PUB-5347

Conceptual Design Report for the Solenoidal Tracker At RHIC

DISCLAIMER

This report was prepared as an account of work sponsored by an agency of the United States Government. Neither the United States Government nor any agency thereof, nor any of their employees, makes any warranty, express or implied, or assumes any legal liability or responsibility for the accuracy, completeness, or usefulness of any information, apparatus, product, or process disclosed, or represents that its use would not infringe privately owned rights. Reference herein to any specific commercial product, process, or service by trade name, trademark, manufacturer, or otherwise does not necessarily constitute or imply its endorsement, recommendation, or favoring by the United States Government or any agency thereof. The views and opinions of authors expressed herein do not necessarily state or reflect those of the United States Government or any agency thereof.

June 15, 1992

The STAR Collaboration

DISTRIBUTION OF THIS DOCUMENT IS UNLIMITED

This work was supported in part by the Director, Office of Energy Reserach, Office of High Energy and Nuclear Physics, Division of Nuclear Physics and by the Office of Basic Energy Sciences, Division of Nuclear Sciences, of the U.S. Department of Energy under Contract No. DE-AC03-76SF00098

MASTER

LBL-PUB--5347

DE92 041174

The STAR Collaboration

M.E. Beddo, J. W. Dawson, D.P. Grosnick, V.J. Guarino, W.N. Haberichter, D.A. Hill, N. Hill, T. Kasprzyk, D.X. Lopiano, J. Nasiatka, E. Petereit, H.M. Spinka, D.G. Underwood, and A. Yokosawa
Argonne National Laboratory, Argonne, Illinois 60439, U.S.A.

P. Buncic, D. Ferenc, K. Kadija, G. Palc, and D. Vranic
Rudjer Boskovic Institute, 41001 Zagreb, Croatia

S.E. Eiseman, A. Etkin, K.J. Foley, R.W. Hackenburg, M.J. LeVine, R.S. Longacre, W. A. Love, E.D. Platner, P. Rehak, A.C. Saulys, and J.H. Van Dijk
Brookhaven National Laboratory, Upton, New York, 11973, U.S.A.

H.J. Crawford, J.M. Engelage, and L. Greiner
University of California, Berkeley, California 94720, U.S.A.

F.P. Brady, J.E. Draper, and J.L. Romero
University of California, Davis, California 95616, U.S.A.

J.B. Carroll, V. Ghazikhanian, E. Gulmez, T. Hallman, G.J. Igo, S. Trentalange, and C. Whitten, Jr.
University of California, Los Angeles, California 90024, U.S.A.

M. Kaplan, P.J. Karol, Z. Milosevich, and E. Vardaci
Carnegie Mellon University, Pittsburgh, Pennsylvania 15213, U.S.A.

M. Cherney, T.G. McShane, and J. Seger
Creighton University, Omaha, Nebraska 68178, U.S.A.

M. Gazdzicki, R.E. Renfordt, D. Röhrich, R. Stock, H. Ströbele, and S. Wenig
University of Frankfurt, D-6000 Frankfurt am Main 90, Germany

L. Madansky and R. Welsh
The Johns Hopkins University, Baltimore, Maryland 21218, U.S.A.

B. Anderson, M. L. Justice, D. Keane, Y. Shao, and J. Watson
Kent State University, Kent, Ohio 44242, U.S.A.

J. Berkovitz, F. Bieser, M.A. Bloomer, D. Cebra, S.I. Chase, W. Christie, W.R. Edwards, M. Green, D. Greiner, J.W. Harris, H. Huang, P. Jacobs, P. Jones, S. Kleinfelder, R. LaPierre, P. Lindstrom, S. Margetis, J. Marx, H.S. Matis, C. McParland, J. Mitchell, R. Morse, C. Naudet, T. Noggle, G. Odyniec, D. Olson, A.M. Poskanzer, G. Rai, J. Rasson, H.-G. Ritter, I. Sakrejda, J. Schambach, L.S. Schroeder, D. Shuman, R. Stone, T.J.M. Symons, L. Teitelbaum, H. Wieman, and W.K. Wilson
Lawrence Berkeley Laboratory, Berkeley, California 94720, U.S.A.

C.S. Chan, M.A. Kramer, S.J. Lindenbaum, K.H. Zhao, and Y. Zhu
City College of New York, New York, New York 10031, U.S.A.

A. Aprahamian, N.N. Biswas, U. Garg, V.P. Kenney, and J. Piekarz
University of Notre Dame, Notre Dame, Indiana 46556, U.S.A.

T. Humanic
University of Pittsburgh, Pittsburgh, Pennsylvania 15213, U.S.A.

S.A. Akimenko, Y.I. Arestov, N.I. Belikov, A.M. Davidenko, A.A. Dereschikov, V. Erin, A. Grachov, P. Meschanin, S.B. Nurushev, A.I. Ronjin, V.L. Rykov, and A.N. Vasiliev
Institute of High Energy Physics, Protvino, Russia

D.D. Carmony, Y. Choi, A. Hirsch, E. Hjort, N. Porile, R.P. Scharenberg, B. Srivastava, and M.L. Tincknell
Purdue University, West Lafayette, Indiana 47907, U.S.A.

D.L. Adams, S. Ahmad, B.E. Bonner, J.A. Buchanan, C.N. Chiou, J.M. Clement, M.D. Corcoran, T. Empl, H.E. Miettinen, G.S. Mutchler, J.B. Roberts, J. Skeens, and I. Stancu
Rice University, Houston, Texas 77251, U.S.A.

A. D. Chacon, R.K. Choudhury, and K. L. Wolf
Texas A & M University, College Station, Texas 77843, U.S.A.

W. Dominik
Warsaw University, Warsaw, Poland

T. Pawlak, W. Peryt, and J. Pluta
Warsaw University of Technology, Warsaw, Poland

R. Bellwied, S. Bennett, J. Bielecki, T.M. Cormier, F. Gang, J. Hall, Q. Li, A. Lukaszew, R. Matheus, C. Pruneau, and G. Roger
Wayne State University, Detroit, Michigan 48201, U.S.A.

W.J. Braithwaite, J.G. Cramer, D. Prindle, T.A. Trainor, and X.-Z. Zhu
University of Washington, Seattle, Washington 98195, U.S.A.

Z. Fraenkel and I. Tserruya
Weizmann Institute of Science, Rehovot 76100, Israel

Spokesperson: J.W. Harris
Deputy Spokespersons: T. Hallman, E.D. Platner

Technical Director: J. Marx

Table of Contents

1. Conceptual Design Summary 1-1
   - 1.A. Scientific Motivation for STAR 1-1
   - 1.B. Detector Concept 1-1
   - 1.C. Cost and Schedule 1-2

2. Overview of Experiment 2-1
   - 2.A. Design Criteria of Experiment 2-1
   - 2.B. Magnetic Field 2-2
   - 2.C. Time Projection Chamber (TPC) 2-4
   - 2.D. Silicon Vertex Tracker (SVT) 2-7
   - 2.E. Electromagnetic Calorimeter (EMC) 2-7
   - 2.F. Triggering and Trigger Detectors. 2-10
   - 2.G. Data Acquisition (DAQ) 2-11
   - 2.H. Time-of-Flight (TOF) Detector - Upgrade 2-12
   - 2.I. External TPCs -Upgrade 2-12

3. Physics of STAR 3-1
   - 3.A. Particle Production 3-1
   - 3.B. Parton Physics 3-9
   - 3.C. Correlations between Event Observables 3-14

4. Conceptual Design 4A-1
   - 4.A. Implementation Plan for the Experiment 4A-1
   - 4.B. Solenoid 4B-1
   - 4.C. Time Projection Chamber 4C-1
   - 4.D. Front End Electronics 4D-1
   - 4.E. Trigger Detectors 4E-1
   - 4.F. Data Acquisition 4F-1
   - 4.G. Computing 4G-1
   - 4.H. Silicon Vertex Tracker 4H-1
   - 4.I. Electromagnetic Calorimeter 4I-1
   - 4.J. Time-of-Flight Detector 4J-1
   - 4.K. External Time Projection Chambers 4K-1

5. Integration of Experiment 5-1
   - 5.A. Subsystems Integration 5-1
   - 5.B. Plumbing & Cabling Plans and Issues 5-13

5.C. Access and Maintenance Requirements. 5-13
5.D. Miscellaneous Subsystem Design 5-16
5.E. Detector Interface with Wide Angle Hall 5-22
5.F. Interface with RHIC Accelerator 5-25

6. Facility Requirements 6-1
6.A. Assembly Areas 6-1
6.B. Shop Requirements 6-1
6.C. Computing Facility Requirements 6-2
6.D. Utility Requirements (HVAC, water, power, gas, cryogenic, etc.) 6-3

7. Safety and Environmental Protection Issues 7-1
7.A. Shielding 7-1
7.B. Access Control 7-1
7.C. Hazardous Materials and Systems 7-1

8. Management Structure of STAR 8-1

9. Cost, Schedule, Manpower and Funding 9-1
9.A. Detector Scope 9-1
9.B. Detector Summary Cost and Schedule Estimates 9-1
9.C. Project Manpower Resources by Subsystem 9-5
9.D. Funding Profile 9-7

Appendix 1: Hit-finding Algorithms in the Simulated TPC A-1

Appendix 2: Alternate Technology Choices for the DAQ Architecture A-4
Use of Fibre Channel Gigabit Networks in STAR DAQS A-4
Fibre Channel Gigabit Networks A-4
Fibre Channel Performance A-5
DAQS Design A-5
A Fibre Channel Testbed A-6
DAQS Costs A-7

Appendix 3: SVT: Transport Code in Silicon A-9
Simulations of Si Drift Detector Response A-9

Appendix 4: Table of Materials at $\eta = 0$ in STAR A-12

STAR

1. Conceptual Design Summary

1. Conceptual Design Summary

1.A. Scientific Motivation for STAR

The Solenoidal Tracker At RHIC (STAR) will search for signatures of quark-gluon plasma (QGP) formation and investigate the behavior of strongly interacting matter at high energy density. The emphasis will be the correlation of many observables on an *event-by-event* basis. In the absence of definitive signatures for the QGP, it is imperative that such correlations be used to identify special events and possible signatures. This requires a flexible detection system that can simultaneously measure many experimental observables.

The STAR experiment will utilize two aspects of hadron production that are fundamentally new at RHIC: correlations between *global observables on an event-by-event basis* and the use of *hard scattering of partons* as a probe of the properties of high density nuclear matter. The event-by-event measurement of global observables – such as temperature, flavor composition, collision geometry, reaction dynamics, and energy or entropy density fluctuations – is possible because of the very high charged particle densities, $dn_{ch}/d\eta \approx 700$ expected in nucleus-nucleus collisions at RHIC. Event-by-event fluctuations are expected in the vicinity of a phase transition, so this experiment will be sensitive to threshold behavior of the experimental observables as a function of energy density. Full azimuthal coverage with particle identification and continuous tracking is required to perform these measurements at momenta where the particle yields are maximal. Measurable jet yields at RHIC will allow investigations of hard QCD processes via tracking combined with segmented electromagnetic calorimetry and high p_t single particle measurements. Measurements of the hadronic cascades of hard-scattered partons will be used as a penetrating probe of the QGP, and will provide important new information on the nucleon structure function and parton shadowing in nuclei. The scientific program of the STAR Collaboration will require measurements of inclusive and event-by-event observables for 1) proton-proton, 2) proton-nucleus and 3) nucleus-nucleus interactions. These observables will be studied as a function of impact parameter and incident energy, in order to understand reactions at RHIC and to detect and conclusively identify the signatures of QGP formation.

1.B. Detector Concept

The physics goals dictate the design of this experiment. To meet the design criteria, tracking, momentum analysis, and particle identification of most of the charged particles at midrapidity are necessary. The tracking must operate in conditions at higher than the expected maximum charged particle multiplicities ($n_{ch} = 3000$ in the range $|\eta| < 1$ at midrapidity within the acceptance of the experiment) for central Au + Au collisions. Particle identification of pions/kaons for $p < 0.7$ GeV/c and kaons/protons for $p < 1$ GeV/c, as well as measurement of decay particles and reconstruction of secondary vertices will be possible. A two-track resolution of 2 cm at 2 m radial distance from the interaction is expected. Momentum resolution of $\Delta p/p \approx 0.02$ at $p = 0.1$ GeV/c is required to accomplish the physics, and $\Delta p/p$ of several percent at $p = 10$ GeV/c is sufficient to accurately measure the rapidly falling spectra at high p_t and particles from mini-jets and jets. The momentum resolution at low p_t is limited by multiple scattering.

To minimize multiple scattering and photon conversion after π^0 decay, which also creates non-primary vertex tracks, detector material will be kept to a minimum throughout the tracking system.

The configuration of the STAR experiment is shown in Fig. 1.1. Momentum measurements will be made at midrapidity over a large pseudo-rapidity range ($|\eta| < 2$) with full azimuthal coverage ($\Delta\phi = 2\pi$). Particle identification will be performed within $|\eta| < 1$. The detection system will consist of a time projection chamber (TPC) and a silicon vertex tracker (SVT) inside a solenoidal magnet to enable tracking, momentum analysis, particle identification via dE/dx and location of primary and secondary vertices. Detectors will be installed to provide a collision geometry trigger. These include a central trigger scintillator barrel around the TPC, vertex position detectors near the beamline just outside the magnet, and calorimeters located in the region of the beam insertion magnets to selectively veto events according to the number of spectators. An electromagnetic calorimeter, for which outside funding is being sought, will be located outside the magnet and used to trigger on transverse energy and measure jet cross sections. The major physics goals of STAR can be accomplished with this configuration of detectors. A time-of-flight system surrounding the TPC for particle identification at higher momenta and external time projection chambers outside the magnet to extend the η coverage are anticipated as upgrades. A summary of the detector systems is presented in Table 1-1.

1.C. Cost and Schedule

The STAR detector system will contain the TPC, SVT, EMC, TOF, external TPC, solenoid magnet, electronics, data acquisition, and trigger as major systems. The cost of the detector has been developed in four iterations, over a 6-month period, each subject to review. The estimates made in FY92 dollars include materials, labor, EDIA and contingency, and are based on a variety of inputs including vendor quotes, estimates from comparable systems, and engineering estimates. The TPC, solenoid magnet, electronics, data acquisition, trigger system, controls, on-line computing, detector conventional systems, detector testing, detector installation, systems integration and project management will be funded primarily by the RHIC construction project. Funding for the TOF, EMC, and external TPC systems will be sought from other sources. The SVT—which is especially important to the initial physics program—will be supported through the prototype phase by RHIC R&D funds and constructed thereafter using other resources.

The cost estimates for the portion of the detector to be funded from RHIC construction funds includes a detailed contingency analysis leading to an average contingency of 30%. Since the RHIC management will maintain $2M in reserves for the two large RHIC detectors, it has been agreed that the STAR contingency for the RHIC-funded part of the detector be reduced to 25%.

The estimated cost of the TPC, solenoid magnet, electronics, data acquisition, trigger system, controls, on-line computing, detector conventional systems, detector testing, detector installation, systems integration and project management and an overall contingency of 25%, is $35.9M in FY92 dollars.

The STAR collaboration is investigating a warm-coil option for the solenoid magnet. Preliminary cost estimates of the option (without the iterations and reviews that characterize the superconducting-coil option) indicate that the warm-coil option could reduce the cost of the magnet by $2.1M in FY92 dollars provided that necessary facility/utility upgrades required by the warm-coil option are supplied by RHIC/BNL. More refined estimates, and a decision between coil options will be completed in the near future.

The STAR collaboration has also evaluated the level of resources available within the collaboration to offset costs associated with the RHIC-funded portion of the detector and found it to be approximately $2.5M. Therefore, assuming that the cost savings of the normal-coil option are confirmed with additional estimates and vendor quotes, the amount of capital funding required from the RHIC construction project for the TPC, solenoid magnet, electronics, data acquisition, trigger system, controls, on-line computing, detector conventional systems, detector testing, detector installation, systems integration and project management is $31.3M in FY92 dollars. In addition, an R&D budget of approximately $4.0M in the years FY93–95 is necessary and is expected to be provided by the RHIC project.

The individual detector sub-systems will be designed, fabricated and tested at individual institutions prior to shipping to BNL for installation at RHIC. The schedule for STAR requires an occupancy date of January 1, 1995 for the Wide Angle Hall, into which the STAR detector system will be installed. An assembly and testing period at RHIC of approximately 2 years is expected prior to installation in the interaction region. With this schedule STAR will be operational at RHIC turn-on.

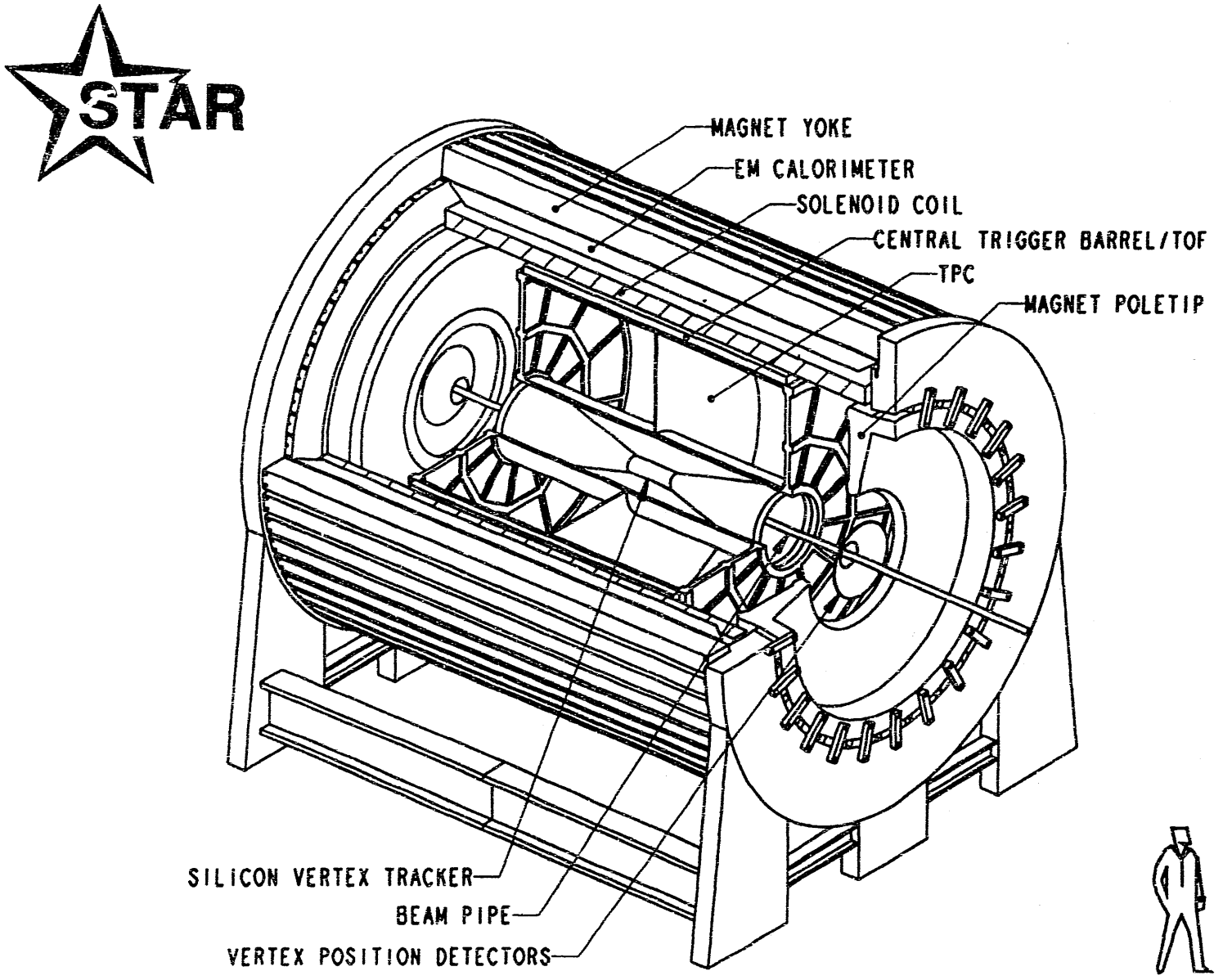

Figure 1.1 Perspective view of the STAR experimental configuration.

Table 1-1 Overview of STAR detector systems.

Solenoidal Magnet	
Coil Radius	2.32 m
Length	6.9 m
Field Strength	0.25 - 0.5 T
Time Projection Chamber (TPC)	
Inner Radius	0.5 m
Outer Radius	2.0 m
Length	4.2 m
# of Channels	140,000
Acceptance	$\lvert\eta\rvert \leq 2.0$
Silicon Vertex Tracker (SVT)	
Type	Si Drift Chambers
Radius 1st layer	5 cm
Radius 2nd layer	8 cm
Radius 3rd layer	11 cm
Length	42 cm
# of Channels	72,000
Acceptance - 1st, 2nd, 3rd layers	$\lvert\eta\rvert \leq 2.1, 1.7, 1.4$
Trigger Detectors	
Vertex Position Detectors	
Segmentation	50 elements
Acceptance	$3.3 < \lvert\eta\rvert < 3.8$
TPC Endcaps (MWPC)	
Segmentation	2,000
Acceptance	$1.0 \leq \lvert\eta\rvert \leq 2.0$
Veto Calorimeters	
Segmentation	to be determined
Acceptance	$\lvert\eta\rvert > 5$
Central Trigger Barrel (Scintillator)	
Segmentation	200
Acceptance	$\lvert\eta\rvert \leq 1$
EM Calorimeter	
Inner Radius	2.53 m
Thickness	0.325 m, 21 X_0
Segmentation	$\Delta\eta, \Delta\phi = 0.105, 0.105$
# of Channels	1200
Acceptance	$\lvert\eta\rvert \leq 1.05$
Time-of-Flight Upgrade	
Type	shingle slats
Radius	2.05 m
# of Channels	7776
Acceptance	$\lvert\eta\rvert \leq 1.0$
External TPC Upgrade	
Dimensions of Each (LxWxD)	$2.2 \times 2.0 \times 1.0\ m^3$
Distance of Front Face	7.0 m
Total # of Channels	22,000
Acceptance	$2.0 \leq \lvert\eta\rvert \leq 4.5$

2. Overview of Experiment

2. Overview of Experiment

2.A. Design Criteria of Experiment

The physics goals of STAR require a large acceptance device having the capability of measuring simultaneously many different observables, representing both soft and hard physics. The design criteria to measure both soft (0.04 GeV/c < p_t < 1.5 GeV/c) and hard physics (single particles with p_t > 1.5 GeV/c and jets) observables are given below:

Soft Physics (0.04 GeV/c < p_t < 1.5 GeV/c)

- Detection of as many charged particles as possible with high efficiency, to provide high statistics for event-by-event observables and fluctuation studies
- 2π continuous azimuthal coverage for reliable event characterization
- High tracking efficiency as close to the vertex as possible, to contain the size and cost of the experiment
- Adequate track length for tracking, momentum measurement and particle identification for a majority of the particles
- High kaon detection efficiency for event-by-event observables and for inclusive measurement of the ϕ--meson
- Momentum resolution $\Delta p/p \leq 0.02$ for p_t < 1.5 GeV/c
- Two-track resolution providing a momentum difference resolution of a few MeV/c for HBT correlation studies
- Accurate determination of the primary vertex for high momentum resolution and to be able to identify particles from the primary interaction
- Accurate determination of secondary vertices for detecting strange particle decays such as Λ, $\bar{\Lambda}$, K^0_s, $\Xi^{\pm}$, Ω^-.

Hard Physics (p_t > 1.5 GeV/c and jets)

- Large uniform acceptance to maximize rates and minimize edge effects in jet reconstruction
- Accurate determination of the primary vertex in order to achieve a momentum resolution $\Delta p/p$ < 0.05 for p_t = 10 GeV/c for high p_t particle spectra and jets
- Electromagnetic calorimetry combined with tracking and good momentum resolution up to p_t = 10 GeV/c to measure and trigger on high E_t jets
- 2π azimuthal coverage of electromagnetic calorimetry for event characterization
- Linear response of electromagnetic calorimetry for accurate energy measurements
- Segmentation of electromagnetic calorimeters which is an order of magnitude finer than the typical jet size, i.e. jet radius $r = \sqrt{(d\eta^2 + d\phi^2)} \sim 1$

The experiment will consist of tracking, particle identification and electromagnetic calorimetry covering a large acceptance ($|\eta| < 1$, $\Delta\phi = 2\pi$) at midrapidity. In addition, various triggering detectors will be installed to make it possible to trigger initially on collision geometry and subsequently on more

sophisticated event characteristics and topologies. The tracking system will extend to $|\eta| < 2$. It will consist of a silicon vertex tracker (SVT), which can precisely locate primary and secondary vertices, and a time projection chamber (TPC) inside a solenoidal magnet for *continuous* tracking, optimum momentum resolution and particle identification. Electromagnetic calorimetry will be used to measure and trigger on jets and the transverse energy of events.

A side view of a quadrant of the experiment is presented in Fig. 2-1. The trigger detectors will consist of a combination of the following systems. Beam position detectors will be installed upstream and downstream of the solenoid to trigger on interactions and to locate the interaction vertex within ± 6 cm in first level triggering. A central trigger scintillator barrel will surround the TPC for triggering on the charged particle multiplicity in the central region of $|\eta| < 1$ and thus the centrality of events. The TPC endcaps will be readout for rapid triggering on charged particle multiplicity for $1 < |\eta| < 2$. Calorimeters will be installed between the insertion magnets near the beam to veto on the number of leading particles. A summary of the detector systems can be found in Table 1-1. A list of the expected materials, thicknesses, and radiation and interaction lengths appear in Appendix 4. An overview of each major detector subsystem will be presented in the remainder of this chapter. Details of the conceptual design of each subsystem of STAR can be found in Chapter 4.

The physics goals of this experiment require a systematic program utilizing a range of projectiles (from protons to Au), available beam energies, and impact parameters. Initially a survey of the soft processes will be undertaken with a variety of collision geometry triggers ranging from minimum bias to highly central. The development of more refined triggers will be an important part of the ongoing STAR experimental program. It is expected that longer data acquisition periods will be necessary for studies of rare events and jet production.

2.B. Magnetic Field

The magnet will be a solenoid with uniform magnetic field along the beam direction. It will be designed to be able to provide uniform fields with strengths of 0.25 T to 0.5 T. An iron return yoke and shaped pole pieces will transmit the magnetic flux and shape the magnetic field. The magnet design is chosen for high tracking accuracy and azimuthal symmetry. Small correction coils will be used to further improve the field uniformity. A field strength of 0.5 Tesla will provide adequate resolution for momenta as high as 10 GeV/c with only modest spiraling of low p_t particles. The magnetic coil mean radius will be 2.32 m and the radius of the yoke will be 2.87 m. The total magnet length will be 6.9 m. A superconducting coil is presently envisioned and will be presented in this document. A room temperature Al coil design is being investigated in an attempt to reduce construction costs. A brief summary of the magnet parameters is presented in Table 2-1.

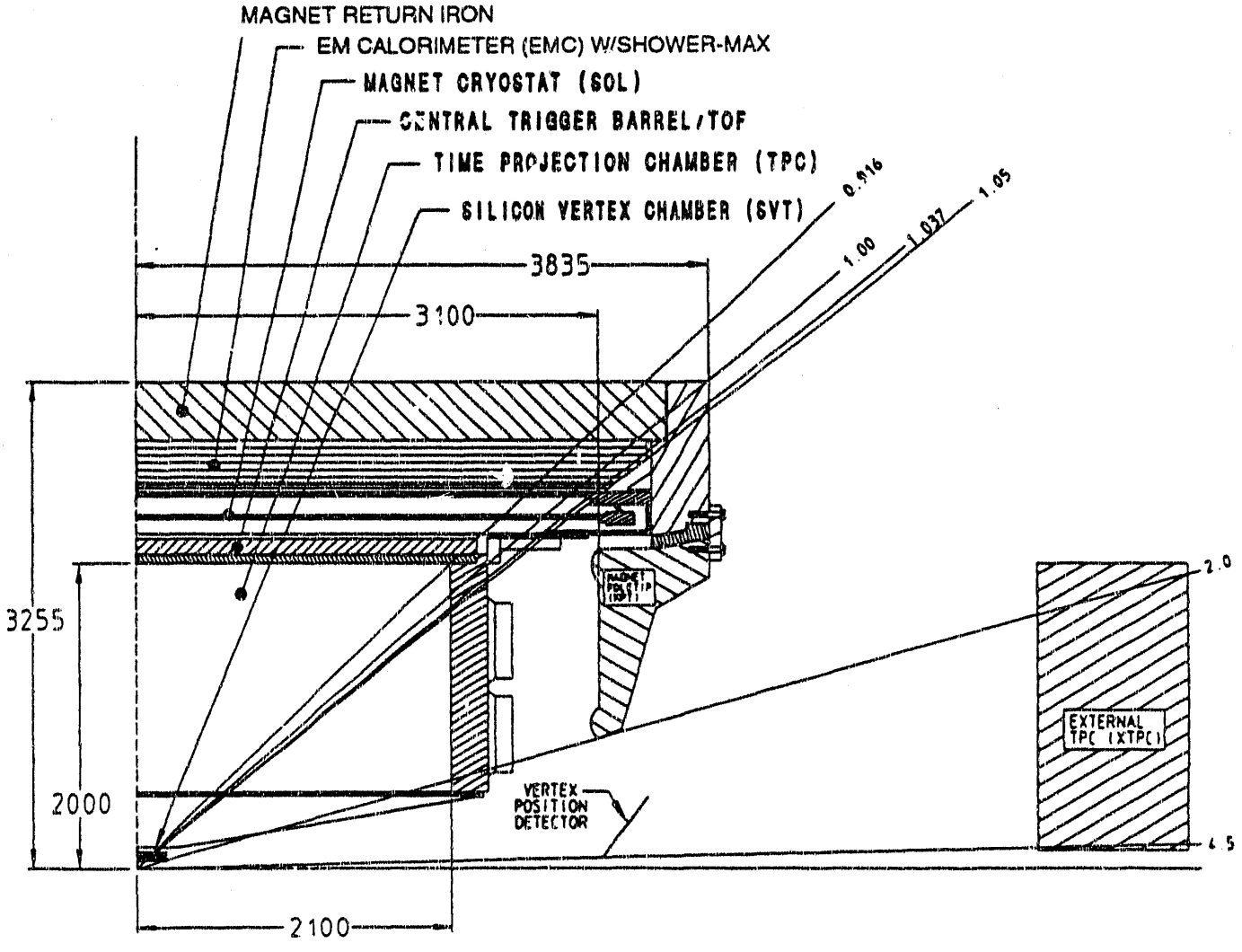

Figure 2-1 Side view of a quadrant of the STAR experiment with dimensions and pseudorapidity lines overlaid.

Table 2-1 Magnet properties.

Solenoid field strength	0.25 - 0.5 T
Length	6.9 m
Superconducting coil	
Radius	2.32 m
Thickness	<0.7 X_0
Yoke	
Radius	2.87 m
Thickness	38.5 cm Fe
Weight	490 tons
Pole tips	
Max. thickness	38.5 cm Fe
Weight of each	25 tons
Total weight of Fe	540 tons

2.C. Time Projection Chamber (TPC)

The TPC will be divided into two longitudinal drift regions, each 2.1 m long, as shown in Fig. 2-2. Electrons created from track ionization will drift in the longitudinal direction, along the TPC electric field lines, to the end-caps of the TPC. Each end-cap is instrumented with 70,000 pads. Two pad sizes will be used, one for the inner sectors (50 cm < radius < 125 cm) and one for the outer sectors (125 cm ≤ radius < 200 cm) as described in Table 2-2. Each pad will be readout into 512 time samples. Neglecting energy loss, singly-charged particles with $p_t < 40$ MeV/c spiral inside the TPC inner radius of 50 cm and do not reach the active volume of the TPC. Particles with 40 MeV/c $< p_t <$ 150 MeV/c spiral inside the TPC volume with most exiting the end-caps. Particles with $p_t >$ 150 MeV/c traverse the TPC and exit the outer edge at radius 200 cm. The TPC geometrical acceptance for particles reaching the outer radius is $|\eta| < 1$ and that for particles reaching the inner radius (i.e. multiplicity with partial dE/dx and tracking) is $|\eta| < 2.0$. A summary of the TPC design can be found in Table 2-2.

The pad plane configuration is designed to maximize the recorded track length for good momentum resolution, minimize the required number of electronics and provide sufficient dE/dx sampling along the track to achieve particle identification in the $1/\beta^2$ region. The inner radius pad plane sectors are composed of small pads arranged in separated rows. These small pads improve the two track resolution permitting position measurements along the track in the high track density region closer to the interaction. These position measurements at the inner radius region are important for extending the measured track and to improve momentum resolution and for accurate projection to the SVT. The outer radius pad sectors are designed with larger pads to achieve continuous sampling along the track for dE/dx. The gas used inside the TPC is expected to be Ar + 10% CH_4.

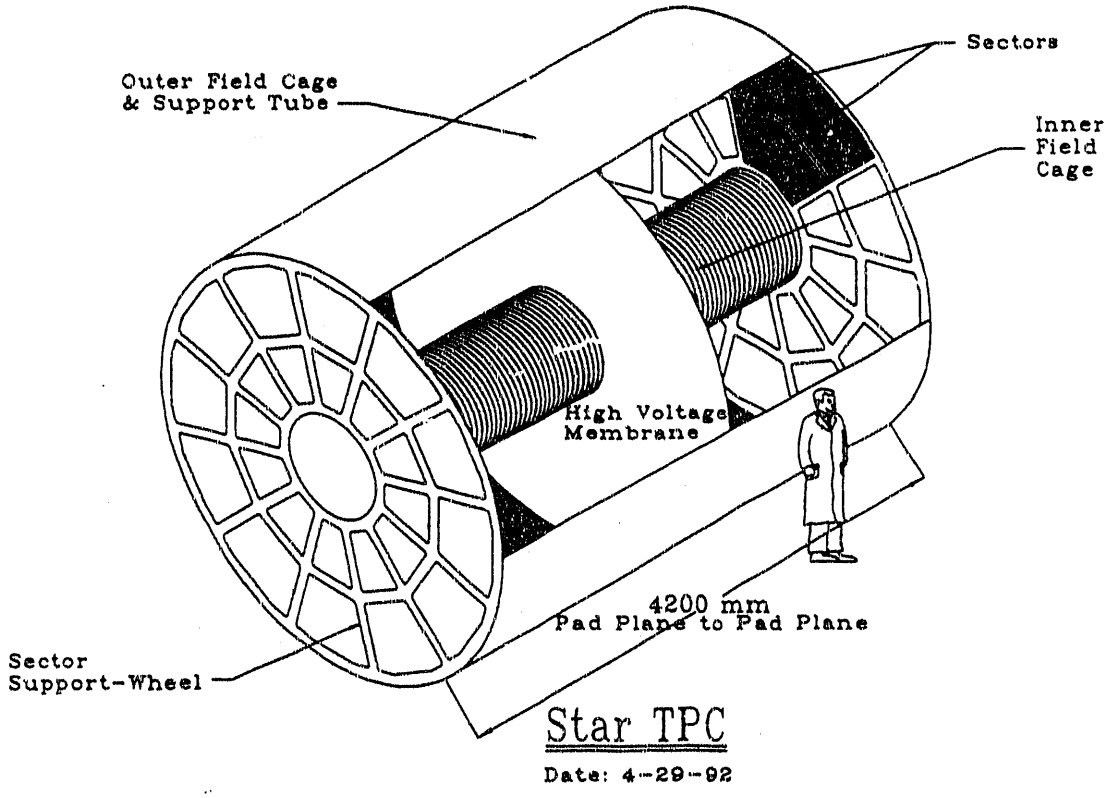

Figure 2-2 Perspective view of the STAR Time Projection Chamber.

The 40 μsec drift time of the TPC limits the interaction rate for each colliding nuclear system below a value where event pileup starts to degrade the detector performance. Discrimination between two primary interactions originating from a single crossing of the circulating beams is dependent upon the vertex resolution of the tracking detectors. At a luminosity an order of magnitude higher than the design luminosity ($\mathcal{L}_0 = 2 \times 10^{26}$ cm^{-2} s^{-1}) for Au + Au interactions at RHIC, events will start to overlap during the drift time of the TPC. However, only in the case when two central Au + Au events occur in the same beam crossing at a distance closer than the detector capability to resolve primary vertices, does this become a problem. When the TPC vertex resolution is used the probability is 1.6×10^{-8} for the overlap of two central collisions and 1.6×10^{-6} for contamination of a central collision by any other interaction. When the SVT vertex resolution is used these probabilities are 1.6×10^{-9} and 1.6×10^{-7}, respectively. For pp collisions at design luminosity ($\mathcal{L}_0 = 1.4 \times 10^{31}$ cm^{-2} s^{-1}), the equivalent probability for two high multiplicity pp interactions (5% σ_R) to occur in the same beam crossing with unresolvable individual vertices is 2.8×10^{-5} using only the TPC and 2.8×10^{-6} using the SVT. Therefore, the TPC is capable of measuring at the interaction rates expected at RHIC.

The effects of positive ion space charge in the TPC have been studied in detail. A gated grid will be used to reduce the positive ion feedback from the avalanche region near the sense wires. Tests have been performed and the results show that the electron suppression in a 1.3 T magnetic field is < 1 part in 7000. In addition, numerical

Table 2-2 Time Projection Chamber.

Drift Volume Inner Radius Outer Radius Length	Coaxial Cylinder - 0.5 m 2.0 m 4.2 m
PID acceptance	$\|\eta\| < 1$
Tracking acceptance	$\|\eta\| < 2$
Drift Gas	Ar + 10% CH4
Pressure	Atmospheric
Sampling Rate	12.3 MHz
Time Samples	512
# of pad rows	50
Pad Sectors Type, Number of rows Pad Size Type, Number of rows Pad Size	Two types Inner, 18 2.85 mm x 11.5 mm Outer, 32 6.2 mm x 19.5 mm
Total number of pads	140,000
Total # pixels	77,000,000
Dynamic range for dE/dx	10 bits
Position resolution ($p_t > 1$ GeV/c)	460 μm in x,y and 700 μm in z
Drift time	40 μs

electrostatic calculations have been performed[1] to determine the effect of the primary ionization of the expected large multiplicity of charged particles in central collisions at RHIC. The accumulation of positive ion charge in the STAR TPC is found to have a small effect on the TPC space points for Au beam luminosities up to 20 times the design luminosity ($\mathcal{L}_0 = 2 \times 10^{26}$ cm^{-2}sec^{-1}).

Tracking performance in the STAR TPC has been simulated using $\sqrt{s_{nn}} = 200$ GeV Au + Au central events, generated using the FRITIOF code and processed by the GEANT detector simulation program. The pattern recognition program for the STAR TPC is based on the ALEPH code.[2] On average 93% of the tracks within the range $|\eta| < 1$ and with momenta above 150 MeV/c that are generated for central Au + Au events are successfully reconstructed. The $\Delta p/p$ of the reconstructed tracks is found to be 1.4% in good agreement with an evaluation based on the track length and momentum distribution in an argon gas-filled TPC.[3]

---

[1] STAR Update to the RHIC Letter of Intent (1991).

[2] W.B. Atwood, et al.. Performance of the Aleph Time Projection Chamber - submitted to Nuclear Instruments and Methods A.

[3] R.K. Bock et al., Formula and Methods in Experimental Data Evaluation, European Physical Society, Geneva, CERN (1984).

The STAR Collaboration has extensive experience in the design, construction and operation of TPCs in high energy particle and heavy ion experiments. PEP4 was the first TPC. The CERN NA36 TPC, with its wire-readout, was the first TPC used in heavy ion experiments. The CERN NA35 TPC, installed in 1990, was the first TPC with pad readout used in heavy ion experiments. The BNL E810 TPC and the LBL EOS TPC are presently in operation at the AGS and the Bevalac, respectively. Various members of the STAR Collaboration have played major roles in the development and operation of these TPCs.

2.D. Silicon Vertex Tracker (SVT)

The silicon vertex tracker (SVT) coupled with the TPC will locate the position of the primary interaction vertex to high accuracy, improve the momentum and dE/dx resolutions, and locate secondary vertices to an accuracy better than 100 μm. It also provides a powerful tool to extend the acceptance of the TPC to low momenta. The lower TPC limit for fully efficient track reconstruction is 150 MeV/c. Therefore a considerable part of the event will be measured by inclusion of tracking in the SVT alone. Thus, the SVT must be able to provide three dimensional space points and tracking vectors with high spatial resolution, so that the tracks measured in the TPC can be linked to those in the SVT. The SVT must be of low mass so as to minimize secondary particle production, photon conversion and multiple scattering.

The SVT will consist of 162 silicon drift detectors (SDD). Individual detectors are grouped into ladders. Each ladder consists of 6 SDDs. The ladders are arranged in three concentric barrels around the interaction at radii of 5, 8 and 11 cm as shown in Fig. 2-3. The SVT contains approximately 72K channels of electronics. Each barrel is 42 cm in length. The range of acceptances for the barrels are listed in Table 1-1. Each SDD is 7 cm in length, 5.7 cm in width and is made from a 4-inch diameter wafer. The thickness of a wafer is 300 microns which is a good compromise between signal strength (24K electrons are created by minimum ionizing particle) and acceptable values of multiple scattering and secondary particle production for particles traversing the detector. A brief summary of the SVT parameters can be found in Table 2-3.

2.E. Electromagnetic Calorimeter (EMC)

The purpose of the EMC is to measure and trigger on the total (E_t) and local ($d^2E_t/d\eta d\phi$) transverse energy deposition in pp, pA, and AA collisions. For soft nuclear processes, analysis of the transverse energy at mid-rapidity leads directly to estimates of the temperature and energy density characterizing the reaction. It is also possible to use the EMC to trigger on jets, high energy direct photons, and high p_t particles. In nucleus-nucleus collisions this provides a unique opportunity to study the interactions of hard scattered partons in the hot nuclear medium and thus infer its properties. In polarized pp collisions the information provided by the EMC can be used to study the spin structure of the proton, as well as single spin transverse asymmetries.

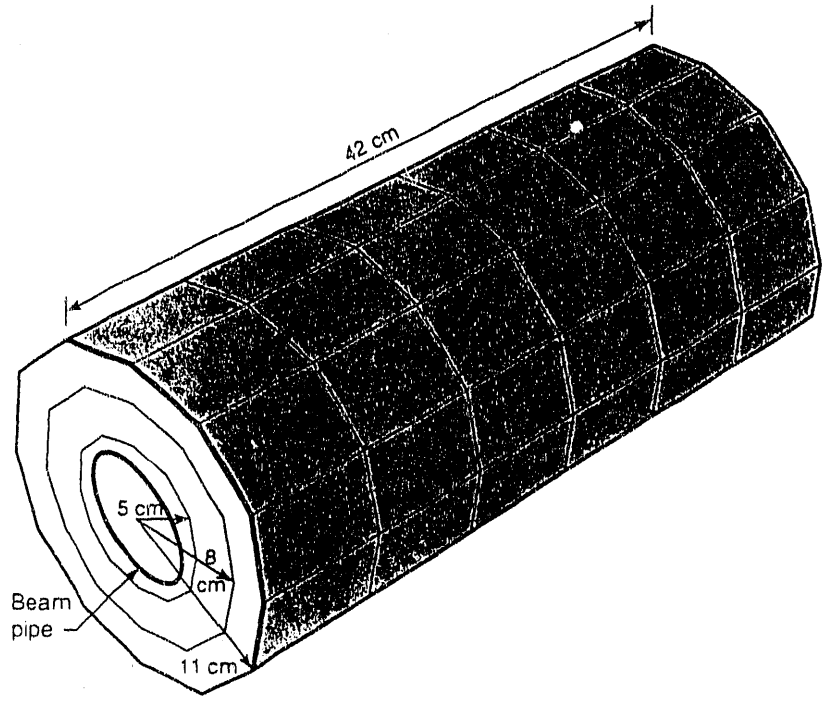

Silicon Vertex Tracker (SVT)

Figure 2-3 Layout of the Silicon Vertex Tracker.

The barrel EM calorimeter is a lead-scintillator sampling calorimeter. It is located outside the superconducting solenoid coil and inside the iron flux return. It covers $|\eta| \leq 1.05$ and 2π in azimuth. At $\eta \sim 0$, the amount of material in front of the EMC is $\sim 1\ X_0$. The inner radius is 2.53 meters and the length is 6.87 meters. It consists of 60 wedge segments of 6 degrees in ϕ and is subdivided into 40 pseudo-projective towers over the η range. Each tower has 21 layers of lead and scintillator. There are therefore 50400 pieces of scintillator of 420 different shapes. Each scintillator tile will be read out with two wavelength shifting optical fibers. In the phase I implementation, to reduce the cost, all the fibers from pairs of towers adjacent in η will couple to one PMT. There will be 1200 PMT's and the effective tower size will initially be 0.105×0.105 ($\Delta\eta$, $\Delta\phi$), similar to many existing calorimeters used in studies of jets and direct photons in high energy physics. The physical construction permits various kinds of upgrades as increased funds become available for more PMT channels. This includes a two-fold increase in η segmentation, and flexible depth segmentation to optimize the separation of hadronic and electromagnetic energy components. The phase I calorimeter will also include a detector with higher granularity at $\sim 5X_0$ to increase the two photon resolution of the EMC and thus, the ability of the detector to separate high energy direct photons from those coming from π^0 decays. This 'shower max' detector will consist of scintillator strips approximately 1 cm in ϕ by 36 cm in η, with each strip read out by a wavelength shifting fiber. The longitudinal dimension of the strips corresponds to the physical size of two η towers in the EMC barrel. The EM energy resolution is expected to be approximately $0.20/\sqrt{E}$. A brief summary of the EMC parameters is presented in Table 2-4.

Table 2-3 Silicon Vertex Tracker.

Length	42 cm
Inner Barrel (radial distance)	5 cm
Middle Barrel (radial distance)	8 cm
Outer Barrel (radial distance)	11 cm
Thickness of detectors (SDD)	300 μm
Total thickness	900 μm ~ 0.9% X_0
Number of detectors	162
Inner Barrel	36
Middle Barrel	54
Outer Barrel	72
Diameter of Si wafer	10.00 cm
Length of detector (SDD)	7.05 cm
Width of detector (SDD)	5.68 cm
Drift length of detector	3.50 cm
Average drift time	~3.5 μs
Time samples	256
Sampling Rate	40 MHz
Anode pitch	250 μm
Number of channels	72576
Position resolution	25 μm

Table 2-4 Electromagnetic Calorimeter Parameters.

Barrel Calorimeter type	21 X_0 lead-scintillator 'EM' section
Segmentation:	60 azimuthal sectors, $\Delta\phi = 0.105$ (6°) 40 projective towers in $\lvert\eta\rvert < 1.05$, $\Delta\eta = 0.0525$
Inner radius:	2.53 m
Length:	6.87 m
Weight:	150 tons
Readout:	Waveshifting fiber (2/tile) to PMT
PMTs:	1200
Shower Max detector:	Scintillator strips parallel to η
Readout:	Waveshifting fiber

2.F. Triggering and Trigger Detectors.

The STAR trigger is designed to cover the dynamic range from pp to central AuAu collisions in an architecture that allows continuous upgradability, as more becomes known about the RHIC environment. It is important to note that a triggerable signature of quark-gluon plasma events has not been identified. Thus the trigger must allow exploration of various paths in the search for these signatures and be flexible enough to implement continuous upgrades as our understanding grows. The trigger is designed with redundancy in mind to allow for application of independent selective criteria which will help to understand and eliminate trigger biases. At the beginning STAR will operate with high deadtime until sufficient information is obtained to be able to increase safely the selectivity of the trigger and thus increase the overall livetime. The trigger goals are summarized in Table 2-5 below.

Table 2-5 STAR Trigger System Goals

Detect AuAu interactions with >95% efficiency
Detect pp interactions with >50% efficiency
Locate AuAu vertex to within +/-6cm within <200ns
Detect multiple events occurring within 40μs w/90% efficiency
Select highest 2.5% of multiplicity or E_t distribution in <200ns
Select high transverse electromagnetic energy
Select based on geometry of hit patterns
Allow simple integration of upgrades to trigger system

Interaction rates are expected to be 1 kHz for AuAu and 1 MHz for pp, while the event recording rate is expected to be 1 Hz and 30 Hz respectively. The trigger system will be used to select events from the available sample according to prioritized selection criteria. A higher priority event can supersede a lower priority event during the TPC readout/digitization but not during the drift time-window. A trigger processor will be constructed to keep track of the rates of each trigger type so that normalized cross sections can be measured.

There are three natural time scales for STAR which provide scales for the trigger decision time: the crossing time of 110 ns, the maximum drift time in the TPC of 40 μs, and the readout/digitization time for the TPC of 10ms. A first level trigger based on vertex location and centrality will be formed within the 110 ns crossing time. This will be distributed and available to other STAR electronics within 200ns of the occurrence of the interaction. A second level trigger based on the geometry of hits in the trigger detectors will be formed in standard computer controlled electronics and available to the STAR electronics within 40μs. Each detector system is expected to include appropriate electronics to perform keep/flush decisions at this point. Finally, third level triggers based on software decisions that include tracking information are expected to be available within 10ms. The keep/flush option can be implemented in software at this point.

The STAR Phase 1 trigger system will consist of the set of detectors described in Table 2-6 below. All detectors cover the full azimuth.

Table 2-6 STAR Trigger System Detectors.

DETECTOR	$\|\eta\|$	# channels
Central Trigger Barrel (CTB)	0 - 1	200
TPC Endcap MWPC	1-2	2000
Vertex Position Detectors (VPD)	3.3 - 3.8	50
Veto Calorimeter (VC)	> 5	2
EM Calorimeter (EMC)	0 - 1	1200

2.G. Data Acquisition (DAQ)

The DAQ subsystem will provide two major functions in STAR. First, it will act as an event builder, by assembling data originating from each detector subsystem into a form suitable for recording and distribution via a network to analysis and monitoring tasks. Second, it will provide for higher level triggering on a time scale short compared with the time required for event building and third-level triggers. Rates >50 events/sec will enter the trigger processors. The data recording rate is limited by available taping speed at reasonable cost.

The DAQ subsystem has been engineered based on an architecture which uses the newest transputer family members, the T9000 RISC processor and the C104 packet router. This technology has been chosen for two reasons: First, the total cost/MIPS (including all necessary ancillary components, interfaces, etc.) is much lower than for any other processor family. Second, the overhead in hardware and in software to network large numbers of processors together is virtually non-existent. Both issues are important in the STAR application. An alternate technology is that of the Fiber Channel. This technology would provide the transport from the readout boards on the detector to an event builder which would be constructed from Fiber Channel components.

The event size for central Au + Au collisions is expected to be 96 MB. After reduction by the average occupancy factor expected for the TPC (10%) and inclusion of a 20% overhead for encoding this becomes approximately 12 MB per event. Events of this size will be recorded to magnetic tape at a rate of 1 event/second. Though p-p collisions have substantially lower multiplicity than Au-Au collisions, their event recording rate is limited by the occupancy in the TPC due to overlapping events at high luminosity. Recording rates for p-p collisions are 30 events/second at $\sqrt{s}$=200 GeV and 10 events/second at $\sqrt{s}$=500 GeV.

Additional compression through online analysis of the data can reduce the event size and increase the overall event rate. It is possible that with some developments in online data reduction and compression through track-finding and fitting the event recording rate could be increased, possibly as much as tenfold.

2.H. Time-of-Flight (TOF) Detector - Upgrade

The purpose of the time-of-flight detector is to extend the particle identification capabilities of the STAR detector to high transverse momenta and to provide a flexible trigger enabling event selection based on inclusive or rapidity-dependent charged particle distributions. The outer surface of the TPC will be covered with 7776 scintillator shingles each of which is read out by one photomultiplier tube. Since the individual detectors are in the magnetic field of the solenoid, special proximity mesh dynode phototubes have to be used. With a timing resolution of 100 ps over 2 m path length the π/K and K/p separation will be extended from ~.65 to 1.1 GeV/c and 1.3 to 2.4 GeV/c, respectively. Inclusive transverse spectra of identified particles can be measured with as little as ~5% coverage in azimuth. Therefore staging of the detector installation is anticipated.

2.I. External TPCs -Upgrade

The purpose of the XTPC is to extend the pseudo-rapidity coverage from $\eta = 2$ to as close to the beam as possible. Conventional uniform drift TPC's can extend this coverage to $\eta = 4$, while the radial TPC under development might extend this to as much as $\eta = 5.5$. The conventional TPC has four quadrants outside each end of the central detector starting at 7 meters and extending one meter with 8 pad rows. This results in 22,000 electronic channels. The conventional TPC extends the charged particle coverage of the central TPC by 40 %. This additional coverage allows identification of events that have regions of anomalously high particle density which may be associated with quark-gluon plasma bubble production.

3. Physics of STAR

3. Physics of STAR

The physics goals of the experiment can be divided into two categories: A) the study of soft physics processes, i.e. hadron production at transverse momenta below 1-2 GeV/c, and B) the study of hard QCD processes, i.e. jet, mini-jet and hard photon production.

3.A. Particle Production

The experiment aims to momentum analyze and identify charged particles (π^+, π^-, K^+, K^-, p, $\bar{p}$, d, $\bar{d}$) directly, as well as various neutral and charged strange particles (K^o_s, ϕ, Λ, $\bar{\Lambda}$, Ξ^-, Ω^-) via charged-particle decay modes. A unique feature of this experiment will be its ability to study observables on an *event-by-event* basis in addition to inclusive measurements. The event-by-event and inclusive measurements that can be made and the physics observables that are studied by these measurements are described below.

3.A.1. Particle Spectra

As a consequence of the high multiplicities expected in central nucleus-nucleus collisions, the slope of the transverse momentum (p_t) distribution for pions and the $\langle p_t \rangle$ for pions and kaons can be determined *event-by-event*. Therefore, individual events can be characterized by "temperature" and events with extremely high temperature, predicted[1] to result from deflagration of a QGP, can be identified. Displayed in Fig. 3-1 are two spectra generated by the Monte Carlo method from Maxwell-Boltzmann distributions with T = 150 and 250 MeV, each containing 1000 pions. This is the average number of charged pions expected in the acceptance $|\eta| < 1$ of this experiment for central Au + Au collisions. The slopes of spectra with T = 150 and 250 MeV derived from fits using a Maxwell-Boltzmann distribution, also shown in Fig. 3-1, can easily be discriminated at the single event level. Fig. 3-2a shows the standard deviation in measuring $\langle p_t \rangle$ as a function of the charged particle multiplicity measured in a single event. The curves are derived from distributions generated with temperatures of 150 and 250 MeV and are labeled by their corresponding $\langle p_t \rangle$ values. From Fig. 3-2a it can be seen that the determination of $\langle p_t \rangle$ for pions can be made very accurately on the single event basis in this experiment, over the expected range of multiplicities in central collisions from Ca + Ca to Au + Au. Even for kaons, with ~ 150 charged kaons per event in the acceptance for central Au + Au events, $\langle p_t \rangle$ can be determined accurately for single events.

Inclusive p_t distributions of charged particles will be measured with high statistics and effects such as collective radial flow[2] and critical temperature[3] at low p_t,

---

[1] E.V. Shuryak and O.V. Zhirov, Phys. Lett. B89 (1980) 253; E.V. Shuryak and O.V. Zhirov, Phys. Lett. B171 (1986) 99.
[2] P.V. Ruuskanen, Z. Phys. C38 (1988) 219.
[3] L. Van Hove, Phys. Lett. 118B (1982) 138; K. Redlich and H. Satz, Phys. Rev. D33 (1986) 3747.

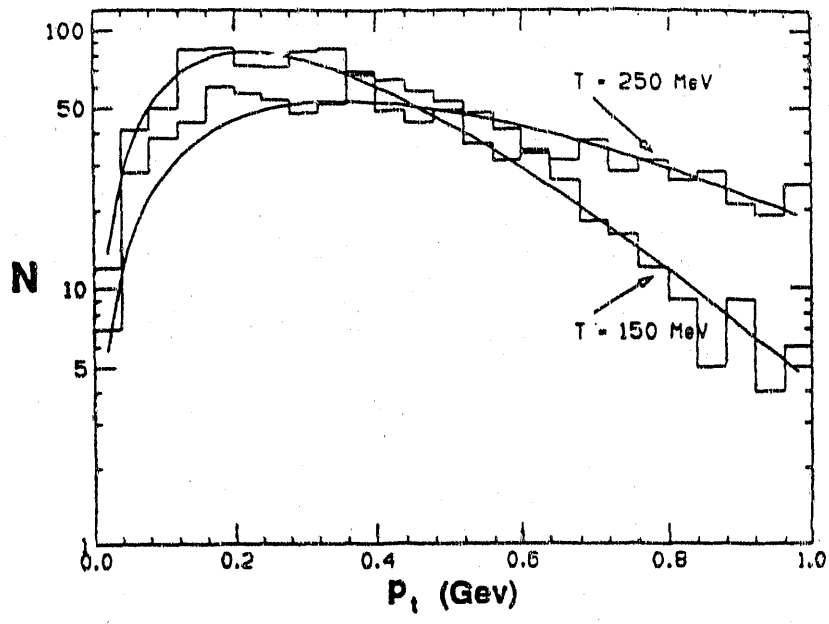

Figure 3-1 Simulation of the p_t spectrum for one event generated using a Boltzmann distribution of 1000 pions. The histograms correspond to single events generated with T = 150 MeV and 250 MeV. The curves are fits to the histogram using a Maxwell-Boltzmann distribution (see text).

and mini-jet attenuation[4] at high p_t will be investigated. Comparison of these spectra for pp and AA as a function of impact parameter is important. Large unexplained differences in spectral shapes have been measured in high multiplicity pp, $\alpha\alpha$ and higher mass nucleus-nucleus collisions at the CERN ISR and SPS.[5,6]

Since the baryo-chemical potential in the central region of heavy ion collisions at RHIC is unknown, and somewhat controversial, the p_t spectra of baryons and anti-baryons at midrapidity are particularly interesting for determining the nuclear matter stopping power. The difference between the p_t spectra obtained for p and $\bar{p}$ or Λ and $\bar{\Lambda}$ will reflect the redistribution in phase space of valence quarks from the nucleons of the target and projectile. This measurement of the net baryon number and net charge is important for establishing the baryo-chemical potential $\mu_B(y)$ at midrapidity.[7]

Measurements of multiplicity and the E_t distributions at midrapidity will provide information on the average matter and energy densities, respectively.

---

[4] P.V. Landshoff, Nucl. Phys. A498 (1989) 217; X.N. Wang, Lawrence Berkeley Laboratory Report LBL-28790 (1990), submitted to Phys. Rev. D.

[5] W. Bell et al., Phys. Lett. 112B (1982) 271; A. Karabarbounis et al., Phys. Lett. 104B (1981) 75; A.L.S. Angelis et al., Phys Lett. 116B (1982) 379.

[6] J.W. Harris et al., Nucl. Phys. A498 (1989) 133c.

[7] R. Anishetty, P. Koehler and L. McLerran, Phys. Rev. D22 (1980) 2793; W. Busza and A.S. Goldhaber, Phys. Lett. 139B (1984) 235; S. Date, M. Gyulassy and H. Sumiyoshi, Phys. Rev. D32 (1985) 619.

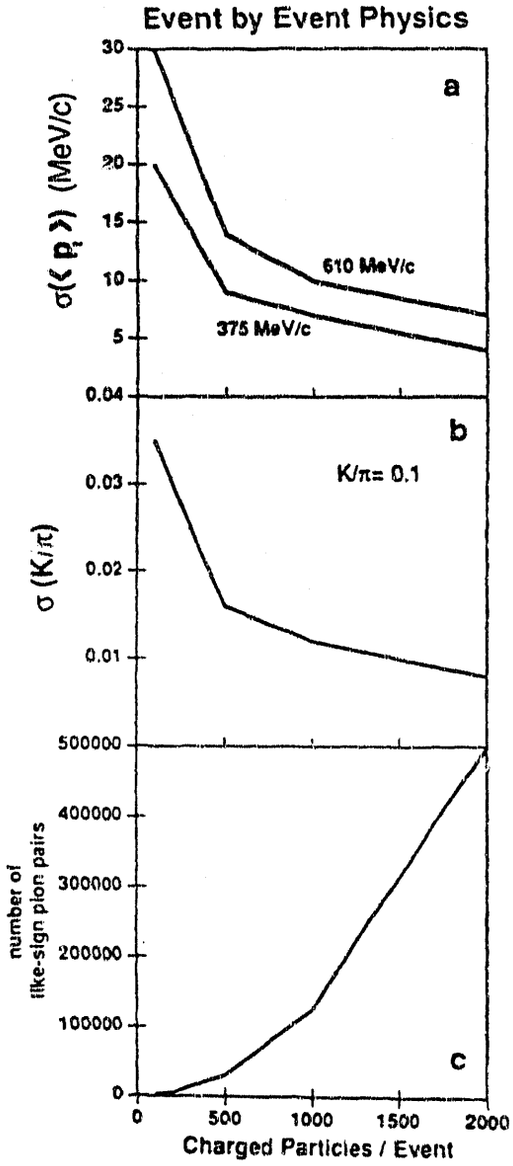

Figure 3-2 Plotted as a function of the charged-particle multiplicity measured in an event are a) the standard deviation of $<p_t>$, (showing the mean p_t values for temperatures of 150 and 250 MeV) b) the standard deviation of the ratio K/π (assuming $<K/\pi> = 0.1$) and c) the number of like-sign pion pairs. A central Au + Au event at RHIC is expected to produce 1000 charged particles in the acceptance of this experiment.

3.A.2. Low p_t Phenomena

By extending the acceptance of the TPC to low momenta via the SVT, low p_t phenomena can be addressed by STAR. The low p_t enhancement measured in pion p_t-spectra below 200 MeV/c emerging from heavy ion interactions at relativistic incident energies[8,9,10,11] is still not understood. A measurement of the low p_t part of the spectrum for a variety of particle species (K,π,p) at RHIC may allow an understanding of the origin of this phenomenon.

Correlations of many low momentum particles has been attributed to collective effects. Recent predictions of localized plasma formation ('Van Hove bubbles'[12]) might lead to correlated hadronization of low p_t particles, which can be investigated by measuring fluctuations of the yield in rapidity.

Bjorken[13] speculates that the orientation of the vacuum in the cold phase could be different from the orientation outside of a QGP bag (disoriented chiral condensate) due to the occurance of a 'cold' QGP. This may lead to coherent emission of low p_t-particles of a given charge. The 'centauro events' which were observed in cosmic ray experiments may be an experimental indication of these fluctuations of the low p_t pion yield. Measuring the yield of low p_t charged pions event-by-event as a function of centrality as well as the correlation with neutral particles measured in the electromagnetic calorimeter may provide information about hadronization of the chiral condensate.

3.A.3. Flavor Composition

At RHIC energies the various stages of the collision, i.e. thermalisation, expansion, and hadronization, will be reflected in the abundance and spectral distribution of particles containing heavy quarks. This should be true for both high density hadronic matter and a QGP. The strongest effect is expected at midrapidity where the energy density will be maximum. A measurement of the corresponding particle yields and spectra as a function of the impact parameter (size of the reaction volume) will elucidate these differences, provide information about soft hadronic processes, and may eventually lead to a decisive signature for the formation of the QGP.

A measurement of the K/π ratio provides information on the relative concentration of strange and nonstrange quarks, i.e. $\langle(s + \bar{s})/(u + \bar{u} + d + \bar{d})\rangle$. This has been suggested[14] as a diagnostic tool to identify hot, dense matter and to study the role

---

[8] T. Akesson et al.,Z.Phys.C46 (1990)361.
[9] H. Stroebele et al.,Z.Phys.C38 (1989)89.
[10] B. Jacak, Nucl.Phys.A525 (1991)77c.
[11] E.V.Shuryak, Nucl.Phys.A525 (1991)3c.
[12] L. Van Hove, Ann. Phys. 192 (1989) 66.
[13] J.Bjorken, 'A FAD detector for SSC', BNL-Colloquium, May 1992
[14] N.K. Glendenning and J. Rafelski, Phys. Rev. C31 (1985) 823; K.S. Lee, M.J. Rhoades-Brown and U. Heinz, Phys. Rev. C37 (1988) 1452.

of the expansion velocity. The K/π ratio will be measured *event-by-event* with sufficient accuracy to classify the events for correlations with other event observables. The capability of STAR can be seen in Fig. 3-2b, where the standard deviation of the measured single event K/π ratio is plotted as a function of the charged particle multiplicity measured in the event. The K/π ratio will be measured very accurately on an *inclusive* basis. It can then be correlated with various observables measured event-by event or on an ensemble basis.

Although the strange quark density in the QGP phase is much higher than in the hadronic gas phase, the total content of strange quarks is less enhanced in a quark-gluon-plasma than in a fully equilibrated hadronic gas at constant total energy or entropy. This is because the volume associated with the hadronic gas is much larger due to the smaller number of available degrees of freedom at fixed energy. Therefore, the observables which depend on the total strangeness abundance, such as Λ, $\bar{\Lambda}$, K^0_S yields or K/π ratios cannot be considered as direct signatures of QGP formation. On the other hand, observables depending on enhanced strangeness density, such as multiply-strange baryons (e.g. Ξ^-, Ω^-), benefit from the higher (near equilibrium) strangeness density reached in the QGP. Their approximate independence from final state effects makes them much more characteristic signatures of QGP formation. Their observation requires detection of secondary decay vertices. Due to the short decay lengths, $c\tau \sim 2 - 8$ cm, a silicon vertex tracker (SVT) close to the beam axis is necessary for these measurements.

The production cross section of ϕ-mesons can be measured *inclusively* from the decay $\phi \Rightarrow K^+ + K^-$. Displayed in Fig. 3-3 is an invariant mass spectrum, in the region of the ϕ mass, constructed from all possible combinations of identifiable K^+ and K^- in the acceptance $|\eta| < 1$. Measurement of the yield of the ϕ, which is an $s\bar{s}$ pair, places a more stringent constraint on the origin of the observed flavor composition[15] than the K/π ratio and is expected to be more sensitive to the presence of a QGP. The ϕ production rate is also expected to be extremely sensitive to changes in the quark masses[16,17,18] due to a chiral phase transition at high energy densities, which is predicted in lattice QCD calculations.[19,20]

A measurement of the predicted QGP enhancement of "open charm", e.g. the yield of D-mesons, would be of extreme interest.[21] The feasibility of identifying and analyzing D-mesons ($c\tau = 0.01 - 0.03$ cm) is near the limit of SVT performance and will depend upon developments in silicon vertex tracking in the RHIC environment. This is currently being investigated.

---

[15] A. Shor, Phys. Rev. Lett. 54 (1985) 1122.
[16] R. D. Pisarski and F. Wilczek, Phys. Rev. D29 (1984) 338.
[17] T. Hatsuda and T. Kunihiro, Phys. Lett. B185 (1987) 304.
[18] E.V. Shuryak, Nucl. Phys. A525 (1991) 3c.
[19] C.E. DeTar and J.B. Kogut, Phys. Rev. Lett. 59 (1987) 399; Phys. Rev. D36 (1987) 2828.
[20] E.V.E. Kovacs et al., Phys. Rev. Lett. 58 (1987) 751; F. Karsch et al., Phys. Lett. 188B (1987) 353.
[21] T. Matsui and H. Satz, Phys. Lett. 178B (1986) 416.

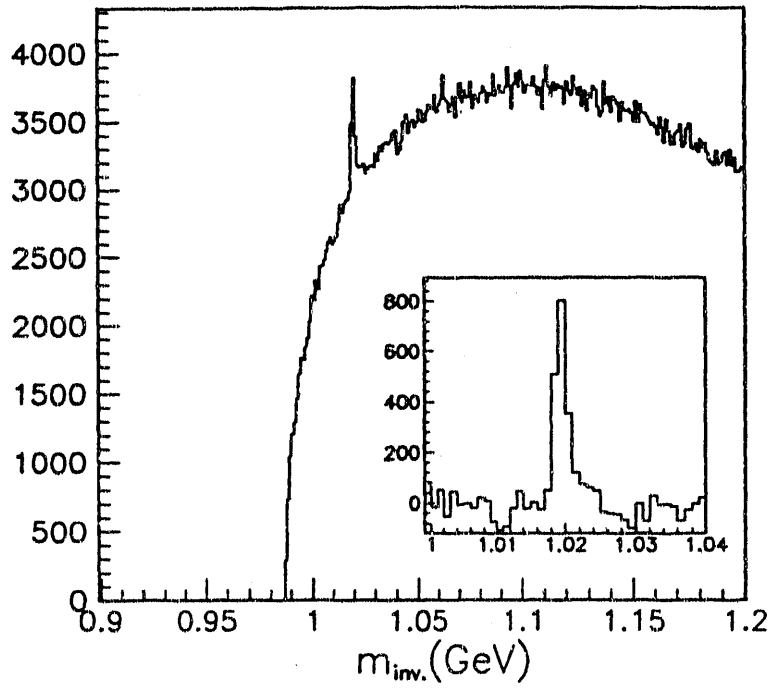

Figure 3-3 Invariant mass distribution for all identifiable K^+K^- pair combinations in the acceptance $|\eta| < 1$ of STAR for 500 Au + Au central events at RHIC. The ϕ signal is the narrow peak at 1.02 GeV. The momentum resolution and tracking efficiencies of the STAR tracking system are included in the simulation. The inset is the result of a subtraction of K^+K^- pairs formed from K^+ and K^-, each from a different event, from the true K^+K^- pairs of the main part of this figure. This effectively subtracts the phase space background yielding the clean ϕ signal observed in the inset. The simulation has no width for the ϕ. Therefore the contribution of the detector to the measurement of the ϕ is observed to be minimal compared to the true width of $\Gamma = 4.4$ MeV. The mean number of reconstructed ϕ's in these events is 6 per event.

3.A.4. Fluctuations in Energy, Entropy, Multiplicity and Transverse Momentum

It has long been known that a prime, general indicator of a phase transition is the appearance of critical dynamical fluctuations in a narrow range of conditions. It is worth emphasizing that such critical fluctuations can only be seen in individual events where the statistics are large enough to overcome uncertainties ($\sqrt{N}$) due to finite particle number fluctuations. The large transverse energy and multiplicity densities at midrapidity in central collisions allow *event-by-event* measurement of fluctuations in particle ratios, energy density, entropy density and flow of different types of particles as a function of p_t, rapidity, and azimuthal angle. They also allow measurements of local fluctuations in the magnitude and azimuthal distribution of p_t. These fluctuations have been predicted to arise from the process of hadronization of a QGP.[22]

---

[22] M. Gyulassy, Nucl. Phys. A400 (1983) 31c; L. Van Hove, Z. Phys. C27 (1985) 135.

Intermittency, or Factorial Moment Analysis[23], is a powerful technique for studying details of the charged particle multiplicity distribution, and is sensitive to multiparticle correlations over many length scales in phase space. There are trivial correlations in the multiplicity distribution due to, for instance, resonances. In order to uncover new physics it is necessary to probe the distribution at resolutions in η and ϕ well below the scale ($\Delta\eta \sim 0.5$) characteristic of these trivial correlations. The two-track resolution, which is the principal experimental parameter limiting the size of bins in phase space, is currently being studied in STAR.

3.A.5. Particle Correlations (Bose-Einstein)

Correlations between identical bosons provide information on the freezeout geometry,[24] the expansion dynamics[25] and possibly the existence of a QGP.[26] It would be interesting and unprecedented to be able to measure the pion source parameters via pion correlation analysis on an *event-by-event* basis and to correlate them with other event observables. In an individual event with 1000 negative pions, the number of $\pi\pi$ pairs within $|\eta| < 1$ is $n_{\pi^-}(n_{\pi^-}-1)/2 = 500{,}000$. The dependence of the number of like-sign pion pairs on the charged particle multiplicity per event is shown in Fig. 3-2c. However, it is necessary to determine precisely the statistics of the correlation function expected in the Bose-Einstein enhancement region of small momentum difference Q, as a function of multiplicity density. An empirical relation for the transverse radius (R_t) of the pion source at midrapidity as a function of the rapidity density (dn/dy) has been derived from the existing pion correlation data[27] shown in Fig. 3-4. This relation, $R_t \sim (dn/dy)^{1/3}$, suggests source sizes, $R_t \sim 10 - 15$ fm, for central Au + Au collisions at RHIC. Such large source sizes would confine the two-pion correlation enhancement to small values of $Q < 10 - 20$ MeV/c. An extrapolation of the CERN NA35 two-pion correlation data[28] to central Au + Au collisions at RHIC, as well as simple phase space density models, suggests that adequate statistics will be available on an event-by-event basis at small Q for these large source sizes, provided that dn/dy exceeds 500 for a given particle species. This value of dn/dy is somewhat larger than that predicted by conventional event generators. However, it may be achievable due to the substantially larger entropy density expected if a phase transition were to occur. At lower dn/dy (~300), sufficient statistics can be obtained with a small number of events (~1000) allowing selection and study of special event classes such as an unusual K/π ratios or unexpected fluctuations. The necessity to accurately measure small values of Q places stringent constraints on the two-track resolution of the tracking system. Using

---

[23] A. Bialas and R. Peshansky, Nucl. Phys. B273 (1986) 703.
[24] F.B. Yano and S.E. Koonin, Phys. Lett. B78 (1978) 556; K. Kolehmainen and M. Gyulassy, Phys. Lett. B180 (1986) 203; B. Andersson and W. Hofmann, Phys. Lett. B169 (1986) 364.
[25] S. Pratt, Phys. Rev. Lett. 53 (1984) 1219.
[26] S. Pratt, Phys. Rev. D33 (1986) 1314; G. Bertsch, M. Gong and M. Tohyama, Phys. Rev. C37 (1988) 1896 and G. Bertsch MSU Preprint (1988).
[27] P. Seyboth, Quark Matter '91 and R. Stock, University of Frankfurt Preprint IKF90-3 (1990) and Annalen der Physik 48 (1991) 195.
[28] A. Bamberger et al., Phys. Lett. B203 (1988) 320.

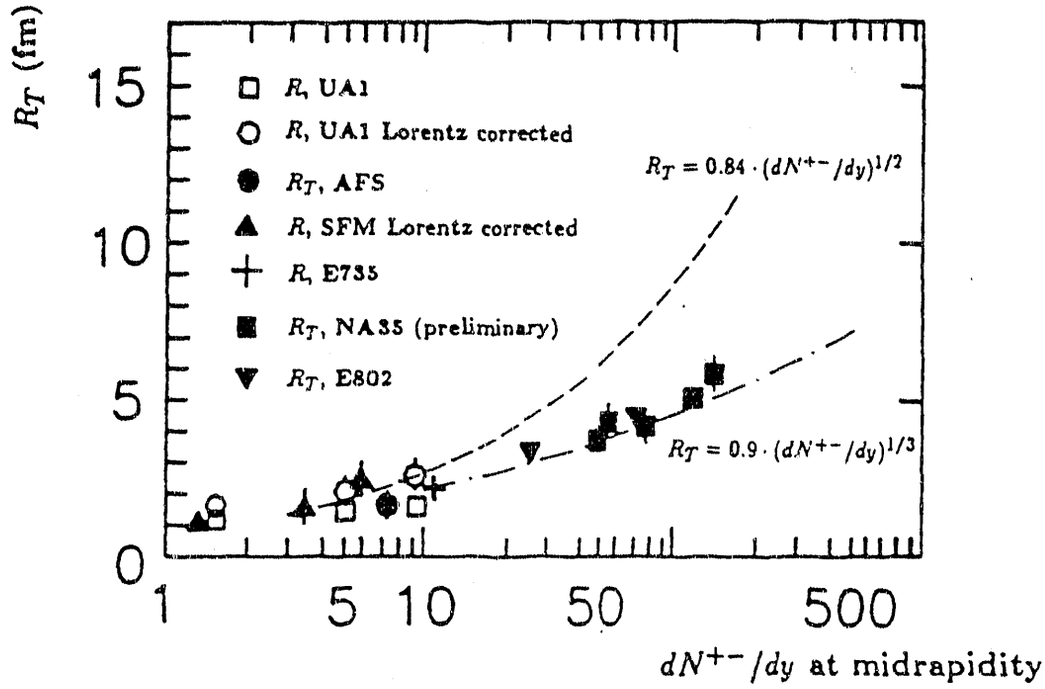

Figure 3-4 Transverse source size parameter versus the charged pion density dN^{+-}/dy at midrapidity. Predictions from models with freezeout at $R_T = \lambda_{\pi\pi}$ (pion mean free path) and at pion density $n_\pi = 0.5\ fm^{-3}$ are shown by dashed and dash-dotted curves respectively.

the present STAR TPC track reconstruction algorithms, which have not been optimized for close track reconstruction, a Q of 5 MeV/c can be measured in the transverse (space) direction and a Q of 10 MeV/c in the longitudinal (time) directions for the mean pion transverse momentum of ~300 MeV/c.

It should be noted that these considerations do not include effects of Coulomb repulsion of like-sign pairs of particles. This can be overcome by using pairs of neutral particles such as K^0_S, which are detected through decays into charged particles. According to simulations, approximately 15 K^0_S decays will be measured per central Au + Au event in the acceptance of STAR. Therefore, a sample of approximately 10^5 events will provide good statistics for a K^0_S-K^0_S correlation analysis.

The correlations of like-sign charged kaons or pions will be measured on an *inclusive* basis to high accuracy. The dependence of the source parameters on the transverse momentum components of the particle pairs will be measured with high statistics. Measurement of correlations between unlike-sign pairs will yield information on the Coulomb corrections and effects of final state interactions, which must be taken into consideration to interpret the like-sign pair distributions. This is important since the Coulomb corrections may also depend upon the spacetime evolution of the source.

The *inclusive* measurement of KK correlations will complement the $\pi\pi$ correlation data. The KK correlation is less affected by resonance decays after hadronic freeze-out

than the $\pi\pi$ correlations[29], thus interpretation of the KK correlation measurements is much less model-dependent than that of the $\pi\pi$ data. Since K's are expected to freeze out earlier[30] than π's in the expansion, the K source sizes are expected to be smaller than those of the π's, resulting in less stringent constraints on the two-track resolution of the tracking system. Depending upon the baryo-chemical potential and the existence of a QGP, the K^+ and K^- are also expected to freeze out at different times. [30] Thus, separate measurements of the K^+K^+ and K^-K^- correlation functions will be of interest.

3.A.6. Expansion Dynamics

Anti-deuterons and heavier anti-nuclei result from the coalescence of combinations of $\bar{p}$ and $\bar{n}$ during expansion, when the anti-nucleon density reaches freezeout density. The "coalescence ratio" $< \bar{d} >/< \bar{p} >^2$ depends not only on the dynamics of source expansion (radial flow, temperature, etc.) at freezeout, but also on the source size. This ratio decreases with increasing source radius, and should provide information complementary to the particle correlation analyses.[31] In a region of zero net baryon number, deuterons will also serve the same purpose.

3.A.7. Electromagnetic/Hadronic Energy

A unique feature of the STAR proposal is its emphasis on event-by-event correlations. Correlation and fluctuation analyses in both azimuth and rapidity are improved considerably by combining the EM and charged particle data. Approximately 1/3 of the energy is electromagnetic (EM) energy. The remaining hadronic energy can be measured by either calorimetry or charged particle tracking. In order to obtain reasonable total energy resolution the fraction of EM energy must also be measured via calorimetry. More important, the measurement of EM energy vs charged-particle energy is one of the correlations that must be measured in the search for signatures of the QGP and other new physics. The unexplained imbalance between charged particle and neutral energy observed in Centauro and other cosmic ray events emphasizes the need for EM/charged particle measurements.[32] Discussions of quark-gluon scattering within the QGP (eg., $qg \rightarrow \gamma q$) also point to the importance of measuring the electromagnetic energy as a possible signature of special events.[33]

3.B. Parton Physics

The goal of studying products of hard QCD processes produced in relativistic heavy ion collisions is to use the propagation of quarks and gluons as a probe of nuclear matter, hot hadronic matter and quark matter. Since the hard scattering processes occur

---

[29] M. Gyulassy and S. S. Padula, Lawrence Berkeley Laboratory Report LBL-26077 (1988).
[30] K.S Lee, M.J. Rhoades-Brown and U. Heinz, Phys. Rev. C37 (1988) 1463.
[31] S. Mrowczynski, Regensburg Report (1990) to be published in Phys. Lett.
[32] J.D. Bjorken and L.D. McLerran, Phys. Rev. D 20 (1979) 2353 and Y. Takahashi and S. Dake, Nucl. Phys. A461 (1987) 263C.
[33] P.V. Ruuskanen, JYFL-3-90, "International Workshop on Quark-Gluon Plasma Signatures," Strasbourg, France, Oct. 2 6 (1990).

at the very earliest stage of the collision ($t < 1$ fm/c), their production rates are dependent only upon the incoming state. Given the quark and gluon structure functions of the colliding nuclei, the rates of hard parton scattering are directly calculable in QCD. RHIC will be the first accelerator to provide nuclear collisions at energies where rates of detectable partonic debris (jets, high-p_t particles and direct photons) from hard partonic scattering permit accurate measurements. Various calculations have predicted that the propagation of quarks and gluons through matter depends strongly upon properties of the medium,[34,35,36,37,38] and that a measurement of the yield of hard scattered partons as a function of transverse energy may be sensitive to the state of the surrounding matter. For example, it has been suggested that there will be observable changes in the energy loss of propagating partons as the energy density of the medium increases, particularly if the medium passes through a phase transition to the QGP.[39] Energy loss in the medium results in jet quenching (i.e. a reduction of the jet yield at a given p_t) which has been observed in deep inelastic lepton scattering from nuclear targets. Jet quenching is expected to lead to significant effects in the spectra of single high p_t particles, di-hadrons and jets in AA collisions at RHIC.[40]

Quark structure functions of hadrons and nuclei are being studied with deep inelastic lepton (DIS) scattering. However, the proton's gluon structure function and its change in nuclei (nuclear shadowing) can only be studied with a hadronic probe. Information on the gluon structure function of the proton at low Feynman x is available from $\bar{p}p$ experiments.[41] However, a complete picture, including the effect of nuclear shadowing, requires a systematic program of pp and pA studies at RHIC.

Reconstruction of the parton scattering kinematics is limited by acceptance and detector resolution effects, and by the superposition of particles from other, incoherent processes which occur during the collision. This latter problem is especially serious in high multiplicity AA collisions, where the jet can be entirely obscured. The technique of jet reconstruction to extract parton information in AA collisions is being investigated with the STAR detector configuration. High p_t particle measurements can be used to extract parton information in pp, pA and AA collisions in STAR.

The distribution of final state particles is represented by the fragmentation function. A few percent of jets fragment into a limited number of hard particles carrying most of the jet momentum. Observing only hard particles above some p_t cut (e.g., $p_t > 2$

---

[34] J.D. Bjorken, Fermilab Report 82/59/59-THY (1982).
[35] D. Appel, Phys. Rev. D33 (1986) 717.
[36] J.P. Blaizot and L.D. McLerran, Phys. Rev. D34 (1986) 2739.
[37] M. Rammersdorfer and U. Heinz, Phys. Rev. D41 (1990) 306.
[38] M. Gyulassy and M. Pluemmer, Phys. Lett. B243 (1990) 432.
[39] M. Gyulassy et al, Lawrence Berkeley Laboratory Report LBL-31002, to be published in Proc. of 4th Conference on the Intersections between Particle and Nuclear Physics, Tuscon, Arizona, 1991.
[40] X.N. Wang and M. Gyulassy, Phys. Rev. Lett. 68 (1992) 1480.
[41] R. Baier and J.F. Owens in "QCD Hard Partonic Processes", B. Cox ed., Plenum Press, New York and London (1987); J. Appel et al, Phys. Lett. **B176**, 239 (1982); E.L. Berger and J. Qiu, Proceedings of the Polarized Collider Workshop, AIP Proceedings 223, Collins et al editors (1991).

GeV) may solve the background problem for high multiplicity. However, in order to study parton dynamics in this way the fragmentation functions must be known. These functions are currently being studied by many groups and should be well known by the time RHIC experiments begin. However, these may change for fragmentation in the presence of a QGP or hadronic matter. Means of determining the fragmentation function for nuclear collisions are currently being investigated.

The measurement of structure functions for unpolarized pp collisions can be extended to the case of polarized beams.[42] The importance of understanding how much of the proton spin is carried by the gluons has been emphasized by recent results in polarized DIS experiments, which can only study that portion carried by the quarks.[43]

The STAR experiment with its present complement of detectors will trigger on total transverse electromagnetic energy. Jet energies and single and multiple high-p_t particles will be measured. These capabilities apply for pp collisions and a range of pA and AA collisions. Achievable resolutions and the range of A that can be covered depend upon maximally efficient use of the EM calorimeter and tracking information. Some yields/10^7 sec (~ 100 days of RHIC running) for jets and single hard π^0s in the STAR detector at RHIC design luminosity are shown in Table 3-1. These rates indicate that the programs outlined can be carried out with significant statistics in reasonable time.

3.B.1. Jets

Hard parton-parton collisions will occur within the first fm/c of the start of the nucleus-nucleus collision.[44,45] Hence, the partons in a single hard scattering (dijet or γ-jet) whose products are observed at midrapidity must traverse distances of several fm through high density matter in a nucleus-nucleus collision. The energy loss of these propagating quarks and gluons is predicted[46,47] to be sensitive to the medium and may be a direct method of observing the excitation of the medium, i.e., the QGP.

---

42 See the RHIC Spin Collaboration Letter of Intent (1990).

43 European Muon Collaboration, J. Asham et al, Phys. Lett. **206B** (1988) 364 ; M.J. Alguard et al, Phys. Rev. Lett. **37** (1976) 1258; G. Baum et al. *ibid.* **51** (1983) 1153.

44 E.V. Shuryak in Proceedings of the Workshop on Experiments and Detectors for RHIC, Brookhaven National Laboratory, Upton, New York, 2-7 july 1990 to appear as a BNL report.

45 T. Matsui in Proceedings of the Workshop on Experiments and Detectors for RHIC, Brookhaven National Laboratory, Upton, New York, 2-7 July 1990 to appear as a BNL report.

46 M. Gyulassy and M. Pluemmer, Phys. Lett. B243 (1990) 432.

47 X.N. Wang and M. Gyulassy in Proceedings of the Workshop on Experiments and Detectors for RHIC, Brookhaven National Laboratory, Upton, New York, 2-7 July 1990 to appear as a BNL report.

Table 3-1. Rates for hard proceses expected in STAR.[48]

Observable	NN $\sqrt{s_{nn}}$ (GeV)	System	$\mathcal{L}$ ($cm^{-2}s^{-1}$)	p_t Range (GeV/c)	#/10^7s
jets, inclusive, $\|\eta\|<0.5$	200	pp	5×10^{30}	> 20	2.3×10^6
				> 40	4.2×10^3
		p Au (Ref.48) (min. bias)	3.2×10^{28}	> 20	2.8×10^6
				> 40	5.0×10^3
		Au Au (central)	2×10^{26}	> 20	5.5×10^5
				> 40	1.0×10^3
	500	pp	1.4×10^{31}	> 20	1.1×10^8
				> 40	2.5×10^6
				> 60	1.3×10^5
π^o, $\|\eta\|<1$	200	pp	5×10^{30}	$10 \pm .5$	4.8×10^4
				$15 \pm .5$	1.5×10^3
		p Au (min. bias)	3.2×10^{28}	$10 \pm .5$	5.8×10^4
				$15 \pm .5$	1.8×10^3
		Au Au (central)	2×10^{26}	$10 \pm .5$	1.2×10^4
				$15 \pm .5$	~350
	500	pp	1.4×10^{31}	$10 \pm .5$	4×10^6
				$20 \pm .5$	3×10^4
				$35 \pm .5$	$\sim 1.2 \times 10^3$

Wang and Gyulassy have developed a model to simulate nucleus-nucleus collisions at RHIC using the Pythia model[49] for pp interactions as a basis and including the nucleus-nucleus geometry. Partons are propagated through matter in the collision and their energy loss is calculated depending upon the type of matter traversed (nuclear, hadronic or QGP). Results from these simulations exhibit a strong attenuation of jets and mini-jets in hadronic matter. The attenuation disappears for traversal of deconfined matter (QGP). The results of the calculations are very much dependent upon the dynamics of the collisions, and the effects are largest at midrapidity. A detailed study of the effects of mini-jet and jet attenuation on the transverse energy is underway.

It is essential to measure the energy of both jets in di-jet events. The sum of the jet energies and the di-jet invariant mass are sensitive to interactions of the partons with the medium. The yield as a function of invariant mass of back-to-back jets at

[48] M.A. Bloomer, et al., in Fourth RHIC Workshop (1990), BNL 52262. Their Table 1 assumes a pp luminosity of $1.4 \times 10^{31}/cm^2/sec$ at 100 A GeV/c; we have assumed a pp luminosity for this energy of $5 \times 10^{30}/cm^2/sec$.

[49] T. Sjostrand and M. van Zijl, Phys. Rev. D36 (1987) 2019.

midrapidity may be the best tool for studying effects of the matter on propagation, since in this case the overall path length in the medium is maximized. The difference of di-jet energies may be sensitive to the difference in path lengths traversed by the partons. In addition, measurement of both jets in a di-jet event suppresses background due to fluctuations of soft production processes that can mimic a jet. A measurement of the di-jet differential cross section for p-nucleus collisions will in itself be of interest for understanding the parton structure functions in nuclear matter.

3.B.1.a. Mini-Jets and High p_t Tails of Distributions

Mini-jets are expected to be produced copiously in collisions at RHIC.[50,51] As is the case for high p_t jets, the observed yield of mini-jets is expected to be influenced strongly by the state of the high density medium through which they propagate.[52] However, direct measurement of mini-jets is virtually impossible because of their large opening angle and the strongly varying background. Thus, it is important to study the degree of fluctuation of the transverse energy and multiplicity as a function of pseudo-rapidity and azimuthal angle ($d^2E_t/d\eta d\phi$ and $d^2n/d\eta d\phi$) *event-by-event*, which should be strongly affected by the mini-jets.[53,54] It is essential that this be systematically studied in pp and pA collisions, as well as AA.

Inclusive p_t distributions of hadrons at $p_t > 3$ GeV/c will also be influenced by jets and mini-jets. It should be emphasized that the single particle cross sections fall off more rapidly as a function of p_t than the jet cross sections.[55] However, Wang and Gyulassy[56] have shown that the inclusive single particle yield is very sensitive to the state of the matter through which the parent scattered partons propagate. Fig. 3-5 shows the charged particle pseudorapidity distribution and the ratio of charged particle yields for Au-Au and p-Au collisions compared to p-p collisions as a function of p_t, under various assumptions about the nuclear structure functions (shadowing) and energy loss of the scattered partons (quenching). From the middle panel of Fig. 3-5 it is seen that the introduction of quenching (on top of shadowing) leads to a reduction in yield above p_t~4 GeV/c of a factor 5, which will be easily measurable at STAR.

---

50 K. Kajantie, P.V. Landshoff and J. Lindfors, Phys. Rev. Lett. 59 (1987) 2527.
51 K.J. Eskola, K. Kajantie and J. Lindfors, Nucl. Phys. B323 (1989) 37.
52 P.V. Landshoff, Nucl. Phys. A498 (1989) 217; X.N. Wang, Lawrence Berkeley Laboratory Report LBL-28790 (1990), submitted to Phys. Rev. D.
53 D. Appel, Phys. Rev. D33 (1986) 717.
54 X.N. Wang, Lawrence Berkeley Laboratory Report LBL-28789 (1990), submitted to Phys. Lett. B.
55 See W. Geist et al., CERN/EP Report 89-159 (1989) to be published in Phys. Rep. (1990).
56 X.N. Wang and M. Gyulassy, Phys. Rev. Lett. 68 (1992) 1480.

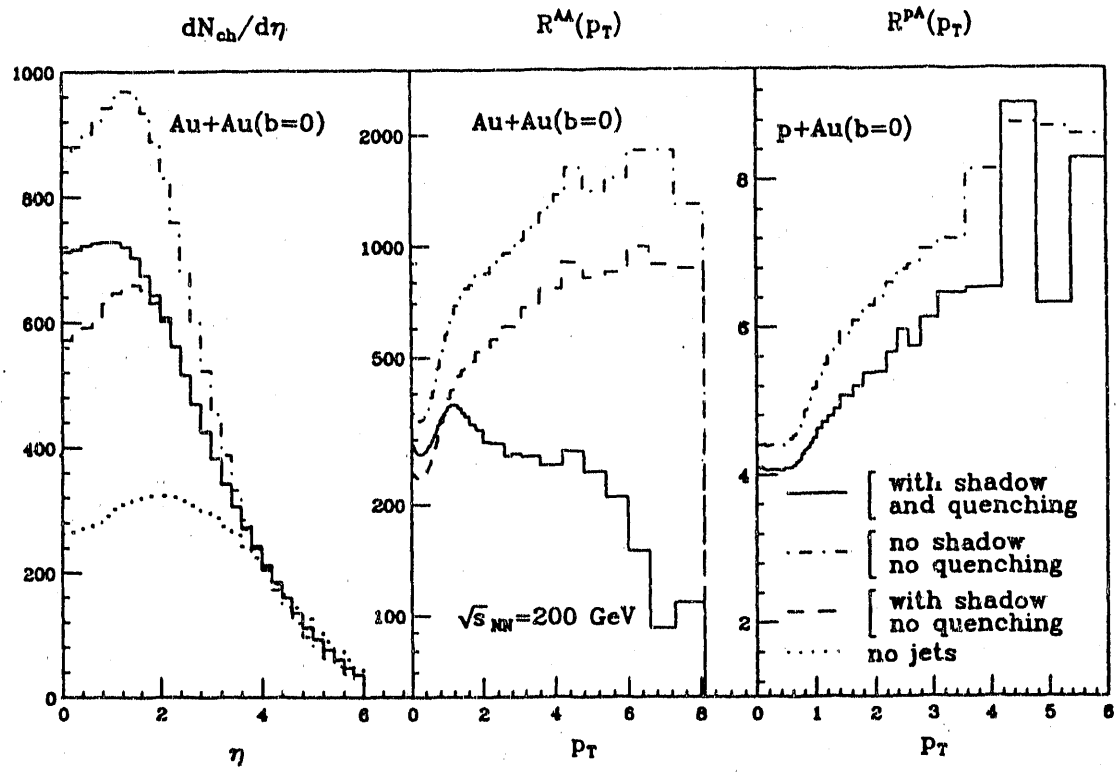

Figure 3-5 Results from HIJING calculations on the dependence of the inclusive charged hadron spectra in central Au + Au and p + Au collisions on minijet production (dash-dotted), gluon shadowing (dashed) and jet quenching (solid) assuming that the gluon shadowing is identical to that of quarks (see text and Ref. 56 for details). R^{AB} (p_t) is the ratio of the inclusive p_t spectrum of charged hadrons in A + B collisions to that of p + p.

3.B.1.b. Di-quarks at High p_t

The formation and attenuation rates of subhadronic objects, such as di-quarks, will also depend upon the state of the medium.[57] Although little theoretical consideration has been given to this subject, an investigation of di-quark scattering and attenuation at high p_t and production of Λ and $\bar{\Lambda}$ at high p_t should provide interesting information on this issue.

3.C. Correlations between Event Observables

It should be emphasized that the capability of measuring several different observables event-by-event is unique to this experiment. Events can be characterized event-by-event by their temperature, flavor content, transverse energy density, multiplicity density, entropy density, degree of fluctuations, occurrence of jets and possibly source size. The presence of a QGP is not likely to be observed in an average event, nor is it expected to be observed in a large fraction of events. Since there is no single clearly established

---

[57] W. Geist, Phys. Lett. B211 (1988) 233.

signature of the QGP, access to many observables simultaneously will be critical for identifying the rare events in which a QGP is formed.

4. Conceptual Design

4.A. Implementation Plan for the Experiment

4. Conceptual Design

4.A. Implementation Plan for the Experiment

The STAR Phase 1 Detector will consist of the Solenoidal Magnet, Time Projection Chamber, Silicon Vertex Tracker, Electromagnetic Calorimeter (EMC), Trigger Detectors for collision geometry, and associated electronics and data acquisition systems. These detectors are expected to be operational and online at RHIC start-up. Funding is being sought for the EMC from sources external to RHIC. This complement of detectors planned for STAR Phase 1 implementation is expected to accomplish most of the physics goals proposed by the STAR Collaboration. Construction and implementation of Time-of-Flight Detectors to extend particle identification to higher momenta, External Time Projection Chambers to extend acceptance to higher pseudorapidity and upgrades to more sophisticated triggering systems will take place as additional funds become available.

4.B.
Solenoid

4.B. Solenoid

4.B.1. Specialized Physics Issues

The TPC detector requires a uniform magnetic field. The average magnetic field uniformity requirement is approximately 1 part in 7000 if no correction is used in the TPC software.[1,2] If magnetic field corrections are applied in the software, the field uniformity requirements are only approximately 1 part in 1000. These field uniformity requirements must be met over the entire volume of the TPC, which is a cylinder 4.0 meters in diameter and 4.2 meters long about the magnetic center of the experiment. The field uniformity requirements have to be met over a range of magnetic inductions from 0.25 Tesla to 0.5 Tesla. The field uniformity requirements of 1 part in 1000 can be met over the entire TPC volume by shaping the iron poles even though there is a hole in the poles at $\eta = 2$ to allow particle transmission to external detectors. Small superconducting and conventional correction coils will be used to further improve the field uniformity.

4.B.2. Description of Subsystem

The STAR magnet includes the following subsystems: 1) a 4.2 meter inside diameter superconducting 0.5 Tesla solenoid magnet, which has an overall length of 6.9 meters and an outside diameter of 5.0 meters, 2) an iron return yoke and shaped pole pieces to carry the magnetic flux generated by the superconducting solenoid and shape the magnetic field to obtain the required uniformity, 3) a liquid helium refrigerator to cool and keep the superconducting solenoid at its operating temperature of 4.7° K or less, with a minimum of heat loss, 4) a vacuum system to provide vacuum for the multilayer insulation system needed to insure that the superconducting solenoid magnet can be kept at its operating temperature of less than 4.7° K, 5) a power supply to deliver up to 2500 amperes at a maximum voltage of 8 volts to the superconducting solenoid system, 6) a quench protection system to protect the solenoid in the event it becomes normal and 7) a system of monitoring electronics to monitor the performance of the superconducting solenoid and all of its subsystems during the life of the experiment.

4.B.4. R&D Issues and Technology Choices

Without pushing the state of the art, a 0.5 Tesla superconducting solenoid which is 0.7 radiation lengths thick can be built for STAR. This makes the magnet and the iron return yoke smaller than with a conventional coil and it allows calorimetry to be done outside of the magnet coil. A conventional solenoid which has been optimized for minimum capital cost of the coil plus power supply and cooling system would be at

---

[1] H. Wieman, "E and B Field Precision Constraints from Momentum Resolution Requirements in the STAR TPC," STAR Note-14, 29 October 1991.

[2] M. A. Green, "Methods for Improving the Magnetic Field Uniformity within the STAR Detector Solenoid," STAR Note-22, LBL Internal Note LBID-1808, 16 December 1991.

least two and a half radiation lengths thick. A thin superconducting solenoid uses about five percent of the power of a two and a half radiation length thick conventional solenoid. This saves a large amount of operating money over the life of the experiment and also saves some cost of new conventional facilities at the RHIC interaction region occupied by STAR.[3] There have been at least nine superconducting solenoids built using thin superconducting solenoid technology. These magnets have been used in physics experiments in the United States, Europe and Japan since 1979. The smallest of these solenoids had a 1.5 meter warm bore; the largest has a 5.2 meter warm bore. The very pure aluminum matrix superconductor proposed for the STAR magnet has been used in seven of these thin solenoids and at least a half dozen other large superconducting magnets. Worldwide, there are at least a dozen companies who are qualified to fabricate the STAR solenoid. Like all of the other thin detector solenoid magnets, the STAR magnet will be cooled indirectly by two phase helium flowing through cooling tubes.

4.B.5. Engineering

4.B.5.a. Brief Technical Description

The basic physical and electrical parameters of the STAR magnet are given in Tab. 4B-1. Fig. 4B-1 shows the magnet coil cryostat in relation to the iron poles and flux return path as well as the other elements of the the STAR experiment. Fig. 4B-2 shows a cross-section of the end of the STAR coil cryostat package. Fig. 4B-2 shows most of the components which make up the magnet coil and cryostat package. Fig. 4B-3 is a schematic diagram for the cryogenic system for cooling the STAR coil and keeping the superconducting coil at its operating temperature of 4.7° K or less. Fig. 4B-4 is a schematic diagram of the magnet coil power supply and quench protection system.

Description and Specifications of Major Components

The superconducting coil is a single layer of pure aluminum matrix superconductor.[4] This type of superconductor has been used in a number of detector solenoids because the energy needed to induce a quench is much higher than for a copper based superconductor which has the same radiation thickness. The STAR coil can carry enough current to generate a central induction of 0.7 Tesla, but the iron is not designed to return the magnetic flux at this level. The 0.7 radiation length thin section of

---

[3] A preliminary study was conducted to determine the cost difference between construction of a conventional coil and a superconducting coil. The capital expense of the conventional coil alone is less than that of the superconducting coil by about one years operating cost for the conventional coil. (Since the cost of operating the supercoinducting coil is much less than any of these other costs, it can be neglected in the present comparison.) Since the initial expense of the superconducting magnet can be amortized by the savings in operating expenditures within 1-2 years, a superconducting magnet operating at least two years is the most cost-effective. Because of potential budgetary savings for the construction project, the conventional coil option is being investigated further. A technology choice will be made within two months, once all the details are known.

[4] M. A. Green, "Preliminary Specification for STAR Superconductor," STAR Note-27, LBL Internal Report LBID-1831, 12 February 1992.

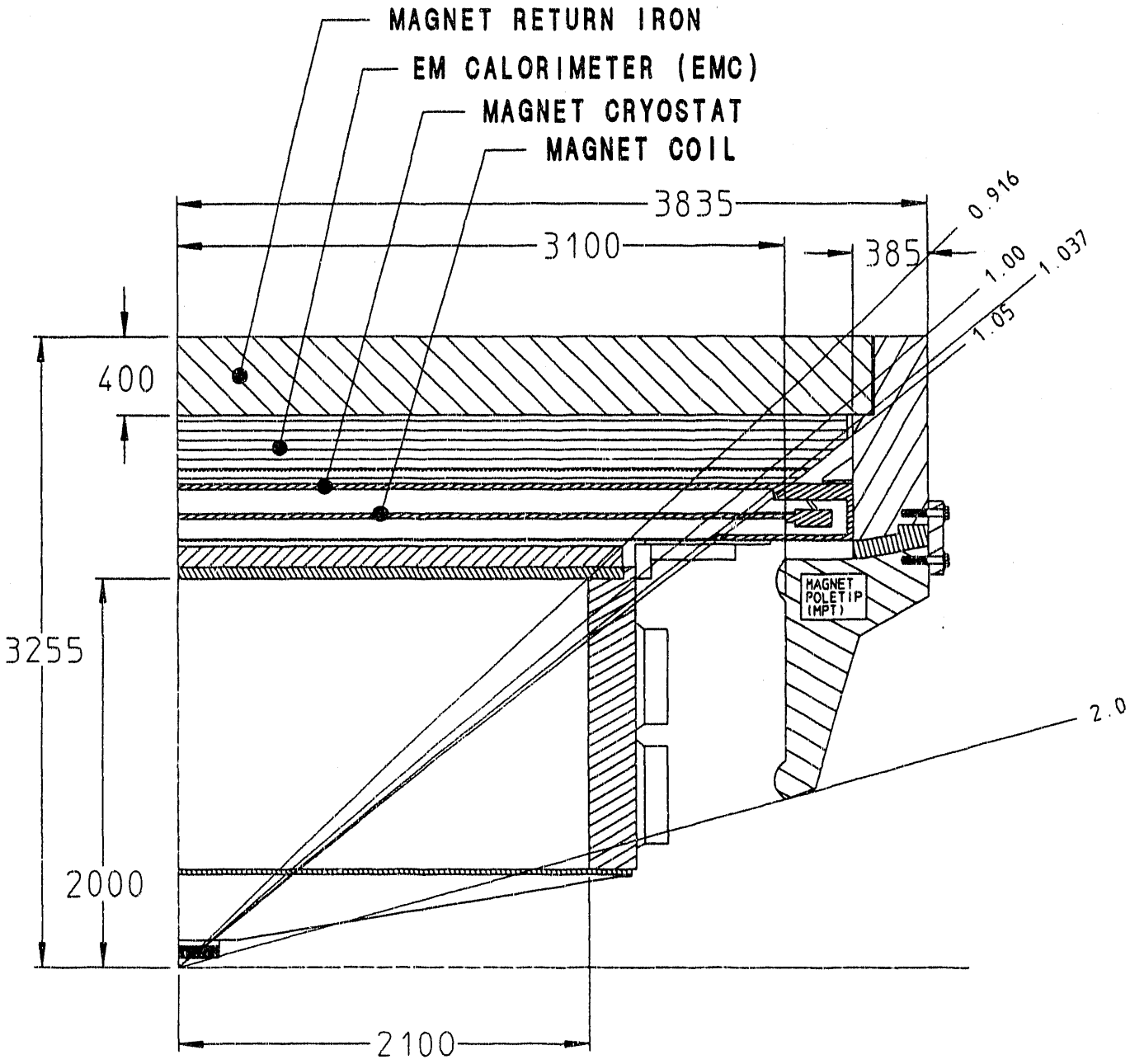

Figure 4B-1 The magnet coil cryostat is shown in relation to the iron poles and flux return path.

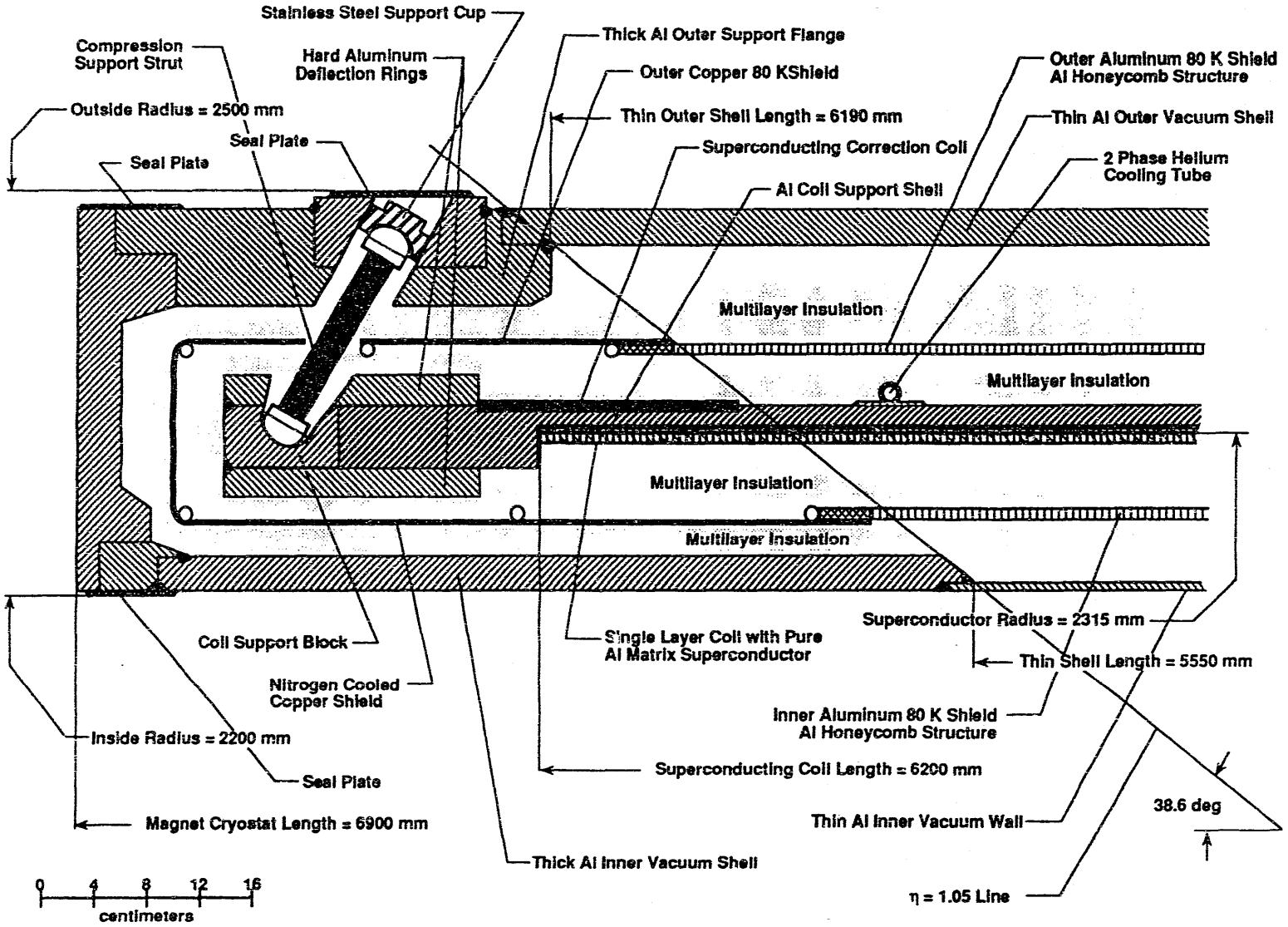

Figure 4B-2 Cross-section of the end of the STAR detector thin solenoid magnet, through the radial compression rod support.

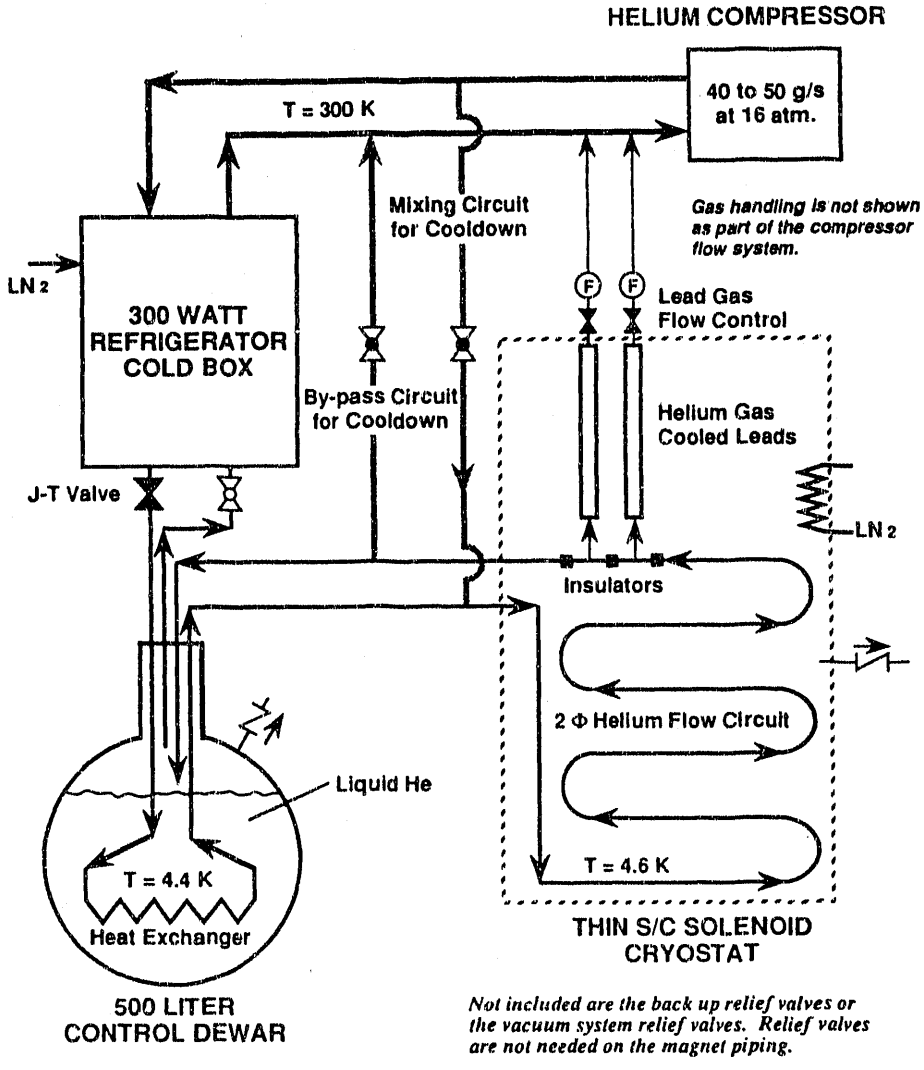

Figure 4B-3 STAR magnet cooling system using a separate refrigerator, forced two-phase coil cooling using the compressor to circulate the helium.

the STAR coil design is 5.43 meters long.[5] The ends of the magnet and cryostat are up to three radiation lengths thick. The end region contains all cryogenic services, the gas cooled electrical leads, the cold mass support system and all vacuum pumping for the cryostat. The coil and cryostat are designed so that all services come out of one end of the cryostat at or near the top of the cryostat. The reference design has cold mass

[5] M. A. Green, "Preliminary Specification for the STAR Superconducting Solenoid Magnet Coil and Cryostat," STAR Note-31, LBL Internal Report LBID-1832, 20 February 1992.

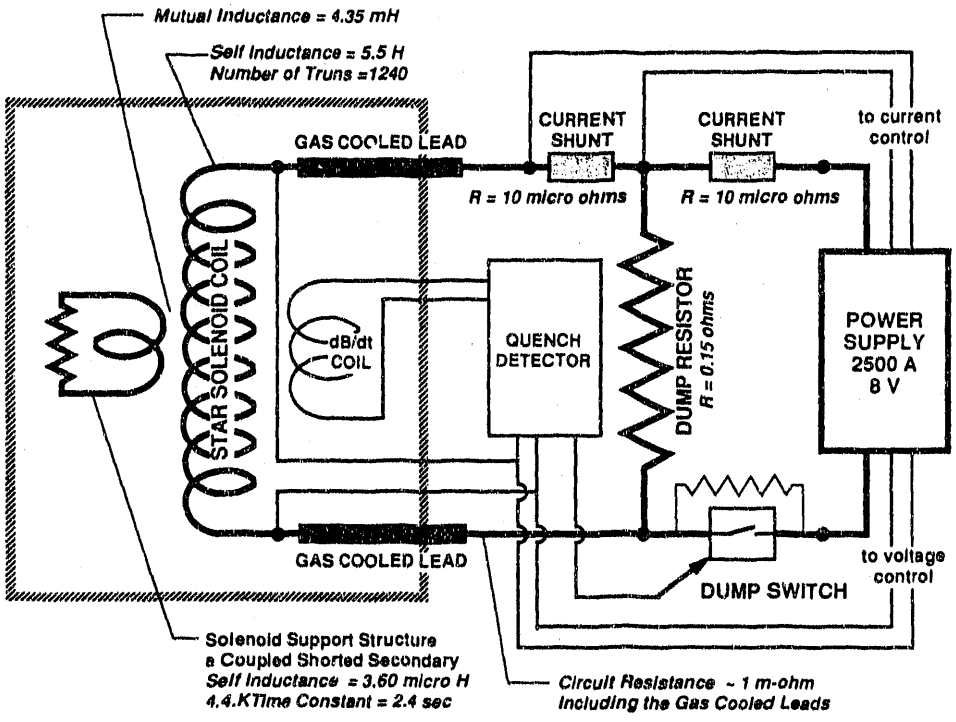

Figure 4B-4 STAR solenoid power supply and quench protection system.

supports in twelve places around each end of the magnet cryostat. The cold magnet cold mass support system is designed to carry accelerations of at least three times gravity in any direction.

The iron return path consists of two end support rings for the STAR experiment, two shaped magnet pole pieces, and sixty flux return bars which also support the EM calorimeter modules. The coil and cryostat are supported from the end rings. The TPC, and SVT are supported from the coil cryostat inner bore at the thick ends. The sixty flux return bars have spaces between them for routing light fibers for the EM calorimeter. The iron return path has sixty-fold symmetry. As a result, the iron return path should present no nonuniform effects on the quality of the magnetic field in the region of the TPC and SVT. The pole pieces are shaped to remove the nonuniform field effects of the gap between the iron pole and the end of the coil and the 1.71 meter diameter $\eta = 2$ hole for particles traveling to the external TPC detectors. The average gap between the iron poles is about 6.2 meters. Additional correction coils around the $\eta = 2$ hole and the end of the superconducting coil can result in further field quality improvement in the region of the central TPC detector. Between pole shaping and the correction coils, the field quality will meet specifications for a central induction range from 0.25 to 0.5 Tesla.

The magnet cooling system is a two phase helium tubular cooling system with tubes attached to the support shell outside of the superconducting solenoid coil. These tubes are spaced about 0.5 meters apart. (See Fig. 4B-2 and Fig. 4B-3.) Two phase helium

cooling has been used for virtually all of the large detector magnets built since 1978. Two phase cooling can be provided by either natural convection (the so called thermal siphon system) or by forced two phase cooling where the pumping is provided by the helium compressor (See Fig. 4B-3.) or a liquid helium pump.[6] The STAR magnet can be cooled by its own refrigerator or the RHIC central liquefier. The use of a tubular cooling system has a number of positive safety implications for the STAR experiment. There is a relatively small amount of the liquid helium (about 15 liters) in contact with the superconducting coil and all of this helium is carried in tubes which are capable of withstanding pressures above 10 MPa.

The power supply and quench protection system for the STAR magnet is similar to that used on other large detector solenoids which use pure aluminum matrix superconductor. The magnet power supply and quench protection system can either be supplied by the magnet vendor or they can be purchased separately. The superconductor matrix current density is rather low (about 4×10^7 A m^{-2}) so the minimum time required for a safe coil quench is long (about 20 seconds). A simple quench detector and dump resistor will protect the coil so that the coil hot spot temperature (at the point where the quench starts) is less than 100 K°.[7] The voltages developed across the superconducting coil during a quench are about 300 V. About half of the solenoid stored energy will end up as heat in the coil at the end of the quench. The other half of the coil stored energy will be dissipated as heat in the dump resistor.

4.B.5.c. Initial Fabrication, Testing and Shipping

The STAR solenoid will be built and tested by industry without the iron return yoke. The coil will be shipped to RHIC by the magnet coil and cryostat vendor. The cost of shipping is included in the cost estimate for coil and cryostat. After the coil and cryostat package has been shipped to RHIC, the coil package will be inspected and then installed in the iron return yoke as the iron is assembled in the STAR assembly building.

4.B.5.d. Assembly & Testing at RHIC

Further testing of the coil will be done at Brookhaven before the internal detectors are installed within the coil bore. This phase of the testing also includes measurement of the magnetic field in the region where the TPC and other detectors are to be located. The measured field map can be used by the TPC detector software to correct for the effect of field nonuniformity up to the level of 1 part in 1000. Once the magnetic field has been mapped, the TPC and the other detectors will be installed within the solenoid magnet warm bore.

---

[6] M. A. Green, "Cryogenic System Options for the STAR Superconducting Thin Solenoid," STAR Note-13, LBL Internal Report LBID-1841, 20 April 1992.

[7] M. A. Green, "Design Parameters for the STAR Solenoid Power Supply and Quench Protection System," STAR Note-53, LBL Internal Report LBID-1848, 23 April 1992.

Table 4B-1 Basic parameters of the STAR superconducting solenoid magnet, its flux return iron, its cryogenic system its power supply and quench protection system .

Solenoid Cryostat Inside Diameter (m)	4.40
Solenoid Cryostat Outside Diameter (m)	5.00
Solenoid Cryostat Length (m)	6.90
Solenoid Coil and Cryostat Mass (metric tons)	23.73
Superconducting Coil Diameter (m)	4.63
Superconducting Coil Length (m)	6.20
Superconducting Magnet Cold Mass (metric tons)	8.34
Maximum Design Central Induction* (T)	0.50
Number of Layers in the Solenoid Coil	1
Number of Coil Conductor Turns	1240
Solenoid Design Current* (A)	1989
Solenoid Coil Self Inductance with Iron* (H)	5.27
Magnet Stored Energy at Design Current* (MJ)	10.43
Length of the Return Iron (m)	7.67
Outside Diameter of the Return Iron (m)	6.51
Average Gap between the Iron Poles (m)	6.20
Number of Iron Pieces	64
Return Yoke Frame Mass (metric tons)	~50
Magnet Pole Piece Mass (metric tons)	~45
One of 60 Return Iron Bars Mass (metric tons)	~6.5
Total Iron Pole and Return Yoke Mass (metric tons)	~540
Estimated Refrigeration Required at 4.5° K (W)	110
Estimated Helium Liquefaction Required** (g s^{-1})	0.70
Cool Down Time with a 300 W Refrigerator (hr)	~120
Minimum Magnet Charge Time (min)	60
Power Supply Maximum Voltage (V)	8.0
Power Supply Maximum Current (A)	2500
Dump Resistor Resistance (ohms)	0.15
Dump Time for the Solenoid (s)	~20
Conductor Hot Spot Temperature (K)	~60

*At the solenoid design current needed to produce a 0.5 Tesla central induction. The design current will be a little higher due to iron saturation in the pole pieces and return yoke.

**The helium liquefaction requirements assume 0.25 g s^{-1} for the gas cooled electrical leads and 0.45 g s^{-1} for the coil cryostat and control dewar shields. If the coil cryostat shields are liquid nitrogen cooled, the liquefaction required goes down to 0.27 g s^{-1}.

STAR

4.C. Time Projection Chamber

4.C. Time Projection Chamber

4.C.1. Specialized Physics Issues

The central TPC is the main detector of the STAR experiment and is designed to fulfill the objectives of the basic physics program. The associated detector subsystems mostly work in conjunction with the TPC to refine and improve its measurements. Charged particles are detected, identified, and their momenta measured for $|\eta| < 1.0$. Tracking alone is performed over $1.0 < |\eta| < 2.0$. This allows the study of particle spectra, flavor composition, fluctuations, momentum distributions, source size (HBT), and source expansion (d and $\bar{d}$). Parton physics is accessible through studies of leading particles, as well as jet production when the TPC is used in conjunction with the EM calorimeter.

4.C.2. Description of Subsystem

4.C.2.a. General Description

The TPC (Fig. 4C-1) is a continuous tracking detector capable of handling high multiplicity events. It determines the momenta of an individual particles by tracking them through a solenoidal magnetic field and identifies them by making multiple energy loss measurements. The active gas volume of the TPC is bounded by coaxial field cage cylinders with instrumented pad plane end-caps at both ends. A high voltage membrane at the center creates an E field, such that ionization electrons drift towards the end-caps. The end-caps contain thin-gap, multiwire proportional chambers (MWPC) in which the primary signal electrons are amplified by avalanche multiplication at the anode wires. Image charges are induced on an array of pads located behind the anode wires and are recorded as a function of time. For each track segment, the drift time provides one coordinate, while the induced signals on the pad rows provide the coordinates in the plane of the MWPC. The basic parameters of the TPC are summarized in Table 4C-1.

Each end cap is comprised of 12 sectors, each of which is divided into two parts: an outer and an inner radius module as shown in Fig. 4C-2. The two modules are optimized for performance in either the high track-density environment that exists close to the interaction vertex or the lower track-density in the outer regions of the TPC. The inner module is distinguished by its ability to provide good two track separation while the outer module is optimized for dE/dx measurements which allows good particle identification.

Each sector module contains several wire planes in front of a cathode plane that is segmented into individual pads. These pads are arranged in concentric rows to optimize performance with regard to position and momentum resolution for straight (i.e. high p_t) tracks. This reason for adopting the radial geometry as opposed to a geometry with straight pad rows (which eases construction and analysis) applies to the STAR TPC even though a large fraction of tracks are of relatively low momentum. The momentum resolution for these low p_t tracks is dominated by multiple scattering and is therefore not affected by the choice of pad row geometry.

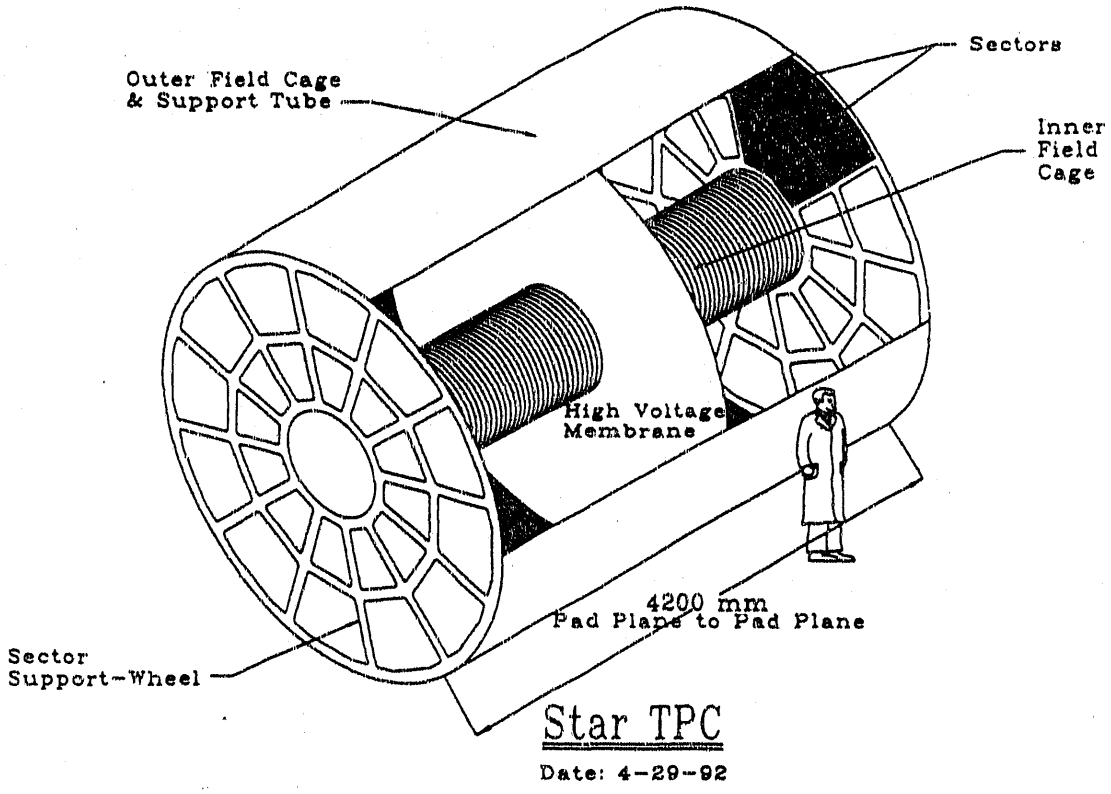

Figure 4C-1 A diagram of the STAR central TPC.

The outer module contains pads that are 19.5 mm long in the radial direction and 6.2 mm wide in the azimuthal direction. They are arranged in circular rows and cover, as much as possible, the full surface area of the module for good dE/dx resolution. There is a 0.5 mm gap between the pads. The widths of the pads and the distance from the pad plane to the anode wire plane (4 mm) is chosen to ensure that signals appear on three contiguous pads above noise threshold for a minimum ionizing particle having the most probable track crossing angle. This has the advantage that the centroid can be located with a three point Gaussian fit and does not require independent knowledge of the width of the distribution.

The inner sector module is also arranged with circular pad rows but the pads are smaller, 11.5 mm long in the radial direction and 2.85 mm wide in the azimuthal direction. There are 18 regularly spaced pad rows instead of complete pad plane coverage. The distance from pad plane to anode wire plane is correspondingly smaller to preserve the proper signal spreading required to achieve three pad hits for the same reason mentioned above. The smaller dimensions will improve the two track separation at the inner radius where the track density is largest. The uninstrumented space between these pad rows compromises the dE/dx measurement in this region.

Table 4C-1

Drift Volume	Coaxial Cylinder - Inner Radius 0.5 m Outer Radius 2.0 m Length 4.2 m
B Field	0.5 T (Axial)
Drift Gas	Ar + 10% CH_4
Pressure	Atmospheric (not regulated)
E Field	130 V/cm
Drift Velocity	5.5 cm/μs
Diffusion	Transverse 185 μm/√cm @ 0.5 T, Longitudinal 320 μm/√cm
Shaping Time	180 ns (FWHM)
Sampling Rate	12.3 MHz
Sampling Depth	512 time buckets
Gas Gain	10^4 (avalanche multiplication)
Anode Voltage	1265 V
Anode Wires	20 μm diameter. Gold plated tungsten (2 Ω/cm)
Anode Readout	4 fold coupling for multiplicity trigger readout
Pad Size	Inner: 2.85 × 11.5 mm, Outer: 6.2 × 19.5 mm
Pad Pitch	Inner: 3.35 × 12.0 mm, Outer: 6.7 × 20.0 mm
Number of Pads	140,000 (total)
Dynamic Range	10 bits (required for dE/dx)
Laser System	Nd:YAG (frequency quadrupled, 266 nm) 60 beams

4.C.2.b. Drift Volume

The necessary phase space coverage of the STAR TPC can be determined to a large extent by simple considerations. In order to detect anomalous behavior in the reaction volume (unusual entropy densities, temperatures, excess strangeness production, etc.) on an event-by-event level, it is necessary to collect as many of the final state particles as possible so that the measurements are not dominated by statistical fluctuations. The distribution of particles radiated isotropically from a point source behaves as $d\sigma/d\eta \approx 1/\cosh^2(\eta)$. Thus, most of the yield is contained within the interval $\Delta\eta = \pm 1$. This sets the *minimum* window necessary for observing nucleus-nucleus collisions on an event-by-event basis. In reality, the reaction volume will have considerable longitudinal extent. The Bjorken picture implies a correspondence between z and η; this means that different pieces of the expanding fluid radiate into different windows of η. The baryon-free region is centered about $z=\eta=0$; thus, observation of the baryon-free zone is best carried out by a device covering at least $-1<\eta<1$. Larger coverage than this is clearly desirable in order to provide sensitivity to fluctuations in the observables between causally disconnected pieces of the "fluid". In addition, jets are

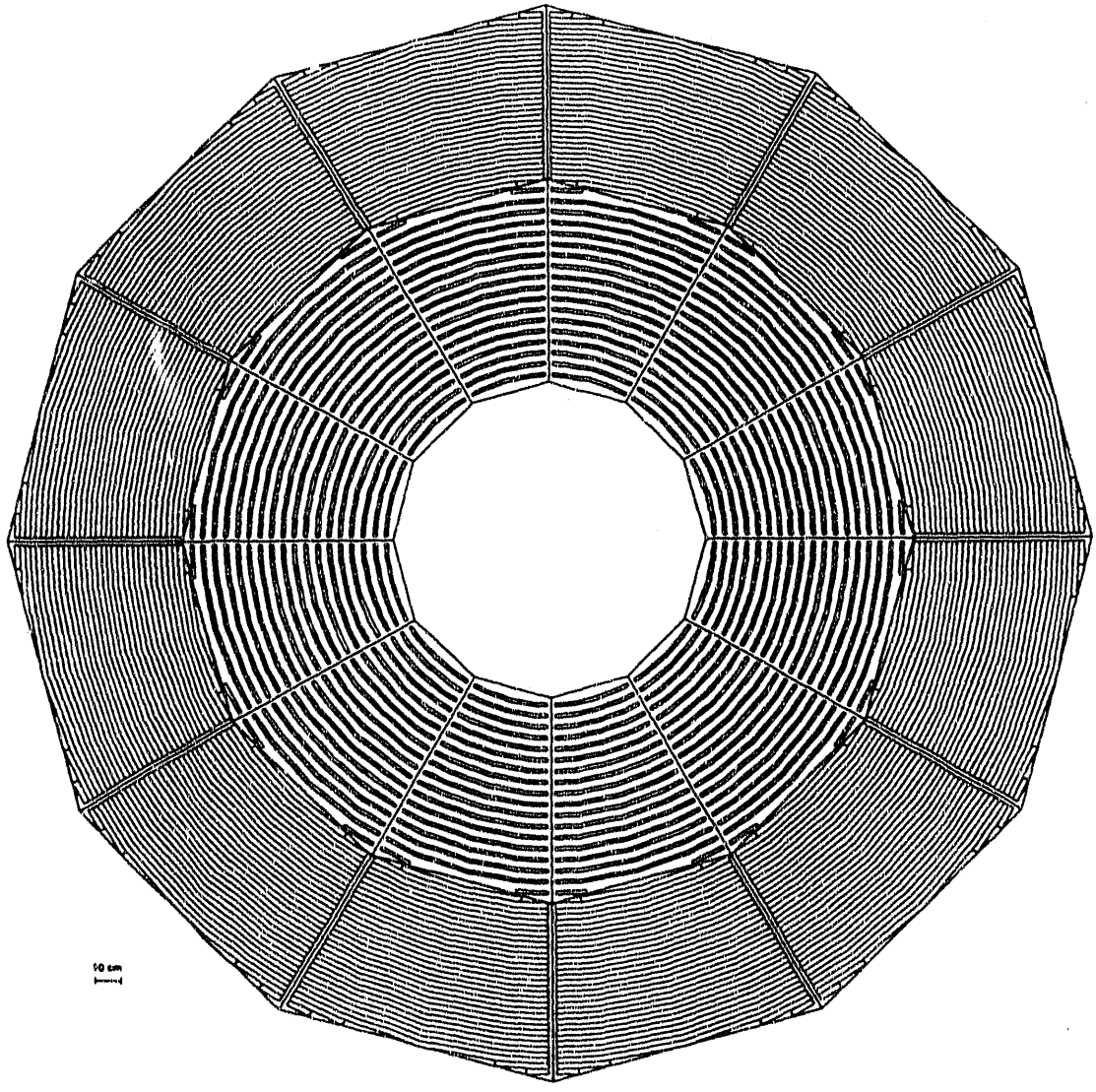

Figure 4C-2 A diagram of the TPC end-cap indicating the locations for the pad plane sectors and the pad rows.

known to radiate their final state particles over an interval of roughly $|\Delta\eta|=1$ about the jet center, so that accurate reconstruction of the jet energy requires detection over this η interval. TPC coverage of $-1<\eta<1$ is adequate for particle ID via dE/dx in the $1/\beta^2$ region. At larger η, a large fraction of the tracks cannot be identified via dE/dx. The η coverage requirement constrains the ratio of the outer radius to length for the TPC. Full azimuthal coverage is dictated by the requirements of observing as many final state particles as possible in a single event, and having adequate coverage for jets (which also have azimuthal extent $|\Delta\phi|=1$ radian).

The magnetic field strength and radial dimensions of the TPC were set by more detailed considerations. These parameters are intimately connected and balanced. The field strength of 0.5 T is a compromise between good momentum resolution and good

acceptance into the TPC at low p_t (~ 150 MeV/c). Momentum resolution is a strong function of the measured path length, requiring as small an inner radius and as large an outer radius as is feasible. In addition, a small inner radius is desirable for accurate pointing to the primary vertex or connecting to tracks from the SVT. Due to the expected track density in central Au-Au collisions, an inner radius of 50 cm is the practical limit; this is the point at which the percentage of merged track hits begins to rise rapidly. This is because of overlapping tracks which cannot be disentangled. An outer radius of 2 m, at 0.5 T, gives sufficient path length for adequate momentum resolution at p_t ~ 10-12 GeV/c, which is the practical p_t limit for STAR from the point of view of count rate. The outer radius is constrained primarily by cost, as increasing the radius causes considerable increase in the cost of the surrounding trigger scintillator barrel (or TOF), the solenoid, and the EM calorimeter. The size is also constrained by the track density expected from a central Au + Au event. It would not be feasible, for example, to increase the field strength while reducing the outer and inner radii. This would result in track densities which render the inner regions of the TPC unusable.

4.C.2.c. Drift Gas

The choice of gas for the active volume of the STAR TPC is made based on a compromise between the following 10 features:

1) The gas mixture has to work at atmospheric pressure.
2) The electron drift velocity must be > 2.0 cm/μs at E < 300 V/cm. This is a strict limit on the electric field, which is determined by the tolerances of the insulators on the field cages. It would be highly desirable to run well below this field. The drift velocity is restricted by the sampling rate and the limit of the SCA memory available.
3) The drift velocity should be saturated at the nominal working drift field. This property is desirable in order to minimize variation in the drift velocity due to: inhomogeneities in the electric field, pressure variations, and temperature variations. If it is not possible to operate on the saturation plateau, a H.V. feedback system will be implemented. It may be desirable to use a feedback system for velocity saturated gases and operate slightly off saturation.
4) Small transverse and longitudinal diffusion to allow for good two-track separation.
5) A large $\omega\tau$ factor to reduce transverse diffusion in the presence of the 0.5 T **B** field and to reduce sensitivity to field errors.
6) A high efficiency; this provides good dE/dx resolution and operation of the sense wires at low gain, which in turn permits low voltage on the sense wires and reduces the risk of sparking near dielectric boundaries. A gain of 10^4 should be achievable for a sense wire potential in the range of 1250 to 1500 volts.
7) Negligible signal attenuation, caused by electron reattachment over the drift length (2.1 m) in the TPC.
8) High drift velocity for positive ions in order to minimize the accumulation of space charge in the TPC drift volume.

9) A low rate of aging and high resistance to high voltage breakdown.

10) The gas should be affordable in view of the large quantities needed. It should be nonflammable, nontoxic, and should not require special safety precautions.

These requirements cannot all be satisfied simultaneously and one therefore must make a compromise. We have studied the literature, including recent SSC results. In addition, we have measured the properties of possible gas mixtures. Based on our findings and experience with TPCs (NA36, E810, NA35, EOS, ALEPH), we have chosen P10, an Argon/methane mixture (90:10), as the most suitable gas for the STAR TPC. However, we are still exploring mixtures based on neon, which would provide better momentum resolution because of the reduced multiple Coulomb scattering within the drift volume. The drawbacks to neon mixtures are that the gas is more expensive, a higher drift voltage is needed to keep the drift velocity above 2 cm/μs, and the primary ionization is lower, requiring that the anode wires be run at a higher bias. Also under consideration are various "slow-cool" gas mixtures. Table 4C-2 gives some of the relevant characteristics of these gas mixtures. Figures 4C-3, 4C-4, and 4C-5 show these characteristics as a function of drift field.

The longitudinal diffusion for Ar/CH_4 is normally taken to be 420 μm/√(cm) at E=120 V/cm. This is derived from detailed calculations of Biagi[1] and confirmed by measurments.[2] However, there are new results from two independent measurements which we have made that show that the longitudinal diffusion is lower than previously thought. A value of 290 μm/√(cm) has been obtained for P10 with a drift field of 200 V/cm. It is interesting to find that this value is nearly the same for all gases, regardless of their specific composition, as shown in Fig. 4C-4 and again is entirely consistent with Biagi's calculations. The use of Ar/CO_2, for example, would not provide significant improvement over P10.

The shaper amplifier time constant has been chosen to be 180 ns which is well suited for P10 (diffusion = 320 μm/√(cm), at E=130 V/cm) or other similar gases. The time constant (FWHM) is in fact calculated and made comparable to the dispersion in

Table 4C-2 The drift velocity and diffusion of some gas mixtures under consideration. Note that σ_{trans} does not include the magnetic field as in Table 4C-1.

Gas Mixture	V_{drift} (cm/μs)	σ_{long} (μm/√(cm))	σ_{trans} (μm/√(cm))
Ar/CH_4 (90:10)	5.5 @ E = 130 V/cm	320	540
Ar/CO_2 (95:5)	2.5 @ E = 200 V/cm	250	300
Ar/CF_4 (80:20)	3.5 @ E = 100 V/cm	—	—
$Ar/CH_4/CO2$	1.8 @ E = 150 V/cm	290	288

[1] R. Brockmann, et al., GSI Annual Progress Report (1989). Thomas Alber, Diplomarbeit der Fakultat fur Physik, Technische Universitat Munchen (1992).
[2] S.F. Biagi, NIM A283 (1989) 716.

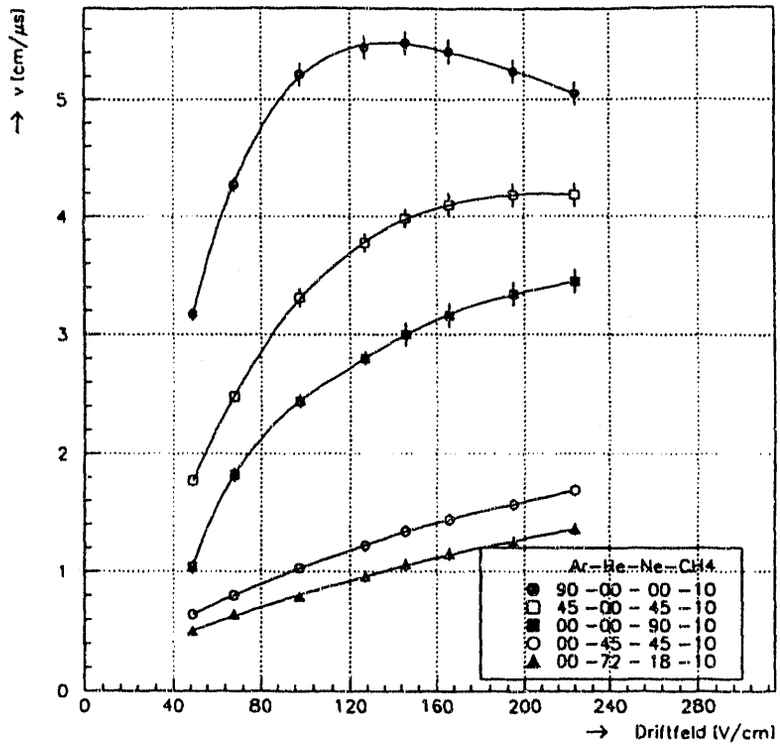

Figure 4C-3 Drift velocity as a function of field for P10 and other gas mixtures.

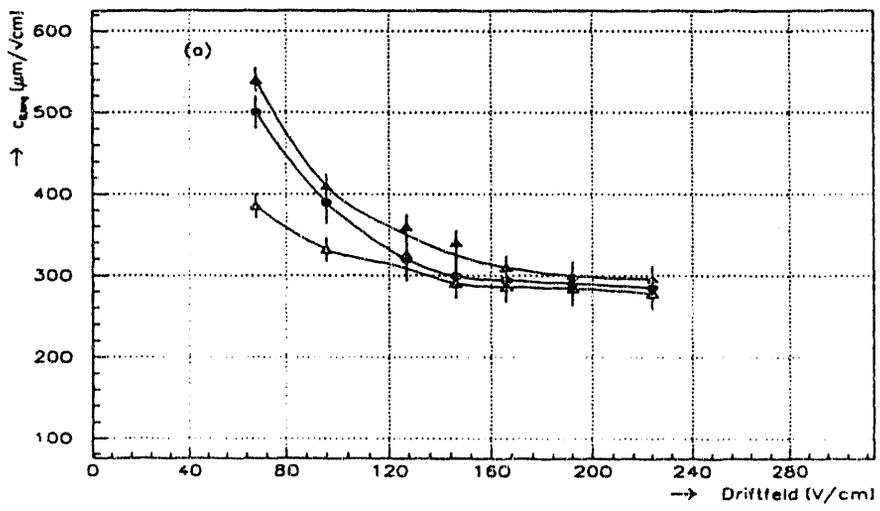

Figure 4C-4 Longitudinal diffusion as a function of field for P10 and other gas mixtures.

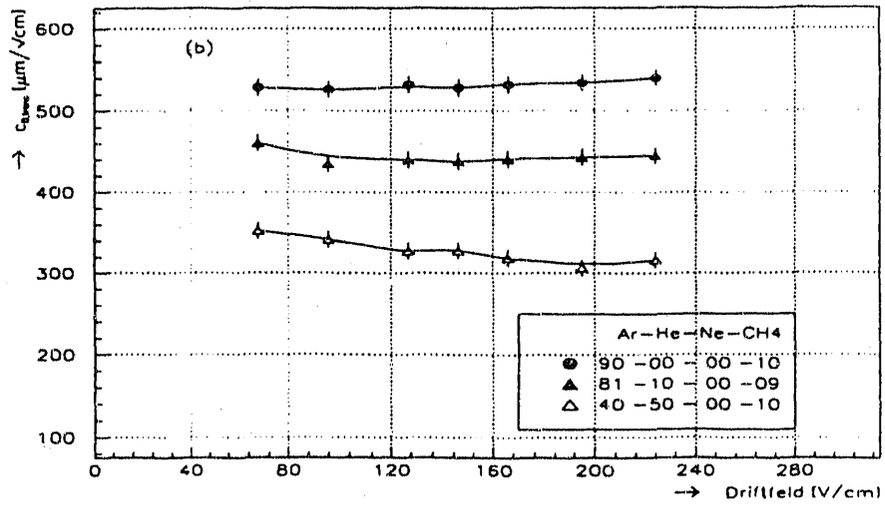

Figure 4C-5 Transverse diffusion as a function of field for P10 and other gas mixtures.

the signal collection time for a cluster of ionization produced 2 m away from the pad plane. In this way ballistic pulse height deficit effects are avoided.

There is one disadvantage in trying to seek out a gas with significantly less longitudinal diffusion which affects the shaper amplifier. The reason has to do with the shaping time constant and the fraction of the input signal which effectively contributes to the final output pulse. The formation of the input signal is mainly determined by the drift motion of the positive ions away from the avalanche region, which in turn, leads to the characteristic "1/t" dependence. Proceeding on the assumption that behaviour of the positive ions is unchanged in going to a cooler gas (with the same electron drift velocity), it follows that a shorter shaping time constant will integrate less of the 1/t signal and consequently reduce the output signal. In fact, because the mobility of a positive ion is directly related to its mass, a cool gas which has a quenching component heavier than the CH_4 will also yield a proportionately longer 1/t tail signal. In that case, the output pulse is further diminished.

The slow gases that have been studied so far have marginally lower diffusion and their use adversely impacts the design of the electric field cage and the depth of the SCAs. The additional cost involved in fabricating a field cage with increased high voltage isolation is not justifiable.

One has to keep in mind that cool gases, with their lower $\omega\tau$ factor, will suffer greater drift distortions as a result of non-uniformities and misalignment of the fields.

P10 is less sensitive to fluctuations in ambient pressure and temperature when operated on the drift velocity plateau. Nevertheless, small variations are still possible. We believe that it is well worth the effort to provide some means of compensation as this will simplify offline corrections.

The idea of stabilizing the drift velocity by using an active feedback system, based on photoelectrons emitted from the central TPC HV membrane during

illumination by a UV laser has been tried and verified using the EOS TPC. This TPC was operated at just below the saturation velocity (E=100 V/cm). The time of arrival of the electrons at the sense wires was recorded with a TDC. We concluded that drift time variations on the order of 1 ns are measureable using a multiple signal averaging technique. In terms of spatial disturbance, this corresponds to 50 μm after drift over a distance of 80 cm. For the STAR TPC we intend to 'lock-in' a 200 μm resolution (corresponding to a 10 ns time shift) at the furthest point away from the pad plane. Our results show that a 1 volt change on the field cage causes a 0.5 ns time difference. A swing of ± 20 V is therefore sufficient to achieve the desired amount of stabilization. Technically, it is easy to implement a computer controlled feedback loop which periodically adjusts the field cage high voltage power supply unit.

4.C.2.d. Pressure

The TPC will operate at atmospheric pressure. The disadvantages of increased pressure outweigh the advantages. The advantages are:

- Increased signal.
- Improved dE/dx in the $1/\beta^2$ region.
- Reduced longitudinal diffusion.

The disadvantages are:

- Increased expense for the pressure vessel.
- Increased difficulty in accessing electronics and other components requiring service.
- Increased multiple scattering in the drift gas.
- Increased multiple scattering in the thicker inner field cage.
- Increased field cage voltage to reach velocity saturation.
- Increased anode voltage required to achieve gas gain.
- Increased drift distortion due to reduced $\omega\tau$

4.C.2.e. E Field

The required magnitude of the electric field is determined by the point at which the drift velocity is saturated. For P10 this corresponds to 130 V/cm. It is important to either run at saturation or control the drift velocity through active feedback to minimize the effect of environmental variations in atmospheric pressure and ambient temperature.

4.C.2.f. Drift Velocity

For the P10 gas mixture, the saturation velocity is 5.5 cm/μs.

4.C.2.g. Diffusion

The longitudinal and transverse diffusion were estimated from recent measurements on P10 performed by V. Eckhart (refer to Figs. 4C-4 and 4C-5). The effect of the axial magnetic field was included on the transverse diffusion term (see Eq. 4C-11). The slow cool gases studied so far would have only marginally lower diffusion than P10

(at most 20%). Therefore, it was not deemed worth the additional cost to enhance the field cages to stand off the higher required voltages and to increase the size of the SCAs (additional time buckets would be required for a slower gas). The cool gases also have the disadvantage of increased vulnerability to drift distortions caused by field errors as the result of reduced $\omega\tau$ and to distortions caused by greater sensitivity to temperature and pressure gradients.

4.C.2.h. Shaping Time

The time constant of the shaping amplifier is designed to be equal to the time dispersion in the collection of an ionization cloud which traverses the maximum drift length of the TPC. For P10 this is 180 ns.

4.C.2.i. Sampling Rate

The sampling frequency is required to be sufficiently high so that at least 5 samples over threshold are taken for each hit; thus, the centroid in the time dimension can be determined with reasonable accuracy, ~ 1 mm. It is also important that the sampling frequency be an integral fraction of the RHIC RF. RF noise is thus synchronous with the readout and can be subtracted on a pixel by pixel basis. We have selected 12.3 MHz.

4.C.2.j. Sampling Depth

The number of time samples needed is determined by the drift velocity, drift length, and sampling frequency. For P10, an SCA depth of 512 samples is sufficient.

4.C.2.k. Gas Gain

The gas gain is the amplification factor of a primary ionization cloud caused by the avalanche in the proportional region of the TPC. The gas gain must be high enough to give adequate position resolution. The signal-to-noise on the pad directly under the track should be $\geq$ 20:1, i.e. the signal from a minimum ionizing particle must be amplified such that it is 20 times the magnitude of the electronic noise (which comes primarily from the pre-amplifier). The gain must be low enough to be well within the proportional region in order to maintain dE/dx resolution. A gain of 10^4 fulfills both of these requirements.

4.C.2.l. Anode Voltage

The gas gain is determined by the anode voltage, the wire diameters, and the wire plane separations. In order to achieve the required gain from the wire planes as they are designed, 1265 V must to be applied to the anode wire planes.

4.C.2.m. Anode Wires

The smaller the anode wires the higher the gas gain. However, the probability of wire failure also increases with reduced wire diameter. 20 μm diameter wires are strong enough to minimize the number of wire failures expected during the lifetime of the STAR TPC and still small enough to produce sufficient gas gain. Wires 20 μm in

diameter have performed well in several TPCs (PEP4, TOPAZ, ALEPH, DELPHI, and EOS), both in terms of stable gain operation and wire longevity.

4.C.2.n. Anode Readout

The signal on the anode wires which results from primary particles within the window $1 < |\eta| < 2$ can be used as a fast measure of the multiplicity, and could be used as an inexpensive centrality trigger in that region.

4.C.2.o. Dynamic Range

The STAR TPC will require 10 bits of dynamic range in the electronics channels for the pad readout. This resolution is needed in order to be able to avoid saturation for slow protons while still resolving the tails of the ionization distributions from minimum ionizing tracks (necessary for good position resolution). For minimum ionizing particles, a 20:1 signal to noise ratio is required. The most heavily ionizing tracks will have a dE/dx which is 10 times minimum ionizing, in addition tracks passing through the TPC at an oblique angle will deposit up to a factor of four more energy in a given pixel than a straight track. Thus at least 10 bits of dynamic range are needed.

4.C.2.p. TPC Tolerances Imposed by Momentum Resolution

Stringent tolerance constraints are imposed on the TPC by the desire to measure particle momenta in excess of 10 GeV/c. The position resolution required to achieve a given momentum resolution is obtained from the following expression for momentum resolution. This formula is valid for high momenta where multiple scattering is not the limiting factor:

$$\frac{\Delta P}{P} = \frac{P\sigma_\phi \sqrt{720}}{eBs^2\sqrt{n+6}} = \frac{P\sigma_\phi \sqrt{720}}{eBs^2\sqrt{\frac{s}{s_p}+6}} \qquad (4C\text{-}1)^3$$

where

P	(GeV/c)	–	Projected momentum
σ_ϕ	(m)	–	Azimuthal position resolution
e	(GeV/c $T^{-1}m^{-1}$)	–	charge = 0.2998
B	(T)	–	Magnetic field
s	(m)	–	Track length
n		–	number of position measurements
s_p	(m)	–	Pad length

This expression is for the measurement of a track with evenly spaced points. This is not exactly the configuration chosen for the final TPC design, but the expression provides a useful approximation for determining tolerance parameters. The azimuthal position

[3] STAR note #14.

resolution, σ_ϕ, which is required can be determined from Eq. 4C-1 if we input the TPC's characteristics (B = 0.5 T, n = 50, s = 1.5 m) and the desired momentum resolution ($\Delta P/P$ = 5% for P = 10 GeV/c). For this case, σ_ϕ must be less than 570 μm which can be achieved with current TPC technology. It is, however, necessary to limit global position tolerances in the TPC to smaller dimensions to achieve this level of momentum resolution. Again, the azimuthal tolerances are the most important in the determination of the sagitta for the stiff tracks for which momentum resolution is an issue. The global position tolerance, or sagitta error, can be expressed in terms of the individual position errors with the following formula:

$$\Delta f = \frac{\sqrt{720}}{8\sqrt{n+6}}\sigma_\phi \qquad \text{(4C-2)}$$

where Δf is the sagitta error for relatively straight tracks. The formula gives Δf = 250 μm for a single point azimuthal resolution of 570 μm and n, the number of measurement points along the track, equal to 50. The value 250 μm sets the limit on azimuthal errors that can be tolerated in the data. Distortions and mechanical errors in the TPC must be either held to this level or correctable to this level.

4.C.2.q. B and E Field Uniformity

This distortion limit sets tolerances on imperfections in the **B** and E fields in the following manner. In the following calculations, electron drift distortions are estimated from an expression for the electron drift velocity which is explained in the following section quoted directly from ALEPH.[4]

> "The drift velocity of electrons in the gas as derived from the Langevin equation can be written as a function of electric field, $\vec{E}$, and magnetic field, $\vec{B}$,
>
> $$\vec{v}_D = \frac{\mu}{1+(\omega\tau)^2}\left(\vec{E} + \omega\tau\frac{\vec{E}\times\vec{B}}{|\vec{B}|} + (\omega\tau)^2\frac{\vec{B}(\vec{E}\cdot\vec{B})}{\vec{B}^2}\right) \qquad \text{(4C-3)}$$
>
> where μ ($=e\tau/m_e$) is the electron mobility, ω ($=eB/m_e$) is the cyclotron frequency and τ is the mean drift time between two collisions with gas molecules. At small magnetic field (small $\omega\tau$) the first term dominates and the particles drift along the electric field lines; at large magnetic field (large $\omega\tau$) the third term is large, and $\vec{v}_D$ is almost parallel to $\vec{B}$.
>
> In the ideal TPC, $\vec{E}$ and $\vec{B}$ are exactly parallel and Eq. 4C–3 simplifies to $\vec{v}_D = \mu\vec{E}$. In reality, however, one expects deviations due to small but finite angles between the fields. These can have two origins:
>
> a) A global angle between $\vec{E}$ and $\vec{B}$ arising from a tilt of the TPC field cage in the magnet.

[4] W.B. Atwood et al., NIM A306, 439 (1991).

b) Transverse field components due to inhomogeneities. These are expected to be dominated by the radial components E_r, B_r, since the azimuthal components $E_{\varphi r}$, $B_{\varphi r}$ are constrained by the cylindrical symmetry of the TPC and the magnet.

The field components producing azimuthal coordinate shifts are more important than those producing radial shifts since the momentum resolution is mainly determined by the azimuthal coordinate resolution."

As explained above, the most significant drift distortion in the azimuthal direction comes from the second term in Eq. 4C-3 which can be expressed as

$$v_\phi = \frac{\mu E_z \omega\tau}{1+(\omega\tau)^2}\left(\frac{B_r}{B_z} - \frac{E_r}{E_z}\right) \tag{4C-4}$$

The azimuthal shift at the end cap is then

$$\begin{aligned}\Delta x_{\varphi r} &= \int v_{\varphi r} dt = \frac{1}{v_z}\int_z v_{\varphi r} dz \\ &= \frac{\omega\tau}{1+(\omega\tau)^2}\int_z \left(\frac{B_r}{B_z} - \frac{E_r}{E_z}\right) dz\end{aligned} \tag{4C-5}$$

This expression makes it clear that one is most sensitive to the radial components when $\omega\tau = 1$. In this case the factor in front of the line integral is 0.5. This was the operating value for PEP4. For ALEPH, the factor is 0.11 ($\omega\tau = 9$). For the operating parameters of STAR (90% Ar + 10% CH_4 and **B** = 0.5 T), the factor is 0.4 ($\omega\tau = 2.34$). Operation with a cooler gas with $\omega\tau$ somewhat less than 1 would be comparable.

With the above formulas we can now consider a quantitative estimate of the allowable field uncertainties by setting the above expression equal to the permitted distortion.

$$\int_z \left(\frac{Br}{Bz} - \frac{Er}{Ez}\right) dz = \Delta f \frac{1+(\omega\tau)^2}{\omega\tau} = 0.7\ \text{mm} \tag{4C-6}$$

for $\Delta f = 250\ \mu m$ and $\omega\tau = 2.34$. This corresponds to an average value of

$$\left|\frac{Br}{Bz}\right| = \left|\frac{Er}{Ez}\right| = 3.3 \times 10^{-4} \tag{4C-7}$$

for a drift distance of 2.1 m. This also corresponds to an alignment angle error between the **E** and **B** field of 0.3 mrad. Likewise an end cap deflection of 0.5 mm over the 1.5 m distance from inner to outer field cage gives the same error, $\left|\frac{Er}{Ez}\right| = 3.3 \times 10^{-4}$.

4.C.2.r. Pad Plane

Pad Response Function and Two-Track Resolution

The pad response function describes the signal observed on a pad as a function of the position of the avalanche. Two points from different tracks are deemed indistinguishable if, at the same radius, they are close in both $r\phi$ and the z-direction. The resolution in the $r\phi$ plane (i.e. in the pad plane) is determined by the width of the signal induced along a pad row. Its variance depends on the wire-pad plane geometry, the amount of diffusion a single electron suffers while drifting through the TPC gas volume, and the crossing angle of the track. We have studied the pad response function and have determined the response widths for two configurations using short (8×12 mm^2) and long (8×20 mm^2) pads. In either case an Ar/Methane (90:10) gas mixture was assumed. Note that these calculations do not use the final pad dimensions for the STAR TPC; they do, however, illustrate the effect of pad length. This exercise helped influence the decision to use 20 mm long pads in the outer sectors and 12 mm pads in the inner sectors. The narrower pad widths finally chosen for the TPC (6.7 and 3.35 mm) were selected to increase the likelihood of 3 pad hits, for which the best spatial resolution is achieved.

Parameterization:

The pad response function is approximately $e^{-(x - x_o)^2/2\sigma^2}$ where x is the position of the avalanche along the pad row and x_o is the center of the pad. The characteristic width given by,

$$\sigma_{prf}^2 = \sigma_o^2 + \sigma_D^2 \lambda (1 + \tan^2 \alpha) + D^2\left(\frac{1}{12}(\tan \alpha - \tan \beta)^2 + S_2 \tan^2 \alpha\right) \qquad (4C\text{-}8)$$

where,

λ - is the drift length (in meters)
D - is the sense wire spacing (4 mm)
β - is the Lorentz angle
α - is the wire crossing angle
$S_2 = \Sigma_i\, i\, \omega_i$ - is the sum over wire weights ω_i (where $\Sigma_i\, i\, \omega_i = 1$)

The three terms correspond to an intrinsic pad response σ_o, determined by the wire-pad geometry in the amplification region, a diffusion term σ_D, and a term which accounts for the crossing angle of the track relative to the normal of the wire direction σ_α. The angular dependence in the diffusion term originates from the projection of the effective track width onto the sense wire. By ignoring $\mathbf{E} \times \mathbf{B}$ effects[5] , $\beta = 0$ and the third term reduces to,

[5] The $\tan\beta$ term accounts for the displacement of an electron trajectory along the sense wire due to the non-parallel *E* and *B* field components in the vicinity of the wire. The parameterization assumes a straight line approximation when in fact the actual $v \times B$ force is dependent on the local electrostatic field.

$$\sigma_\alpha^2 \tan^2 \alpha \tag{4C-9}$$

where,

$$\sigma_\alpha^2 = D^2\left(\frac{1}{12} + S_2\right) \tag{4C-10}$$

The intrinsic pad response, σ_0:

This has been measured by D.L. Fancher and A.C. Schaffer[6] for 8×8 mm^2 pads, using a wire-pad geometry similar to that proposed for the STAR TPC. The measured value of 0.362 cm was found to be in close agreement with a value obtained from the EOS simulation utilizing 8×12 mm^2 pads.[7]

The diffusion term, σ_D:

The coefficient of the diffusion term may be written as,

$$\sigma_D^2 = \frac{\sigma_D^2(0)}{(C + \omega^2\tau^2)} \tag{4C-11}$$

where $\sigma_D^2(0)$ is the free field single electron diffusion, ω is the electron cyclotron frequency, τ the mean collision time and C is a constant.

A value of $\sigma_D(0) = 540\ \mu m/\sqrt{cm}$ was recently measured by V. Eckardt for P10 at 130 V/cm. The values of $\omega\tau$ and C were determined from the measurements made by S.R. Amendolia et al. [8], which yielded a value of $\omega\tau = 2.34$ (B = 0.5 T) and C = 2.8. Inserting these values into Eq. 4C-11, a value of $\sigma_D = 185\ \mu m/\sqrt{cm}$ was obtained.

The angular wire term, σ_α:

The final term in Eq. 4C-8 arises from the fact that the pad response is broadened for inclined tracks due to the effect of adding displaced Gaussian distributions from the contributing wires. The functional form of the summation, S_2, is derived simply by calculating the dispersion in the signals induced on the pad due to each sense wire. The weights measure the relative wire-to-pad couplings of the wires. These were deduced from the measurements of the pad response function for 8×8 mm^2 and 4×4 mm^2 pads by D.L. Fancher and A.C Schaffer[9], who measured the pad response both perpendicular and parallel to the direction of the sense wires. The results are consistent with an approximately Gaussian response with equal width in the perpendicular and parallel directions. The pad response for an 8×12 mm^2 and 8×20 mm^2 pad may thus be built

---

[6] D.L. Fancher and A.C. Schafer, IEEE Transactions on Nuclear Science, Vol. NS-26 (1979), 150.
[7] PEP4: G. Lynch, PEP4 note TPC-LBL-78-17 (1978). ALEPH: S.R. Armendolia, et al., NIM A283 (1989), 573. DELPHI: C. Brand, et al., Delphi 85-56, Trak-15.
[8] S.R. Armendolia et al., NIM A244 (1986), 516.
[9] D.L. Fancher and A.C. Schafer, IEEE Transactions on Nuclear Science, Vol. NS-26 (1979), 150.

up from summing the contributions of an appropriate number of 8×8 mm^2 and 4×4 mm^2 pads. This procedure had already been undertaken for the 8×12 mm^2 pad case to calculate the response for the EOS TPC[10] and was calculated separately for the 8×20 mm^2 pads. These values are summarized in Table 4C-3 together with other calculated and measured responses.

Table 4C-3 Summary of the values for σ_α for various pad sizes.

	σ_α (cm) 8×8 mm^2	σ_α (cm) 8×12 mm^2	σ_α (cm) 8×16 mm^2	σ_α (cm) 8×20 mm^2
G.L [11]	0.415			
G.R.[12]	0.400	0.490†	0.567	0.632†
H.W.[13]		0.446		
STAR				0.637
DELPHI[14]	0.382			

† Result of simply scaling by the pad length, h. Scale factor = $\sqrt{\frac{h2}{h1}}$

The values obtained for the coefficients of the three terms in the pad response function in Eq. 4C-8 are listed below in Table 4C-4.

Table 4C-4 Summary of the three σ measures for various pad sizes.

	8×12 mm^2	8×20 mm^2
σ_0 (cm)	0.362	0.362
σ_D (cm)	0.185	0.185
σ_α (cm)	0.446	0.637

The difference between the two pad configurations is reflected in their angular behavior as illustrated in the Table 4C-5. Short pads have a smaller value of σ_α which in turn provides better two-track separation of low momentum tracks with large crossing angles.

10 H. Wieman, EOSTPC note 174.
11 G. Lynch, PEP4 note TPC-LBL-78-17.
12 G. Rai, EOSTPC note 112.
13 H. Wieman, EOSTPC note 174.
14 C. Brand, et al., Delphi 85-56, Track-15.

Table 4C-5 Summary of the angular behavior for the two pad sizes.

	σ_{prf}(cm)			
Pad Size	$\alpha = 0°$ $\lambda = 0$ cm	$\alpha = 0°$ $\lambda = 200$ cm	$\alpha = 45°$ $\lambda = 0$ cm	$\alpha = 45°$ $\lambda = 200$ cm
8×12 mm^2	0.36	0.49	0.57	0.74
8×20 mm^2	0.36	0.49	0.73	0.87

In order to quantify two track separation, we have adopted a simple criterion that double 'hits' are considered clearly resolved provided the signal peaks along the pads are separated by at least the sum of the width of their respective pad response functions, σ_{prf}, plus the width of one pad. This is a conservative estimate but one which realistically describes the performance of traditional cluster finding algorithms. Therefore, the two track separation for the STAR TPC ranges from 1.5 cm to 2.5 cm (for $\alpha = 45°$ and $\lambda = 200$ cm) along the pad row. Note that this is improved for the inner sectors which have 3.35×12.0 mm pads.

Two signal pulses cannot be separated in time if their centroids are less than Δz apart, and this value is determined by three factors: electron diffusion, shaping time and the projected track segment along the drift axis. The latter is calculated from the pad length (h) and the polar (dip) angle θ of the track. Let Δz represent the width of the pulse at 10% of full height and $\tau(\mu s)$ the FWHM shaping time. The total width σ_T is the quadratic sum of the shaping time constant and diffusion, that is simply given by the expression $([\tau V_D/2.3]^2 + \sigma_D^2\lambda)^{1/2}$ where $V_D(cm/\mu s)$ is the drift velocity, σ_D the diffusion constant for Argon/Methane (= 300 $\mu m/\sqrt{cm}$), and λ(cm) is the drift length. The resolution function, Δz, depends on the ratio of the projected track length ($h/\tan(\theta)$) to σ_T, which is denoted by β. For β greater than 3

$$\Delta z = h/_{\tan(\theta)} + 2.8\,([\tau V_D/2.3]^2 + \sigma_D^2\lambda)^{1/2} \qquad (4C\text{-}12)$$

whereas for β less than 3,

$$\Delta z = 4.6\,[1 + h/12\tan(\theta)]^{1/2}\,([\tau V_D/2.3]^2 + \sigma_D^2\lambda)^{1/2} \qquad (4C\text{-}13)$$

The intrinsic two-track separation is set by the shaping time and is equal to 2.0 cm for the Ar/Methane P10 gas mixture. The shaping time matches the largest value of the diffusion term, which is at $\lambda = 200$ cm where the resolution decreases to 2.7 cm. Table 4C-6 below lists the values of Δz (cm) for various dip angles and the two pad sizes. The drift length was kept fixed at $\lambda = 100$ cm and the angles where chosen to highlight the various regions of the TPC. The majority of tracks in the TPC will have pad row crossings with dip angles less than 45° which in turn corresponds to a pseudorapidity coverage of approximately ± 1 unit.

Table 4C-6 Resolution as a function of dip angle for the two pad sizes.

Dip Angle (θ) degrees	Short Pad (0.8 × 1.2 cm)	Long Pad (0.8 × 2.0 cm)
60	2.5	2.6
45 (η = 1)	2.6	3.5
30	3.55	4.9
20	4.7	7.0

Projective geometry dominates Δz at small dip angles, and clearly short pads are better than long pads. However, in considering the short pad with dip angles greater than 40°, we find Δz is on the average influenced more by diffusion than projective track geometry. Therefore, since there is no gas mixture to our knowledge whose longitudinal diffusion constant is better than 300 $\mu m/cm^{1/2}$ and satisfies the design parameters, we believe our choice of using 2.0 cm pads at large radius (R > 125 cm) and short 1.2 cm pads in the inner region (50 < R < 125 cm) is the optimum configuration for the STAR TPC.

Basis of Design Choice

The pad plane design for the inner radius module compromises the dE/dx resolution in order to improve the two track resolution in the inner region where track densities are high. Current technology and budget limit the pad number density. Small pads arranged in separated rows have been chosen such that the total number of pads is the same as would have been required to fill the inner sectors with 8 × 20 mm pads. This choice reduces the total amount of track signal available for dE/dx by 35 % due to the gaps between rows on the inner sectors. However, since we only use dE/dx for particle identification in the $1/\beta^2$ region this is not a serious problem, particularly, since dE/dx resolution depends on $1/\sqrt{\text{track length}}$. The small pad size requires that the anode wire plane be moved closer to the pad plane, which results in an asymmetric placement of the anode wire plane with respect to the ground wire plane and the pad plane. Small pads with asymmetric anode plane placement have been tested by V. Eckardt in work on the NA35 and NA49 TPC designs[15], but further testing and prototyping will be required to verify this choice for STAR. Simulations will be performed to verify that tracking is not compromised by adding space between the pad rows.

There are several trade-offs implied by the choice of pad length that have been considered in the STAR design. Longer pads improve signal to noise for straight tracks. This can improve the position resolution. Lower momentum tracks from the main vertex cross the pad row with an angle, α, greater than zero. This contributes a position error that increases linearly with pad length due the tanα term (see Eq. 4C-17 from subsection 4.C.3.d). This effect is quantified in Fig. 4C-6 by using Eq. 4C-3 and the calculated momentum-dependent crossing angle. At low momentum the position resolution deteriorates markedly. However, this position resolution has been used to

[15] V. Eckardt's design work for NA35 pad planes.

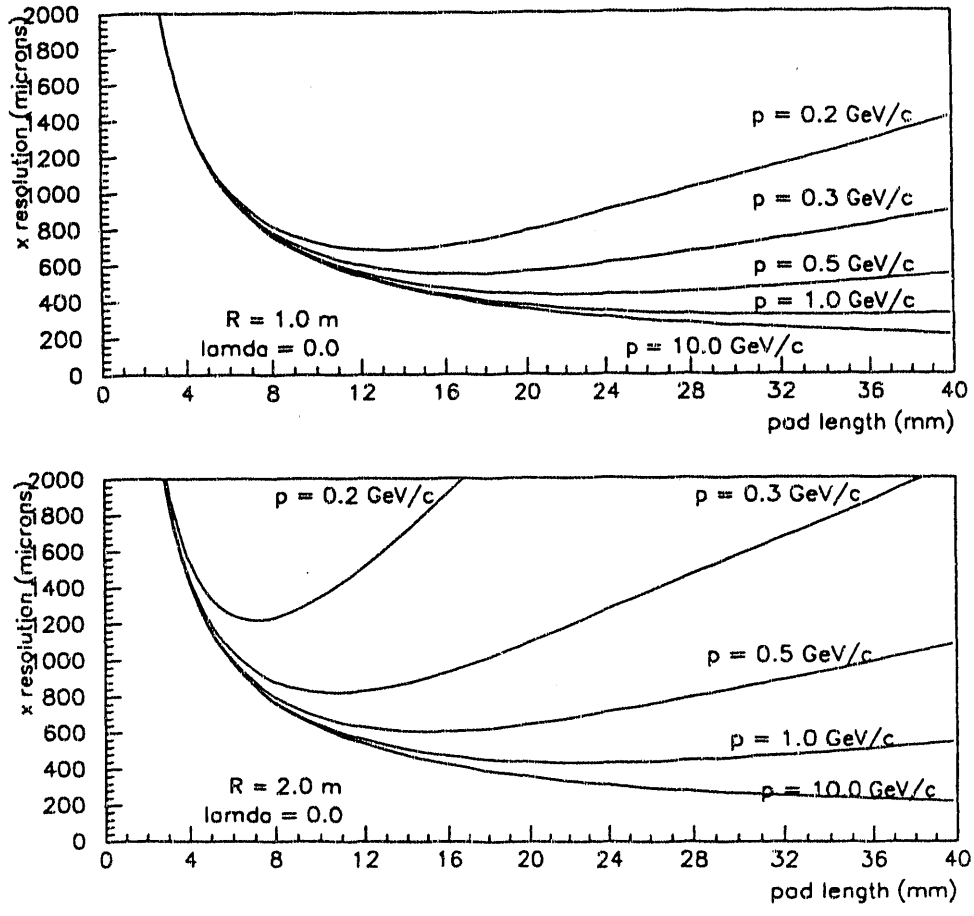

Figure 4C-6 The position resolution as a function of pad length.

calculate the momentum resolution and the results are not quite as might have been expected. This calculation of the momentum resolution was done using the following formula[16] which is the same equation as Eq. 4C-1 with an additional term for multiple scattering:

$$\left(\frac{\Delta P}{P}\right)^2 = \frac{P^2\sigma_\phi{}^2 720}{e^2B^2s^4(n+6)} + \frac{3\times10^{-3}}{B^2sL_R\beta^2} \tag{4C-14}$$

The only new parameters are β, the particle velocity in units of c, and L_R, the radiation length of the drift gas in the TPC. The radiation length of Ar at STP is 110 m. The resulting momentum resolution for π's is shown in Fig. 4C-7 for several pad lengths. This shows that pad length is not an important factor for momentum resolution at low momenta. At lower momentum ($p < 5$ GeV/c) the crossing angle is large, and therefore the position resolution is poor, however, in this momentum region the resolution is

[16] DELPHI and EOS results.

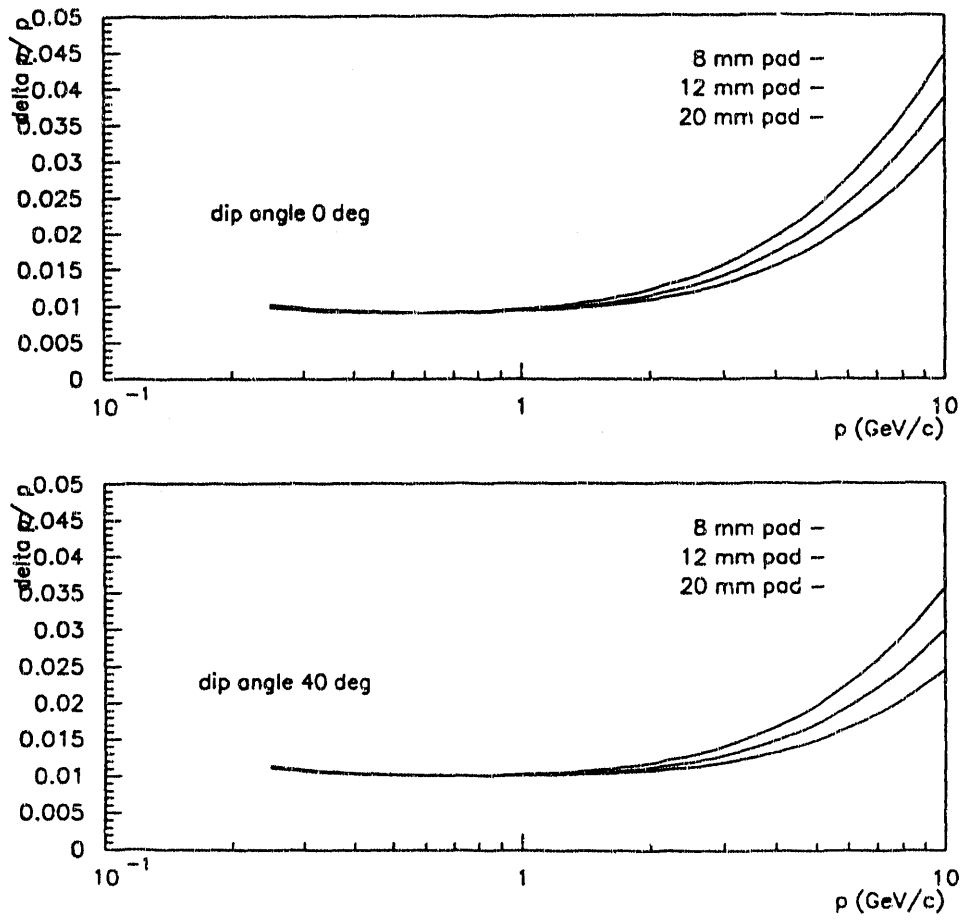

Figure 4C-7 The momentum resolution as a function of momentum for two different dip angles and three pad lengths.

limited by multiple scattering. At higher momentum the longer pad has some slight advantage due to the improved signal to noise.

The main negative consequence of large pad lengths is the increased time projection at larger dip angles. This factor was discussed in the previous subsection.

4.C.2.s Cooling System

The cooling system must hold the gas temperature variation to less than 1°C in order to maintain a constant gas gain and a uniform drift velocity. Note that if it is necessary to operate with a drift gas that is not on the saturation peak of the velocity versus field curve, then the temperature must be controlled to 0.3°C. At this level the position error in the z direction (drift direction) will be 2.3 mm. This position error is monitored using the laser system and can be corrected for offline.

4.C.2.t Laser System

The laser system is designed to produce a set of tracks at well defined θ angles. This coverage will provide an on-line measure of drift velocity and a measure of $\omega\tau$. The beams follow the paths of stiff tracks radiating from the interaction region and can be used for correcting the sagitta of such stiff tracks.

In order to minimize the error in the absolute position measurement of the TPC, it is necessary to account for both static and time-dependent distortions in the drift path of the ionization cloud. Static distortions are the result of non-uniformities in the B and E fields. A calibration system that provides absolute positional references is needed so that a deconvolution procedure, which determines the absolute spatial position from the raw pad and time bucket information, can be developed. Time-dependent distortions can result from changes in gas performance, changes in environmental variables (temperature or atmospheric pressure), or spontaneous failures. A calibration system that can reproduce fiducial tracks is needed to monitor the TPC performance. The positional accuracy of the calibration system must be significantly better than the spatial resolution of the TPC. The system that has been selected to perform these function is a Nd:YAG laser which will produce 60 calibration beams within the active volume of the TPC. This is a sufficient number of beams to calibrate the TPC performance as a function of both η and ϕ.

4.C.3. Capabilities of Subsystem

4.C.3.a Overview

This subsection outlines the ability of the central TPC to achieve the physics goals of the STAR experiment in the RHIC environment. The primary physics goals have been outlined previously in Chapter 3 and in the introduction to section 4.C. These include the inclusive study of particle spectra (subsections 4.C.3.c, e, and f describe the tracking, particle identification, and momentum resolution required to generate spectra), flavor distributions (subsection 4.C.3.f describes particle ID through dE/dx, which demonstrates the capabilities to address K to π ratios), fluctuation analyses (subsection 4.C.3.c), HBT correlations (subsection 4.C.3.g), and leading particle analyses (subsection 4.C.3.e discusses the momentum resolution for stiff tracks.). Note that the simulations and analysis routines developed here focus on technical issues rather than the ultimate physics analyses. The additional constraints on the capabilities of the STAR TPC that are imposed by the RHIC environment are explored in subsections 4.C.3.i though m.

4.C.3.b Simulations of the TPC Response

Simulated events have been generated to test the performance of the central TPC. The Lund-FRITIOF code has been used to create $\sqrt{S_{nn}}$ = 200 GeV Au +Au and $\sqrt{S}$ = 500 GeV p + p events. GEANT is used to process these events. It contains information on the pad plane design as well as the position and composition of the surrounding material. The data are then passed through the STAR FaSt TPC Simulation program (FST) which has been designed to simulate the response of the STAR TPC and the performance of the first level of the analysis software (the hit reconstruction algorithm). Input to the

FST program are the ZEBRA hit-banks which are output from the GEANT Monte Carlo. FST assigns each native Monte Carlo pad crossing a characteristic signal width and a spatial resolution, according to a parameterization which is dependent upon the track trajectory and the length of drift. The hits are smeared about the known track position according to their calculated spatial resolution. Those hits which are then found to overlap in both the pad plane projection and in the drift direction are merged to form larger single hit clusters. The output of FST then forms the input of the STAR pattern recognition program.

The FST simulation has been written with flexibility in mind. The program is controlled by parameter files for easy modification of the TPC running parameters. It allows for investigation of different pad sizes and geometries. However, in the implementation of the simulation chain which is discussed in this document, the STAR TPC is simulated using a straight pad row geometry consisting of 75 rows of 8×20 mm^2 pads. This was the original design for the pad plane of the TPC. Simulations with the current TPC design, consisting of circular padrows and smaller 3.35×12 mm^2 pads for the inner rows, are underway.

Another feature of the simulation program is the ability to merge events prior to and following the triggered event. This is particularly important in the high luminosity environment of proton-proton collisions where non-triggered events will be registered during the time that the TPC volume is being read out. Overlapping events from the non-triggered beam crossings are displaced in time, according to the time elapsed either before or after the triggering event. This creates quite a different event shape from that created by a central silicon-silicon event, which has a similar total multiplicity. The average number of events per crossing are calculated from the beam bunch separation, the beam luminosity, and the inelastic cross section[17] . The actual number of events in any given beam crossing is determined by a Poisson distribution whose mean is the calculated average number of events per crossing.

For crossing angles up to 45°, the induced signal width on the pads are calculated by FST for each GEANT pad crossing. The first is obtained from a parameterization of the pad response[18], which includes terms for the pad-wire geometry, the track crossing angle relative to the pad, and transverse diffusion which is a function of the drift length. Previous measurements have demonstrated that this parameterization of the pad response is good for crossing angles up to approximately 45°. For larger crossing angle tracks, the approximation of a Gaussian pad response breaks down. In this case the pulse width on the pad plane is calculated from either the projected arc length of track subtended by the row or by a simple projection of the tangent to the track from the momentum vector at the center of the pad. The smaller of the two values is chosen and an additional term is added to account for the transverse diffusion which is a function of the drift length. Because the pulse width calculated from the track projection onto the pad plane is always larger than the pad response calculated at the same value of the crossing angle, the pad response is scaled to meet to the projected width for crossing

[17] M.A. Bloomer, P.G. Jones and I.M. Sakrejda,
Evaluation of the performance of the STAR TPC for detecting p+p collisions at RHIC, STAR Note 57.
[18] P.G. Jones and G. Rai, The STAR TPC Pad Response Function, STAR Note 33.

angles between 45° and 72°. Refer to subsection 4.C.2.r Table 4C-4 for more details (note that for the simulations a σ_D of 230 μm was used).

In the drift direction, the spatial extent of the charge distribution is simply calculated according to the track length projected over each pad, the longitudinal diffusion and the electronics shaping time. The hits are smeared with a resolution of 700 μm which is determined by the longitudinal diffusion of the gas, the shaping time, and the sampling frequency[19]. The spatial resolution in the plane transverse to the drift direction is similarly parameterized as a function of the expected signal-to-noise ratio (20:1), the transverse diffusion and the track crossing angle relative to the pad row[20]. The hits are smeared about the known GEANT pad crossing using a Gaussian distribution function whose width (σ_{prf}) is given by the parameterization. The RMS resolution obtained on the pad row is approximately 770 μm for the 8×20 mm^2 pads. For stiff tracks the resolution is 500 μm.

Hits are merged in the simulation according to their separation and calculated spatial width in both the pad row plane and the drift direction. Hits in the same pad row are merged when their separation Δ is given by,

$$\Delta_{pad} < \sigma_{prf}(1) + \sigma_{prf}(2) + 0.8 \text{ cm} \tag{4C-15}$$

and

$$\Delta_z < \sigma_z(1) + \sigma_z(2) + 1.1 \text{ cm} \tag{4C-16}$$

The constant factors relate to one pad width and two time bins respectively, in the initial design specification of the TPC (namely 8×20 mm^2 pads, $v_D = 5.5$ cm/μs and 512 time samples). This places a cut-off on the deconvolution of close hits, related to the expected performance of the hit reconstruction algorithm, and results in a two track separation of approximately 2 cm in the pad plane and 3.5 cm in the drift direction. Merged hits whose combined spatial width is smaller than 10 pad widths (8 cm) and 20 time bins (11 cm) are preserved and written to the output file.

In Fig. 4C-8 the total hit multiplicity for a central Au+Au event is shown as a function of the TPC pad row number. The three distributions show the number of GEANT pad crossings, the number of hits from FST, and the number of those FST hits which are the result of merged hits. This indicates that 60% of the pad crossings are lost due to hit merging at the inner most pad row for 8×20 mm^2 pads. Furthermore, 30% of the remaining hits are clusters of two or more hits. Preliminary results from the simulations employing the new pad plane configuration (circular pad rows, small pads on the inner sectors) suggest that on the inner radius 70% of the pad crossing are reconstructed. This is a substantial improvement over the 40% of the original pad plane design.

---

[19] W.B. Atwood, et al., CERN-PPE/91-24.

[20] P.G. Jones and G. Rai, The STAR TPC Pad Resolution Function, STAR Note 34.

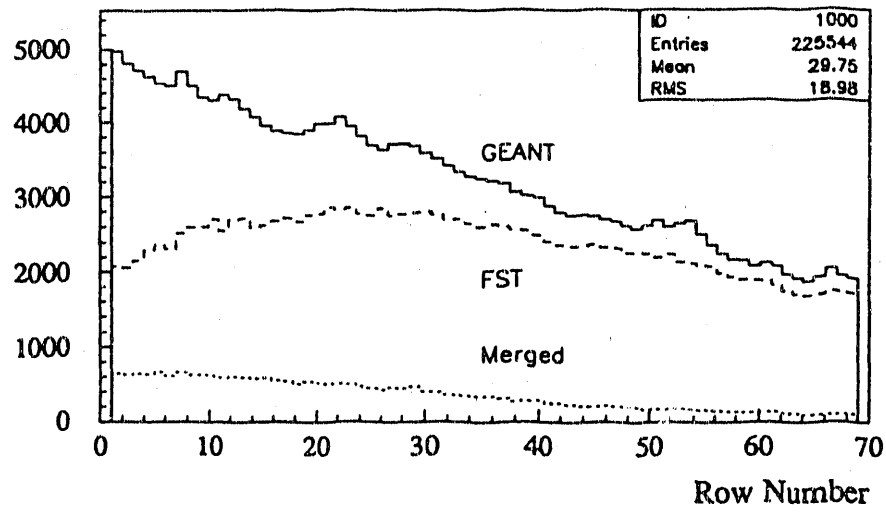

Figure 4C-8 Total hit multiplicity as a function of pad row for a central Au + Au event.

4.C.3.c Track Finding and Fitting

Central collisions at RHIC are expected to produce several thousand particles per central collision. The resulting track densities in the STAR TPC are compared with those measured and successfully tracked in the CERN NA36 experiment in Fig. 4C-9. The track densities measured successfully in the CERN NA35 TPC lie between the STAR and NA36 values. Therefore, tracking in the STAR TPC at RHIC should present no problem even at track densities an order of magnitude higher than expected. Pattern recognition for the STAR TPC has been based on an algorithm developed for the

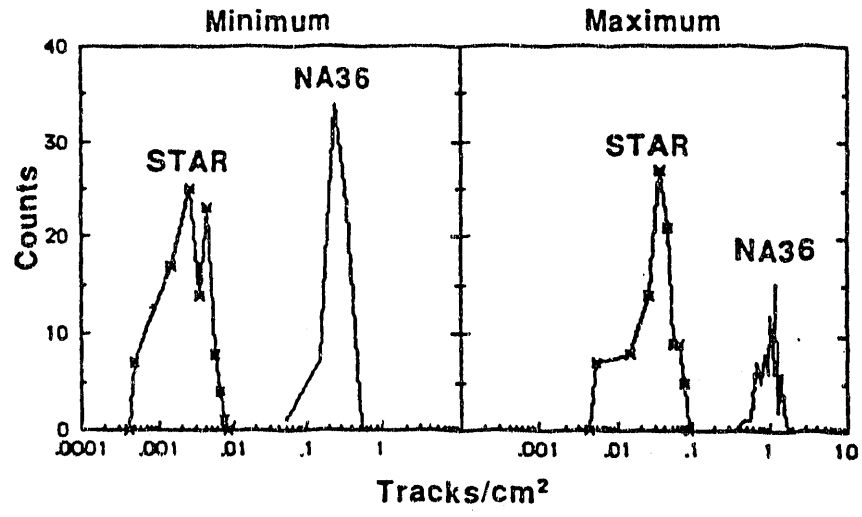

Figure 4C-9 A comparison of track densities between NA36, and STAR.

ALEPH TPC[21] . Modifications for the high track multiplicities encountered in relativistic heavy-ion collisions has been made following experience gained with the CERN experiment NA36.

The procedure for track reconstruction consists of the following steps:

- Short track segments are formed by simple extrapolation.
- A helix fit to each segment is performed .
- The segments are extrapolated using the helix parameterization.
- Track segments from a single spiraling particle are merged.

The formation of track segments starts at the outermost radius of the TPC where the hit density is lowest. Starting from each hit on the outermost pad row all possible 3-hit links are formed with hits on the next inner 2 rows. Each link is then extended using a linear extrapolation based on the local gradient of the track. When the linear extrapolation fails, a helix is fit to each of the segments and the best track candidate originating from any given hit is selected. The criteria for this selection are track length and $\chi 2$ probability of the fit. The best candidate is preserved for later analysis and hits that belong to it are removed from the pool. This procedure is repeated, row-by-row for all of the hits remaining in the pool until the innermost pad row is reached.

In order to extract the parameters which best describe the track, a helix is fit to the first half turn of the spiral. The helix fit consists of two independent components: a circle fit in the x-y (bend) plane and a straight line fit in the s-z plane, where s is the track length. The track length is calculated from the point on the track which is closest to the origin of the coordinate system. From the helix parameters a momentum vector may be calculated at any point along the track trajectory.

In the next step, an attempt is made to assign more hits to each of the reconstructed segments and to merge fragmented tracks. At this point all of the hits are marked as unused and returned to the pool. Then starting from the longest segment, all hits that are consistent with the helix parameterization for each segment are assigned to a track and removed from the pool. After the addition of each hit, the track is refit, providing progressively better predictions for subsequent hits. In the process of track extension, hits may be removed from shorter tracks. If sufficient hits are claimed from another segment, this will result in that segment being dropped as a track candidate. In this way tracks which were reconstructed in two or more segments in the initial stages of track reconstruction, may be merged to form a single track. By starting with the longest track candidates, the most accurate extrapolations are undertaken first. This optimizes the elimination of short track segments.

The procedure described above does not, however, merge pieces of a track which result from different turns of a helix. This is because the helix extrapolation is performed only within one turn. In an attempt to merge pieces of spiraling tracks, the dip angles, momenta in the bend plane and positions of the centers are compared in the final track sample. Tracks with similar values of these parameters may be merged on the condition that they do not overlap in z.

---

[21] Status of Reconstruction Algorithms for ALEPH (Ed. J. Knobloch and P. Norton).

The track reconstruction algorithm is constantly under evaluation, and work continues in determining the efficiency by comparing reconstructed tracks with the Monte-Carlo information output from GEANT. Hits which are lost on the innermost padrows, due to hit-merging in the FST simulation, reduce the available track length for reconstruction and may lead to track fragmentation due to merged hits lying outside the tolerances of either of the parent tracks. In Fig. 4C-10 the number of reconstructed track segments is plotted for each Monte-Carlo primary track in a central Au+Au event within a pseudorapidity interval of $|\eta| < 1$. An additional requirement is imposed that there should be at least 5 hits from FST available for each track since this is the lower limit for track reconstruction. This plot shows that the efficiency for reconstructing tracks in one or more segments is approximately 91%. In detail, 52% are reconstructed as a single track, 30% as two tracks and 8% as three tracks. Over the range of p_t from 150 to 600 MeV/c, the efficiency is a constant 93%, but falls off below 150 MeV/c. The average efficiency of 91% assumes that fine tuning of the track merging algorithm may greatly reduce the number of fragmented tracks. Improvements in the matching procedure are also expected with the better two track resolution which can be obtained by employing to 3.35×12 mm^2 pads in the inner padrows.

The quality of the reconstructed tracks is shown in Fig. 4C-11. This quality is defined as the ratio of correct hits assigned to a reconstructed track to the total number of hits assigned to the reconstructed track. As can be seen in the figure, less than 5% of the reconstructed tracks have a quality ratio of less than 0.8. The low quality tracks are primarily either low momentum or have a short useable track length in the TPC.

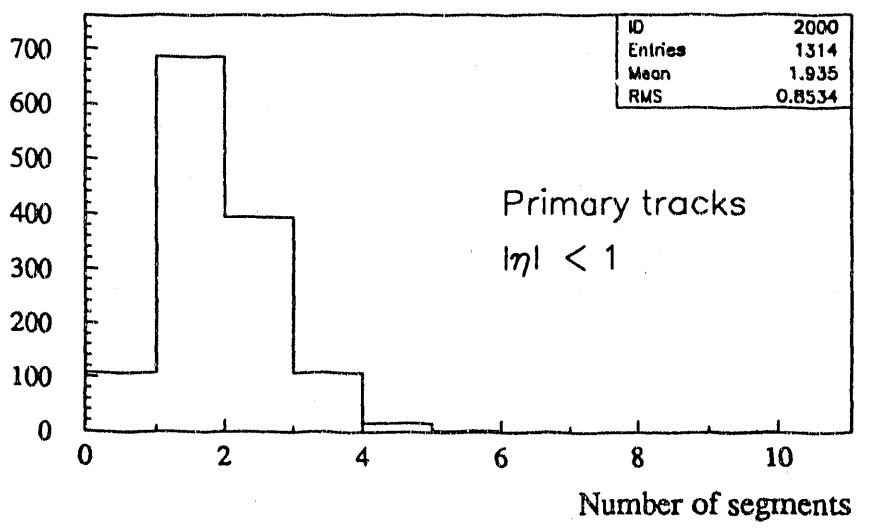

Figure 4C-10 Number of reconstructed segments per primary input track with $|\eta| < 1$ and more than 5 hits in the TPC from an Au + Au central event,

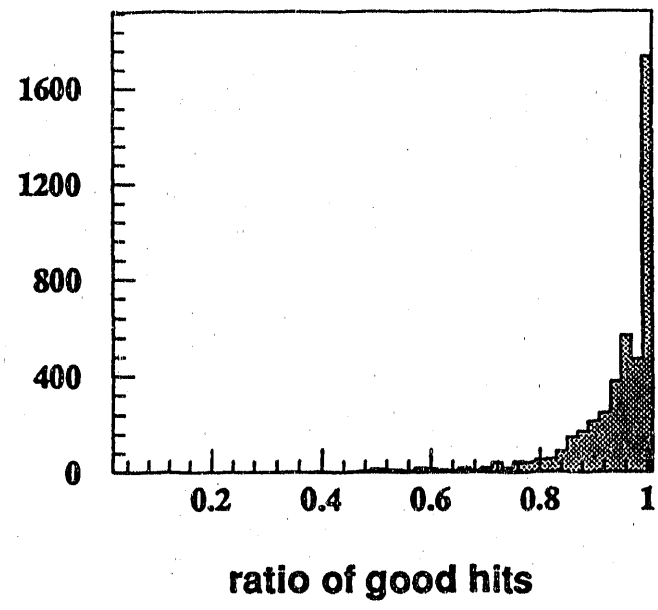

Figure 4C-11 Quality index for reconstructed tracks.

4.C.3.d Spatial Resolution

In this section we briefly outline the expected contributions to the uncertainty in space point reconstruction for two pad sizes: 8×12 mm^2 and 8×20 mm^2. This analysis is similar to that of subsection 4.C.2.r, however, in that subsection the width of the signal at the pad plane was determined in an effort to understand under what circumstances two-tracks could be separated. In this subsection, the uncertainty in the spatial resolution for isolated tracks is analyzed. The pad spatial resolution function is given by[22],

$$\sigma^2 = \sigma_A^2 + \sigma_B^2 \lambda\, e^{\gamma\lambda} \sec\alpha + \sigma_C^2 e^{\gamma\lambda} \cos\alpha \tan^2\alpha \qquad \text{(4C-17)}$$

where,

λ - is the drift length (in meters)
α - is the wire crossing angle
$e^{\gamma\lambda}$ - is the inverse of an attenuation factor appearing in the denominator

The three terms correspond to an intrinsic resolution σ_A, determined by the signal-to-noise ratio on the pads, a diffusion term σ_B, and a term which accounts for the crossing angle of the track relative to the normal of the pad row. Experience with the EOS TPC has found the effect of attenuation, due to electron capture, to be negligible, therefore $\gamma \rightarrow 0$ and $e^{\gamma\lambda} \rightarrow 1$.

[22] R. Sauerwein, TPC-LBL-83-18, and H. Aihara et al., IEEE NS-30(1983)76.

The signal-noise term, σ_A:

The effect on the spatial resolution due to electronic noise on the pads can be determined from the simple prescription of G. Lynch [23]. Here, the hit position is calculated from the pads with the two largest pulse heights. For a given x-position of the hit, $\bar{x}$, the pulse height is determined from the Gaussian response function,

$$h(x - \bar{x}) = A\, e^{-(x - \bar{x})^2/2\sigma^2} \tag{4C-18}$$

where σ is the width of the pad response, x is the pad position and A is the maximum pulse height. For a hit at some point between two pads with centers x_1 and x_2, the hit position may be determined using,

$$\bar{x} = \frac{\sigma^2}{\Delta x} \ln\left(\frac{h_2}{h_1}\right) + \frac{x_1 + x_2}{2} \tag{4C-19}$$

where Δx is the pad pitch (8 mm) and the uncertainty in $\bar{x}$ is then given by,

$$\delta\bar{x} = \frac{\sigma^2}{\Delta x}\left(\frac{dh_2^2}{h_2^2} + \frac{\delta h_1^2}{h_1^2}\right)^{1/2} \tag{4C-20}$$

Arbitrarily setting A = 1 and assuming a signal-to-noise ratio of 20 : 1, $\delta h_2 = \delta h_1 = 0.05$. The best resolution is obtained when the track crosses between the two pads, whereupon the calculated resolution, assuming $\sigma = 0.362$ cm[24], is 213 μm. In the worst case, where the hit is centered above one pad, the resolution deteriorates to 949 μm. However, if a three pad hit were registered, this would considerably improve the resolution. In this case the resolution would be approximately 666 μm.

The diffusion term, σ_B:

The coefficient of the diffusion term may be written as,

$$\sigma_B^2 = \frac{\sigma_D^2}{N_o} \tag{4C-21}$$

where σ_D is the coefficient of the diffusion from the pad response function and N_o is the total number of electrons liberated along the pad length. For a P9 (91% Ar and 9% CH_4) gas mixture at atmospheric pressure the mean ionization for a minimum ionizing particle is 100 electrons per cm[25]. Thus for 20 mm and 12 mm pads the value of σ_B was calculated to be 166 μm and 213 μm respectively.

---

[23] G. Lynch, TPC-LBL-78-17.
[24] P.G. Jones and G. Rai, STAR note 33.
[25] ALEPH Handbook, ALEPH 89-77.

The angular wire term, σ_C:

This term has been measured in the case of PEP4[26], with B = 0.4 T, E = 15 kV/m using a P20 (80% Ar and 20% CH_4) gas mixture at atmospheric pressure. Here, a value of $\sigma_C(8 \times 8\ mm^2) = 665 \pm 25\ \mu m$ was reported. Scaling this value by the pad length, calculated values of σ_C for 20 mm and 12 mm long pads are 1663 μm and 998 μm respectively. ALEPH identifies this term as the angular pad effect,

$$\sigma_C^2 = \frac{h^2}{12\, N_{eff}} \tag{4C-22}$$

where h is the pad length and N_{eff} is the effective number of electrons per unit length sampled by the wire. The value of N_{eff} depends on diffusion, which provides a declustering effect for ionization fluctuations along the track. Equation 4C-22 justifies the simple scaling assumption applied to the PEP4 data. Furthermore, using the measured result from the ALEPH prototype TPC-90, it can be shown that a suitable number for N_{eff} is $N_{eff} = 12$. Inserting this value into Eq. 4C-22, σ_C for 20 mm and 12 mm long pads is found to be 1667 μm and 1000 μm respectively. These values agree with those derived from scaling the PEP4 measurements above.

The final values obtained for the coefficients of the three terms in the pad resolution function of Eq. 4C-17 are listed in Table 4C-7.

Table 4C-7 Summary of the final values obtained for the coefficients in the pad resolution function for 8 × 12 mm² and 8 × 20 mm² pads.

	$8 \times 12\ mm^2$	$8 \times 20\ mm^2$
σ_A (μm)	440†	440†
σ_B (μm)	213	166
σ_C (μm)	999	1665

† Average value

4.C.3.e Transverse Momentum Resolution

An axial magnetic field like that of STAR allows a measurement of the transverse component of the momentum, p_t. Low p_t particles ($p_t \leq 1$ GeV/c) are important for the thermodynamic observables and HBT analysis. Higher p_t particles come from the fragmentation of jets and mini-jets. It has been suggested that the ratio of inclusive p_t spectra at large p_t for pp, pA and AA collisions at RHIC will enable one to investigate the effects of nuclear shadowing and quenching on jet and mini-jet production.[27] The ability to make these physics measurements depends crucially on the single particle momentum resolution at both small and large p_t.

[26] R. Sauerwein, TPC-LBL-83-18.
[27] X. N. Wang and Miklos Gyulassy, Phys. Rev. Lett. 68, 1480 (1992).

A realistic study of the p_t resolution using the standard STAR TPC Monte Carlo and track reconstruction algorithm was carried out in order to ascertain the ability of the TPC, with and without the SVT, to meet the physics objectives of STAR. Particles from central Au+Au FRITIOF events were tracked through the STAR detector setup with all physical processes turned on. In order to enhance the statistics of high p_t tracks, a finite number of high p_t particles were superimposed onto the FRITIOF Au+Au events. For this calculation the TPC were simulated using straight pad rows with 8×20 mm^2 pads. The momentum resolution was evaluated by comparing the transverse momentum of reconstructed and generated tracks.

Figure 4C-12 shows the p_t resolution ($\equiv \Delta p_t/p_t$) as a function of p_t. The inset frame is a blow-up of the results for $p_t < 1$ GeV/c. Track fitting was performed for two cases: 1) using hit information from the TPC alone (shown as black dots), and 2) using hit information from both the TPC and SVT (shown as open triangles). For the low p_t tracks ($p_t < 1$ GeV/c), the momentum resolution (dominated by multiple scattering) reaches a minimum of 1.6% at $p_t \approx 0.4$ GeV/c, where the bulk of particles are produced. Below p_t=0.4 GeV/c $\Delta p_t/p_t$ grows due to the $1/\beta$ factor in the multiple scattering term. As p_t increases beyond 1 GeV/c, $\Delta p_t/p_t$ grows linearly with p_t and is dominated by the position resolution of the TPC hits. The p_t resolution increases from 3% at a p_t of 3 GeV/c to 14% at 12 GeV/c. The curve represents an analytical formula for the p_t resolution[28], where some adjustment of the parameters of the curve have been made to optimize the fit.

The pad size of 8×20 mm^2 is not small enough to differentiate hits from close tracks in the inner rows of the TPC for the high particle density environment of Au+Au collisions. Hence the usable path length for track reconstruction is reduced and the momentum resolution deteriorates. Quantitatively, a track with a p_t of 5 GeV/c has a resolution of 2.9% when it is tracked alone in the TPC and deteriorates to 5.4% when superimposed on a central Au+Au event. The SVT has a much smaller pixel size than the TPC which significantly enhances the hit position resolution close to the primary vertex. The inclusion of SVT hits in the track fitting improves the p_t resolution by a factor of two or more for the high p_t tracks. This improvement is a consequence of the addition of a few well defined hits close to the primary vertex, which increase the effective path length for track fitting. Perfect matching of TPC hits with the SVT hits was assumed. Inclusion of the primary vertex as a point in the helix fit will provide an improvement in the momentum resolution that is comparable to that observed when the SVT points are added. This technique is only helpful for primary tracks.

[28] Data Analysis Techniques for High Energy Physics Experiments, R.K. Bock, H. Grote, D. Notz, M. Regler (Cambrigde: Cambridge University Press, 1990) pp. 310-3.

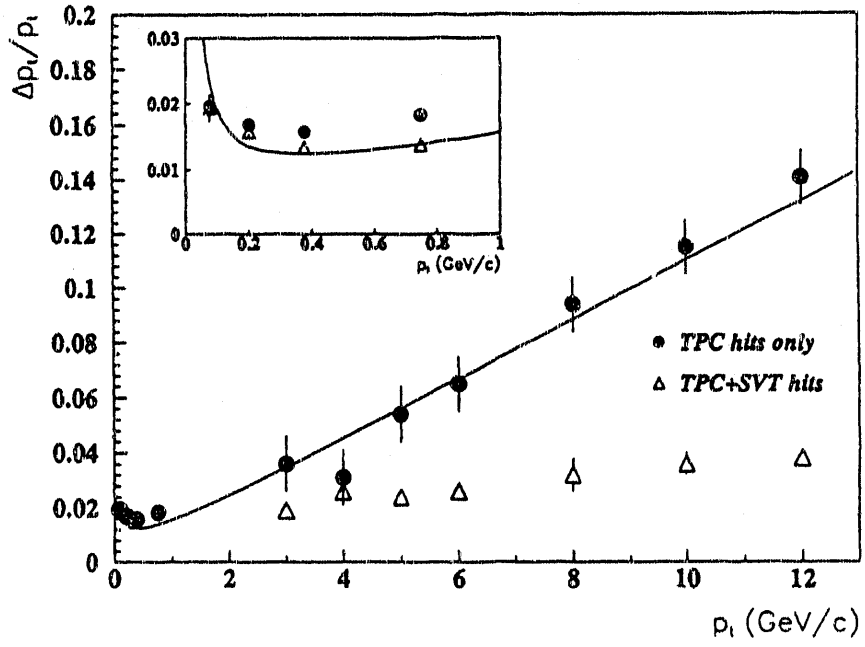

Figure 4C-12 P_t resolution as a function of p_t for both the TPC only and TPC + SVT cases.

A design employing circular pad rows for the TPC should improve the momentum resolution for high p_t tracks. Studies of p_t resolution for circular pad rows and reduced pad size for the inner sectors are in progress. The impact of the momentum resolution on the HBT measurement is discussed in section 4.C.3.g.

For high p_t tracks, the main effect of the momentum resolution on inclusive p_t spectra is to skew the distribution toward higher p_t values. This effect is shown in Fig. 4C-13, which displays the ratio of a momentum resolution "smeared" distribution to the same "unsmeared" distribution, using the p_t resolution of the TPC with and without SVT hits as shown in Fig. 4C-12. The unsmeared distribution is $\propto p_t(1 + p_t/1.8)^{-12.14}$, which is a parameterization of the inclusive charged particle spectrum for $p\bar{p}$ collisions at $\sqrt{S}$ = 200 GeV.[29] Note that the ratio is monotonically increasing with p_t. Gluon shadowing and jet quenching are expected to reduce dramatically the yield of charged particles for $p_t > 2$ GeV/c from central Au+Au collisions.[30] In order to disentangle gluon shadowing from jet quenching, it is necessary to study pp and pAu collisions up to $p_t = 6$ GeV/c as well. The deviation of the smeared distribution from the unsmeared parent distribution is on the order of a few percent in the p_t region of 2-6 GeV/c for TPC tracks without SVT hits. If the SVT hits are included the effect of smearing is minimal all the way out to $p_t = 10$ GeV/c. With the present simulation we conclude that the TPC alone should provide sufficient p_t resolution for a study of inclusive spectra up to $p_t = 6$ GeV/c, and the addition of SVT hits extends this p_t limit to above 10 GeV/c. Note that for stiff tracks, use of the reconstructed primary vertex location would

[29] C. Albajar et al. (UA1 Collaboration), Nucl. Phys. B335, 261 (1990).
[30] X. N. Wang and Miklos Gyulassy, Duke-TH-91-25.

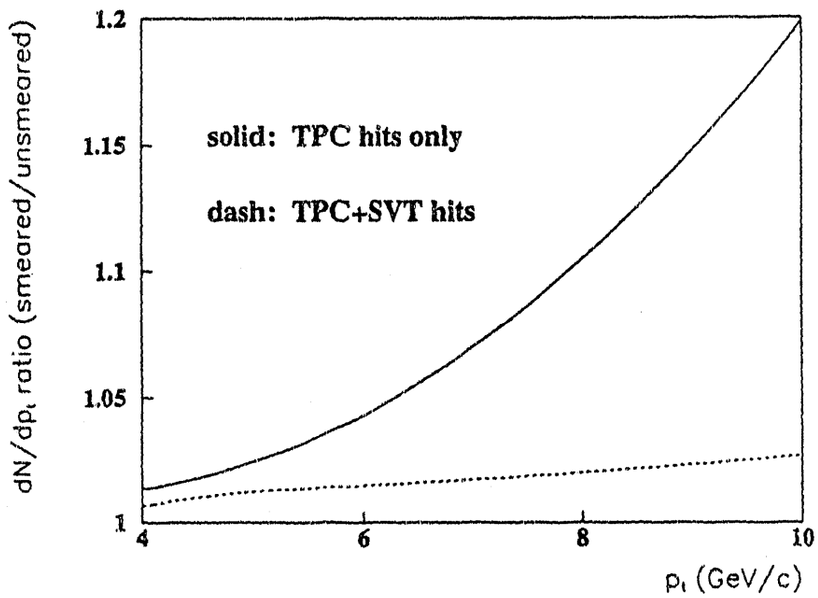

Figure 4C-13 The effect of momentum resolution on the measured yield assuming measurement with TPC alone (solid) and TPC + SVT (dashed).

have an effect comparable in magnitude to that observed when SVT hits are included, and it is safe to assume that stiff tracks originate from the primary vertex.

4.C.3.f dE/dx and Particle Identification

For the purpose of predicting the dE/dx resolution of the STAR TPC, we use the simulation chain consisting of the Lund/FRITIOF event generator, GEANT, the FaST simulator and the tracker. To predict the truncated mean dE/dx signal associated with each reconstructed track, we use empirical expressions (detailed below) which have consistently described dE/dx resolutions of previous detectors. An alternative procedure is to use GEANT to generate the individual dE/dx samples associated with each hit on each track and then to apply a truncation. This scheme has not yet been tested for STAR, but in the case of the EOS TPC, the empirical approach gives a more accurate description of the experimental data.

Cowan[31] has reported the following parameterization for the dE/dx resolution observed in the PEP4 TPC for both minimum ionizing particles, and particles in the relativistic rise region:

$$\sigma_{dE/dx} = \sqrt{a/N + b}\,(1 + cN + d\,|90^\circ - \theta|)\,(dE/dx)_{trunc.} \qquad (4C\text{-}23)$$

where N is the number of samples and θ is the polar angle with respect to the beam direction; the fitted coefficients a, b, c , and d are 0.168, 4.62×10^{-4}, -5.46×10^{-4}, and -0.258, respectively. Cowan has also reported that the resolution improves as $(dE/dx)^{-0.35}$ in the $1/\beta^2$ region.

[31] Glen Cowan, Ph. D. thesis, LBL-24715 (1988).

A widely used empirical expression, first described by Walenta[32] and by Allison and Cobb[33], describes the resolution at minimum ionization, for N dE/dx samples of length h cm in argon gas with up to 20% CH_4 at a pressure of P atmospheres:

$$\sigma_{dE/dx} = 0.47N^{-0.46}(Ph)^{-0.32}(dE/dx)_{trunc.} \quad (4C\text{-}24)$$

The N-dependences specified by Eqs. 4C-23 and 4C-24 are quite similar, and Eq. 4C-24 is averaged over the relatively weak θ-dependence described by Eq. 4C-23. Many detector groups have reported resolutions[34] consistent with Eq. 4C-24. Their results are summarized in Table 4C-8:

Table 4C-8 A summary of the dE/dx resolution from other detectors.

	Detector	N	h (cm)	P (atm)	Observed σ (%)	Eq. 4C-24
SLC	MARKII	72	0.83	1.0	7.2	7.0
CESR	CLEO	51	1.4	1.0	6.5	6.9
TRISTAN	TOPAZ	175	0.4	3.5	4.6	3.9
LEP	DELPHI	192	0.4	1.0	5.5	5.6
PEP	PEP TPC	183	0.4	8.5	3.4	2.9
LEP	ALEPH	340	0.4	1.0	5.1	4.3
LEP	OPAL	120	1.3	4.0	3.4	3.1

We use Cowan's formula, scaled for P = 1 atmosphere and h = 2 cm using Eq. 4C-24.

Figure 4C-14 shows the simulated distribution of N for reconstructed tracks with $40^\circ \le \theta \le 140^\circ$ ($|\eta| < 1.01$) in a central Au + Au event. About 1/5 of the reconstructed π's and more than 1/3 of the reconstructed K's decay in the TPC, so even for an ideal tracking detector with perfect reconstruction efficiency, the distribution of N within $|\eta| < 1$ will include many entries at low N. Figure 4C-15 shows the corresponding prediction for dE/dx versus momentum for all tracks with $N \ge 20$ in 4 central Au + Au events. Near 100 MeV/c and below, some marginal separation begins to open up between the band for pions and the band for muons resulting from the decay of slow pions. However in such cases we can more efficiently identify the muons by decay topology rather than dE/dx. We find that N, which is the most important parameter in determining the dE/dx resolution, is only weakly correlated with other variables such as momentum in this range of θ. Consequently, we can greatly improve statistics while preserving the main features of Fig. 4C-15 by bypassing the normal simulation chain and randomly assigning N-values according to Fig. 4C-14. Figure 4C-16 shows this simplified simulation of dE/dx versus momentum for tracks from 100 central Au + Au events. Above about 2 GeV/c, dE/dx resolution is good enough to separate most kaons

[32] A.H. Walenta, Nucl. Instr. and Meth. **161**, 435 (1979).
[33] W.W.M. Allison and J.H. Cobb, Ann. Rev. Nucl. Part. Sci. 30, 253 (1980).
[34] Compilation from *Symposium on Particle Identification at High Luminosity Hadron Colliders*, Fermilab, G. Lynch (1989).

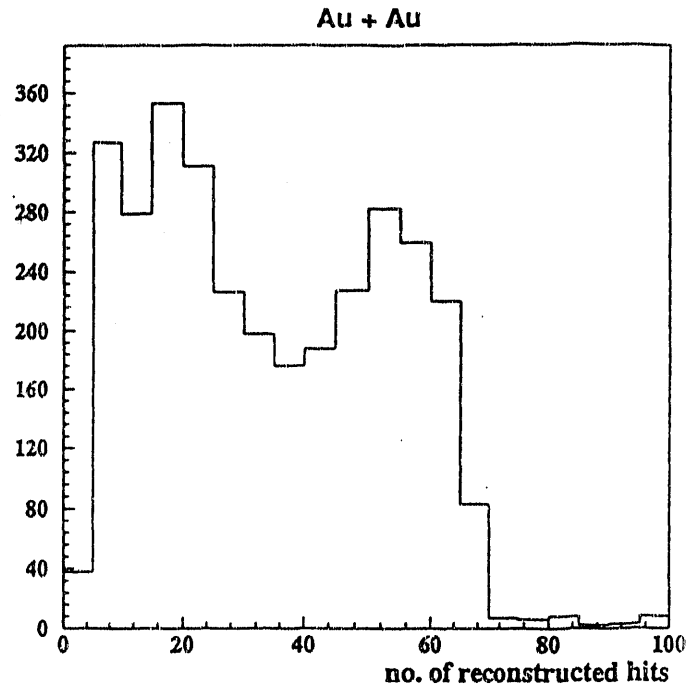

Figure 4C-14 The distribution of the number of usable dE/dx samples associated with each track within $|\eta| < 1$ for one central Au + Au event.

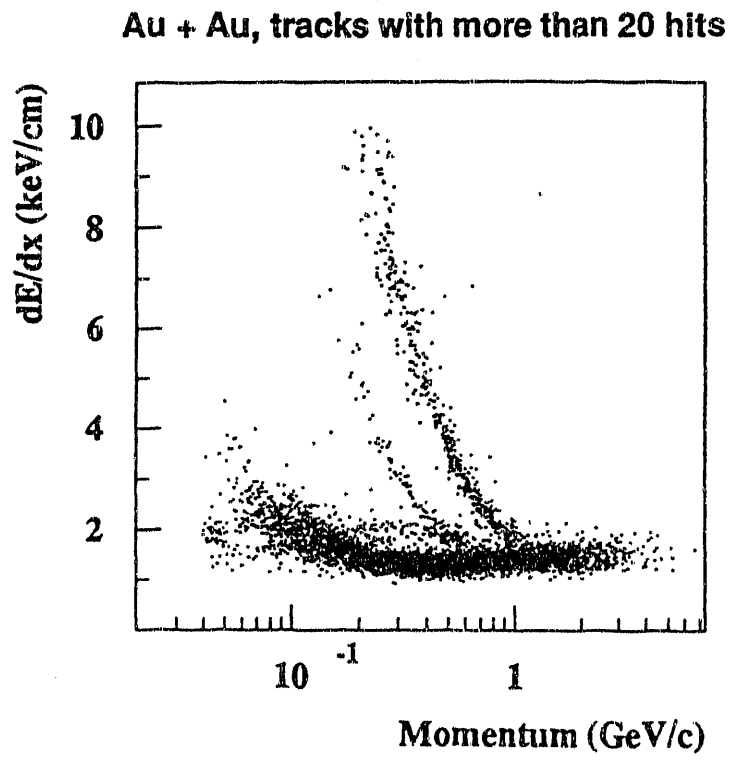

Figure 4C-15 dE/dx vs. momentum for all tracks within $|\eta| < 1$ and with $N \geq 20$ for 4 central Au + Au events.

and protons from pions (but not from each other). Figure 4C-16 demonstrates that the population of tracks in the relativistic rise region is very low, and dE/dx information from this region is insignificant in terms of its contribution to the overall percentage of identified particles. However, for the purpose of flavor tagging of leading particles in jets, dE/dx might still provide some useful information; this question deserves further study. Assuming that we utilize dE/dx information only in the $1/\beta^2$ region, where the separation between bands increases very strongly with decreasing momentum, some degradation of dE/dx resolution due to uncorrected instabilities in gas gain could be tolerated. Overall, we conclude that reliable identification of kaons and protons can be achieved below momenta of 0.6 - 0.7 GeV/c and 1.0 - 1.1 GeV/c, respectively.

Figures 4C-15 and 4C-16 show the expected incidence of electrons from Dalitz decays of the π^0 and from γ conversions. The contamination of the pion sample by such electrons is only at the level of a couple of percent where the pion and electron bands intersect. There is even less contamination in the case of kaons. Because of this relatively small number of electrons, the dE/dx information from the TPC is not critical for separating electrons from other particle species.

An important consideration for HBT studies is whether global tracking algorithms such as elastic tracking[35] might be used to measure the relative momentum of pion and kaon pairs in cases where the two particles are unresolved for most of their track length in the TPC. For those cases identified by elastic tracking as overlapping tracks, identification of the particle species via dE/dx can be made as shown in Fig. 4C-16. The lower (upper) dashed line in this figure shows the position of the dE/dx band for two overlapped pions (kaons) and the dotted lines show the positions of other possible overlapped cases: πe, πk, πp, ke, and kp. Since an overlapped pion pair is much more probable than any other overlapped pair, Fig. 4C-16 indicates that dE/dx could help identify overlapped pions over most of the available phase space. Identification of overlapped kaon pairs through dE/dx is much more difficult because of the low rate of such pairs and the fact that they are close to the proton band for momenta above about 0.3 GeV/c.

[35] M. Gyulassy and M. Harlander, Nucl. Instr. and Meth. (in press, 1992).

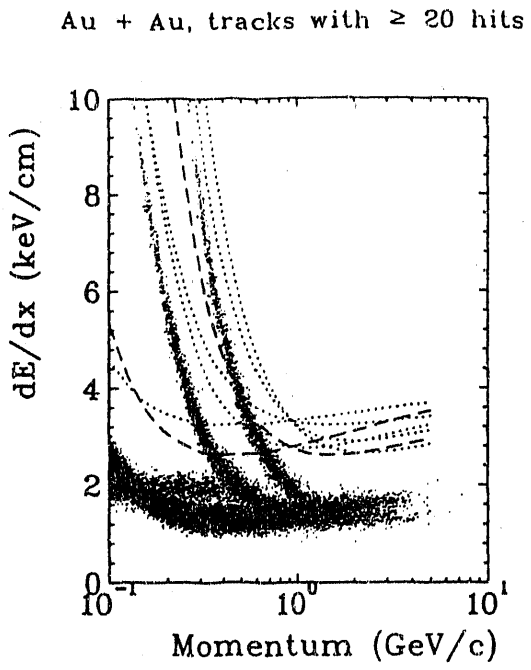

Figure 4C-16 Same as previous figure, except that a simplified simulation has been performed which allows higher statistics (100 events). The dashed and dotted lines show the expected dE/dx for particle pairs whose relative momentum is too small for them to be resolved as separate tracks (see text).

4.C.3.g Hanbury-Brown Twiss (HBT) Correlation Analysis

Correlation functions of identical final state particles contain information on the space-time dimensions of an emitting source. Many experimental efforts have utilized two-particle correlation functions of identical particles to gain an understanding of the dynamics of nucleus-nucleus collisions. There are several physical effects (hydrodynamical evolution, resonance decays, presence or absence of a phase transition) that may contribute to the source lifetimes and radii extracted from such correlation functions[36], so that only a detailed experimental study may significantly constrain theoretical models describing the collisions and give insight into the contributions of the various physical effects. The large value of $dN/d\eta$ expected in central Au-Au collisions raises the possibility of measuring the source radius on a *single event* basis, so that anomalous radii can be correlated with other measures of unusual dynamics to identify interesting events. However, this is a demanding task requiring sufficient statistics at small relative momenta to give a sufficiently precise result.

The phase space of a pair of identical particles can be described by six variables: the rapidity y, transverse momentum p_t, azimuthal orientation ϕ of the mean momentum vector of the pair, and the components of the three-momentum difference vector $q=p_1-p_2$ defined in the laboratory frame of reference. The Lorentz invariant 4-momentum difference Q is related to q via $Q^2 = q_0^2 - q^2$. In the following discussion, we

[36] S. Padula, M. Gyulassy and S. Gavin, Nucl. Phys. B329 (1990) 357.

will consider the components of q which are in the beam direction q_{beam}, parallel to the mean momentum of the pair in the transverse plane q_{par}, and perpendicular to the mean p_t q_{perp}. These are the appropriate components for studying a boost invariant, longitudinally expanding source [37]. In addition, due to the cylindrical symmetry of STAR, the resolution of the transverse components of q are independent of z.

The azimuthal orientation of the pair is not relevant for inclusive measurements. The interval covered by the STAR TPC with particle identification is $|\eta|<1$. This is expected to lie within the plateau (boost invariant) region, and the physics of the reaction volume is not expected to depend on η in this range. Though there may be interesting classes of events with varying structure within $|\eta| < 1$, we do not consider this possibility for the calculations presented here. Rather, we discuss correlation functions integrated over $|\eta|<1$. We therefore expect four dimensions of phase space, namely (p_t,q), to be fruitfully explored with identical particle correlation functions.

The transverse radii that will be measured at RHIC are unknown; however, extrapolation from current, lower energy measurements[38] suggests radii of magnitude 12-15 fm. We therefore set as our goal the ability to measure radii as large as 20 fm. In order to study STAR's capability of doing this it is necessary to track correlated pions generated from such a source through the full simulation and then fit the resulting correlation function. We have not yet performed such a detailed simulation. However, we can obtain an idea of what is required as follows: the conjugate momentum to 20 fm is 10 MeV/c, which will roughly be the value of the inflection point in the correlation function. If we demand at least two bins within the inflection point, we arrive at the requirement to resolve pairs having momentum difference ~5 MeV/c.

From the experimental point of view, there are four principal difficulties in carrying out correlation measurements: q resolution (i.e. two-track momentum difference resolution), particle identification, rate, and pair reconstruction efficiency. The pair reconstruction efficiency in the TPC is strongly dependent upon the tracking algorithm used. We have not implemented an algorithm optimized for tracking close pairs, so we do not discuss the efficiency here. We address each of the other points separately.

(i) q Resolution:

q_{par} probes the longitudinal source radius and temporal extent of the source, and q_{perp} probes the transverse source radius. The resolutions of q_{par} and q_{perp} in the STAR TPC have been studied using the standard STAR simulation and tracking algorithms (sections 4.C.3.b and 4.C.3.c). Pion pairs of a given q_{par} and q_{perp}, for a single particle p_t around 250 MeV/c in the region of central pseudorapidity, were tracked in the TPC and the resolution was obtained by comparing the reconstructed q values with that of the input pairs. A pad size of 8×20 mm^2 was used in the simulation, and a minimum of 15 hits was required for each track of the pair.

---

[37] M. Gyulassy and S. Padula, Phys. Lett. B217 (1988) 181.
[38] R. Stock, Ann. der Physik, 48 (1991) 195.

Figure 4C-17 shows typical q_{par} and q_{perp} resolutions for either q_{par} or q_{perp} restricted to a 5 MeV wide bin and the other component with the indicated value. Typical resolution of q_{perp} is 5 MeV/c, while that of q_{par} is 10 MeV/c. Using the criterion of at least two bins within the inflection point of the correlation function, the corresponding maximum measurable source parameters are 20 fm in the transverse direction and 10 fm in the longitudinal-temporal direction.

The inclusion of hits from the the SVT is expected to improve the q_{perp} resolution but not the q_{par} resolution. Future developments that may improve the resolution for HBT are the development of tracking algorithms specifically targeted to close pairs, and the implementation of smaller pads in the inner and outer radius of the TPC to enhance the two-track separation capability.

(ii) Particle Identification:

The particle identification (PID) capabilities of the STAR TPC are addressed in sub-section 4.C.3.f. For HBT, the PID requirement is to identify a pair of tracks that are close in momentum space and which are possibly overlapping through a large portion of the TPC. This is especially important for KK HBT measurements, where positive identification is essential. It has been shown[39] that the increase in pulse height for two tracks integrated together relative to one track leads to an increase in dE/dx resolution. However, distinguishing a pair of kaons from a pair of pions requires higher resolution than the single track case because of the presence of "interpolating" πK pairs between the dE/dx bands of $\pi\pi$ and KK. In addition, in some momentum ranges the dE/dx band for KK overlaps that for single protons (Fig. 4C-16), so that unique identification of a pair of tracks using only dE/dx information is not possible. Global tracking algorithms such as Elastic Tracking [40] must be used to recover q resolution for such overlapping tracks. A basic property of these algorithms is their ability to distinguish single from double tracks based on the geometry of the charge distribution as a function of distance along the track. Thus, dE/dx information combined with geometrical charge distribution information may permit q resolution and unambiguous identification for close-lying pairs. However, this procedure contains many uncertainties and requires significant development before it can be shown to be feasible.

[39] P.Jacobs, STAR Note #12.
[40] M.Gyulassy and M. Harlander, NIM in press, Comp. Phys. Comm. 66 (1991) 31.

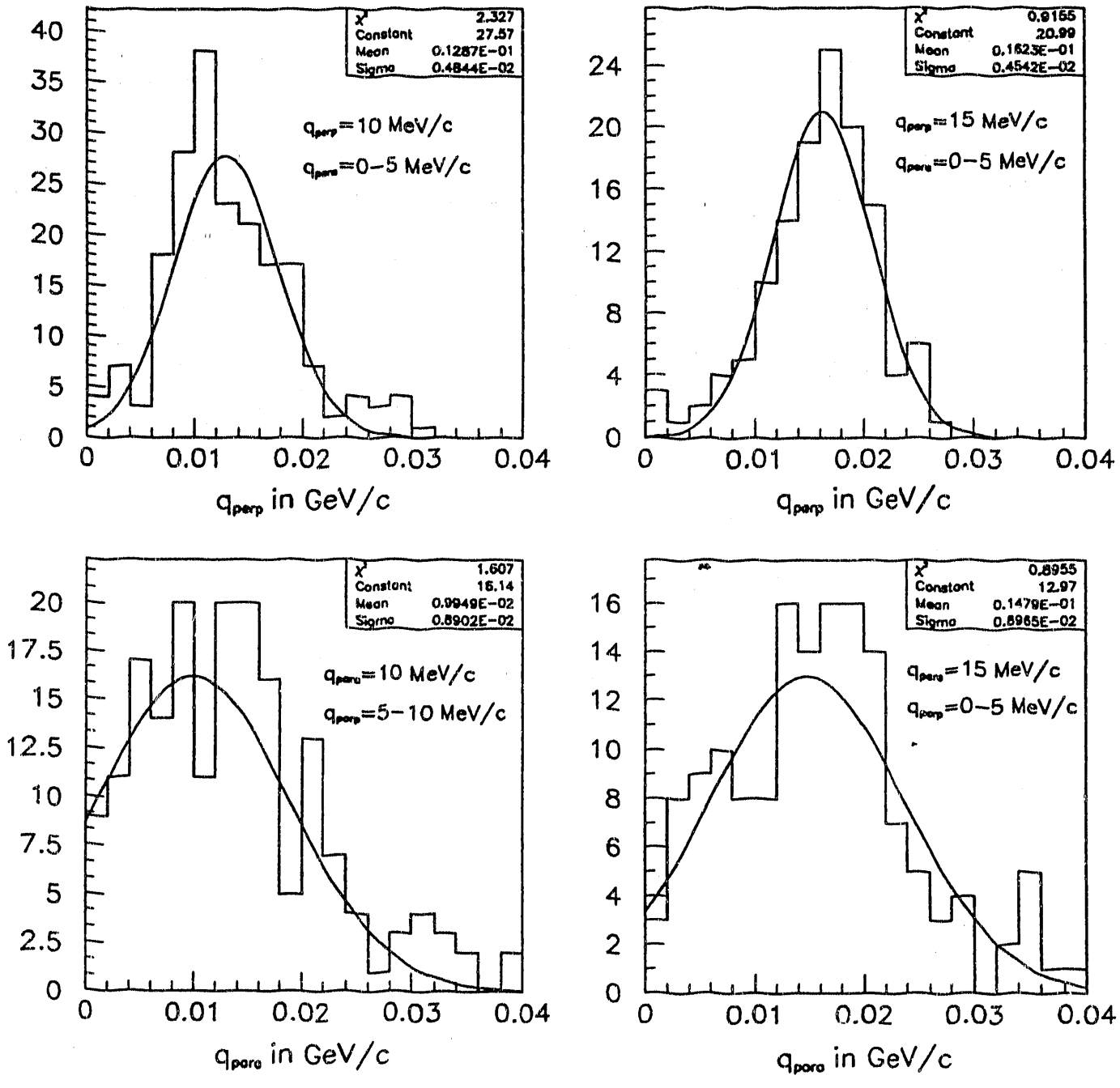

Figure 4C-17 Reconstructed Lorentz invariant momentum resolution in the STAR TPC for a pair of pions; η=0, p_T=250 MeV/c. Upper panels: reconstructed q_{perp} for input q_{par} < 5 MeV/c, input q_{perp} = 10 MeV/c (left) and 15 MeV/c (right). Lower panels: reconstructed q_{par} for input 5 < q_{perp} < 10 MeV/c, q_{par} = 10 MeV/c (left) and q_{perp} < 5 MeV/c, q_{par} = 15 MeV/c (right)

(iii) Rate:

To investigate the rate question, we have studied the phase space density of **q** within a simple but representative Monte Carlo model for which high statistics could be generated. Uncorrelated particles were generated uniformly in azimuth and rapidity and with single particle p_t distribution

$$P(p_t)dp_t = \frac{p_t \cdot e^{-(p_t/T)}}{T^2} dp_t \qquad \text{(4C-25)}$$

with T≈200 MeV/c for pions and T=400 MeV/c for kaons. This distribution is a reasonable match to the p_t distributions generated by FRITIOF, given in Figure 10 of the original STAR LOI. The different T parameters account for the differing $\langle p_t \rangle$ between pions and kaons. $dN/d\eta$ was chosen to be the number of pions or kaons of a single species identified via dE/dx in the STAR TPC[41]: $dN/d\eta(\pi)=200$, $dN/d\eta(K)=10$. The following results can be scaled by $(dN/d\eta)^2$ to obtain rates for other multiplicity densities.

Dynamical information may be obtainable by studying correlation functions through multi-dimensional binning of (p_t,q) space. Such binning of phase space is clearly only achievable on an inclusive basis, especially for high p_t. Table 4C-9 shows the number of pairs per 100 days for a single species of pion or kaon within various bins of p_t and magnitude of the Lorentz invariant momentum difference Q. Correlation, Coulomb and strong interaction effects have not been accounted for. Coulomb repulsion is especially important for kaons, where the net effect of correlation and Coulomb repulsion is expected to decrease the rate by a factor ~5 at small Q . Since Table 4C-9 gives rates only as a function of Q, rates for binning simultaneously in components of **q** will necessarily be smaller than those given in the table. The expected rate of pion pairs is adequate for fine phase space binning at low Q (<10 MeV/c) up to at least p_t = 700 MeV/c, which is the limit for π-K particle identification via dE/dx. The rate for close kaon pairs is much smaller, reflecting the much lower $dN/d\eta$ for kaons. Fine phase space binning appears impossible in this case. K-K correlation measurements at STAR will be possible only on an inclusive basis.

[41] W. Christie, STAR Note #7.

Table 4C-9 Rates within $|\eta|<1$ for uncorrelated pairs of close tracks for a single species of π or K in central Au-Au events at STAR, within selected bins of mean p_t of the pair and Lorentz invariant momentum difference Q. $dN/d\eta(\pi)=200$, $dN/d\eta(K)=10$; these are roughly what is expected for one species of charged π or K identified via dE/dx in the STAR TPC. Calculation of the number of pairs per 100 days is based on a rate of 1 central Au-Au event recorded per second.

p_t bin (MeV/c)	Q bin (MeV/c)	# pairs /100 days (1 event/sec)	
		π	K
$75 < p_t < 125$	$5 < Q < 10$	3×10^6	500
	$20 < Q < 25$	2×10^7	5×10^3
$175 < p_t < 225$	$5 < Q < 10$	2×10^6	300
	$20 < Q < 25$	10^7	3×10^3
$275 < p_t < 325$	$5 < Q < 10$	9×10^5	200
	$20 < Q < 25$	7×10^6	2×10^3
$575 < p_t < 625$	$5 < Q < 10$	7×10^4	< 10
	$20 < Q < 25$	6×10^5	300
$875 < p_t < 925$	$5 < Q < 10$	10^3	< 10
	$20 < Q < 25$	2×10^4	50

In order to study in more detail the STAR detector's sensitivity to the pion source parameters, we have generated correlation functions and analyzed them according to a procedure which involved: i) generating the two particle phase space distribution associated with a given number of events, N, ii) creating a Monte Carlo correlation function, with its error bars, by using a Gaussian (in Q) source parameterization with an assumed radius, R, and iii) extracting the source parameters and their associated confidence intervals. The effect of the di-pion Coulomb interaction has been included (this increases the error bars in the low Q region), and the assumed chaoticity parameter, λ, is unity. No attempt has been made to include the effects of two-particle acceptance or the pair tracking efficiency. The assumed source radii are 1, 10 and 20 fm. The motivations for the selection of these radii are: i) the observation of pp collisions, strong correlations between the momentum and spatial distributions of the secondaries, or of spatial inhomogeneities during rehadronisation[42], ii) the observation of the projectile radius, and iii) the observation of a source whose size follows $(dN/d\eta)^{1/3}$ scaling. The results for data sub-samples of 1, 10, 100, and 1000 events are presented in Fig. 4C-18. This figure provides a gauge of the number of interesting events of a given class (i.e. events with anomalously large charged multiplicity, anomalous K/π ratio, etc.) necessary in order to determine the invariant source radius for this class to a given

[42]RE2 Hadron Subgroup Report, p. 10.

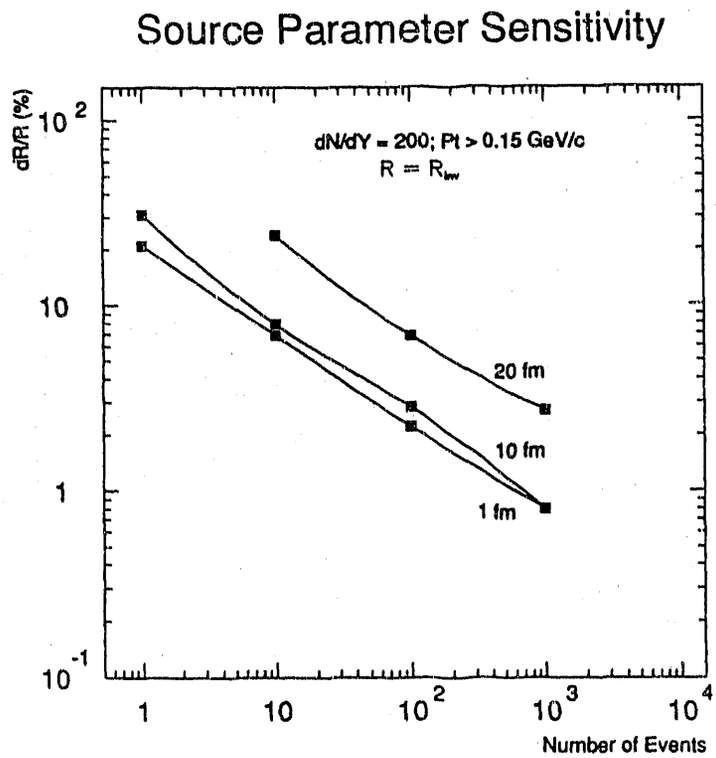

Figure 4C-18 A plot of the sensitivity to the (invariant) source radius as a function of event sub-sample size. Note that $dN_{\pi^-}/d\eta = 200$ and $p_t > 150$ MeV/c.

level of sensitivity. It also demonstrates that for the cases of 1 and 10 fm, single-event HBT can be performed to the 20-30% level of sensitivity; note that there is effectively no sensitivity to the invariant source radius for the single-event analysis of a 20 fm source. In order to further pursue single-event HBT analyses for 20 fm sources, cases with $p_t >$ 40 MeV/c, and $dN/d\eta(\pi^-) = 500$ were considered. The increased acceptance at low p_t is provided by tracks reconstructed in the SVT. This enhances the number of pairs at low Q as there is a correlation between low relative momentum and low p_t. The assumed pion multiplicity density is exotic when compared with the predictions of conventional Monte Carlo calculations such as FRITIOF, but is not at the extremes predicted by simple calculations based upon the Bjorken picture and entropy conservation throughout hadronization[43,44]. A typical correlation, function generated according to these relaxed assumptions is presented in Fig. 4C-19. We conclude that single-event HBT is feasible with sensitivity at the 30% level for a 20 fm source.

4.C.3.h Primary Vertex Localization

Reconstruction of the primary vertex is important for identifying multiple events in STAR. Tracks reconstructed in the TPC can be used to determine the primary vertex

[43] J.D. Bjorken, PRD 27 (1983) 140.
[44] G. Bertsch et al., PRD 37 (1988) 1202.

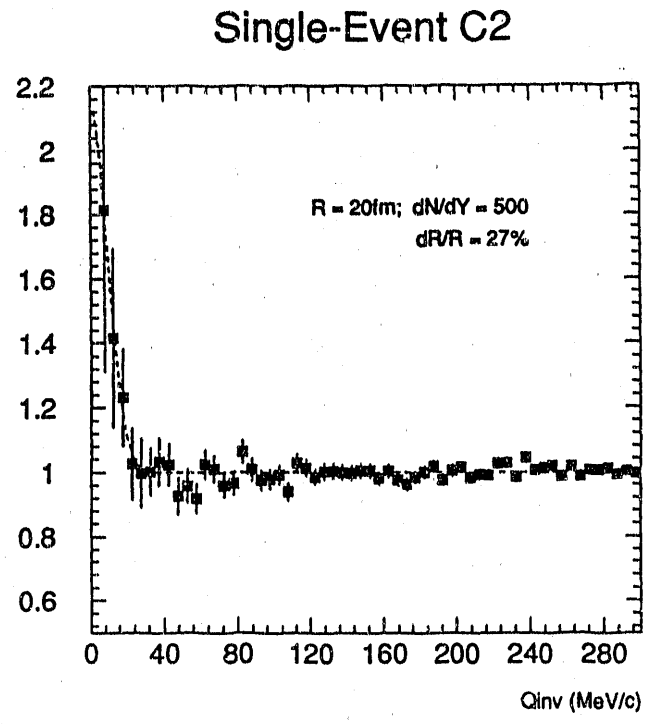

Figure 4C-19 A single event correlation function for the case of R_{inv} = 20 fm, $dN_{\pi^-}/d\eta$ = 500, and p_t > 40 MeV/c.

of the interaction. For the best vertex resolution only high momentum tracks, which suffer least from multiple scattering, can be used. Figure 4C-20 shows a histogram of the distance of closest approach to the found vertex for the set of tracks from a single Au + Au central event. The accuracy of the primary vertex localization is indicated in the top corner for an analysis using tracks with p_t > 200 MeV/c. The corresponding widths σ_z = 140 μm and σ_x = 60 μm (as defined in Fig. 4C-20) are found. These results will improve when more sophisticated methods of vertex finding[45] are implemented.

4.C.3.i Separation of Overlapping Interactions

Due to the 40 μs readout time of the TPC, multiple events which occur within this window must be resolved. Results from studies of multiple Au + Au events are shown in Fig. 4C-21 for tracks with p_t > 800 MeV/c. From Fig. 4C-21 it is seen that two Au + Au events can be separated if they are more than 2 mm (FWHM = 2 mm for a single peak) apart. The corresponding widths of the distributions when all tracks are used in an event are slightly worse than in Fig. 4C-21a with values of σ = 1.1-1.5 mm. Furthermore, even if they are at the limit of this resolution (Fig. 4C-21c), the structure of the two-event peak is distinctly different from that of a peak for a single event (Fig. 4C-21b) of the same total multiplicity. Only in the case when two Au + Au events occur in

[45] E. Andersen et al., Determination of the Primary Vertex Position in the NA36 Experiment, Nucl. Instrum. and Methods Phys. Res. A, Accel. Spectrom. Detect. Assoc. Equip. A301 (1991) 69.

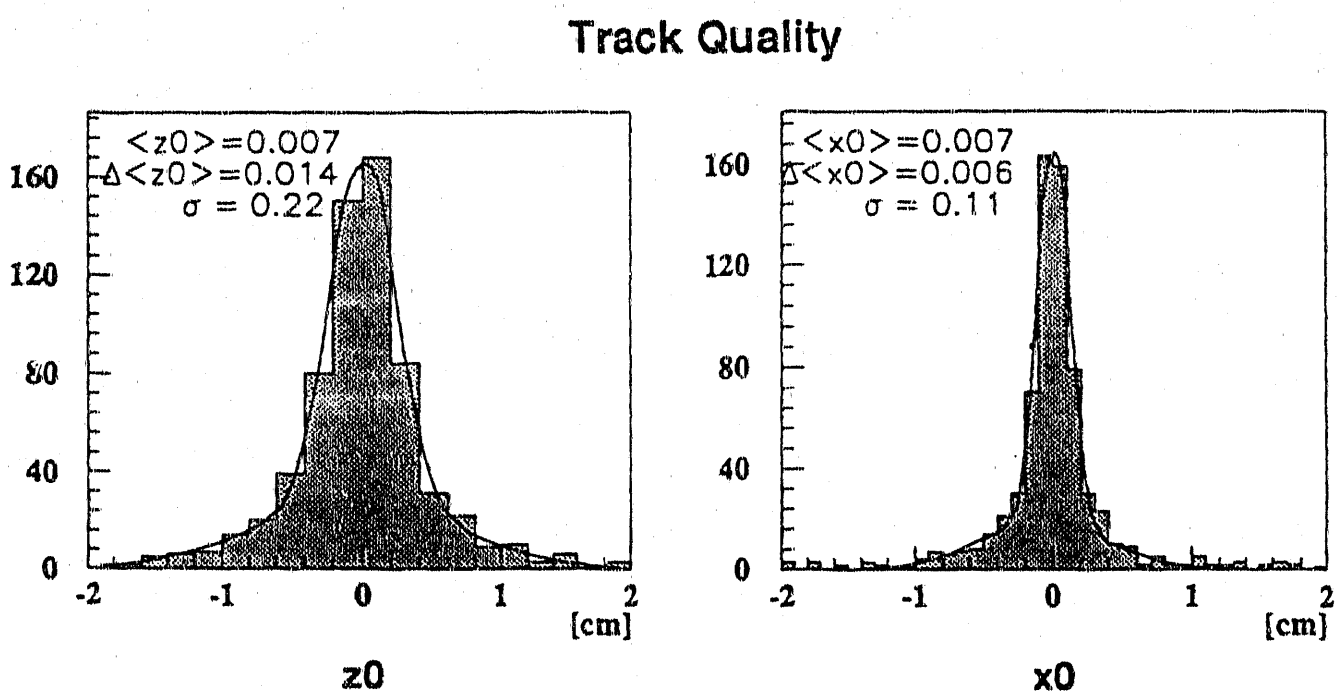

Figure 4C-20 Distance of closest approach of tracks to the found primary vertex in z and x.

the same beam crossing at a distance closer than the detector capability to resolve primary vertices, do overlapping events become problematic.

During the p+p data taking period at RHIC a high luminosity is foreseen. It will result in a high interaction rate and consequently many events may be registered during the time when the TPC gate is open. These events will show up in addition to the triggered event and will look like secondary tracks. The goal of this study is to show that such compound events can be analyzed and that different events can be distinguished.

In order to answer the questions raised above, the following procedure was adopted:

- Time when the chamber is sensitive was evaluated.
- Number of events that occur within this time was calculated assuming the pp cross section and the design luminosity.
- Appropriate number of minimum bias FRITIOF p+p events was generated.
- Events were processed by GEANT.
- Fast TPC simulator was used to assign each point a spatial resolution and diffusion that corresponds to its true position in the chamber.
- Z coordinates of the hits from the different events were modified according to the drift time.
- Events were combined to make 1 full event.
- Overlapping hits were merged.
- Pattern recognition was run and results were evaluated.

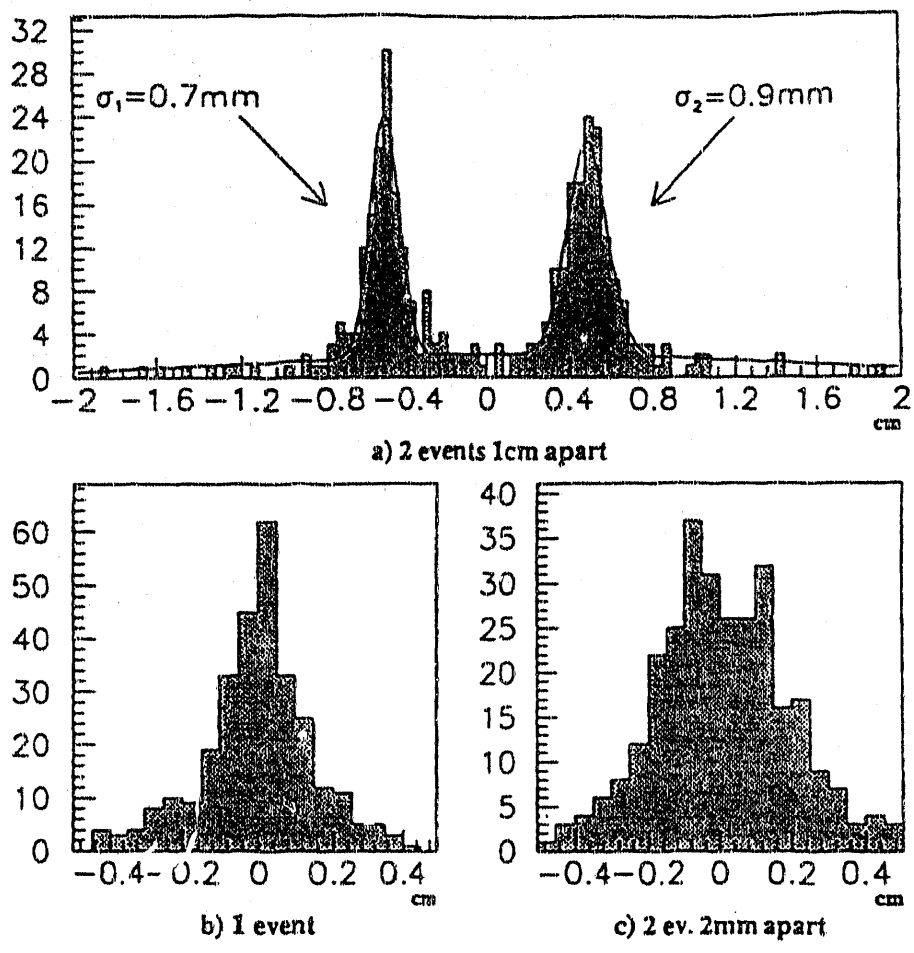

Figure 4C-21 Coordinate, z, of the closest approach to the origin for tracks with p_t > 800 MeV/c: a) Two events 1 cm apart. b) one event with twice normal multiplicity. c) two events 2 mm apart.

Due to the 40μs drift time in the TPC[46], the detector is sensitive to events in a 80μs window around the triggered event. At the beginning of the triggered event, midrapidity tracks from an event 40μs earlier will just be arriving at the end plate. The last event that has any chance to be recorded is one that occurred just before the gate was closed, 40μs after the triggered event. In this case ionization that is very close to the end plate will be registered and will appear in the triggered event as short tracks about the mid-plane. All the events that occurred between these two extremes will contribute to the signal. The total time during which the chamber is sensitive to pileup events is therefore 80μs.

The number of events (N_{ev}) that occur within the time that the chamber is sensitive can be derived from the pp inelastic cross-section (σ_{inel}) and the design luminosity ($\mathcal{L}_0$).

[46] Update to the RHIC Letter of Intent for an Experiment on Particle and Jet Production at Midrapidity, The STAR Collaboration, LBL-31040 (July 1991).

$$N_{ev} = \sigma_{inel} * \mathcal{L}o \qquad (4C\text{-}26)$$

If we take the design luminosity[47] of 1.4×10^{31} $cm^{-2}s^{-1}$ and an inelastic pp cross-section (45 mb for $\sqrt{s}$ 500 GeV[48]), then we get 6.3×10^5 events per second. This combined with the 80 μs sensitive time gives us on average 50 events registered together with the trigger event in the TPC.

Since the spacing between two consecutive bunch crossings is 220 ns, during the 80 μs "sensitive time" 364 bunch crossings will occur, and thus we should expect 0.11 minimum bias events per crossing. This was taken into account when the z coordinates were modified. On average events are separated by 10 cm along the drift direction. A detailed description of the event merging procedure is given in the TPC Fast Simulator User's Guide[49].

The combined pp event was then reconstructed and the results evaluated. Evaluation shows that such multi-pp events are reconstructed well. Comparison of Fig. 4C-22a and 4C-22b shows that most of the available hits were assigned to tracks. The level of the confusion (hits from different MC tracks assigned to the same reconstructed tracks) is low (Fig. 4C-23). The momentum resolution was not affected. Figure 4C-24 shows the $\Delta p/p$ histogram which has $\sigma = 1.6\%$ averaged over all p_t (refer to Fig. 4C-12 for the resolution for Au + Au events).

Another crucial question is whether the different events can be distinguished. In order to investigate this problem, the position of the vertex for each reconstructed track of p_t >150MeV/c was calculated. Figure 4C-25 shows a histogram of the reconstructed z coordinates of the vertices for these tracks. We observe that they cluster in groups spaced by approximately 10 cm. This corresponds to the average spacing between consecutive events. Thus we conclude that we can properly assign high p_t tracks to different events. Further study of lower momentum tracks needs to be completed.

4.C.3.j Space Charge

Considerable attention has been paid to possible distortions in the electric drift fields caused by positive ion space charge effects in the TPC. In the NA35 experiment at CERN, ^{32}S beams at intensities of 25,000 ions/s were sent through the TPC to determine possible effects of distortions in the electric drift fields and the trajectories of tracks, due to positive ion space charge. This corresponds to 6×10^6 minimum ionizing particles per second in a cross sectional area of less than 1 cm^2 in the TPC. No measurable distortions in the trajectories of tracks were observed. Likewise, the E810 experiment at BNL studied the behavior of TPCs in a high flux environment.[50] The E810 TPC was exposed to a flux equivalent to 10^7 minimum ionizing particles per second in 1 cm^2 spot size. This caused a distortion in the drift direction of 1.5 mm which agreed with predictions from a numerical calculation described below. In comparison, the maximum

[47] Conceptual Design of ... Relativistic Heavy Ion Collider RHIC, BNL 52195 (May 1989).
[48] Review of Particle Properties, Particle Data Group, Phys. Letters B 239 (1990).
[49] P. Jones, STAR note #56.
[50] Behavior of TPCs in a High Flux Environment, A. Etkin, et al., Vienna Wire Chamber Conference proceedings. To be published.

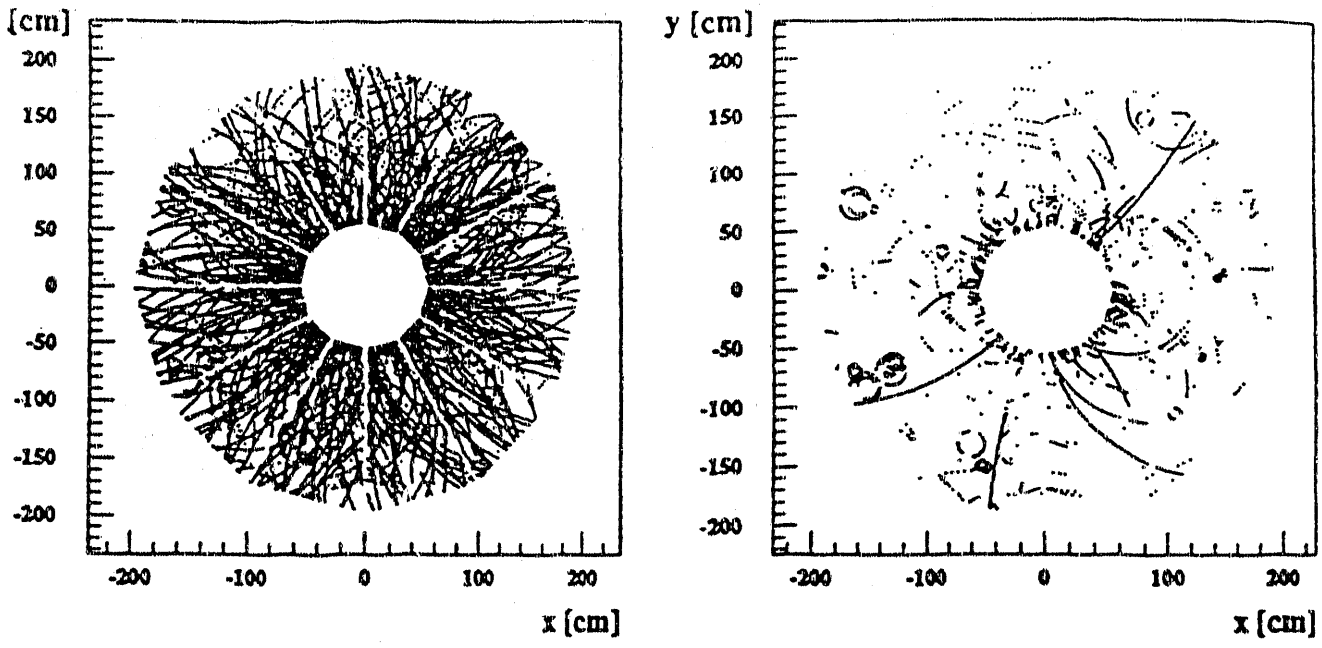

Figure 4C-22 TPC hits from a multiple pp event projected to the TPC end plate. a) all the hits, b) hits that were not assigned to any tracks.

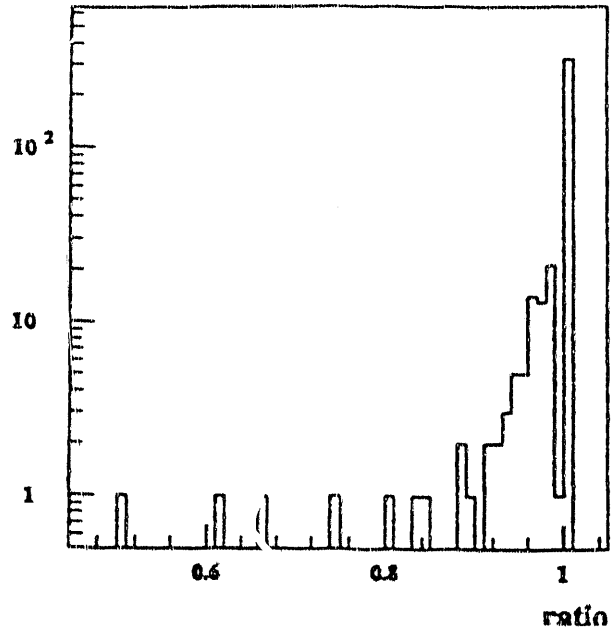

Figure 4C-23 Ratio of good hits to the total number of hits per track.

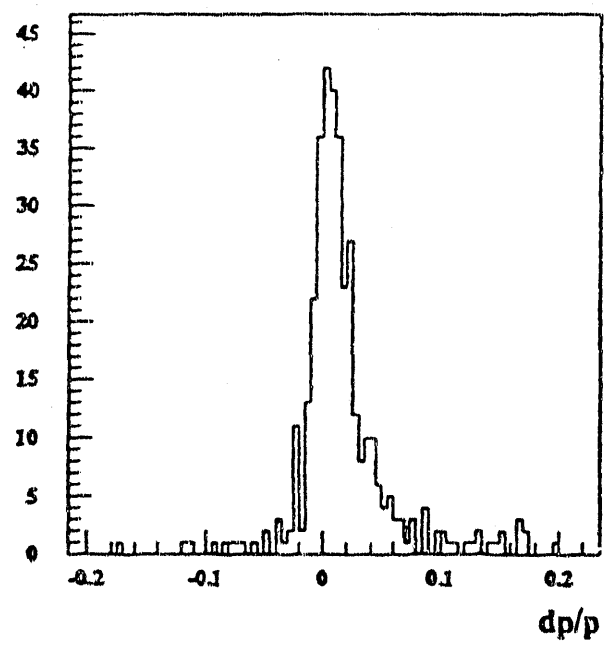

Figure 4C-24 Momentum resolution for the pp events.

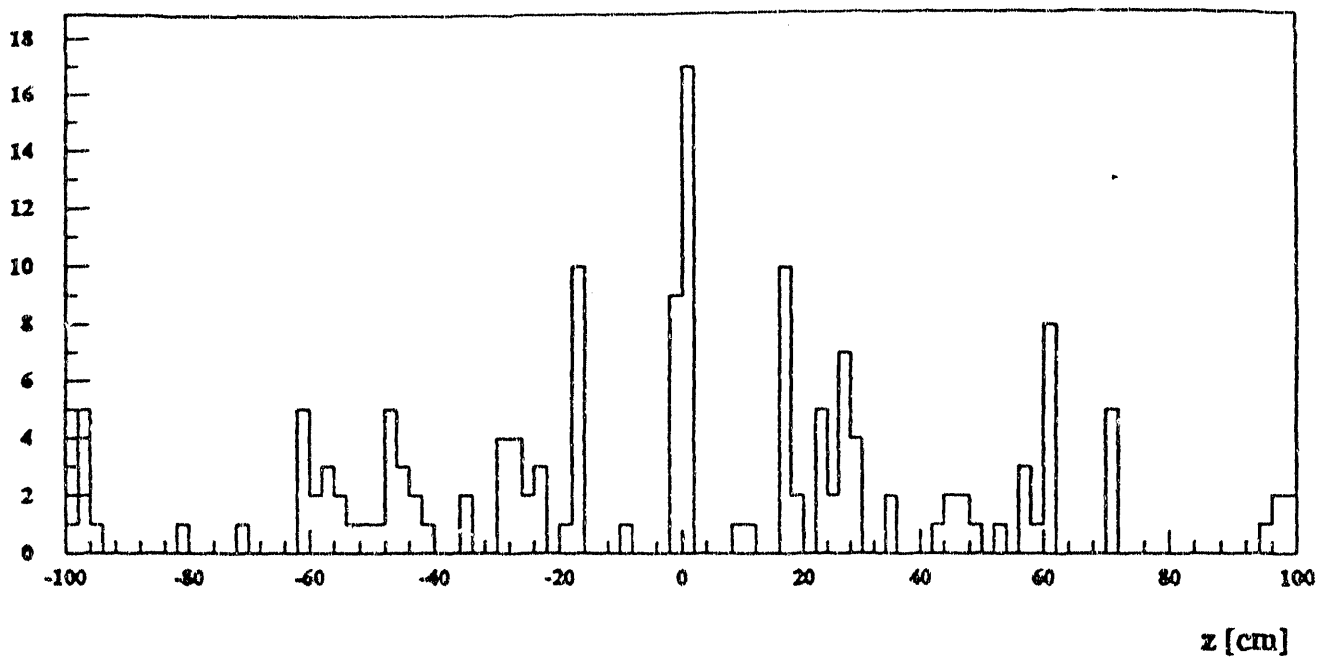

Figure 4C-25 Reconstructed z coordinate of the vertex for tracks with momenta greater than 150 MeV/c. Separate clusters correspond to different events.

charge density in the STAR TPC is only 600 ions/cc but is typically much less than 50 ions/cc, orders of magnitude smaller than the space charge loading created by the beam tests. Therefore, we do not expect any significant distortions in the STAR TPC arising from primary ionization.

The NA35 and EOS TPCs each use gated grids to reduce, significantly, positive ion feedback from the avalanche region near the sense wires. Tests have been performed on the new EOS gated grid and the results show that the suppression is better than 10^{-4}.

Detailed numerical electrostatic calculations have been performed[51] to determine the effect of the primary ionization as a result of the expected large multiplicity of charged particles in central Au+Au collisions at RHIC. The accumulation of positive ion charge in the STAR TPC is found to have a small effect on the TPC space points for Au beam luminosities up to 20 times the design luminosity ($\mathcal{L}_0 = 2 \times 10^{26}$ cm^{-2}sec^{-1}). Displayed in Fig. 4C-26 are the errors for space points along the azimuthal and radial directions as a function of the distance along the beam axis away from the detector center. These errors represent the systematic displacement of electrons as they drift through the perturbation potential and are calculated from a transport equation. For radial distances of 75 cm to 200 cm, the outer radius of the TPC, the errors are < 20 μm in the azimuthal direction and < 10 μm in the radial direction. The azimuthal and radial distortions reach maxima at the inner radius, 50 cm, of the TPC, with space point errors of 100 μm and 48 μm, respectively. On average, displacement errors range 20-50 μm depending on the track geometry. The rms resolution in $\Delta p/p$ due to space charge averaged over all reconstructed tracks in the TPC is found to be less than 0.07%. Even at $10\mathcal{L}_0$ the performance of the TPC will not be degraded by this effect. Figure 4C-27 shows the averaged momentum resolution as a function of beam luminosity. The space charge distortions become comparable to multiple scattering at ~ $18\mathcal{L}_0$ for argon chamber gas.

4.C.3.k QED Electrons

One concern is the potential background of low-mass lepton pairs[52] produced by the electromagnetic interaction between the heavy ion colliding beams. Tables of the calculated double differential cross-sections ($d^2\sigma/dp_t d|y|$) for $\sqrt{S_{nn}}$= 200 GeV Au + Au were obtained from M. Rhoades-Brown, integrated over the appropriate rapidity ranges for the TPC and SVT, and scaled by the design luminosity to calculate the flux of electrons expected in the detectors. Shown in Fig. 4C-28 is the number of electrons per detector clearing time as a function of p_t for the two devices.

---

[51] G. Rai, LBL- STAR note 3.

[52] Mark J. Rhoades-Brown and T. Ludlam, Proceedings of Fourth Workshop on Experiments and Detectors for a Relativistic Heavy Ion Collider, July 2-7, 1990, p. 325.

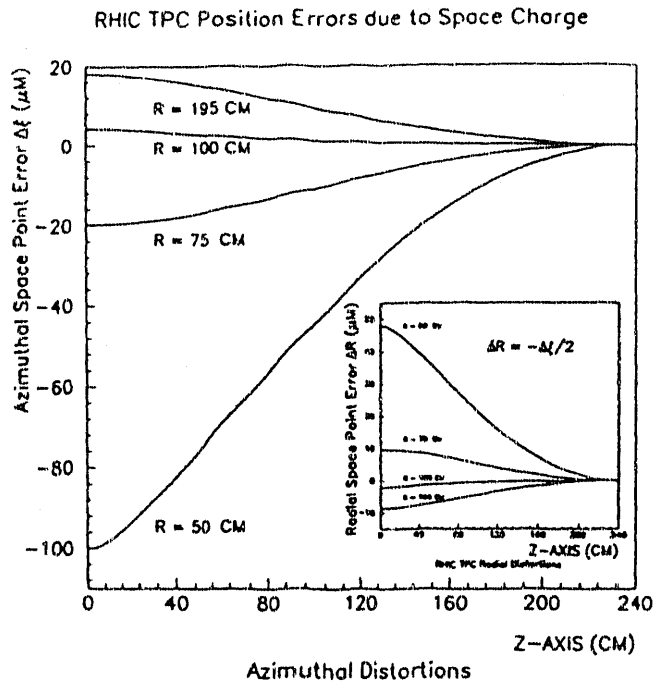

Figure 4C-26 Results of an electrostatic calculation showing the displacement errors due to space charge along the azimuthal and radial (inset) directions as a function of distance in z.

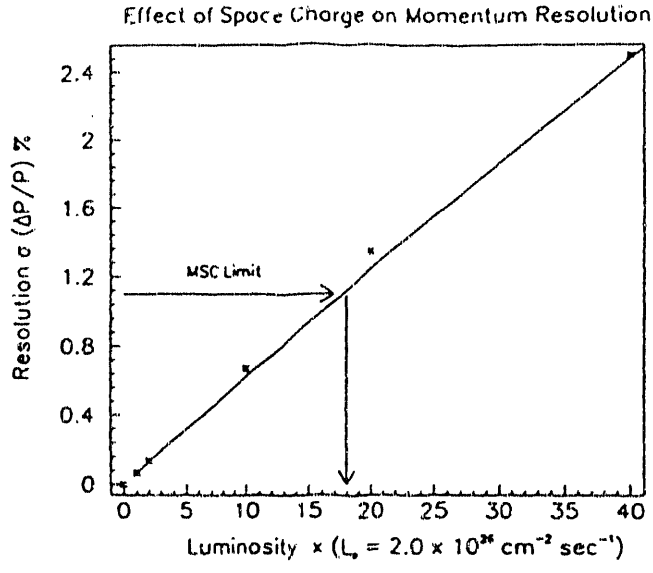

Figure 4C-27 The average momentum resolution due to space charge effects as a function of luminosity. The multiple scattering limit in argon gas is shown.

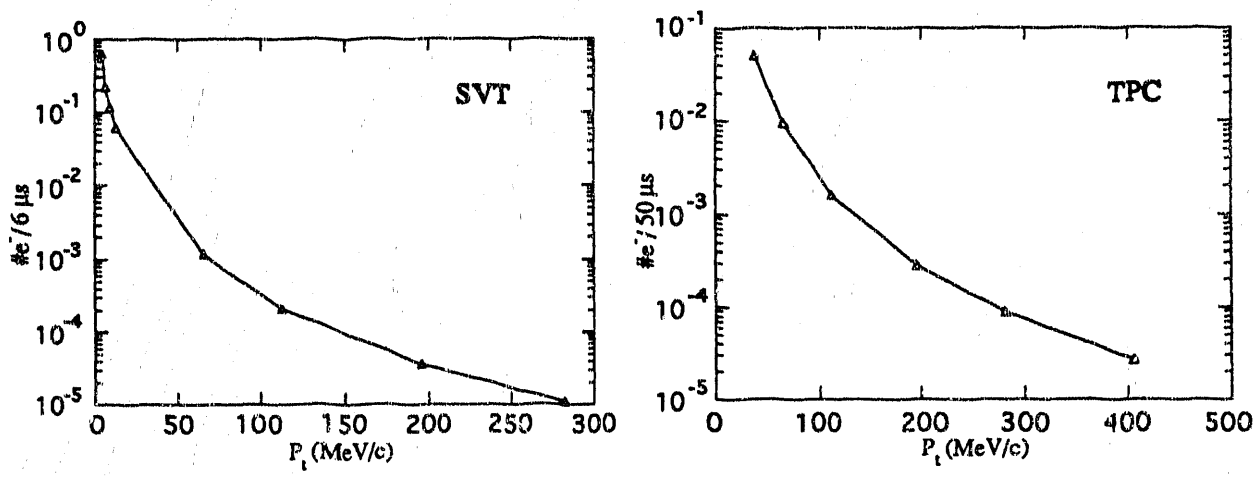

Figure 4C-28 Expected rate for QED electrons.

It can be concluded that this source of background is not a problem for the proposed STAR configuration.

4.C.3.1 Wire Aging Effects

The wire aging effect upon the anode wires of the STAR TPC has been estimated. The charge loading on the anode wires, when the TPC is in operating mode, derives from three sources: 1) ionizing particles from triggered events, 2) ionizing particles from leak-through events when the gating grid is closed, and 3) ionizing particles traversing the multiplication region of the TPC whose ionizing charges cannot be suppressed by the gating grid. The contributions from sources 1) and 3) are of the same magnitude while that from source 2) is much smaller. Using a maximum allowable loading of 0.1 Coulomb/cm on the anode wires, we conclude that the TPC can operate for its expected lifetime without experiencing serious aging effects at the RHIC luminosity of $2 \times 10^{26}/cm^2/sec$. Normal precautions will be taken during TPC construction and test phases to ensure good chamber performance.

4.C.4. R&D Issues and Technology Choices

4.C.4.a Low Diffusion Gas Tests

Studies are required to investigate alternative gases to Ar + CH_4 which will give reduced longitudinal diffusion. Theoretical calculations suggest that Ar + CO_2 + CH_4 could give a significant improvement in longitudinal diffusion while operating at a workable field of 290 V/cm. This means that the field cage can be operated at a relatively low potential (60 kV). At this potential an insulating layer is not required on the inner field cage, thus allowing a significant reduction in multiple scattering. Several characteristics of the gas must be measured:

- Longitudinal diffusion; at present there is considerable uncertainty on this issue.
- $\omega\tau$
- dV_D/dT, Drift velocity dependence on temperature
- Gas gain characteristics
- 1/t tail shape

The first three items will be measured at MPI Munich by V. Eckardt's group and at BNL. The last two items will be measured at LBL with the EOS prototype chamber.

4.C.4.b Reduced Pad Size Studies

We have proposed constructing the inner pad modules with small pads (2.85 mm × 11.5 mm) and reduced anode to pad spacing in order to improve the two track resolution. The pads will be arranged on circular rows with the row centers separated by 4 cm in radius. This design has received some testing[53]. However, it has not been used in an operating experiment. A number of issues must be thoroughly investigated before this approach is ready for production.

Simulations are required to verify improved tracking efficiency and check that the added projection between hits does not degrade tracking efficiency. These simulations are under way and it is expected that they will be complete by mid-August 92.

A prototype series of pads will be checked with X-ray sources and laser generated point electron sources. The following issues are of interest in this study:

- Gain stability along the wire. The compact geometry will increase sensitivity to spacing errors, but since dE/dx has already been compromised in the inner radius region of the TPC some error can be tolerated.
- Pad response function - does an avalanche give three pads with amplitudes above threshold.
- Pad position resolution.
- 1/t signal characteristics - to determine required correction in the shaping amplifier.
- Test the ability to extract dE/dx to a σ of 5% from pad signals for which the pads vary in position relative to the wires as a result of the circular pad row geometry.

4.C.4.c Increased Gain and Wire Termination Studies

Since it is planned to use smaller pads than those of previous TPCs, it may be necessary to operate at a factor of 2 higher gain than has been used routinely in atmospheric pressure TPCs such as ALEPH, DELPHI and EOS. With 20 μm anode wires this will require increasing the voltage from 1265 to 1325 volts[54]. Stable performance at this voltage has been demonstrated, but it is important to perform careful tests. The

[53] Volker Eckardt, MPI.
[54] H. Wieman, EOS note 128.

main potential problem area is the boundary region where the anode wires are captured in the supporting epoxy bead. A testing program is planned to examine wire termination at elevated voltage. Various epoxies and curing conditions will be studied as well as anti-spark coatings of polyurethane. The effect of cathode wire radius will also be analyzed.

4.C.4.d Drift Velocity Feed Back System

The drift velocity in the TPC can vary because of changes in temperature, pressure and gas composition. It is desirable to have a detection and feedback system which holds the drift velocity to one part in 2000. Development has started on a system which directly measures the electron drift time in the TPC volume. A UV laser is used to generate a pulse of electrons from the field cage cathode plane. The drift time is monitored with a large dynamic range TDC which records the time between the laser flash and the anode signal marking the arrival of the electrons at the pad plane. By operating the drift field slightly off the peak of the velocity distribution, the voltage can be adjusted to hold the drift time constant. Initial testing of this approach with the EOS TPC shows that the drift time can be consistently measured to an accuracy of 1 ns. This corresponds to a position accuracy of 55 μm. This system would be particularly useful if a low diffusion gas is found which must be operated in the linear region well removed from the velocity saturation peak.

4.C.4.e Micro-Strip-Gas-Chamber (MSGC) Read Out for TPC

An R&D program is planned to explore a new technology for amplifying and reading out the electron track signals in the TPC. This technology is too new to include in the baseline, but it does have several potential advantages which make it worthy of study. This new approach is based on the Micro-Strip-Gas-Chamber which works like the traditional MWPC with a high field at the anode for gas gain and cathode pads for picking up the induced signal. The MSGC is made from aluminum structures deposited on a thin glass substrate using photolithography techniques. The added geometrical precision achieved with photolithography permits construction of devices with small dimensions without compromising gas gain uniformity. The ultimate two track separation, as set by the diffusion width of the electron cloud, can be achieved using this approach.

Some issues to be explored are:

- Gas gain uniformity.
- Possible variations with time and loading due to surface charge build up.
- Ultimate gas gain without high voltage breakdown.
- Detector life time.
- Suitable pad dimensions for use in the inner radius region of the STAR TPC.

4.C.4.f Multi-layer Pad Plane Board

The multilayer concept has not been used in this application before and is not conventional for boards of this size. We will contract out the fabrication of the pad

planes. The pad planes will be received with front end board connectors installed. Some prototyping is required.

4.C.4.g Pad Plane Sector Casting

Castings often take some amount of time in initial pattern adjustment. Thus it is wise to start this process early. This work will also be contracted out, probably locally so that we can monitor the foundry's progress. Other areas of responsibility for the foundry contractor are the stress relief of the casting and its machining to finished size. Since there are a large number (24) of sectors, we will construct a representative generic prototype sector to engineer/optimize the production methods.

4.C.5. Engineering

4.C.5.a Brief Technical Description & Specifications

The STAR Time Projection Chamber (TPC) has a tracking volume enclosed by a 4 m inside diameter outer field cage (OFC), a 1 m outside diameter inner field cage (IFC) and pad planes 4.2 m apart. The basic TPC configuration is shown in Fig. 4C-1. The tracking volume is divided into two chambers by a high voltage membrane held at the midpoint of the outer field cage. A negative potential is placed on this membrane which, with the two field cages, defines a constant electric field. As particles pass through the tracking volume, electrons are knocked off detector gas molecules. These electrons drift away from the negative central membrane and toward the pad planes. The time of arrival of this ionization gives information on the z location of the electron source. The pad location gives the x and y coordinates. A 0.5 T axial magnetic field causes the particles to follow helical trajectories, which allows momentum determination. The magnetic field also reduces the dispersion of the electrons as they drift toward the pad plane, which increases the precision of particle track measurements. Other major components of the TPC are a laser calibration system, a gas supply, cooling systems, two large sector support structures (called wheels), and slow controls to monitor various parameters such as the temperatures of the components.

4.C.5.b Description of Major Components

Outer Field Cage (OFC)

The primary function of the OFC is to constrain the electric potential along one boundary of the active volume of the TPC. In addition, the OFC performs secondary functions as the gas containment vessel for the TPC and as a structural support for both the TPC and the central Trigger barrel (or the TOF upgrade). The OFC is a 4.56-m-long cylinder with a 4.01-m inner diameter. It is composed of a voltage gradient cage, a support structure, an insulating layer between the two, and a load-attachment ring at each end of the cylinder. Figure 4C-29 shows the overall OFC configuration and some details. The voltage gradient cage is a cylinder made from sheets of 0.035 mm copper plated on both sides of a 0.075-mm thick Kapton film. The copper has been etched into stripes as shown on Fig. 4C-29. The copper stripes on the Kapton film surfaces overlap in z to minimize the local field perturbations. A high voltage cable is attached to the

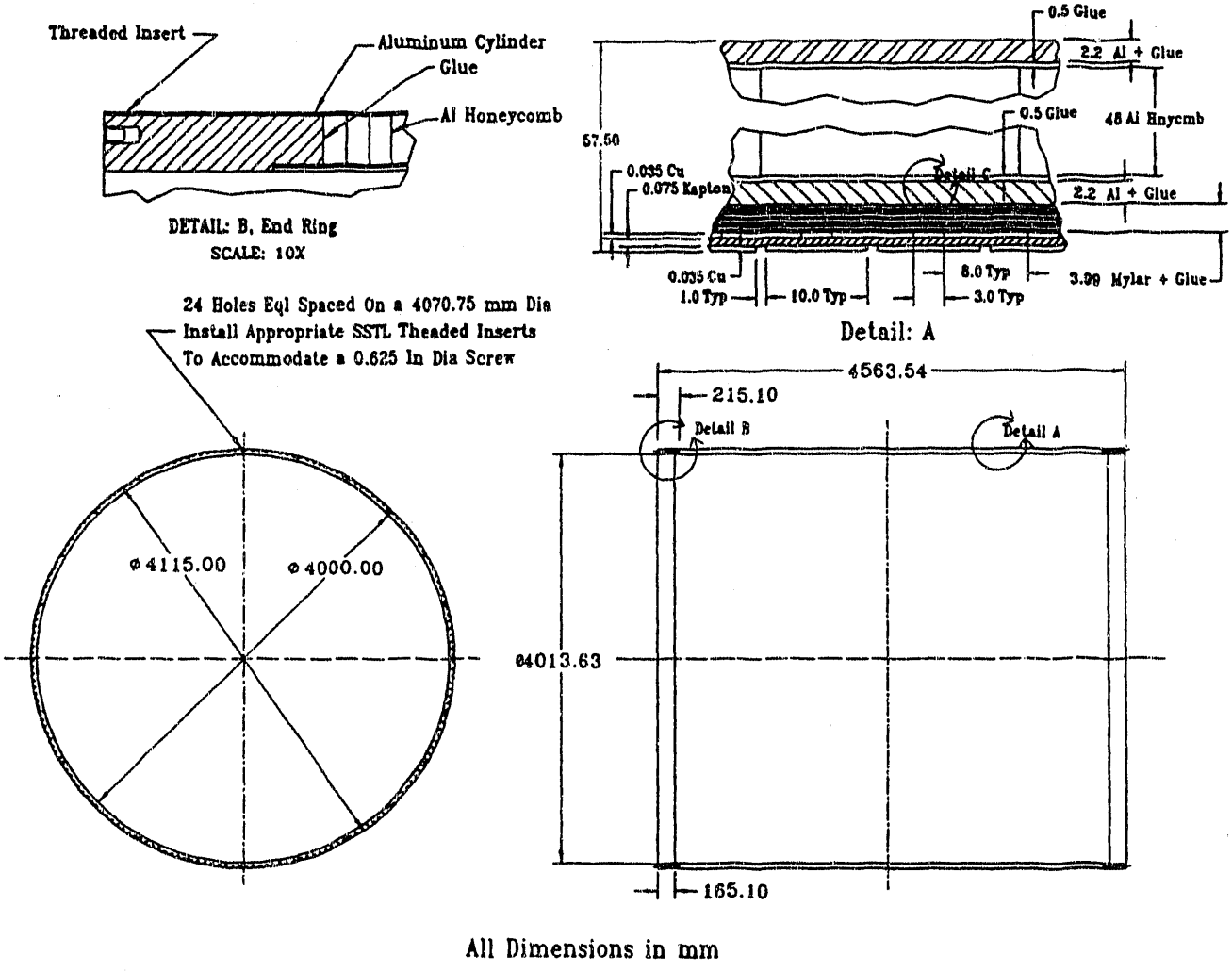

Figure 4C-29 The STAR outer field cage.

copper stripe located at z = 0 and the remaining stripes are held at constantly increasing voltage in z by connecting them to a precision resistor chain. This same method of producing a precise electric field gradient is also used for the inner field cage.

The OFC is in close proximity to other subsystems of STAR which are held at ground potential and therefore, the voltage gradient cage must be electrically shielded. A mylar insulator and a grounded inner aluminum skin are formed by wrapping layers of material around the outside of the voltage gradient cage and continuously bonding each new layer to the previous one with adhesive. This method of fabrication was chosen to minimize the size and number of inter-layer bubbles formed during fabrication. This is necessary to preclude high voltage breakdown between the high voltage gradient cage and the grounded support structure due to faults initiated within the bubbles. This technique was used successfully in the fabrication of the ALEPH TPC outer field cage.

The two OFC end rings provide the interface between the central part of the OFC support structure and the sector support wheels. In addition, these rings help maintain a round OFC. The estimated weight of the OFC is 2724 kg (6110 lb).

The OFC support structure must support the voltage gradient cage on its interior, and the central trigger barrel (and time of flight upgrade) on its exterior. Additionally, for ease of maintenance, it is desirable to have a structure that will support a person working inside. The central aluminum-honeycomb support structure is supported by the OFC end rings, which mount to the wheels. The wheels, and therefore the TPC, are supported by the magnet cryostat. A finite element analysis (FEA) was completed using the ANSYS code with the following specifications:

Total deflection during operation < 1 mm
Weight of OFC plus TOF - 6406 kg (14,110 lb)
Weight of person inside - 91 kg (200 lb)

The results of this study are shown in Table 4C-10.

Table 4C-10 Results of OFC deflection study.

t_{skin} (mm)	t_{core} (mm)	y Deflection (mm)	x Deflection (mm)
1	16	5.0	7.5
2	16	3.1	4.6
1	32	2.4	3.8
2	32	1.0	1.4
2	48	0.5	0.7

Detail A of Fig. 4C-29 shows that a 52-mm thick cylinder with 2-mm laminated aluminum face skins is specified to support the TOF upgrade and limit the deflection to <1 mm. In addition, the stress generated in the support structure is low with the assumed maintenance person inside.

The proposed assembly procedures and type of equipment for the OFC fabrication are similar to those used by ALEPH personnel. A 4-m diameter foam-covered mandrel will be fabricated and supported between two bearings. One layer of piano wire will be wound over the metal mandrel and another layer will be imbedded in the foam. The OFC end rings will be mounted inboard of the support bearings before the winding operation commences. One of the bearing supports will have a motor drive. Parallel to the axis of the mandrel, a winding head will be mounted on a carriage which moves over fully supported rails that are slightly longer than the mandrel. The head will be moved by use of a powered lead screw. The final mandrel rotation and the lead screw turning rate will be determined during the initial winding tests. The first use of the head will be to true the hard foam covering to the axis determined by the support bearings. The foam will serve as the base for further winding operations. The head will contain a feed bobbin that holds the material being wound, a roller to press the material against the cylinder, an automatic adhesive mixer and dispenser, and a servo mechanism to control the tension in the material. The finished winding machine will be

similar to a 4.3 m (14 ft) diameter lathe. Fabrication of the OFC is planned to occur in building 77A at LBL. The cost estimate for the TPC provides for facility upgrades to maintain the air at low humidity in the winding equipment workroom. Tests are planed to determine the allowable humidity for the winding room. An adhesive (Uralite 6108), different from that used on ALEPH, may be employed for the OFC fabrication. This adhesive may set properly at normal or high humidity.

The order of fabrication is to first lay up the voltage gradient cage using 200 mm wide Cu/Kapton sheets in the configuration shown in Fig. 4C-29. The copper stripes are positioned perpendicular to the axis of the mandrel. The relative alignment of the last copper stripe on one Cu/Kapton sheet must be within 0.1 mm of the first copper stripe on the adjacent sheet in order to maintain field uniformity. A telescope optical tooling bar system will be used to position the edge of each first copper stripe as the sheet is placed onto the mandrel (see Fig. 4C-30). After the voltage gradient cage is in place, the winding of the Mylar insulation begins. About 42 layers of 200 mm wide Mylar sheets will be wound with each layer shifted by half of a sheet-width to overlay the butt joints of the previous layer. It is anticipated that four to five layers of Mylar per day can be wound using Hexcel 6108 urethane adhesive with an overnight drying period required prior to winding the next series of layers. Care will be exercised to prevent the inclusion of air bubbles among the Mylar layers. After the Mylar has been wound, the 20 layers of 0.1 mm thick 200 mm wide aluminum sheets will be wound. The aluminum sheets may be anodized to provide a better surface for the adhesive.

The two pre-machined end rings then will be moved into position over the inner aluminum skin. The ring inside diameter will be slightly oversized. Spacers will hold the ring off of the aluminum skin and adhesive will be injected through holes in the ring to fill the space between the ring and aluminum skin. The position of the end rings relative to the mandrel axis and each other will be determined by the use of theodolites or an autocollimator and mirrors.

A 48 mm thick 38 kg/m^3 (2.4 pcf) honeycomb layer will then be placed over and bonded to the first aluminum skin. The outer aluminum layer of the support structure may be wound sheets equal to the inner skin, or it may be large rolled sheets. Either would be glued onto the honeycomb and the end rings. Since the inner aluminum skin

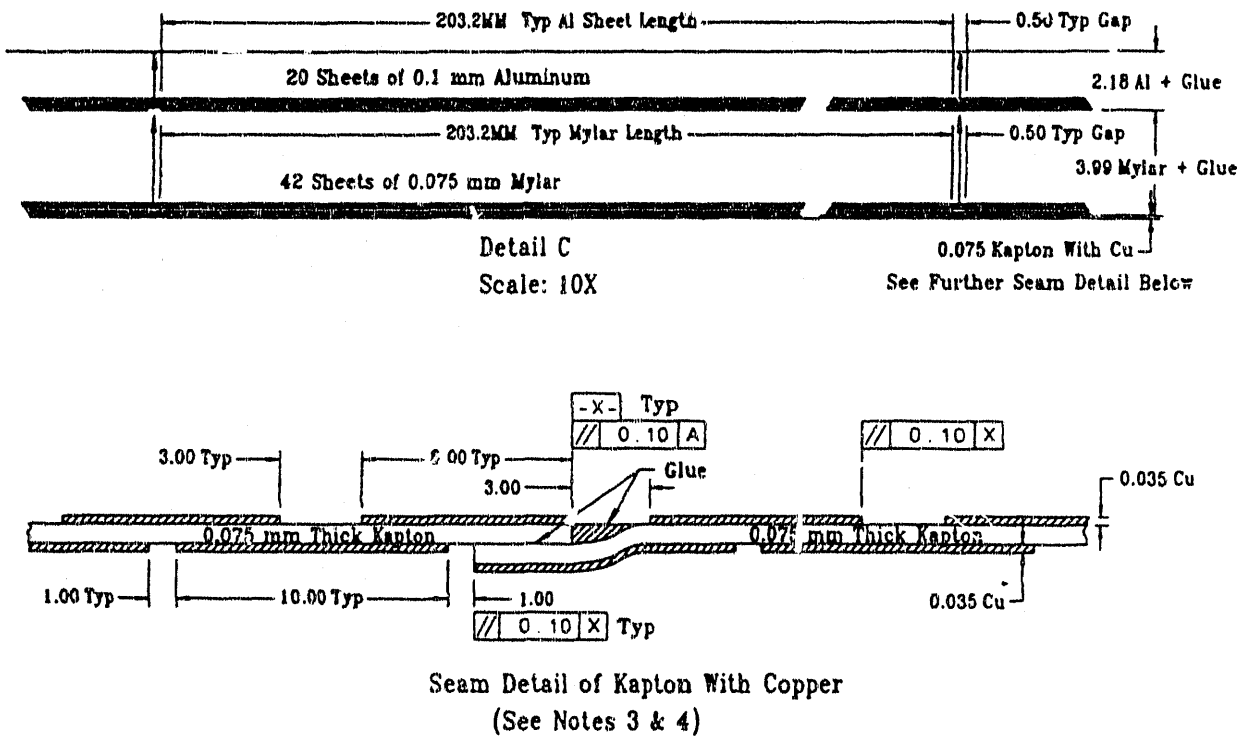

Figure 4C-30 Details of the OFC construction.

is the ground plane, bubbles between the honeycomb and the inner and outer aluminum skins are not an electrical concern.

After fabrication of the OFC, the embedded piano wires will be pulled through the foam. This will remove most of the foam providing a clearance between the mandrel and the inside diameter of the OFC. The OFC is then removed from the mandrel and placed onto an assembly/test stand. The resistor chain and high voltage feed are then placed along the inside of the OFC parallel to its axis. The OFC is now ready for both mechanical and electrical tests.

Inner Field Cage (IFC)

The IFC performs the primary function of defining the electrical potential along the inner radius of the active volume of the TPC. It also performs the secondary function of gas containment. Its support structure is not as substantial as that of the OFC as it is required only to support itself. An insulating layer is not required as the closest grounded structure at z = 0 (the SVT mount) will be about 320 mm away. A dry gas such as nitrogen will fill the space between the field cage and the SVT support. This configuration is shown in Fig. 4C-31. Figure 4C-32 shows the overall IFC configuration and some flange details are shown in Fig. 4C-33.

The support structure for the IFC has to support only the voltage gradient cage (Cu/Kapton sheets). The IFC must perform its functions and at the same time minimize the radiation length for particles passing through it into the TPC's tracking volume. The

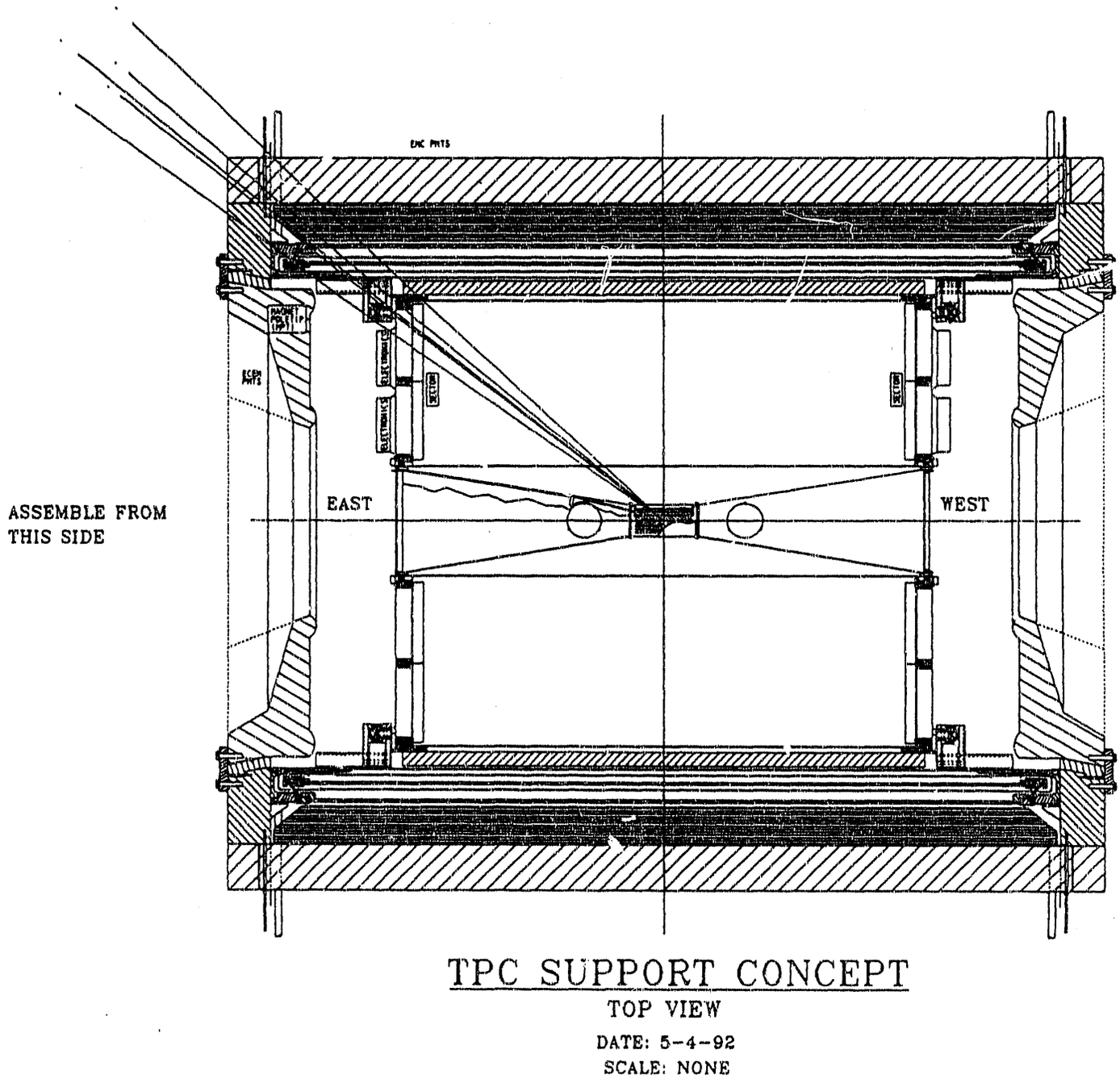

Figure 4C-31 A top view of the TPC inside the cyrostat displaying the mounting structures.

requirement of low radiation length encourages the use of composite material or foam for support. A finite element analysis (FEA) was completed using the ANSYS code demanding a 1-mm deflection limitation during operations. In addition, the deflection and stress under a 23 kg (50 lb) point load was also determined. This type of load might occur if a person leaned on the IFC for balance while doing maintenance work inside the TPC.

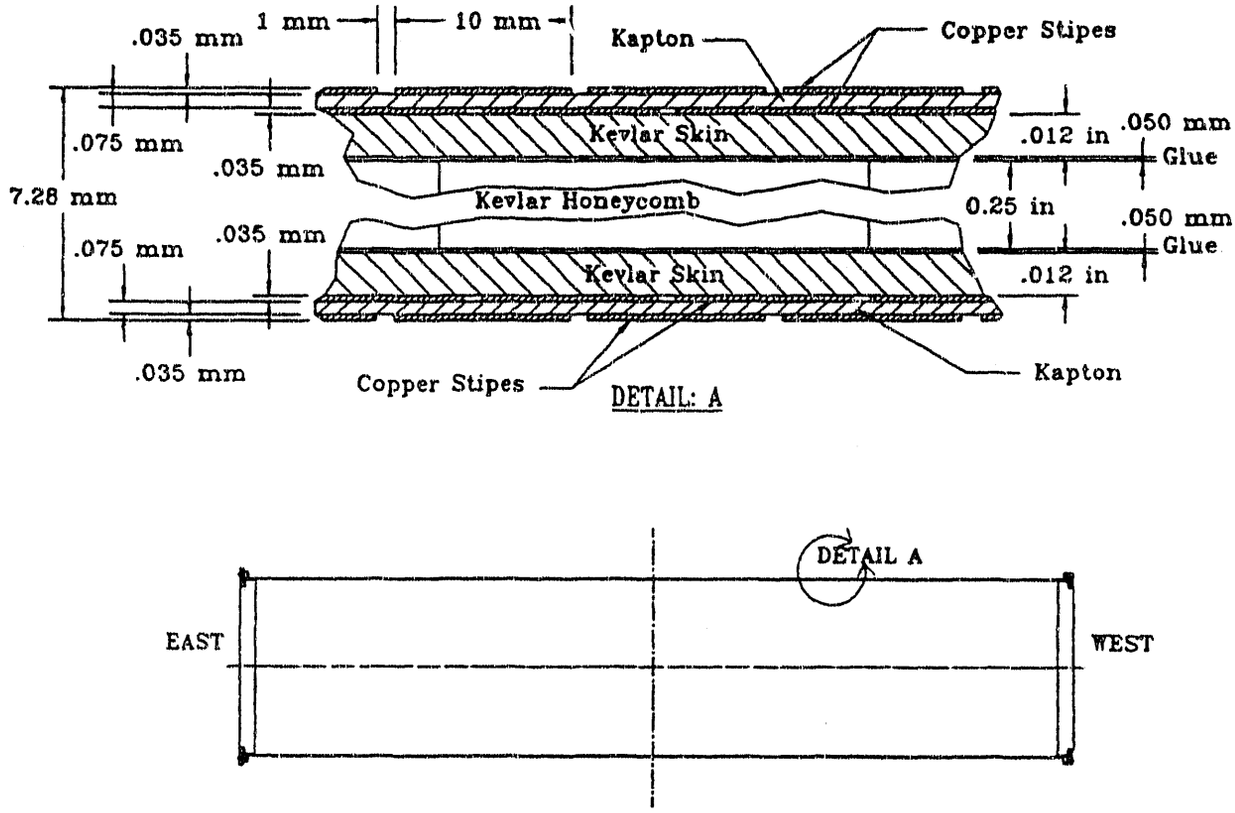

Figure 4C-32 Inner field cage construction.

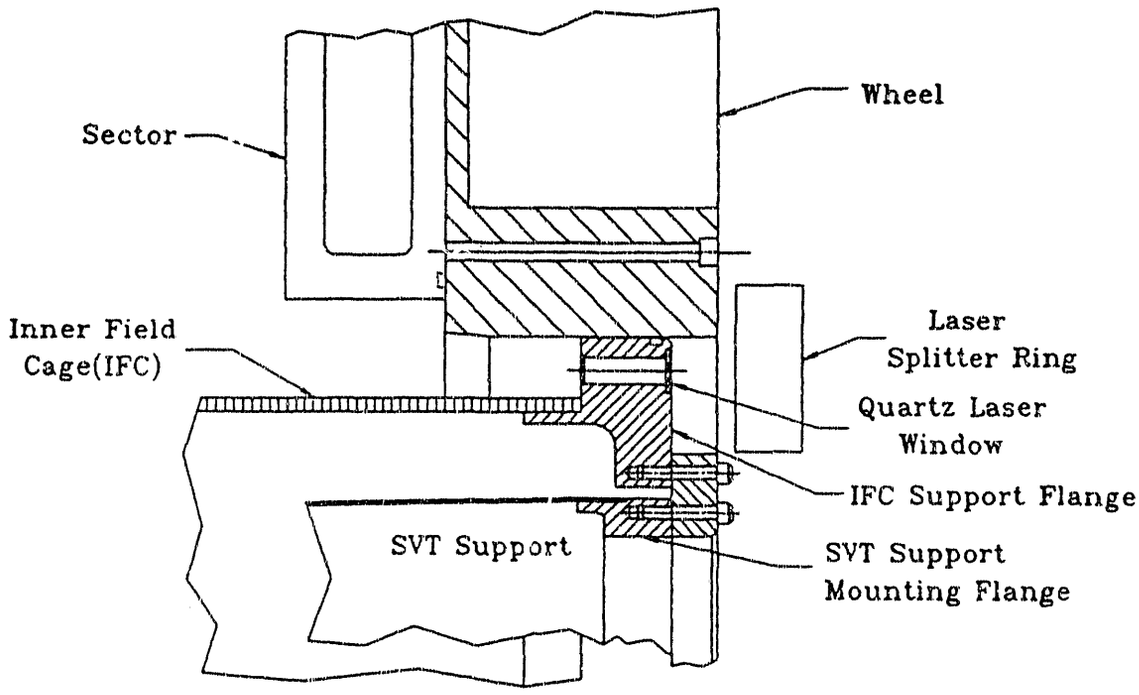

Figure 4C-33 Inner field cage and SVT support mounting to the end-cap wheel (east end).

Although the deflection for the Rohacell/Cu/Kapton configuration met the specifications during operations, the stress in the Kapton was relatively high. It has been observed that Rohacell covered with Kapton will creep significantly over time. Comparing the calculated 38.0 MPa (5000 psi) stress in the Kapton film with vendor data indicated that creep might be a problem. The proposed solution is to replace the Rohacell foam with a support made of Kevlar, or equivalent, face skins and Kevlar honeycomb. The resulting radiation length, deflection and stress are summarized in Table 4C-11.

Fabrication of the IFC will be much simpler than the OFC. The nominal 1-m diameter is well within the present fabrication capability of several manufacturers. The 4.2-m length however may necessitate a two-section tube. In addition, since the Cu/Kapton sheets must be on the inside of the tube, they must be placed on the mandrel first. If the composite material to be wound next requires a high temperature cure, problems might be encountered due to the temperature limit of Kapton. For this reason, the optimum composite material has not yet been selected. The winder used for the OFC might be used for the IFC, but the preferred fabrication method may be determined by outside vendors.

Central Membrane

The central membrane will serve as the high voltage cathode plane. It will be fabricated from Aquadag-painted mylar sheets and will be electrically connected to the z=0 copper stripe on both the IFC and OFC.

Table 4C-11 Deflection and stress results for the IFC support structure.

Radiation Length (%)	Support structure Rohacell Foam	Support structure Kevlar Honeycomb
Structure	0.05	0.3
Cu/Kapton	0.7	0.7
Al/Kapton	0.2	0.2
Deflection (mm)		
Static	0.28	0.02
Concentrated load		31.0
Maximum Stress (MPa)		
50 lb. concentrated load	38.0	0.5

Sector Support Wheels

The sector support structures are two 4.1-m diameter spoked wheels, one at each end of the TPC ($|z| = 2.1$ m). Each wheel consists of an inner ring, a medial ring, an outer ring, and 12 T-section spokes extending radially from the inner ring to the outer ring (see Fig. 4C-34).The medial ring is actually a dodecagon and defines the juncture of the inner and outer pad plane sectors (see Sectors, below). The inner and outer field cages as well as the pad plane sectors are supported by these wheels. In addition, the load of the central trigger barrel, TOF upgrade, and SVT will be born by the wheels.

To simplify the fabrication of these structures, the wheels will be cast from the aluminum alloy A356. Although this is a very large casting, it can be done at a reasonable cost. The raw castings could either be sent to an outside machine shop for finish machining or could be done in-house by the caster if his shop is adequate. After machining and inspection, the finished wheels would be shipped to LBL for additional work and assembly into the TPC.

Sector location bushings must be installed in the wheel. These bushings define the individual sector locations, and therefore the pad locations on one sector relative to those on other sectors. Oversized holes will be machined into the wheel, and the sector location bushings will be placed into the holes. After accurately locating these parts, adhesive will be injected into the clearance between the hole and the OD of the bushing. After the adhesive sets, the bushings will be permanently located at the proper position in the wheel.

TPC Supports

The STAR TPC is supported by four compact, rigid mounts, located at or close to the horizontal plane of the detector. They are located at the extreme "corners" of the detector and transfer the entire load of the TPC, central trigger barrel, SVT, and TOF upgrade from the wheels to the inner wall of the magnet cryostat. One of the mounts at each end will be slightly off the horizontal to allow a TOF module to be inserted. All mounts incorporate a ball and cone arrangement to insure repeatability. These mounts allow the TPC to be adjusted in x, y and z through the use of a combination of horizontal and vertical jacking screws. One of the supports is adjustable (constrained) in x, y and z . On the same side but at the opposite end of the detector is a second support which is adjustable in x and y but has freedom of motion (is not constrained) in z. The remaining two supports are adjustable only in x but have freedom of motion in y and z. This scheme results in a semi-kinematic mounting system which with care will minimize strain in the TPC.

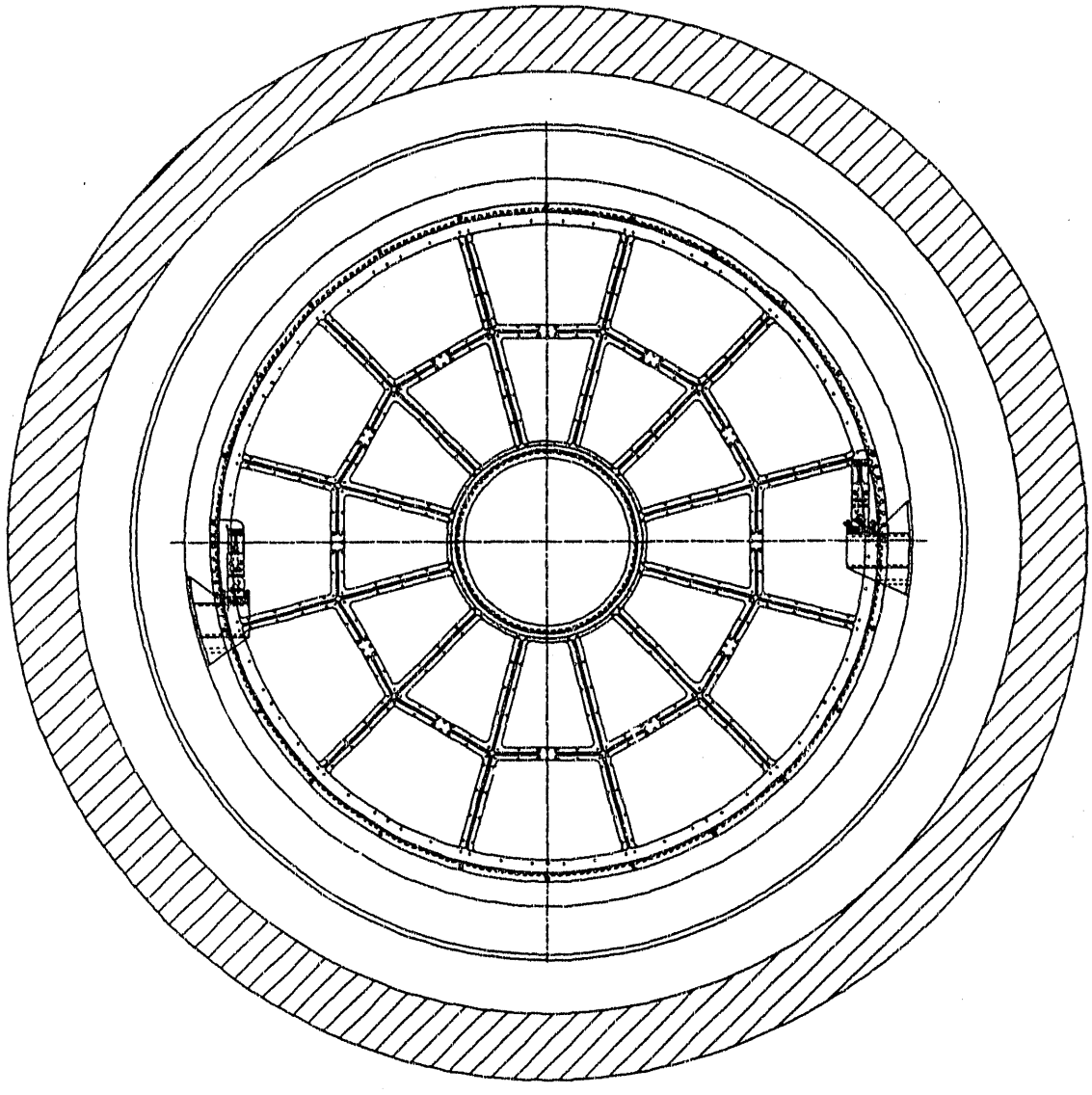

Figure 4C-34 A end view of the TPC inside the cyrostat displaying the mounting structures. The end-cap wheel structure is clearly displayed.

Pad Plane Sectors

The pad plane sectors are the active elements of the TPC. On these sectors are mounted the wire grids that create the high field regions in which the drifting ionization clouds form avalanches. Also mounted on these sectors are the pads which detect these avalanches. The sectors also serve as part of the gas containment vessel for the active region of the TPC. There are two types of sectors which mount to the "O" ring surfaces on the spokes of each wheel. There are 12 inner sectors which fill in the space between the inner and medial rings and 12 outer sectors that fill the space between the medial and outer rings. The medial ring is actually a dodecagon so that the inner and outer sectors abut each other on a straight line. The mechanical support for the sector is

the sector casting. This is an aluminum (A356) casting which resembles half of a waffle iron, i.e., a thick plate containing many pockets. The pockets are separated by ribs as shown on Figs. 4C-35 and 4C-36.

The cathode pads are etched onto large multilayer NEMA G-10 printed circuit boards. These assemblies are called the pad planes. Figure 4C-37 illustrates the pad layout for both the inner and outer sectors. Note that the pad size and row spacing is different between the inner and outer sectors. A pad plane is glued to the flat, unpocketed side of the sector casting. The flatness of the pad planes and the positioning of the pad plane sectors relative to each other and to the **E** and **B** fields will affect the position of tracks relative to the pads and will affect track arrival times. The accumulated tolerance for all of these factors inclusive is ± 0.5 mm. The side of the pad plane away from the sector casting contains the cathode pads and the side of the pad plane toward the casting has connectors soldered to it. The casting has holes in it so that these connectors can protrude into the casting's pockets. The pad plane is manufactured on a gas tight multilayer board. In the multilayer board, the vias (plated-through holes

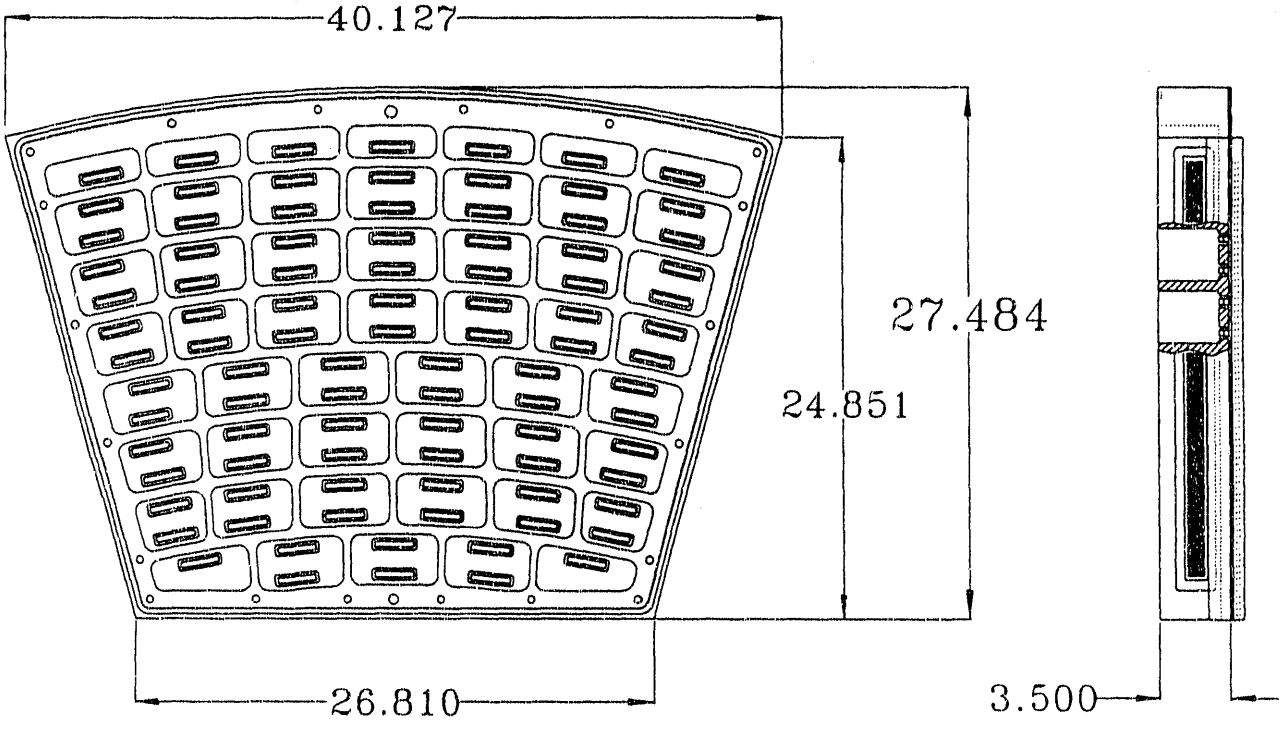

OUTER SECTOR ASSEMBLY

Date: 5-21-92

Scale: None

Figure 4C-35 Outer pad plane sector assembly.

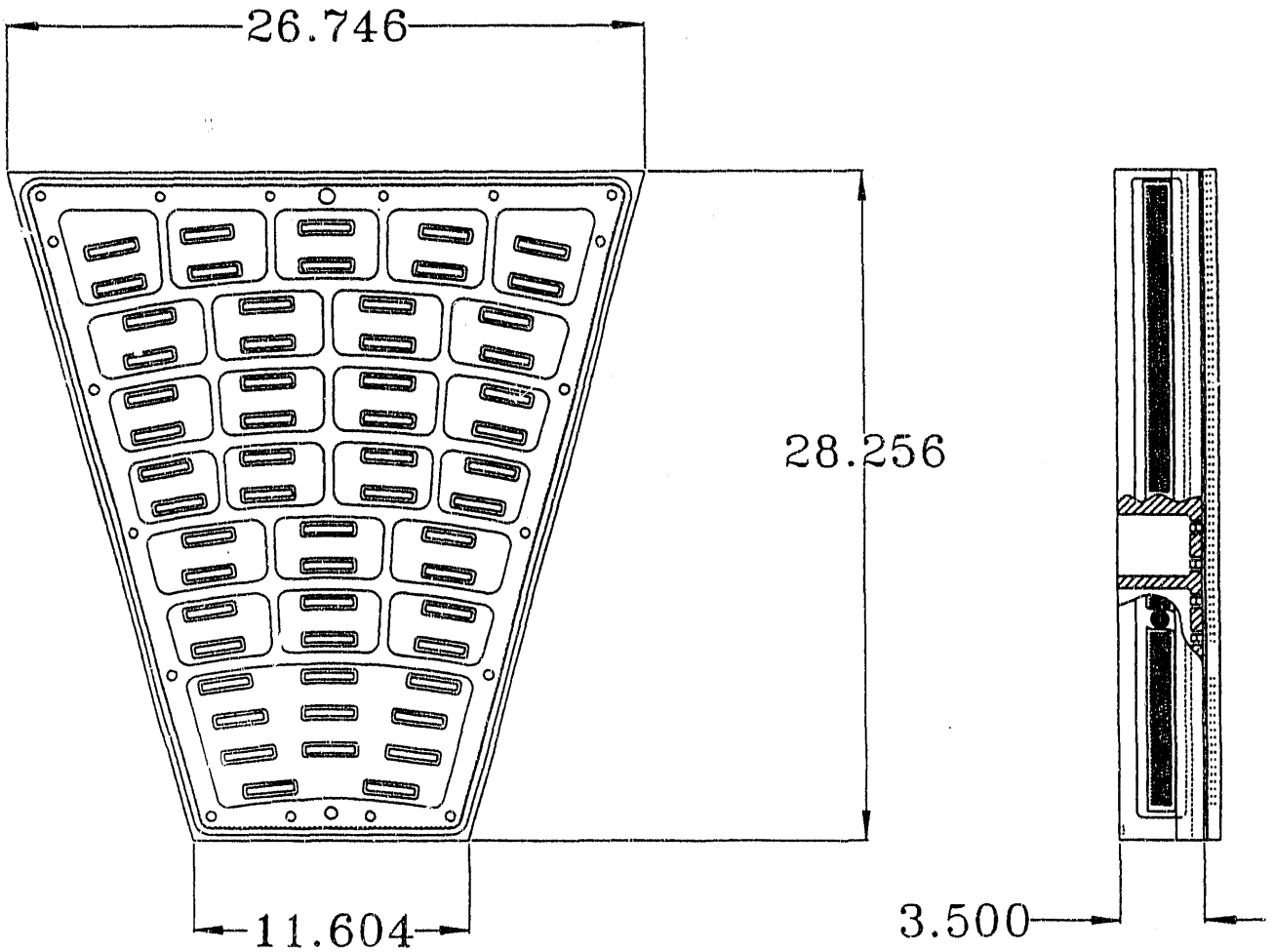

INNER SECTOR ASSEMBLY

Date: 5-21-92

Scale: None

Figure 4C-36 Inner pad pad sector assembly.

which are part of the electrical path carrying signal from pad to connector) do not go all the way through the board. Hence there are no perforations which must be sealed. The construction materials for all structures that contact the active region must be free of gas-poisoning volatiles in order to maintain TPC performance. The materials approved for interior use are listed in ALEPH and PEP4 reports.

As pictured in Fig. 4C-38 and summarized in Table 4C-12 below, there are three wire grids mounted above the pads. The first grid is composed of alternate field and anode wires. The anode wires are gold-plated tungsten with a 20 μm diameter. The

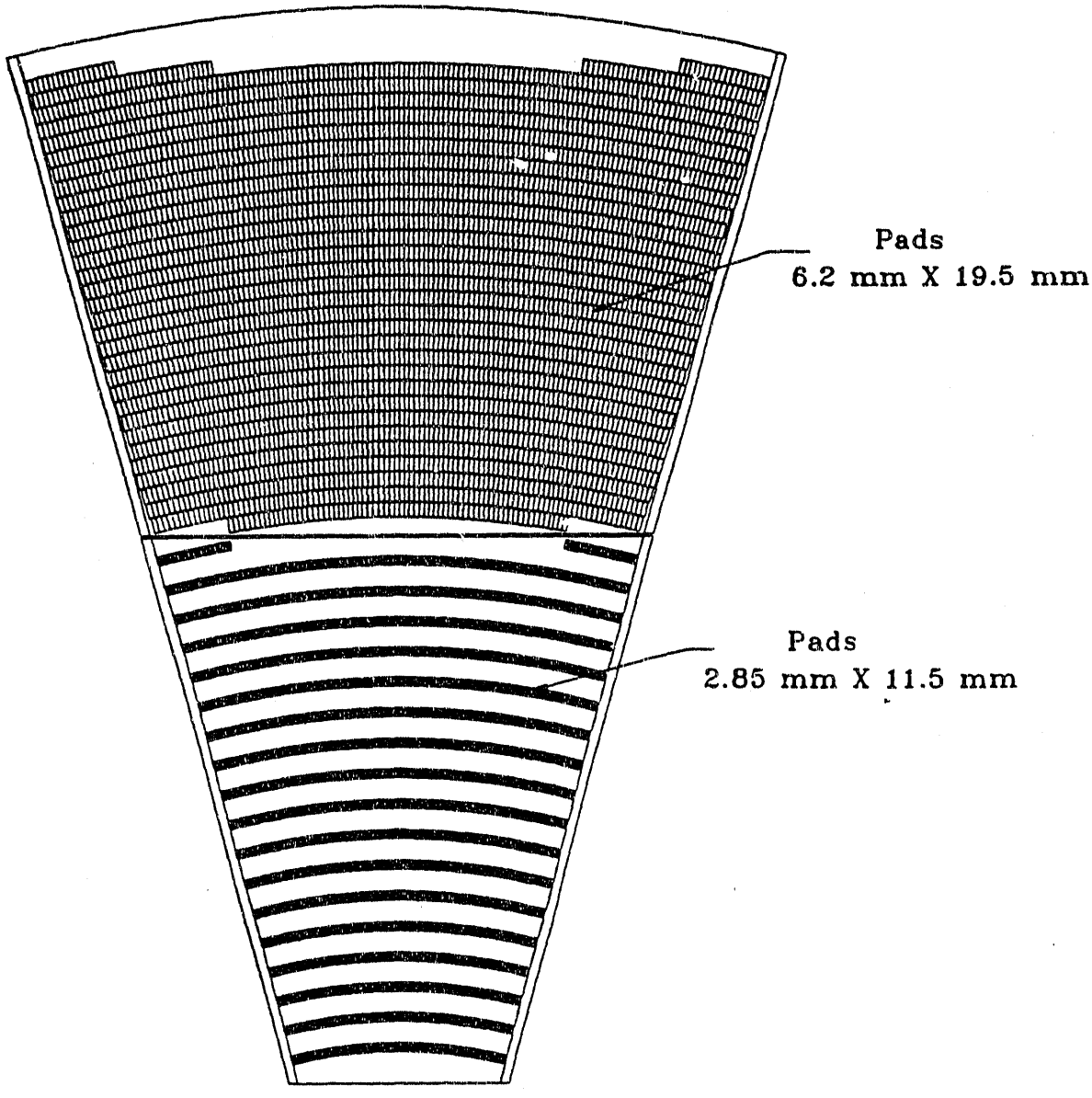

Figure 4C-37 The pad layout for the inner and outer pad plane sectors.

Be-Cu field wires are 125 μm in diameter. Their large radius reduces the field at the cathode to improve resistance to high voltage breakdown. This is particularly important at the gas-conductor-dielectric triple point where the wire enters the support epoxy. The second grid is a ground plane and the third grid is the gating grid which blocks electrons from unwanted events and captures positive ions from the avalanche before they can enter the main drift region. The tolerances, listed in Table 4C-12 for distances from wire to pad, are based on the wire gain uniformity required for dE/dx and the calculations of F. Ragusa and L. Rolandi[55] . The ±100-μm tolerance on the ground

[55] F. Ragusa and L. Rolandi, ALEPH-LEP Note: 89, Feb. 1, 1983.

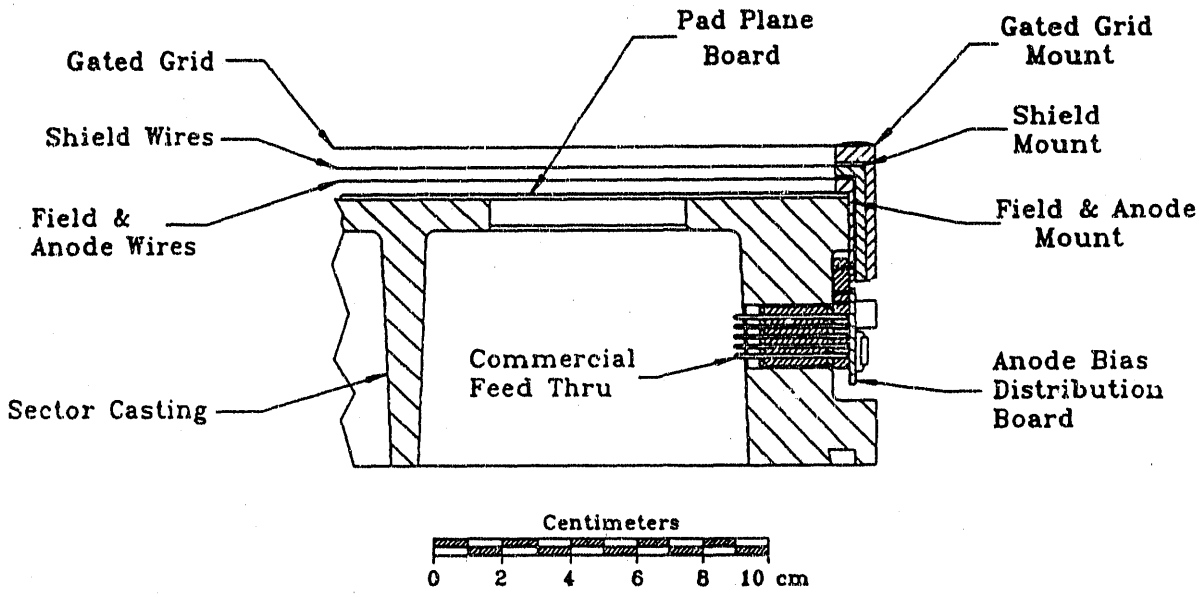

Figure 4C-38 A detail of the edge of a pad plane sector illustrating the wire grid mounts and the anode bias distribution board.

Table 4C-12 Specification for the wire grids

Grid	Distance ± tolerance from pad plane (mm)	Wire spacing (mm)	Material	Diameter (mm)	Stringing tension (N)
Outer Sectors					
Anode	4 ± 0.1	4 ± 0.1	W	0.020	0.5
Field	4 ± 0.1	4 ± 0.1	Cu + Be	0.125	3
Ground	8 ± 0.1	1	Cu + Be	0.075	1.2
Gating	14 ± 0.1	1	Cu + Be	0.075	1.2
Inner Sectors					
Anode	2 ± 0.1	4	W	0.020	0.5
Field	4 ± 0.1	4	Cu + Be	0.125	3
Ground	8 ± 0.1	1	Cu + Be	0.075	1.2
Gating	14 ± 0.1	1	Cu + Be	0.075	1.2

plane position will give a gain variation of $\Delta G/G = 4\%$. The tolerance on the in-plane displacement of a single field wire of $\pm$ 100 μm will cause $\Delta G/G = 6\%$, but for dE/dx this is not important since the gain shifts on adjacent sense wires will tend to cancel. This kind of wire gain error will increase the tanα error, but not significantly compared to Landau fluctuations. In-plane shifts of the anode wires by $\pm$ 100 μm produce gain variations of only $\Delta G/G = 2\%$. These calculations are based on total surface charge on the wires and neglect the fact that avalanches are localized on one side of the wire. The actual gain variations could be somewhat larger for displacements in distance to the pad plane. The gain errors will also be different for the inner radius sectors where the anode wire plane is not centered between the ground wire plane and the pad plane. The flatness and parallelism of the pad plane and the wires will be maintained by the stiffness of the sector casting. These wires are glued to and supported by wire mounts which are located along the two radial edges of each sector. To minimize the 'dead' area of each pad plane sector, the wire plane mounts are stacked on top of each other (see Fig. 4C-38).

It should be noted at the outset that the sector fabrication procedures which follow are basically a description of the assembly of the corresponding section of the EOS TPC, with modifications as appropriate for the larger production volume of STAR. The description below is for a single sector. Due to the large number of sectors and the tight schedule, sectors will be built in parallel.

The required equipment is one wire winder, a minimum of six granite tables of minimum size 8 feet by 12 feet, and a low-humidity clean room with crane capability and large enough to hold four of the granite tables and four two-man tech teams. In order to meet the schedule, two shifts a day are required for a total of eight two-person teams. As an alternative, by adding four more tables and one more crane, all eight two-person teams may be on the day shift.

The first task is to bond the pad plane to the sector casting. The basic workstation is shown on Fig. 4C-39. The pad plane is held down to a granite table (surface plate) by vacuum. A fine mesh screen lies between the pad plane and the table to make gaps for the air to escape as the vacuum is drawn. The edges around the pad plane are sealed with tape. This tape barrier is penetrated by hypodermic needles which serve as vacuum lines. Epoxy adhesive is rolled onto the sector casting and the casting is lowered onto the connector side of the pad plane. Fiducial points on the pad plane and the sector casting are positioned relative to each other during this process. The casting is held on the pad plane by its own weight; any additional force might well deform it from its free state. Any lack of flatness in the casting's free state is filled in by the epoxy adhesive.

The next step is to take a very fine precision finish cut (a few thousandths of an inch) across the back of the sector casting producing the desired thickness for the sector assembly. This brings the reference surface from the front of the pad plane to the back of the sector casting. This reference transfer eases subsequent fabrication operations and provides a precision mounting surface for the sector/wheel interface. It also provides a flat surface to mate with the cold plate.

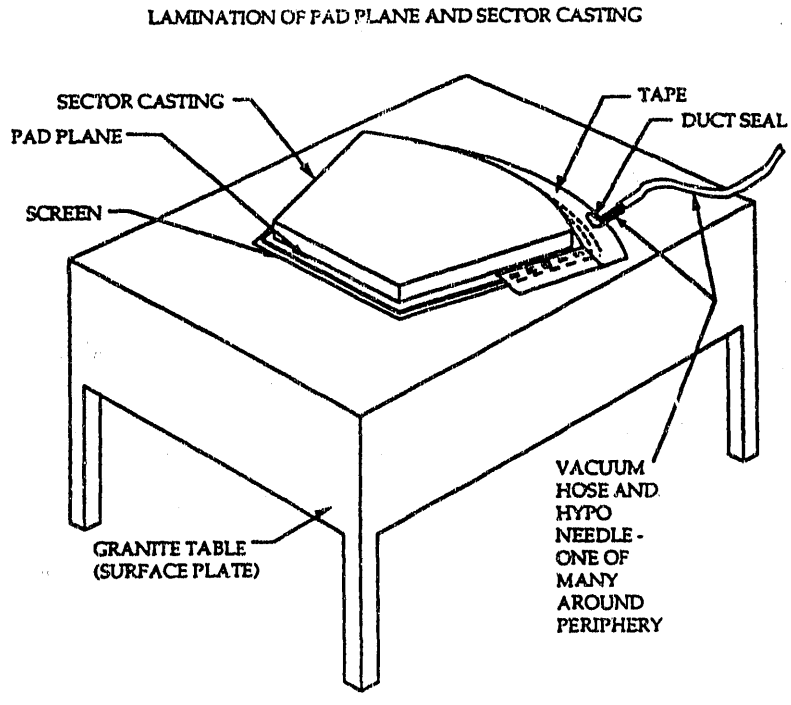

Figure 4C-39 A diagram showing the basic workstation for pad plane assembly. The procedure for gluing the pad plane onto the sector casting is illustrated.

The last operation to be performed outside of a clean room is the installation of the sector location bushings. These are bushings which locate the sectors relative to the wheel and, therefore, to each other. Taking a tip from our predecessors, the bushings will be optically located relative to a set of fiducials on a fixture mounted to a surface plate. Then the sector, with the pads facing upward, with epoxy in its slightly-oversized bushing holes, will be lowered over the bushings. Using previously-set microscopes and the pad-plane fiducials, the subassembly will be moved into position. After the epoxy sets, the bushings will be permanently located at the proper position relative to the pad plane.

The following operations must be performed in a low-humidity clean room. If the epoxy which bonds the wire grids to their mounts does not cure in a low-humidity environment, surface tracking of the epoxy will occur at a lower voltage. If the room is not clean, dust particles will settle on the grid wires precipitating arc-overs.

At this stage, the wire mounts for the field and anode wires are fastened to the sides of the sector casting. The mounts overhang the periphery of the pad plane slightly. The assembly is set on a granite table (surface plate) with the precision surface of the casting down. This puts the wire mounts and pad plane facing up and at known heights. As illustrated in Fig. 4C-40, wire combs are set along the radial sides of the assembly and aligned to the pads. The combs are grooved fixtures which define the height of the wires relative to the pad plane and also the wire spacing. The wire heights are such that they are not actually in contact with the top of the mounts. If they were, the mounts would determine the height, and occasionally lateral position, rather than

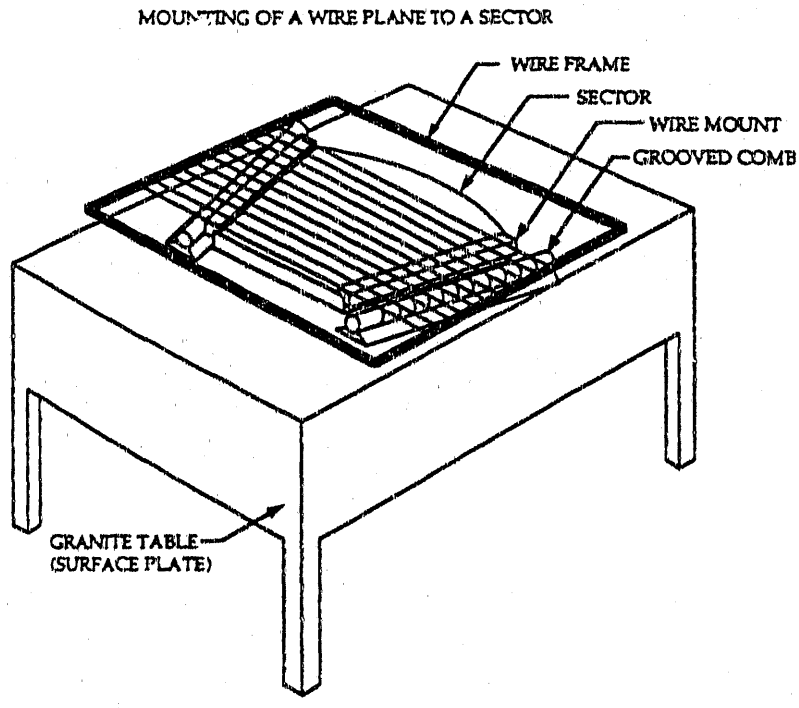

Figure 4C-40 A diagram illustrating the procedure for mounting the wire grids onto the pad plane sectors.

the combs, which are more accurate. A bead of epoxy is laid over the wires. It sinks around the wires to bond them to the mount while they are held at the proper elevation. The anode wires will be soldered to termination pads on the wire mount structures. Anode HV distribution cards with isolation resistors and bypass capacitors plug into the wire mount structures and provide a fan out of one external high voltage connection per group of 36 anodes. This arrangement will result in 5 bias supply channels per sector and will require two LeCroy 1440 bins to service the whole detector. The distribution cards are located in the drift gas volume to control surface current leakage. Figure 4C-41 shows a schematic diagram of the circuitry for the anode bias distribution system.

The wire mount for the shield grid is installed on top of the wire mount for the anode and field grid, and then the grid itself is laid down and glued by the same method as described above.

The wire mount for the gating grid is installed on top of the wire mount for the shield grid and the shield grid wires are installed as described above.

Final inspection of the completed sector assemblies will be performed by physicists aided by technicians. They will be looking for shorts, inadequate voltage standoff capabilities, and gas gain uniformity.

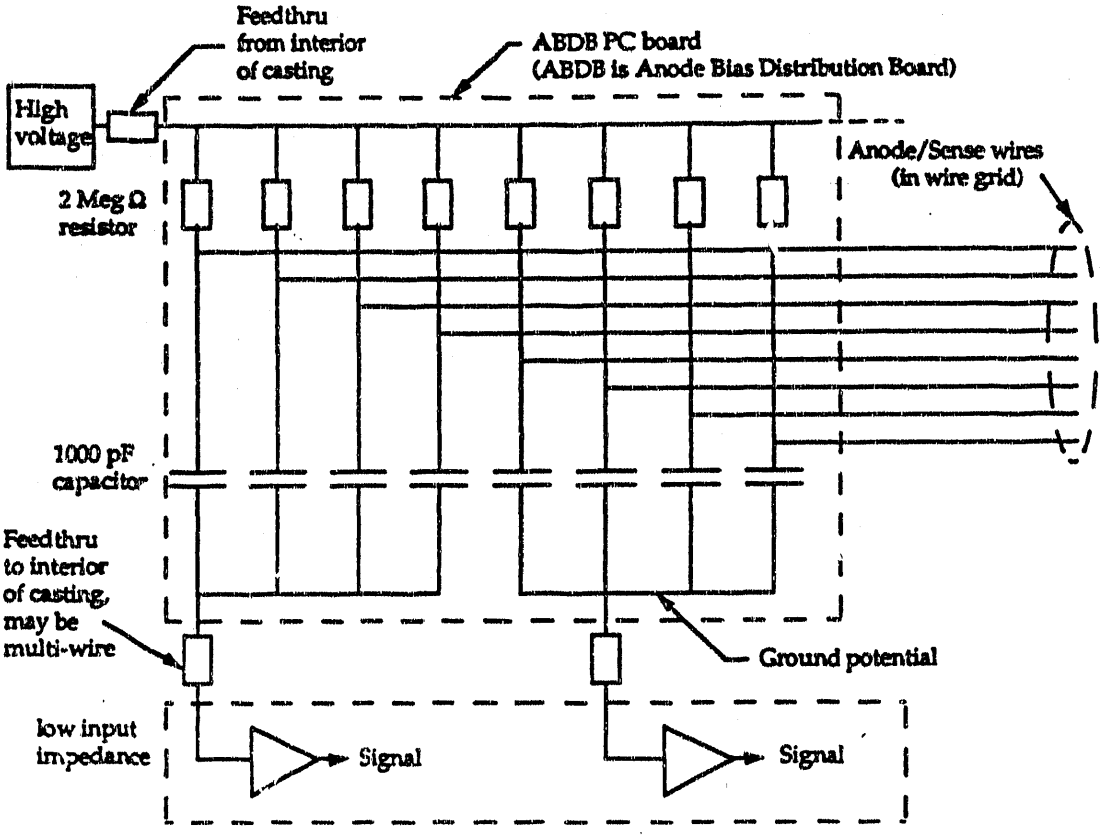

Figure 4C-41 A diagram of the anode bias distribution circuit.

Cooling System

The primary function of the cooling system is to maintain a temperature variation of < 1.0° C for all components in contact with the gas. The sources of heat in the TPC are the front end electronics, the mother board immediately following, and the resistor chains on the IFC and OFC. When the TOF upgrade is installed, there may be an additional heat source equal to 8 kW, from the TOF PMTs, distributed over the OFC. The cooling system is broken down into several circuits for the purpose of this discussion. These are the wheel, the sectors, the OFC cooling water distribution systems, and the chilled gas cooling for the IFC.

Cooling manifolds will be mounted on the wheels for distribution of coolant to each sector and to the OFC. The coolant temperature can be controlled by use of slow controls and heat exchangers. The expected temperature gradients will determine the amount of manifolding that must be provided. Trace cooling lines can be placed on the OFC and on the wheels.

Excellent temperature uniformity must be maintained over the gas side of the pad plane. The source of heat for this region is the front end electronics board. Figure 4C-42 shows a cross section of the front end electronics board and the surrounding components. The flow of coolant through the cold-plate passages will be such that the

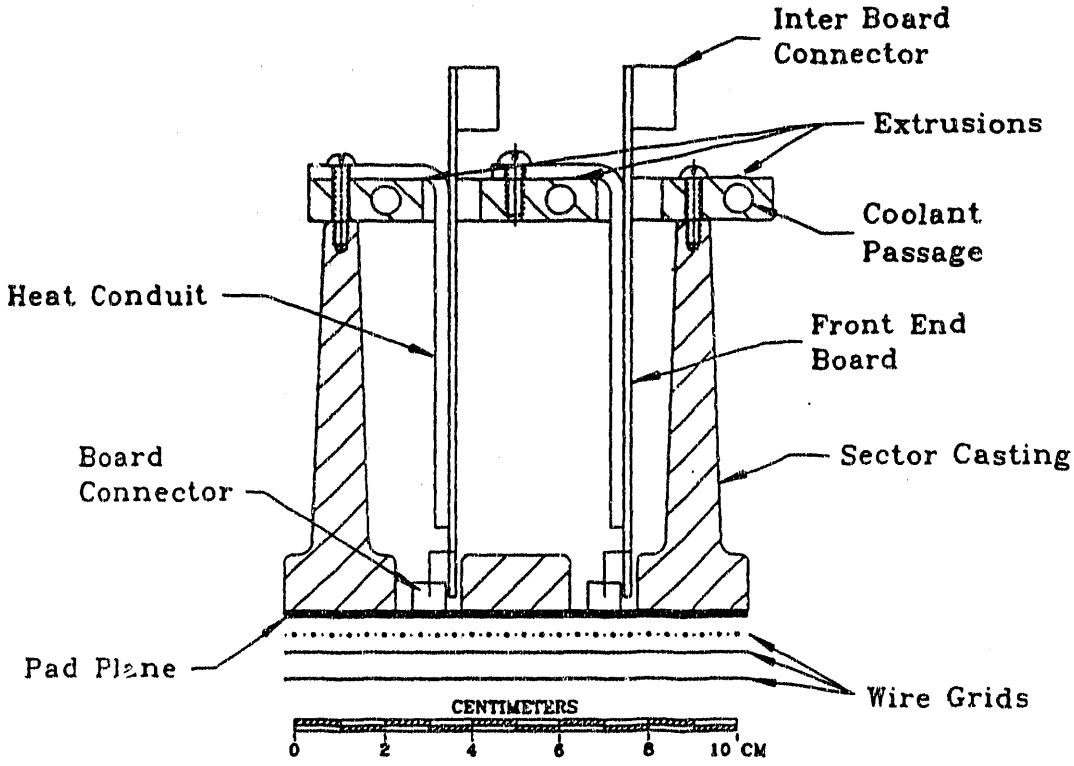

Figure 4C-42 Cooling of the front-end electronics cards using heat conduits to a cold plate which contains extrusions with internal coolant passages.

direction of flow in a given line is opposite that in its immediate neighbors. Since the cold plate is a low-resistance thermal path, this scheme will result in good temperature uniformity over the plate. The expected power dissipation on the front end electronics chip is 100 mW per channel. Each front end electronics board will be connected to 32 pads and will generate 3.2 W. The estimated size of the board is 142 × 96 mm. This G-10 front end board will be laminated with an aluminum plate. The aluminum plate has one end bent 90° and this tab is attached to the cold plate as shown in Fig. 4C-42. The cold plate is attached to the sector casting rib. This plate has ports in it which allow the installation of the front end boards. The cold plate may be an aluminum plate traced with cooling tubes or be made from many bar extrusions with water passages in them. Each cold plate will have an inlet and an outlet connector. If one of the front end electronics boards has to be removed, no water connections will have to be broken.

A preliminary heat transfer calculation was made using the ANSYS code to determine the gradients that may occur on the gas side of the pad plane. This model is shown in Fig. 4C-43 and assumes the heat to flow toward the pad plane through the connector. The connector model assumes that all the heat goes through the leads. This is a result of the very low thermal conductivity of the plastic molded material. It was assumed that there were two rows of 2.54-mm pitch copper leads. The length of the leads was estimated to be 15 mm. The thermal resistance of the leads was calculated to be 0.075° C/W/m. Elements modelling the leads were assigned a thermal conductivity that, with the heat flow area, matched the value above. A convection film coefficient of

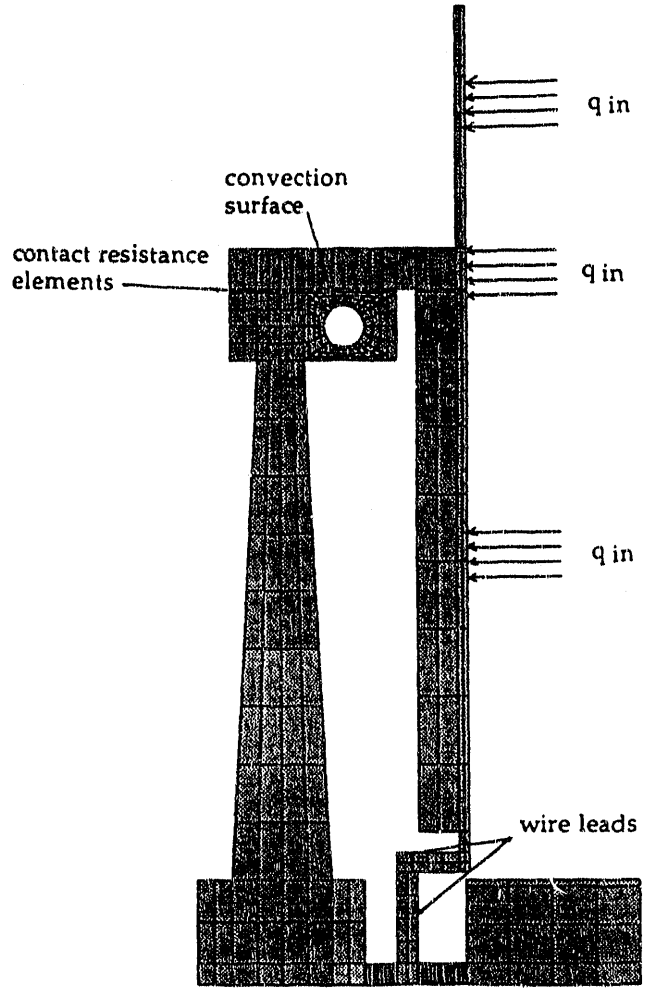

Figure 4C-43 A diagram of the thermal model used to study heat flow in the pad plane sectors.

10,000 W/m^2/°C was assumed in the cooling passage. This corresponds to a typical value with reasonable water velocity. The contact resistance at the aluminum plate/cold plate interface was estimated to be 6.5×10^{-5} m^2 °C/W. This value can be achieved with a reasonable force exerted by the attachment screws. The equivalent conductivity of the pad plane was calculated using results from a submodel consisting of a 3.2-mm (1/8 in) thick G-10 plate with and without Cu strips along the underside. Subjected to a dummy heat load, the conductivity of the submodel with Cu was found to be about three times that of the same model without Cu.

The results of the ANSYS calculations, with the above nominal values, indicate that the maximum temperature difference at the gas side of the pad plane is <0.5° C. The contact resistance value was increased by a factor of 2 and the temperature difference still did not exceed 1° C.

The IFC cooling can be accomplished by controlling the temperature of the insulating gas. A slow flow of gas will be necessary for temperature control. Since the

IFC is expected to be fabricated from a low heat transfer material, variations in temperature will only occur over long periods of time.

Gas Handling System

The gas handling system must maintain high purity gas at well defined mixture percentages. Mass flow meters and controllers will be used to measure and control the individual components of each mixture. Gaseous components will be measured or controlled using the standard mass flow meters/controllers that are presently used in the semiconductor industry. These units can be provided with an absolute accuracy of better than 1 percent and a reproducibility of 0.2 percent. For liquid components, custom flow meters will be used. BNL is presently using one based upon thermal transfer but there also exist units based on timing a temperature pulse. Each system will use a microprocessor based read-out/interface supplied by the mass flow meter manufacturer to set the flows and to interface to the slow control system using the IEEE-488 standard. All plumbing will use standard Swagelok stainless steel fittings and bellows sealed valves which are air pressure and hand operated. Chamber pressure will be regulated with a closed loop system using capacitance manometer pressure sensors and proportional solenoid valves. Both items will be supplied by the manufacturer of the flow meters. In systems where several chambers share a common gas mixture, a mixer will be employed that uses one component as a reference to proportionally control the flow of the other components, and each chamber will be supplied by a separate flow controller. A sub-atmospheric exhaust system will be used to remove gas from the chambers and vent it to the outside. All on-line primary gas supplies will be located in a specially constructed room along with the mixers and associated control system interface. Cryogenic sources will be used for inert gases where possible. The entire system will be monitored and controlled using the experiment slow control system. Monitor chambers will be used with each system to measure changes in gas composition. Figure 4C-44 shows one possible system for supplying P-10 to the main TPC.

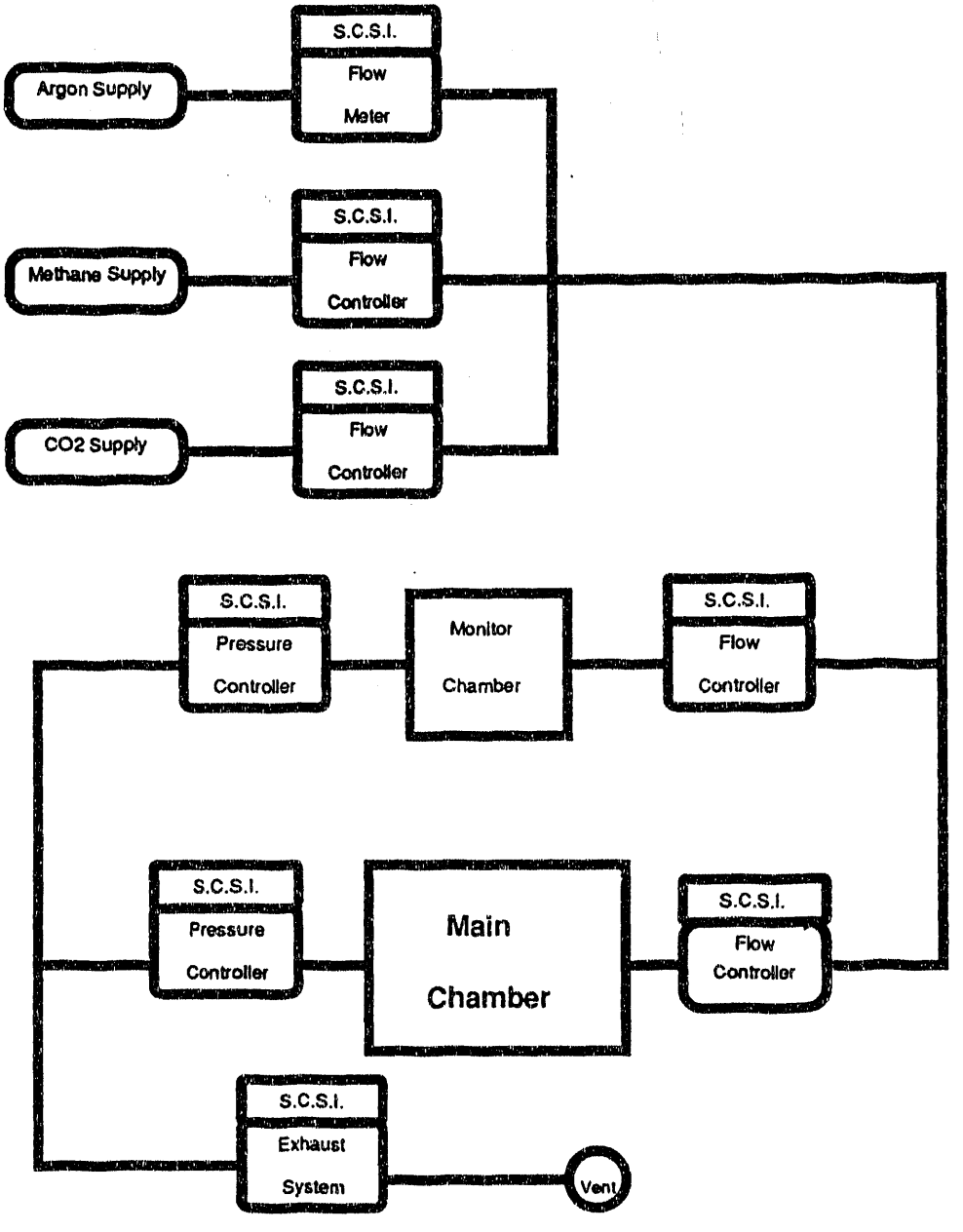

Figure 4C-44 A schematic diagram of the gas handling system.

Laser Calibration System

The laser calibration system will use two Nd:YAG lasers which will be mounted on platforms above the return iron for the magnetic flux (and above the PMTs for the EM calorimeter). Each laser will service one half of the central TPC. The primary beam from the Nd:YAG laser has a wavelength of 1064 nm (IR). The frequency will be quadrupled with two frequency doubling crystals and the resulting 266 nm (near UV) component will be isolated with a harmonic separator prism. At this frequency, laser light will induce ionization through two-photon excitation of contaminants in the gas. The pulse duration of the Nd:YAG lasers is 5 ns, the energy per pulse is up to 45 mJ,

and the maximum repetition rate is 10 Hz. The beam intensity and polarization are controlled by a system consisting of a half-wave plate and a Glan polarizer. The laser beam is focused with a two-lens system which produces a waist through the active volume of the TPC. The incident vector of the beam is defined by a two-mirror system with each mirror on a remotely controllable kinematic mount with two degrees of freedom.

The beam is then transported through aluminum beam pipes to the pole tip and then into the magnetic field volume via one of the cable conduits. Inside, the beam is brought to a splitter ring which is mounted to the TPC wheel. On this splitter ring, the beam is divided by optical elements into six parallel paths that enter the TPC volume axially through quartz windows in the IFC support ring and one path that is used for alignment monitoring. This beam terminates on a quadrant silicon detector which serves as a fiducial point for the origination of the beam vector into the TPC. Figure 4C-45 provides a diagram of the system.

Inside the active volume of the TPC, rails are mounted along the IFC which hold five beam splitters each. The semi-transparent beam splitters and their mounts will be electrostatically shielded so as not to influence the E field within the active volume. These splitters direct beams through the active region of the TPC along lines of constant η. In total, there will be 30 calibration beams per TPC half. An effort will be made to balance the power of the beams inside the TPC, but due to the variations in the production of the partially reflecting surfaces it is not expected that this can be done to better than a factor of two. In addition to the 5 calibration beams, the remaining fraction of each beam passes through the opposite TPC half and finally terminates on a quadrant silicon detector on the back side of the beam splitter ring. Thus the absolute position of each beam that passes through the TPC is measured at its entry to and exit from the TPC. This defines the vectors and allows detailed monitoring of individual beam alignment.

4.C.5.c Initial Assembly & Alignment

The assembly procedures proposed have relied strongly on information obtained from ALEPH TPC personnel. Some of the estimated cost and activity durations are based upon their experience.

Miscellaneous Fixtures

Several fixtures are required to facilitate certain tasks during TPC assembly and maintenance. One major item is a test stand that serves as an assembly and insertion device. Initially, it supports the OFC to which all other components are attached. After the assembly is complete, tests are run while the TPC is on the test stand. After testing, it may be possible to use this stand as a shipping fixture. After inspection at RHIC, the stand may be used as part of the insertion fixture.

The TPC will be installed into the cyrostat using a central beam. The installation procedures are discussed in section 5.A.3.

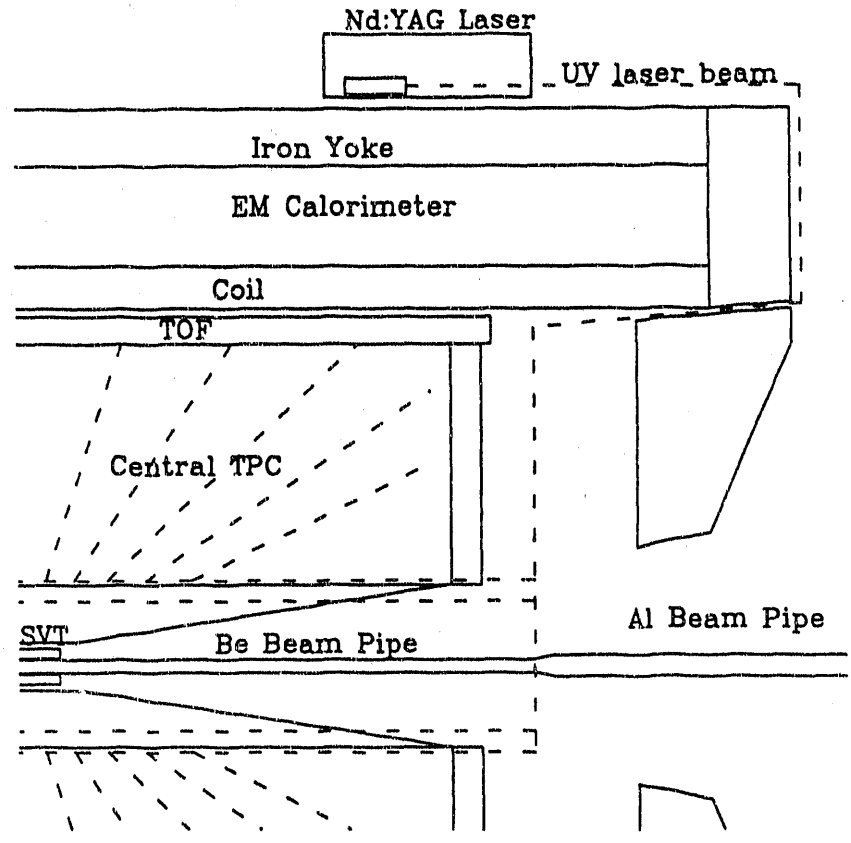

Figure 4C-45 A schematic of the laser calibration system.

Another important fixture is the sector removal tool. This tool is used to initially place the sectors on the wheels and is then used to remove and replace any sectors that fail during operation. It must have a minimum of 3 degrees of freedom. The sector removal tool must be sufficiently stiff that it can maintain the sector to within 1 mm of its true position when the sector is being removed or replaced. The space between sectors is about 3 mm when on the wheel. If the sector removal tool cannot be made sufficiently stiff, then adjustments in the x, y plane must be available to allow the use of fiducials and telescopes to guide the sectors into position.

TPC Assembly

The TPC assembly follows a logical sequence of steps that is summarized below. At specific points in the assembly, the position of specific components relative to each other must be determined. The method of accomplishing this will be discussed later.

1. The OFC is placed on the test stand.
2. The high voltage membrane is attached to the OFC.
3. The sector support wheels are attached to the OFC.
4. The sectors are installed using the sector removal tool.
5. The IFC is attached to the wheels.
6. The cooling distribution lines and manifolds are attached.

7. The laser system is installed, including the splitter ring.
8. The gas supply and return are connected.
9. The pressure tests are conducted.
10. The front end electronics are connected.
11. The mother boards are connected.
12. The cables and optical fibers are connected.
13. The TPC power is applied – ready for testing.

The IFC/wheel joint is shown in Fig. 4C-46. It must have provisions for the SVT support and also provide access for the laser calibration beams. The IFC and SVT supports are inserted into the east end. The west end has a slip flange. Since the OFC and IFC have different coefficients of thermal expansion, compliance is provided by fixing one end of the IFC but letting the other end float longitudinally. This type of joint should preclude loading the IFC excessively if the operational temperature is different from the assembly temperature. During shipping, the IFC will not be attached tightly to the wheel since large temperature swings are expected during the trip across the US.

Alignment Methods

The accuracy of component machining and placement must be verified at the end of several tasks during the fabrication and assembly of the TPC. This section will describe those tasks requiring precision alignment and how it is proposed that they be accomplished. For clarity, the discussions will be by components.

The two OFC rings (shown in Fig. 4C-29) define the parallelism of the pad planes. The distance between the pad planes is also established by the distance between these rings. While the OFC is on the mandrel, the two rings are brought into position over the wound inner aluminum skin. The rings are centered on the aluminum by spacers. As the mandrel is slowly spun, dial indicators will measure the runout. The ring on one end is adjusted until the average runout is a minimum. Dial indicators can easily detect 10 μm (0.4 mil) of deviation as the cylinder turns. Adhesive is injected into the gap through holes in the ring. This fixes one of the rings in place. On the side of the mandrel opposite the winding head a 5-m horizontal tooling bar can be set up with its axis parallel to the axis of the cylinder. Two optical transit squares are placed onto the tooling bar carriage. One of the optical transit squares is placed at the other end of the mandrel. The vernier on the horizontal tooling bar will provide the position of this square relative to the first one to about 25 μm. Optical tooling scales and the transit

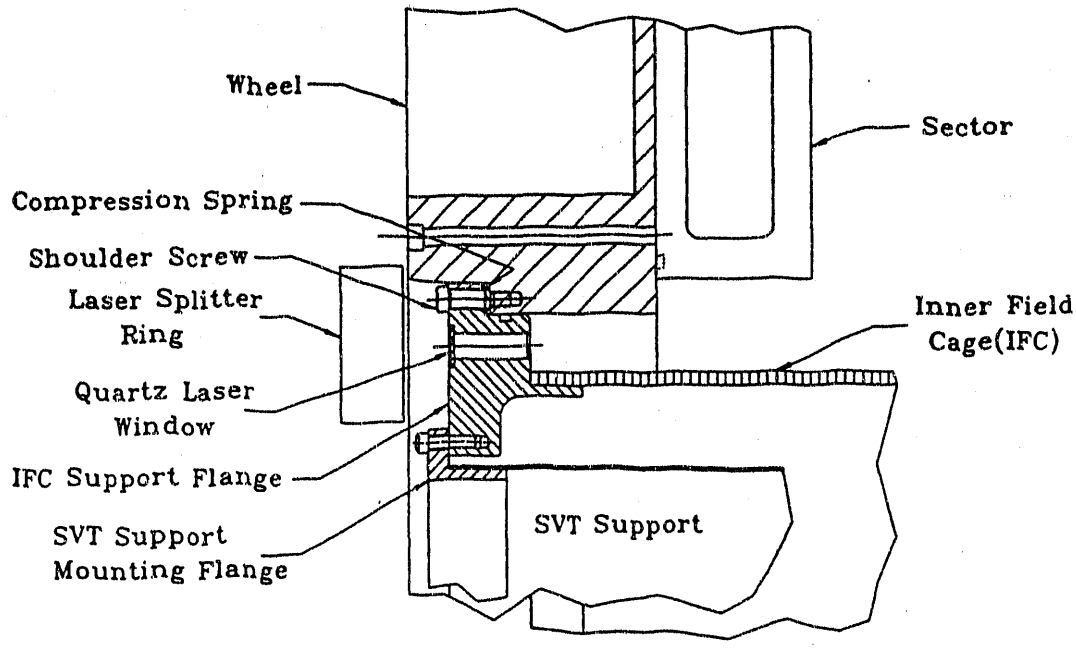

Figure 4C-46 Inner field cage and SVT support mounting to the west end of the end cap wheel.

square can be used to position the other ring edge parallel to the fixed one and locate it at the proper distance. This setup will also be used to determine the squareness and location of each sector and, therefore, of the pad planes.

The pad locations can be fixed within the artwork to about ±10 μm. On the same artwork as the pads, fiducials will be drawn at each corner. A bushing placement fixture will be fabricated with locations accurate to ±10 μm. The use of this fixture has been described earlier. This is the same method of bushing placement used in the fabrication of the ALEPH TPC.

After the sectors have been installed on the two wheels, the pad plane positions and squareness must be determined. The optical transit squares and tooling scales can be used for these measurements. This technique requires that three reference locations (relative to the pads) be available at the back of each sector. These can be precision machined after the pad plane has been attached to the aluminum casting. Their location relative to the pad plane can be held to about 25 μm. After the wheels have been attached to the OFC, the sectors will be installed. Each sector can be inspected by three tooling scales and the transit square. Errors of about 50 μm can be detected. This corresponds to an angle of about 0.1 mrad over the pad plane of a sector. If a sector is out of tolerance, another one must be installed. It may be possible to re-machine the back of a flawed sector depending upon the type of tolerance error measured. A small amount of shimming may be allowable since the O ring seal is fairly large and compliant and the differential pressure across it is almost zero. If another sector indicates the same out-of- tolerance, the machining in that area of the wheel may be at fault. This must be noted and a replacement sector must be shimmed to fit.

Another method of determining the relative positions of the various components is the use of theodolites. Various locator points are provided with permanent holders for balls and targets. The balls allow an accurate measure of relative locations by coordinate measurement machines (CMM), and when replaced by targets, these same locations can be determined by theodolites. It is felt that the optical transit squares and tooling bars and scales will be faster and will provide adequate precision.

Maintenance

Based upon the operating experience of the DELPHI and ALEPH TPCs, it will eventually be necessary to work inside the STAR TPC. The mother boards and front end electronics boards are accessible from the back of the sectors and sectors themselve can be removed for service to the pads or wire planes. Any problems with the resistor chain, central membrane, the copper stripes, or the laser calibration beam mirrors must be handled by personnel entering the tracking volume. The structural support of the OFC has been specified to allow a 90 kg (200 lb) person to stand on the interior surface. The IFC configuration has been chosen to withstand a point load of 23 kg (50 lb). This load corresponds to a person leaning on the IFC cylinder, but not standing on it. The resistor chain and high voltage cable will be located at about the –45° level relative to the center horizontal plane for easy access once a person is inside.

Sectors can be removed and replaced by disconnecting the cables and the mother boards and attaching the sector removal tool. This tool should be sufficiently stiff to allow removal without using optical sights and mechanical adjustments. If not, then the procedures would be the same as those presently used by ALEPH personnel. If possible, the design will allow removal without disconnecting the front end electronics, but further design work must be completed before this is certain. The installation of a new sector is the reverse of its removal. It is anticipated that about 24 hours will be required to change a sector.

4.C.5.d Engineering Testing

4.C.5.e Transportation, Reassembly & Alignment at RHIC

Shipping

It is proposed to ship the TPC assembled on the test stand. The OFC and wheel provide excellent protection for the sectors. The test stand, which must accompany the TPC, is a stable base that can be supported on shock isolators to provide protection comparable to that of a typical air-ride truck. The total weight of the assembled TPC is 7260 kg (8 tons) and the overall shipping size is about 4.3 × 4.3 × 5 m high (14 × 14 × 16 ft). Conversations with a shipping company indicate that the size and weight are not severe obstacles to truck transport. Other means of shipping will be considered, both sea and air transport. Although the TPC could be shipped fully assembled, a more conservative plan would be to disassemble it and ship the parts separately. The cost estimate includes the tasks of shipping using this plan.

4.C.6 Testing and Calibration Issues

Testing and calibration of the STAR TPC will be done using the laser system (described in section 4.C.2.b).

4.D.
Front End Electronics

4.D. Front End Electronics

4.D.1. Specialized Physics Issues

The TPC and the SVT operate on similar principles. In both cases a position is determined by measuring the time the electron cloud generated by primary ionization drifts towards an anode. The charge is integrated and shaped consecutively by a shaping amplifier. The pulse height spectrum covering the maximal drift time is stored in an analog store and digitized. The position of the centroid is then a measure of the drift time and the amplitude depends on the amount of primary ionization, leading to a position and to a specific energy loss measurement.

4.D.2. Description of Subsystem

Drift velocity, drift length and degree of diffusion determine most of the parameters for the front-end electronics. For the TPC the standard gas P10 with a drift velocity of 5.5cm/μs has been chosen as the most probable candidate. The average longitudinal diffusion determines the peaking time of the shaper. It is chosen so that the shaping time of 180 ns is comparable to the diffusion width of the pulse in the time domain. From the shaping time a sampling frequency of approximately 12 MHz can be derived. Thus the total drift space of 210 cm is divided into about 500 time samples. The dynamic range of the ADC is determined by several factors:

a) the signal to noise ratio is 40:1 for a mean minimum ionizing particle.

b) The difference in ionization between a minimum ionizing particle and a 200MeV/c proton is a factor of 10.

c) Due to large tail in ionization one has to accommodate at least a factor of two for fluctuations.

Those factors add up to a requirement of 10 bit range for the ADC. Pending precise simulations it is felt that the performance of the TPC would not deteriorate by storing 8 bit words provided that the ADC has a nonlinear response. That could be achieved by a nonlinear clock to the ADC or by a look-up table later in the data stream.

4.D.2.a. TPC Front-end Electronics

The charge collected on the TPC pads is amplified and integrated by a low noise, low capacitance preamplifier. The step function generated by the preamplifier is transformed into a near gaussian shape by a multipole shaping amplifier that corrects as well for the 1/t tail generated by the slow drift of the positive ions. The time history is stored on a 512 sample switched capacitor array (SCA) analog memory that is clocked at approximately 12MHz (synchronized to the RHIC Collider frequency). After the total event is stored on the SCA the cells are clocked out to an ADC (one per channel) for digitization. The digitized data are then transmitted to a read-out board for data collection and zero suppression before being transmitted off-chamber.

The preamplifier/shaping amplifier and SCA/ADC devices are two 16 channel integrated circuits realized in full custom CMOS technology. The IC's are mounted on a

front-end board that is attached to the pad plane by a connector. Each front-end card contains the electronics for 32 channels and is connected by a cable to the TPC readout board.

4.D.2.b. SVT Front-end Electronics

The SVT front-end electronics differs from the TPC electronics since the preamplifier is integrated into the detector in the form of a Darlington amplifier and the shaper amplifier does not contain the long time constants necessary for the 1/t tail compensation. A more detailed description can be found in 4.H.4.2. The shaping time constants of the shaping amplifier and the sampling rate of the SCA are adapted to the drift velocity, drift distance, and to the double pulse resolution of the SVT. The precise way of packaging the electronics has not yet been decided. A possible solution is described in 4.D.4.f.

4.D.3. R&D Issues and Technology Choices

The concept for the front-end electronics is entirely based on custom designed integrated circuits. The use of those circuits for TPC electronics was pioneered by the EOS TPC[1], where a four channel low noise integrated preamplifier and a 256 sample SCA[2] have been developed. The IC development for fully integrated TPC front-end electronics has been supported for several years by RHIC R&D funds (RD13). This approach is to develop the individual components separately and combine the preamplifier with the shaping amplifier and the SCA with the ADC.

4.D.3.a. Preamplifier

A new layout for the 4 channel preamplifier has been completed that is compatible with the current design tools. This design can be easily extended to 16 channels and can be combined with the shaping amplifier.

4.D.3.b. Shaping Amplifier

The main emphasis of the R&D program for integrated TPC electronics has been the development of an integrated shaping amplifier with time constants that are reproducible within a few percent. This is a complicated task since discrete component circuit techniques are not directly applicable to IC design. It is difficult to achieve the precision and consistency for the resistors and capacitors needed for uniformity of the time constants in all channels. It has been decided to solve this problem with a simple approach which allows us to trim the time constants by adjusting the capacitance. This is done on the chip by using switchable trimming capacitors in parallel with the main capacitors. In the final product the trim capacitors will be selected by blowing fuses. During the development and test phase the capacitors will be selected with digital

[1] G. Rai, A.A. Arthur, F. Bieser, C.W. Harnden, R. Jones, S.A. Kleinfelder, K. Lee, H.S. Matis, M. Nakamura, C. McParland, D. Nesbitt, G. Odyniec, D. Olson, H.G. Pugh, H.G. Ritter, T.J.M. Symons, H. Wieman, M. Wright, and R. Wright, IEEE Trans. on Nucl. Sci. 37, 56 (1990).
[2] S.A. Kleinfelder, IEEE Trans. on Nucl. Sci. 37, 1230-1236 (1990).

registers. The adjustment will be used to compensate for variations in the process parameters. Figure 4D-1 schematically shows this principle.

Work on the shaping amplifier has progressed in stages. It was started with a digitally trimmed integrator chip and then proceeded to a integrator-differentiator. At this stage the amplifier was combined with the existing EOS preamplifier and is now being designed with the the digitally trimmed multipole shaping amplifier. All IC's are built in CMOS integrated circuit technology using the 2-metal 2-poly process. No external components are required to define the shaping time.

The matching of peaking times between shaper channels was tested extensively. From several Quad Shaper IC's it was verified that the variation in time constants between the different channels on the same chip was sufficiently small to allow for all channels to be tuned simultaneously. Thus variations between wafers and process variations may be compensated for by setting a three-bit digital code on each chip and blowing metal fuses on the chip during testing.

For the implementation of the shaping amplifiers a high speed operational amplifier has been developed that has good bandwidth, is highly stable, and easy to compensate. It is capable of closed loop bandwidth of over 25 MHz at a gain of up to 30. This operational amplifier has potential for additional future applications. It is a single stage design with open loop gain of about 70 db.

A new 16 channel multipole shaping amplifier has been submitted. The principles of this design are similar to the shaper described here except that it provides complex poles and has implemented all the necessary shaping including the 1/t tail compensation.

4.D.3.c. SCA

The SCA (Switched Capacitor Array) is designed to operate as an inexpensive, dense, low power, and high dynamic range analog memory, replacing CCD's and

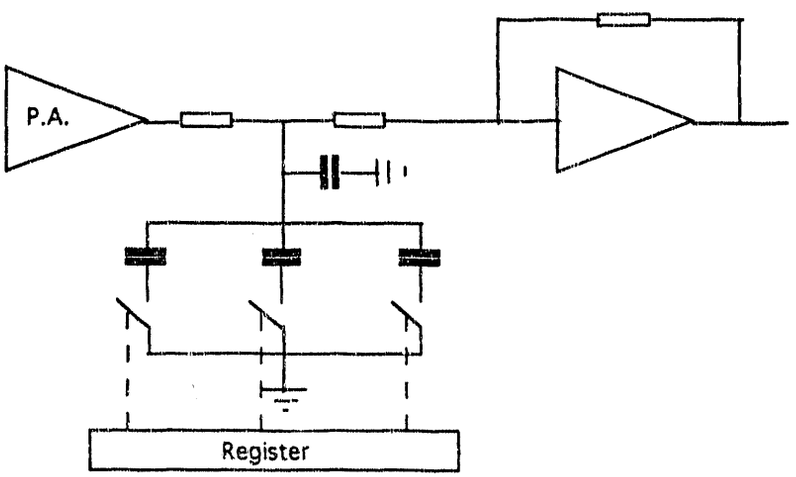

Figure 4D-1 Schematic representation of the correction capacitors.

FADC/memory devices in large data acquisition systems. A 256 sample 16 channel SCA has been developed for EOS and this design has been improved to 512 samples in 1.2μ CMOS technology for NA35. Presently we are working to improve the control and to eliminate the odd-even effect for the 512 sample design.

The main features and performance parameters of the latest 512 sample per channel SCA IC include:

1.2 micron double metal, double polysilicon CMOS process.
16 Channels per chip, 512 cells per channel.
Die size 6.8 x 4.6 mm.
Serial cell addressing, multiplexed and buffered analog output.
Storage cell capacitance = 1 pF.
Input capacitance = 15 pF.
Average readout rate of 1 MHz.
10 mW power consumption per channel at 5 Volts.
Analog bandwidth of >50 MHz.
Rail to rail input and output range.
Output noise of ~1 mV.
Dynamic range (single cell, 10MHz) of >4000:1 or >12 bits.
Non-linearity of ~1% over entire range.

4.D.3.d. ADC

A pitch-compatible 16 channel 12 bit ADC sub-section (Figures 4D-2 and 4D-3) has been fabricated. This follows several single channel prototype fabrications that proved monotonic 12 bit conversion with about 11 bit linearity. The single slope design is flexible enough for use in less than 12 bit applications. For SSC applications, a 62 MHz digitization clock is applied for a 12 bit conversion in 32 μs. A 10 bit conversion would take 8 μs.

4.D.3.e. Alternate Technology

The set of IC's described above is a continuous development derived from the EOS effort. There is a parallel ongoing effort to develop a complementary design with industry participation. This effort is described in section 4K on the XTPC. Once both lines of electronics are available for testing a decision between the alternatives will be made based on performance and expected price. This technology choice will have to be made no later than January 1993 .

4.D.4. Engineering

4.D.4.a. Brief Technical Description & Specifications

The front-end electronics is located on a printed circuit board that is connected with the pad plane at one end by a connector and at the other end to the readout board

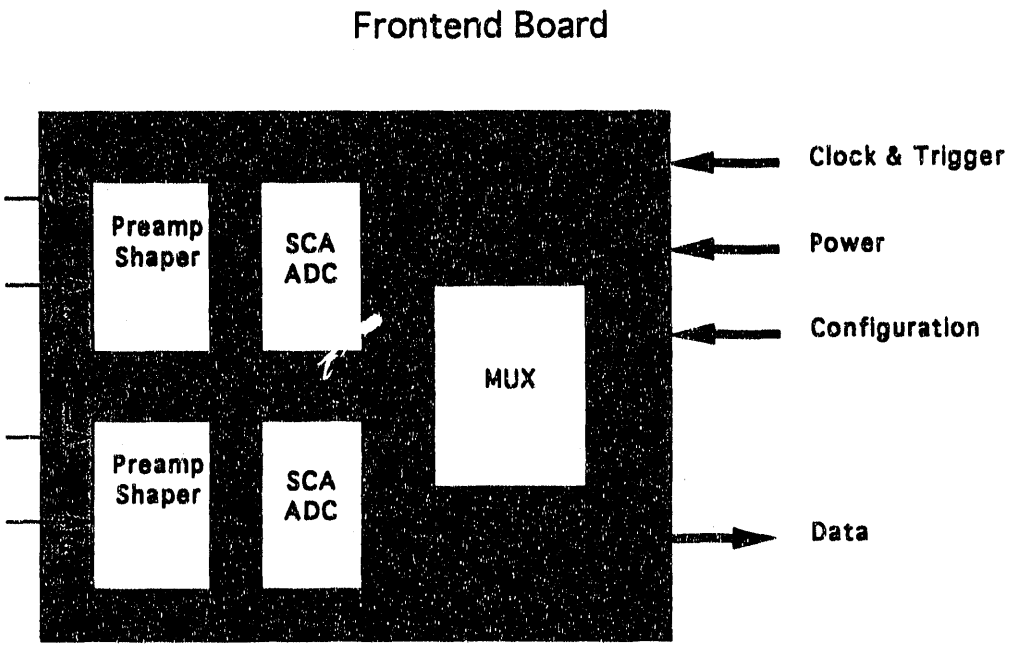

Figure 4D-2 Front end board containing 32 channels of amplifier/shaper and 32 channels of SCA/ADC with multiplexing to readout board.

by a cable. The arrangement is schematically shown in Figures 4D-2 and 4D-3 and the main parameters are listed in Table 4D-1.

Table 4D-1. Front-end board.

	TPC	SVT
PA noise	700e rms	
Min Ionizing Pulse (MIP) input (mean)	28000 e	24000e
PA linearity range	110 MIP	
input protection	1000pf @ 1300V	n/a
# of channels per IC	16	40
# of channels per board	32	448
1/t tail correction	yes	no
peaking time	180ns	30ns
power cons. per channel	55mW	15mW
time constant uniformity	+/- 5%	
# of time buckets	512	256
analog acquisition rate	12.3MHz	40MHz
# of effective bits for ADC	10	10

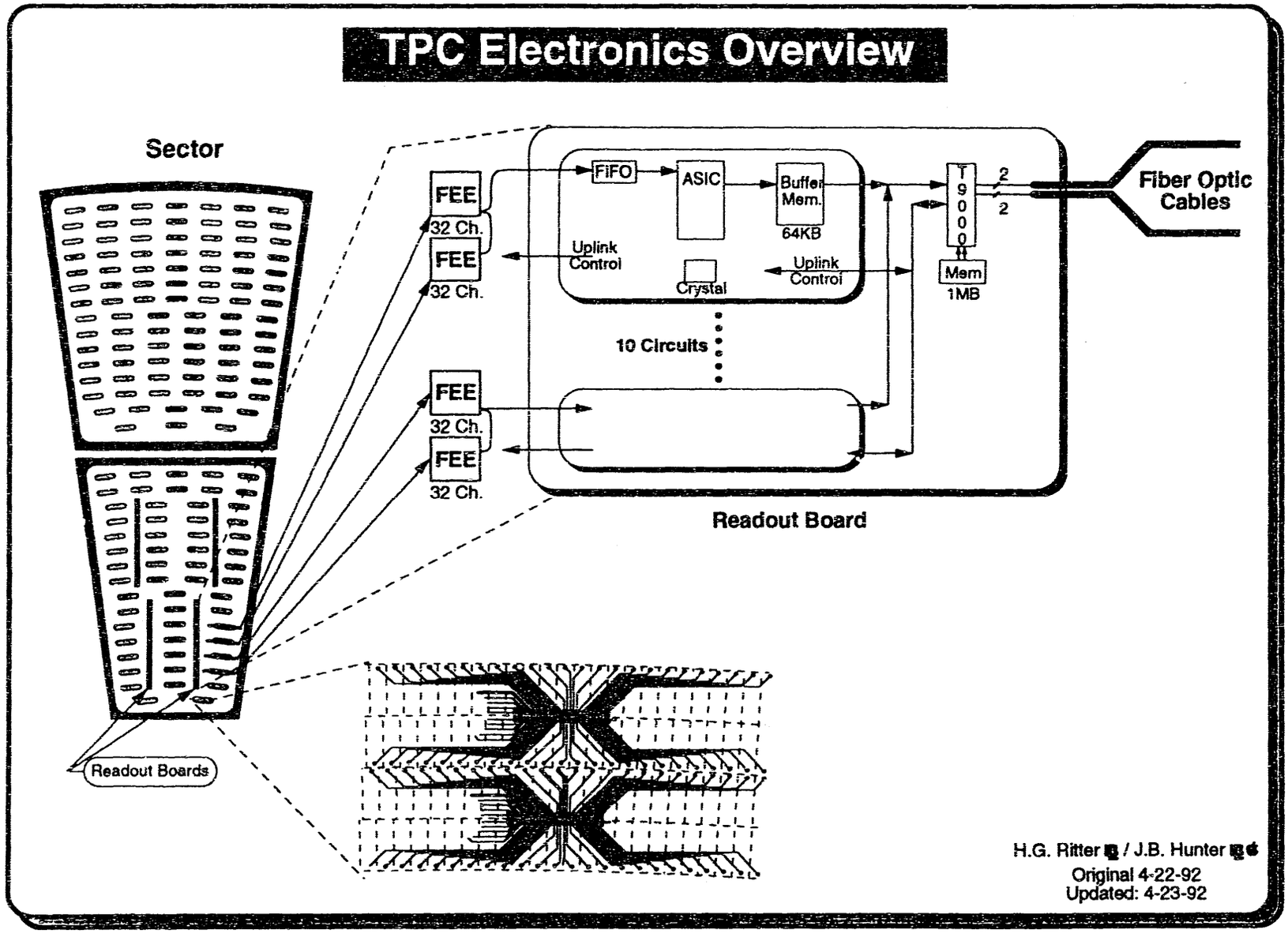

Figure 4D-3 TPC electronics overview showing sector layout with pad interconnection to front end boards and readout boards with fiber optic connection to off chamber electronics.

The configuration information and the power for the front-end board comes from the readout board as described in the data acquisition section. The digitized data from the ADC's are sent to that board. Front-end boards are daisy-chained in pairs; 20 are serviced by one read-out board.

The functionality of the SVT front-end electronics and the components will be very similar to those of the TPC electronics but the actual assembly and packaging will have to be optimized for the SVT. Engineering studies are not yet completed.

4.D.4.b. Description of Major Components

The design and the layout for the front-end board for the TPC will be done at LBL. Prototypes will be fabricated and tested extensively on test sectors. After a final design review the production of the boards will be awarded to a PC manufacturer and the individual components will be loaded by a specialized manufacturer.

The custom designed integrated circuits will be manufactured by the foundry that has done the prototype production. The wafers will be cut and packaged by the foundry or by a firm specializing in integrated circuit packaging.

4.D.4.c. Initial Assembly & Alignment

Manufactured and tested boards will be assembled on a prototype sector of the TPC. By populating a sector of the TPC, it will be possible to bring enough front-end and readout boards together to evaluate the performance of the complete system.

4.D.4.d. Engineering Testing

Production testing is of key importance to well functioning electronics. Testing at all levels of production is important. The integrated circuits will be tested on the wafer with automatic probe stations and only those dies that pass the on-wafer tests will be packaged. Packaged dies will be subjected to a complete dynamic functionality test on a custom test station that has been designed and developed during the IC development cycle.

The printed circuit boards are tested as part of the production contract and then are loaded with the completely tested IC's. The assembled boards will be tested on a prototype sector for full functionality and system performance. In addition to providing a system mock-up suitable for further testing and software debug, this prototype sector will be used during the production cycle for board burn-in.

4.D.4.e. Transportation, Reassembly & Alignment at RHIC

There are two options for the final assembly at RHIC. The TPC sectors and front-end electronics could be shipped to RHIC separately and then assembled and tested at the final installation site. As an alternative, each sector could be fully assembled and tested at LBL and then shipped to RHIC as a complete unit.

4.D.4.f Issues Specific to SVT Front-End Electronics

4.D.4.f.1 Conceptual Design:

The present working assumption is that the front end electronics consist of a Darlington amplifier as an integral part of the detector chip. This is followed by a shaping amplifier that has a single differentiation pole zero and four 9 ns integration poles leading to a pseudo-gaussian waveform with a σ of 18 ns. This amplifier has a voltage gain of 10 and will deliver pulses up to 2 volts on 110 ohm stripline (possibly not terminated). The stripline (up to one meter long) is received by the analog memory (SCA/ASA). The data are digitized, desparsified by an ASIC, and stored in digital memory. Then I/O is done on fiber optic cables.

4.D.4.f.2 Functional Block Diagram:

A preliminary electronics block diagram is shown in Figure 4D-4. Table 4D-2 gives the electrical specifications. Each detector contains 224 anodes on each end. The shaper amplifiers have 40 channels per IC. Six chips will serve on each end of the detector. There are a total of 30 16 channel SCA/ASA chips for analog memory per assembly. Eight ASIC's are used to read data from the SCA/ASA chips which also contain ADC's and calibration circuitry. The ASIC's serve to compact the data and organize it for transmission over fiber optic lines. Locally but not on the FEE boards will be about 75 T9000 transputers with fiber optic links to remote modular logic as part of the DAQ chain. Cooling using low pressure "leakless" water is being concidered for both the detector end and the FEE board end of the system. There are 72k channels in 162 detector-cable-FEE assemblies.

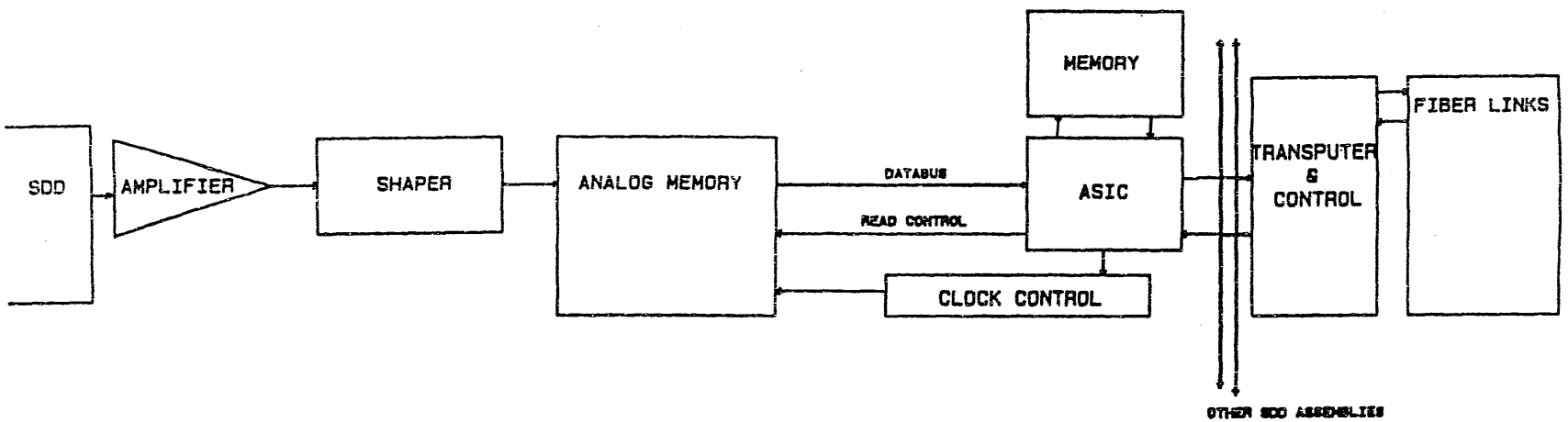

Figure 4D-4 SVT detector and electronics assembly.

Table 4D-2 SVT Electronics subsystem performance.

Amplifier - Shaper	
Channels/IC	40
Gain	10
Risetime	10ns
Power	2 mw/channel
Analog Memory/ADC	
Channels/IC	16
Segment Size	Variable
Power	10 mw/channel
ASIC/Memory	
Digitization Time	< 8 ms
Power	1 watt/60 channels
Transputer/Input-Output	
Total Digitization Time	< 10 ms
Power	2.8 watts/448 channels

4.E. Trigger Detectors

4.E. Trigger Detectors

4.E.1. Specialized Physics Issues

The goals of the STAR trigger system are listed in Table 4E-1 below. Because the expected QGP observables will involve a combination of signals, a large emphasis will be placed on a minimum bias survey for p-p to Au-Au collisions at turn-on, with the addition of simple selection on the centrality of the event. The STAR Phase 1 trigger system is expected to provide a reliable minimum bias trigger for all systems from pp to Au-Au with sufficient redundancy to understand biases and efficiencies and to provide the ability to select varying degrees of centrality and asymmetry. As the interesting physics becomes better defined, the trigger system will require a continuous evolution during the experiment. *Thus, the flexibility for trigger upgrades is essential to the program of the STAR detector.* Following the initial survey runs of central and peripheral A-A collisions the trigger system must be able to select rare events which are characterized by unusual η, ϕ distributions and signals from hard scattering processes.

Table 4E-1 STAR Trigger system goals.

Minimum Bias
Detect Au-Au interactions with > 95% efficiency
Detect pp interactions with > 50% efficiency
Locate Au-Au vertex to within ± 6cm in < 200ns
Detect multiple events occurring within 40μs
Detailed Event Selection
Select highest 2.5% of multiplicity distribution in < 200ns
Select high transverse electromagnetic energy
Select on geometry of hit patterns
Allow simple integration of upgrades to trigger system

4.E.2. Description of Trigger System

The Phase 1 trigger system is shown in Figure 4E-1 and listed in Table 4E-2 below. It consists of a central trigger barrel (CTB), vertex position detectors (VPD), TPC endcap MWPC's (MWPC), veto calorimeters (VC) and output from the EMC. The CTB is a cylindrical array of scintillator slats with photomultiplier tubes at each end, surrounding the outer surface of the TPC and designed to record charged particle multiplicity for $|\eta| < 1$. Hits are recorded in a pipeline TDC and total light output is integrated to give multiplicity. The TPC endcap MWPC's are instrumented to yield hits on each anode wire, providing multiplicity in the range $1 < |\eta| < 2$. The VPD's are Cherenkov radiators directly coupled to rings of PMTs. The radiators are located at $z = \pm 3$ m to determine vertex position and to detect multiplicity from $3.3 < |\eta| < 3.8$. The VC is placed at $z = \pm 17$ m to detect spectator fragments remaining from peripheral collisions as a means of detecting large impact parameter events. Output from the EMC

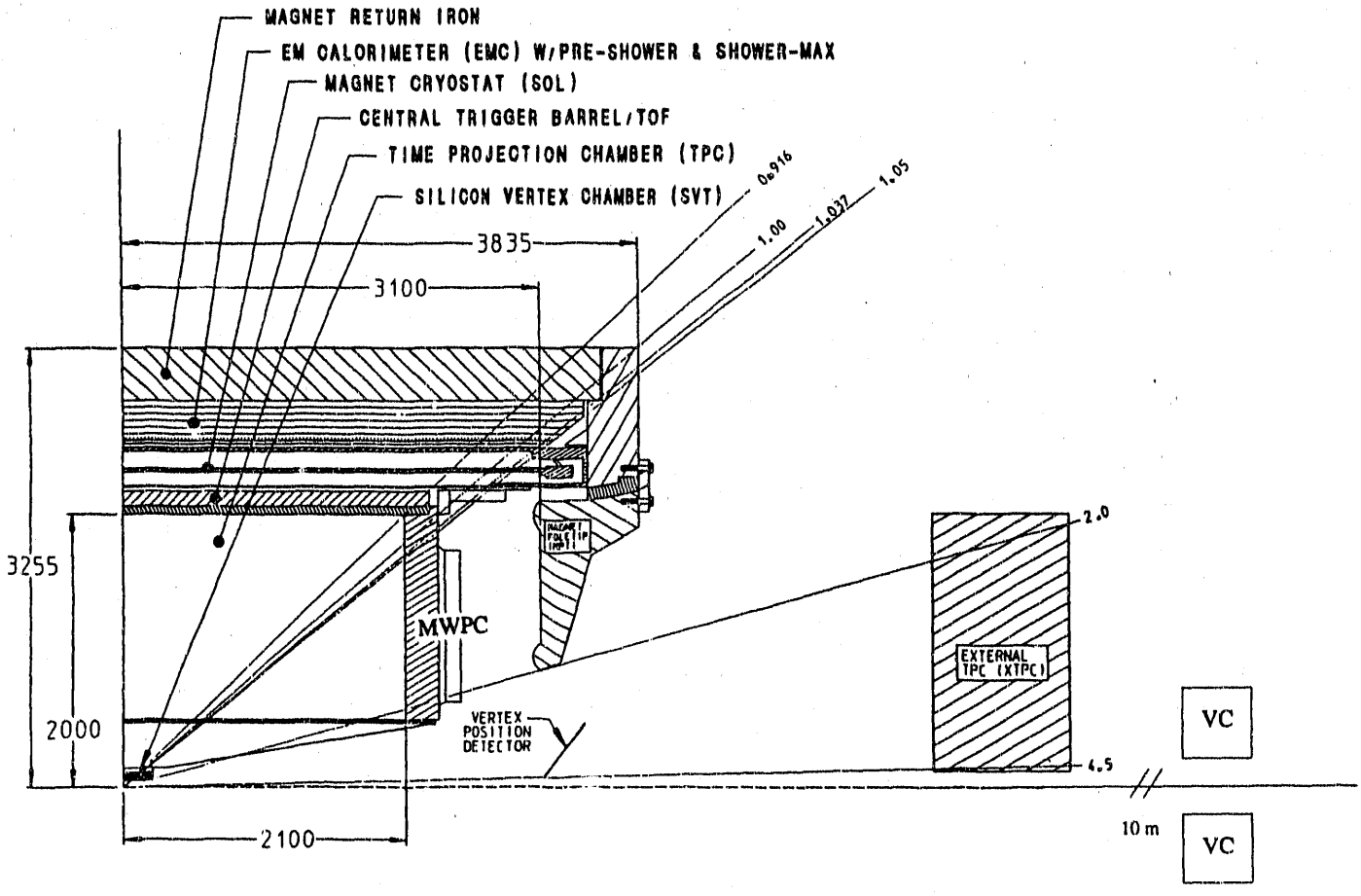

Figure 4E-1 Quadrant view of the STAR detector system showing baseline trigger detectors: EM Calorimeter (EMC), Central Trigger Barrel (CTB), Vertex Position Detector (VPD), TPC endcap MWPC's and Veto Calorimeter (VC).

Table 4E-2 STAR Trigger System Detectors.

DETECTOR	$\|\eta\|$	# channels
Central Trigger Barrel (CTB)	0 - 1	200
TPC Endcap MWPC	1-2	2000
Vertex Position Detectors (VPD)	3.3 - 3.8	50
Veto Calorimeter (VC)	> 5	2
EM Calorimeter (EMC)	0 - 1	1200

is used in the first and second level triggers to select on transverse electromagnetic energy and $d^2E_t/d\eta d\phi$. The first level trigger is formed by a threshold on the hardware sum of all PMT signals. The second level trigger is formed in a dedicated CPU which receives digitized signals from each PMT. A block diagram of the trigger system electronics is shown in Figure 4E-2. Figure 4E-3 shows a central Au-Au RHIC event

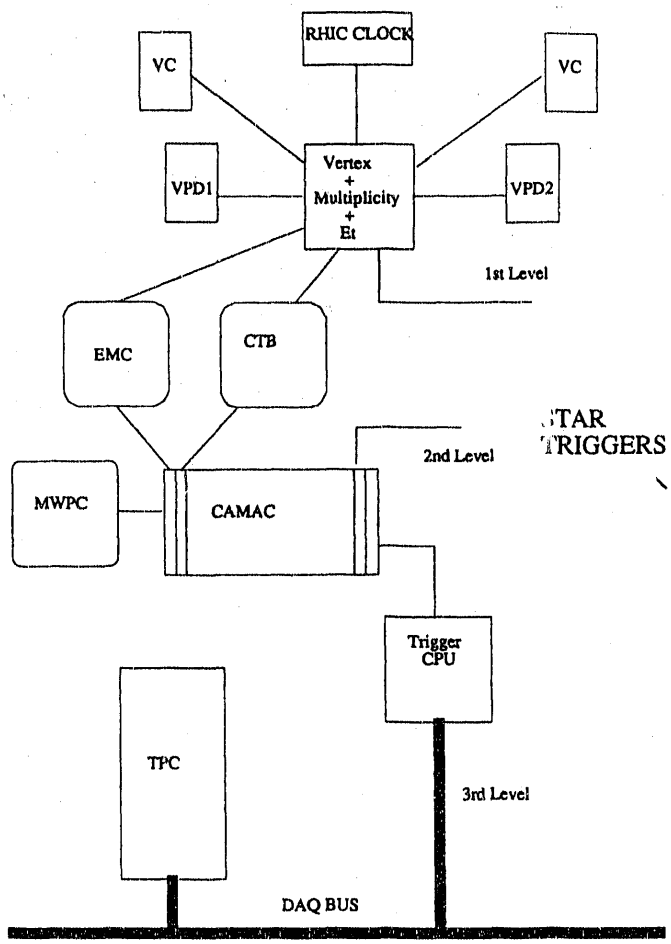

Figure 4E-2 Block diagram of trigger electronics. Shown are the VPD, EMC and CTB multiplicity units forming the first level trigger coincidence with the Veto Calorimeters, the pattern unit in CAMAC, and the trigger control computer. The first level trigger in the baseline has VPD, EMC, CTB and VC as switchable inputs. The second level is made in the computer from input register input from each PMT hit and from the MWPC hits, and can be programmed for any hit pattern. This can be based on existing CAMAC units, with trigger "yes" indicated using an output register. The third level assumes input from the TPC and uses a control CPU to determine real track patterns of interest. Note that level 2 and 3 will benefit from learning from the simplest triggers what patterns will enrich the data stream, although the pattern can be selected a priori from any model.

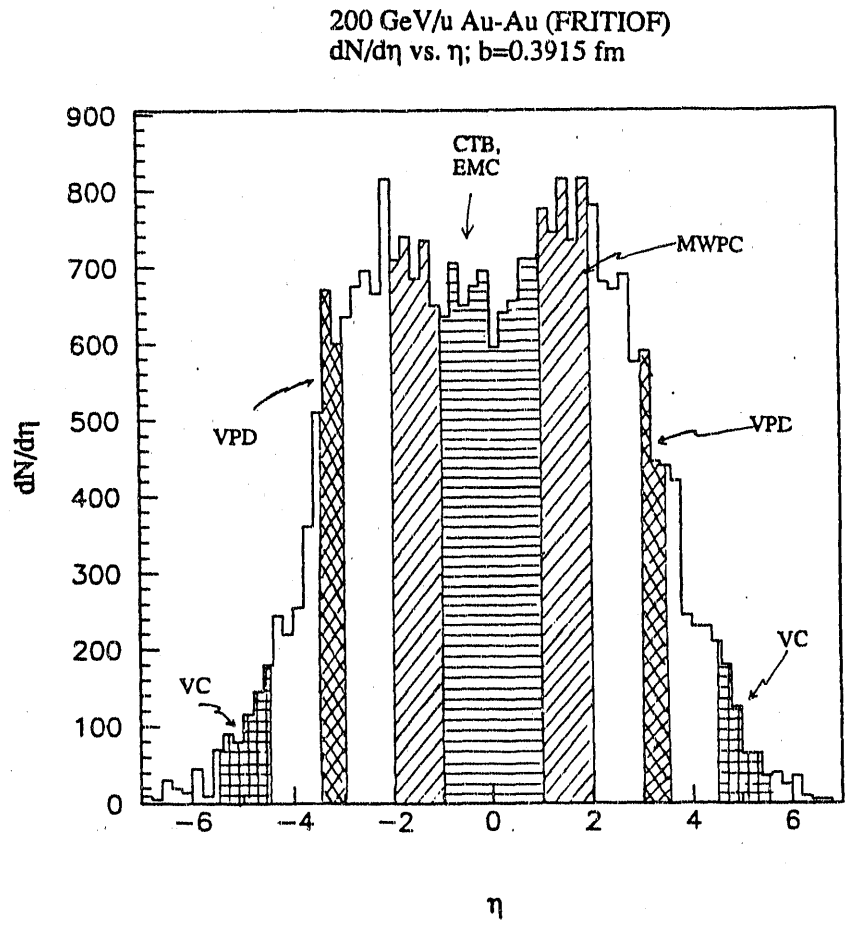

Figure 4E-3 Central 200 GeV Au-Au event (FRITIOF), to show the "typical" particle density in rapidity. Shaded regions indicate the coverage of the CBT, EMC, MWPC and VPD trigger detectors.

generated by FRITIOF with the pseudorapidity coverage of various detectors indicated. Note that the trigger detectors serve to sample the multiplicity and transverse energy distributions, but clearly cannot give a complete picture of large scale fluctuations over a range as large as $|\eta| < 5$.

Level 1 Trigger

We expect the STAR detector to be capable of recording at least one central Au-Au collision or 30 p-p interactions per second. The RHIC luminosity is expected to produce 10^3 Au-Au collisions or 10^6 p-p interactions per second in the diamond volume. We have devised a flexible trigger, configurable to select a wide variety of event types, from minimum bias to the highest multiplicity "central" events selected on the basis of both multiplicity and transverse energy. The system will be able to determine that an interaction has occurred, determine its location in the diamond, and decide if the multiplicity or transverse energy is high enough and the number of spectators low enough to flag a central event. It will work for both p-p and Au-Au collisions. The specifications of the level 1 trigger system are listed in Table 4E-3.

Table 4E-3 Specifications of the level 1 trigger system.

Specifications of the level 1 trigger
Decision available within 200 ns
Selection of the highest 2.5% of multiplicity distribution with 90% efficiency (based on CTB and MWPC hits)
Determination of z-position to ± 6 cm to keep events inside optimum SVT acceptance (based on VPD)
Detection of multiple events within the TPC drift time
Detection of projectile spectator nucleons (based on VC)
Determination of the total transverse electromagnetic energy for collision centrality selection (based on EMC)

Level 2 Trigger

A second trigger level will provide more elaborate signals within 50 μs. These are preselected patterns in the CTB, the MWPC, and the EMC. Level two triggers will be based on level one trigger detectors and require in addition a computer controlled multiplicity logic unit. The specifications of the level 2 trigger system are listed in Table 4E-4.

Table 4E-4 Specifications of the level 2 trigger system.

Specifications of the level 2 trigger
Decision available within 40μs
Detection of multiple events
Determine geometrical hit patterns for asymmetry selections on multiplicity
Determination of the transverse electromagnetic energy for $d^2E_t/d\eta d\phi$
Correlation of EMC and multiplicity detectors for rare events

Level 3 Trigger

Decisions on the time scale of ms will be based on extensive processing of track and calorimeter data in real time to look for high-p_t tracks and energy clusters correlated with jets or for large scale fluctuations in multiplicity or E_t. High level algorithms will determine energy and charge cluster centroids, track parameters and momenta for some subset of the detector output.

As more information is gained about the RHIC environment and as the STAR system evolves this system will be augmented with additional information from other detectors such as a high granularity TOF array and the silicon vertex tracker to constrain $\langle N_c \rangle$ and geometry. The system is expected to evolve from small livetime operation, reflecting selection uncertainty, to large livetime operation resulting from highly selective triggers that reflect increased knowledge of the collision topologies. The Phase 1 trigger system has been designed with evolution in mind.

4.E.3. Capabilities of Subsystem

Central Trigger Barrel (CTB)

A barrel of 200 slats on the TPC outer surface subtends $|\eta| < 1$. Each slat counter consists of two R3432-01 proximity focusing mesh dynode phototubes optically coupled to a radiator 1.5 cm x 6.25 cm x 4.2 m . The fabrication and assembly for the slat counters proceeds in a similar manner to the shingle counters (see section 4.J). The slat counters are mounted two abreast in the module trays foreseen for the shingles. Note that there is an effective sweeping field that curls up charged particles with transverse momentum less than 0.15 GeV/c before they reach the outer surface. This cut eliminates 15% of the charged particles that would otherwise hit the barrel. The total multiplicity distribution for 500 Au-Au events is shown in Fig. 4E-4. Also shown is the correlation of total multiplicity with hits in the CTB. To trigger with 90% efficiency on the top 2.5% of this distribution means that we must be able to detect multiplicities greater than 1750 in the barrel. Shown in Figure 4E-5 is the total number of photoelectrons seen in the CTB. There is a strong correlation suggesting the system will be able to select the upper 2.5% with minimal contamination.

Vertex Position Detectors (VPD)

Figure 4E-6 shows $dN/d\eta$ vs η for 1000 pp collisions, with 95% inclusion bars on each point. Assuming the VPD are 5m apart, and that we need to determine time differences to $\Delta t < 180$ps (6cm at $\beta = 1$), we need to confine our analysis to particles having $\beta > 0.988$. The flux of such particles at 2.5m from the target at an angle of 4/250=0.016 rad is seen to be > 50 for Au-Au but ~1 for pp. Since the VPD subtends ~0.5 units of pseudorapidity, the coincidence rate for pp will be only 26%. However, 70% of the pp collisions will cause at least one hit in the VPD and > 99% of the Au-Au collisions will lead to multiple hits in each VPD.

TPC Prompt Output (MWPC)

There are about 9,000 MWPC outputs which can gather the charge deposited by tracks which directly impinge on the TPC endcaps covering $1 < |\eta| < 2$. Similar considerations to those discussed for the barrel apply to this system. The two systems each cover two units of pseudorapidity. The direct readout of the TPC, however, can have finer pseudorapidity granularity which will allow triggering on $dNc/d\eta$ fluctuations on an event-by-event basis.

A fast multiplicity trigger will be made using the TPC endcap MWPC's. By reading out the 9K anode wires in 2 K separate segments it will be possible to measure the number of particles in the range $1 < |\eta| < 2$. The segmentation in ϕ is determined by the endcap design and in η by the requirement that the density of particles per segment be uniform. The electronics will be mounted directly on the individual endcap segments with a minimum number of connections to the rest of the system.

This trigger requires an amplifier discriminator combination for each segment which has a low effective input impedance (less than 100 ohms), a peaking time of 30 ns, system noise of less than 1500 electrons and ECL output levels (this circuit could be

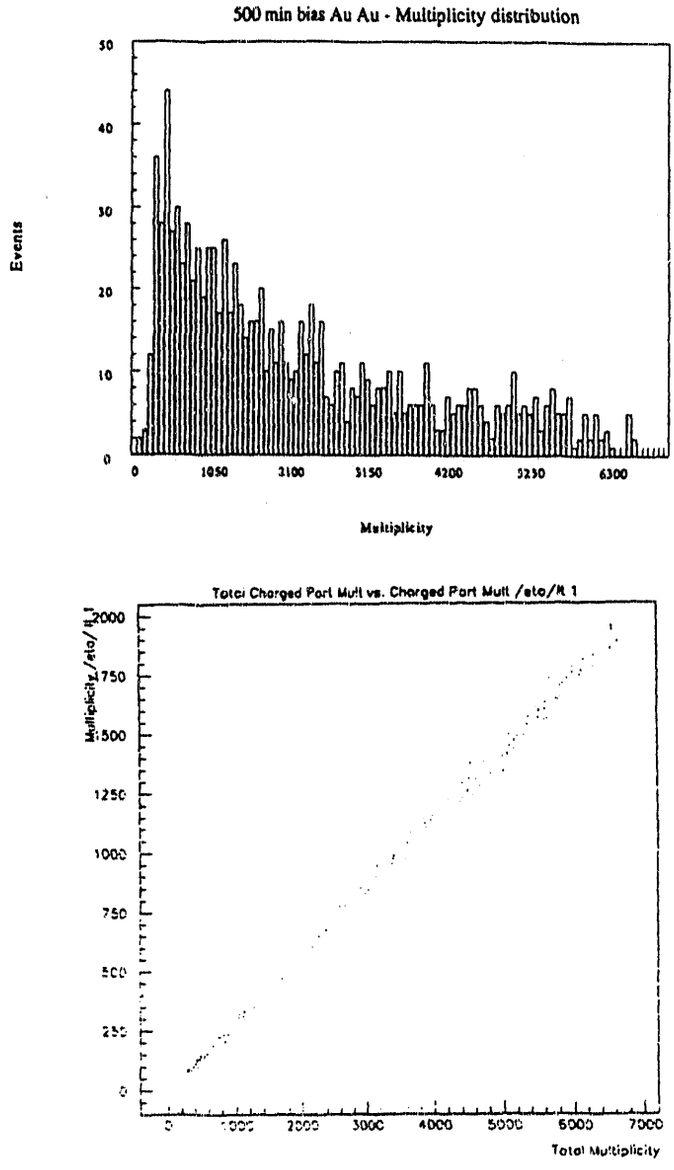

Figure 4E-4 Charged particle multiplicity distribution for 500 minimum bias AuAu events and the scatter plot of charged multiplicity vs multiplicity in the barrel region $|\eta| < 1$. Note that the top 2.5% of the histogram have M > 6000. This implies that the barrel must count reliably above 1750. However, the correlation for AuAu is quite tight, so selecting on M > 1750 will not lead to serious contamination from lower M events.

based upon an IC being developed for the SSC). An ASIC would be designed that would act as a gated latch with multi-layer buffers for each input. This circuit would have a prompt logical OR output along with a prompt cluster multiplicity output (this could be generated using an adder tree). Multi-layer buffers would also be provided for these outputs. Test and mask inputs for each channel would be provided using serial data transmission. Each chip could have all outputs remotely disabled. Multi-layer

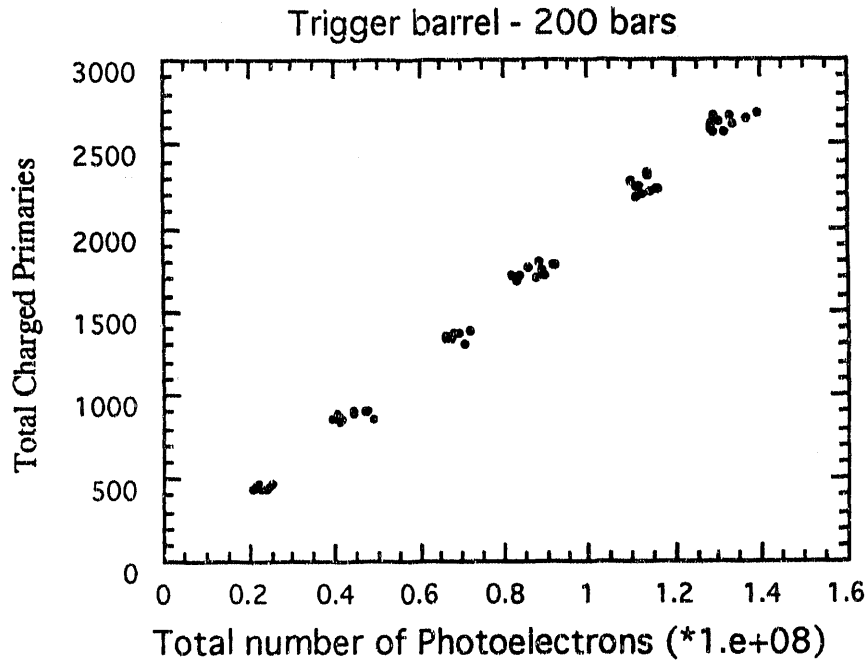

Figure 4E-5 Total charged primaries vs number of photoelectrons generated in the 200 slat barrel. Note that this is an almost linear function, but that it assumes ideally matched PMT's. It will be difficult to match PMT gains to better than a few percent, so that this method may limit the overall efficiency of the trigger for selecting the highest multiplicities.

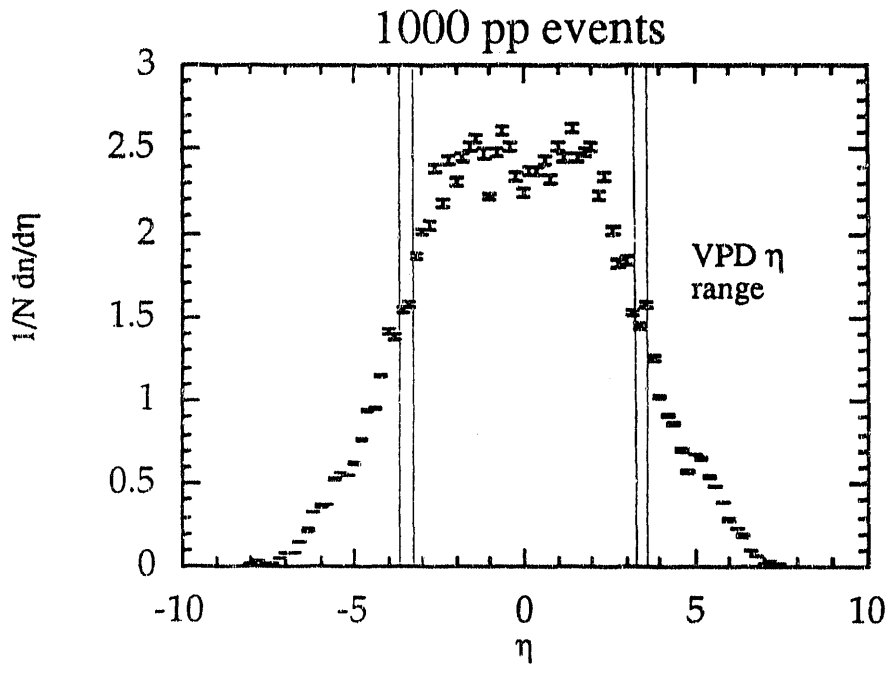

Figure 4E-6 The 1/N(dn/dη) distribution for 1000 pp interactions. Error bars are 2σ to show the dispersion in the densities at each pseudorapidity. For the pp case, only 26% of the events will yield one or more hits on each VPD. However, at least one VPD will be hit 70% of the time.

buffers are provided in order to store for the several crossing intervals that it is anticipated it will take to form the final hardware trigger. It should be noted that this ASIC could be used with other detectors (e.g., barrel array) to form a part of the overall trigger system.

EM Calorimeter

The Electromagnetic Calorimeter is described in section 4.I. It measures a fraction of the total transverse energy which stems to a large extent from photons and electrons which in turn result from π^0 decays. It will be used alone to select centrality and fluctuations in E_t, and together with the CTB to select events with unusual ratios of E_t to charged multiplicity.

Veto Calorimeter (VC)

Addition of veto calorimeters beyond the first dipole magnets in the beam transport system provide information on collision geometry (impact parameter) independent of the E_t and N_c values at midrapidity. Proton and neutron spectators are well separated from the collider beams at a distance of 17 m from the interaction point. At this point calorimeters with slots to allow passage of the beams could be raised into position after a beam fill to detect spectator energy. This possibility is now being investigated to determine the additional information such detectors provide in increasing the efficiency for detecting large impact parameter collisions.

Trigger Electronics

The trigger electronics has three main components, reflecting the three levels of triggers. The first is a specially designed fast circuit to determine the vertex location based on VPD signals; the second is a computer controlled multiplicity logic unit to select fast hit patterns; the third is a dedicated CPU for making tracking level trigger decisions. The block diagram is shown in Figure 4.E-2. All single PMT's and logic nodes are expected to be read into event scalers to monitor system integrity and provide overall normalization for cross section determination. The first level trigger includes selection of the CTB multiplicity and E_t, and for events that give hits in both VPDs, selection of the vertex location. CTB and EMC anode currents are summed for first level multiplicity and E_t information. A trigger processor will be used to form the first level trigger and to keep track of the different first and second level triggers formed.

The vertex location unit accepts inputs from all VPD discriminators. These are to be stable at better than 30ps electronically. Each input has a separate trimmable delay line. VPD PMT's within a given detector unit are equidistant from the vertex to better than 1cm. The detector is timed by taking a sample of high multiplicity events and tuning the delay lines so that the fastest signal from each PMT arrives at the same time within 50ps to the vertex locator coincidence unit (VLCU). The VLCU requires a coincidence between the first arrival of any VPD ring signal and the first arrival of any opposite side VPD ring within 360ps. The mean time for this coincidence is delayable to select regions within the interaction diamond.

The second level trigger is determined by a computer controlled pattern recognition unit. Each CTB and EMC PMT and MWPC discriminator signal is sent to this unit and different masks are applied to determine whether events satisfy various asymmetry conditions. This unit can incorporate EMC upgrades without change in architecture.

Third level triggers will evolve as we understand the RHIC environment better. It is the third level trigger which should focus on definite signatures which suggest the new physics. Such a system needs to be managed on an interactive basis.

TMC

The Trigger Manager Computer (TMC) is an interactive work station which manages the trigger system in a stand-alone mode, but which shares a bus system with the main DAQ structure. It displays the trigger status with a variety of pictorial representations, it controls prescaling, and modifies the trigger structure for calibration purposes and for time-share among various trigger configurations with different physics goals.

4.E.4. R&D Issues and Technology Choices

The technical constraints on the CTB trigger system are summarized below in Table 4E-5.

Table 4E-5

Constraints
1. magnetic field interference $\delta B/B < 0.001$
2. mass for interference with downstream detectors $< 5\ \chi_0$
3. radiation hardness survive 10 MGy
4. slat insertion access; need to swap out individual detectors in situ.
5. radial thickness at r=2.06m for barrel volume > 11cm
6. upwards compatible with TOF arrays and SVT

Research and development is required for the various trigger detectors.

- PMT bases : We expect local HV generation and discriminators on each barrel PMT, with fiber optic communication from the trigger computer to set thresholds and voltages. This has been solved in principle but not in our identical application.
- Fiber communication : We expect all logic levels and computer communication to be accomplished via optical fiber. This requires implementation of the receive/transmit operations for our PMT's and register logic.
- Slat response : We would like to compare the response of fast scintillator and wave shifted Cherenkov radiator for this application.

- Variable 10ps delay line : for tuning the leading edges of the PMT signals from the VPD PMT's, we will need a computer controlled delay line having a precision of better than 50ps. This is an interesting development project which can be accomplished with variable numbers of gates on a chip for each delay line.
- PMT timing : Much progress has been made in testing the mesh anode PMT's that have small effect on or by the magnetic fields expected at the locations of the barrel and VPD's. However, we would like to continue this investigation and test process so that we select the best possible PMT's for the experiment.

Note that the trigger system will undergo a vigorous upgrade program and will require continuous R & D.

4.E.5. Engineering

4.E.5.a. Brief Technical Description & Specifications

The CTB, VPD and VC all require significant engineering to fit within the STAR environment with minimal impact on other systems.

4.E.5.b. Description of Major Components

The CTB and VPD will be fabricated from standard materials at LBL and the participating university labs. The VC will be fabricated at Frankfurt.

4.E.5.c. Initial Assembly & Alignment

The VPD is a simple and small detector that fits snugly around the beam pipe in easily removed segments. Thus it presents no particular assembly problems. The CTB will require special attention to assemble within the STAR detector. The VC sits well outside the area occupied by the STAR magnet and TPC.

4.E.5.d. Engineering Testing

This centers primarily on the electronics issues associated with the trigger processor and the vertex locating unit.

4.E.5.e. Transportation, Reassembly & Alignment at RHIC

The trigger barrel and VPD are easily shipped and assembled at BNL. Slats will have an assembly jig for uniformity. The VC will arrive as separate detector units for installation.

4.E.6. Testing and Calibration Issues

Test beams will be required for PMT, slat and VPD unit testing during FY93 and FY94. Each unit can thereafter be tested using a laser.

4.F.
Data Acquisition

4.F. Data Acquisition

4.F.1. Specialized Physics Issues

The STAR detectors represent a challenge for data acquisition. First, the amount of data arising from a single Au-Au interaction is much larger than an event encountered in any previous detector system. Even at the modest interaction rates expected for the heaviest systems, the data rate is more than an order of magnitude greater than can be reasonably accommodated by a magnetic tape logging system or by subsequent analysis requirements. The bulk of the data (80%) for the STAR phase I detector arises from the TPC. Much of the remaining data is generated by the Silicon Vertex Tracker (SVT). The structure of the data is similar for both devices. This discussion will focus on the TPC data however, and more specifically, the central TPC. There are 140K pads in the central TPC. Each pad represents 512 time samples. Thus the number of pixels in the central TPC is 72 million. For a 10-bit digitization per time sample, the full pixel space of the TPC corresponds to 90 MByte per event. While most of these pixels are empty (pedestal only) for a given event, the STAR detector represents a departure from previous collider TPC experiments in that the pixel occupancy for STAR is significantly larger than has been previously encountered. As predicted by event generators for the case of a central Au-Au collision, the pixel occupancy varies as a function of radius from 28% (at r=53 cm) to 3 % (at r=190 cm), with an average occupancy of 10%.

Merely suppressing the sub-threshold (empty) pixels in the data stream reduces the TPC contribution to the event size to ~12 MByte, including a 20% overhead for encoding the zero-suppressed data. It will be possible to record events of this size on magnetic medium at the rate of ~1 event/sec. It should be pointed out that there are two separate limitations to the performance of the DAQ system:

1) The system is *event rate* limited (independent of the nature of the event) by the ~5 msec digitization time of the ADCs, but

2) The back end of the system is *data rate* limited to ~20 MByte/sec by the capabilities of the taping hardware that can be purchased within the STAR budget.

For the case of p-p, the multiplicity of any triggered event will be considerably smaller than that of a central Au-Au event. However, because of the 40 μs drift time of the TPC, there will be many overlapping, non-trigger events read out in addition (see Section 4.C.3). Simulations show that the zero-suppressed size of a p-p event relative to a central Au-Au event is roughly 3% for p-p at design luminosity for $\sqrt{s}$=200 GeV and 10% at design luminosity for $\sqrt{s}$=500 GeV. Thus, a system capable of writing central Au-Au events to tape at 1/sec will write p-p events to tape at 30/sec at $\sqrt{s}$=200 GeV and 10/sec at $\sqrt{s}$=500 GeV. Even for p-p collisions, the performance is limited by taping speed rather than by the digitization time of the ADCs.

An increase in the recorded event rate is possible by further compressing the event. This could be accomplished by converting the stream of above-threshold samples to space points (centroids, areas, widths) corresponding to each cluster. Due to the density of tracks, especially at the inner radius of the TPC, extraction of space points

from the pad response is a non-trivial matter. The TPC data from the outermost padrows, however, are relatively uncomplicated. The low pixel occupancy makes simple hit-finding algorithms quite effective in dealing with these data from this region (see Appendix 1). This suggests the possibility of using these data as the basis of a (third-level) trigger based on, e.g., rapidity distributions, cuts in p_t.

4.F.2. Description of Subsystem

The DAQ subsystem is designed to meet this challenge in a variety of ways. First, in order to record events at the highest possible rate, the events will be reduced in size by either of two methods. The least problematic of these is to remove the sub-threshold pixels from the data stream, retaining pad responses for only those pixels above threshold. Additionally, an effort is being made to develop algorithms to convert responses for a cluster of neighboring pads to space point co-ordinates: centroids, widths, and correlation coefficients. The most difficult part of this task is recognizing problem situations (e.g., overlapping clusters) and dealing with them, either by retaining the information in its original form, or by developing alternative methods. It is recognized that delivery of the entire event (empty pixels included) from the TPC readout boards to the receiver crates would present a bottleneck which would limit throughput to ~15 Au-Au events/sec. This is to be compared with the Au-Au central collision rate, ~50/sec. In other words, transportation of the entire event would result in a dead time of >70 per-cent. In the STAR DAQ subsystem, the below-threshold pixels will be removed from the data stream on the detector readout board, using a custom IC (ASIC), allowing a data transfer rate of >50 events/sec, limited only by the conversion time of the digitizers.

4.F.3. Capabilities of Subsystem

The DAQ subsystem will provide two major functions in STAR. First, it will act as an event builder. That is, it will assemble data originating from digitizers appropriate to each detector subsystem, into a form suitable for recording on a logging medium and for distribution via a network to analysis and monitoring tasks. Second, it will allow for information arising from the detector subsystems to play a role in the decision to keep or reject each event, on a time scale short compared with the time required for event building (third-level trigger). It is expected that rates >50 events/sec will enter the trigger processors and that data will be recorded at rates from 1 to 10 events/sec, depending on the technology choice for tape recording systems (see below).

It is expected that future upgrades to the system will not result in a larger data rate to tape. Rather, it will involve better event selection which will arise from improved third-level trigger algorithms and from increased processing power (larger trigger farm) to implement these algorithms.

4.F.4. R&D Issues and Technology Choices

The DAQ subsystem has been engineered based on an architecture which uses the newest transputer family members, the T9000 RISC processor and the C104 packet router. This technology has been chosen for two reasons: First, the total cost/MIPS (including all necessary ancillary components, interfaces, etc.) is much lower than for

any other processor family. Second, the overhead in hardware and in software to network large numbers of processors together is virtually non-existent. Both issues are important in the STAR application. Some of the parameters which characterize the performance of the T9000 CPU are listed below:

T9000 Characteristics
Pipelined, superscalar RISC architecture
200 MIPS peak performance (75 MIPS sustained)
Multitasking scheduler implemented in hardware
4 bi-directional links (total throughput 80 MBytes/sec)
Programmable memory interface (160 MByte/sec bandwidth)
On-chip cache

C104 Switch Characteristics
32 bi-directional ports
Packet routing switch
Aggregate bandwidth 640 MByte/sec
Packet latency 1 μsec

An R&D project is underway to provide sufficient familiarity with transputer technology to allow an evaluation based on hands-on experience. This will include simulation of T9000 performance, which has been carried out using a simulator provided by Inmos, for STAR benchmarks, e.g., hit-finding algorithms. Early in 1993 this effort will be expanded to running code fragments on two communicating T9000 CPUs. Neither the T9000 nor the C104 router is available for purchase at the time of this writing. While the manufacturer (Inmos-SGS Thomson) insists that both will be available by the fourth quarter of 1992, the STAR collaboration must be prepared for the eventuality that the appearance of these products is delayed beyond the time when a technology choice must be made. To this end, other technologies are being examined to assess their suitability for this application. One of these alternate technologies is that of the Fibre Channel (see Appendix 1). This technology would provide the transport from the receiver crates to an event builder which would use the Fibre Channel as its backbone. An R&D project (see Appendix 1) will provide realistic benchmarks for a scaled-down version of the switching network necessary for STAR. In order to meet the scheduling goals for DAQ, a technology choice will have to be made no later than July, 1993.

A second technology decision that has to be made is the choice of the recording system. This decision will be postponed as long as possible. Tape recording technology continues to evolve; presently a recording system can be purchased which will provide a data rate capability of ~16 MByte/sec for a cost of $100K. It is expected that, in 2 years,

a system with equivalent performance will be available for $50K. Earlier recording needs, related to requirements for detector testing, will be met with modest tape systems (e.g., Exabyte 8mm drives with rate capabilities of 0.5 MByte/sec).

4.F.5. Engineering

4.F.5.a. Description of Major Components

The DAQ system consists of several parts: the readout boards, the optical fiber transport, the receiver crates, the third-level trigger, the logger, and the workstation interfaces.

1. The readout boards.

In the case of the TPC, each of the readout boards (Fig. 4F-1) contains a custom chip (ASIC) which moves the data from the SCA-ADC chips to a RAM, re-ordering the data and pedestal correcting them in the process. A second function of the ASIC is to generate lists of pointers to clusters of above-threshold samples in the RAM. One ASIC serves 64 pads (4 SCA-ADC chips).

The readout board also contains a T9000 transputer, which fetches the data pointed to by the cluster pointers generated by the ASICs. One T9000 transputer serves from 4 to 16 ASICs (256 to 1024 pads), depending on the radial location of the padrow. The transputer performs the additional function of formatting the data and managing its output via a 10 MByte/sec link which is transported off the detector, using optical fiber technology, to the receiver crate system. The T9000 can also respond to incoming commands to perform housekeeping functions, including calibration management, loading pedestal tables, or shutting down a malfunctioning SCA-ADC.

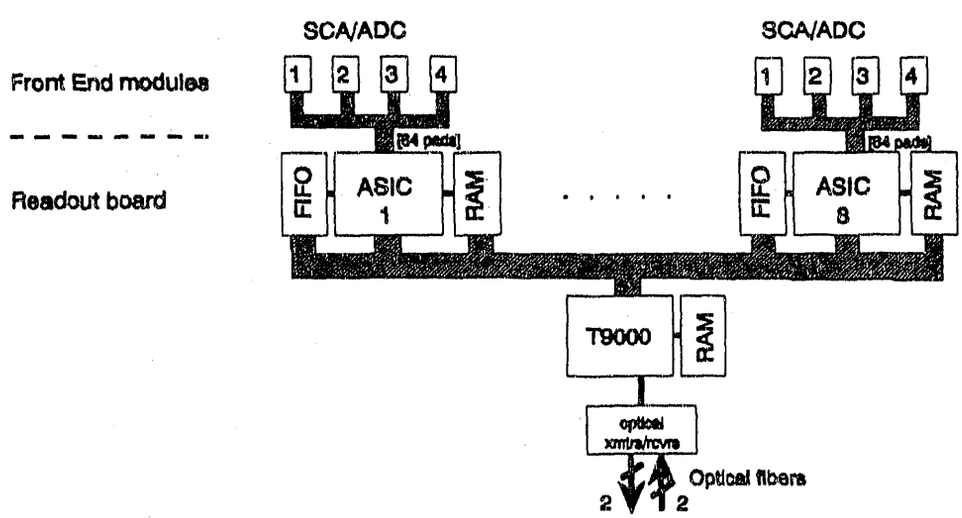

Figure 4F-1 Block diagram of a readout board for the TPC (for the case of 512 pads served by one readout board).

The readout scheme for the XTP is identical to that for the TPC. The SVT readout is similar in principle; however, the number of channels served by one readout board is different from that for the TPC (see SVT FEE description, section 4.D.2.b).

2. The optical fiber transport.

The optical fiber transport implements a bi-directional 10 MByte/sec T9000 link between the readout board on the detector and the receiver crate. Each bi-directional link is based on 4 optical fibers (2 in each direction) using 125 Mbit/sec technology.

3. Receiver crates.

The receiver crates contain the event builder and the third-level trigger, both implemented using T9000 processors and C104 packet routers. The incoming data are transformed from optical fiber media to T9000 link signals, then fed into C104 routers. Each C104 router contains 32 bi-directional ports. The incoming packet, formatted at the detector readout board, contains a header which is used by the router chip to determine the exit port to which it is directed by the router chip. Thus each packet finds its way to the appropriate T9000 in the event builder and/or trigger processor based on information embedded in the packet on the readout board.

The receiver crates will be implemented using an industry standard backplane, e.g., Fastbus or FutureBus-plus. In neither case will engineering be required to implement the crate hardware, power distribution, or cooling. A preliminary configuration for the boards which fill the crates is illustrated in Fig. 4F-2. The external logic or "glue" necessary to support a T9000 is negligible: RAM and a 5 MHz crystal. Thus a large number (>10) of the processors can occupy a single board. The number of detector-mounted readout cards which can be served by a single receiver board is limited to ~8 by the real estate required at the card edge to mount the fiber optic connectors. The physical configuration shown in Fig. 4F-2 can support a variety of logical configurations due to the flexibility offered by the C104 router switch; two of these logical configurations are discussed in the following sections. It should be noted that the T9000 network spans board boundaries by the use of two links on each board connected to its nearest neighbors.

4. Event builder.

The event builder must funnel the information from ~200 readout boards from the TPC and a smaller number from the remaining detectors into a single event, whence it can be committed to a recording device and made available globally via the network. For both of these ends, a backplane interface will be used. One of the T9000 processors on each board will interface to the crate backplane through its memory interface, thus allowing the use of commercially available tape systems and network interfaces.

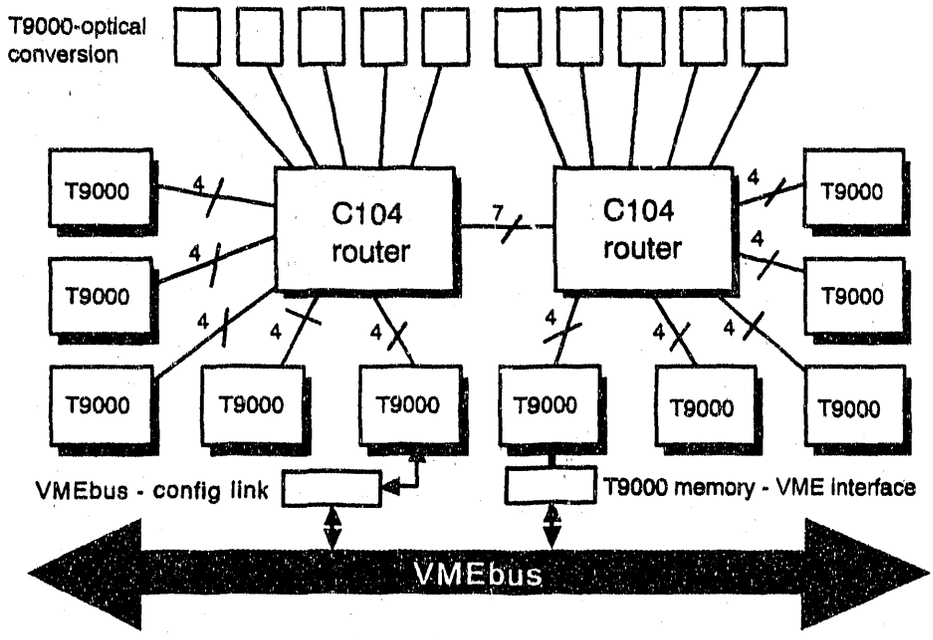

A VMEbus implementation of the crate system unit

Figure 4F-2 Block diagram of VMEbus implementation of the crate system board, containing 10 T9000 transputers. The RAM associated with each T9000 is not shown. This board serves 8 readout boards.

A fragment of the event builder topology is illustrated in Fig. 4F-3. This arrangement is realized using the physical layout shown in Fig. 4F-2. The connections between T9000s are virtual links; i.e., they do not correspond one-to-one with the physical links shown in Fig. 4F-2. The virtual links are connected by the C104 routers (not shown in this figure).

The architecture shown, with event fragments funneling into a single T9000 which provides the interface to the backplane, provides throughput of up to 40 MByte/sec. This is well in excess of STAR's requirement for backplane bandwidth, which is ~20 MByte/sec, dictated by the performance of affordable tape systems.

5. Third-level trigger.

The third-level trigger makes use of information obtained from the outermost readout board in each sector (8 padrows). The packets are directed to the trigger processors as described in the preceding paragraph. In general, the workload will be divided up so that a small patch (for example, 8 padrows by 64 pads) is assigned to each T9000 processor. Dividing up the real estate in this fashion creates boundary problems: each processor needs information on pad responses which is now in the memory of a neighboring processor. In the transputer architecture sharing this information is effortless; ease of communication among processors is one of the strongest arguments for this architecture.

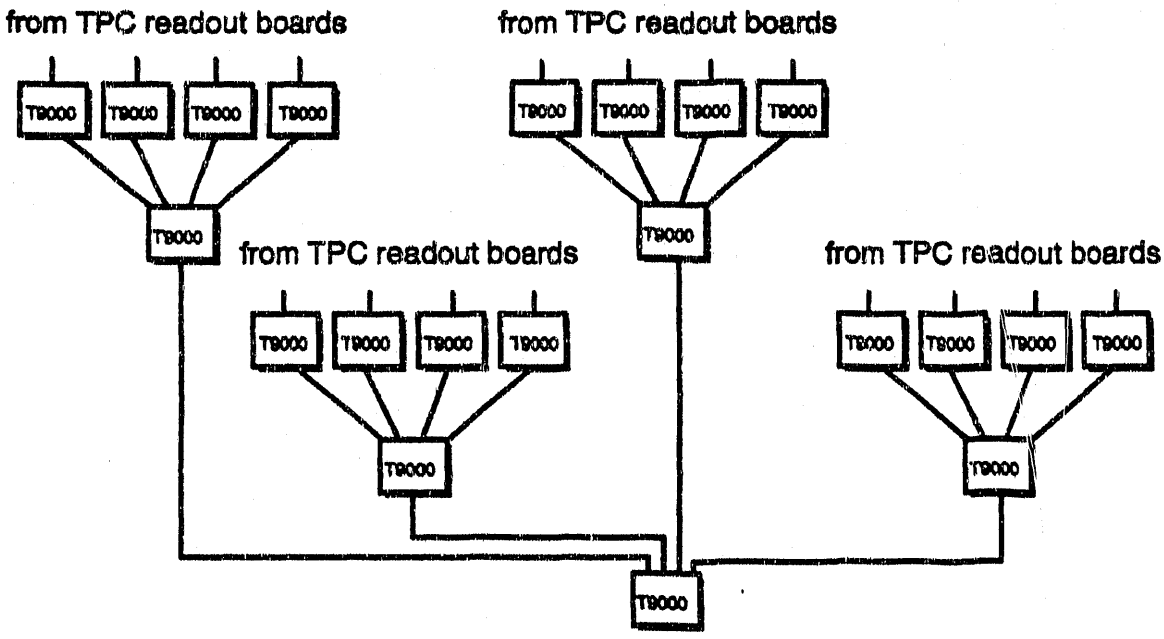

Figure 4F-3 A fragment of the event builder. The connections between T9000s are virtual links (see text).

Figure 4F-4 shows the kind of arrangement that can be realized using the C104 router to implement the logical links necessary to connect neighboring T9000s which share the hit-finding task for a single padrow.

6. Tape logger.

The tape logging device will make use of a commercially interfaced system if at all possible. Interfaces to high-performance tape drives through HIPPI are likely to be available in the required time frame. The choice of a tape technology will be made at the latest possible time (end of 1993). The rationale for this is that the number of drives required is not small: 2 are required online, 2 more are required for offline analysis and copying, and collaborating institutions will require drives as well. (Thus, the difference between a $50K and a $100K unit might well be $400K!)

7. Workstation interfaces.

It is expected that all of the human interface to the DAQ system will take place through workstations with good graphics and high-speed network communications. These workstations will be used to host tools used in development and debugging of code running on the detector readout boards and in the receiver crates. Heavy use will be made of X-Windows-based tools and techniques.

4.F.5.b. SVT Data Acquisition

The silicon drift vertex detector (SVT) consists of 162 detectors. Each detector is read out on two edges with each edge containing 224 anodes, for a total of 72,576

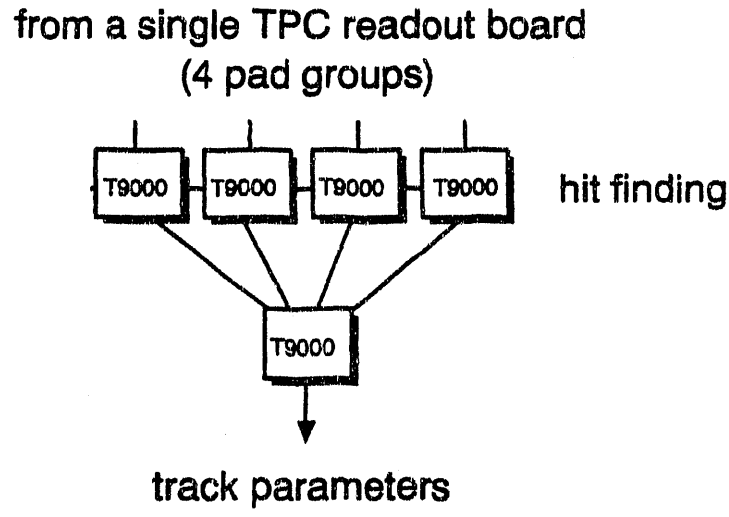

Figure 4F-4 A fragment of the arrangement necessary to perform tracking calculations for trigger purposes.

readout channels. The disposition of readout hardware at the detector is somewhat different from that of the central TPC (see section 4.D.2.b). The number of T9000 boards required is approximately 75 (Fig. 4F-5).

4.F.5.c. XTP Data Acquisition

The external TPCs (XTP) are not part of the STAR phase I detector system, and thus have not been discussed in any detail. The readout requirements are similar to those of the central TPC. The principal difference is the smaller number of pads (22000) in the XTP, requiring ~1/4 the number of T9000 boards and associated fiber optic links compared to the central TPC.

4.F.5.d. EMC Data Acquisition

The requirements for the electromagnetic calorimeter (EMC) are rather different from those of the systems discussed above. Because of the small (1200) number of channels, the need to store the analog signals during the time a first-level trigger is being formed will be addressed by cable delays. The digitizers will be commercially available Fastbus ADCs. Thus the readout requirements for EMC consist of reading the contents of the ADCs contained in a single Fastbus crate. This system will be integrated into the STAR DAQ by an interface which connects a commercial Fastbus master via an optical fiber pair to a dedicated interface in the standard STAR receiver crate system.

Upgrades to the EMC detector, notably 30K channels of shower-max detector, will require a totally different approach to this problem, based on analog pipelines implemented in custom chips. Such solutions are currently being developed for several collider experiments, and it is expected that any upgrade to the EMC will make use of one of these developments.

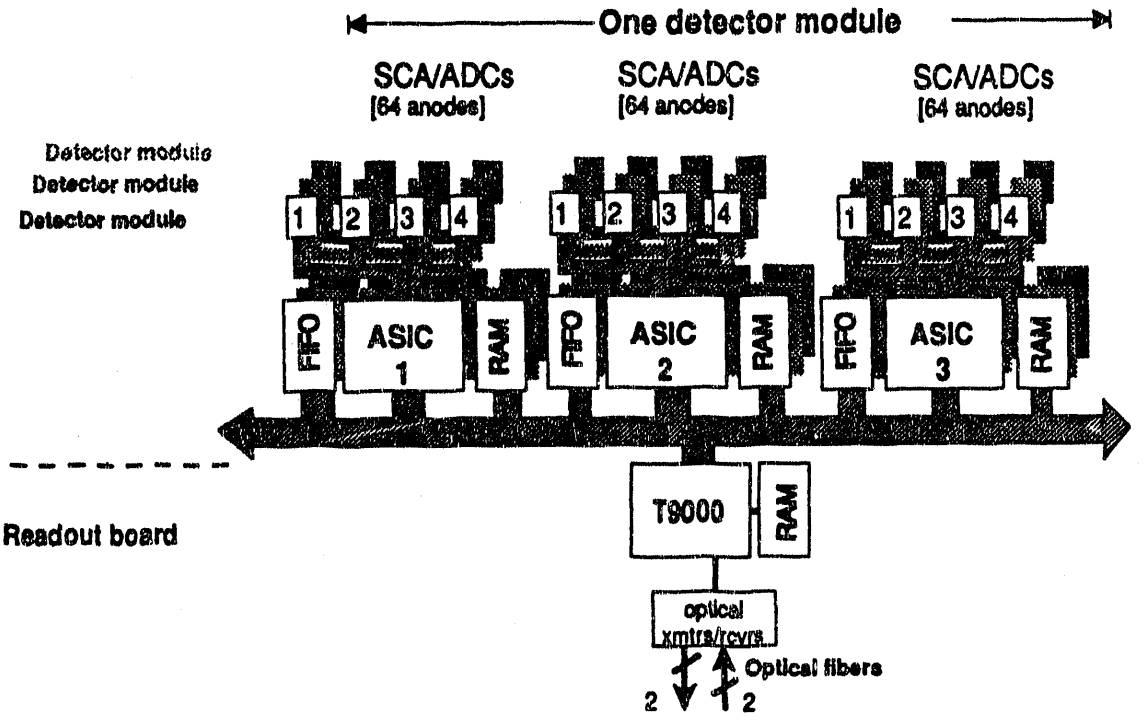

Figure 4F-5 Block diagram of the SVT readout. Each detector module contains 3 ASICs (one per 64 anodes). Three detector modules are linked together to the readout board, which contains the T9000 and the optical links to the receiver crates. The T9000 assembles data prepared by the ASICs.

4.F.5.e. DAQ Requirements During Initial Assembly

The final installation of the detector subsystems in the Wide Angle Hall will be finished in early 1996. At that time, the DAQ subsystem must be functional in all important respects. Much earlier, however, there will be a need to test parts or prototypes of the STAR detector components using cosmic rays, lasers, radioactive sources, or test beams. To accommodate this need, a few mini-DAQ systems must be available by mid-1994. They should be capable of running independently of each other, should be capable of recording data, and should be functionally as similar to the final DAQ system as possible. In particular, the parts of the DAQ system which reside on the detector and which perform operations on the data stream (i.e., pedestal suppression) should be available for testing at this time. While having these systems identical to the final product would be desirable from the point of view of improving the final DAQ system, it is not necessary in order to test detector performance. For example, these systems could be configured using workstations, 8mm tape systems, and an interface to the readout electronics to be used in the final system. Such a configuration would provide the required functionality without impacting on limited resources.

4.F.6. Engineering Testing

A prototype of a part of the planned readout board will be built and tested using the SCA-ADC chips appropriate to the final design, prototypes of the ASIC, etc.

Completion is anticipated by 4Q 1993. A single optical link (4 fibers) will be built and tested in conjunction with the prototype readout board. Completion is anticipated by 2Q 1993. A prototype of the receiver card, partially populated, will be tested in conjunction with the above-mentioned prototypes. This card prototype should be completed by 4Q 1993.

4.G. Online Computing

4.G. Computing

The job of the on-line computing is to establish a high degree of reliability in the data recording process. If the recorded data are incomplete or incorrect, then the on-line computing has failed. An important part of this process is to alert the experimenters to any failures of the apparatus of the STAR detectors in a timely way so that repairs can be made with minimum loss of running time. One of the best ways quality assurance measures that can be applied is to carry the analysis of on-line data through to physics analysis. This is accomplished by performing the analysis steps which are traditionally part of the off-line analysis on a sample of the data on-line.

4.G.1. Specialized Physics Issues

Significant issues for the online computation are:

1) The large number of tracks in the TPC for Au beam operation. A single central Au-Au collision at RHIC energies is expected to put more than 5000 primary charged tracks in the central TPC. This causes serious loading of the available TPC pixel space and loss of information from the merging of overlapping hits. The efficient and accurate reconstruction of the tracks from Au-Au collisions is the benchmark for the design of the TPC and the TPC tracking code. This has a direct impact on the global on-line event reconstruction task.

2) The need for resolution adequate for some HBT measurements. The measurement of the predicted size of the plasma source, tens of fermi in radius, by detecting the enhancement in identical particle correlation at small momentum differences, will require a momentum resolution significantly better than 10 MeV/c. This also pushes the capabilities of the TPC design and the accuracy attainable by the TPC, SVT and global event reconstruction codes.

3) The goal of reconstructing strange particle decays using the SVT and the TPC together. We propose to detect strange particle decays by reconstructing vertices in the SVT detector and measuring the momenta of the secondary tracks in the TPC. Matching the tracks from the two detectors is another challenge for the tracking and event reconstruction code.

4) Evaluating the efficiency, bias and stability of the various triggers is another important aspect of the on-line computing system. This reflects on the accuracy and reproducibility of all the physics measurements performed with this detector.

5) Monitoring the performance of the various detector subsystems, i.e. the efficiency for particle detection and particle identification and position resolutions is also a critical feature of the on-line computing which has a direct impact on the physics measurements.

4.G.2. Description of Subsystem

The on-line computing is essentially a complex software system. The hardware requirements of the on-line computing system are determined largely by the rate at which data is to be processed for the monitoring functions mentioned above and the

large size of the individual event data. The software requirements are driven by the functions to be performed, including monitoring and control of the detectors and presentation of information about the state of the experiment to the operating crew. The user interface will be designed so that this crew need not, in general, be specialists in the on-line software.

The computing hardware is describable in terms of the scale of the resources needed. We have no special hardware requirements beyond the current state-of-the-art, although the choice of a good architecture can reduce costs and improve efficiency. Perhaps the most worrisome hardware issue is the storage of the massive data generated by the experiment. However, this is largely the purview of the data acquisition system designer and will mostly impact the offline computing task.

It is envisioned that each detector subsystem will, in the course of designing and testing prototypes and through the final construction phase, acquire a computing system for the diagnosis of the performance of the detector hardware. These systems will communicate with their users and with other computers over Ethernet. These systems are expected to continue to provide significant monitoring of the detector hardware during on-line operations and to contribute to the on-line information database by responding to queries over the network. Some of the software developed for these systems will serve as prototypes for the complete on-line monitoring system.

The complete reconstruction, on-line, of a small sample of the events is the chosen goal which sets the scale of the main on-line computer hardware. If we choose for the most complicated events to set that sample at 5%, we need 250 Mflops for the on-line event reconstruction, which is a large enough system to make its cost a significant factor in the choice.

The software must be well designed and will require unwonted discipline on the part of the writers, who must be the physicists and graduate students of the collaboration for the most part. The size of the project mandates an organized and professional approach to the software. No part of the on-line software can be regarded as "private" code. For reliability, on-line programs must be fault tolerant to the extent that they are virtually immune to the appearance of any spurious bit pattern whatsoever in the data.

The performance monitoring and control requirements provide the goals for defining the majority of the on-line software components. The distributed nature of the computing hardware defines the base level environment for the software systems. Given these considerations the software components must provide for: (a) management of calibration, configuration, and performance data, (b) a software development environment which defines interfaces enabling individuals to contribute to the larger system, (c) standard user interfaces for operation and control of the various processes and (d) other utility services that all programs will require, e.g.. error handling, message service, etc.

The goal of on-line reconstruction of the largest events means that there is a large overlap between the on-line and offline code. A special requirement of the on-line software is a tool for queries to the ephemeral database and presentation of the returned

information to physicists and engineers in control of the experiment. This tool must have an intuitive graphical interface that is easy to use by people who are not computer specialists. These tools must provide information about the data and the detector to all levels of detail.

4.G.3. Capabilities of Subsystem

The scale of the system is designed to provide full analysis of event data on-line at a rate of 0.05 to 0.1 events/second, i.e. 5% to 10% of the data acquisition rate. There are many other tasks on the menu of the on-line computing system. Indeed, the shakedown and startup of the apparatus finds physicists and engineers often staring at hexadecimal dumps of the data. Nevertheless, the need at a later stage for a good analyzed event sample in the on-line database sets the scale of computing needed. Present analysis of simulated event uses about 1 Mflop-second per track. Thus the event analyzer task requires 250 Mflop on-line. Input to the system is mostly via a high speed direct connection to the DAQ event recording system. In advance of the actual on-line analysis, major computer support is needed for the code developers. The generation of simulated events and especially the simulation of the interaction of the event particles with the detector materials requires more CPU power than the actual event analysis.

The performance monitoring and experiment control capabilities of the on-line computing system amount to the major portion of the software system to be built. This system needs to be able to display a history of experiment performance (total multiplicity, dN/dY, $N^+ - N^-$, etc.) as a function of time and trigger conditions. It also must be able to display detector-element position resolutions as functions of time, trigger type and other slow control parameters (drift velocity, pressure, temperature, high voltage). In addition to displays, the monitoring programs must be able to sound alarms when any of the necessary performance parameters drift out of tolerances. These capabilities impact the data management and information display characteristics of the on-line computing.

4.G.4. R&D Issues and Technology Choices

The design of the software is the major task. Acquisition of hardware should be timed to anticipate needs and to capitalize on progress in cost/performance. This means that software must be platform independent to maximize hardware choice. As the most platform independent operating system around, UNIX must necessarily be a part of every physicist's environment. Most of the code will still be written in FORTRAN, with a gradual implementation of the newer features of Fortran90.

In addition to defining and carefully designing the features and functions of the on-line computing system, it is clear that one of the first things required in order to take advantage of the available labor pool of non-computer professional physicists (graduate students, post-docs, etc.) is a framework providing the interfaces that can be used in developing the various functions of the on-line system. A joint (STAR and SDC) R&D effort to develop such a framework is underway at LBL.

In light of the rapidly evolving computing industry it is necessary to make careful decisions on which industry standards, both hardware and software, are used in developing the on-line computing system. Identifying the current standards that are best suited to STAR is one of the tasks that should be completed soon. Following the development of new standards is an ongoing effort.

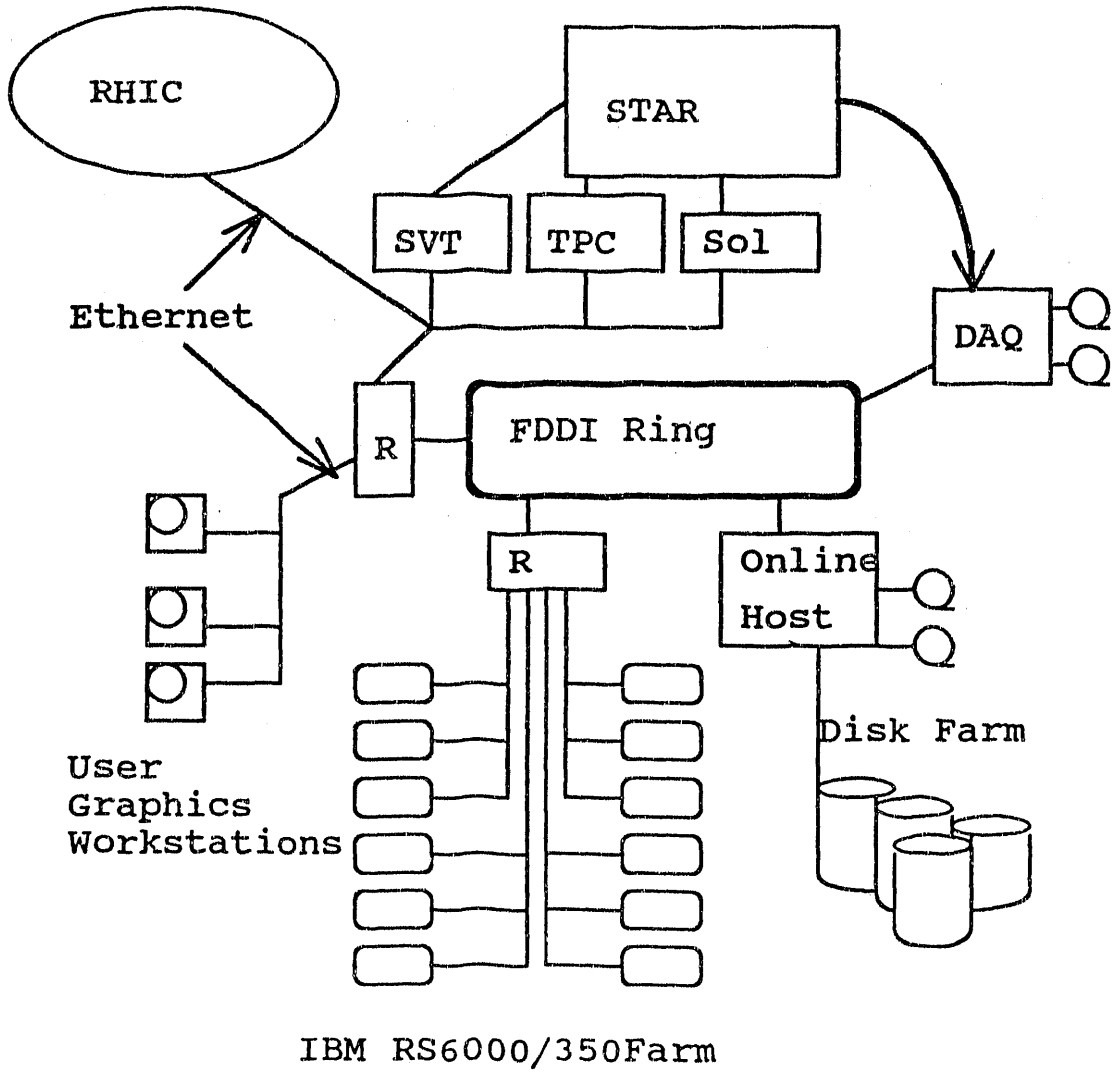

Figure 4G-1 Hardware components of the on-line computing system. Connected to a central FDDI ring over Ethernet are the subsystem hardware monitors labeled SVT, TPC, and Sol (for the magnet). The main data acquisition system with its high speed VHS tapes is marked DAQ. The on-line host computer (OLH) controls the event processor, shown as a set of 12 RS6000/350 RISC workstations. OLH also maintains the on-line database. The User Graphics Workstations provide the consoles for the experimenters to interact with the online system.

4.G.5. Engineering

4.G.5.a. Brief Technical Description & Specifications

The figure shows the components of the system located at the 6 o'clock hall. Connected to a central FDDI ring over Ethernet are the subsystem hardware monitors labeled SVT, TPC, and Sol (for the magnet). These systems are the main providers of so-called "slow" control and monitoring. The main data acquisition system with its high speed VHS tapes is marked DAQ. The on-line host computer (OLH) controls the event processor, shown as a set of 12 RS6000/350 RISC workstations. OLH also maintains the on-line database, the hardware for which is labeled Disk Farm in the figure. The presentation of the data to the experimenters is accomplished by code running in the User Graphics Workstations (UGW), at least one of which has a very high resolution event display.

Not shown are the code development workstations which have no reason to be located at the experimental equipment. Indeed, given the distribution of the personnel of the collaboration, code development will take place on three continents.

The schedule for delivery of computer hardware will be driven by the detector development and will be placed late in the cycle to take maximum advantage of the steady improvement of the cost-performance ratio that characterizes the computer industry. The schedule for the software development is much more pressing and mandates the early formation of a core group to work together on design and implementation of the infrastructure that will facilitate the work of the programmers contributing to the sub-system and physics code.

4.G.5.b. Description of Major Hardware Components

Code Development Systems

Currently the STAR share of the RHIC computer system supports about a half dozen workers at their own workstations or X terminals. The expected doubling of the CPU and some increase in file support should handle twice that number. To reach full productivity a central STAR system will be acquired of about the same capacity unless the RHIC system expands to that level (i.e. about four times present CPU power and disk capacity). In any case there will be a need for perhaps twenty personal workstations to serve as access ports to the central systems and local support during network failures. The reliability and capacity of the international networks should continue to improve so that workers can contribute from home institutions in the U.S. and outside.

On-line Detector Subsystem Computers

These will range from a PC for small detector elements (e.g. magnet monitor) to larger workstation systems (for the TPC). All must conform to network and STAR communication standards.

On-line Event Processor System

This system will require a multiprocessor computer of at least 250 Mflops total capacity with 25 GBytes of disk. The choice of system will depend on the market at the time. Coarse grained parallelism is adequate to provide timely event analysis, that is the use of multiple processors can be on an event-by-event basis. Possible solutions could be three or four of the SGI multiprocessor RISC systems or a larger farm of IBM RS6000's (say about 1/7th of the current FNAL IBM system) or of DEC alpha computers.

On-line Event Processing Host System (OLH)

The host of this system will have a high speed link (FDDI) to the DAQ system for rapid on-line sampling of raw event data. Slower network (Ethernet) access to all the detector subsystem computers will enable this system to maintain a rotating up-to-date database of all experimental parameters as well as some raw and processed complete events. This database will be stored in a disk farm of at least 25 GBytes which with current designs requires 15 disk drives on two SCSI (or faster) buses. User workstations will access this database over Ethernet for on-line event display and monitoring of the complete detector. Also in the OLH system will be two tape drives capable of reading the main DAQ tapes, baselined as VHS systems. This is to enable quick recovery into the on-line event pool of the raw data for previously recorded events. This is in addition to the tape systems of the DAQ system itself.

Network Capacity

The processor farm will be served raw event data at an aggregate rate of 500 KB/sec (10 MB Au-Au events processed at 3/minute) and the return of processed events will add a similar load. Thus the processor farm backbone must sustain 1 MB/sec total, a rate currently achievable over Ethernet. To allow for expansion and the possibility of handling larger events, the system is shown as configured around an FDDI ring with the use of two CISCO AGS/2 routers (boxes labeled R in the figure) to interface the Ethernets of the processor farm and that serving the hardware subsystem computers and supplying processed event data to the experimenters. The DAQ computer and the OLH are interfaced directly to the FDDI ring.

4.G.5.c. Description of Major Software Components

The code development system includes:

1) A centrally located library of all current software with tools for installation, program generation, and version control.
2) A database of real and simulated event data from all detectors.
3) A set of parameter files describing all detector components.
4) A documentation system mostly derived directly from the operating software.

The online operating system includes:

A manager process to handle systematic replacement of the on-line database with up-to-date records of event data and slow monitor data and to service requests for data records from the UGWs. The database must be large enough to hold a fairly complete record of running configuration data and data summaries for a period of months as well as complete data for a recent raw event sample (hours) and an accumulation of "interesting" events (days). This will be an independent process from the on-line event analysis control. The latter will supply the processor farm nodes with event records and retrieve processed data records.

An on-line database inquiry and display system running in the UGWs will use graphics based on the X11 standard. The future development of the CERN library tools such as KUIP and PAW will be important. STAR software needn't reinvent the histogram. Unfortunately CERN support for projects with no CERN basis is desultory. A staff of STAR CERNlib experts will be necessary.

We must reconcile the desirable features of commercial databases with the special needs of physics data. If a commercial database is chosen it must have user "hooks" and considerable user customization is required. If a physics-inspired tool like ZEBRA is the basis, then the user interface can be built to specification.

4.G.5.d. Engineering Testing

Some Computer Aided Software Engineering (CASE) tools will be needed. Any such tools need to be usable over the network and on the systems where the code must be used. This rules out most PC-based tools. No theoretical model of software engineering is yet established as a panacea but techniques like Object Oriented Programming have demonstrated advantages. No automatic system or principle can take the place of serious design effort by experienced people and thorough testing of all software modules.

4.G.6. Testing and Calibration Issues

Full simulation of all detector subsystem data outputs will be produced to serve as testbeds for all software components before construction. As detector components are built and operated, simulation will be upgraded to match measured performance. A means of examining the calibration of single channels and complete detector subsystems will be part of the on-line software system.

4.G.7. Off-line Computing

The nature of the off-line computing load will change rapidly in the early stages of the experiment. The following is a likely scenario. Data will initially be passed through the DAQ system without benefit of on-line filtering in order to provide a data base from which to develop an efficient algorithm for the filter. The size of these events will be large. For the TPC it is 140000 pads times 512 time buckets times 10 bit ADC = 90 MB+. A few hours of such running (at a rate limited to maybe 0.25 Hz by the taping speed) once the TPC is functioning well, should provide an adequate database for the filter tests. This kind of data taking will be repeated at regular intervals for a while until the filter algorithm is stable. It is likely that the optimum filter will be developed in

stages, simple zero-suppression coming first, time cluster finding second, full 3-D cluster finding later. Of course, the initial filter algorithms will be developed before RHIC turn-on, but final tuning will be done on RHIC produced data.

A few hundred hours of level 1 trigger running should give an adequate sample of minimum bias and coarsely selected "central collision events" to test and develop secondary triggers.

With well developed hardware triggers and DAQ pre-processing, a selective run of central collision events will give a survey of "soft" physics at RHIC. At a 1 Hz rate the database will grow at the rate of one million events for every 300 hours of RHIC operation. Note that 1 Hz is still only a few percent of the essentially central collision rate at nominal RHIC luminosity. This event database will form the resource for the first searches for rare processes as well as for the physics signals expected for common events. The characteristics of the "rare" events will drive the development of sophisticated triggers so that the 1 Hz recording rate can contain the highest yield of "rare" phenomena.

The critical system requirement for the off-line computing is that events be reconstructed at a rate that keeps pace with the recording rate of experimental data. That rate will vary with the sophistication of the trigger system and at the beginning will be limited by the recording rate of the data acquisition system. The scale of the off-line system is set so that at each stage it will be possible to reconstruct the most difficult events at a 1 Hz rate. At present the simulation of events by the CERN GEANT program requires about three times the reconstruction time. It will eventually be necessary to use large-statistics samples of simulated events to evaluate acceptances and event reconstruction efficiencies as well as derived particle identification, momentum, and angle resolutions. This will require improving the event simulation efficiency by using hybrid simulations that replace full simulation of some detector features by parametrizations where possible. Nevertheless, the total scale of computing required is several times that needed for a 1 Hz event processing.

After event analysis, physics output will require handling a large database of processed events with inquiry and event selection from multiple high performance workstations, some of which must have excellent graphics displays. The design of this system to meet real user needs is more challenging than the relatively straightforward processor farm. The database must provide a hierarchical structure of data summary files, allowing rapid summing for statistics of small data records, backed up by more complete event data (all the way back to the raw data) to allow closer examination of selected events. The Monte Carlo events generated for acceptance and resolution measurement are kept in the same database. The software for manipulating this database would either be built on a commercial database system, adding features required by the special needs of large physics experiments, or by developing the necessary tools around an existing system for handling physics event data, like ZEBRA. Either approach requires substantial design and implementation effort, though much of it could be developed in common with other experiments in heavy ion and high energy physics.

STAR

4.H. Silicon Vertex Tracker

4.H. Silicon Vertex Tracker

4.H.1. Specialized Physics Issues

The Silicon Vertex Tracker is a high resolution tracking device with a spatial resolution that is equivalent to 18 million pixels (72576 channels x 256 time samples) distributed over 3 layers at radial distances of 5, 8 and 11 cm from the interaction point. It greatly improves the tracking capabilities of the STAR detector below transverse momenta of 150 MeV/c, extends the particle detection scheme to short lived neutral and charged strange particles, and allows the study of K°_{S}-K°_{S} correlations. In this chapter the specific physics issues addressed by the SVT are discussed.

4.H.1.1. Flavor Physics

Particles containing strange or heavy quarks are of particular interest for the study of hot and dense hadronic matter and the possible formation of a quark-gluon-plasma. Strange quarks will be the most frequently produced heavy quarks. Therefore strange particle detection is one of the primary goals of STAR. For the determination of the total strange quark content in an average event both, mesons and baryons must be considered, since it is unclear what fraction of all s-$\bar{s}$ pairs appear in hyperon-antihyperon pairs. This fraction was found to be 0.09 in the baryon-rich regime at lower energies[1] and around 0.15 in Tevatron p-$\bar{p}$ interactions.[2]

The various types of strange particles are detected and identified by different methods. Charged long-lived kaons will be identified by measuring their energy loss (dE/dx) in both TPC and SVT. Short-lived particles (K°_{S}, Λ, $\bar{\Lambda}$, Ξ^{-}, Ω^{-}, 1cm < $c\tau$ < 10cm) are detected via their weak decay into charged particles. Identification of strange particle decays, i.e. the separation of the decay tracks from those tracks which originate from the primary interaction point, requires precise information on the track position close to the interaction point. Therefore a high granularity SVT placed just outside the beam pipe is foreseen. Its capabilities will be described in detail below.

The STAR tracking detector system will address also the detection of the ϕ meson which contains "hidden" strangeness. Its detection efficiency will be enhanced due to the fact that the STAR vertex tracking detector will allow the detection of the asymmetric decays (see chapter 4.H.1.2.). The ϕ meson has a short lifetime and thus a measurable width. The measurement of the invariant mass with a resolution of the order of the ϕ width (4 MeV) may allow a study of the variation of the width of the ϕ meson with the size of the reaction volume. This requires an excellent invariant mass resolution provided by the SVT.

The experimental situation is much more complicated in the case of charmed particles due to significantly shorter life times (e.g. $c\tau(D^{\circ})$ = 126 µm, $c\tau(D^{\pm})$ =300 µm as compared to $c\tau(K^{\circ}_{S})$ = 2.7 cm) and small production cross section ($\sigma(c)/\sigma(s)$ about 10^{-2}). However the existence of a high resolution SVT detector positioned close to the

[1] H. Bialkowska et al., Warsaw Univ. Preprint IFD/1/1992, J. Bartke et al, Z.Phys. C48(1990)91.
[2] T.Alexopulos et al., Nucl.Phys. A525(1991)165c.

interaction point may allow the measurement of charmed particle production. The detection efficiency of $D^{\circ}(\bar{D}^{\circ})$ decays into $K^{-}+\pi^{+}(K^{+}+\pi^{-})$ has been studied via Monte Carlo simulations.[3] This reaction was chosen because of its relatively large branching ratio (3.7%), the high efficiency of identifying the decay products and the relatively low combinatorial background. The analysis has shown that the open charm signal to noise ratio is 1:1 for 10^6 central Au + Au collisions. The development of new algorithms is in progress.[4]

4.H.1.2. Extension of STAR Acceptance to Low P_t

The Silicon Vertex Tracker in STAR provides a powerful tool to extend the acceptance of the TPC to low momentum tracks. FRITIOF simulations of central Au+Au events show that the transverse momentum distribution of emitted particles at midrapidity will in general be peaked around 300 MeV/c. The lower TPC limit for fully efficient track reconstruction is 150 MeV/c. Therefore a considerable part of the event will be measured by inclusion of tracking in the SVT alone. In addition, recent results of AGS and CERN experiments have shown that low p_t physics is an interesting topic in relativistic heavy ion physics in itself.[5,6,7] In the following we state the main physics issues that can be addressed by STAR if a detector like the SVT is employed in connection with the TPC. In chapter 4.H.3.2 we describe a first attempt of tracking in the SVT.

a) The low p_t enhancement measured in pion p_t spectra below 200 MeV/c emerging from heavy ion interactions at relativistic incident energies[8,9,10] is still not understood. An overview of the diversity of recent theoretical approaches is given in [11]. A measurement of the low p_t part of the spectrum for a variety of particle species (K,π,p etc.) at RHIC may allow an understanding of the origin of this phenomenon. It also allows a more accurate assessment of the rapidity distribution of identified particles in the pseudorapidity range covered by the TPC, by integrating over the full p_t range in each rapidity bin. A probable uncertainty based on the extrapolation of a p_t spectrum measured by the TPC to $p_t = 0$ is eliminated. This uncertainty is increased by effects like a low p_t enhancement.

b) The correlations of many low momentum particles is in general attributed to collective effects. Recent predictions of localized plasma formation ('Van Hove bubbles',[12]) might lead to correlated hadronization of low p_t particles, which can be investigated by measuring fluctuations of the yield in rapidity.

---

[3] S. Margetis, K. Wilson, STAR-SVT note 9/20/91.
[4] M.Gazdzicki, W.Retyk, STAR note Warsaw 1/92.
[5] T. Akesson et al.,Z.Phys.C46 (1990)361.
[6] H. Stroebele et al.,Z.Phys.C38 (1989)89.
[7] B. Jacak, Nucl.Phys.A525 (1991)77c.
[8] T. Akesson et al.,Z.Phys.C46 (1990)361.
[9] H. Stroebele et al.,Z.Phys.C38 (1989)89.
[10] B. Jacak, Nucl.Phys.A525 (1991)77c.
[11] E.V.Shuryak, Nucl.Phys.A525 (1991)3c.
[12] L. van Hove, Ann.Phys.192 (1989)66.

c) Many particle short-range correlations in rapidity can be measured with high accuracy. Factorial moment calculations and other more general intermittency theories could be verified on an event by event basis because of the high multiplicity in a central Au+Au event. Measuring these correlations at low p_t would shed some light on the scale invariance of short range correlation functions.[13]

d) Since the phase space density is highest at low p_t , coverage of this part of the spectrum will enhance considerably the number of close pairs per event and thus single event two particle correlation capabilities (HBT measurements). The two track resolution will be improved considerably compared to a TPC standalone performance (see chapter 4.H.3.3.).

e) The low p_t capability of the SVT also provides an extension of the TPC measurement of ϕ-decays into charged kaons. Since the most probable ϕ decays are asymmetric, this results in at least one decay particle with transverse momentum below 500 MeV/c.

f) Based on a theory by T.D.Lee which postulates the occurrence of a 'cold' QGP, Bjorken[14] speculates that the orientation of the vacuum in the cold phase (chiral condensate) could be different from the orientation outside of a QGP bag. If this is valid at hadronization time, the plasma emits on an event by event basis an unusual particle ratio during relaxation (reorientation) into the exterior vacuum direction. Production of particles with charges in the interior vacuum direction are preferred. Bjorken calls this interior phase a disoriented chiral condensate. He postulates a coherent emission of low p_t particles of a certain charge. The so called 'centauro events' which were observed in cosmic ray experiments may be an experimental indication of possible fluctuations of the low p_t pion yield. By measuring the cross sections of charged low p_t pions event by event in the SVT as a function of centrality it should be possible to sort out unusual particle fluctuations. A correlation with neutral particles measured in the calorimeter also determines the $\pi^{\pm}/\pi^{0}$ ratio.

4.H.1.3. K^{0}_{S} Interferometry

4.H.1.3.1 Motivation

Two-particle Bose-Einstein correlations have the potential to probe the space-time structure of the particle emitting source and may carry a signature for QGP formation.[15,16] In order to extract space-time information, final state interactions[17,18] and

[13] N.M.Agababyan et al.,Phys.Lett.B261 (1991)165.
[14] J.Bjorken, 'A FAD detector for SSC', BNL-Colloquium, May 1992.
[15] S. Pratt, Phys. Rev. Lett. 53, 1219 (1984).
[16] G. Bertsch, M. Gong, and M. Tohyama, Phys. Rev. C 37, 1896 (1988).
[17] M. Gyulassy, S. K. Kauffmann, L. W. Wilson, Phys. Rev. C 20, 2267 (1979).
[18] M. G. Bowler, Z. Phys. C39, 81 (1988).

resonance formation[19,20] must be understood. Kaons offer significant advantages over pions in these regards[21,22,23,24,25,26,27,28]. In particular resonance production, which increases the apparent size and lifetime of the source, is less important for charged and neutral kaons[29,30]. Moreover K^+ and K°_s correlation functions can in principle be used to remove the distortions due to resonances.[31] Another argument for K°_s HBT studies is the absence of Coulomb repulsion which plays an important role for charged kaons. A comparison between the correlations functions measured for charged and neutral kaons would enable a quantitative assessment of the effect of Coulomb repulsion if the same phase space is covered for both particle species. Finally some interesting and potentially important consequences arise from the fact that the K°_s is not a strangeness eigenstate. The K°_s-K°_s correlation includes a unique interference term that provides additional space-time information[32] as well as insight into possible strangeness distillation effects[33,34,35,36] in cases where the baryon density of the source is appreciable. If the kaons come from a baryon-free region, the expected K°_s correlation function has the conventional form.[37]

Central Au+Au collisions at RHIC are expected to produce on the order of 230 short lived neutral Kaons per event. Of these we expect to actually detect 10-20%. The corresponding sample of K°_s constitutes the basis for the study of K°_s-K°_s Bose Einstein correlations. Such a study is helped significantly by the fact that it is not affected by two-particle resolution limitations which are crucial in charged particle correlations: K° mesons are identified and measured by their decay into charged pions and these pions are emitted back-to-back along a line oriented randomly in the kaon rest frame. Even for two K°_s at exactly zero relative momentum the decay pions are well separated in (configuration and momentum) space and can be measured with the same efficiency as if the relative momentum of the kaons was large.

---

19 S. S. Padula and M. Gyulassy, Phys. Lett. B217, 181 (1989).
20 M. Gyulassy and S. S. Padula, Phys. Rev. C 41, R21 (1989).
21 S. S. Padula and M. Gyulassy, Phys. Lett. B217, 181 (1989).
22 M. Gyulassy and S. S. Padula, Phys. Rev. C 41, R21 (1989).
23 S. S. Padula, M. Gyulassy, and S. Gavin, Nucl. Phys. B329, 357 (1990); Nucl. Phys. B339, 378 (1990).
24 C. Greiner, P. Koch and H. Stocker, Phys. Rev. Lett. 58, 1825(1987).
25 C. Greiner, D.-H. Rischke, H. Stocker, and P. Koch, Phys. Rev. D 38, 2797 (1988).
26 C. Greiner and B. Muller, Phys. Lett. B219, 199 (1989).
27 S. Pratt, P. J. Siemens, and A. P. Vischer, Phys. Rev. Lett. 68, 1109 (1992).
28 M. Gyulassy, preprint LBL-32051 (1992).
29 S. S. Padula and M. Gyulassy, Phys. Lett. B217, 181 (1989).
30 M. Gyulassy, preprint LBL-32051 (1992).
31 M. Gyulassy, preprint LBL-32051 (1992).
32 M. Gyulassy, preprint LBL-32051 (1992).
33 C. Greiner, P. Koch and H. Stocker, Phys. Rev. Lett. 58, 1825(1987).
34 C. Greiner, D.-H. Rischke, H. Stocker, and P. Koch, Phys. Rev. D 38, 2797 (1988).
35 M. Gyulassy, preprint LBL-32051 (1992).
36 U. Heinz, K. S. Lee, and M. J. Rhoades-Brown, Phys. Rev. Lett. 58, 2292 (1987); Mod. Phys. Lett. A2, 153 (1987).
37 M. Gyulassy, preprint LBL-32051 (1992).

4.H.1.3.2 Simulations of HBT Capabilities for K°_{s}

The K°_{s} HBT performance of STAR has been simulated using the neutral kaons from central ($0 < b < 1$ fm) Au + Au events generated by HIJING[38] with a Bose enhancement imposed as per an incoherent spherical source of radius 10 fm. Considering that kaons can be expected to freeze-out earlier than pions, this radius is plausible. These events have not yet been processed through the full STAR simulation chain which includes TPC track finding and reconstruction, but have been analyzed using a simpler and much faster simulation. The latter incorporates parameterizations of the K°_{s} finding and reconstruction efficiencies and resolutions of the SVT/TPC, obtained from relatively small samples subjected to the full simulation. Further details can be found in STAR note #47. Fig. 4H-1 shows the correlation functions $C(Q_{out})$ and $C(Q_{side})$[39,40] with the condition that the K°_{s} rapidity lies in the range $-0.5 < y < 0.5$ after application of the experimental filter. Q_{out} refers to the relative transverse momentum along the direction of the average pair momentum. This is the direction predicted to offer the best discrimination between plasma and hadron gas scenarios[41,42,43] . The intercept at $Q = 0$ is mostly determined by the binning and the condition imposed on the other two dimensions of Q. The solid line shows the symmetrized HIJING without any detector distortions but with the same binning. The dashed line in Fig. 4H-1 was calculated by assigning a charge to the kaons represented by the solid line, and applying the standard Gamow factor.[44] The width of this "Coulomb hole" underlines the benefit of neutral particle HBT when the particle is relatively heavy and the source radius is large.

This first simulation suggests that K°_{s} interferometry offers substantive advantages over charged-particle HBT, and the K°_{s} enhancement is a robust signal. The SVT is crucial for K°_{s} HBT, because of its tracking capability for secondary vertices.

---

[38] X. N. Wang and M. Gyulassy, LBL-29390.
[39] S. Pratt, Phys. Rev. Lett. 53, 1219 (1984).
[40] G. Bertsch, M. Gong, and M. Tohyama, Phys. Rev. C 37, 1896 (1988).
[41] G.Bertsch, M. Gong, and M. Tohyama, Phys. Rev. C 37, 1896(1988).
[42] S.S.Padula and M. Gyulassy, Phys. Lett. B217,181(1989).
[43] M. Gyulassy, preprint LBL-32051 (1992).
[44] S. Pratt, Phys. Rev. Lett. 53, 1219 (1984).

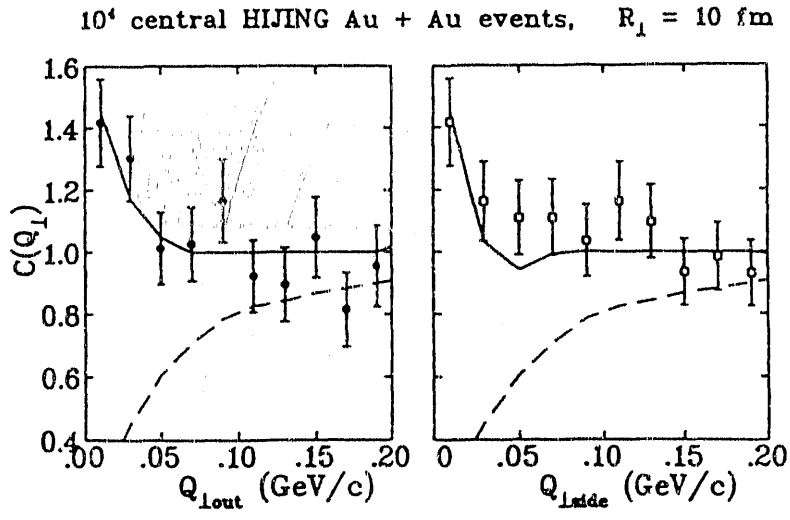

Figure 4H-1 Simulated STAR performance.

4.H.2. Description of Subsystem

4.H.2.1. Silicon Drift Detector (SDD)

The choice of the SDD, a relatively new but well tested semiconductor detector [45,46,47], as the basic component of the SVT system is motivated by its excellent spatial resolution which leads to a space point precision of better than 25 μm and, based on our electronics choice, to a two-track resolution of 500 μm. The two track resolution can be improved to 150 μm by performing a waveform analysis which allows one to separate peaks in adjacent time buckets by knowing their widths.[48] This peak width depends on the incident angle which can be determined via track reconstruction in the SVT. Further advantages of this detector are that it has no dead time, a low number of electronic channels (as compared to pixel detectors) and the capability to measure the energy loss of the traversing particle. A perspective view of the drift detector is shown in Fig. 4H-2.

The volume of the detector is fully depleted of mobile electrons. The field created by the remaining fixed charges confines electrons generated by an ionizing particle in a buried potential channel. An electrostatic field parallel to the surface is superimposed. This field forces electrons liberated by particle passage to drift toward a collecting electrode. The transit time inside the detector measures the distance of an incident particle from the anode.

[45] E. Gatti, P. Rehak, M. Sempietro, NIM A274(1989)469.
[46] P. Rehak and E. Gatti, NIM A289(1990)410.
[47] P.Rehak et al.,NIM A248(1986)367
[48] T. Humanic et al.,'Double Particle Resolution Measured in a Silicon Drift Chamber', Preprint Univ. of Pittsburgh, November 1991.

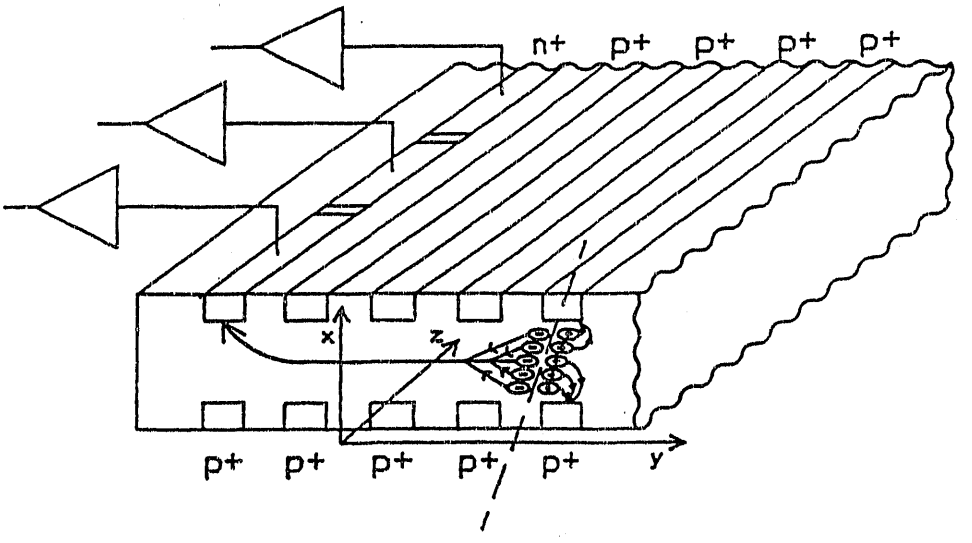

Figure 4H-2 Perspective view (not to scale) of a semiconductor drift detector. Electrons created by ionizing particles are transported long distances parallel to the detector surface. The anode is divided into short segments to measure the coordinate perpendicular to the drift direction

An important difference with respect to standard (wire) drift chambers is the absence of gas amplification and of the corresponding dead time. All electrons are continuously drained at the anode so that the maximum drift time is not the dead time of the detector. Electrons drifting toward the anode have their charges screened by the electrode structure of the silicon drift detector and do not interfere with other signals or with the signal processing at the anode. The signals are stored within the detector for the duration of their drift. As a direct consequence of this electron transport method the anode capacitance is much lower than the anode capacitance of classical semiconductor detectors of the same dimensions. The amplifier noise can be made much smaller which is the main reason for the excellent position resolution of silicon drift detectors. A detailed description of the exact shape of the electric potential in silicon drift detectors can be found in [49]. Simulations to study the anode response of Si drift detectors are in progress (see Appendix 3: Transport code in Silicon). These simulations include diffusion, the applied drift field, and the self field of the electron cloud created by the passage of a charged particle through the detector. The effects of the magnetic field on the transport of the cloud of electrons to the anode plane are also being addressed.

4.H.2.2. Silicon Vertex Tracker (SVT)

Figure 4H-3 shows the SVT layout presently envisioned for the final design. Individual detectors are grouped into ladders. Each ladder holds a row of 6 silicon detectors. The ladders are arranged in three concentric barrels around the interaction point at radii of about 5, 8 and 11 cm. At an inter barrel distance of 3 cm the multiple Coulomb scattering compares to the intrinsic resolution of the detector. This was chosen

[49] P. Rehak, E. Catti "Semiconductor Memory Detectors", Scuola Normale Superiore, Pisa 1989.

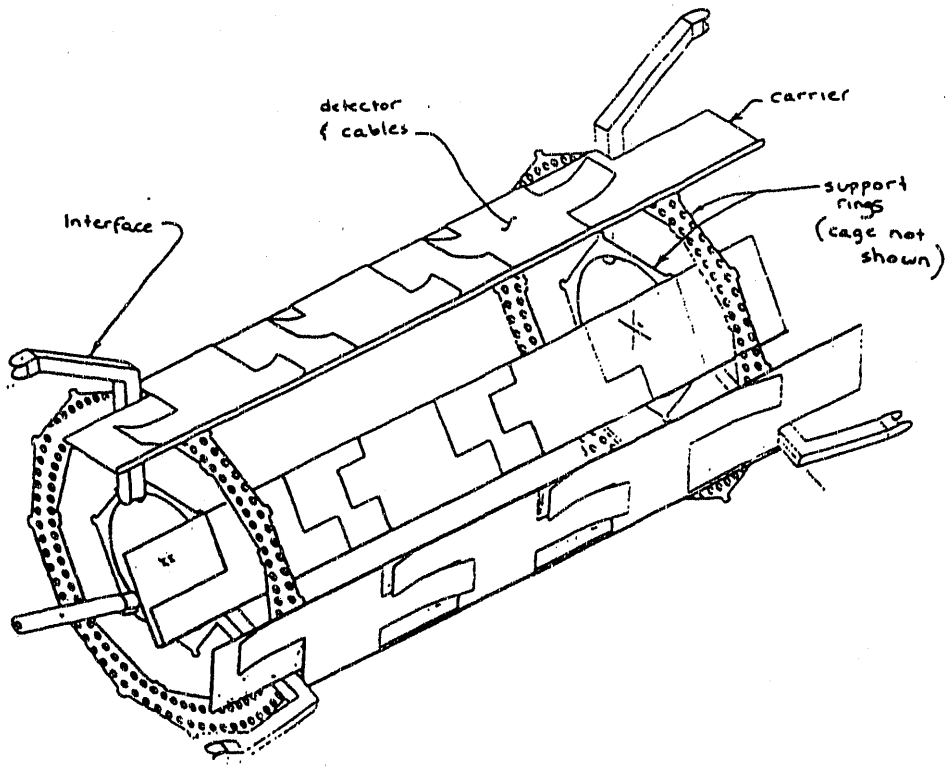

Figure 4H-3 SVT layout used in simulations.

to be close enough for efficient spacepoint matching between neighboring layers and at the same time to be far enough to construct a vector from the three resulting spacepoints. The goal of the SVT design was to accomplish the physics goals (see chapter 4.H.1.) with the simplest possible detector layout. Three layers in addition to the vertex point, are the minimum to perform a helix fit. In addition, secondary vertex reconstruction requires a complete phase space coverage close to the vertex. The addition of a fourth layer would improve the standalone tracking capabilities of the SVT, but it will not affect significantly the dE/dx (particle identification) or vertex finding capabilities. All three barrels together contain 162 detectors (4 inch diameter wafers) with around 72,000 readout channels, each having 256 time buckets in the drift direction, which accounts for 18 million pixels. The 4 inch wafer technique is pursued instead of the more common 3 inch technique to reduce the number of electronics channels. The anode pitch of 250 micron and the channel count were optimized for a good balance between resolution and performance/cost issues. Some design choices are still under consideration (see chapter 4.H.4.1.). Each barrel is about 42 cm in length to cover ± 2 units of η (the same coverage as the TPC). The design of barrels of equal length has been chosen to a) enhance the capabilities for vertex finding and track reconstruction for events with a non-zero vertex and b) to ease the construction and cost of a barrel support structure. The thickness of a wafer is 300 microns which appears to be a good compromise between signal strength (24K electrons are created by each minimum ionizing particle) and acceptable values of multiple scattering and secondary particle production for particles traversing the detector. The optimization of the drift velocity (voltage on detector) is still subject to tests. The required sampling frequency of

40 MHz is due to the attempted two-track resolution. Matching front-end electronics with a short rise time were chosen (see chapter 4.H.4.2.). A more detailed description of the support structure, cooling and cabling can be found in chapter 4.H.5. of this report.

4.H.2.2.1 Tiling the STAR SVT for Complete Geometric Coverage

The detection elements of the SVT are assumed to be silicon drift detectors (SDD) of the "STAR-2" design (see 4.H.4.1). At each end of the active region is a non-detecting (dead) row of pads for charge collection. The active area of the detector is also pi ed in along its mid line by a triangular dead region bounding each side and cont ing "guard electrodes" that reduce the local potential to zero near the cut edges of the device. The resulting active region of the detector has an "hour-glass" shape bounded by dead regions on all four edges.

The geometry of the SDD creates a problem of efficiency, in that, if the devices are simply mounted end-to-end on adjacent parallel "ladders" there will be significant dead regions at the ends and edges of each SDD, leading to a reduced coverage of about 89%. This problem can be solved by "tiling" the SDD units along the long axis of the ladder. Such longitudinal tiling is accomplished by mounting alternate SDDs on the top and bottom ladder surfaces and adjusting their positions so that the boundary of the active area of an upper detector is immediately above the equivalent boundary of the lower detector.

Similarly the problem of the triangular dead areas at the sides of the SDD is solved by using an offset lateral tiling geometry. Figure 4H-4 illustrates both the longitudinal and lateral tiling strategies. The two SDD elements on the left of the drawing are longitudinally overlapped with their active regions butted together so that the dead pad region of each detector is covered by the active region of the other.

If the laterally adjacent SDD element is offset along the longitudinal axis by half the length of an SDD (35.25 mm) then the "bulge" of one detector can be made to line up with the "waist" of a neighboring detector, as illustrated in Fig. 4H-4. However, this strategy is not sufficient in itself, because the SVT ladders are not coplanar, and the overlapping edges must not interfere. This problem can be dealt with by arranging the ladders so that each has an "overhang" on one side, as illustrated for a 6-sided SVT layer in Fig. 4H-5. Then, a particle traveling through the dead waist area of one SDD will also pass through the active bulge region of its neighbor, resulting in full azimuthal coverage by the SVT.

This tiling strategy will provide essentially 100% efficiency for the STAR SVT in its region of coverage. However it will require an even number of ladders in each SVT layer. Simulations to optimize this geometry are in progress. The "price" of full coverage is that about 11% of the particles will have to pass through twice as much silicon (600 μm instead of 300 μm) in a given SVT layer. This may result in an overall γ conversion on the order of 40 electrons per event. This yield seems acceptable for full SVT coverage. Beyond that, the necessity for an addition of small overlapping active detector areas for alignment purposes will be investigated.

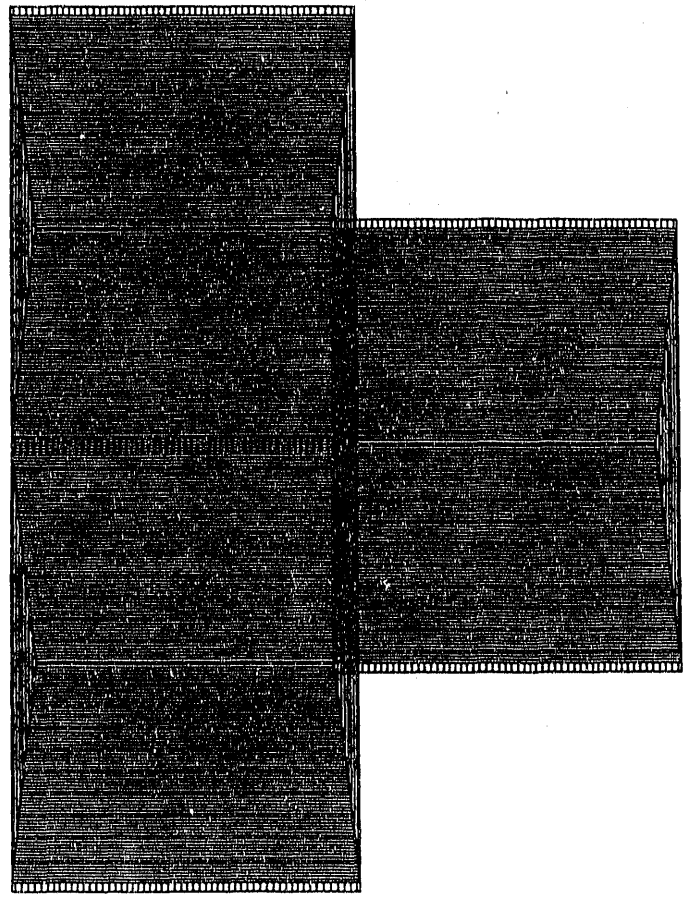

Figure 4H-4 Tiling of SDD units.

4.H.3. Capabilities of Subsystem

4.H.3.1. Detection of Primary and Secondary Vertices

4.H.3.1.1. Strangeness in STAR

The high multiplicity RHIC environment will be a challenge for every current detection technique. About half of the 8000 produced particles in a central Au+Au event are seen by the central tracking detectors at STAR which are located around mid-rapidity. Therefore, for the strange particles which are less numerous, the combinatorial background is expected to be high. Table 4H-1 shows the FRITIOF data rates for the relevant particles, and their decay characteristics.

The mean momentum of most of these particles is well below 1 GeV and therefore multiple Coulomb scattering plays an important role. At the same time, there is no significant Lorentz boost around mid-rapidity. Therefore most of the strange particles decay very close to the interaction point. This, combined with the very high track density around the main vertex results in stringent requirements on track impact parameter resolution (extrapolation accuracy). A very good vertex detector with vectoring/tracking capabilities seems to be the only possible solution to the problem.

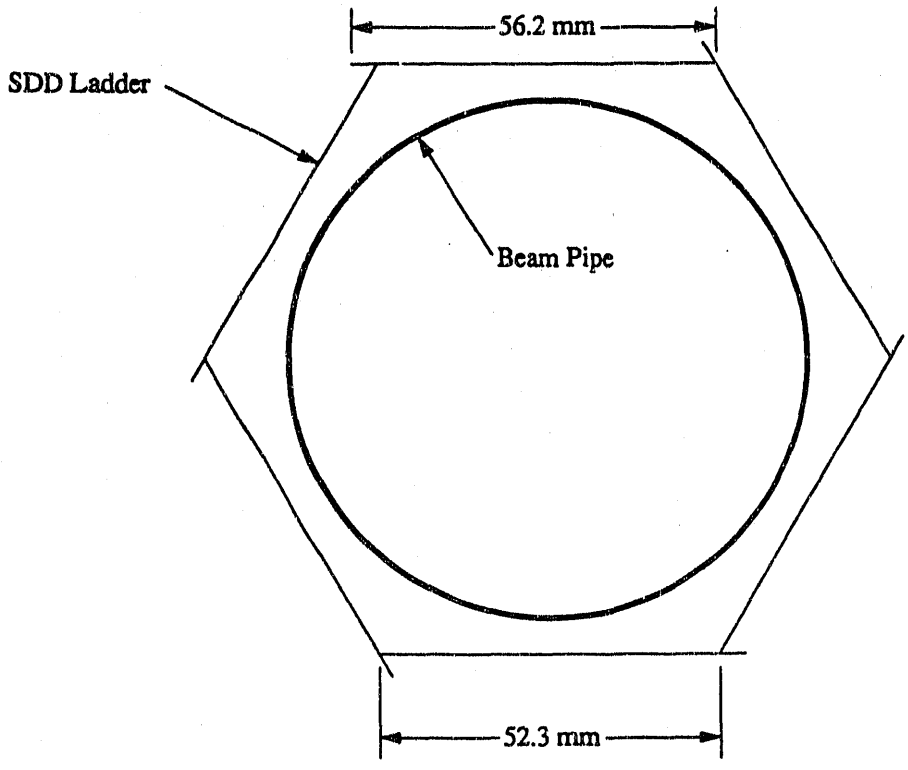

Figure 4H-5 End view of SVT layer 1 with lateral tiling.

Table 4H-1 FRITIOF (4π) predictions for the average central Au+Au event.

Particle	No. per event	Mass (GeV)	Decay mode (%)	$c\tau$ (cm)
π^+	2200	0.1396	$\mu^+\nu_\mu$ (100.)	780.4
K°_s	230	0.4977	$\pi^+\pi^-$ (68.6)	2.7
Λ	60	1.1156	$p\,\pi^-$ (64.1)	7.9
$\bar{\Lambda}$	35	1.1156	$\bar{p}\pi^+$ (64.1)	7.9
Ξ^-	3-4	1.3213	$\Lambda\,\pi^-$ (100.)	4.9
$\bar{\Xi}^-$	3	1.3213	$\bar{\Lambda}\pi^+$ (100.)	4.9
ϕ	30	1.0200	K^+K^- (50.)	0.0

The detailed simulations of such a detector, with the detection of specific physics observables in mind for a high multiplicity environment, were carried out in order to specify the parameters of the initial design of the SVT.

4.H.3.1.2. Simulation Procedure

The SVT was represented in simulations by the layout shown in Fig. 4H-6.

Individual detectors are grouped into ladders made of 500 μm beryllium. Each ladder holds a row of 6 silicon drift detectors (SDD, STAR2). The ladders are arranged in three concentric barrels around the interaction at radii of 5, 8, and 11 cm. Each barrel is about 42 cm in length. Each SDD is 7 cm in length and is made from a 4-inch diameter wafer. The thickness of a wafer is 300 μm. The beam pipe thickness was assumed to be 1 mm beryllium. Inactive area of the wafers (high voltage guard) is about 11% of the total surface of STAR2.

The FRITIOF event generator was used to create Au+Au central events at $\sqrt{S_{nn}}$ = 200 GeV. The events were then passed through the STAR detector systems using GEANT. The spatial resolution used in simulations was σ = 25μm for the SVT and σ = 500 μm for the TPC in the transverse directions and 700 μm in the drift direction. Interactions with all materials in the present STAR design were taken into account. Multiple scattering, energy loss, secondary interactions, and all other physics processes in GEANT were included.

A typical central Au+Au FRITIOF event at RHIC energies gives rise to about 2900 charged particles that leave at least 20 hits in the TPC. There are about 3000 hits in SVT layer 1 (at 5 cm), 2400 hits in layer 2 (at 8 cm) and 2000 hits in layer 3 (at 11 cm). The average hit densities are 2.3 hits/cm^2, 1.2 hits/cm^2 and 0.71 hits/cm^2 in layers 1, 2 and 3, respectively.

4.H.3.1.3. Main Vertex

Figure 4H-7 shows the precision of finding the primary vertex along the beam axis (z axis) with and without the SVT. A substantially improved resolution is obtained with the SVT. The solid line represents tracks originating from the interaction vertex, whereas the dotted one, tracks from decays of short lived particles. The precision of finding the main vertex position in the perpendicular directions (Fig. 4H-8) is significantly better than along the beam axis.

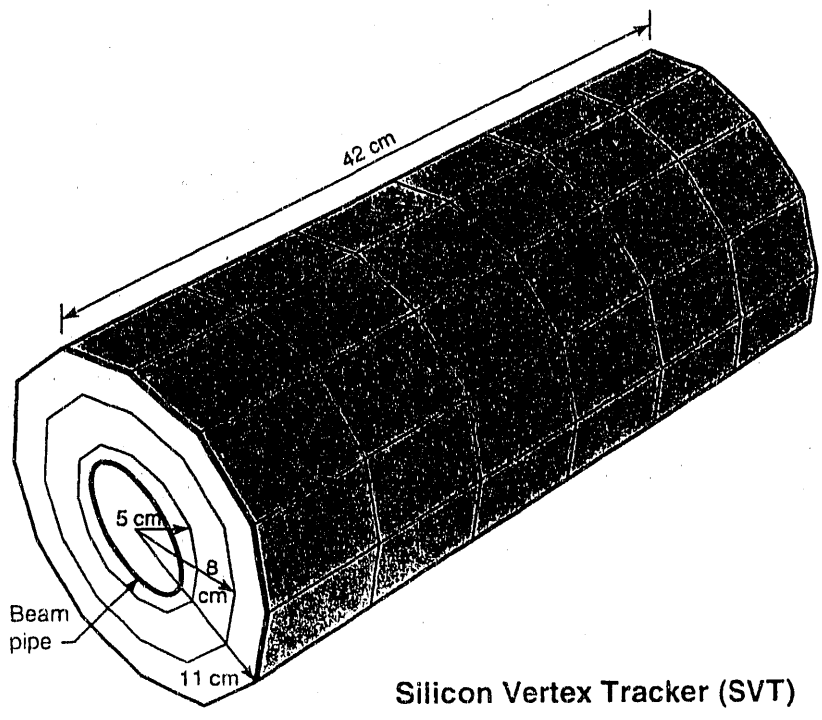

Figure 4H-6 SVT layout used in the present simulations.

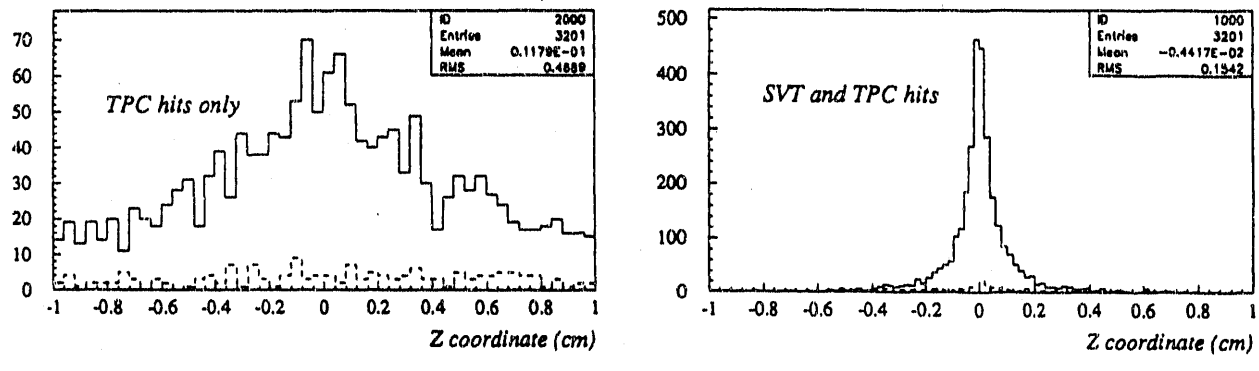

Figure 4H-7 Primary vertex resolution (along the beam direction) using: (a) TPC tracking only and (b) TPC + SVT tracking.

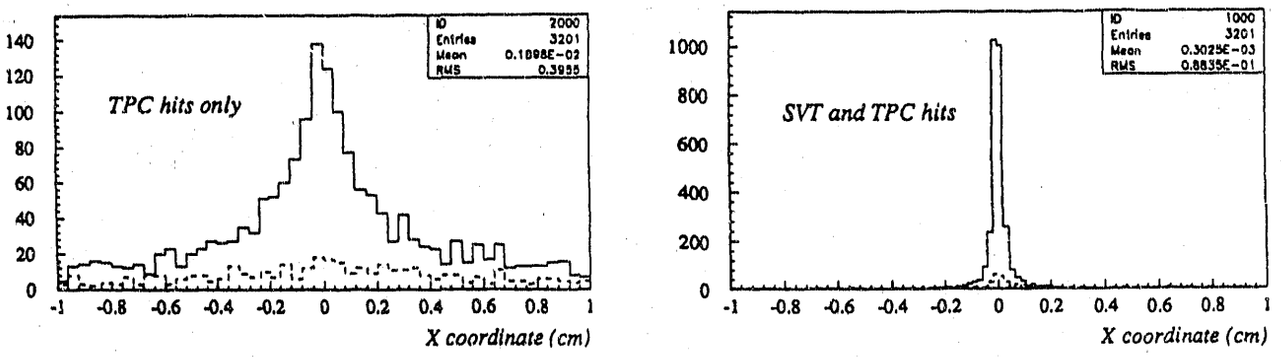

Figure 4H-8 The same as Fig. 4H-7 but in transverse direction.

4.H.3.1.4 Secondary Vertices

4.H.3.1.4.1 Singly Strange Particles: K°_{s} Λ, $\bar{\Lambda}$

The K°_{s}, Λ and $\bar{\Lambda}$ produced in FRITIOF Au+Au events were used to evaluate the efficiency of detection of neutral strange particle decays. About 25% of K°_{s} and 20% of Λ and $\bar{\Lambda}$ are within the detector acceptance. The majority of losses are due to non-charge decays. To reduce the combinatorial background due to high track density, the following cuts were applied:

- minimum track length cut r_d (= cut on distance from main vertex to the secondary one).
- impact parameter cut for parent particle r_{min}.
- for any pair of decay candidates cut on the closest approach to two trajectories (crossing between two tracks) in 3 dimensions r_c.

The following table contains cut values

cut	K°	Λ	$\bar{\Lambda}$
r_c (cm)	0.15	0.20	0.20
r_d (cm)	1.00	1.50	2.50
r_{min}.(cm)	0.15	0.20	0.15

Combining the TPC and SVT information, track parameters were refitted and an invariant mass analysis was performed. Figures 4H-9, 4H-10, and 4H-11 show the effective mass distributions for reconstructed K°_{s} (σ=4.0 MeV), Λ (σ=2.5 MeV) and $\bar{\Lambda}$ (σ=2.5 MeV) in three Au+Au events. Sharp peaks at the correct masses are obtained above a flat background.

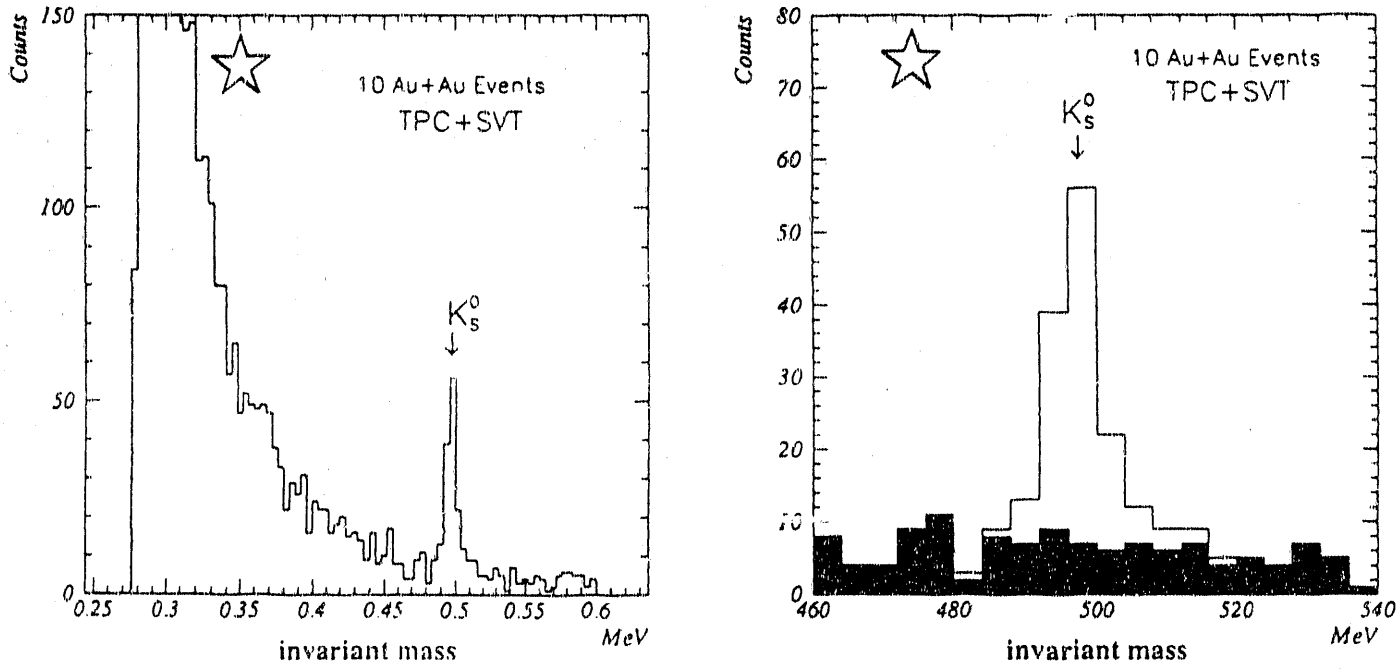

Figure 4H-9 Invariant mass distribution for K°_s reconstructed in STAR SVT/TPC system: a) full range of spectrum b) enlarged area in K°_s mass vicinity.

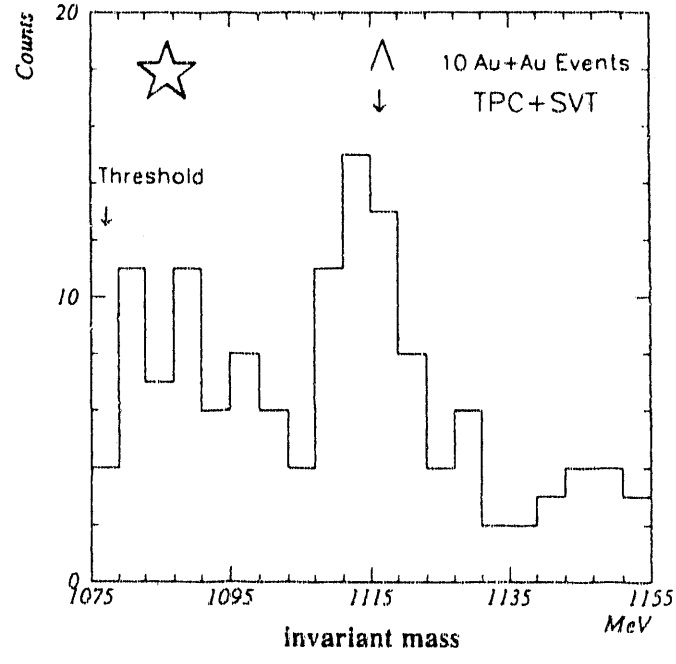

Figure 4H-10 Invariant mass distribution for Λ reconstructed in STAR SVT/TPC system.

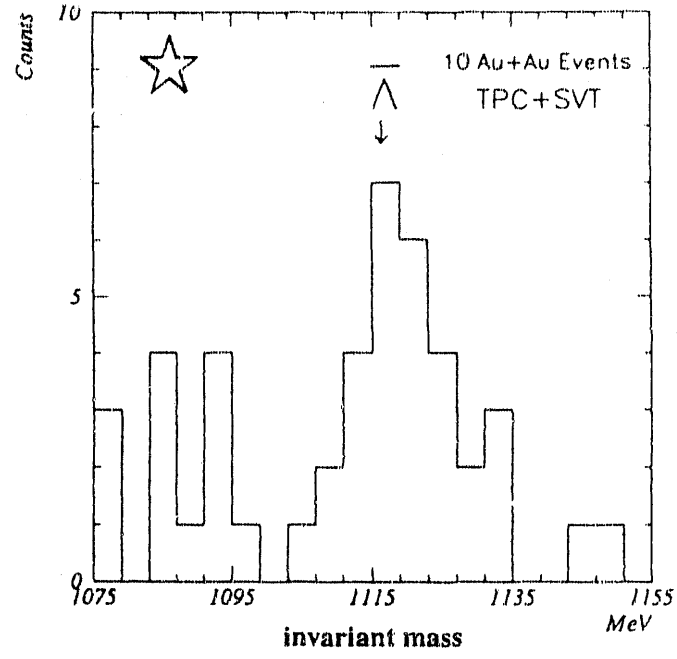

Figure 4H-11 Invariant mass distribution for $\bar{\Lambda}$ reconstructed in STAR SVT/TPC system.

4.H.3.1.4.2. Charged Hyperons : Ξ^-, Ω^-

Among the multistrange particle decays only $\Xi^- \rightarrow \pi^- + \Lambda$. and $\Omega^- \rightarrow K^- + \Lambda$ channels can be studied at STAR. The 15000 Ξ's (13000 $\bar{\Xi}$'s) and 300 Ω's (300 $\bar{\Omega}$'s) produced in 4000 FRITIOF Au+Au events were analyzed. They were passed through GEANT with an assumed TPC space point resolution of 200 μm. Note that the Ξ and Ω decays have the same topology. As a consequence of the very short lifetime (down to 10^{-13} s), the track length of the decaying particle is small and its momentum cannot be determined.To optimize the signal to background ratio, a number of cuts were imposed (analogous to those for K°_{s}, Λ, and $\bar{\Lambda}$). Tracks which miss the main vertex by less than 2 cm for Ξ 's and 1 cm for Ω's were excluded, a reconstructed hyperon was required to point back to the main vertex within 1.5 mm, and the distance of closest approach of the decay products at the decay vertices should not exceed 5 mm. Overall about 15% of multistrange baryons which were within the STAR acceptance were reconstructed (which corresponds to ~5 % of all Ξ's, $\bar{\Xi}$'s, Ω's, $\bar{\Omega}$'s produced in full phase space). The bulk of the losses (~ 85%) are due to the limited acceptance of STAR and, to the branching ratios(67% for $\Omega^- \rightarrow K^- + \Lambda$ and 64% for $\Lambda \rightarrow p + \pi^-$). Figure 4H-12 shows the invariant mass of Ξ (TPC+ SVT) for a TPC momentum resolution of $dp/p = 1\%$ taken into account. A sharp peak at the correct mass is obtained above a flat background. Similar results were obtained for $\bar{\Xi}$'s, Ω's and $\bar{\Omega}$'s. A more detailed description of the performed analysis can be found in [50]. A space point resolution of the TPC of 500 μm (x,y) and 700 μm (in z), which corresponds to the most recent simulations, will slightly increase the combinatorial background.

[50] G. Odyniec et al, LBL preprint - LBL-31773

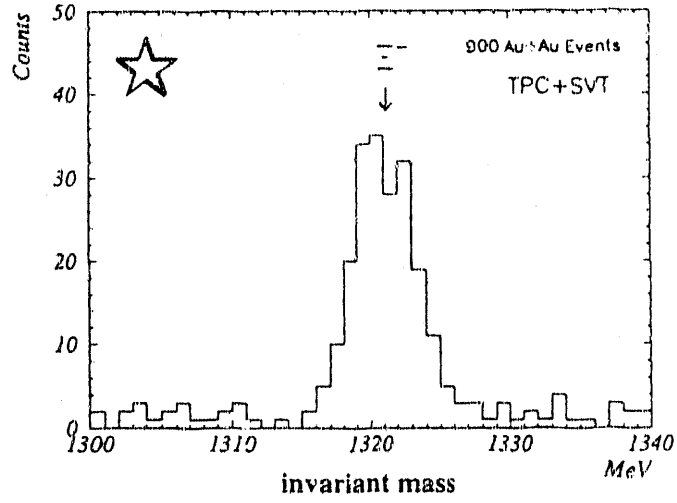

Figure 4H-12 Invariant mass distribution of Ξ (TPC+SVT) with TPC momentum resolution taken into account. Shaded areas represent the contribution from random background.

4H.3.1.4.3. Matching SVT hits with TPC tracks

The results of the previous sections were based on the assumption that a perfect assignment of SVT hits with tracks identified in the TPC was possible. An algorithm to examine how well this assignment can be performed was developed and tested with Au+Au events, generated by FRITIOF, and processed with GEANT, assuming 200 μm TPC space point resolution. A track was required to have at least 20 hits in the TPC, to ensure good tracking information, and three SVT hits. A helix was fitted to the TPC points and its parameters were used to calculate the expected hit position in SVT layer 3. The expected multiple scattering of the track was calculated and used to define a 3 σ 'search' area. The deviation between the expected position and the actual position is well described by a multiple scattering calculation and the chosen 3 σ area contains the correct hit over 98 % of the time. In 30% of the tracks there is only one hit in the search area. All candidates in layer 3 were tested by adding them (one at a time) to the TPC points and re-doing the helical fit. Using the improved helix parameters, extrapolation to layer 2 was made, and subsequently to SVT layer 1. After this procedure, sets of three candidate points for each track were found. For cases with more than one helix the one with the lowest χ^2 was chosen. The helix is defined as being 'correct' when all three SVT points and the TPC points come from the same GEANT track. A measure of how well matching is done is expressed by the ratio of 'correct' helices to the number of track finding attempts . This efficiency as a function of p_T is plotted in Fig. 4H-13. The overall average efficiency, for a p_t above 100 MeV/c, is 91%. For a p_t above 200 MeV/c, the matching efficiency is over 97%.

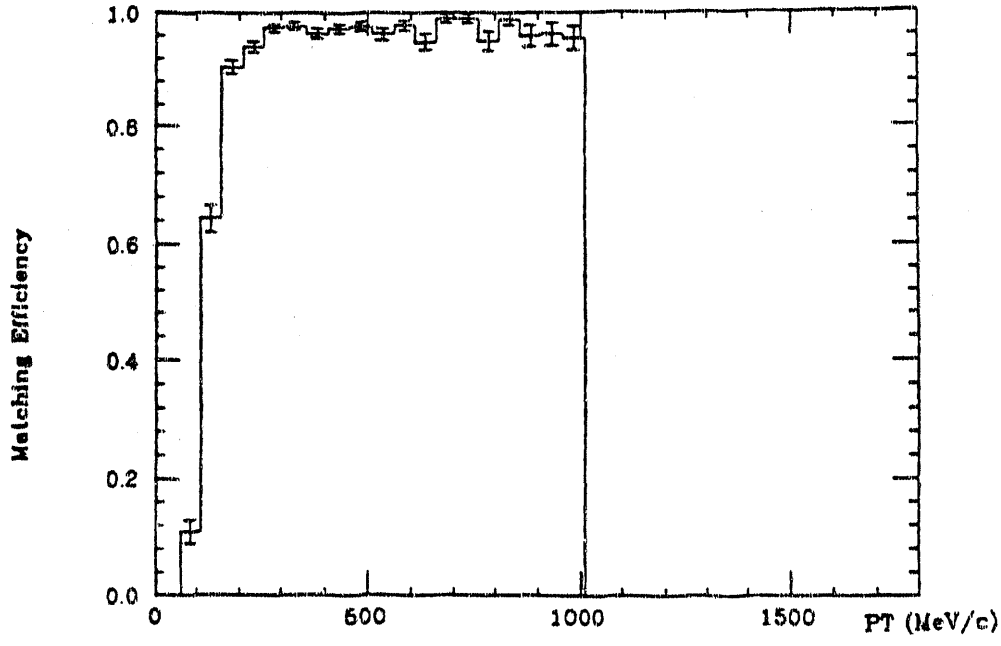

Figure 4H-13 Matching efficiency as a function of pT.

For tracks with lower pt there are serious problems with multiple scattering. There are two obvious software improvements to make. The first is the use of KALMAN filter techniques.[51] The second is to assign the tracks to a vertex and use this as a constraint. Regardless of software optimizations FRITIOF predicts a significant number of tracks at low enough p_t such that, due to interactions or scattering in the TPC walls, their track parameters are altered before they are measured in the TPC. For those tracks, the SVT acts as an independent tracker (with efficiency close to 90%, see chapter 4.H.3.2.) and consequently enlarges the STAR acceptance significantly.

4.H.3.2. Reconstruction of Low p_t Tracks with the SVT

4.H.3.2.1. Introduction

A first round of detailed simulations has been performed with a standalone tracking program for the Silicon Vertex Tracker. The geometry of the STAR2 detector (see 4.H.4.1.) was implemented in GEANT and used to simulate the response of the SVT for central Au+Au FRITIOF events. At this point the algorithm assumes that the efficiency of matching a TPC track with a spacepoint on the outermost layer of the SVT is 100% down to a well defined momentum (input parameter). First estimates of the efficiency of track reconstruction above 200 MeV/c with SVT and TPC resulted in 97% tracking efficiency (see [52]). Consequently SVT hits from higher momentum tracks are removed, because they belong to tracks which were successfully reconstructed by the

[51] R. Fruehwirth, 'Application of filter methods to the reconstruction of tracks and vertices in events of experimental high energy physics', HEPHY-PVB 516/88, Vienna, Dec.88.
[52] Updated Letter of Intent, STAR-collaboration 1991

SVT+TPC system. By applying this p_t cutoff, the fraction of non reconstructed hits in the SVT decreases by a dramatic factor. For example removing tracks with momenta greater than 200 MeV/c reduces the number of tracks by a factor 6. One is then left with a relatively small number of tracks in the SVT (around 7 hits per wafer on the outer barrel, 15 per wafer on the inner barrel, whereas one wafer consists of around 100,000 pixels). For the track reconstruction in the SVT layers a position resolution of 150 μm in x and z is assumed. This number is a conservative estimate of the SVT capabilities. A position resolution of better than 25 μm was reported. To define a helix one needs at least three points. So every track would have no free parameter if one takes only the three SVT layers into account. But besides the high momentum track reconstruction the TPC tracking also provides a rough vertex point with a 2mm position resolution. This vertex is incorporated into the SVT pattern recognition as a fourth point for each track. Based on this algorithm the present simulation can only reconstruct particles originating from the main vertex. Particles from secondary vertices require a fourth layer in the SVT.

4H.3.2.2. Results

Preliminary results show an 89 % tracking efficiency for particles between 40 - 200 MeV/c. An increase of the p_t cutoff for perfect track reconstruction by the TPC from 200 MeV/c to 300 MeV/c decreases the efficiency in the SVT algorithm only by 10 % although the occupancy doubles. Figure 4H-14 shows the reconstruction efficiency as a function of the p_t cutoff. For a given TPC cutoff the SVT tracking efficiency is almost constant over the p_t range covered by the SVT alone. The momentum resolution for the reconstructed tracks is, in the low p_t part, dominated by multiple scattering. At higher p_t (p_t > 200 MeV/c) the resolution depends only on the position resolution in the silicon detector. Figure 4H-15 shows the momentum dependence of the transverse momentum resolution based on tracks only identified by the SVT. The results show that the SVT is capable of reconstructing low p_t tracks with good momentum resolution in a 'standalone' mode if the data sample was successfully preprocessed by the TPC track algorithm.

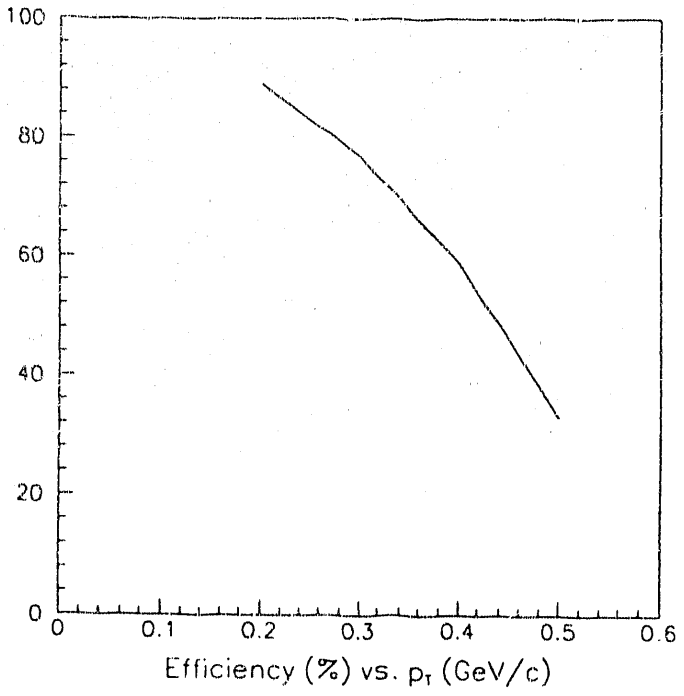

Figure 4H-14 Reconstruction efficiency in SVT as a function of the p_t-cutoff for successful track reconstruction in the TPC.

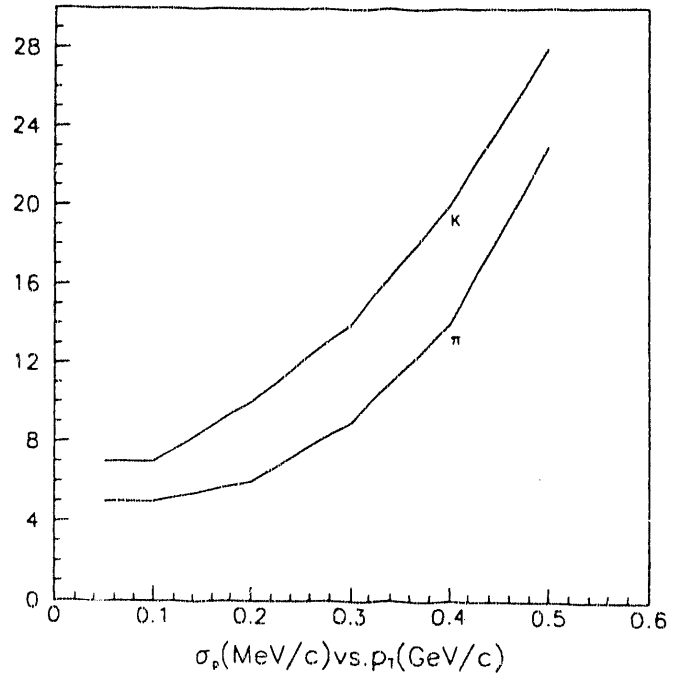

Figure 4H-15 Transverse momentum resolution for π and K in SVT alone.

Another topic that was investigated with the track algorithm in the SVT is the reconstruction of 'straight' tracks only. In general this algorithm works on defining a cone to match from one spacepoint in layer A to a spacepoint in layer B. The opening of the cone is proportional to the bending of the particle with the lowest possible momentum (p_T = 40 MeV/c). For the case of straight tracks this parameter was decreased considerably to allow only for high momentum particle reconstruction. In a window between p_t = 400-500 MeV/c the SVT alone reconstructs 98 % of the tracks, which should enable a software alignment of the SVT and TPC by vector to vector matching between the two detectors (see alignment requirements in chapter 4.H.5.5.)

4H.3.2.3 Outlook and Improvements

Certain improvements to this first approach to tracking in the SVT can be made:

a) 4 spacepoints are required per track. Thus tracks which hit the dead area in one of the barrels are excluded although they have a non zero tracking efficiency. A switch to the tiled STAR2 design, with no dead area will solve this problem.

b) The fourth point is the vertex obtained from the TPC, which causes a position resolution of an estimated 2 mm in the fourth point. This is pessimistic, based on the fact that the vertex can also be defined by the tracks in the SVT even before the start of the pattern recognition. An improvement to a vertex resolution of 150 μm can be achieved. We are in the process of investigating this further.

c) As mentioned above the measured spacepoint resolution in the SVT is actually known to be better than 25 μm instead of the conservative assessment of 150 μm.

d) The efficiency will be increased by enhancing the number of track finding loops in the original program with simultaneous application of more realistic elimination processes for 'ghost' tracks. This process is relevant for tracks which 'share' a spacepoint in one of the layers because of merging. Right now each spacepoint only contributes to one track.

The open question at present is how reliably the TPC can reconstruct tracks down to a certain p_t in central Au+Au collisions. Assuming a high threshold of 400-500 MeV/c for the standalone SVT program, most of the improvement originates from the inclusion of tracks that do not have 4 points in the SVT. All the tracks above 100 MeV/c will also have some tracklength in the inner layers of the TPC. The corresponding points can be used efficiently even in the case of high occupancy in the TPC layers.

A Kalman filter method[53] can only be applied for SVT tracks if at least 10 TPC points are included in the tracking recognition with the 4 spacepoints from the SVT + vertex. This emphasizes the concept of a combined tracking algorithm for at least part of the p_t spectrum. Work on a matching program between the SVT and the TPC is in progress.

[53] R.K. Bock et al, 'Data analysis techniques for high energy physics experiments, Cambridge, University Press, 1990

4.H.3.3. Two-track Resolution

In the high particle density environment of RHIC, the ability of an SDD to resolve close hits in space is crucial for good track reconstruction efficiency. This is particularly important for two particle interferometry studies[54] where interference effects are most sensitive to close hits. We performed a series of measurements to determine the two-hit resolution of SDD (we used STAR0 detector with an active area of 1×1.8 cm^2) and compared measurements with theoretical predictions.[55] These are the first measurements on SDD two-track resolution (results are submitted for publication to NIM).

The procedure we have adopted for two-hit measurements is the following: Two particle hits are simulated using a 8 ns pulse of 1064 nm light from Nd:Yag laser split into two pulses using light fibers. These fibers illuminated a microscope objective which was used to focus the light pulses to 20 μm spots on the SDD. The separation between the fibers at the microscope was adjustable using a precision set screw. The anode signal was amplified, shaped (σ=27ns) and fed into a 50Mhz digitizer. The digitized signal was then stored into a computer and analyzed offline. The off-line analysis consisted of fitting a two-gaussian function to the two-hit anode signals and comparing the fitted positions of the peaks with the known positions of the light fibers having been set with the precision set screw above. A typical two-hit spectra is shown in Figure 4H-16 for a hit spacing of 500 micron with the drift field of 284 volts/cm.

A relatively low electric field has been chosen to have a drift time (and amount of diffusion) close to that expected for the STAR1 detector (see 4.H.4.1). Critical in this analysis is the assumption that the width of a single pulse is well understood. This is illustrated in Figure 4H-17 where the measured σ^2 distribution is plotted as a function of applied potential (E^3). The solid line which represents a calculation of the expected dependence (using as inputs only the measured mobility and shaping time) describes the measurements very well. Comparable agreement is observed when studying the s dependence with distance from the anode pad.

---

[54] T.J. Humanic et al. "Pion Interferometry with Ultrarelativistic heavy-ion collisions from the NA35 experiment," Z. Phys C38,79(1988).
[55] E. Gatti et al. "Double particle resolution in semiconductor drift detectors", NIM A274,469 (1989).

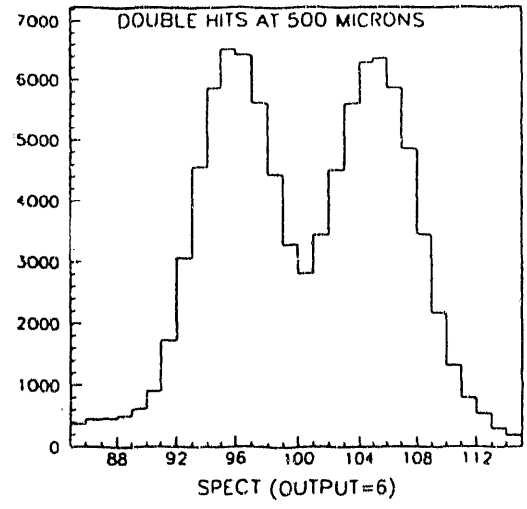

Figure 4H-16 Typical two-hit spectra.

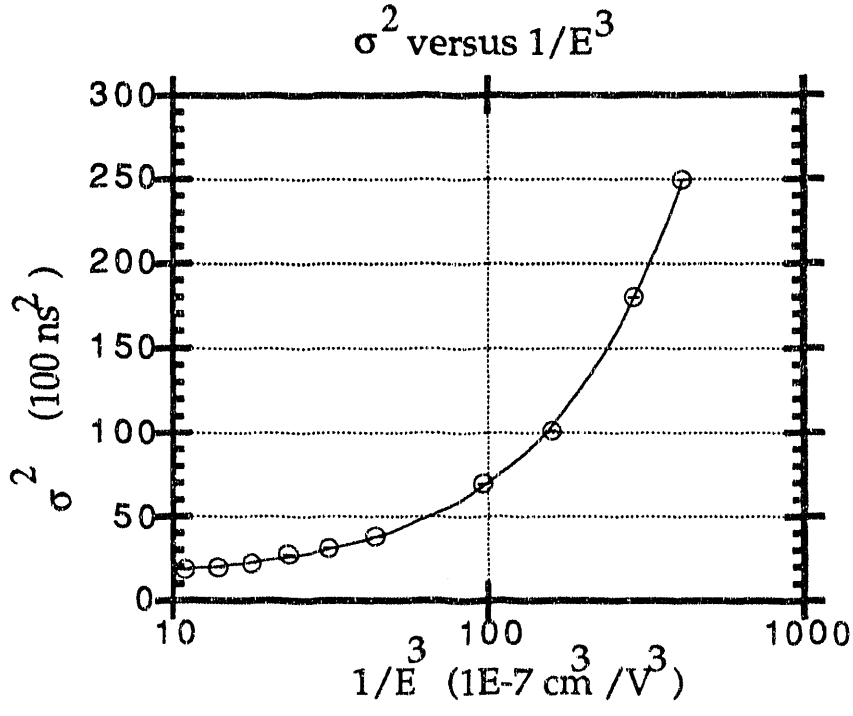

Figure 4H-17 Measured σ^2 distribution.

The variable of importance in two-hit measurements is the hit spacing error relative to the hit width sigma.[56] Shown in Figure 4H-18 is the relative two-track error, the hit spacing error divided by the hit width sigma, as a function of the two-hit spacing. Several measurements were made at both high and low drift fields and from one to four times the minimum ionizing intensity. The solid line is the predicted error.[57] At 500 μm separation the measured separation error is 25 μm, approximately the same as predicted.

4.H.3.4. Energy Loss Measurements with the STAR SVT

It has been investigated both by simulation and by experiment whether energy loss measurements with the SVT can provide particle identification in the STAR detector. The relativistic rise phenomenon is suppressed by coherence effects in crystalline solids like silicon, therefore only the $1/\beta^2$ region is considered.

Monte Carlo calculations were performed to prove that a dE/dx measurement with good resolution can be obtained with a few samplings only. A piece wise-continuous analytic representation of the energy loss distribution function expected for 300 MeV/c pions passing at normal incidence through a 300 μm slab of silicon was used. The approximate function consists of two Gaussian and two exponential functions and agrees well with measured[58,59] and calculated[60,61] distributions. The piece wise function is shown in Fig. 4H-19, as plotted on logarithmic vertical scale with a horizontal scale chosen to give a most probable energy loss ε_o=1.00. We have used this basic distribution function to provide random energy loss samples ε_i.

These Monte Carlo tools were used to simulate the measurement and analysis of energy loss information from n layers of a silicon vertex detector, where n = 1 to 4. In combining the measured energy loss samples ε_i to extract the most probable energy loss ε_o we have compared various analysis strategies:

(i) a straight arithmetic average of n samples

(ii) the minimum value of n samples

(iii) a truncated mean in which only the lowest m of n samples are averaged

(iv) the most probable energy loss obtained from maximum likelihood analysis of n samples.

---

[56] M. Clemen et al. "Double particle resolution measured in a silicon drift chamber", to be published in NIM 1992.
[57] E. Gatti et al. "Double particle resolution in semiconductor drift detectors", NIM A274,469 (1989).
[58] J. Schukraft,CERN, Geneva, Switzerland (1992), private communication.
[59] J.F. Bak et al., Nucl. Phys. B288(1987)681 and CERN-EP/87-62.
[60] J.F. Bak et al., Nucl. Phys. B288(1987)681 and CERN-EP/87-62.
[61] Hans Bichsel, Reviews of Modern Physics 60 , 663 (1988).

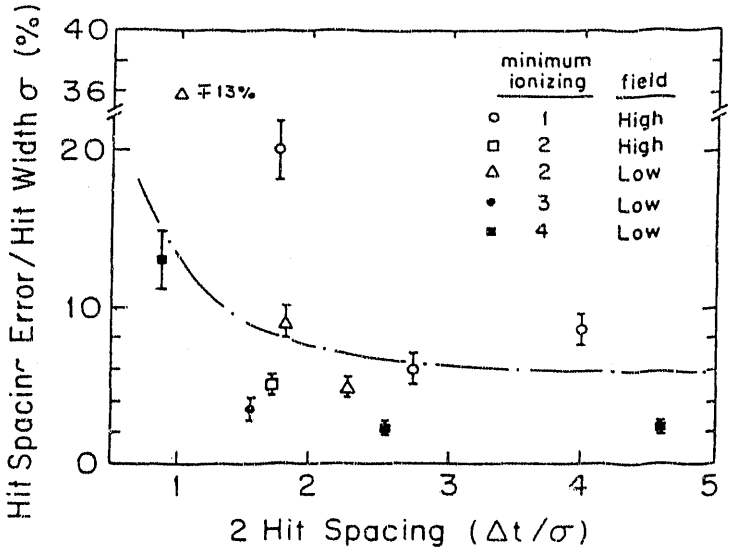

Figure 4H-18. Relative two track error.

Figure 4H-20a shows the distribution of 10^5 energy loss samples in a single layer of silicon, as shown on a logarithmic vertical scale and a horizontal scale chosen so that the most probable energy loss $\varepsilon_0 = 200$. In this histogram the Landau tail is quite apparent. Figs. 4H-20b–d show, for a three layer detector, the estimated most probable energy loss obtained from procedures (i), (iii), and (iv), where in (iii) the lowest two of three samples are averaged. In all figures the smooth curves through the histograms

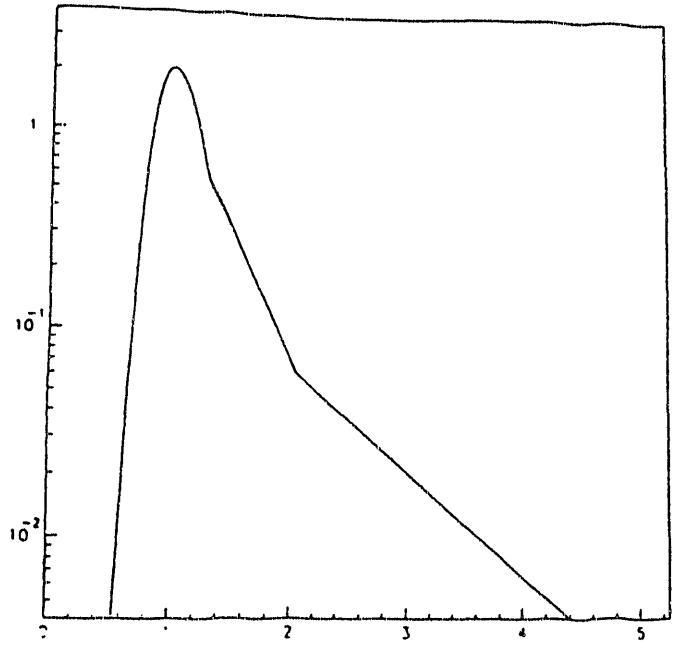

Figure 4H-19 A piece wise-continuous representation of the energy loss distribution function used in Monte Carlo calculations.

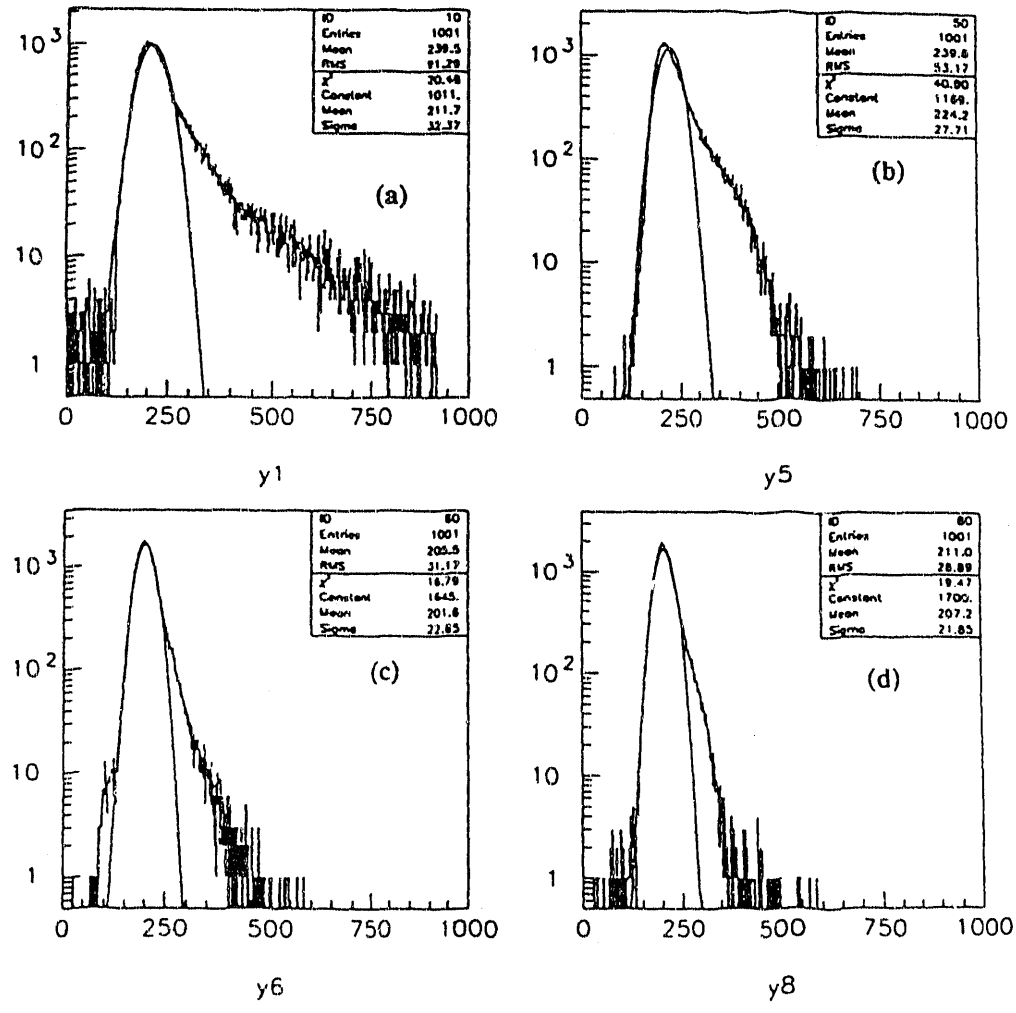

Figure 4H-20 Energy-loss distribution in single (a) and three layer (b-d) detector.

represent 3-parameter Gaussian fits, the parameters of which are given in the lower boxes of the figures. As is apparent in Figs. 4H-20c, averaging the lowest two of n values provide narrow peaks corresponding to good estimates $< \varepsilon_0 >$, as do the maximum likelihood analyses shown in Figs. 4H.3.5-2d. These simulations show that a dE/dx resolution of 15% seems to be possible for particles from the $1/\beta^2$–region. As a rule of thumb, each particle type (except muons) can be distinguished from all others provided its momentum p is such that $pc < m_0 c^2$.

The outcome of the above Monte Carlo simulation was verified by a measurement of the energy loss in a single SDD (STAR0 with thickness of 300 μm) of 300 MeV/c pions at the TRIUMF accelerator in Vancouver, Canada. The detector had 15 pads instrumented. Data were acquired with the detector operating at two different drift fields, 284 and 500 Volts/cm. This allows a study of dE/dx resolution at different drift velocities. The measured signal to noise ratio was found to be 55 to 1. The signal to noise ratio is defined to be the maximal pulse amplitude on one pad to the rms of the pedestal on this pad. The energy scale was calibrated using the 60 keV gamma rays from an ^{241}Am source. The energy calibration is accurate to approximately 10%.

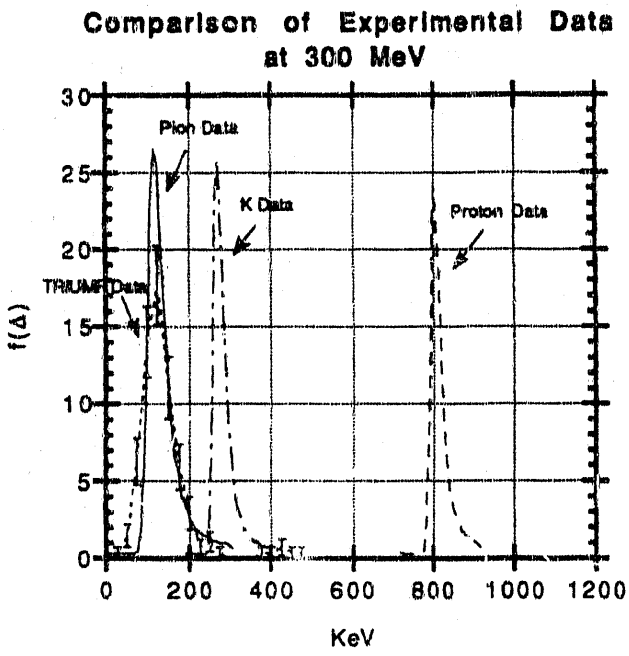

Figure 4H-21 dE/dx distribution for various particles.

Figure 4H-21 shows the measured dE/dx distribution obtained with STAR0. The solid line represents results from earlier measurements at 2 GeV/c [62] which have been properly scaled according to the model in Ref. 62. Qualitative agreement is seen. It is also essential to compare the measured dE/dx distribution of 300 MeV/c pions with the expected distributions for 300 MeV/c kaons and protons (also from Ref. 62). Figure 4H-21 clearly illustrates that the dE/dx resolution achieved by the SVT will be sufficient for particle identification in the $1/\beta^2$ range.

4.H.4. R&D Issues and Technology Choices

4.H.4.1. STAR1 vs. STAR2

Parallel field silicon drift detectors with an active area of about 1 cm^2 have already been successfully built and tested.[63,64] STAR1 is the first attempt to build a detector with the largest active area compatible with a 3-inch wafer (14 cm^2). Figure 4H-22-1 shows a schematic view of the STAR1 SDD with high voltage cathode on one side and collecting segmented anode on the other. The drift distance is about 4 cm.

Immediately after completion of STAR1 production and the first order tests (June/July 1992), the design and fabrication of STAR2 detectors will be initiated. The solution chosen for STAR2 was to split the sensitive area of each detector into two drift regions so that electrons drift in opposite directions in the two halves (Fig. 4H-22-2). In this way the maximum drift length and the required drift field are reduced by a factor

---

62 J.F. Bak et al., Nucl. Phys. B288(1987)681 and CERN-EP/87-62.
63 E. Gatti and P. Rehak, NIM A225(1984)608.
64 P. Rehak et al., NIM A248(1986)367.

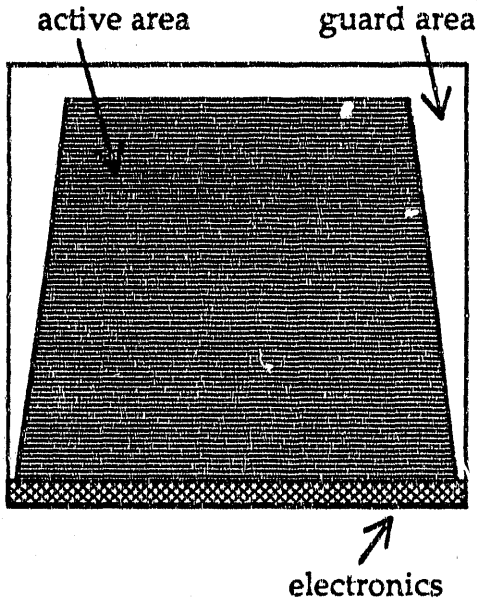

Figure 4H-22-1 Schematic view of STAR1.

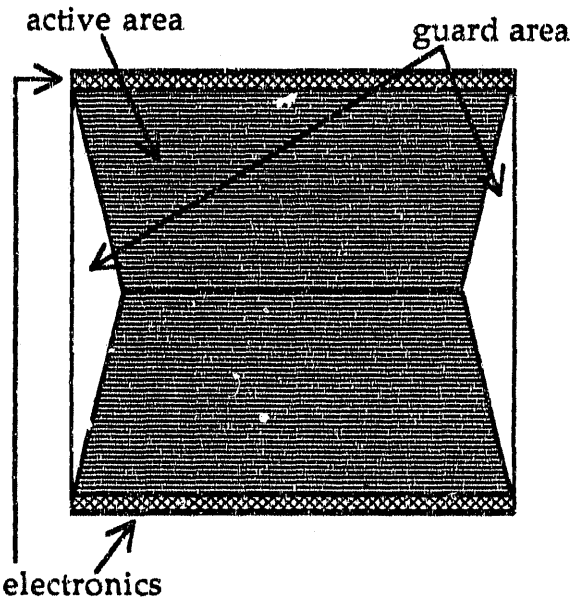

Figure 4H-22-2 Schematic view of STAR2.

of two. Fig 4H-22-2. shows a schematic view of the STAR2 SDD detector. A 4-inch version of STAR2 is used in the present version of the baseline. A similar detector was designed and successfully built to use in the experiment UA6 at the CERN p-p collider.[65]

The advantages of each design are listed below:

STAR1	STAR2
Less electronics needed to connect channels to SCA's (~1/2).	Smaller memory time of the detector. Maximum drift time ~1/2 of STAR1. Smaller dead areas - at 3 + 4" diameter STAR1 is 69% active, whereas STAR2 is 88% active (31% dead area vs. 12%). Shorter drift distance requires less voltage Maximum voltage = 2450V = 1/2 of STAR1

[65] A. Vacchi et al., NIM A 306(1991)187.

Power dissipated at the wafer is about the same for both solutions. The decrease of the power dissipation in the divider for the STAR2 is compensated for by an increase of the power in the front end electronics.

The requirements on the SCA are also similar. STAR2 requires twice as many channels however, each channel has only 1/2 of the capacitors as a channel in STAR1.

The decision on detector geometry for SVT at STAR will be made after completion of the final tests of the STAR2 detector (End of 1992). Assuming that there are no major drawbacks in the geometry of either of the designs, cost may be the deciding factor. For the costing in the CDR we have used the STAR2 design.

4.H.4.2. SDD Front End Electronics

A decision must be made as to the location of the first amplification stage for the SDD electronics. From a standpoint of signal-to-noise performance the optimum circumstance holds for a system where the preamplifier is brought as close as possible to the charge source (in this case an anode pad on the SDD).This reduces channel capacitance to a minimum and thereby maximizes the voltage signal compared to irreducible white noise sources. A proposal currently under consideration is to integrate Darlington transistor pairs (DP) into the lithography of the SDD in close proximity to the anode pads, thereby achieving an extremely small channel capacitance dominated by the anode pad size itself. The first stage of the SDD amplifier is part of the detector and is a two stage Darlington, the first gate of which is the anode. This leads to a predicted signal to noise ratio of at least 500 and produces signals of a few millivolts amplitude that are about 30 ns wide after differentiation. The transistors of the Darlington follower are p-channel junction field effect transistors (JFETs) with one gate only. The first p-channel FET operates with the gate forward biased relative to the source. The forward bias is exactly such that the average detector leakage current continues to flow from the anode and gate to the source. No high value resistor or switch to take away the leakage current is needed. The size (width) of the first transistor was determined to have the gate to source capacitance close to the anode capacitance. This matched condition gives the best possible noise performance for the given anode capacitance and the given transistor technology. The equivalent noise charge (ENC) of about 100 electrons is expected for the detector with a leakage current of several nA and for a shaping pulse which peaks at about 100 ns.

While successful inclusion of Darlington pairs would enhance the signal integrity it does so at some cost. First, the yield for SDD production might decrease by implanting the DP directly on the detector. An alternative would be to mount the DP's 'off-board' an a separate silicon segment. Tests to determine the signal degradation due to the additional wire bonding are planned. Secondly, the Darlington pairs, along the pad row edge of the SDD, become the largest heat source on the SDD (290 mW) on STAR1, exceeding that of the potential grading resistor strings on each side of the STAR1 SDD (4 x 50 mW). The flow of this heat to sinks establishes a temperature profile across the SDD which may vary in time. Stability of the temperature profile is of great importance for the determination of the drift speed in silicon, and hence to correct

inference of z position of a hit in the SDD. Ideally one would like not only to have a stable profile but to have it as uniform as possible to minimize the extent of systematic corrections to inferred hit positions. Overall the DP amplifier produces 1.3 mW of heat and with the other sources of heat, i.e. the HV divider and nearby shaper amplifier leads to a need for water cooling in order to keep the temperature rise to less than 0.1°C. The cooling system is discussed elsewhere (see chapter 4.H.5.6.). The Darlington amplifier in high resistivity Si is rather poor having an output impedance of 2K. Therefore, either an additional transistor stage to drive the signal cable or the preamplifier itself must be very close so that the connection can be made by wire bonds. However to minimize the mass on the detector, a design with a preamp/shaper board mounted to the field cage is preferred.The shaper amplifier differentiates the charge and has four pole zero filters, which leads to integration of the high frequency components with a pseudo gaussian output peaking time of 40 ns. The amplifier has a voltage gain of 10 and is expected to dissipate less than 2 mW per channel. It is designed in bipolar and should be ready for first prototyping in July. After amplification the signal can be driven to the SCA board which will be located on the inner field cage (see 4.H.5.5.). This board connects to the readout board described in 4.F.5.2. which contains the T9000 transputer as well as the ASIC chip. Six frontend boards are multiplexed at this point into one readout board. From there the zero suppressed data will be processed by fiber connections.

The SDD prototype with DP incorporated into the wafer is presently undergoing fabrication at BNL by the SVT group. Completion is scheduled for mid-June. First order tests will be finished by mid-July. Necessary measurements to finally decide on integrating DP's into the SDD wafer for further development are planned for summer 92 by testing SDD channels with DP, with DP on separate pad and without DP. The decision on the optimum configuration will be made not later than September 92.

4.H.5. Engineering

4.H.5. Brief Technical Description and Specifications

The basic cylindrical configuration of the SVT is shown on Figure 4H-23. There are 6 detectors per face arranged in a tiled fashion in z. Coverage in the z direction is ±211 mm with the assumed active length of 70.5 mm per detector. The detectors and cables will be assembled into a module which facilitates testing and replacement. Figure 4H-24 shows a STAR2 module. The same configuration would be used for the STAR1 detector modules except the cable will exit from only one end. For the baseline configuration, six of these modules will be placed on a carrier which is then mounted onto the main support framework of the SVT. Figure 4H-25 shows the tiling of the detectors in z and the design of the carrier. Material is removed from the carrier where possible to reduce the average radiation length of the assembly. During each stage of assembly, testing of the completed components will occur prior to the next step. After all the detectors have been tested on the carrier, it is placed on the end plates. The end plates are connected together by interface/support beams. This is shown by Figure 4H-26. These interface/support beams are connected to a support tube which is joined to

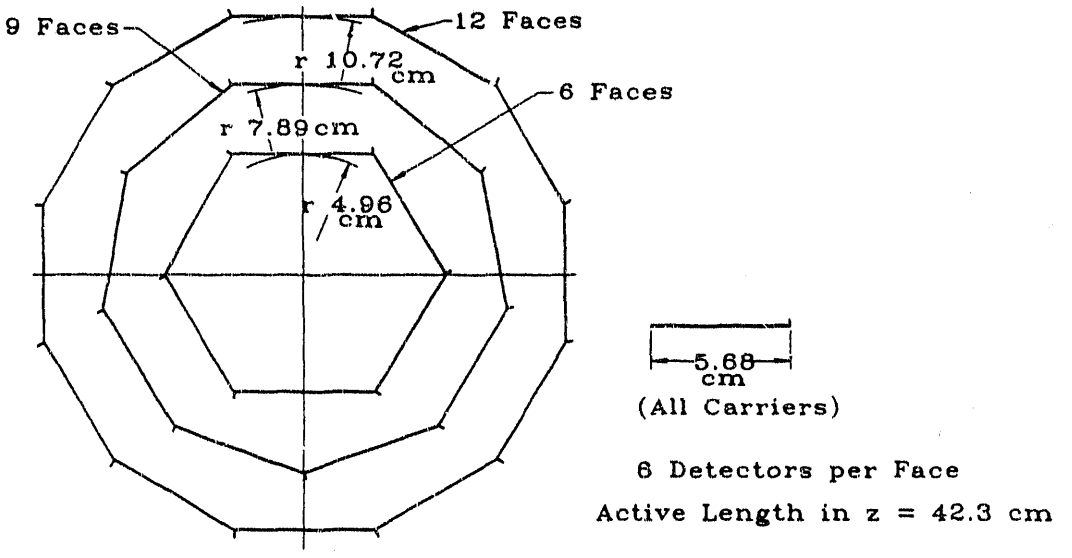

Figure 4H-23 An end view of the SVT with radii indicated.

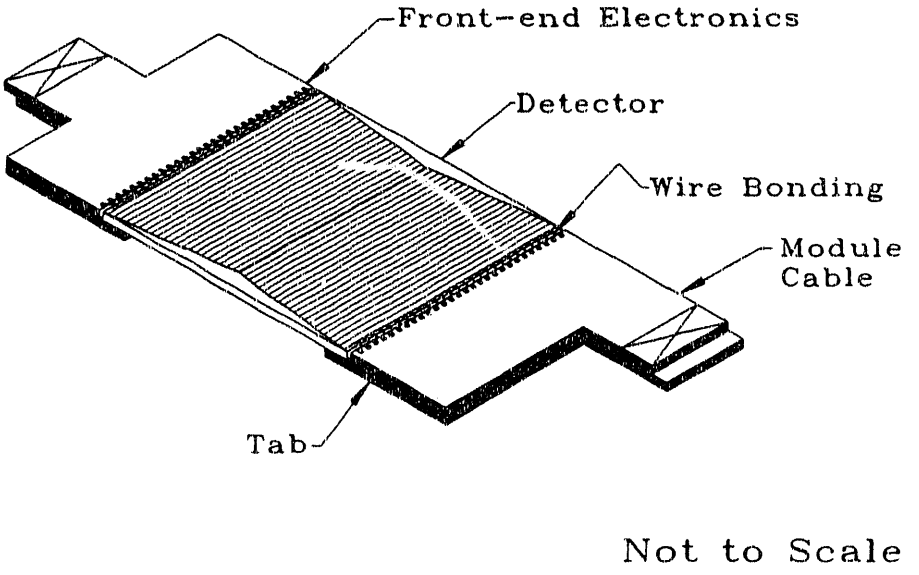

Figure 4H-24 View of typical module with STAR2 detector.

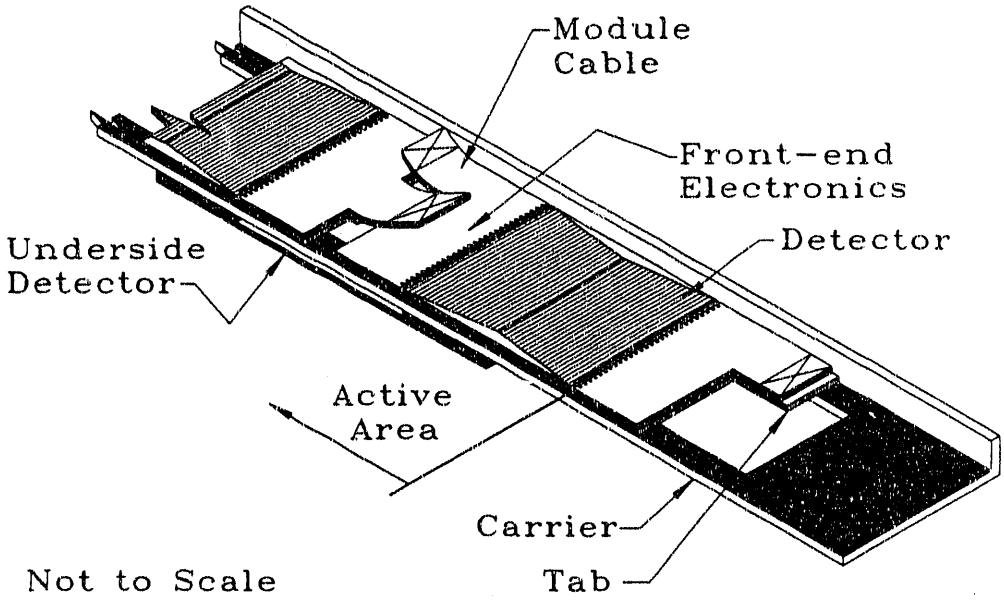

Figure 4H-25 Overview of modules mounted onto a carrier.

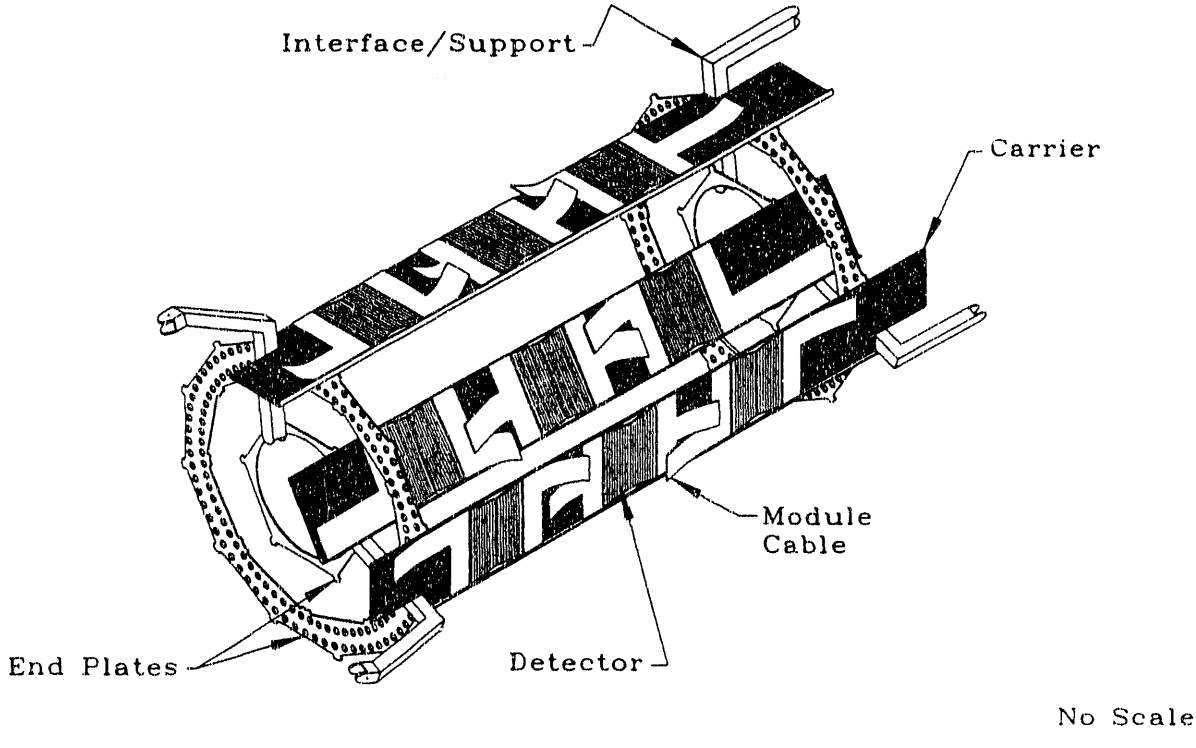

Figure 4H-26 Partial view of assembled SVT.

support cones. These support cones have flanges that connect to the TPC. This basic configuration is shown on Figure 4H-27.

4.H.5.1. Material Selection

There have been several comparisons of material to be used in silicon-based detectors. Table 4H-2 shows several candidate materials with their applicable parameters.

It can be seen that beryllium is an excellent choice for the structural material for an SVT. It has high stiffness and radiation length. It's disadvantages are high coefficient of thermal expansion and cost. The expected operating temperature of the SVT is equal to or near the assembly temperature, therefore, the CTE of support material compared to silicon is not critical. If it is necessary to match the CTE of silicon with the structural material, composite materials can be used. These type of materials have there own unique set of problems. Since there are only a few parts required, the cost of the initial tooling may make them more expensive than beryllium. These materials also absorb moisture and move slightly over time until they stabilize. Work is proceeding at LANL to develop and characterize composite materials for other programs. Their results may be applicable to the SVT.

The end plates are the most expensive part of the assembly. If possible, these may be made of aluminum which could reduce the cost of the main frame. Since another different CTE will be introduced with this change, a detailed thermal analysis must be completed prior to making this decision.

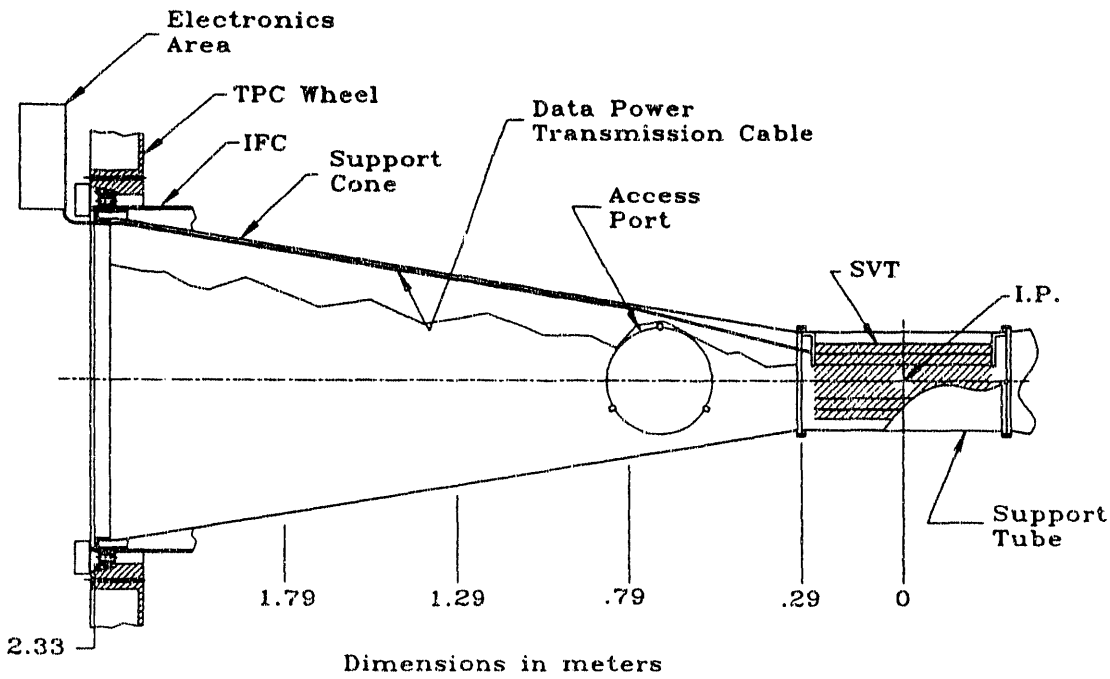

Figure 4H-27 Elevation view of the assembled SVT mounted in the tube/cone support.

Table 4H-2 Selected material properties.

Material	Elastic Modulus E-GPa	Density p (gm/cm³)	Specific Stiffness E/p-10⁸ cm	CTE å ppm/K	Thermal Conductivity k W/M-K	Specific Heat c_p J/gm-K	Effective Radiation Length L-cm
Beryllium	290.0	1.84	16.08	11.60	146.0	1.88	35.43
Carbon-Carbon	152.0	1.90	8.16	0.10	246.0	1.00	18.80
P75/1939-3 G/E	311.7	1.68	20.00	-1.13	46.2	0.92	25.00
Al-MMC (AZ91)	190.3	2.03	9.56	-0.35	412.0	?	16.80
Al-MMC (6061-T6)	196.5	2.39	8.39	0	409.0	?	13.22
Silicon	131.0	2.33	5.74	2.60	129.0	0.70	9.37
Al (6061-T6)	68.9	2.70	2.59	23.58	168.0	0.90	8.89
Copper	117.2	8.91	1.34	16.90	400.0	0.39	1.43
SiC	325.0	3.00	11.05	2.30	200.0	0.89	8.52
Kapton	2.5	1.42		20	0.12	1.09	28.3

4.H.5.2. Description of Major Components

Carrier

The baseline carrier, shown on Figure 4H-23, is fabricated from beryllium. It is 0.5-mm (20 mil) thick. This thickness is chosen since it is a standard size available from a local vendor. An optimization study considering the stiffness required and the effect on average radiation length has not yet been completed . The length of the bent tab was calculated to provide sufficient stiffness to limit the sag to 50 μm. Since the stiffness is provided primarily by the bent tab, some material in the detector support section is removed to reduce the overall radiation thickness of the part. Extra length is added to each end to include an area for cable attachment. This should provide some strain isolation between the long transmission and the module cables.

If water cooling is required, the carrier may be made as a laminate with flow channels between the two layers. Although this requirement has not been finalized, the cost estimate includes carrier with flow channels. Discussions with a local vendor indicate that a multilayered beryllium carrier is feasible.

End Plates

The carriers are attached to the end plates which are also constructed of beryllium. It may be possible to fabricate them out of aluminum, but the baseline material is beryllium. The end plates are joined together by interface links that also

support the SVT. These end plates are the most complex part of the mechanical assembly. The method of attaching the carriers to the end plates has not been selected, although other silicon-based trackers have used the same basic configuration.

The end plates shown in Figure 4H-26 have many holes in them to allow gas to flow into the assembly. If a water-cooled SVT is required, these holes will not be necessary.

It was recently decided to utilize a clamshell design for the end plates. This allows removal of the SVT without removing the accelerator beam tube. The SVT can also be installed over the beam tube after beam operation has stabilized. Although the clamshell design is not shown on Figure 4H-26, funds have been allocated in the cost estimate for this feature. It is assumed that the ALEPH clamshell design will be usable for STAR as is or with minor modifications.

Tube/Cone

The SVT will be attached to a support tube as shown on Figure 4H-27. This tube is constructed from graphite-epoxy and has a radiation length of about 0.5%. Development of this configuration is being conducted at LANL. The tube is attached to support cones that are then connected to a flange on the TPC inner field cage. It may be necessary to transfer fiducials from the SVT to the end of the support cone. Some adjustment at the cone/IFC flange attachment point will be provided.

4.H.5.3. Cabling Requirements

The cables attached to the detector will be fabricated using aluminum data and power strips. These metal layers will be laminated with kapton. The technology development of aluminum cables is being carried out by another program at LBL. Some development will be required for the specific SVT module cable due to its configuration. Also under development at LBL is a minimum mass demountable connector. This may have application at the end of the module cable.

The baseline configuration has the first amplifier on the detector. This amplifier may not be capable of driving the signal down a long cable, therefore, an intermediate amplifier may be needed. A flat ribbon cable will connect the electronics in the assembly to the main electronic boards mounted at the ends of the TPC. The ribbon cable attaches to the aluminum/kapton module cable at the end of the carrier. Area is available at the end of the carrier to attach the cables to the carrier relieving the strain from the modules. The number of signal lines going into each module is 224. These can be accommodated with a metal signal line pitch of 250 μm. If a two-metal layer cable is used, the module cable will be about 30 mm wide as it leaves the module. Past the end of the carrier, a single layer cable can be used. Aluminum cables are being developed at LBL and beryllium cables are being developed by LANL. A low mass connector is being developed at LBL.

Power must also be brought into the SVT. The total power input to the DP amplifiers is 0.34 W and into the high voltage divider is 0.2 W. If a 5% loss is allowed in the 2-m distribution cables, an aluminum DP power trace could be 1-mm wide by 0.013-mm thick. The high voltage distribution cable requires a smaller area due to the low

current in this circuit. The exact configuration of these signal and power cables will be determined after the basic DP amplifier location has been fixed.

4.H.5.4. Initial Assembly

Detectors onto Carriers

The detectors will have fiducials located at each corner. These can be used to define an axis for each detector. The carriers will also have fiducials at each end which define a local axis. These will be used to align the carrier along the workstation axis. After the first detector is attached to the carrier, it's axis then determines the reference axes. All other detectors are placed relative to this axis instead of the carrier axis. This is because one of the most important tolerances is the parallelism of each detector axis relative to each other. Present equipment can locate fiducials over the area of a detector to better than 2 μm and determine their absolute location to better than 5 μm. After all the detectors have been place onto a carrier, a measurement will be made of the location of all fiducials. This will then allow the fiducials on the carrier to be used for the next assembly step. Initial work on the workstation arrangement is being conducted at LBL.

Carriers onto End Plates

The method of attachment of the carriers to the end plates has not been finalized. The two halves of the end plates will be joined while the carriers are being placed. In order to accurately place the carriers onto the end plate, it is necessary to first define a workstation z axis. Using this axis, microscopes can be located at two perpendicular axes. These microscopes can then look at the carrier fiducials and guide the carrier placement onto the end plates. The location in phi can be accurately determined by either using a rotary table or machining an index plate. The location in radius can be determined by use of a focusing scale. After all the carriers are mounted on end plates, the x, y and z location of each outboard detector can be measured. From these measurements, fiducials on the end plates can be calibrated and used for the final assembly and alignment steps. Each end plate can then be separated and reassembled to determine the adequacy of the clamshell design. Off--the-shelf equipment exists that can determine axes and locate fiducials to the required accuracy. Development of a complete workstation is proceeding at LANL. This work is directed toward assembly of the SDC silicon tracker.

Assembly to TPC

The SVT assembly shall be preassembled into the support tube/cone and aligned relative to fiducials located at the cone flanges. Access ports are provided in the two cones to allow adjustments to be made on the SVT/tube supports. The SVT/tube supports will have to provide x, y and z adjustment for this alignment task. A special fixture can be used to lift and translate the SVT slightly to clear its supports. The SVT can then be translated on temporary tracks to the end of the cone supports. There, it can be broken into two halves and removed from the beam tube. These steps will be performed several times during the initial assembly to determine how accurately the assembly can be repositioned. When the SVT is ready to be installed at BNL, the

tube/cone will be installed and fastened to the TPC without the SVT. The two halves of the SVT will be placed around the beam pipe, joined together and placed on the temporary tracks. After positioning in the tube, a fixture will lift the SVT off the tracks and translate it over the SVT/tube supports. After lowering the SVT onto the supports, the fixture and the tracks will be removed. It is expected that it will be difficult to see the SVT end plate fiducials, so the fiducials on the two support cones will be used to guide the final alignment of the SVT relative to fiducials on the TPC.

4.H.5.5. Alignment

4.H.5.5.1. Specifications for Alignment

The following are the specifications for the allowed error (5%) of the detector from the known position:

Phi ± 7 μm
Radial ± 15 μm
Z ± 7 μm

This set of specifications limits the relative structural movement after placement and turnon. Analyses and prototype testing are required to verify meeting these values. The SVT will be assembled using precision equipment, such as coordinate measuring machines (CMM), that can locate fiducials over the required volume to less than 25 μm. These machines now have optical heads with corresponding smart software that can find centroids of fiducials to about ±5 μm. Work is presently proceeding at LANL and LBL to develop techniques and equipment that will allow attainment of these goals.

The sag (due to gravity) in the module carrier is estimated to be 50 μm for the worst case. It was assumed that all the bending stress is taken by the bent tab and any contribution due to the silicon was neglected.

The location of the SVT with respect to the TPC and the remaining detector is:

SVT axis parallel to magnetic field ± 5 mrad
SVT x-y location ± 250 μm to TPC center
SVT z location ± 250 μm to defined interaction point

These goals must be met after the SVT is put into place at RHIC. The support points at the SVT/tube interface is about 2 m from the edge of the TPC. This makes it difficult to see fiducials and adjust the SVT assembly. For this reason, it is proposed to align the SVT with the tube/cone support and transfer fiducials out to the tube/cone flanges.

4.H.5.5.2. Alignment Constraints Based on Physics Goals

The precision requirements of barrel detectors are discussed in ref. [66]. They are specifically determined by the physics requirements [momentum and vertex resolution (primary and secondaries) needed], and the intrinsic limitation of the device. Most of the SVT physics involves precise determination of the impact parameter (extrapolation

[66] A. Seiden, Note on `Systematic errors and Alignment in Barrel Detectors'.

accuracy to a vertex), which is significantly more affected by any misalignment than momentum. By assuming the maximum acceptable degradation on impact parameter and the intrinsic point resolution of the SVT (25 μm for STAR1) one can determine alignment precision requirements. To propagate the requirements on impact parameter resolution into requirements for SVT position precision, one must understand how an SVT misalignment affects the impact parameter. To understand this connection, we consider a simple model of STAR tracking including the SVT which assumes that the high space point precision of the SVT would force the tracks through the SVT points. Taking the SDD wafer as a rigid object, the misalignments break down into 4 categories (6 parameters):

- planar translation (2 parameters)
- planar rotation (1 parameter)
- radial translation (1 parameter)
- out-of-plane rotation (2 parameters)

The four categories, in order, have a decreasing effect on the impact parameter precision, but show a basic linear relation between misalignment and impact parameter (Fig. 4H-28).

To estimate tolerances, we will adopt the results obtained for the ALEPH vertex detector using Monte Carlo with smeared positions of the vertex detector hits to account for alignment effects before refitting the track. The results, expressed in the wafer local coordinate system (Fig. 4H-29) are shown in Fig. 4H-30.

As an example for the derivation of the points in these plots (Fig. 4H-30) we assume a V displaced by 20 μm. For each event, the position of each wafer is smeared in V by a Gaussian of width 20 μm, in addition to the intrinsic vertex detector point resolution. The track is then refit with the vertex detector hits. Next, the impact parameter resolution is calculated as the width of the distribution comparing the reconstructed impact parameter with the Monte Carlo "true" value. This impact parameter resolution is then divided by the resolution with no smearing for alignment affects. The plots in Fig. 4H-30. show that the impact parameter resolution in z is more sensitive than that in R-ϕ for 4 of the 6 alignment parameters: V, W, α_u, α_w. This is because the tracks cross the wafers closer to normal incidence in the R- ϕ plane than in the R-z plane. The effect of the planar rotation, α_v, is almost the same in both dimensions.

Taking the limit of 5% (10%) degradation of the impact parameter resolution one can set requirements for alignment of the vertex detector :

- V = 15 (20) μm
- U = 7 (12) μm
- W = 7 (10) μm
- α_v = 0.5 (0.7) mrad
- $\alpha_u = \alpha_w$ = 0.8 (1.3) mrad.

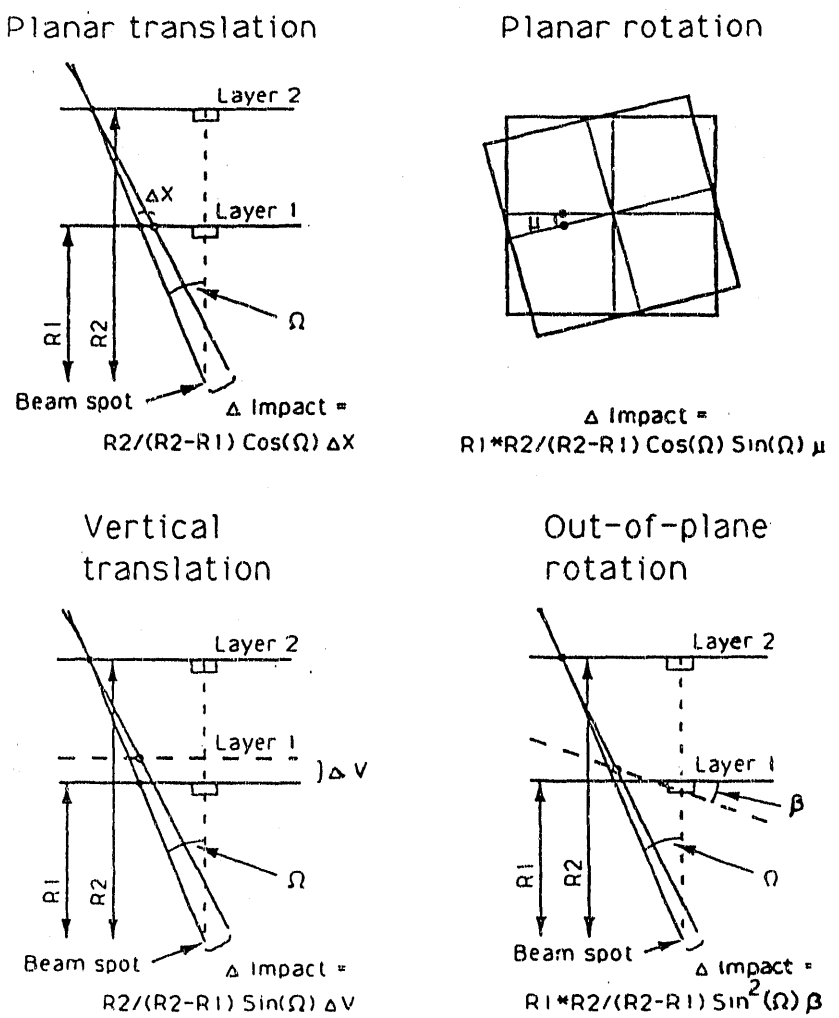

Figure 4H-28 Impact parameter dependence on misalignment.

One should remember that the above numbers represent **final precision** needs, not mechanical alignment tolerances.

Table 4H-3 shows (in general) how misalignment influences the space point resolution of the detector[67].

Since the STAR SVT consist of 162 silicon tiles positioned around the interaction point, proper alignment of these elements becomes crucial. It can be factored into 2 problems, namely the alignment of the wafers relative to each other (**Local** alignment), and the alignment of the SVT as a single rigid body with respect to the rest of STAR (**Global** alignment).

---

[67] Note that Fig. 3 demonstrates that 10 μm final precision is satisfactory to preserve the goodness of the impact parameter.

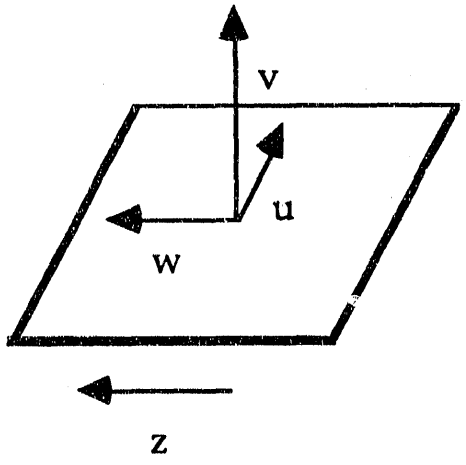

Figure 4H-29 V points perpendicular to the wafer surface outwards from the interaction point, U lies in the wafer plane, while W points along the z axis (beam) VUW is a right-handed system.

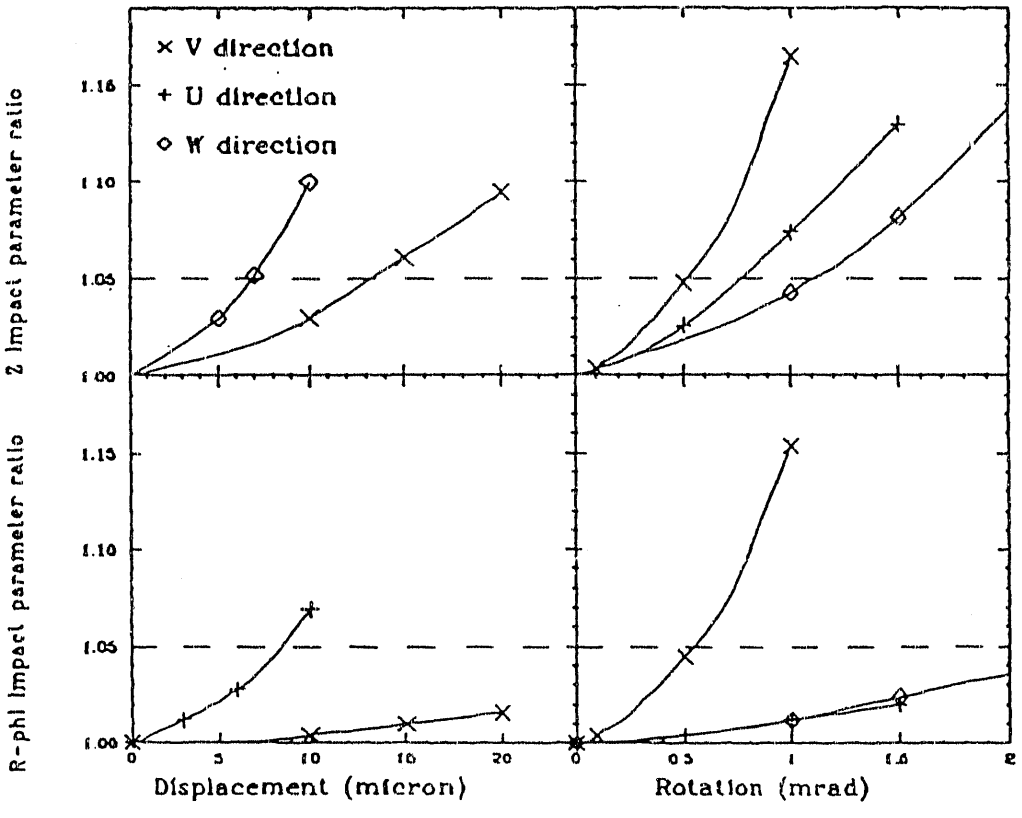

Figure 4H-30 Impact parameter dependence on alignment error.

Table 4H-3

intrinsic resolution σ_1	misalignment error σ_2	total error $\sigma = \sqrt{(\sigma_1^2 + \sigma_2^2)}$
25 μm	20%	25.5μm
	33%	26.3
	50%	27.9
	100%	35.4

4.H.5.5.3. Global Alignment

The global alignment in fact is hardly more than a convention, as the position resolution of the SVT is much better than the other STAR detectors. The requirement on global alignment is therefore very relaxed, namely that the SVT global position lie within the (relatively large) TPC errors of the origin defined by the TPC. In the reconstruction, the errors on the global alignment are not used, as they are redundant with the local alignment errors. Thus the degrees of freedom represented by the global alignment are completely redundant with the local alignment. The only real function of the global alignment is therefore to insure that the local alignment corrections are kept small, so that the (linearized) correction routines used for the local alignment are not extended beyond their proper limit. For global alignment, we will adopt, after ALEPH, a simple software procedure,[68] which operates by taking a sample of TPC tracks (about 10K), and minimizing the discrepancy between SVT hits and associated track extrapolation points, taking as free parameters 3 translations and 3 rotations of the SVT as a single rigid object.

4.H.5.5.4. Local Alignment

The local alignment is by far the more important, and the more difficult. It will be discussed here in steps:

- **SDD internal alignment:**
  addresses how precisely the E field is aligned with the geometry of the pad row. The present technology of fabrication of silicon drift chambers allows for accuracy better than 1 μm. Therefore, this is not a concern.
- **SDD alignment on the ladder:**
  The literature on alignment of silicon strip detectors refers to an achievable precision of 2 μm. We adopt here the conservative number of 5 μm, which is easily obtainable with the present LBL mechanical shop equipment. Each SDD wafer, for this reason, will have fiducials at each end which can be located with a microscope. The same will be done for each carrier. The detectors will be placed relative to one another and the carrier fiducials with a variance of 5

[68] ALEPH Note 91-43.

μm. After placement on the carrier, the carrier fiducials can be used for all other references.

- **Vertical tilt of SDD's on the ladders:**
  SDD's will be glued to the ladders. The glue thickness will be 20–25 μm. The tilt can be controlled very accurately by using 25 μm wires or balls to determine the distance between surfaces. This way the glue only fills in the void and does not determine the actual gap. Accuracy of this procedure can not cause a tilt greater than 0.2 mrad.

- **Positioning carrier on frame:**
  will be done using a microscope and precision rotary assembly jig. Anticipated precision should not be worse than 25 μm. The attachment strategy has not been determined yet. (LANL is working on this problem and expects a timely solution).

Summarizing, it is planned (and it seems feasible) to measure relative SDD wafer positions **prior to insertion** into STAR, to an accuracy of 5-30 μm. However, because of numerous physical effects (thermal expansion, stress during insertion, magnetic field effects, etc.), these positions may not be a correct set for the detector after insertion. Therefore, it is necessary:

1) to determine the distortion of the SVT **in situ,**

2) to **monitor** changes of the SVT position as a function of time.

The most direct method for measuring the position of the detector is with straight track data. Even if not absolutely required, the data-driven alignment will still be a necessary test of the consistency of the data. Two alignment methods, **vertex constraint technique** and **2 (3) layer technique**, can be used in STAR for this purpose. The latter one uses only information from the SVT itself, so it can be used to **bootstrap** the detector into alignment, thus avoiding the **systematic accuracy limits** of the TPC. This can also be used as an accurate monitor of stability of TPC performance in time. This software alignment is usually performed only periodically. Therefore, one needs an on-line monitoring system to check continuously the position of the vertex detector. Techniques like capacitive position sensors or laser beams pointing to CCD chips installed on the SVT end caps are being considered. The detailed descriptions of similar procedure can be found in [69,70].

4.H.5.6. Cooling Considerations

A preliminary study has been completed to determine the magnitude of the cooling required. The input model and typical thermal contours with gas convection cooling are shown on Figure 4H-31.

---

[69] ALEPH Note 91-43.
[70] ALEPH Note 92-10.

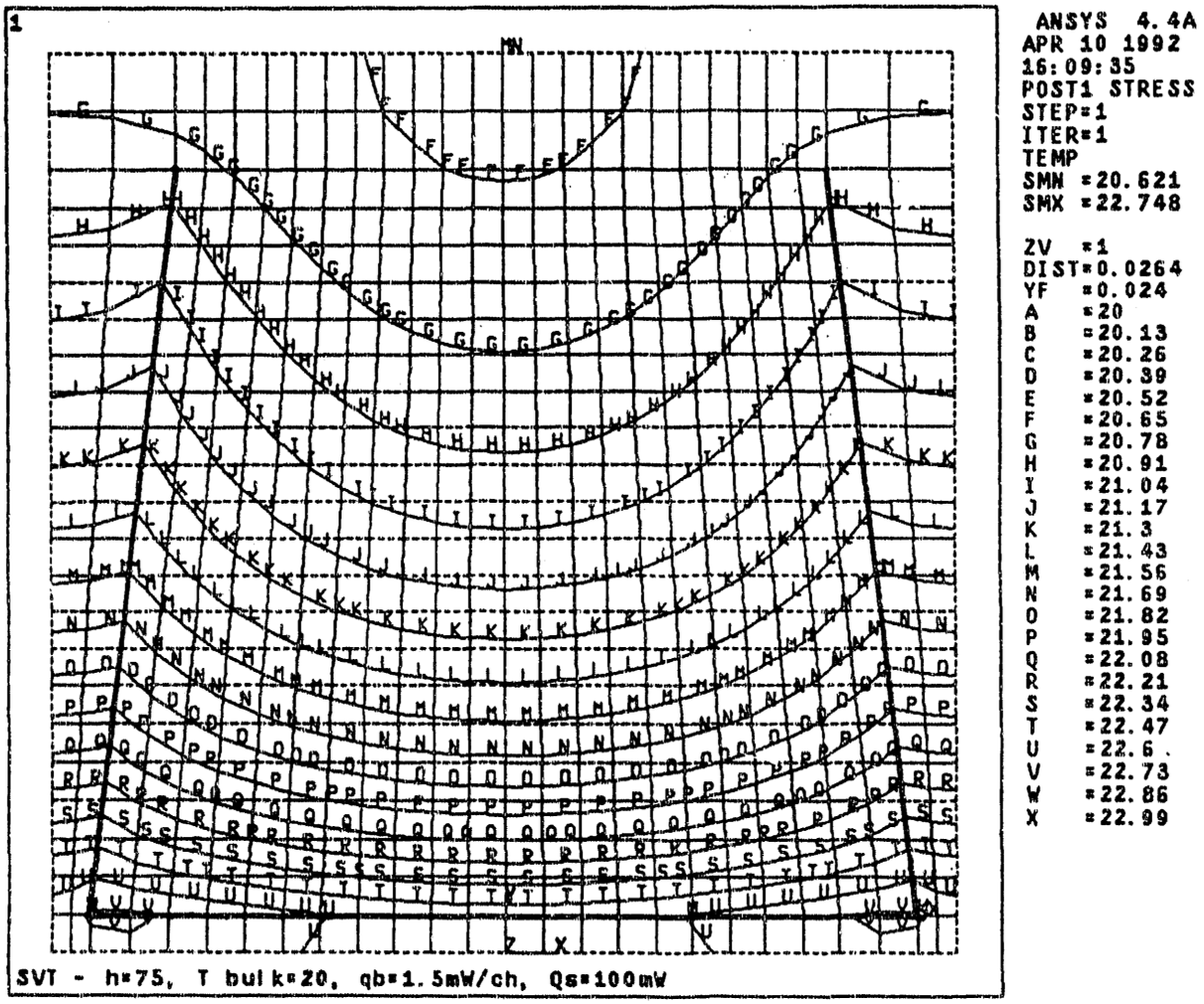

Figure 4H-31 Thermal model of the prototype detector and typical thermal contours. Heat was input along the dark lines.

Different convection film coefficients were assumed for this initial study. The smallest of 5 W/m^2-C corresponds to that achieved by natural convection and the highest, 75 W/m^2-C would be obtained by blowing high velocity gas (75 mph) over the detector surface. The results of these calculations are shown by Table 4H-4. The maximum temperature gradient was along the detector centerline.

Assuming a power of 1.5 mW/channel it can be seen that the drop in the maximum gradient is not significant if the film coefficient is increased above about 20 W/m^2-C. None of the cases studied predicted an achievable gradient less than 1° C. For a reasonable film coefficient (20 W/m^2-C), the maximum gradient was about 2.6^o C. Early indications from physics are that gradients in the detector must be below 0.1^o C. From these results it can be assumed that cooling by gas only may not be sufficient to obtain the required thermal profiles.

Table 4H-4 Results of gas cooling study.

Film Coef. W/m^2-C	Power/chan mW	Max Temp gradient, C	Max Temp. C
5	1.0	2.16	37.9
5	1.5	3.19	42.4
5	2.0	4.21	46.9
10	1.5	3.03	32.2
20	1.5	2.55	25.9
75	1.0	1.3	22.1
75	1.5	1.92	22.7
75	2.0	2.55	23.4

Initial studies were conducted to determine the possible thermal profiles using liquid cooling. During these studies, three edges of the detector were held at 20° C. The forth edge, corresponding to the middle of the STAR2 design, was assumed to be insulated. This is an idealized case similar to aggressive liquid cooling around the detector where it is attached to the carriers. The results indicated that the gradients were below about 0.1° C with and without the assistance of natural convection. Additional physics analysis and prototyping must be completed prior to determining the final detector cooling method. It is expected that a decision will be made at the end of summer. The cost estimate assumed liquid cooling as a baseline.

4.H.5.7. Installation and Access

The SVT will be assembled as described earlier. During the initial assembly, it will be installed in the tube portion of the tube/cone support. This tube will provide excellent protection during shipping. The SVT will be aligned relative to the tube/cone support using fiducials on each end plate of the SVT and the two flanges on the tube/cone support. During the final installation in the STAR detector, these fiducials can be seen by theodolites that can determine their position relative to fiducials on the TPC. It may be possible to use a long-focal length microscope to look at the fiducial on the SVT which would provide a more accurate relative placement. After alignment of the fiducials, the SVT will be removed from the tube/cone supports. When it is time to install the SVT in the STAR detector, the tube/cone support will be inserted into one end of the TPC inner field cage. One end of the support will have a fixed flange and the other will have a rotatable removable flange. This removable flange will contain two O rings, one for the TPC connection and one for the tube/cone support. Prior to tightening the flange bolts, the external fiducials can be aligned relative to those on the wheel of the TPC. Temporary tracks will then be attached to the tube/cone support. The two halves of the SVT will be placed over the beam tube and attached together. The SVT will then be moved down the tracks to a position next to the SVT/tube supports. A fixture will then lift the SVT off of the tracks and translate it to the supports. After lowering the SVT onto its supports, the fixture and temporary tracks will be removed. The accuracy

of SVT placement relative to the fiducials on the cones will have been determined earlier during initial assembly. The cost of the special fixture and the temporary tracks are included in the cost estimate.

Access to the onboard SVT electronics will not be possible without removing the SVT. It will be possible to gain access to the end of the SVT by moving the tube/cone assembly toward one end of the detector. Ports will be available in the cone supports to allow access to the end of the carriers. The SVT must be completely removed for any work on the detectors. To remove the SVT, the cables must be disconnected at one end. A temporary support may be necessary to hold these pigtails. Temporary tracks will be installed at the opposite end and a special fixture will be used to lift and translate the SVT onto these tracks. The SVT can then be rolled to one end of the TPC. After the cables have been removed, the SVT can be split into two halves and moved to the STAR clean room for maintenance. If detectors must be replaced, the carriers must be removed from the end plates. These tasks must be accomplished using precision instruments equivalent to those used during initial assembly.

4.H.5.8. Engineering Issues

The outstanding issue that has the greatest impact on the mechanical design of the SVT is the type and amount of cooling required. As discussed above, liquid cooling may be required. Although the amount of heat to be removed is small, the requirement for very low radiation lengths makes the cooling configuration design a challenging one. To obtain low radiation lengths, the flow channels must be kept small and even with small flow, pressure may be an issue. Fabrication of small channels using beryllium must be investigated prior to a final decision on the configuration.

Another mechanical uncertainly for the SVT is the ability of the frame to hold the tight tolerance for unknown positions after turnon. The placement requirements are within the present capability of coordinate measuring machines with optical heads. Micro manipulators are available to assist in fine movement during assembly. A CMM available at LBL has a measurement volume of $1 \times 1 \times 1$ m. Over this volume the accuracy is about 25 mm in x, y and z. While placing the detector modules onto the carrier, a smaller CMM can be used that can locate fiducials relative to each other by about ± 2 μm. Once the assembly is complete, the location of the inner modules can not be determined optically. The expected location will be determined by analysis and prototype testing. The final, most accurate position location will be by the use of stiff particles and software.

4.H.5.9. Testing and Calibration Issues

Prototyping

In the near future we will build a full size Al prototype of the support structure for the SVT in order to test the assembly procedure and address integration and alignment issues. In connection with the support prototype we will test a number cooling system designs for comparison with thermal calculations. We attempt to perform deflection measurements which will help us to determine the mechanical distortions due to the selection of a certain cooling technique, e.g. vibrational effects due

to high pressure air cooling or under pressure water cooling. This prototype also enables us to test the integration of the various carrier designs and carrier material choices under discussion. The tiling and the cable integration of the STAR2 detectors will be investigated as well (see chapter 4.H.5.6.)

Test Beam

As a next step we plan to mount a few STAR2 prototypes, which are available by the end of 1992 onto the structure prototype and perform detector tests by utilizing available test beam facilities. The plan foresees beam times at TRIUMF (up to 300 MeV/c pions), BNL (SEB and RHIC heavy ion test beam) and WSU (5 MeV/c electrons). In these varying environments it will be possible to determine effects like enhanced γ conversion due to the cooling pipes, cooling material (if liquid cooling) and the detector tiling, cross talk between the detectors, performance in high multiplicity environment, optimization of readout chain. Besides that the main physics requirements like spatial, momentum and two track resolution as well as dE/dx capabilities will be investigated by utilizing test beam. A detailed plan for test beam requirements for the next year is in progress.

Calibration Issues

The relative as well as the absolute position calibration on the SVT wafers can be determined either by straight (high p_t) tracks (see chapter 4.H.5.5.4) or by induced laser beams. For the energy calibration one uses radiation sources or, for higher energies, a particle beam of well known energy A third alternative would be to induce current onto the detector. All these methods will be used to calibrate the system offline. For online calibration, tracks whose momentum is well determined by the TPC seem adequate.

4.I. Electromagnetic Calorimeter

4.I. Electromagnetic Calorimeter

4.I.1. Specialized Physics Issues

Soft Processes in Nucleus-Nucleus Collisions

Measurement of the total (E_t) and local ($dE_t/d\eta$,) transverse energy deposition in relativistic nucleus-nucleus collisions is essential in determining the degree of nuclear stopping which occurs. Analysis of the total transverse energy at mid-rapidity leads directly to estimates of the energy density characterizing the reaction, allowing further determination of the likelihood of plasma formation. Detailed examination of the local transverse energy deposition ($d^2E_t/d\eta\, d\phi$) may be used to search for fluctuations resulting from unusual particle production processes. Furthermore, event by event correlation of the $dn/d\eta$ and $dE_t/d\eta$ distributions allows not only a systematic description of the reaction dynamics appropriate for the description of "ordinary" nucleus-nucleus collisions, but facilitates the identification of rare events as well. Events in which the ratio of charged to neutral transverse energy (E_t^{chg}/E_t^0) is uncharacteristically high or low in view of normal isospin considerations have also been proposed as a possible signature of novel phenomena. The scintillator trigger barrel, time projection chambers, and SVT will provide offline information allowing studies of some of these effects. However, because the STAR electromagnetic calorimeter (EMC) is unique in its ability to detect neutral electromagnetic energy, and is inherently a fast device, it will perform several essential functions in the study of these phenomena.

For "soft" nuclear processes ($p_t \leq 1$ GeV), the STAR EMC detects approximately 50% of the total transverse energy deposited in the range $|\eta| < 1.05$ (Fig. 4I-1). Approximately 40% of the detected energy is from low energy hadrons entering the calorimeter and depositing energy by dE/dx. The remaining 60% is due to neutral electromagnetic energy, for which the calorimeter is essentially 100% efficient. Ordinarily in high energy hadronic collisions the $dn/d\eta$ and $dE_t/d\eta$ distributions are simply related by the $< p_t >$ of the produced particles. It is predicted therefore by models such as FRITIOF[1] and HIJING[2] that these distributions will be strongly correlated in relativistic nucleus-nucleus collisions as well (Fig. 4I-2). The observed experimental correlation may therefore provide important information on the reaction dynamics characterizing these collisions. As the STAR EMC efficiently detects the neutral transverse electromagnetic energy, the resolution of the STAR detector for studying this correlation is improved. More generally, the improved resolution afforded by the EMC enhances the STAR physics capability in all studies where the flow of transverse energy is an observable.

Another study facilitated by the STAR EMC is the search for events in which the ratio of charged to neutral transverse energy (E_t^{chg}/E_t^0) is uncharacteristically high or low. Speculation concerning the origin of so-called Centauro events[3], for example , has

---

[1] Bo Nilsson-Almquist and E. Stenlund, Computer Physics Communications 43(1987).
[2] Xin-Nian Wang and Miklos Gyulassy, LBL report LBL-31036; X.-N. Wang and M. Gyulassy, Phys. Rev. D41, 3501 (1991).
[3] Panagioutou et al., Phys. Rev. D45, 3134 (1992).

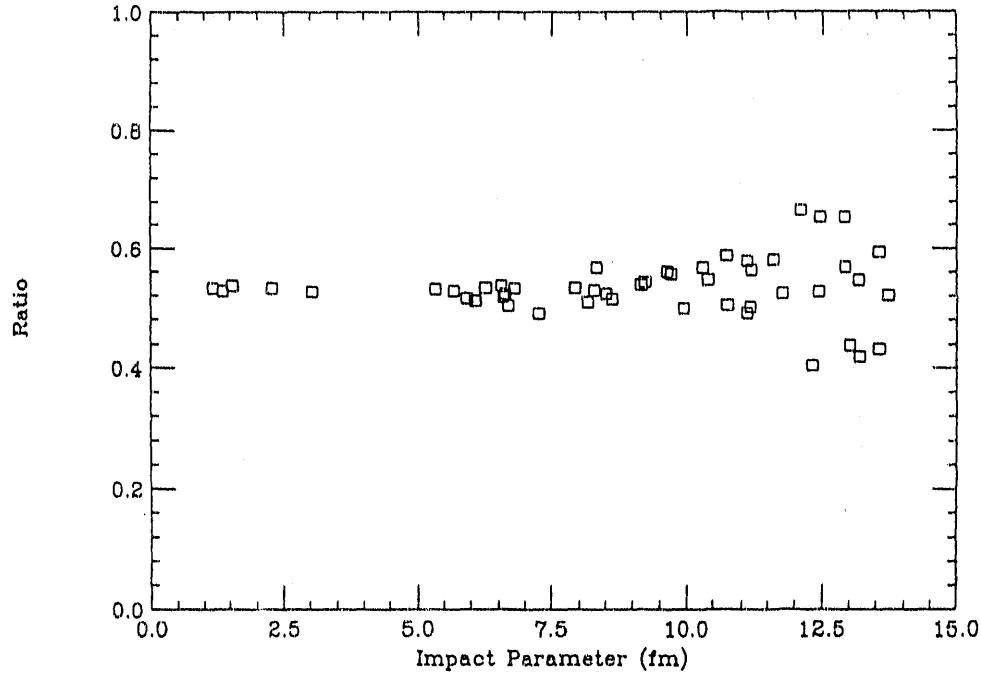

Figure 4I-1 The ratio as a function of impact parameter of the transverse energy detected in the STAR EMC to the total transverse energy within $|\eta| \leq 1.05$ for AuAu collisions at $\sqrt{s_{nn}} = 200$ GeV.

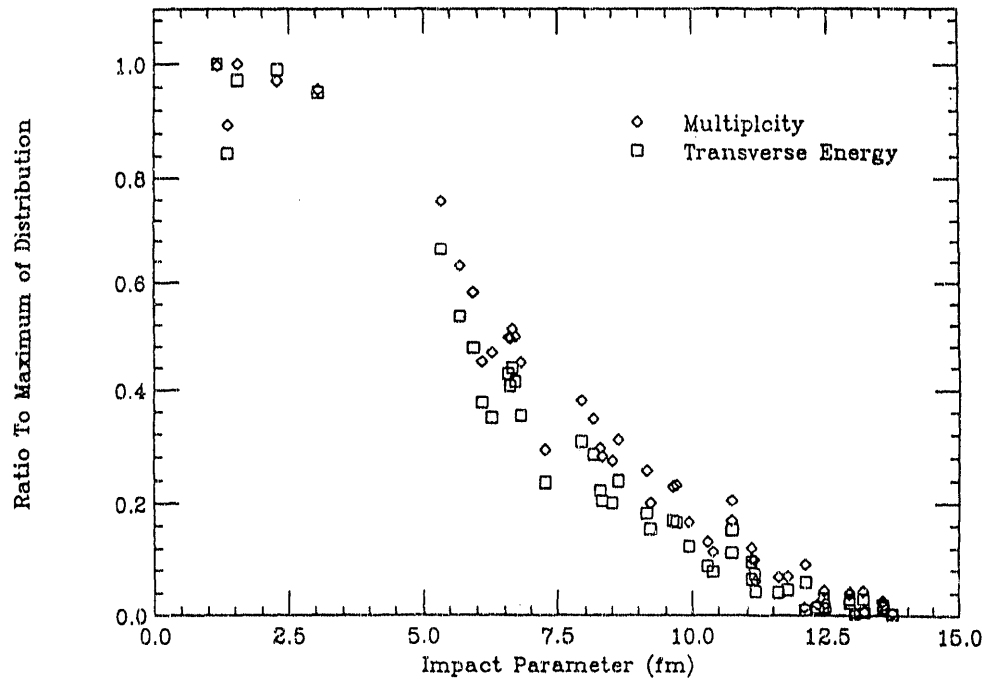

Figure 4I-2 A comparison as a function of impact parameter of the particle multiplicity and transverse energy within $|\eta| \leq 1.05$ for AuAu collisions at $\sqrt{s_{nn}} = 200$ GeV. Both distributions are plotted as a ratio of the value at a given impact parameter to the maximum of the distribution.

lead to the possibility that unusual fluctuations in this ratio could signal the onset of novel phenomena. Since the EMC is the only detector in the Phase I baseline to detect neutral electromagnetic energy, these phenomena can only be studied with information provided by this detector system. Information on the transverse energy carried by charged particles will be provided by TPC and SVT tracking, and to some extent by the longitudinal segmentation in the EMC as well. An example of the expected change in this ratio if only neutral pions were produced is shown in Fig. 4I-3 for central AuAu collisions. The input for this scatterplot was derived by replacing the charged pion ID presented to GEANT for normal AuAu collisions by the corresponding neutral pion ID, given the STAR geometry. Momentum and energy are therefore conserved. What is evident from this plot, is that even though the increase in detected energy is ~ 25% in the case where all the produced pions are neutral, the correlation of the information from the EMC with multiplicity information provided, for example, by the scintillator trigger barrel would provide a powerful means of triggering on events in which the correlation between the < M > and E_t distributions may signal the production of rare events of unique origin. This is an important consideration since events in which "new physics" occurs may be produced at very low cross section.

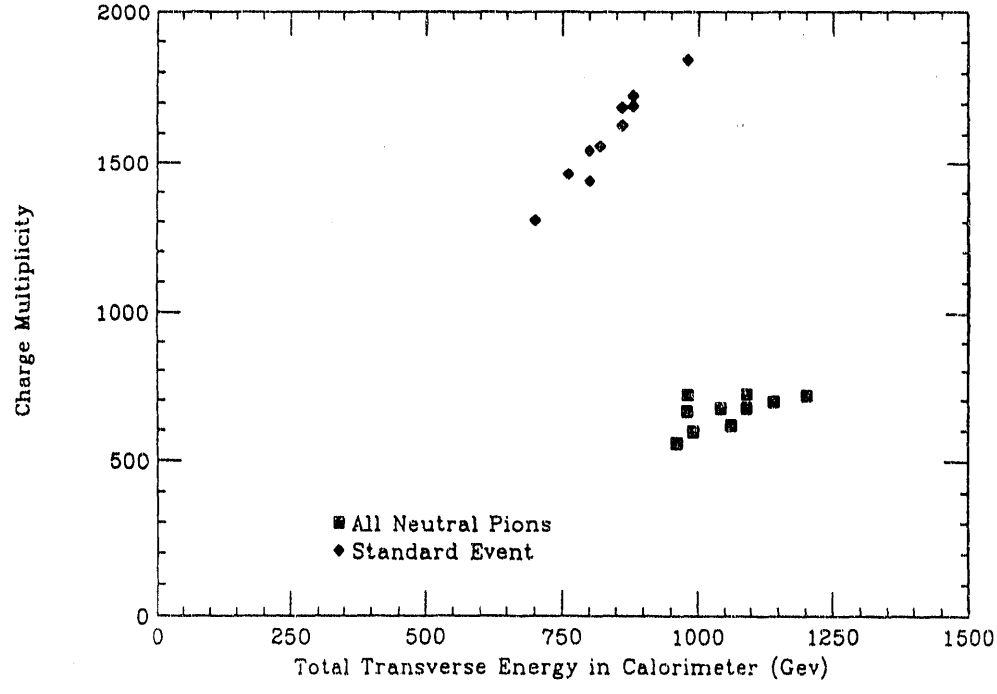

Figure 4I-3 A scatterplot of the charge particle multiplicity and the transverse energy detected in the STAR EMC for 1) standard HIJING AuAu events at $\sqrt{s_{nn}}$= 200 GeV, and 2) HIJING AuAu events in which only neutral pions are produced. Data shown are for b < 1 fm.

Hard Parton Scattering In Nucleus-Nucleus Collisions

Another interesting possibility pointed out by Gyulassy and Plumer[4] is the use of hard parton scattering to probe nucleus-nucleus collisions. RHIC will be the first accelerator to provide nuclear collisions at energies where perturbative QCD gives an accurate description of hard parton scattering, and where the rates of detectable partonic debris (jets and high p_t particles) permit accurate measurements. Because the hard parton scatterings occur before hot matter forms in the region between the two receding nuclei, the rate of hard parton scattering can be reliably calculated. RHIC therefore offers a unique opportunity to study the interactions of partons in the hot medium and thus infer its properties.

There are data[5] which suggest the interaction of hard scattered partons passing through nuclear matter is strong enough to be observed. Ideally, this physics is best studied in back to back jet-jet or γ-jet events. A detailed understanding of the effect of the nuclear medium in such events requires a systematic program of pp, pA, and AA studies, in which the effects of parton shadowing and the structure function of the proton can be unfolded as well.

The full capability of the STAR EMC to pursue these studies, as well as the possible use of this probe to search for the quark-gluon plasma is still under investigation. Since, for example, jet-jet and γ-jet events are produced at low cross section, the generation of a sufficient number of fully simulated nucleus-nucleus collisions to accurately estimate the backgrounds which are present is difficult. Furthermore, although some data for low p_t hadrons do exist[6], in general the response of sampling calorimeters to hadrons of this energy is not well studied. The large flux of low p_t hadrons present in these reactions may preclude the study of jets, except for the study of leading high p_t particle production. There is evidence[7] which suggests it is still possible in this instance to investigate nuclear effects. Simulations to determine the real capability of the STAR EMC for detecting hard parton scattering in nucleus-nucleus collisions are continuing.

Direct Photon and Jet Physics in Polarized pp Interactions

Although years of experimental efforts at the CERN and FNAL colliders have provided much information about the structure of QCD hard scatterings and the parton structure of the proton, there is no corresponding body of data on the spin-dependence of the elementary interactions and the spin structure of the proton. High luminosity polarized proton beams in RHIC offer the opportunity to use the unique properties of the spin variable to increase the understanding of these fundamental quantities. Measurements[8] at SLAC and CERN of deep inelastic scattering of longitudinally

---

[4] M. Gyulassy and M. Plumer, Phys. Lett. **B243**, 432 (1990).
[5] L. S. Osborne et al., Phys. Rev. Lett. **40** 1624 (1978); M. Gyulassy and M. Plumer, LBL Report LBL-27234 (1989).
[6] C.W. Fabjan and R. Wigmans, Rep. Prog. Phys. **52**, 1519(1989).
[7] X.N. Wang and M. Gyulassy, Phys. Rev. Lett. **68**, 1480 (1992).
[8] V.W. Hughes and J. Kuti, Ann. Rev. Nucl. Part. Sci. **33**, 611 (1983); J. Ashman et al., Nucl. Phys B328, **1** (1989).

polarized leptons by longitudinally polarized protons suggest that a surprisingly small fraction of the proton's spin may be carried by the valence quarks. This is in contrast to the fraction of the proton's longitudinal momentum carried by the valence quarks, and may indicate that the present understanding of the proton's internal structure is deficient. The fraction of spin carried by gluons must be measured to clarify this situation.

There are two areas of proton-proton spin physics which can be best done with the combination of RHIC and STAR. The first area is the proton spin structure functions of gluons with longitudinal spin. The gluon spin structure function, ΔG, can be determined crudely with inclusive jets, better with inclusive direct gammas, and best (with actual measurement of the x dependence) by using a direct gamma in coincidence with production of an away-side jet. A second clear category of physics to be done is the measurement of single-spin transverse asymmetries. These are variously described as twist-3, non-local, or orbital effects. In the past, the theoretical expectation was that such effects would disappear at high p_t. The fact that they have not vanished, but appear to remain constant at a given x_t up to Fermilab fixed-target energies, has stimulated much theoretical work and there is now great interest in doing such measurements at the higher energies available at RHIC, where it is unarguable that perturbative QCD should be fully applicable. STAR is in a unique position to measure jets in the relevant kinematic region, with full acceptance for parton scatters within $|\eta| < 0.3$ and p_t up to 50 GeV at $\sqrt{s} = 200$ GeV. In pp collisions, STAR can also measure the inclusive π^0 yield in the x_t region up to 0.4, and direct photons having $p_t \geq$ 2-3 GeV. The necessity of electromagnetic calorimetry for making the measurements of direct photons and π^0's is obvious, and is also essential to remove the energy fluctuations that would otherwise occur in measurement of jet properties. The x_t range that can be covered in measurements of γ-jet events can be considerably extended by the future addition of an end-cap EM calorimeter, and space is being reserved for this possibility.

4.I.2. Description of Subsystem

Conceptual Design of the STAR EMC

The barrel EM calorimeter, Figs. 4I-(4-6), is a lead-scintillator sampling calorimeter. It is located outside the superconducting solenoid coil and inside the iron flux return. It covers $|\eta| \leq 1.05$ and 2π in azimuth. At $\eta \sim 0$, the amount of material in front of the EMC is $\sim 1X_0$. The inner radius is 2.53 meters and the length is 6.87 meters. It consists of 60 wedge segments of 6 degrees in ϕ and is subdivided into 40 pseudo-projective towers over the η range. Each tower has 21 layers of lead and scintillator. Thus there are 50400 pieces of scintillator of 420 different shapes. Each scintillator tile will be read out with two wavelength shifting optical fibers which go to Hamamatsu R580 PMT's (Fig. 4I-7). In the phase I implementation, to reduce the cost, all the fibers from pairs of towers adjacent in η will go to one PMT. There will be 1200 PMT's and the effective tower size will be 0.105 x 0.105 ($\Delta\eta$, $\Delta\phi$), similar to many existing calorimeters used in studies of jets and direct photons in high energy physics. The physical construction permits various kinds of upgrades as increased funds become available for more PMT channels such as a two-fold increase in η segmentation, and flexible

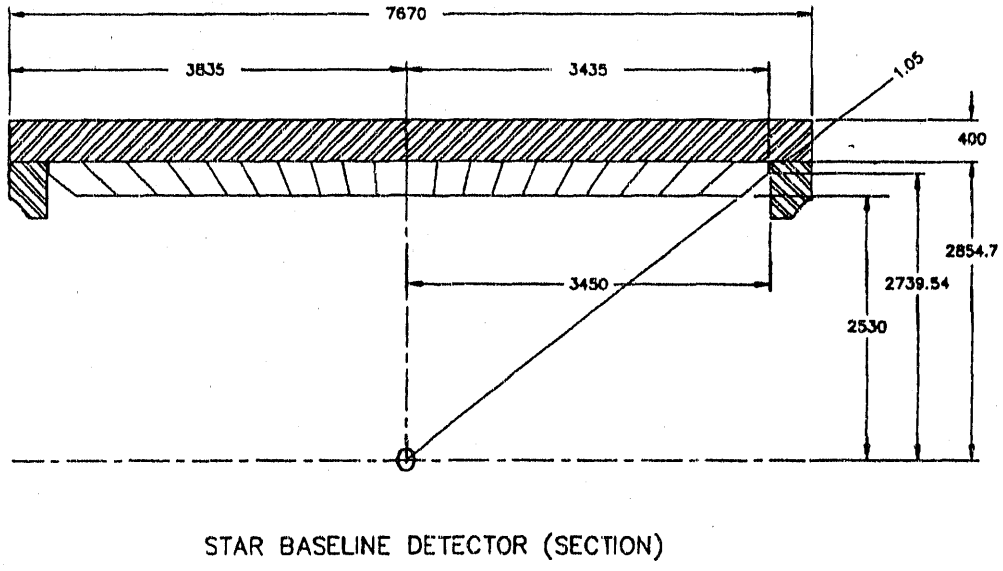

Figure 4I-4. A cross section of the STAR EMC barrel.

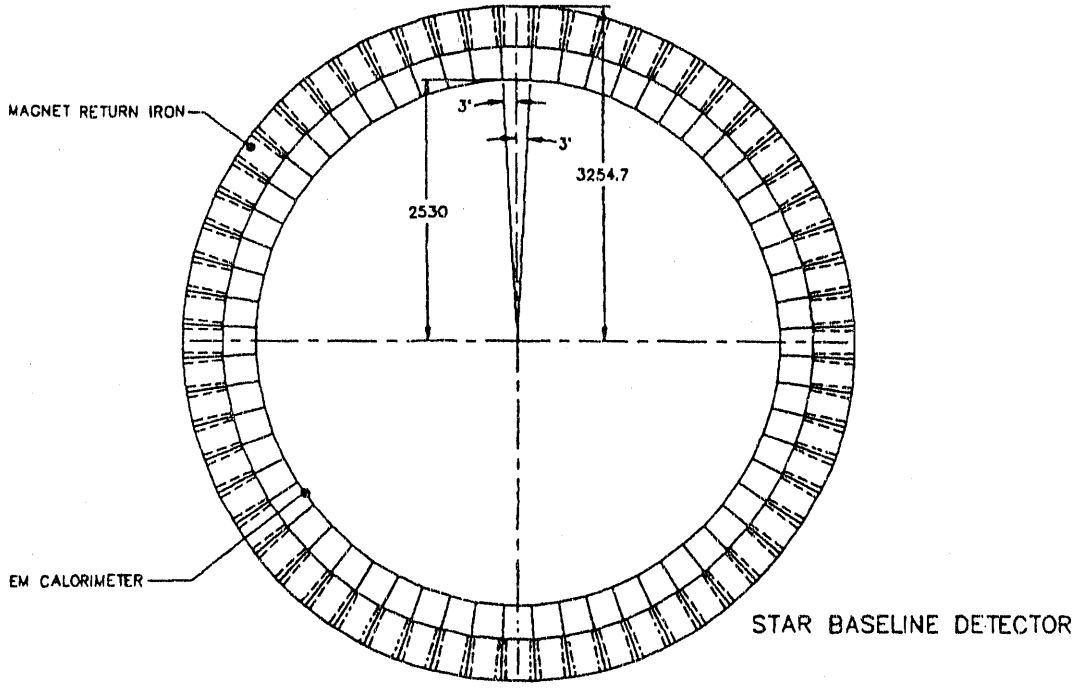

Figure 4I-5 An end view of the STAR EMC barrel. The EMC wedges are titled at an angle of 3° to eliminate projective cracks in the barrel.

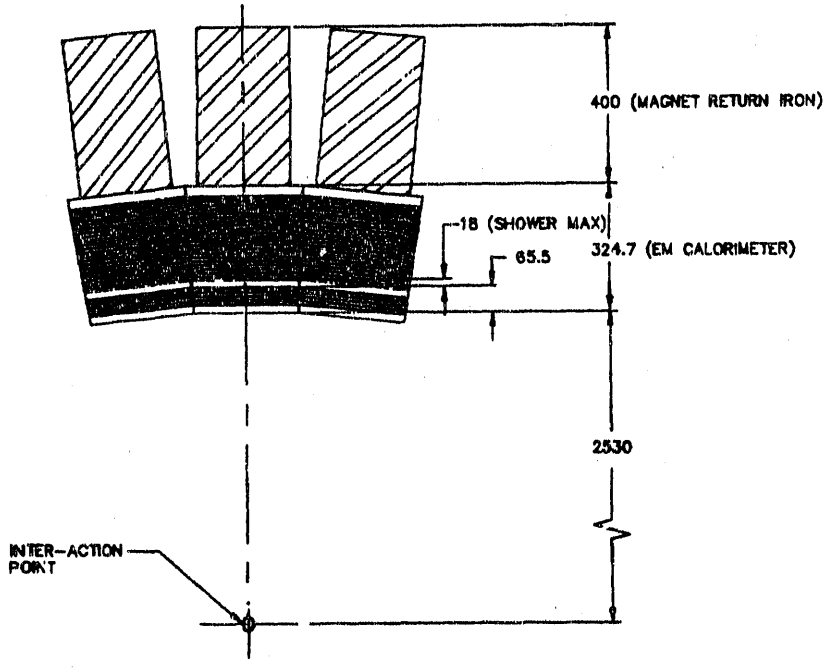

Figure 4I-6 A cross section of several of the EMC wedges mounted on the iron flux return bars. The shower max box is located at a depth of ~ $5X_0$.

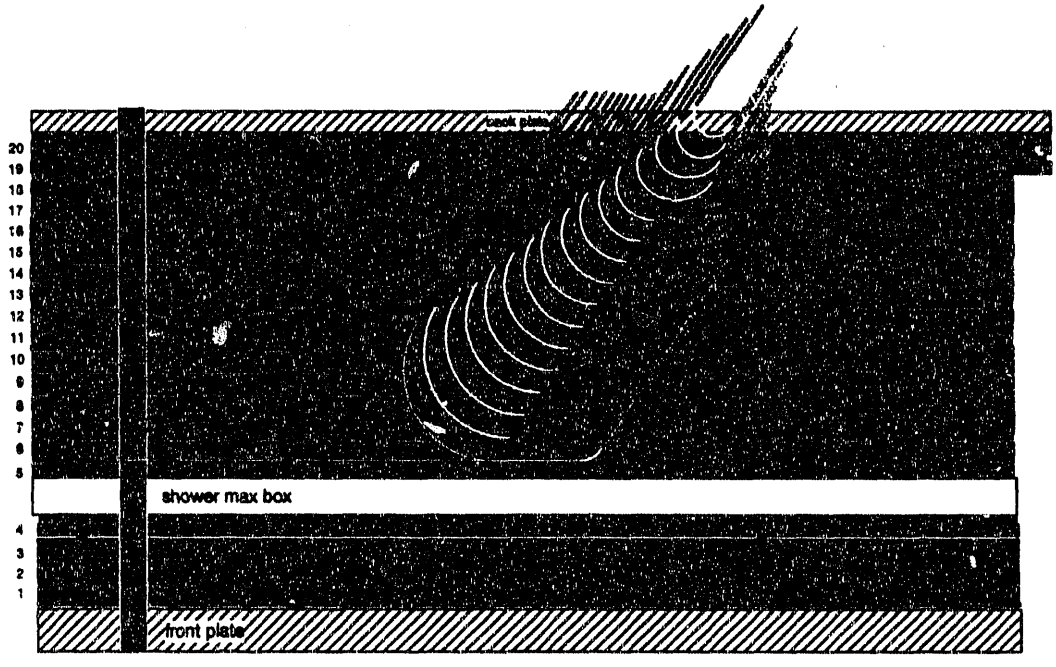

Figure 4I-7 A cross section of the lead-scintillator stack in one of the EMC wedges. Each η tower contains two scintillator tiles, each of which is read out by two WLS fibers.. The locations of the front plate, shower max box, compression strap, and strong-back support are also indicated.

depth segmentation to optimize the separation of hadronic and electromagnetic energy components.

The phase I calorimeter will also include a detector with higher granularity at ~ $5X_0$ to increase the two photon resolution of the EMC and thus, the ability of the detector to separate high energy direct photons from those coming from π^0 decays. The shower max detector that is planned is similar in design to prototypes that were made for ZEUS, CDF, and SDC (see for example Rainwater et al.[9]). It consists of scintillator strips approximately 1 cm in ϕ by 36 cm in η, located at a depth of ~ $5X_0$. Each strip is read out by a wavelength shifting fiber. The longitudinal dimension of the strips corresponds to the physical size of two η towers which facilitates bringing the fibers to the outside of the barrel. The construction of the strips is accomplished using a single piece of scintillator which is slotted. The scintillator itself is in the form of 1200 tiles which are approximately 27 cm in the ϕ direction by 28-45 cm in η. This technique minimizes the handling of small parts, and provides good alignment. The phase I shower max detector will therefore consist of 28800 scintillating strips fabricated from 1200 scintillator tiles, with 28800 WLS fibers aluminized on one end. The read-out for this detector, which could make use of multi-anode phototubes, will be added as an upgrade.

For calibration of the detector, small radioactive sources, such as Cesium 137, can be positioned accurately inside small steel tubes, typically 1 to 1.5 mm diameter. The positioning accuracy is very important since the energy deposited in a tile has a $1/r^2$ dependence as well as an exponential factor due to absorption of the gammas. There will be two source tubes in the η direction at the shower maximum depth in each wedge, approximately positioned at the center of the wedge in the ϕ direction. This will allow relative gain checks of the towers, and an absolute calibration if correlated to test beam calibrations. There will also be one source tube in the radial direction on each side of each tower of each wedge. This will allow monitoring of the depth response of towers and possibly be the only absolute calibration of each tower once the wedges are installed. The sources can be put in manually on the ends of wires or with a motorized driver system using flexible tubes which couple to the steel tubes. There are 2400 radial source tubes and 120 axial ones. Motorized source drivers will be permanently installed on the end of each wedge if there is space. Laser calibration of the EMC PMT's will be used to monitor gain stability. Distribution of the laser light will be accomplished using clear uv transmitting optic fiber.

The dynamic range required for the ADC's used to digitize the information from the calorimeter towers is determined by two general considerations. The maximum electromagnetic energy in a tower will be ~20 GeV. This corresponds to the maximum energy at which the yield of direct photons is still measurable. This energy is also approximately the same as that of leading particles or the electromagnetic component in the highest energy (~50 GeV) jets that will have measurable yields. At the low end, a minimum ionizing track traversing the entire calorimeter stack will deposit ~20 MeV (400 MeV electromagnetic equivalent). This signal must be observed above the pedestal, with some resolution, to account for tower energy sharing and for use in trackfinding at

[9] Rainwater et al., ZEUS Note AMZEUS No. 107, Oct. 25, 1991.

high luminosity where there are many out-of-time events in the TPC. Thus, the required range of the ADCs is approximately 12 bits in either a single device or in parallel devices with different gains. The dynamic range of the ADC's for the shower max scintillators is determined by the number of minimum ionizing tracks in a maximum energy shower at $5X_0$, about 100 at 35 GeV. If the pulse height from one track is to be a few counts above pedestal, the dynamic range required is roughly 500, or 9 bits.

The DAQ requirements for the EMC are somewhat different from those of the TPC or SVT. Because of the small number of channels (1200), the need to store the analog signals during the time required to make up a first level trigger will be addressed by cable delays. The digitizers will be commercially available Fastbus ADC's. Upgrades to the EMC detector, notably the 30k channels of shower max detector, will require a totally different approach to this problem based on analog pipelines implemented in custom chips.

The relevant design parameters of the STAR EMC barrel are summarized in Table 4I-1 below.

Table 4I-1 Calorimeter parameters.

Barrel Calorimeter type	21 X_0 lead-scintillator 'EM' section
Segmentation:	60 azimuthal sectors, $\Delta\phi = 0.105$ (6 °) 40 projective towers in $\lvert\eta\rvert < 1.05$, $\Delta\eta = 0.0525$
Inner radius:	2.53 m
Length:	6.87 m
Weight:	150 tons
Absorber: pieces:	5 mm lead (= 0.9 X_0) in 21 layers 21 x 60 pieces total, each ~ (25 x 650) cm^2
Scintillator: pieces:	3 mm plastic in 21 layers 60 x 21 x 40; pieces, 420 sizes each ~ (25 x 25) cm^2
Readout:	Waveshifting fiber (2/tile) to PMT
PMTs:	1200 (Phase I: 2 η towers/PMT)
Shower Max detector:	Scintillator strips parallel to η
Strip size: pieces:	1 cm x (25-45) cm 28800 total
Readout:	Waveshifting fiber (no PMTs in Phase I)

4.I.3. Capabilities of the STAR EMC

The performance goals for the STAR EMC can be described in terms of energy resolution, spatial resolution, and ability to separate EM from hadronic energy. Additionally, the response of the STAR EMC is constrained to be fast in order to provide a trigger for high p_t particles. Unlike similar devices currently planned or in use at other colliders, however, the STAR EMC is intended to provide both "soft"

nuclear physics and high p_t parton physics data. The implications for the design of this detector therefore vary, depending on which physics goals are discussed.

Full calorimetry in STAR is accomplished using a combination of TPC tracking and electromagnetic calorimetry. This question was studied by simulating jet events in pp collisions at $\sqrt{s_{nn}}$= 200 GeV using the HIJING generator, decaying all produced particles with lifetimes shorter than the K^o_L, and considering the energy produced in the form of photons, charged particles and hadrons (both charged and neutral). The effect of the STAR solenoidal field on the location of the energy deposited by the charged particles in the hadronic calorimeter was taken into account, and then the energies of the hadrons and photons were binned into an η-ϕ grid with bin sizes of 0.1 and 0.028, respectively. (These bins are much larger than necessary for the 'Tracking' and EM components, but are used for comparison with the bin sizes typical of collider calorimeters.) The resulting binned energies were folded with resolutions of $0.40/\sqrt{E}$ for the hadron calorimeter, and $0.22/\sqrt{E}$ for the EM calorimeter. The spatial resolution, momentum resolution, and reconstruction efficiency of the tracking system were assumed to be perfect. An implementation of the CDF cluster-finding algorithm was then applied to the binned data sets and, for each found cluster, E_t was summed within $R = \sqrt{(\Delta\eta^2 + \Delta\phi^2)} \leq 0.7$ for both the [EM + hadronic] and [EM + Tracking] data sets. A grand sum over all clusters found in each event was then made in both cases. The mean detected jet energies and fractional RMS widths for these data are listed in the table below.

E_t (jet)	20 GeV/c	40 GeV/c	80 GeV/c
EM + Hadronic			
mean detected	13.77	29.70	65.32
detected/generated	0.83	0.65	0.65
RMS width	6.60	9.59	13.99
% RMS width	40	24	14.5
EM + Tracking			
mean detected	13.98	26.79	59.01
detected/generated	0.81	0.76	0.79
RMS width	5.21	8.49	13.50
% RMS width	32	25	17

The energy resolutions in [EM + Tracking] are not appreciably worse than those in [EM + Hadronic] for the higher p_t jets, and are even somewhat better for the lowest p_t, presumably because of the rapidly decreasing hadronic calorimeter resolution.

Further results of this study are presented in Figs. 4I-(8-9), where the energy of clusters found using the CDF style cluster finding algorithm in 40 GeV pp jet events is compared for (EM plus tracking) and (EM plus hadronic) calorimetry on an event by event basis. The primary losses in the former technique are a consequence of transverse energy carried by neutrons and K^o_L mesons which are detected with low probability in

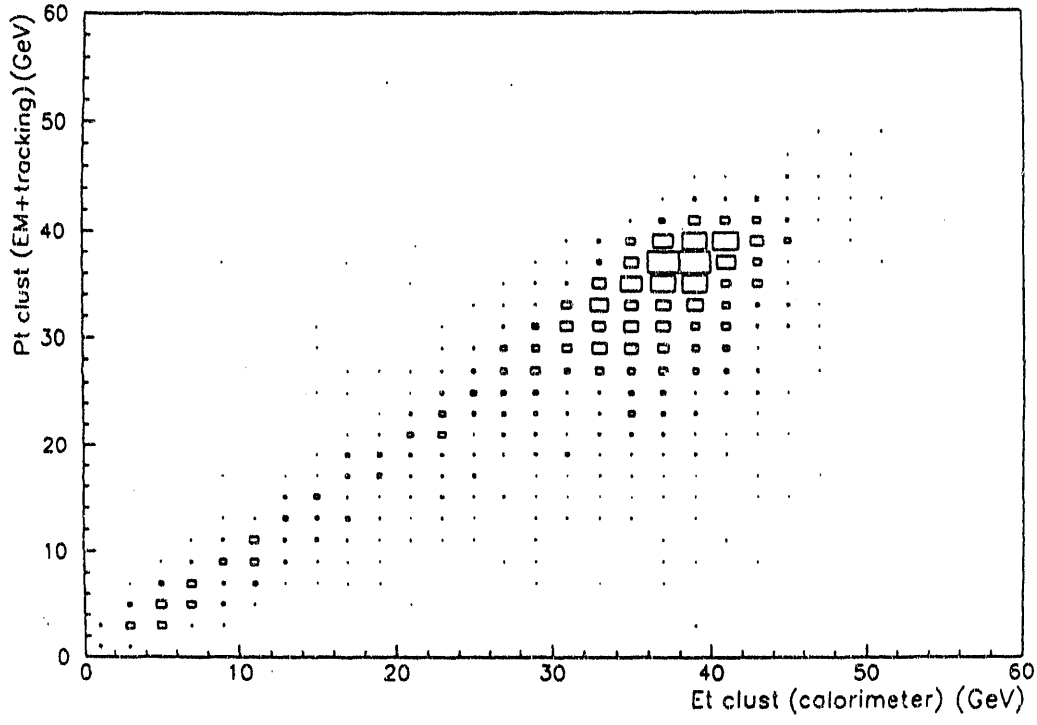

Figure 4I-8 A scatterplot of the energy of clusters found using electromagnetic energy from the STAR EMC plus tracking and momentum information from the TPC versus EM plus hadronic calorimetry, Data shown are for 40 GeV jet events from pp collisions at $\sqrt{s}$ = 200 GeV. The asymmetry in the distribution is due primarily to the transverse energy of neutrons and K°_{L} mesons which are detected using EM plus hadronic calorimetry but are detected in the EMC alone with low probability.

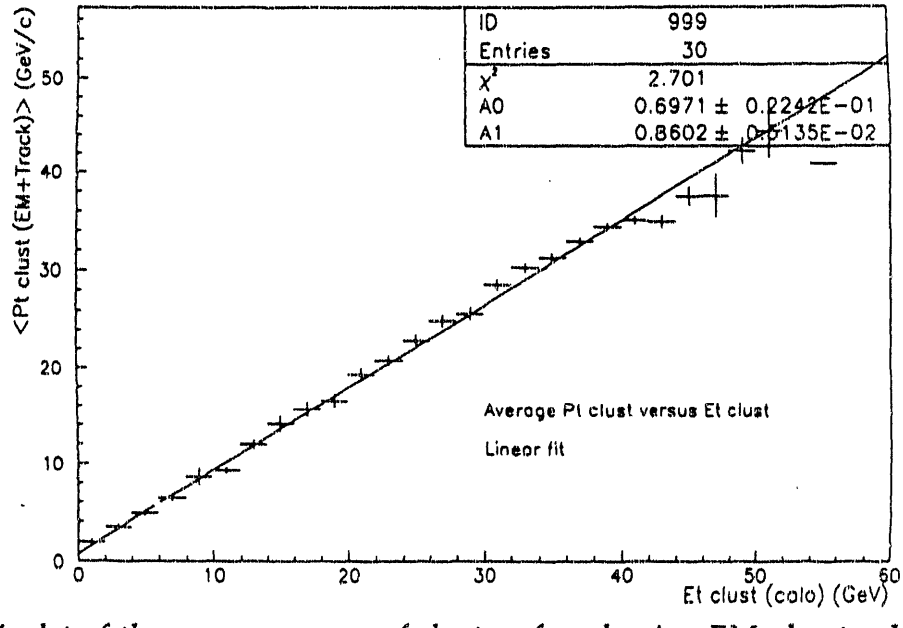

Figure 4I-9 A plot of the average energy of clusters found using EM plus tracking versus the average energy found using EM plus hadronic calorimetry for 40 GeV jet events from pp collisions at $\sqrt{s}$ = 200 GeV.

the EMC section. There is a clear correspondence between the energy of clusters found using these two techniques, which is further evident in Figs. 4I-(10-11), in which slices in energy on the (EMC plus hadronic) calorimetry axis have been projected on to the (EMC plus tracking) axis. There are also data from a recent experiment at KEK which support the feasibility of studying jets and direct photons using tracking and electromagnetic calorimetry.[10]

For nucleus-nucleus collisions, it is also envisioned the EM plus tracking technique will be used, both for high p_t and soft physics studies. For the latter, accurate measurement of the local transverse energy flow ($d^2E_t/d\eta d\phi$) is complicated by the fact that the response of the EMC to low energy hadrons entering the detector is subject to fluctuations, despite the information available from the TPC tracking. Correction of the measured energy flow will require careful test beam calibrations, to document the response to low energy hadrons, and will, in any event, be subject to a loss of resolution due this effect.

An important question in the study of jets and direct photons in both pp and AA reactions is the ability of the STAR EMC to trigger efficiently on events containing hard parton scatters, while rejecting minimum bias events. This is particularly important in

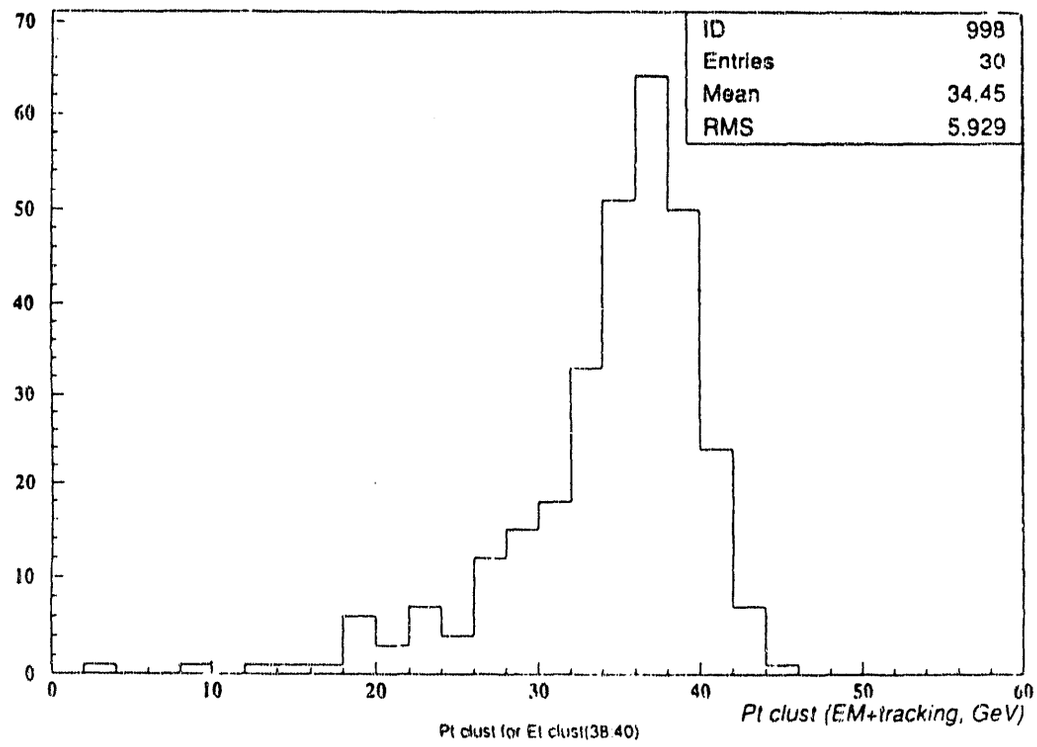

Figure 4I-10 A projection on the EM plus tracking axis of a slice of the EM plus hadronic calorimetry axis from 38 to 40 GeV.

[10] Y. Kim, University of Rochester Report UR-1182; I. H. Park, Ph.D. dissertation, Rutgers University 1989, unpublished.

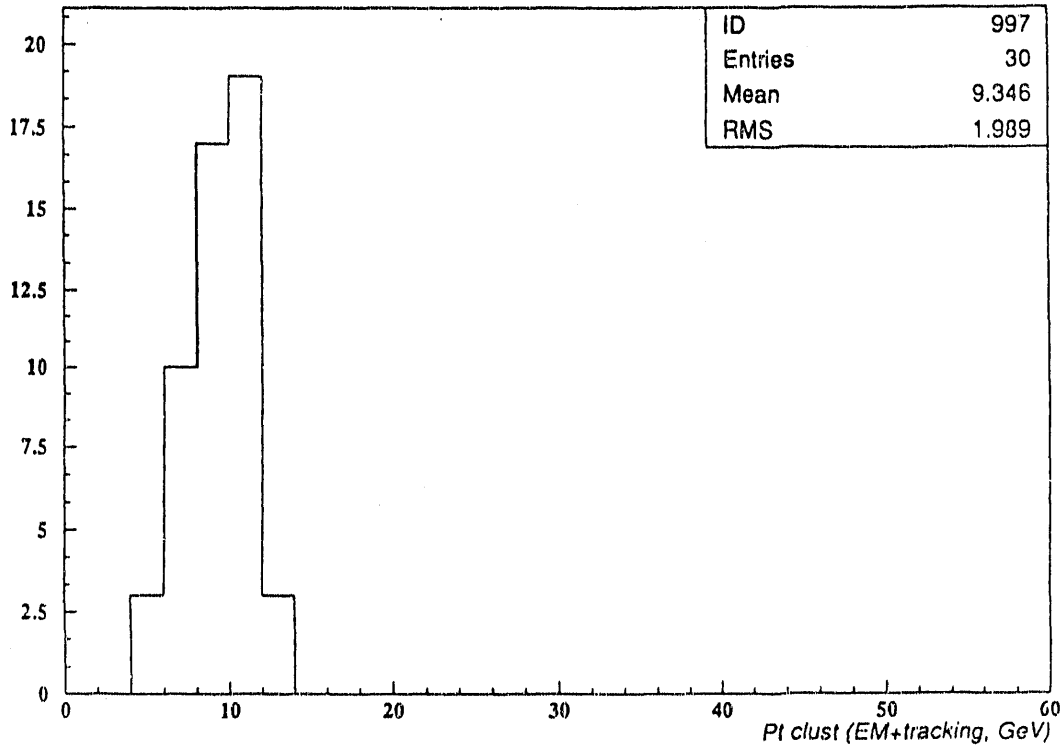

Figure 4I-11 A projection on the EM plus tracking axis of a slice of the EM plus hadronic calorimetry axis from 10 to 12 GeV.

pp studies where the design luminosity for $\sqrt{s}$ =200 yields approximately $2 \cdot 10^6$ minimum bias events per second. The results of a study to examine the efficiency of a calorimeter trigger based on discriminating energy on a tower by tower basis are presented in Fig. 4I-12 for pp collisions. From the data presented, it is evident that for a discrimination threshold of 3 GeV, the trigger efficiency for jets having transverse momenta of 10 GeV for example is ~ 10%. The trigger rate for this threshold is approximately 10 per second (Fig. 4I-13). Consequently, the rate of 10 GeV jet events logged is predicted to be ~ 1 per second.

The corresponding plots for AuAu collisions are presented in Figs. 4I-14 and 4I-15. In this case the trigger thresholds have been increased to account for the increased average E_t deposited in the towers by the large number of secondaries produced in AuAu collisions. Despite this increase, the selectivity of the trigger for events containing a hard parton scatter below $p_t \leq 20$ GeV is considerably worse. This is a consequence of the fact that the observation, for example, of an energy deposition of 7 GeV in a given tower is not as strongly correlated with the presence of a jet in this environment. The efficiency at this threshold for selecting events containing jets of 10 GeV is nevertheless higher than in pp collisions. This is because the number of 10 GeV jets produced in central AuAu collisions is greatly increased, and there is therefore an increased probability of accepting such an event by random chance. Further simulation is necessary to determine if an more selective trigger can be devised. The trigger rate for

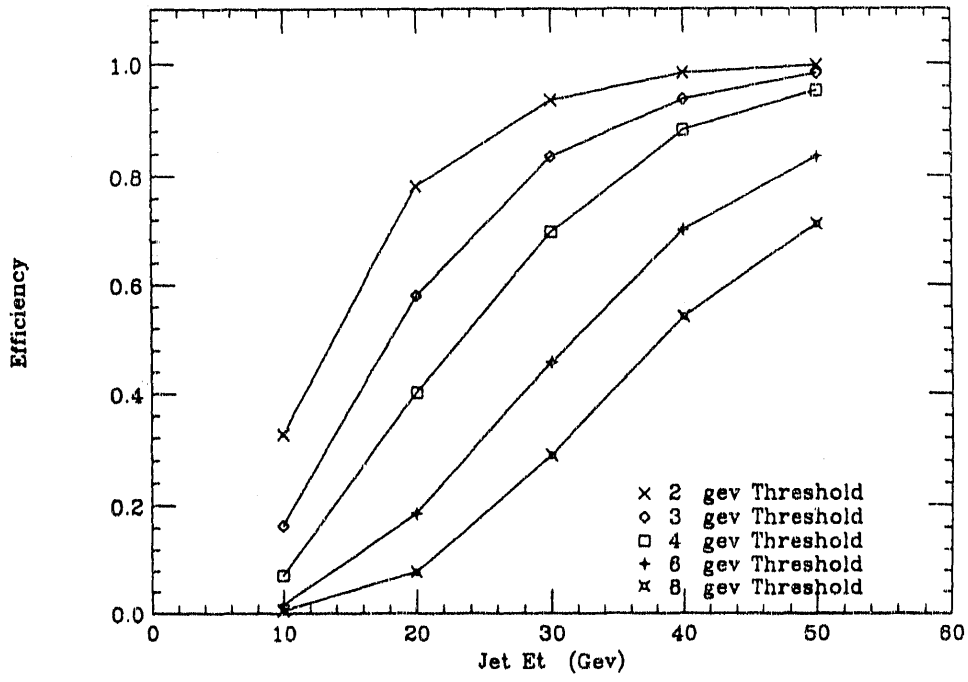

Figure 4I-12 The efficiency as a function of jet energy for triggering on an event containing a jet, for a given single tower discrimination threshold. Data shown are for pp collisions at $\sqrt{s}$ = 200 GeV.

AuAu events containing a parton scatter with a p_t of 10 GeV or more is approximately 1 per second which is well within the STAR capability. This is a consequence primarily of the reduced luminosity for Au. It is noted with regard to triggering, that the STAR EMC is presently the only detector in the STAR Phase I capable of triggering on high p_t particles.

A related question is the ability of the TPC to track in the high luminosity pp environment. For the RHIC design luminosity of ~ $1.4 \cdot 10^{31}$ cm^{-2} sec^{-1} the number of minimum bias events which occur within ± 40 μsec of a triggered event in the TPC is ~60. Recent simulations (c.f. section 4.C.3.I) to examine the response of the TPC under these conditions indicate that identification of the proper vertex for the triggered event in the presence of other events which both precede and follow the triggered event is not a problem. The corresponding track reconstruction efficiency is also good. Given the average multiplicity of secondaries produced in minimum bias pp collisions, and the number of tracks produced in central AuAu collisions, it is anticipated that the STAR TPC will accommodate at least a factor of 10 increase in the pp luminosity.

Another important consideration, which bears on the capability of the STAR EMC to detect direct photons, is the ability of the EMC to discriminate against π^0 photons which are close together. This discrimination can in principle be performed either on a statistical basis, using a pre-shower detector ~ 2 X_0 thick in front of the calorimeter, or by measuring the shower shape and therefore the two γ separation on an

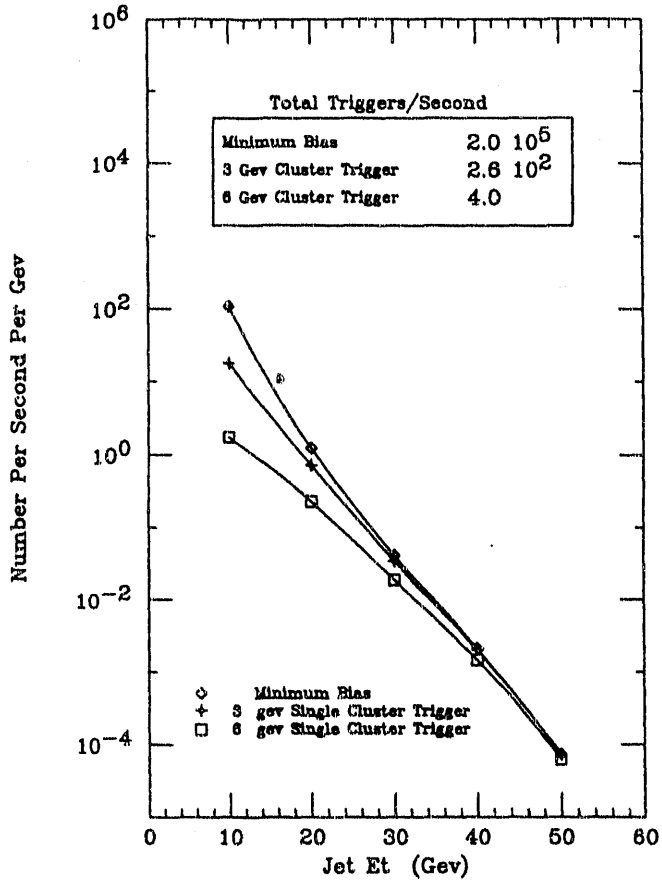

Figure 4I-13 The rate per second per GeV of events containing jets of a given E_t for various single tower discrimination thresholds. Data shown are for pp collisions at $\sqrt{s}$ = 200 GeV ($|\eta| < 1.05$).

event by event basis with a 'shower max' detector. Simulations[11] have shown the latter method is superior given the STAR geometry, and results in a much higher sensitivity to the spin dependent scattering asymmetries of interest in the STAR polarized pp physics program (Fig. 4I-16).

The limiting resolution of a sampling EM calorimeter depends on the frequency of sampling. This resolution has been parameterized as shown in Fig. 4I-17. The choice of 5 mm thick lead (0.9 X_0) and 3 to 4 mm scintillator (0.01 X_0) will provide approximately $\Delta E/E = 20\%/\sqrt{E}$. This resolution is adequate for direct gamma and jet physics above p_t of 10 GeV/c, based on experience from previous collider detectors which have successfully studied similar physics. Other limiting factors in jet resolution come from the TPC resolution ($\Delta p/p \sim 1.5$ % at high momentum) , and from missing neutrals such as K^0_L's, Λ^0's, and neutrons . The sampling depth of 19 X_0 is adequate based on experience with 19 X_0 lead glass at FNAL and from EGS calculations done for other experiments. Contributions to the resolution from fluctuations in energy loss through the back of the calorimeter are expected to be negligible below 50 GeV/c. The

[11] M. Beddo, et al., Argonne National Lab, private communication.

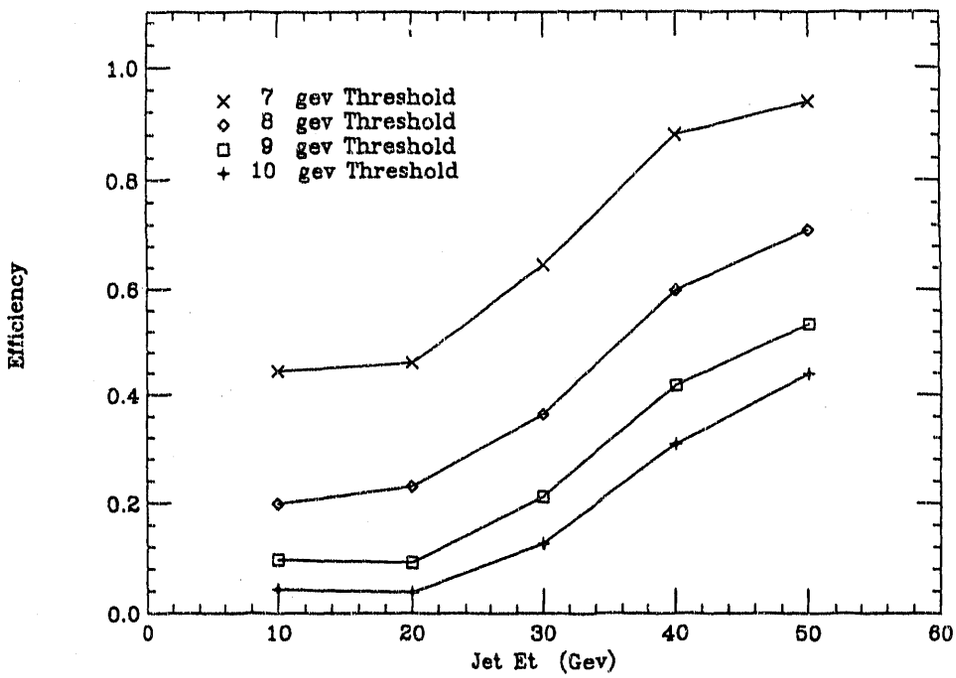

Figure 4I-14 The efficiency as a function of jet energy for triggering on an event containing a jet, for a given single tower discrimination threshold. Data shown are for AuAu collisions at $\sqrt{s_{nn}}$= 200 GeV.

coupling scheme between the scintillator and fiber has been shown to give 2-4 photo-electrons/MIP and does not contribute significantly to the overall stochastic resolution.

Tile-to-tile or tower-to-tower variations in response lead to degraded resolution as an energy independent term and can also lead to poor trigger selectivity (hot-spots). These effects can be controlled by proper calibration procedures before, during and after assembly of the detector.

Trigger capability for both total summed energy and local energy, (2x2 and 3x3 clusters of towers for gammas, π^0's and jets) will be provided with buffered electronics similar to that in the ZEUS experiment.

4.I.4. R&D Issues and Technology Choices

Basic areas where R&D is required for the STAR EMC include specification of the mechanical structure of the lead-scintillator stack, determination of the optimal technique for waveshifter readout of the sampling scintillator tiles, the choice of photomultiplier tube, and the design and fabrication of the shower max detector. Additionally, it is of particular interest to investigate design options which enhance the linearity of the calorimeter response to low energy hadrons. These areas have recently been under study for ZEUS, SDC, and the CDF endcap upgrade, and much information is already available. However, the detailed requirements for the STAR EMC are specific to this project, and somewhat different solutions must be investigated to determine where cost savings may be achieved.

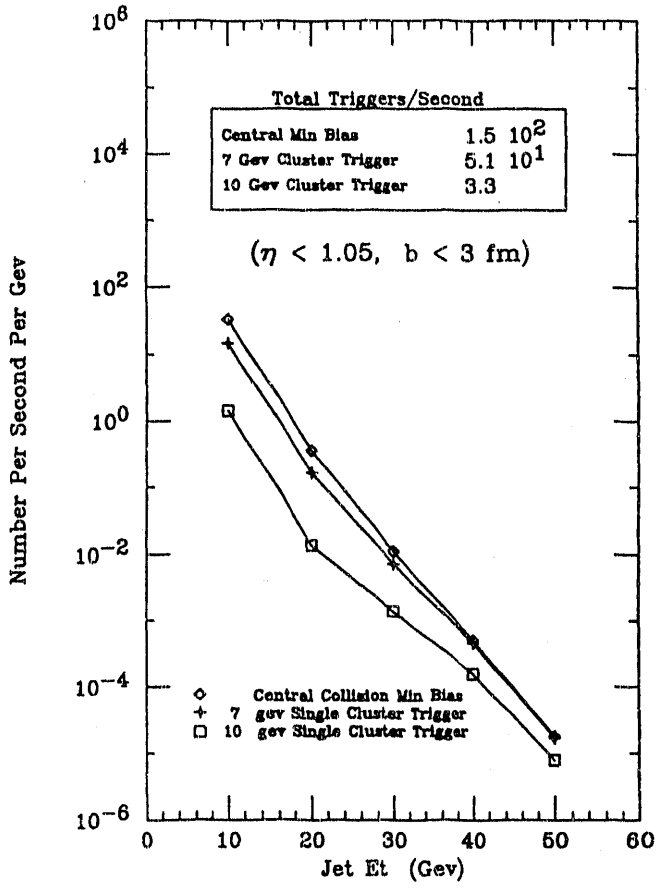

Figure 4I-15 The rate per second per GeV of events containing jets of a given E_t for various single tower discrimination thresholds. Data shown are for AuAu collisions at $\sqrt{s_{nn}}$ = 200 GeV.

Several important considerations enter into the mechanical structure of the EMC. One option, which requires the most R&D, but could lead to significant cost savings, is to stack the lead and scintillator without spacers so the pressure is evenly distributed over the scintillator. The pressure on the scintillator due to the weight of the stack is ~15 psi in this instance, similar to that in the CDF barrel calorimeter. Unlike CDF however, a difficulty arises due to the additional compression loading necessary to keep the stack mechanically stable. Concern over the possible long term crazing of the scintillator in this instance has lead to the initiation of pressure tests in which the light output of a number of scintillator tiles containing embedded WLS fibers was monitored as a function of pressure. It was found, for example, that at 100 psi the light output from the tiles decreased by ~8%, although it returned to its initial value when the pressure was once again reduced to zero. This observation suggests a lack of irreversible damage due to crazing at this pressure, although further study is clearly needed to determine the long term effects of pressure on the scintillator tiles.

A second option is to again stack alternating layers of lead and scintillator, but to separate consecutive layers of lead absorber with small I-beam shaped spacers having a web of ~3mm. The scintillator tiles forming the towers fit between the spacers and do not experience any load due either to the weight or the compression loading of the stack. They are held in place by soft foam. In this instance however, the pressure on the

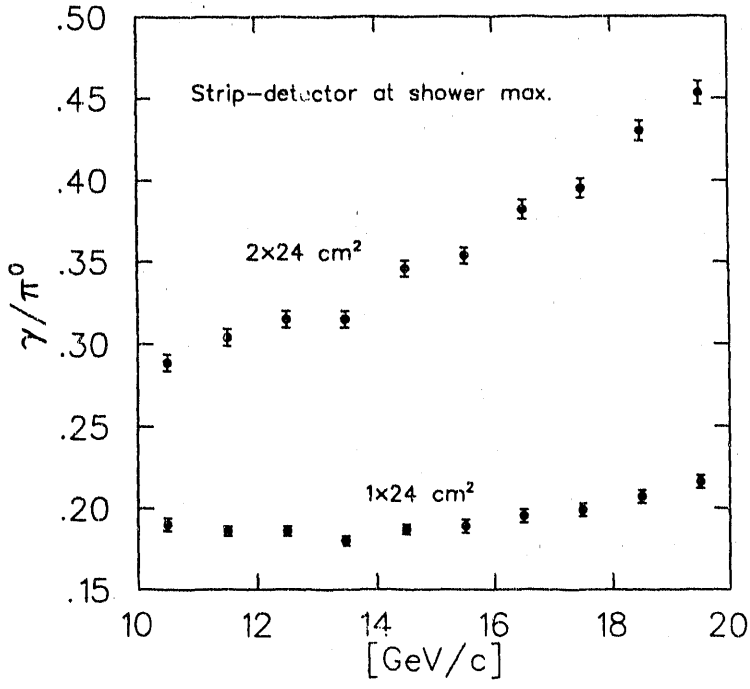

Figure 4I-16 Ratio of 'fake' γto π° yields for model strip detectors placed at shower maximum in the EM calorimeter.

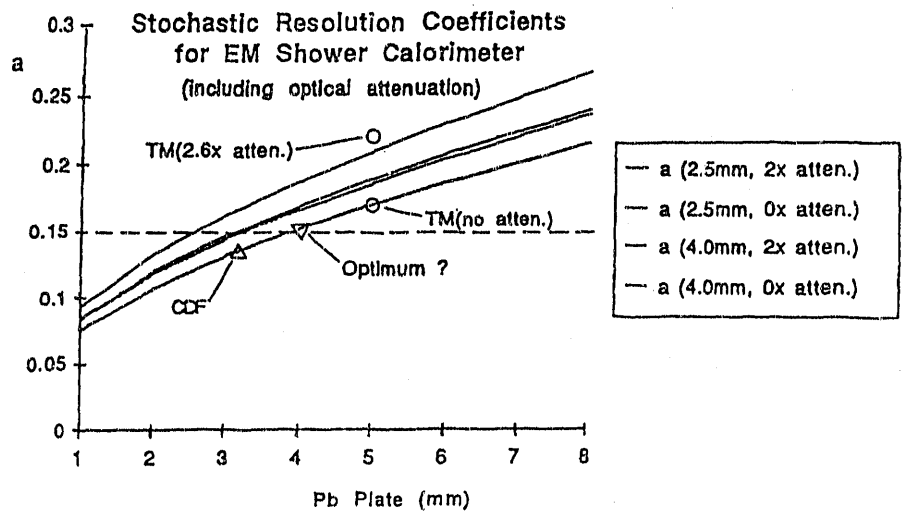

Figure 4I-17 Scaling of the stochastic term in EM shower counter geometries and comparison to the ANL/WSTC Test Module and CDF shower counters.

spacers is ~2000 psi which leads to a potential difficulty with "coining" (i.e. point deformation) of the lead, despite the fact that the lead alloy used contains small concentrations of calcium and tin to improve its structural integrity. Tests are presently being conducted to determine the compression loading necessary given the measured

coefficient of friction. Additional tests will indicate the extent of the coining of the lead which occurs when the lead experiences the proper load while in contact with the spacers. It is noted that this stacking technique was successfully used for the ZEUS barrel calorimeter. In this instance however, the absorber plates were fabricated from billets of depleted uranium, which is both stiffer and more expensive than the lead absorber contemplated for the STAR EMC. One potential solution to the problem of coining is to clad the lead with thin (.015") sheets of stainless steel bonded to both sides of the absorber plates. This possibility is presently being investigated.

A second difficulty with this stacking technique arises from the positioning of the I-beam spacers. Ideally they are placed along the boundaries of towers so as not to conflict with the segmenting of the scintillator tiles. Since the spacers at different radial depths are not located at the same longitudinal location however, there are bending moments in the stack which tend to deform the layers locally in the vicinity of the spacers. The influence of this effect, as well as the ability of the stainless steel cladding to resist it are currently under investigation.

A cast-lead structure with internal steel membranes cast inside the lead is a known solution to the structural problems discussed above. This option reflects the technology of choice for SDC and has been studied in some detail. Many finite-element stress-studies have been done, and two prototype calorimeters have been built and studied under test beam conditions. The documentation of costs has also been done in great detail.

For STAR, the choice of a cast lead option would require building the barrel calorimeter in two segments longitudinally, and would potentially increase the cost of the mechanical structure by ~10%. The precise increase in cost is difficult to determine since the costs of the other options are not as well documented. Choice of a cast lead option also has potential consequences for the project schedule, since casting the lead absorber structure is a critical path item, subject to delays surrounding the casting procedure and the availability of multiple molds.

One uncertainty in the optical design is related to the option of stacked lead with pressure on the scintillator. The current solution involves wrapping the scintillator with aluminized mylar and making the wrapping function as a focusing element in coupling light to the waveshifter fibers. With pressure on the stack, the mylar might optically "wet" the surface and cause loss of light in an unpredictable manner. A study of the potential difficulties due to this effect has begun, as well as a search to identify other materials which would not wet the surface of the scintillator under these conditions. It has already been found that acid-free typing paper functions reasonably well in not wetting the surface and in protecting the scintillator at 100 psi.

The type of waveshifter readout and the overall optical system will also be investigated. Several options for the waveshifter readout are under consideration. The favored option involves the coupling of a WLS fiber to both longitudinal edges of each scintillator tile. The fibers are 1 mm in diameter, about 2.0 meters long, and aluminized on one end. Facilities for aluminizing the fiber ends must be found and the method improved. Ways to protect the aluminum coating from mechanical abrasion must also be found. Krylon spray has been suggested. The fiber material may be Bicron BCF-91A,

which has the shifter dye K27 and is similar to the Kuraray fiber with Y7 shifter. Its effectively shifts the light from approximately 440 nm to 550 nm. It must also be determined whether the fibers must cover the full length of the edge of the scintillator or if partial coverage will give an adequate number of photoelectrons. If partial coverage would suffice, the fiber routing might be re-arranged to eliminate fiber crossings and reduce the gap between calorimeter wedges. In the present design, the routing of the fibers on the face of the calorimeter wedges requires 2 mm of space plus tolerance on each side of the calorimeter stack. This will require mapping the tile response for various fiber configurations. At the same time, the uniformity of tile response can be checked and correction masks developed if necessary.

A related question is the attachment of the WLS fibers to the PMT readout devices. Careful design of the optical coupling will facilitate future upgrades, making it possible to further segment the towers in both the η and longitudinal directions by running groups of fibers to different phototubes. A simple method is to glue the fibers initially to a light mixing cookie. For future upgrades, the fibers can then be cut off, and the ends resurfaced with razor blade trimming before gluing them onto another cookie. There will be 100800 fibers to resurface if this method is chosen. Another possibility which has been adopted in principal for SDC, is to segment the cookies initially so that the segments from an entire tower fit onto one large (1.5") or several small (.75") phototubes. The mapping of the cookies can then be rearranged as necessary for subsequent applications. For this method however, the optimum segmentation must be known beforehand.

R&D testing is also required for the multi-channel phototubes potentially used to read out the shower max detector. This method of readout is being contemplated as a possible means of reducing the cost, given the relatively large number (~30k) of channels required for this device. If these phototubes are shown to have low cross talk, and sufficient linearity, they might also be used in the main calorimeter to reduce the cost as well.

Finally, as a means to study all the potential R&D issues associated with construction of the STAR EMC, a small lead-scintillator stack of full calorimeter depth will be built. This prototype will be constructed of typical materials including scintillator, aluminized mylar, and lead. It will be mounted in cantilevered position, and subjected to typical loads and accelerations. Additionally, it will be transported to an accelerator and tested for its response to low energy hadrons. It is thought this prototype can be constructed quickly and cheaply to give guidance before a cast lead SDC prototype module becomes available for additional testing.

4.I.5. Engineering

4.I.5.a. Technical Description & Specifications

The barrel EM calorimeter is a lead-scintillator sampling calorimeter. It is outside the superconducting solenoid coil and inside the iron flux return. It covers ±1.05 in rapidity and the full 2π in ϕ. The inner radius is 2.53 meters and the length is 6.87 meters. It consists of 60 wedge segments of 6 degrees in ϕ and is subdivided into 20

projective towers over the η range. The physical construction will allow easy upgrade to 40 segments in η with the addition of twice as many photomultiplier tubes (PMTs). It can also be segmented in depth in an arbitrary way with the addition of more photomultiplier tubes. The scintillator tiles will be read out with waveshifting optical fibers which go to photomultiplier tubes. The tubes are on the outside of the iron flux return bars. There are 42 scintillator tiles per tower arranged in 21 layers. The total number of scintillator tiles is 50400. The present design includes 100800 optical fibers, two fibers per scintillator, and 1200 phototubes. There are 20 lead absorber plates per ϕ wedge. Each wedge weighs 2.2 tons and is attached to a flux return bar which weighs 5.5 tons. A shower maximum detector will be built into each wedge at a depth of 5 X_0. It consists of thin strips of scintillation plastic with optical waveshifter fibers going to the outside of the iron flux return bars. There will be 28800 fibers. The shower max detector for each of the 1200 towers will be contained in a thin-walled box for the case of stacked lead plate construction. Multi-channel phototubes to readout the shower max detectors are being considered as an upgrade option.

Another future option is an EM end cap calorimeter inside the iron pole piece. It would cover $1.05 \leq |\eta| \leq 2.0$. The desire to measure direct photons in this acceptance would require a shower max detector in the endcap calorimeter as well.

4.I.5.b. Description of Major Components

Lead Plate Mechanical Structure

The absorber plates for the STAR EMC are continuous sheets of "calcium-tin" lead approximately 6.3 meters long at the inner face of each "wedge". The absorber sheets at the outer face are 6.87 meters in length. This distance is shorter than that between iron pole pieces by ~1.5 cm on each end to provide clearance for optical fibers from the shower max detector and the drive mechanism for the radioactive calibration sources. The present design uses 5 mm thick lead plates with 0.38 mm (.015") steel bonded on both surfaces.

The present plan is to hold each wedge together by compression and friction. using a rigid faceplate and strong-back support. The inner face plate of each calorimeter wedge is 26.5 cm wide. Metal spacers of I-beam shape are located between the lead absorber plates at each scintillator tile boundary in order to avoid any pressure on the scintillator itself. Since the spacers are aligned along lines of constant η, there are bending moments on the plates. The purpose of the bonded stainless steel is to prevent excessive bending which might lead to mechanical instabilities. The calorimeter wedges will be attached to the inside surface of the iron flux return bars. The stiffness of the bars may be required to prevent bending of the calorimeter structure.

Optical System

The scintillator tiles are arranged in 21 layers in each tower. They are separated by pseudo-rapidity boundaries which are integer multiples of $\Delta\eta = .0525$ which is half the distance corresponding to the tower boundaries ($\Delta\eta = .105$). In the start-up configuration, each pair of tiles within a given layer in a given tower will have the same readout PMT. The light output will also be summed over tiles at all depths in each

projective tower. The smallest tiles are about 266 mm in the ϕ direction and 136 mm in the η direction. The largest are 285 mm in ϕ and 220 mm in η.

The favored option for optical readout is to use a waveshifting fiber on each of the two η edges of each scintillator tile. The fibers are 1 mm in diameter, ~2.0 meters long, and are aluminized on one end. One method to couple the fiber to the scintillator by wrapping them both tightly in aluminized mylar has been prototyped and has demonstrated uniform light collection.

The shower maximum detector is within the EM calorimeter, located at ~5 X_0. It consists of scintillator strips approximately 1 cm in ϕ by 36 cm in η. The strips are constructed from 1200 scintillator plates having approximate dimensions of 27 cm in ϕ by 28 -45 cm in η. Each scintillator plate is formed into 24 shower max strips by cutting partially through the scintillator. This technique minimizes handling of small parts and provides good alignment.

4.I.5.c. Initial Assembly & Alignment

The gap between adjacent ϕ wedges of the calorimeter modules is ~1 mm and the tolerance is (+ 1 - 0) mm. The wedges are 6.87 meters long, and 8 tons in weight, including the weight of the iron flux return bar. The outside surface is a thin aluminum covering which serves both to light tight the calorimeter sectors and protect the delicate fiber optics used for optical readout. The alignment of the wedges is provided by either the iron pole piece or the sides of the flux bars themselves. The precise means of alignment is under study.

During construction of the wedges, the shape and size of each wedge must be controlled to better than 1 mm tolerance. This can be accomplished with a jig during stacking. The calorimeter wedges must also be aligned with respect to the iron flux bars, both in the η and ϕ directions. The flux bars provide the alignment of the calorimeter segments both with respect to each other and with respect to the rest of the detector. It is presently assumed that nothing else is supported by the flux bars, so that they can be removed one at a time for repairs or installation. Removal of the wedges at the bottom of the detector may require a special fixture due to constraints resulting from their proximity to the floor of the experimental hall.

4.I.5.d. Engineering Testing

Engineering testing is needed both to make a technology choice for the design for the lead plate structure and to evaluate a full scale version of the design chosen. There are two basic options for the lead plate structure. These involve either casting the lead structure of a wedge as one piece or building it up of stacked plates. There is a further choice within the stacked version of using spacers or allowing the scintillator to be compressed. The version which is costed is quite similar to the ZEUS calorimeter. In this version the plates are separated by metal spacers and held in place by compression on the entire stack. There is no mechanical pressure on the scintillator. To evaluate this option, tests will be required on the uniformity and flatness of the plate dimensions in order to meet the stated tolerances between wedges. The cost of the stacked lead option would be reduced if the use of spacers were not necessary. However, there are presently

several uncertainties in such a design. A major concern is that the amount of pressure which would damage the scintillator over an extended period is not well known.

Another area which requires engineering testing is the design of the shower max support box. It will have to support over 4000 lbs in each wedge, and must be designed with as few inner structural members as possible. The inner structures must also be as thin as possible to minimize dead areas in the detector.

After a technology choice is made for the mechanical structure of the calorimeter wedges, a full size wedge with active scintillator in a small fraction of the towers will be built. It will then be necessary to test this prototype for deflections and the effect of deflections on light output for various orientations of the wedge. The module will then be shipped from the location where it was assembled to BNL to check whether it is possible to maintain structural integrity under shipping conditions. In the instance that the stacked option is chosen the compression of the stack would be rechecked. The light output from the active towers would also be rechecked under test beam conditions. The module would then be shipped back to the location where it was assembled, where a "post-mortem" would be performed. It would once again be checked for light output, and then disassembled to search for evidence of unanticipated mechanical stress.

Finally, if the wedge modules are constructed at a site other than Brookhaven, several modules will be assembled into a portion of the barrel. This will test for possible tolerance problems or other unforeseen difficulties encountered with assembly of the full barrel calorimeter.

4.I.5.e. Transportation, Reassembly & Alignment at RHIC

It is likely that the calorimeter wedges will require the attachment of the iron flux return bars for structural strength. For this reason, it is anticipated that each will be shipped as a single unit, with the wedge structure either up or down and the iron flux return bar held in a shipping fixture. The iron bars are ~ 7m long. The bars weigh 5.5 tons and the calorimeter wedges weigh 2.2 tons. The optical readout fibers will have to be protected very well. This may require that the wedges have the fibers put into final position into the phototube cookies after shipment The phototubes will be shipped separately and then be re-attached. It is not known at present where the wedges will be assembled.

The wedges at the bottom of the barrel will be installed early in the process of assembling the whole STAR detector. They will be the "floor" during installation of the magnet coil and TPC, and some protection will therefore be required.

The installation of the calorimeter wedges will be a delicate operation. The outer faces will have a thin aluminum covering over delicate fiber optics. While final alignment may depend on the placement of pins and bolts between the pole piece and the bars, some additional structure will also be needed during installation. The options being considered are guides attached to the pole pieces or bearing plates attached to the sides of the flux bars.

4.I.6. Testing and Calibration Issues

Test

To understand the response of the STAR EMC in nucleus-nucleus collisions, it will be necessary to calibrate its response to low energy hadrons in a test beam. Although there are CERN data[6] down to 200 MeV which can serve as a guide, in general the response of sampling calorimeters to hadrons of this energy is not well studied. Further testing will be required to determine if the longitudinal profile of the energy deposition for low energy hadrons can be used to help discriminate between electromagnetic and hadronic energy in this range.

Funding for construction of two STAR prototype calorimeter segments has been requested from RHIC R & D funds. These modules will consist of two wedges of two towers each, one near $\eta = 0$ and one near $\eta = 1.05$. These will be used for studies of resolution, electromagnetic and hadronic response, response uniformity and the effects of boundary gaps. A single tower prototype will also be constructed on a shorter time scale to study these issues quickly, and indicate where modifications to the calorimeter and to the shower max design may be in order.

Calibration

There are a number of stages to the calibration of the calorimeter. The first stage involves the measurement of the light output of scintillator tile assemblies before installation into the lead mechanical structure using a radioactive source. In the next stage, these measurements are correlated with the corresponding response in a test beam. It is then necessary to map the calorimeter modules with the radioactive sources calibration system before installing them in the STAR detector. The last stage is maintenance of calibration over long time scales.

The reconstruction of π^0 and η^0 mesons can also be used to calibrate in situ. One difficulty with this technique however, is that there is a correlation between the systematic error associated with the opening angle as a function of momentum and the systematic error in the determination of the energy. A second method is to use electrons from J/Ψ events measured in the TPC to calibrate the EM calorimeter. In this case, the systematics depend on the position and momentum resolution in the TPC. The accuracy which can be obtained also depends on the rate of J/Ψ production. Other processes will be considered.

A green LED system will be incorporated into the calorimeter for long term relative monitoring of PMT's. It is also possible that a separate similar system of blue LEDs' may be used to check the optical fibers. A similar green system was built for CDF, and a prototype for a blue system already exists.

The only non-physics-event means of monitoring the scintillator itself appears to be the injection of UV laser light into the scintillator. This may be necessary in the event the stacked lead option without spacers is chosen in which case there is mechanical pressure on the scintillator. The bend radius necessary for quartz fibers to transmit the UV may however be so large as to preclude the UV option.

4.J. Time-of-Flight Detector

4.J. Time-of-Flight Detector

A number of the physics goals of STAR require particle identification for a large fraction of the particles emitted from central collisions. In order to accomplish these goals, the dE/dx capabilities of the TPC and SVT will be complemented by a comprehensive Time of Flight (TOF) system. The system must measure the flight time of as many charged particles as possible in the central region of the STAR detector with a timing resolution of at least 100 picoseconds. This requires a highly segmented cylindrical counter outside of the TPC having a 2 m inner radius and 4.2 m length and able to operate in a 5 kG magnetic field.

The design developed to satisfy the STAR requirements is the "shingle" design, consisting of tiling the cylinder with 7776 single ended scintillators arranged in 216 trays of 36 scintillators each. Each tray is 2.25 meters long and 11.8 cm wide. Individual trays can be inserted from one end of the magnet. The required rails are mounted and supported on the TPC outer field cage.

Because of budget constraints this detector will be installed only when additional funds become available for the experiment. A first stage of the construction will consist of 300 shingles to cover the intervals $|\eta| \leq 1$ and $\Delta\phi = 13°$ for inclusive measurements of identified particles up to high transverse momenta. The integration of the TOF detector will be designed now, R&D efforts will continue, and its support structure will be implemented prior to start-up of the experiment. This structure will also support the central trigger scintillator barrel.

4.J.1 Specialized Physics Issues

Particle identification over the full phase space accessible to momentum measurements by the STAR detector is essential to meet the full physics goals of STAR. Full pseudorapidity coverage within $|\eta|<1$ and full ϕ coverage ensure that the number of identified particles is maximum, that the events can be characterized by particle ratios and that particle number fluctuations can be studied in three dimensions. PID coverage up to high transverse momentum is necessary for complete spectra and precision measurements of mean momenta for all particle species (π,K,p) and their respective ratios. The dE/dx measurements in the TPC separate π–K up to 0.65 GeV/c and K-p up to 1 GeV/c (see chapter 4.C.3). The TOF detector will double the range of π-K and K-p separation capabilities by moving the upper threshold to 1.3 and 2.4 GeV/c respectively, as can be seen in Fig. 4J-1 .

4.J.2 Description of Subsystem

Introduction

The design developed for the TOF system is the shingle design, which consists of tiling the cylindrical outer field cage of the TPC with 7776 single ended scintillators arranged in 216 trays (108 in +z ; 108 in -z direction). Figure 4J-2 shows a cross sectional view of 108 trays arranged outside the TPC at a radius of 205 cm. Each tray positions

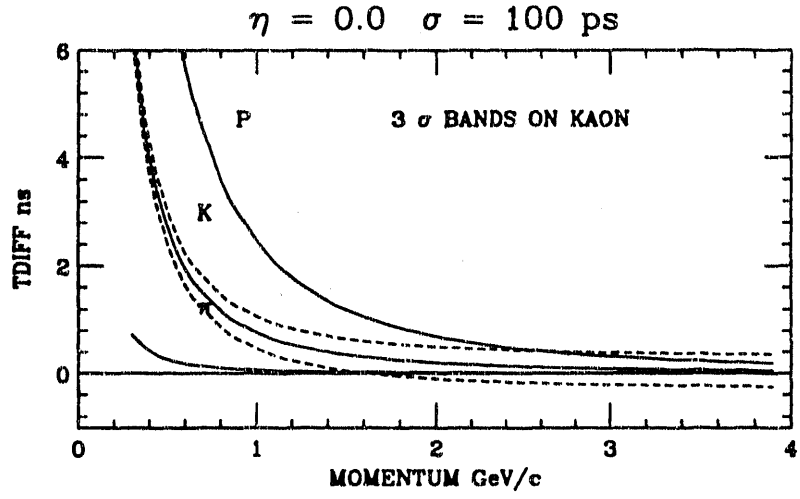

Figure 4J-1 A plot of the difference in time of flight from $\beta = 1$ for π, K, and p at $\eta = 0.0$. For a time resolution of 100 ps, the 3σ band on the kaon time of flight intersects the π and p lines at the PID limits quoted in the text.

and supports 36 scintillators and covers ~3.3° in ϕ as shown in Fig. 4J-3. A tray is 11.8 cm wide and 2.25 meters long. The trays are individually inserted onto the rails mounted on the outside surface of the TPC. The reference timing signal is obtained either from the vertex position trigger detectors or by means of the self-consistent determination of the shortest arrival time.

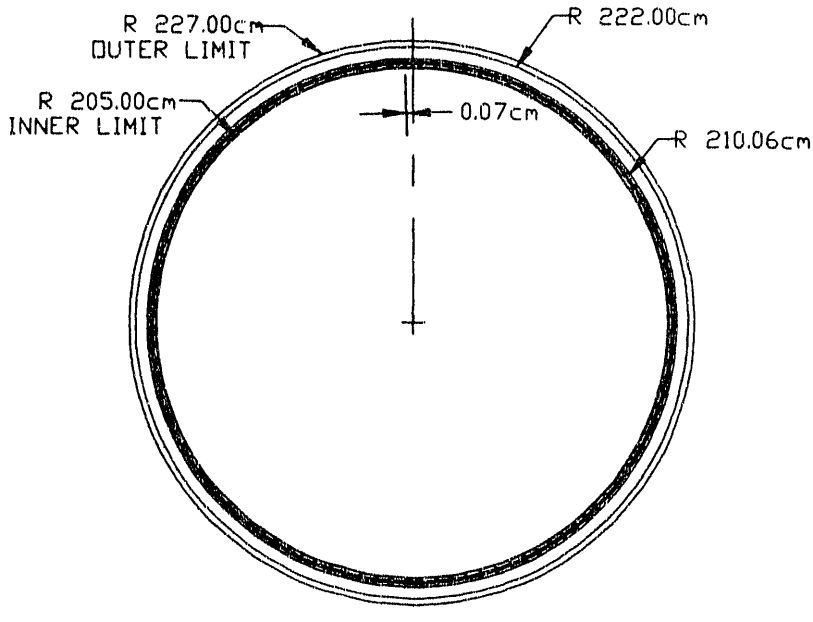

Figure 4J-2 A drawing of the 108 trays that will house the TOF shingle counters covering one half of the TPC.

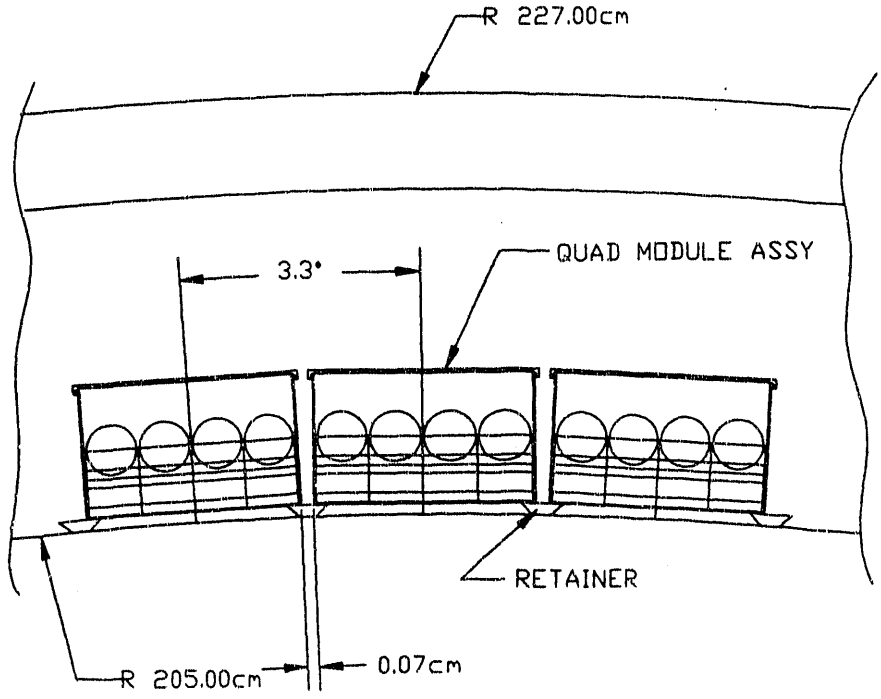

Figure 4J-3 A cross section of the TOF shingle counters and trays.

Fabrication, Assembly and Installation

Each shingle counter consists of a 1 inch diameter 15 stage R3432-01 Hamamatsu proximity mesh dynode phototube optically coupled to a scintillator with a plexiglas light guide. The scintillator is Bicron BC404 with dimensions 1.5 cm x 2.6 cm x 23.5 cm with diamond cut edges. A light guide provides a transition from the 1.6 cm diameter active area of the phototube to the 2.6 cm x 1.5 cm area of the scintillator. The light guides are machined from acrylic sheets with all machined edges flame polished. Calibration fibers for time and amplitude calibration with laser pulses are glued to the scintillators. Each counter is wrapped in aluminized mylar and enclosed in a molded light-tight bag. The gain will be measured as a function of voltage under standardized conditions and documented for each counter. Then the 36 shingle counters are mounted four abreast in a tray.

The module tray parts are fabricated out of extruded plastic. These are considered expendable items during repairs. Therefore a larger number than is required for the complete system will be fabricated at the outset in order to provide for ample spares. Each group of four shingle counters will be supported inside the tray by a molded foam wedge or block and secured by two extruded plastic restraint struts. Retainers will be used to hold the tubes in position. The preliminary engineering drawing for a shingle counter assembly is shown in Fig. 4J-4 .

The mechanical support system will consist of 108 aluminum rails bolted to the TPC outer frame. Each module tray containing 36 shingle counters will be inserted into the slots formed by the support rails. Trays will be inserted from each end of the STAR

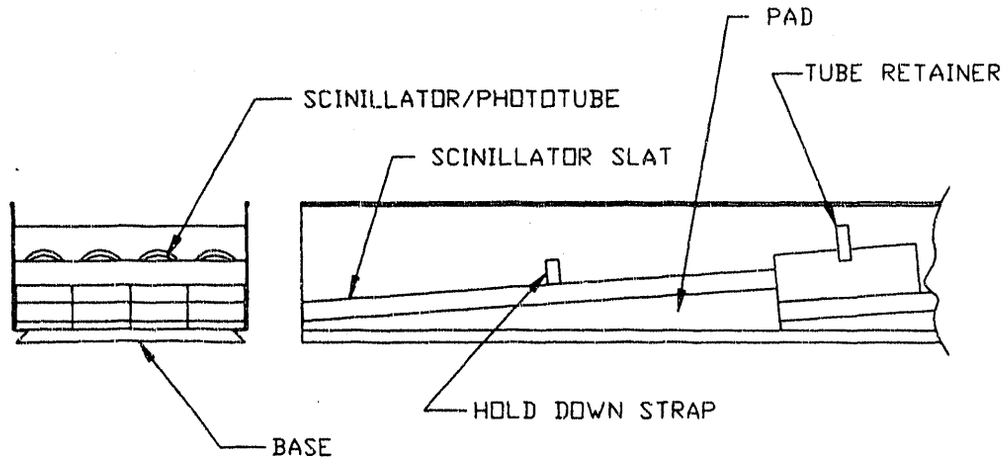

Figure 4J-4 An engineering drawing of a shingle counter assembly.

detector. Power and signal cables, calibration fibers and cooling support will be run inside the module trays. An assembly unit will be used to support a loaded tray module while it is being inserted into the STAR detector.

TOF Front End Electronics

The front end electronics consists of two subsystems: the active high voltage (HV) divider and monitoring system in the phototube bases and the TOF signal path that consists of discriminators, cables and TDCs. The 7776 phototubes will have dc-dc converters built into the tube bases that will set and regulate the HV with appropriate divide ratios under remote digital control. This includes readout of the HV. An R&D effort is underway to find the optimum discrimination method to extract the TOF information. It is expected that this method can be implemented locally in the phototube bases. The "shingles" will require only a single time measurement for each beam crossing.

Fabrication Concepts:

The HV system with control and monitoring will be developed from a model in use at LANL. If it proves possible for optimum timing the discriminator will also be included in the tube bases. The TDC system with multiple buffering will be housed in a standard bus structure such as FASTBUS or VME.

Testing and Costing

The HV and discriminator electronics housed in the tube bases will be extensively cycled and tested using Automatic Test Equipment (ATE) methods. The costing is based on a similar system now in use. A buffered TDC system is under

development at Neologic[1]. When developed it will be highly integrated and should fall within cost level of currently commercially available TDC systems.

Maintenance and Servicing

Once the TOF system is debugged and operational, minimal maintenance and upkeep is envisioned. During regularly scheduled maintenance periods, it would be a simple operation to replace defective counters. Such maintenance may not require a major disassembly of the system and will not have a significant impact on other detector elements.

4.J.3 Capabilities of Subsystem

Extensive Monte Carlo simulations have been conducted to study the performance of a de-scoped TOF system.[2] The simulated configuration consists of 16+16=32 trays with shingle counters, which covers approximately 53 degrees in phi. Ten FRITIOF 200 GeV/c/A Au+Au events were used as input to GEANT 3.14. The program tallies the primary tracks that make it to the TOF; this provides a direct measure of the effective coverage. The known properties of the scintillators were used in simulating the response of the shingles (Bicron BC404). The response was parameterized in terms of the particle's beta and path length in the scintillator. The resultant light was transported to the phototube assuming a delay time of 75 ps/cm. The light attenuation for a given scintillator was calculated from the bulk attenuation length divided by the cosine of the critical angle. A 20% photocathode efficiency was used. A threshold of 100 photoelectrons was required for a light pulse to produce a signal in the PMT. The time spread of the hit was modeled by throwing a Gaussian distribution with a sigma given by $\sigma(ps)=a\sqrt{L}$ where L is the distance in cm from the hit to the PMT and a is an empirically determined constant equal to 20 for the BC404 shingles. This value and the value for the delay time were determined experimentally.[3] Figure 4J-5 shows the distribution of the average time resolution. Its sigma is 64 ps.

The distribution of the number of tracks and hits in the shingles averaged over 10 events is shown in Table 4J-1 for both primary and secondary tracks. The data presented in Table 4J-1 are for the descoped TOF configuration in which two back to back segments of 16 trays each cover $|\eta| \leq 1$ and a total of 53° in ϕ. Note that the number of hits is typically larger than the number of tracks, since a track can go through more than one scintillator. Figure 4J-6 shows the hit multiplicity in the shingles for a typical event.

---

[1] Neologic, Inc., Beverly, Mass.
[2] S. Ahmad, et al., Use of Time of Flight Detectors in the Trigger, STAR NOTE #52, 1992.
[3] S. Ahmad, et al., Tests of Proximity Mesh Dynode Tubes and Evaluation of Shingle Counters, STAR NOTE #50,1992.

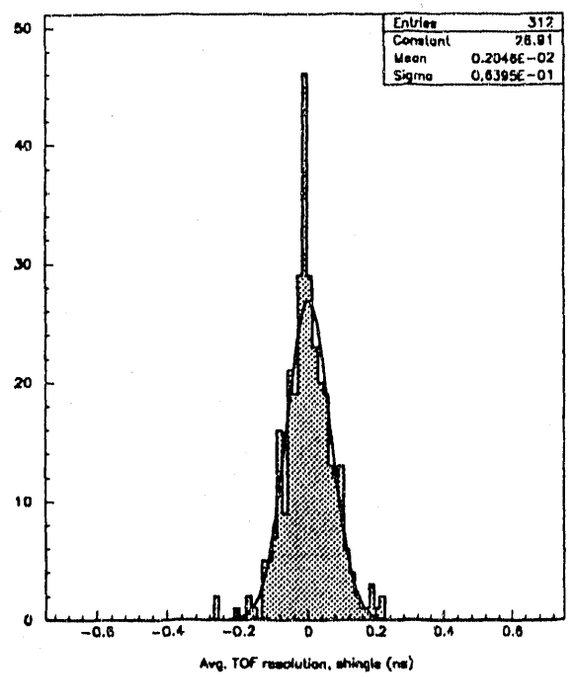

Figure 4J-5 The time resolution found in simulation for the 1.5 cm × 2.6 cm × 23.5 cm shingle counter geometry.

Figure 4J-7a shows the typical p_t distribution of all primary pions which hit the shingles, and in Fig. 4J-7b we see the p_t distribution of the primary pions which have been correctly identified. The cross-hatched entries represent the primary pions which were not found. The pion reconstructed mass is shown in Fig. 4J-8. The reconstruction efficiencies for primary pions, kaons and protons are shown in Table 4J-2, averaged over the 10 events. One should note that the efficiencies were calculated using a lower limit of 0.2 GeV/c rather than 0.3 GeV/c which is the effective momentum cutoff for a magnetic field of .5 Tesla.

Table 4J-1 Average Hit and Track Multiplicities in the Shingles for the Descoped TOF Configuration.

Total hits delivered	414
Total tracks	326
Secondary tracks	201
Primary tracks	125
Primary pion tracks	110
Primary kaon tracks	8
Primary proton tracks	7

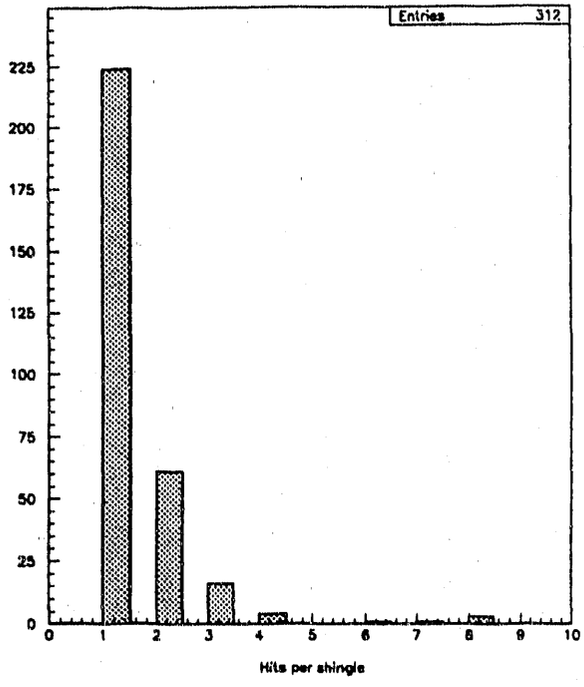

Figure 4J-6 The distribution of hit multiplicity in a TOF shingle counter resulting from a central AuAu FRITIOF event at $\sqrt{s_{nn}} = 200$ *GeV.*

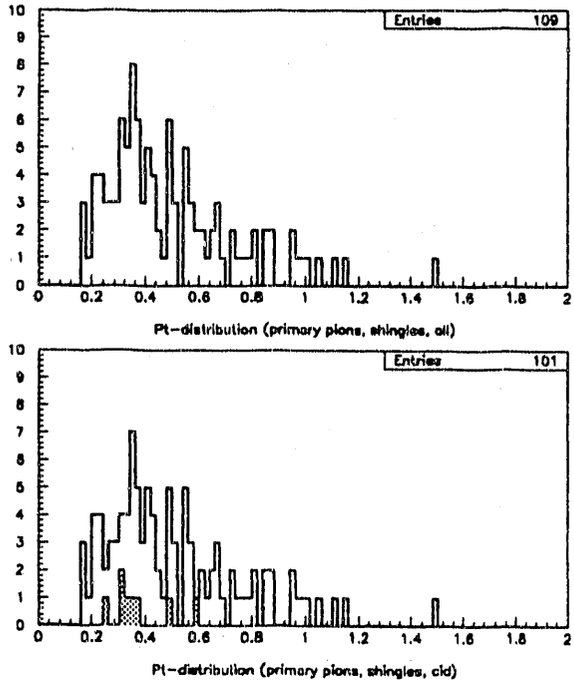

Figure 4J-7 The pion p_t *distribution for (a) all primary pions, that struck the shingle counters and (b) those that were correctly identified in the shingle counters. The shaded entries represent particles that were not found.*

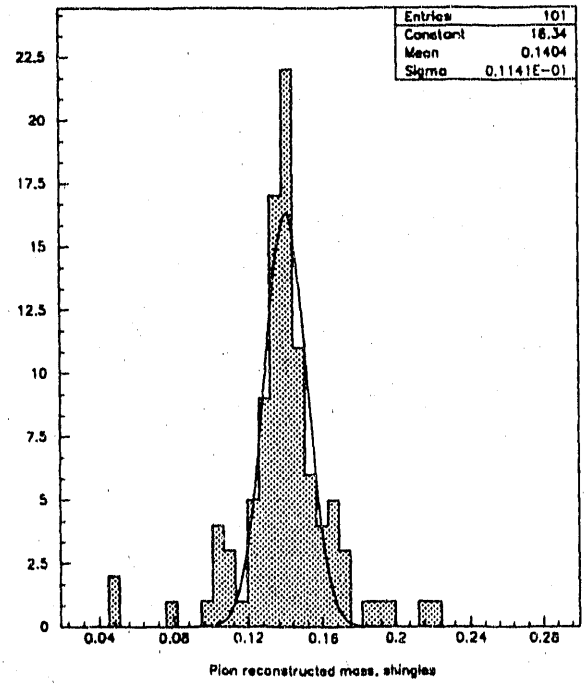

Figure 4J-8 Reconstruction of the pion mass using particle momentum and velocity information from the TOF shingle counters.

Table 4J-2 Average reconstruction efficiencies for primary particles for the descoped TOF configuration.

Particle	Shingles
Pions	93%
Kaons	88%
Protons	90%

4.J.4 R&D Issues and Technology Choices

The foremost R&D issue facing the TOF subsystem is to verify the performance of the proposed baseline design. This includes the phototube and counter for the shingle design.

Photomultiplier Tube Choice and Evaluation

It is now a technical reality to be able to place the TOF phototubes directly in the 5 kG field used for STAR. This was made possible by the advent of a new phototube design, the mesh dynode tube.[4,5] A further advance in the development of this tube

[4] S. Suzuki, et al., IEEE Trans. on Nucl. Sci. Vol. 33, No. 1, 1986, p. 377.
[5] G. Finset, et al., NIM A290 (1990) 450-466.

design was to place the dynodes close to the photocathode to reduce the transit time spread (TTS). This has resulted in a magnetic field insensitive tube with a single electron TTS of 100 to 150 ps. Four such tubes, Hammamatsu R3432-01, have been evaluated. These are 15 stage, one inch diameter tubes, with an active area of 2 cm^2. Tube bases supplied by Hammamatsu were used. These bases used a standard linear dynode resistor string. No attempt was made to optimize the performance of the bases. The anode output was fed into a 50 ohm splitter to provide signals for the discriminator and ADC. At 2000 V the one MIP signal was approximately 900 mV before the splitter.

A series of tests of the shingle geometry using the R3432 phototube at zero field on BC408 and BC420 scintillators were done with 300 MeV/c π^- beams at TRIUMF. Timing was done with leading edge and constant fraction discriminators. The results, corrected for time walk, are given in Table 4J-3.

For the data presented, the beam traversed the length shown first in the cross section column. X is the distance from the beam spot to the phototube. σ gives the results. LE means leading edge timing (Phillips 708) with pulse height corrections. CFD means constant fraction timing (Phillips 715).

The results of the test measurements are summarized in Fig. 4J-9 for BC408 and Fig. 4J-10 for BC420. From these figures we can estimate the behavior of the proposed 2.6 cm x 1.5 cm x 23 cm shingle counters. The worst resolution, at L = 23 cm, is 87 ps for BC420 and 103 ps for BC408. Near the phototube the rms σ is ~ 50 ps. These results have been corrected for the contribution to the resolution from the start detector.

The transit time of the pulse is shown in Figs. 4J-11 and 4J-12. The time is given by a linear relation to the length with constants of 74.7 ps/cm for BC408 and 80.2 ps/cm for BC420. The time delay for light in material with index of refraction 1.58 is 53 ps/cm for straight travel and 83 ps/cm for rays traveling at the critical angle. Clearly the latter was more nearly the case for our tests. This suggests that by optimizing the gain of the phototube to efficiently detect the light traveling in a straight line, it may be possible to achieve further improvement in the resolution, if the number of photons traveling in a straight line is sufficient.

Finally, in Figs. 4J-13 and 4J-14, we show the spread of the individual measurements around the transit time fit in Figs. 4J-11 and 4J-12. It should be noted that the worst deviation of 42 ps for BC420 represents a beam position error of only 0.5 cm. This is consistent with the uncertainty in the alignment of the detector. The worst case for BC408 is due to low pulse height. The difference between the results for pathlengths of 3 cm and 1.5 cm is due to slewing, which is at most a correction of 125 ps for the 25 cm data.

Table 4J-3 Timing results.

Type	Cross Section (cm)	X(cm)	σ(ps)	DISC
BC408	1.5 x 3.0	5	85	LE
	1.5 x 3.0	25	113	LE
BC420	1.5 x 3.0	5	55	LE
	1.5 x 3.0	10	75	LE
	1.5 x 3.0	25	100	LE
	1.5 x 3.0	25	123	CFD

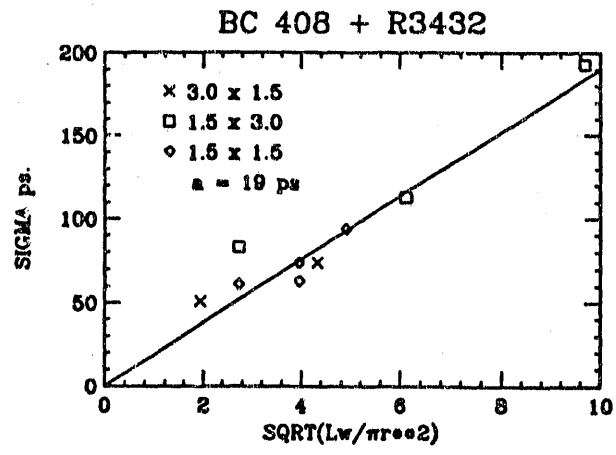

Figure 4J-9 The time resolution measured as a function of position using the Hamamatsu R3432 mesh dynode tube and BC408 scintillation counters of varying geometry. The abscissa, $\sqrt{Lw/\pi r^2}$, is related linearly to the resolution predicted empirically by the constant 'a', which is dependent on the photoelectron density per unit time characterizing the leading edge of the photon pulse. In this instance L is the distance from the beam to the photomultiplier, w is the width of the scintillator through which the beam passes, and r is the radius of the photocathode. A linear fit to the experimental data yields a value of 'a' of 19 ps.

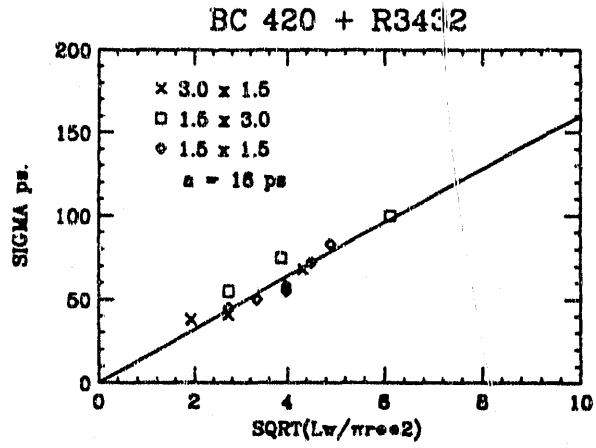

Figure 4J-10 As in 4J-9, but plotted for the BC420 and R3432 combination. A linear fit to the data yields a value for the constant 'a' of 16 ps.

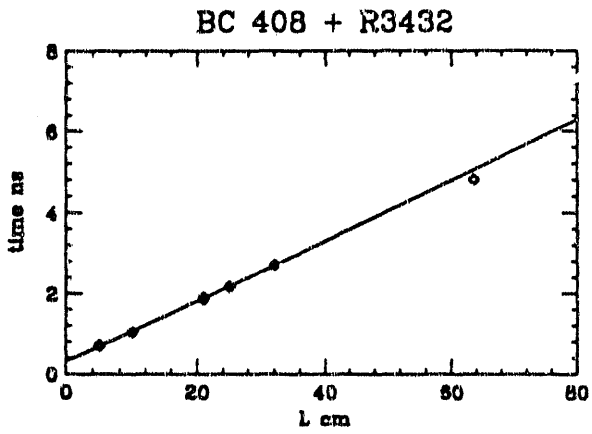

Figure 4J-11 Transit time of light through BC408.

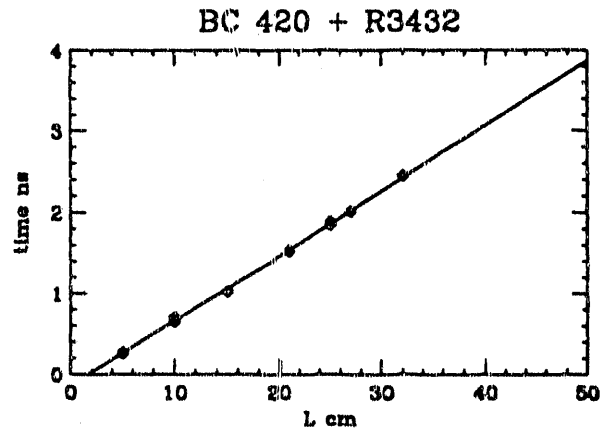

Figure 4J-12 Transit time of light through BC420.

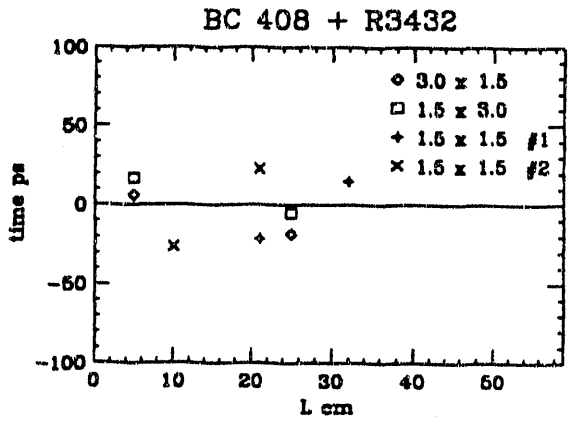

Figure 4J-13 The deviation of the data points from the fit of transit time vs. position for BC408 in Fig. 4J-11.

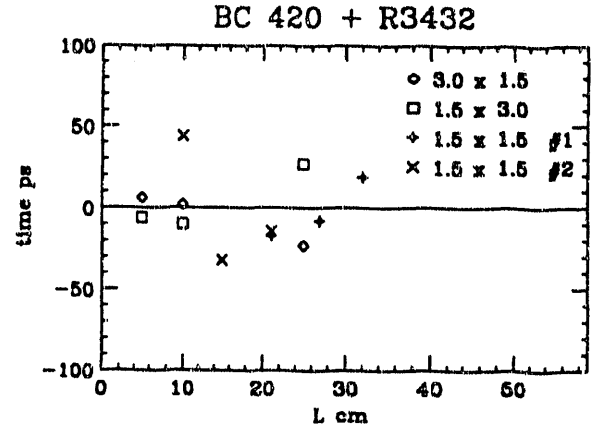

Figure 4J-14 The deviation of the data points from the fit of transit time vs. position for BC402 in Fig. 4J-12.

Conclusions and Further Tests

We have evaluated the scintillator performance for BC408 and BC420 using the R3432 proximity mesh dynode photomultiplier at zero field. Very good results were obtained. A slew corrected resolution of better than 100 ps seems feasible. Price quotes from BICRON indicate the BC404, which is faster than BC408, is actually cheaper. Price quotes from PolyCast indicate that acrylic based scintillators will be much cheaper, as little as one forth the cost of BC408. Samples of these two scintillators have been obtained for evaluation. Tests in a 5 kG field are also planned. From the literature,[6] the field is not expected to degrade the time resolution by more than 20%.

[6] c.f. Ref. 5.

STAR

4.K. External Time Projection Chambers

4.K. External Time Projection Chambers

4.K.1. Specialized Physics Issues

4.K.1.a. Enhanced Particle Production in the Forward Regions

Nucleus-nucleus collisions at RHIC are expected to produce baryon-rich matter near beam rapidity and baryon-free matter at midrapidity. While the latter is the more interesting case for the study of the transition between hadronic matter and the QGP, understanding the transfer of energy from beam rapidity to midrapidity is essential for understanding the later development of the collision. Energy transfer can be studied by following the fate of the baryons brought into the collision, in particular by measuring the net baryon number at intermediate rapidities. If the baryon number flow can be determined on an event-by-event basis, events can be tagged by the energy deposition at midrapidity and other observables can then be studied for unusual behavior. Simpler measures of the state of matter at intermediate rapidities are also very useful for tagging unusual events. Because the matter radiating at midrapidity and intermediate rapidity (η=3-5) are causally disconnected, the entropy densities (proportional to $dN/d\eta$) at midrapidity and intermediate rapidity can be compared in order to label events with unusually high entropy generation at central rapidity, corresponding to a first order phase transition.

The external time projection chambers (XTPCs) extend the kinematic range covered by the STAR spectrometer. The central TPC covers the pseudorapidity (η) range from +2 to -2 into which about 50% of the charged primary particle distribution from central gold on gold events is emitted. The XTPCs increase the covered range to at least η from +4.0 to –4.0 with complete and uniform azimuthal (ϕ) coverage; an additional 40% of the charged primary particles are emitted into this range. The XTPCs therefore give STAR almost complete event characterization (see Fig. 4K-1). Note that the utilization of radial TPCs that are currently under development could extend the covered range as high as $|\eta| = 6.0$, which would give a total of 99% coverage of the production cross-section. The coverage of the central TPC extends across the η region where $dN/d\eta$ is approximately constant. The additional coverage provided by the XTPCs at high η extends into the regions where the particle production is expected to be falling off rapidly as a function of increasing η. In these regions, the $dN/d\eta$ distributions are qualitatively different in the two detection systems. The coverage added by the XTPCs allows an accurate measurement of the width of the region of maximum $dN/d\eta$, allows an accurate determination of where the production fall-off occurs, and enhances the ability to resolve regions of anomalously high particle production. These regions of anomalously high particle production are expected to be associated with the decay of a quark gluon plasma bubble. As the plasma is transformed into normal nuclear matter, large numbers of particles should be produced in the rest frame of the bubble. If a bubble of plasma were to be moving in the laboratory frame, its products would be focused into small region of η space. These regions can be identified through analyses of the $dN/d\eta$, the $dN/d\phi$, and the two-dimensional intermittency.

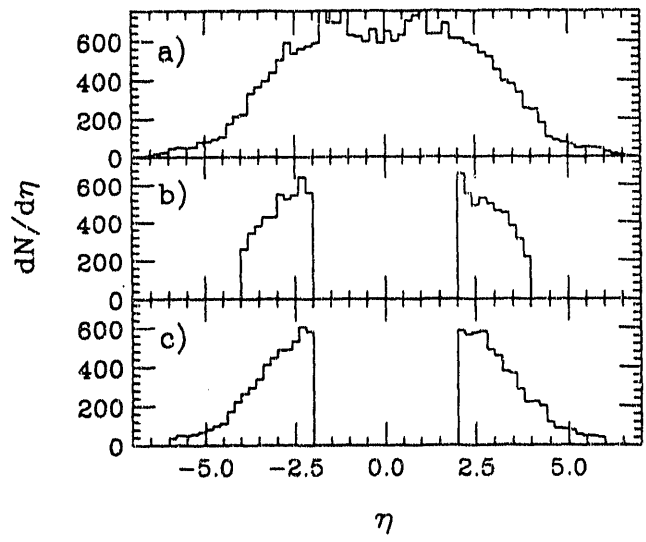

Figure 4K-1 dN/dη distributions: a) primary particles, b) particles identified in the external TPCs, c) particles that would be detected in a radial TPC.

4.K.1.b. The Fate of the Projectile Remnants

FRITIOF simulations suggest that the projectile nucleons from central collisions should be distributed at $|\eta|$ from 3.5 to 6.5. Coverage in these regions would permit studies of the nuclear stopping and of possible collective effects in the spectator matter. These studies would be pursued through an analysis of the differences in the distributions of positively charged and negatively charged particles (plus - minus) as a function of η (see Fig. 4K-2). Additionally the ϕ distribution could be studied to search for evidence of collective effects. There should be an excess of the positively charged particle distribution due to the protons from the projectiles. The distribution of the excess positive charge could be studied on an event-by-event basis and correlated with the particle distributions at mid-rapidity.

4.K.2. Description of Subsystem

4.K.2.a. Specifications Required to Achieve Physics Goals

In order to determine the primary particle distribution, it is necessary to be able both to detect all particles and to reject those which are the result of secondary interactions. The FRITIOF and GEANT simulations predict that in the forward regions, secondary particles constitute a large part of the total charged particle flux. These secondary particles are the result of interactions in the materials of the beam pipe, the silicon vertex tracker, and the central TPC, and from the decay of short lived particles. Detection of all particles requires good two-track separation at high η where the particle densities are the highest. The ability of the detector system to resolve two close tracks is determined by the precision of the device and the diffusion of the signal from each track.

Rejection of tracks from secondary interaction products requires that tracking chambers, rather than detectors that simply measure the particle flux, be employed, so

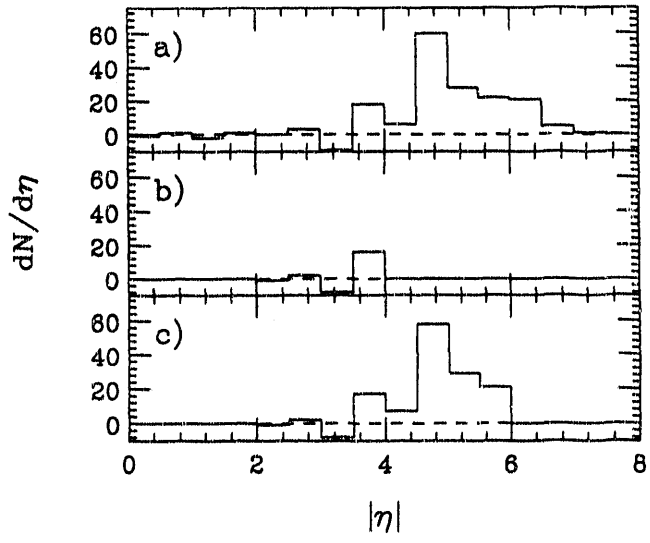

Figure 4K-2 The difference between the distribution of positive charges and the distribution of negative charges as a function of $|\eta|$. a) Primary distribution from FRITIOF, b) Signal detected in the external TPCs, c) Signal that would be seen in a radial TPC.

that the point of closest approach to the interaction vertex can be determined. Tracks that are a result of particles created in secondary interaction with materials that make up the detector apparatus will not originate from the interaction vertex, therefore, a cut on the point of closest approach will allow a rejection of most of these secondaries. For an XTPC at z = 7 m, an angular resolution of 0.6 degrees is needed to distinguish particles from the primary vertex from those which originated in the beam pipe, which is only 5 cm away.

In order to undertake an analysis of the residual baryonic matter it is necessary to identify the charge of the particle that created each track in the active region of the detector. This is done by determining whether the magnetic field bent a given track to either the left or the right. For the very rigid tracks that are left by the remnants of the projectiles this bending is extremely slight. In order to determine the charge of a proton with a momentum of 20 GeV/c, an angular resolution of 0.1 degrees would be needed (see Fig. 4K-3).

A measurement of the amount of bending that a given particle experiences allows one to determine the momentum of that particle. The charge identification is a crude momentum measurement, however, it requires a resolution of only 50%. With 0.1 degree resolution, which is the best attainable with the current detector design, the momentum could be determined to 10% for tracks of momentum less than 3 GeV/c. The resolution rapidly deteriorates for higher momenta.

The angular requirements for secondary rejection, charge identification, and momentum measurement will determine the necessary spatial resolution and detector depth. The key parameters for any detector systems in the high η region would be the two-track separation and the angular resolution.

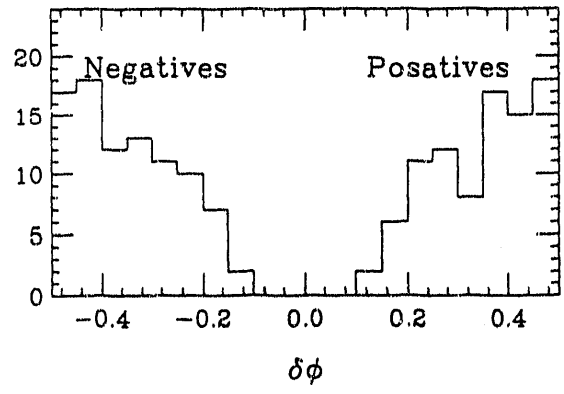

Figure 4K-3 A histogram of the change in ϕ angle from the front to the back of the external TPC. This is a measure of the degree of deflection in the magnetic field for tracks that originate from the primary vertex.

4.K.2.b. Detector Description

The baseline design of the high η tracking chambers would use a total of 4 rectangular TPCs on each side of the interaction. The TPCs would be situated 7 m from the intersection region and would be arranged as shown in Fig. 4K-4. TPCs have been chosen for this region because they provide tracking, which is necessary for both secondary track rejection and charge identification. The drift direction is perpendicular to the beam axis and is indicated by the arrows on the figure. By employing drift perpendicular to the beam axis, the analog storage capabilities of a TPC are optimized allowing for a minimum in the required number of channels of electronics. Perpendicular drift does, however, require that the TPCs be situated external to the solenoidal magnetic field in a region where the fringe fields will not significantly distort the drifting of the ionization to the pad plane. The position of the XTPCs at 7 meters from the interaction region was a compromise between cost and performance. The electronics would be similar to that used in the central TPC. However, since there will be no effort to identify particles through dE/dx a high gas gain could be used to reduce the effect of noise. This may allow the cost of the electronics to be reduced. Note that it

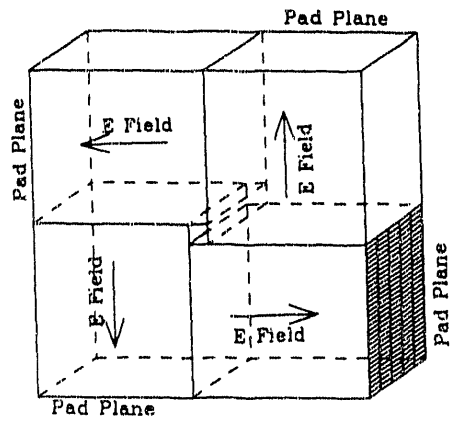

Figure 4K-4 A schematic diagram of the configuration of the external TPCs.

is necessary to record the pulse height as a function of time for good spatial resolution and two-track separation. The current design has readout via cathode pads, each 0.5 cm wide in the ϕ direction. There are approximately 22K readout channels arranged in 8 pad rows. The expected track density varies from $0.01/cm^2$ at η=2.0 to $0.10/cm^2$ at η=4.0 if the chambers are located 7 m from the intersection.

4.K.3. Capabilities of Subsystem

The capabilities of the XTPCs have been studied using FRITIOF and GEANT simulations for $\sqrt{S_{nn}}$ = 200 GeV Au + Au central events.[1] As the XTPCs are situated in a field free region, the tracks are all nearly straight line trajectories from the point that the particles leave the magnetic field. Vectoring to reject secondaries is extremely important; of an estimated 4200 particles in the XTPCs, 2200 are from the primary vertex, 1500 are the result of interactions with the beam pipe, SVT, central TPC, or other associated equipment, and 500 are from decays of short-lived particle species. Figure 4K-5 displays a scatter plot of primary and secondary tracks in $\delta\eta$ and $\delta\phi$ space. A cursory analysis reveals that the primaries tend to be stiff and display little deflection while the secondaries which do not originate from the region of the target display significant apparent deflection.

A more sophisticated analysis employs a road finder pattern recognition routine to reconstruct tracks from space points. This routine is able to reconstruct 93% of the primary tracks and 78% of the secondary tracks that hit the XTPCs. The tracks that are not reconstructed are all low momentum particles that hit the detector at a shallow

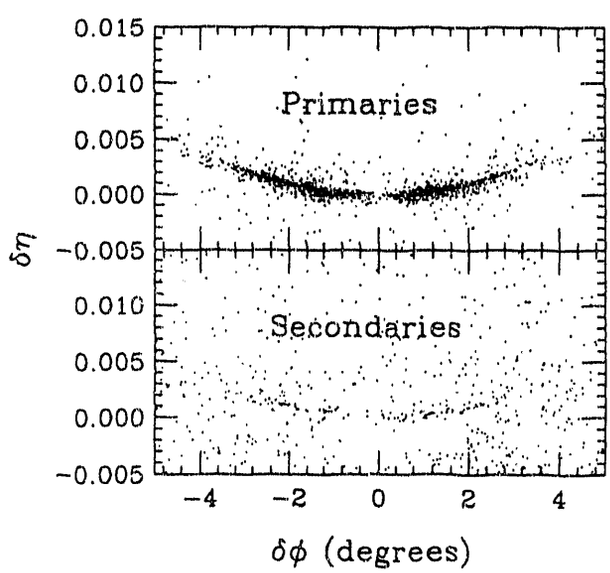

Figure 4K-5 Vectoring in the external TPCs is naturally done in η-ϕ coordinants. A stiff primary track will show little deflection while secondaries will scatter across a wide range.

[1] I. Stancu, submitted as STAR Note.

angle and do not penetrate to the planes furthest back. Of the secondary tracks that are reconstructed, 65% are correctly identified as being not associated with the primary vertex. The remaining 35% are associated with decays of short lived particles. The charge identification is correct 99% of the time. The momentum reconstruction is accurate to 10% only for primary particles of less than 3 GeV/c, which does not constitute a large fraction of the cross-section at high η. The track density gets too high for the present cluster finding and tracking algorithms at the inner edges of the detector ($|\eta|>4.2$). However, it may be possible to extend coverage to higher η through use of more sophisticated tracking routines such as the elastic tracking techniques proposed by M. Gyulassy. This technique does not employ cluster finding, which is the algorithm primarily responsible for merging close hits.

For the XTPCs as currently proposed, the drift distance will be 2.2 meters. Using a cool gas with a slow drift time (2 cm/μs) will reduce diffusion and improve both position resolution and two-track separation. The overall drift time for these XTPCs would be 110 μs. For a beam luminosity of 2×10^{26} one expects 1000 events per second, of which 10% would be naively considered central. This will result in the superposition of two events within the drift volume in 23% of the triggers. This superposition means that tracks from a non-triggering event were created in the active region of the XTPC from interactions that occurred within the window from 110 μs before the trigger to 110 μs after the trigger. However, tracks from events that occur more than 2.5 μs before or after the trigger event will not track back to the primary vertex and will thus be rejected just as secondary tracks are rejected. The 2.5 μs cut comes because a track that was caused by a particle which was created during an interaction more than 2.5 μs before or after the triggering interaction will appear to be displaced by at least 5 cm and will therefore fail the vertex cut. Therefore, less than 1% of triggers events will be contaminated with tracks from overlap events that can not be effectively removed. The trigger system will be able to reject any interactions that occurred outside of the selected beam crossing (±110 ns) which will reduce the potential event pileup to 0.1%. These events will have to be discarded for high η analyses. Thus, we conclude that the XTPCs will be able to operate without difficulty at the design luminosity of RHIC.

4.K.4. R&D Issues and Technology Choices

4.K.4.a. Gas Selection and Performance Optimization

The XTPCs attempt to extend into a region of extreme particle density, thus the two-track separation is a key parameter in the final design. Use of a slow cool gas mixtures such as Argon-Iso-Methylal or Argon-Iso-CO_2 will minimize the diffusion of the electron cloud and thus provide the best two-track separation, however, a much higher drift potential is needed to reach saturation velocity. Studies are currently underway using a test volume at Munich to measure the diffusion and drift velocity for several gas mixtures as a function of the drift potential. At LBL, studies are underway to determine the ability to stabilize the drift velocity using feedback circuity. This could allow operation below saturation velocity. These choices will then drive the specifications for the electronics for the XTPCs. The shaping time should be matched to the maximum diffusion width of an ionization cloud, and the sampling frequency

should be high enough to acquire multiple measurements for all peaks in the time spectrum (the sampling frequency must also be an integral fraction of the accelerator frequency). These decisions will be made by the end of 1992.

4.K.4.b. Radial Time Projection Chambers

4.K.4.b.1 Justification

FRITIOF simulations predict the particle distribution for central Au+Au collisions at RHIC. From the predicted $dN/d\eta$ distribution we can estimate dN/dA as a function of z and θ for small θ; dN/dA (hits/cm^2)= $(dN/d\eta)/2\pi z^2\theta^2$. Figure 4K-6 plots the hit density vs. (θ, η, and r_i) for z=7 m. The two-track density at high η tends to limit the range that can be effectively covered by conventional TPC technology, which can not effectively operate where track densities are above 0.1 per cm^2. Unfortunately this limit occurs at $|\eta|$=4.0 which is on the lower end of the region in which the projectiles protons would be found (refer back to Fig. 4K-2). In order to handle this high hit density region, a different kind of TPC in which the drift field is radial, is being considered. Radial drift leads to smaller effective pixel sizes at the smaller radii which is where the highest hit densities and stiffest tracks would be. This addresses the key design parameters for any detector in the high η region; it achieves better two-track separation and spatial resolution the smaller the radii. The design also has the advantage of true azimuthal symmetry. The designs for radial TPCs envision complete detector barrels so that there are no edge effects. This reduces the effect of the magnetic field distortions and lost active area and allows the detectors to operate closer to the return yoke of the main solenoid. As this is a novel technology a certain amount of development work is in progress to verify that detectors of this sort will work as expected.

4.K.4.b.2 Diffusion

To demonstrate the advantage of a radial drift TPC consider the direction of drift and the diffusion of the ionization cloud. If the diffusion parameter σ in the ϕ direction is constant then the width (standard deviation) of the electron cloud would be:[2]

$$w = \sigma \sqrt{[(R-r_i)\, R/r_i]} \qquad \text{(4K-1)}$$

for a radial drift TPC with a negligible size of electron cloud at the initial radius r_i drifting radially outward to a collection radius R. We use cylindrical coordinates (r, ϕ, z). For a rectangular TPC, Eq. 4K-1 applies, but without the factor of $\sqrt{(R/r_i)}$. In the actual case, the diffusion parameter varies with the electric field strength E (proportional to 1/r). Then w_ϕ can be calculated numerically by iterating

$$w_{j+1}^2 = w_j^2(r_{j+1}/r_j)^2 + \sigma_j(r_j)^2\delta \qquad \text{(4K-2)}$$

[2] J. Draper, STAR Note #45.

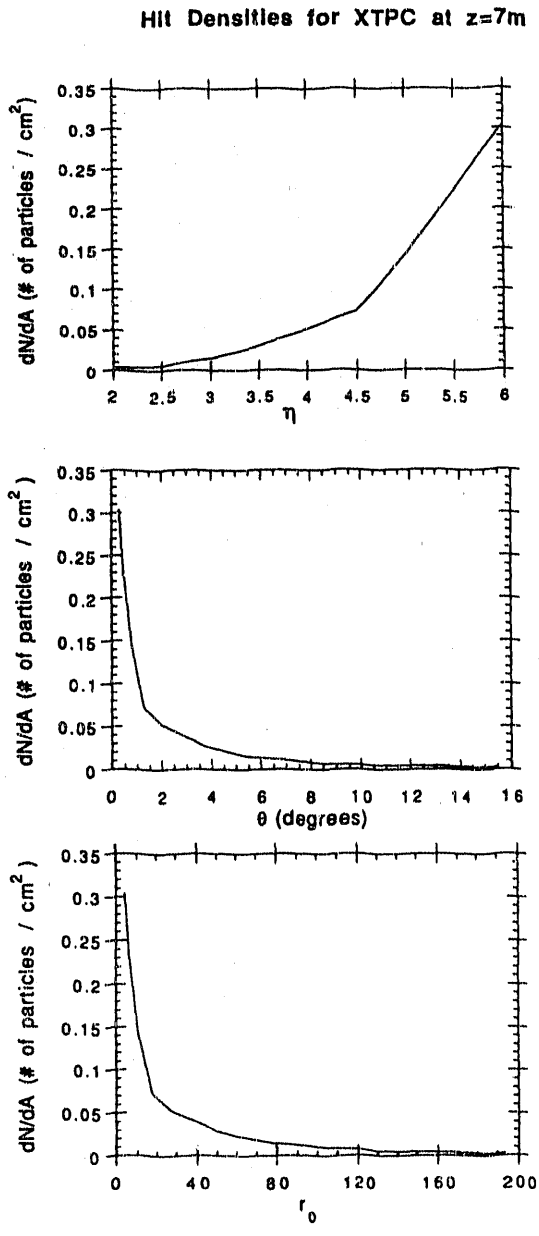

Figure 4K-6 Hit flux densities for the external TPCs as a function of η, θ, and r_0.

varying with r, and $\delta = (r_{j+1} - r_j)$ = const. When σ is constant, Eq. 4K-2 gives Eq. 4K-1. Figure 4K-7 shows a comparison of the calculated results for Eq. 4K-2 for a argon-iso-dimethoxy mixture (80% Ar, 15% isobutane, 5% Methylal). The dots in the figure are Eq. 4K-2 for this mixture, and the curve is for Eq. 4K-1. An exact analytical solution to Eq. 4K-2 is:[3]

$$w_\phi(r) = r\left(\int_{r_i}^{r} (\sigma(r)/r)^2\, dr\right)^{1/2} \qquad \text{(4K-3)}$$

[3] P. Brady and J. Romero, STAR Note #64.

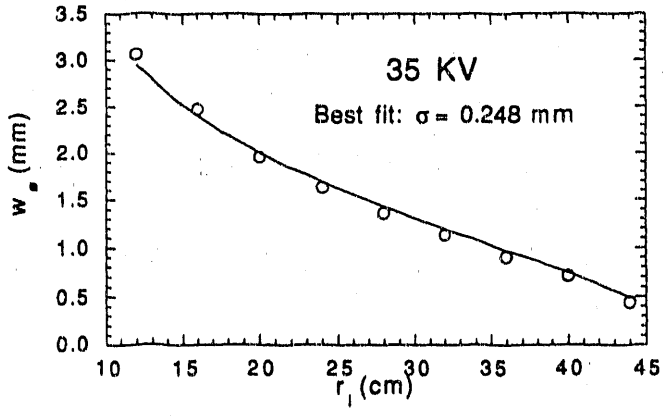

Figure 4K-7 Azimuthal width of an ionization cloud as a function of point of origin.

which agrees with Eq. 4K-2. Diffusion of the ionization cloud in the z and r directions exhibits no expected difference between the radial and conventional geometries. Equation 4K-1 without the factor of $\sqrt{(R/r_i)}$ is then applicable, with the appropriate parameter σ for the directions in question.

Now consider two closely spaced clouds of initial ionization originating from two tracks which we wish to resolve. A Monte Carlo has been written to simulate diffusion and drift in a radial TPC[4]. Figure 4K-8 illustrates the effect of diffusion and drift on the ionization clouds created by particles which hit a detector with a 1 cm separation. The figure displays the separation of the ionization clouds after 35 cm of drift and compares the effectiveness of a radial-drift TPC to that of a conventional design. The advantage of the radial drift design relative to a conventional geometry is that the track separation grows as r/r_i while the cloud width grows only as $\sqrt{(r/r_i)}$. A

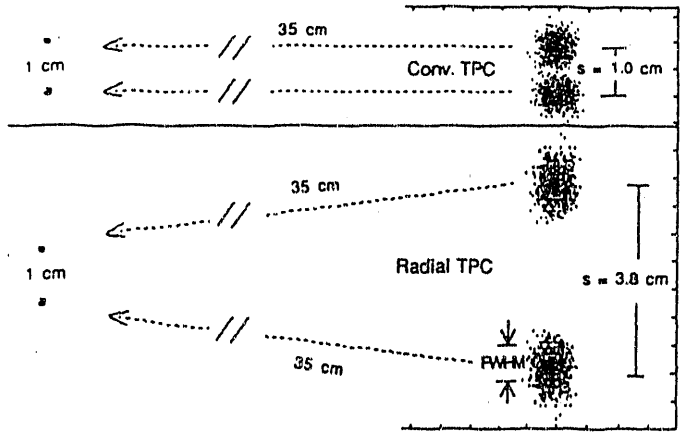

Figure 4K-8 Results of a Monte Carlo simulation to demonstrate the spreading of the ionization clouds in a conventional and radial TPC.

[4] J. Romero, P. Brady, D. Cebra, J. Draper, STAR Note #65.

figure of merit (FOM) is the separation of the clouds at the collection radius R (after drift) divided by the width of each cloud at collection. This FOM is illustrated in Fig. 4K-9 for both the radial and conventional design. For comparison, consider M, defined as the ratio of the FOM for the radial-drift TPC to that of a rectangular TPC. From Eq. 4K-1, a good approximation is $M = \sqrt{(R/r_i)}$ for the ϕ direction. This demonstrates the clear advantage for the radial-drift TPC for the highest η (smallest r_i) region. Furthermore, the advantage increases as the ratio of R/r_i increases. For example, for r_i = 12.5 cm and R = 48 cm (the dimensions of the test radial-drift TPC now under construction), then M = 2, which corresponds to a two-fold advantage for the radial TPC in resolving power.

4.K.4.b.3 Nonlinearity of Time vs Radius

It is not feasible to operate a radial-drift TPC with an electric field of uniform strength as a function of radius. The strength of the field is $E = (V_0/r)[\ln(R_{inner}/R_{outer})]^{-1}$. This 1/r electric field makes the drift velocity vary with radius, so the collection time is not linear with the drift distance ($R-r_i$). Figure 4K-10 displays the drift velocity as a function of radius for the prototype radial TPC for two different biasing options. An attempt has been made to have the electric field straddle the saturation potential. The effect of this non-linear drift velocity has been calculated by integrating the velocity at each step in r along the drift length of the ionization and thereby calculating the collection time T_i for each r_i. The values of T_i vs. r_i were least square fitted to a straight line. The differences between each r_i and the radius extract from comparing T_i to the fitted straight line are plotted in Fig. 4K-11 for the Ar-Iso-Methylal gas mixture. The points (without the "error bars") are the calculated results for two different voltages, 35 and 50 kV across a radial TPC with inner radius 12.5 cm and outer radius 47.5 cm. The different voltages produce different ranges of drift velocity vs

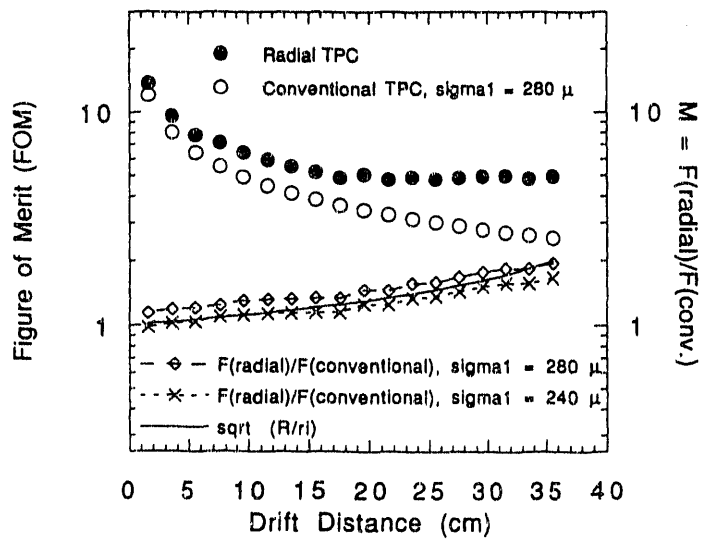

Figure 4K-9 The figure of merit for a radial TPC as a function of drift length. The longer the drift distance the greater the advantage of the radial TPC over the conventional design at separating close tracks.

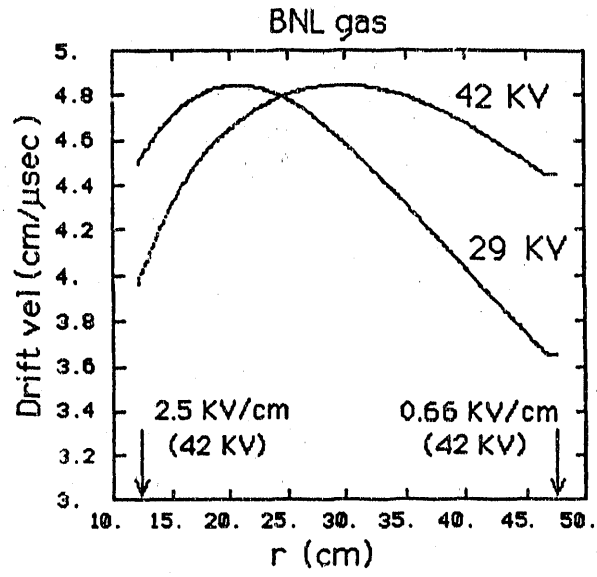

Figure 4K-10 Drift velocity as a function of position within the active volume of the prototype radial TPC for an Ar-Iso-Methylal gas mixture and for two biasing options.

radius. The results displayed on this figure could be used to build a lookup table to convert the collection time T, for a given hit, into the radius r_i. A lookup table of this sort is not considered to be a problem. Also shown in Fig. 4K-11 is the effect of the radial diffusion calculated by Eq. 4K-2 using the same diffusion parameter vs radius as for the ϕ calculations above. This effect is indicated by the "error bars" which indicate the standard deviation (width) of the radial Gaussian shape of the cloud.

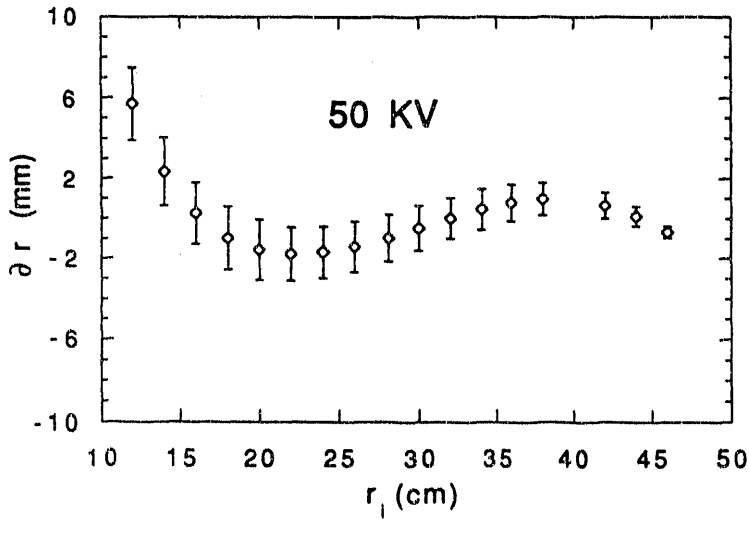

Figure 4K-11 Deviation in extracted radius induced by the varying drift field.

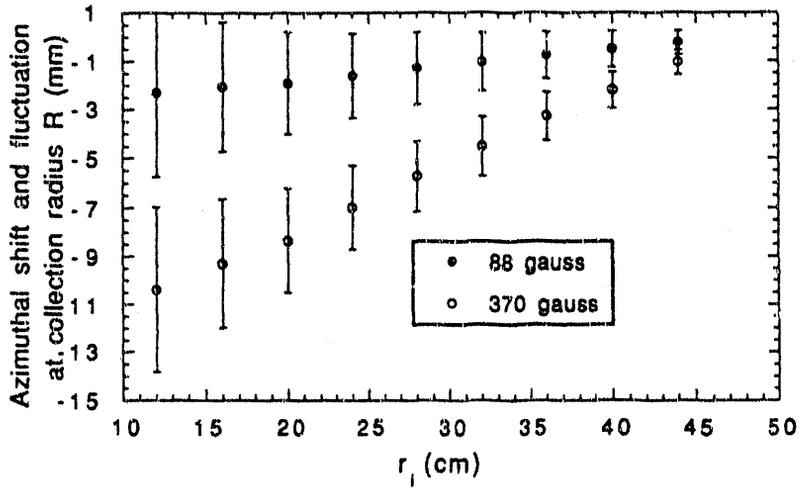

Figure 4K-12 Azimuthal distortions induced if the XTPCs were to operate in the fringe field of the STAR solenoid.

4.K.4.b.4 The Effect of Stray Magnetic field

At the site of a drifting electron in the external TPCs, the stray magnetic field B from the main solenoid will, to high accuracy, be in the plane defined by the accelerator beam and the electric field vector experienced by that cloud. The Langevin equation for the drift velocity v_D of an electron is:

$$\vec{v}_D = \{\mu E/[1 + (\omega\tau)^2]\}\ [\hat{E} + (\hat{E} \times \hat{B})(\omega\tau) + \hat{B}(\hat{E} \bullet \hat{B})(\omega\tau)^2] \qquad \text{4K-4}$$

where $\omega = Be/m_e$ (cyclotron frequency of an electron), and the carat denotes a unit vector.

Since $\mu B = \omega\tau$, we can evaluate the drift velocity at a given E. The result is $\omega\tau << 1$ for any B to be experienced by the XTPCs. Thus the third term of Eq. 4K-4 is completely negligible. The second term produces drift at an angle $\phi_L = \tan^{-1}(\omega\tau|\hat{E} \times \hat{B}|)$ measured in the $(\hat{E} \times \hat{B})$ or ϕ direction from E. This is called the Lorentz angle when $|\hat{E} \times \hat{B}| = 1$.

For purposes of estimation, consider the case where μB and $\hat{E} \times \hat{B}$ are each constant. This is a closer approximation to the conventional rectangular TPCs, in which E is constant, then to the radial TPCs. The fringe field B is not constant in either case. The drift velocity would then be at a constant angle ϕ_L from E. The trajectory would then simply be a straight line for a rectangular TPC.

The change in ϕ in a radial TPC during the course of the drift to the outer radius is shown to be:

$$\phi_f = \phi_L \ln(R/r_i) \qquad \text{4K-5}$$

for drift from radius r_i to R under the approximation that μ and B are uniform. This trajectory has a spiral-like quality. Thus the cloud at radius R is displaced in the ϕ direction by the distance $R\phi_f$ from its location if B were zero. In the actual situation, the calculation must be numerical because neither μ nor B is constant. The drift velocity saturates, and even over saturates, at small radii. The resulting spiral effect is actually not as strong as would be indicated by Eq. 4K-5. Figure 4K-12 shows the calculated azimuthal shifts for two different fringe field strengths with the Ar-Iso-Methylal gas mixture and a 42 kV drift potential across the test radial TPC. The points are the calculated deflections in mm in the ϕ direction at the collection radius R, i.e. each accumulated ϕ deflection multiplied by R. The cloud starts drifting from radius r_i as usual. There is little sign of the spiral-like effect because μB is smaller at smaller radii than at larger radii, so the deflection is nearly linear. The correction for this effect will require a lookup table for either the radial or conventional TPC. For reference, the standard deviation associated with the Gaussian shape of the diffusion in the ϕ direction is shown by the "error bars". The amount of the magnetic deflection is of the same order of magnitude as the Gaussian width caused by diffusion.

4.K.4.b.5 Prototyping Effort

A sector of a prototype radial drift TPC is being built cooperatively between BNL, UC Davis and LBL. The device is illustrated in Fig. 4K-13. It is a 45 degree wedge with an inner radius of 12.5 cm and an outer radius of 50 cm. This prototype TPC will address all the new technology questions introduced by the radial geometry such as: what is the effect of the ratio of inner to outer radii? Will the ionization cloud spread as expected through the non-uniform electric field? Will the use of only field wires in the anode wire plane effect the resolution? Is the two-track separation and spatial resolution as good as expected for tracks at the inner radius? How critical are the various structural specifications? Can a cylindrical pad plane be made to work? What sort of gain uniformity can be achieved?

The construction of the prototype wedge has been shared by three institutions. BNL is manufacturing the readout region. This consists of the wire planes, pad plane, and electronics interface. UC Davis is making the mechanical support structure for the drift region. LBL is building the field cages. The front-end electronics will be borrowed from NA35 and the DAQ electronics from E810. The assembly and testing will take place at BNL, employing first bench tests with sources and lasers and later beam tests at the AGS.

4.K.4.b.6 Schedule of Technology Selection

The manufacture of parts is currently underway at all three institutions. Assembly at BNL will take place in June and testing in the summer. The analysis of the results will occur concurrently with the acquisition of the data and final conclusions from the study will be available by the end of the summer.

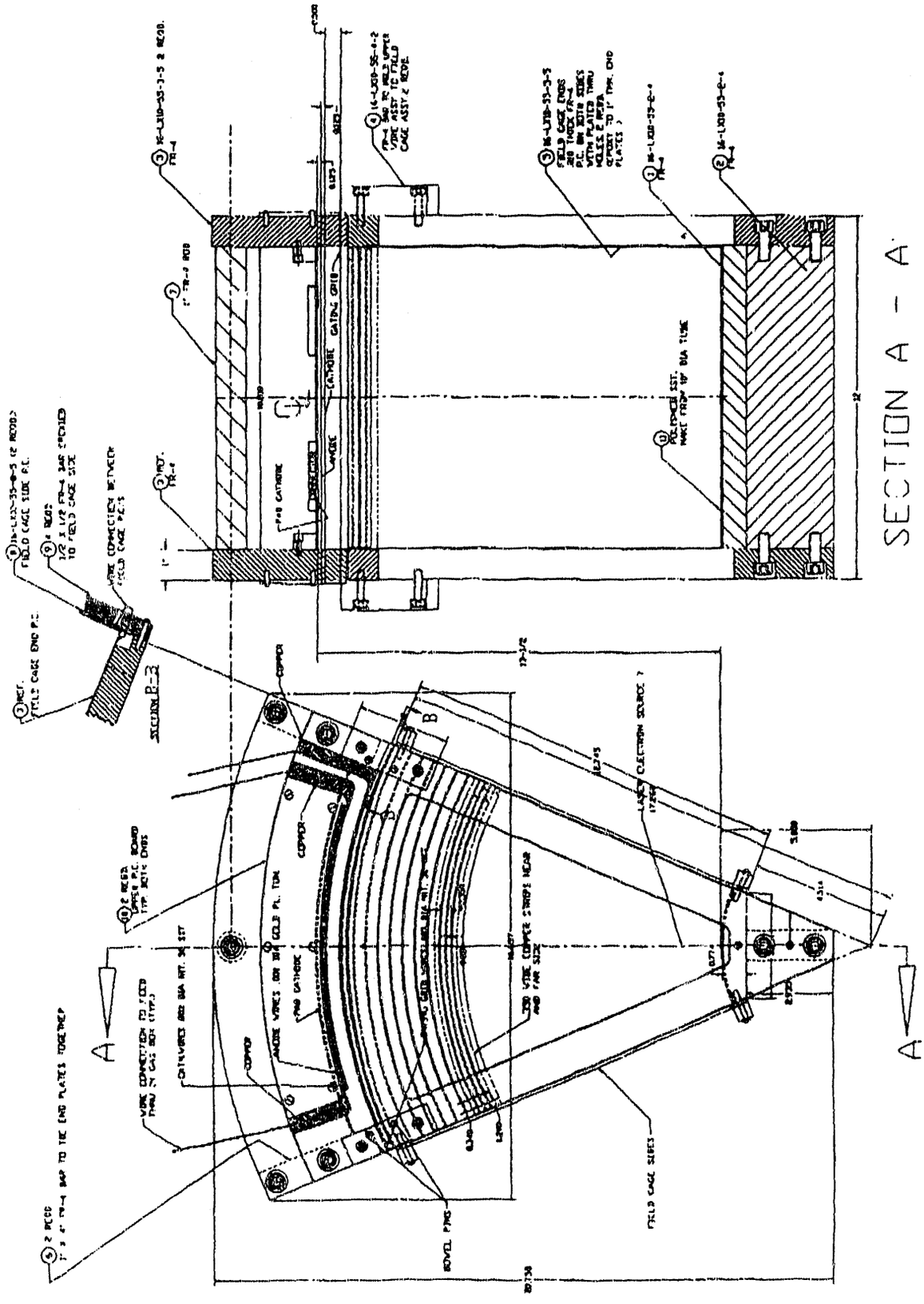

Figure 4K-13 A diagram of the prototype radial TPC sector that is under construction.

4.K.5. Engineering

4.K.5.a. Brief Technical Description & Specifications

4.K.5.b. Description of Major Components

4.K.5.b.1 Detector Hardware

The XTPC detectors will use cathode pad readout, this being the least expensive option in terms of the number of electronics channels required to achieve the needed spatial resolution. This would be true either for the conventional or radial geometry. Above the pad plane will be an anode plane with field wires, a cathode wire plane and a gated grid. The field uniformity in the drift region will be achieved via copper strips on the sides and front and rear ends of the field cage walls. There will be double sided PC boards on the sides, and double sided Kapton for the entrance and exit windows. A resistor string will supply a uniform gradient.

In an effort to control costs and maximize existing manpower, it is anticipated that the project will be broken down into smaller tasks with local testing of subsystems before being assembled into the final package at BNL. A test of this procedure is taking place in the construction of the prototype radial drift chamber, for which parts are being built at UC Davis, LBL, and BNL.

4.K.5.b.2 Front End Electronics

The front end electronics consists of a preamplifier-shaper followed by an analog sampling memory such as the SCA/ASA chips which may or may not contain data desparsification. At this point the FEE shifts to DAQ. Our concerns then are making low noise contact with either pad or anode electrodes, then delivering digitized data (10 bits) to a local bus that receives this data. The bus may further compact the data and pass it to off-chamber electronics. The principle elements in this FEE are: Amplifier-shaper, SCA/ASA, readout logic, and physical mounting of the sub-assembly.

Preliminary electronics block diagrams are shown in Fig. 4K-14. Figure 4K-15 shows an artist's conception of a FEE module. As an integral part of the end cap and interconnection PC (sector) we will have an I/O circuit (T9000 board) that combines digital inputs from the 8 64 channel FEE modules onto a fiber optic channel. This sector configuration is shown in Fig. 4K-16. Thus the on-chamber electronics is part FEE and part DAQ with 45 links (for 22 k pads) going each way to external modules (probably FASTBUS). It should be noted that low pressure (leakless) water cooling is part of all plug in modules as well as the end cap structure.

The 360 FEE modules will be assembled using mass assembly techniques. The water cooling layer will be stamped from two pieces of brass and soldered or glued together with appropriate jig structures, then glued to the heat producing layer of the FEE structure. The three layers of IC will be on multilayer polyimide substrates. The chips will be glued to polyimide and wire bonded.

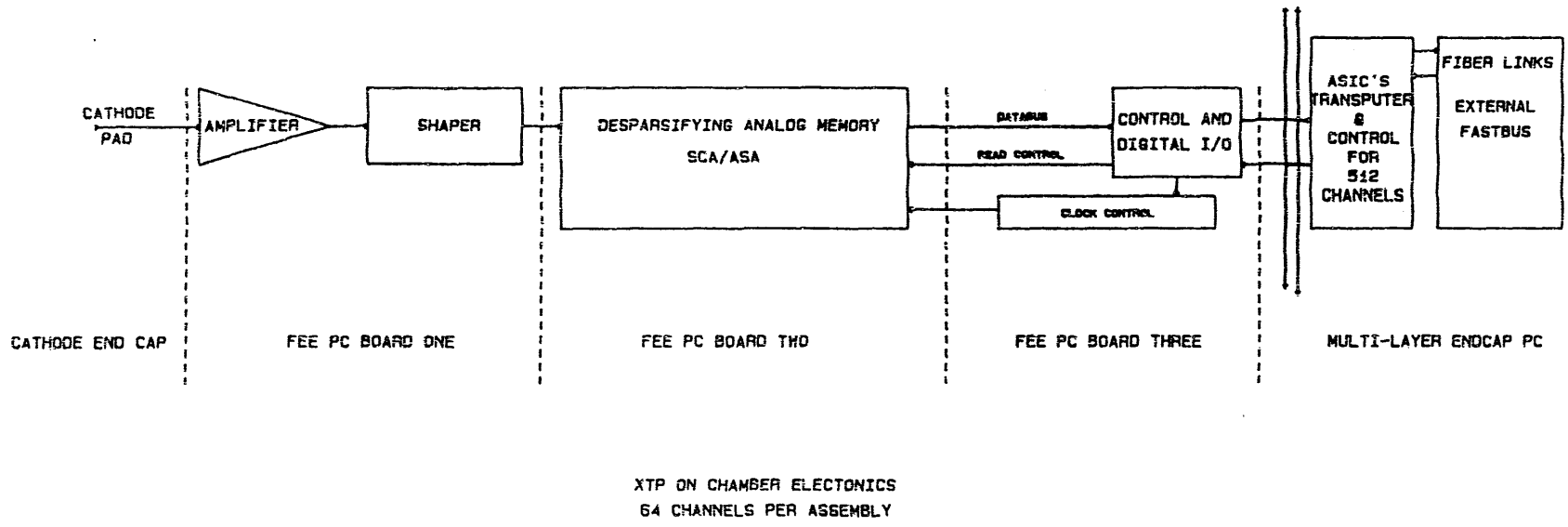

Figure 4K-14 XTPC on-chamber electronics.

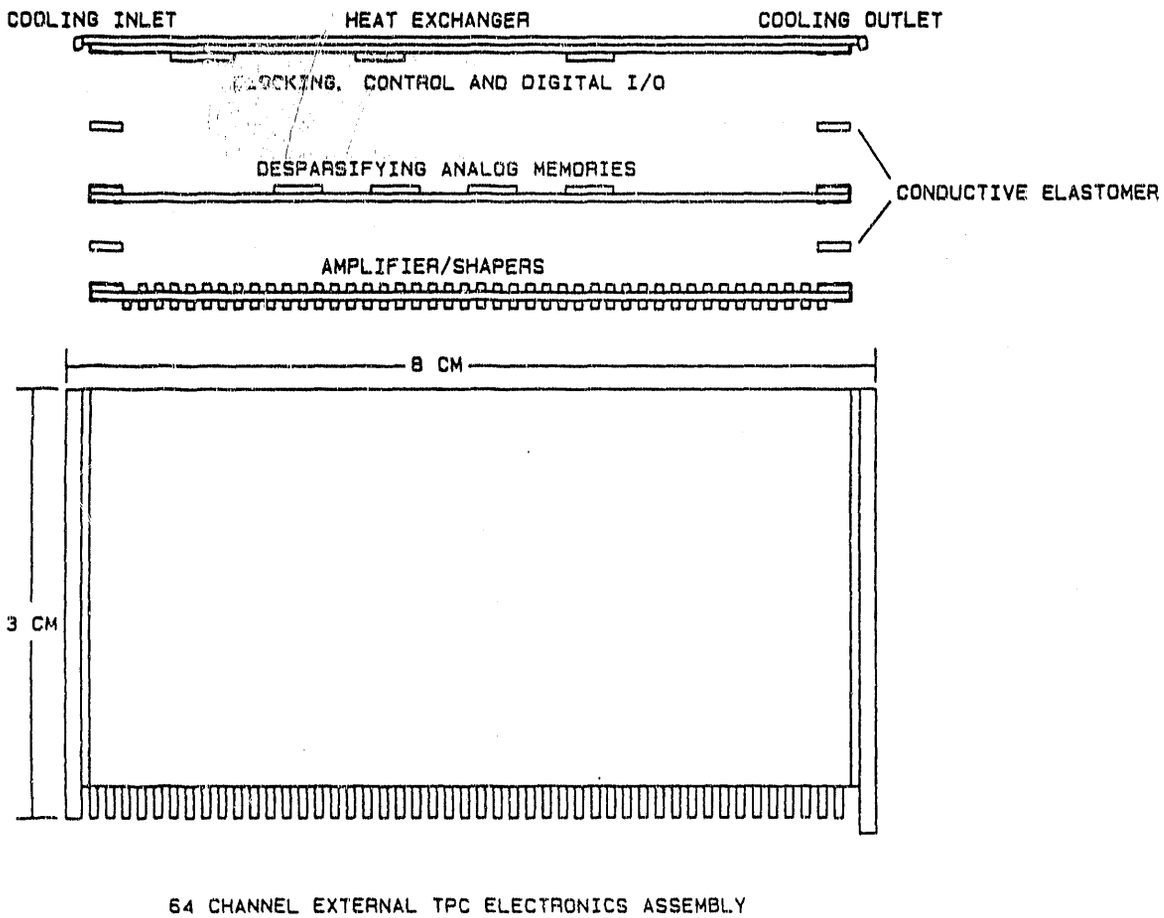

Figure 4K-15 XTPC electronics assembly.

All electronic devices will be fully tested first at the wafer level using automated test equipment, then tested again at the individual PC layer level, and finally tested as complete assemblies. This highly automated test and assembly process is expected to hold the XTPC FEE cost down well below that of previous systems.

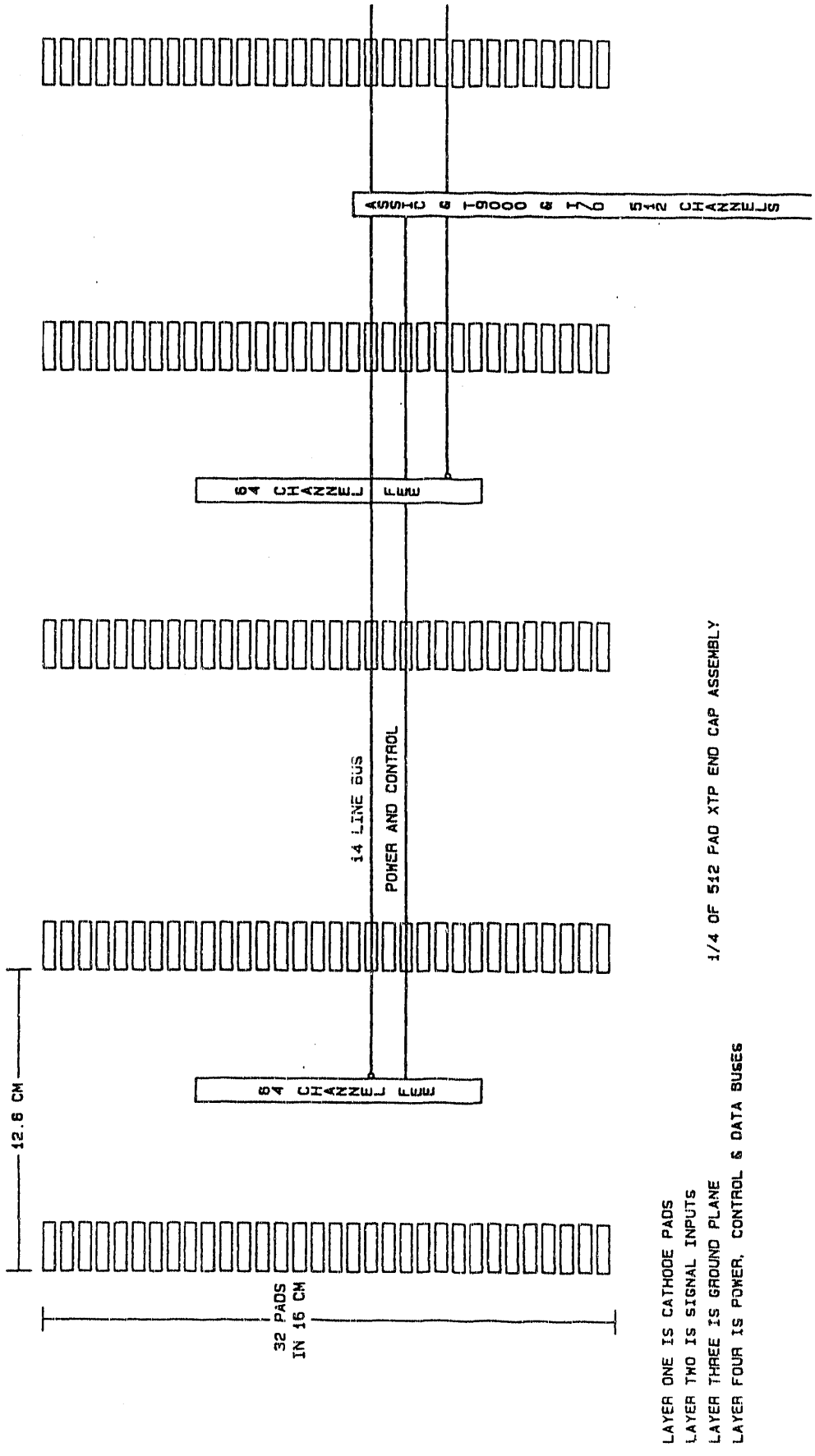

Figure 4K-16 XTPC end-cap electronics.

5.
Integration of Experiment

5. Integration of Experiment

5.A. Subsystems Integration

Subsystem Integration tasks include the following:

- Subsystem Dimension Control
- Routing of cables, pipes, ducts, etc. from detector subsystems
- Assembly and service scenario modeling
- Conceptual design of detector supports, return iron, other miscellaneous subsystems.
- Determination of conventional facilities needs, which include assembly hall requirements and modifications and utility needs (power, HVAC, water, etc.)

5.A.1. Subsystem Dimension Control

Engineering and design effort is being devoted to ensure that subsystems fit together, can be assembled and serviced, and have minimum negative impact on other subsystem's performance. Subsystem overall dimensions have been defined along with assembly clearances. Figure 5-1 shows a cross-section of the STAR detector with some basic dimensions. The subsystem overall dimensions are shown in Table 5-1.

It is important to note that these dimensions represent simple geometrical volumes and maximum subsystem dimensions. A subsystem's nominal dimensions will likely be different due to manufacturing and alignment tolerances. More detailed geometries will be defined as systems evolve. Three-D CAD solid modeling will be used to model these geometries in an unambiguous manner.

5.A.2. Assembly

Initial assembly and subsequent servicing of the detector has been modeled on both 2-D and 3-D CAD in order to determine the dimensions for the new assembly building and to insure adequate fit in the existing Wide Angle Hall. The detector will be assembled, fully cabled, and tested in the assembly building. Figure 5-2 shows the assembled detector with its electronics trailer in the proposed assembly building. The detector with its electronics trailer will then be rolled into place on the beamline, the beampipe will be installed, and the shielding wall/room erected around the electronics trailer. At this point, the detector is ready for testing and operation on the beamline. Figure 5-2 also shows the detector in its operating position.

Assembly of the detector begins with erection of the detector supports onto the steel floor plates as shown in Figure 5-3. Temporary auxiliary supports are used to stabilize the structure against forces in the axial direction. The end iron rings are then mounted onto these supports, and surveyed and aligned into proper position. The lower EMC/barrel return iron segments are then bolted to the end iron ring. They are brought in from the side, then picked up using special lifting fixtures by two cranes (shown conceptually in Figures 5-4 and 5-5) and inserted onto the mounting studs. The mounting nuts are tightened evenly to pull the segments up into final position on the end return iron rings.

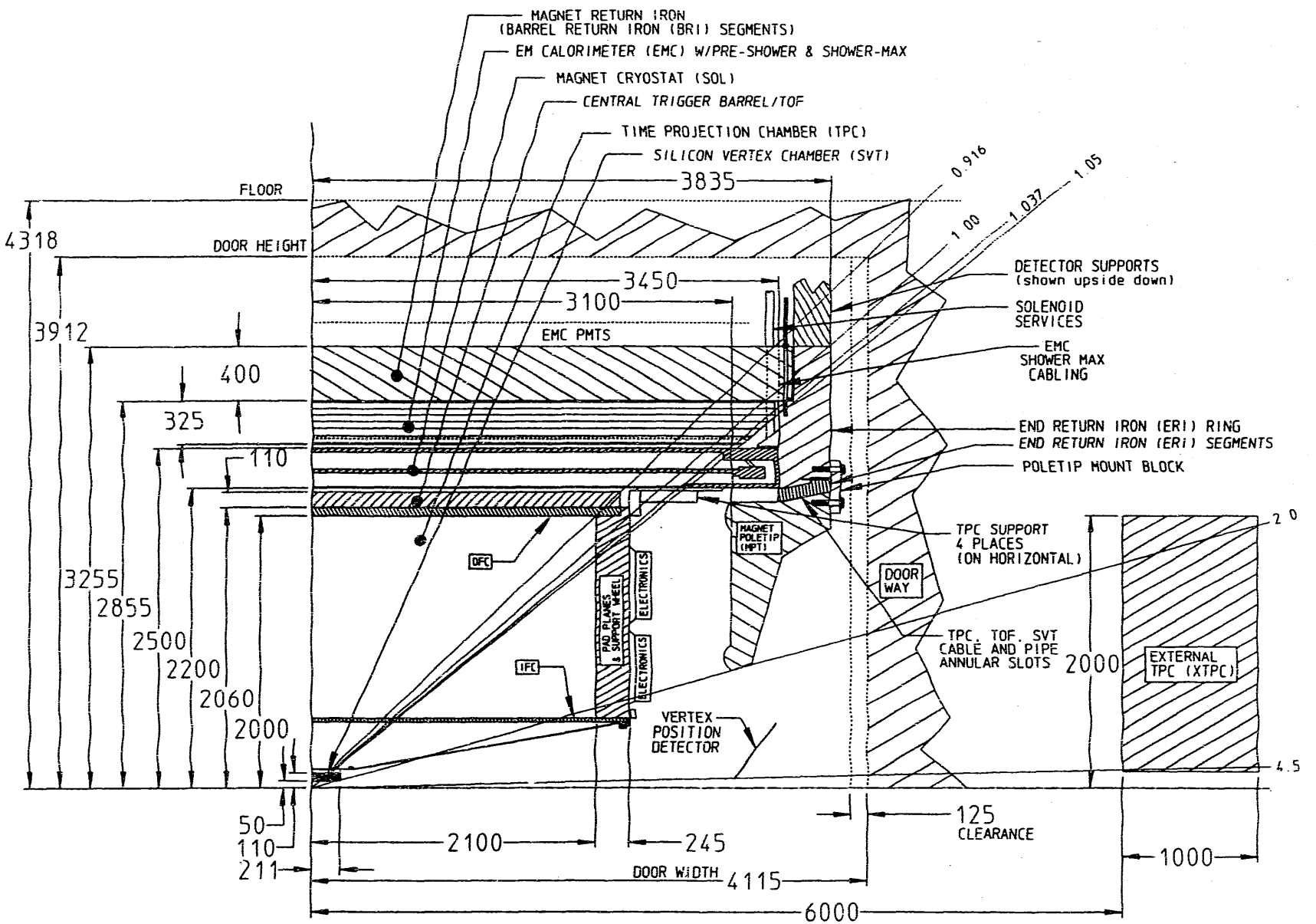

Figure 5-1 STAR Detector, quarter section view.

Table 5-1 STAR subsystem basic dimensions.

SVT		
	Inner Radius	50 mm
	Outer Radius	107 mm
	Half length	211 mm
TPC		
	Inner Radius	500 mm
	Outer Radius	2060 mm
	Half length, Tracking Volume	2100 mm
Trigger Barrel (CTB)		
	Inner Radius	2060 mm
	Outer Radius	2170 mm
	Half length	2280 mm
Solenoid		
	Inner Radius, cryostat	2200 mm
	Outer Radius, cryostat	2500 mm
	Half length, cryostat	3450 mm
	Return Iron Inner Radius	2780 mm
	Return Iron Outer Radius	3180 mm
EMC		
	Inner Radius	2530 mm
	Outer Radius	2780 mm
	Maximum Half Length	3430 mm

The coil is then lowered into the resulting cradle, mounted and aligned, as shown in Figure 5-6. The remaining upper half of the barrel return iron segments are then assembled onto the end iron rings. Once most of the barrel iron is assembled, the detector becomes self stabilized against axial forces, and the auxiliary detector supports may be removed. Coil mounts for the upper half are installed as the segments are installed.

After the iron and coil are assembled, the detector is ready for field mapping, which must be done without the TPC in place. Field measurement equipment is installed in the magnetic volume, and the poletips are then installed. The poletips have their own rolling supports. The supports may be left on when the detector is in the operating position or in the testing position in the assembly hall. They must be removed before the detector can be moved through the door of the wide angle hall, because of the limited WAH door width.

After field mapping is complete, the poletips are removed while on their supports, and a TPC installation beam is installed through the detector. This beam is

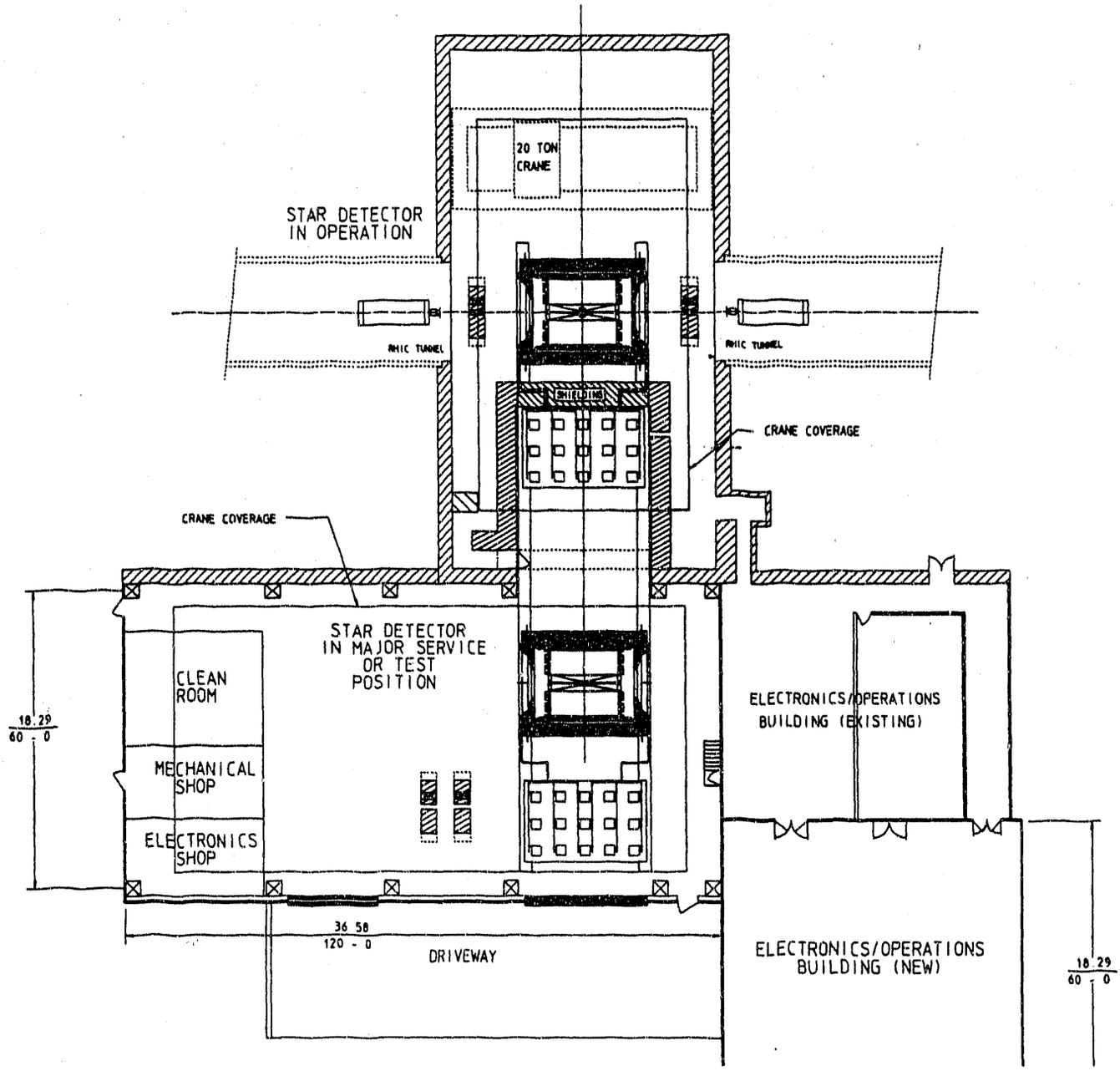

Figure 5-2 STAR Detector in Wide Angle hall.

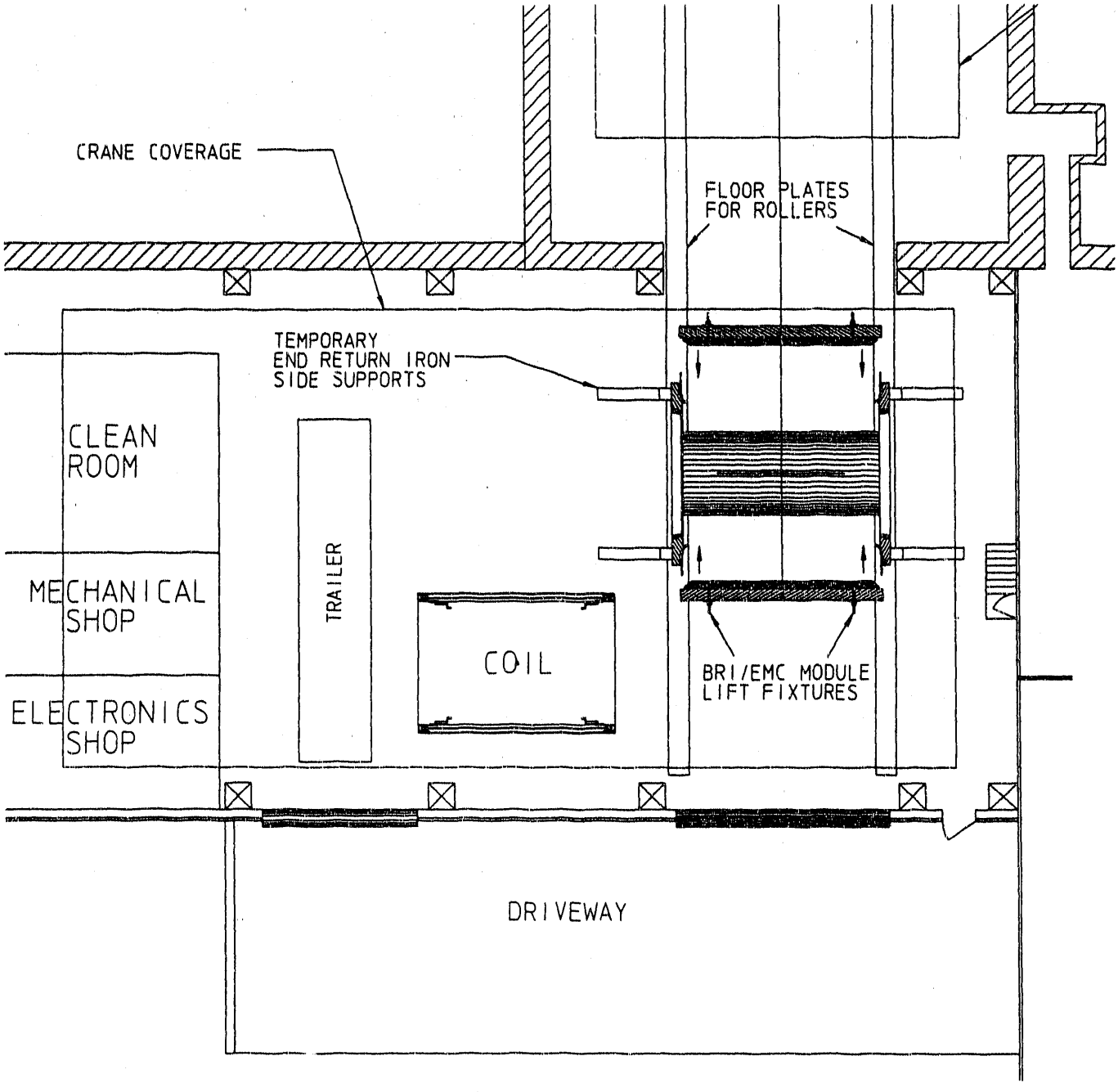

Figure 5-3 Barrel return iron (BRI)/EMC module assembly.

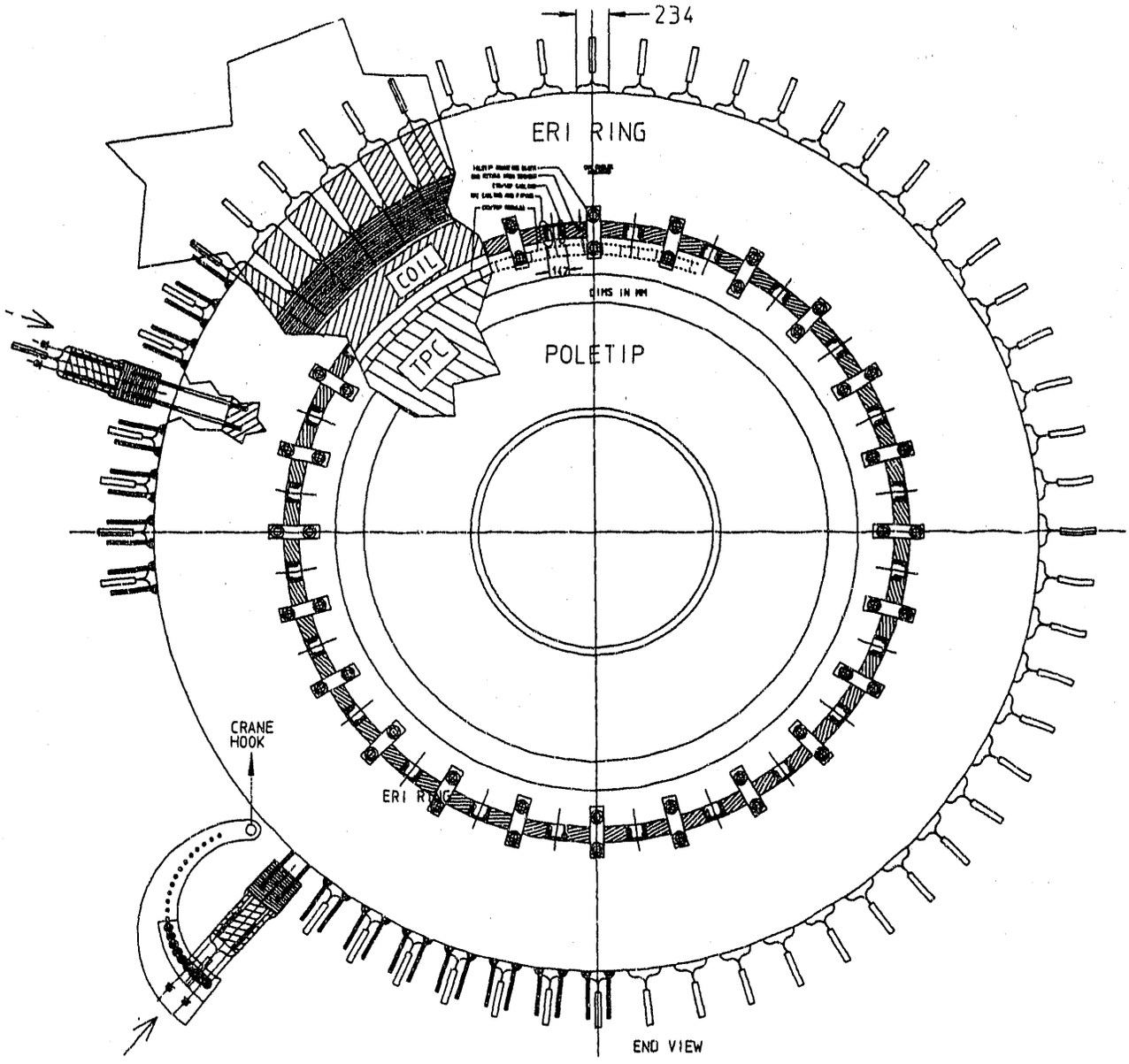

Figure 5-4 STAR Detector, end view.

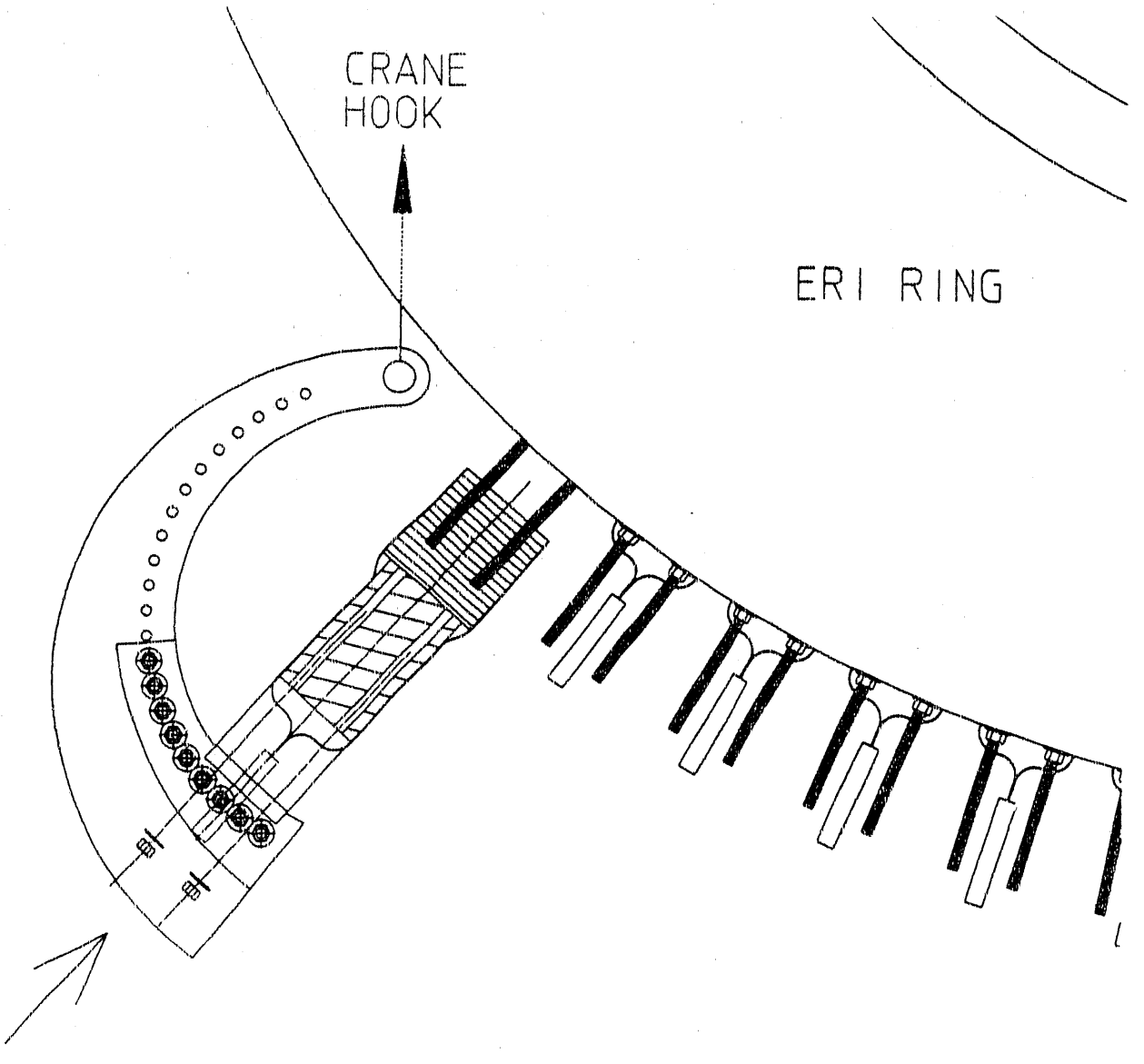

Figure 5-5 Detail, BRI/EMC assembly, end view.

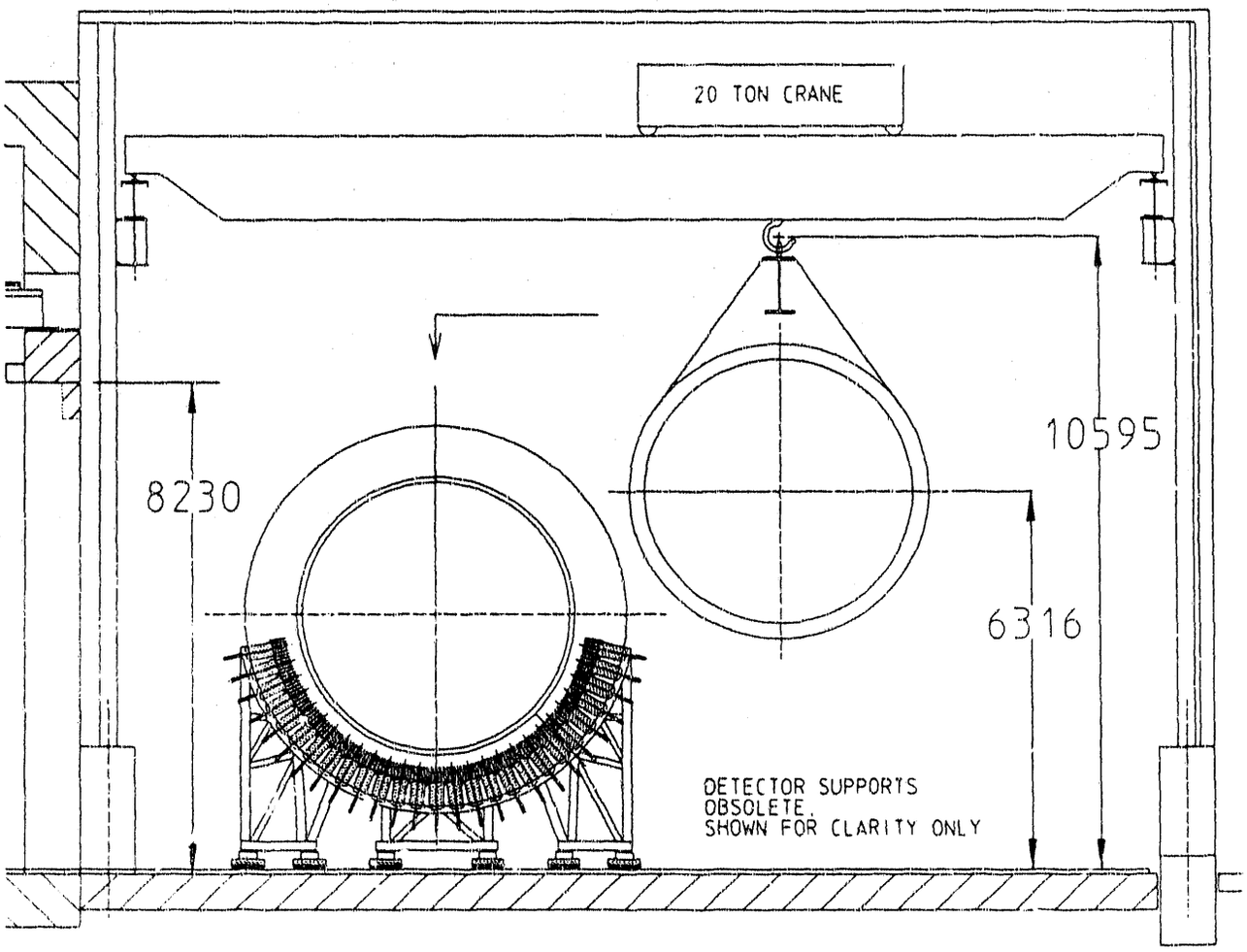

Figure 5-6 Assembly of coil into detector.

more than twice as long as the detector to allow three possible supporting points. Twin double-arm TPC supports roll along this beam. This allows the TPC, without Central Trigger Barrel (CTB) modules, to be installed onto the beam. The TPC can then (by removing the central beam support) be rolled along the beam into place inside the magnet cryostat, where it is mounted. The beam is then withdrawn from the detector. This sequence is shown in Figures 5-7 through 5-9.

After the TPC is installed and roughly aligned, the CTB modules are installed. Figure 5-10 shows a CTB module being either installed or removed for servicing. The SVT can also be installed at this time. After installation, the SVT, TPC, and CTB cables are connected and routed between the end return iron segments. The poletips are then replaced and the cabling to the electronics trailer is completed. The complete detector is then ready for testing.

After testing of the assembled detector, the detector together with its electronics trailer can be rolled into the experimental hall, as noted above. This is accomplished by installing anchor blocks into the holes in the steel floor plates and jacks between the

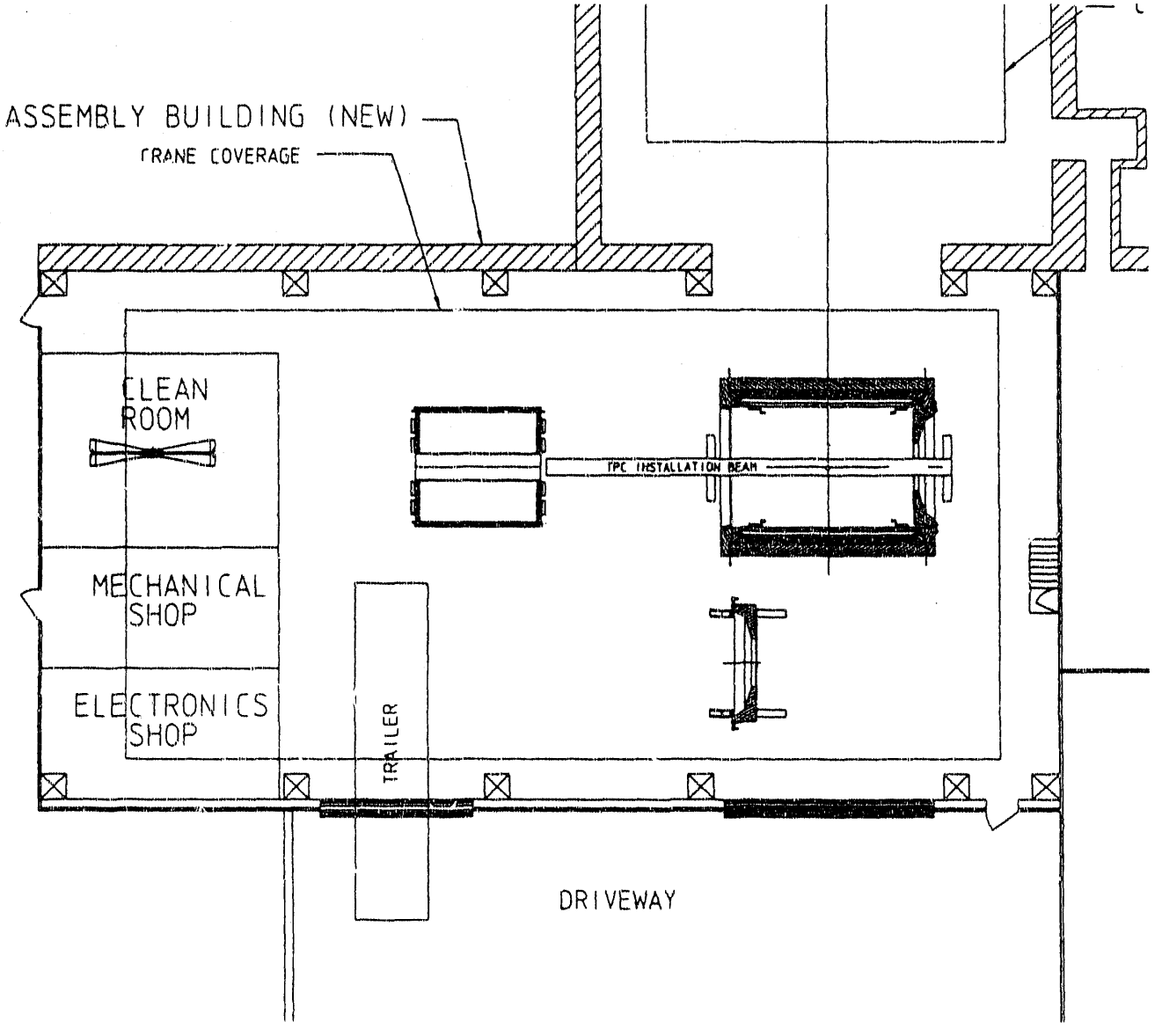

Figure 5-7 Installation of TPC, initial set-up.

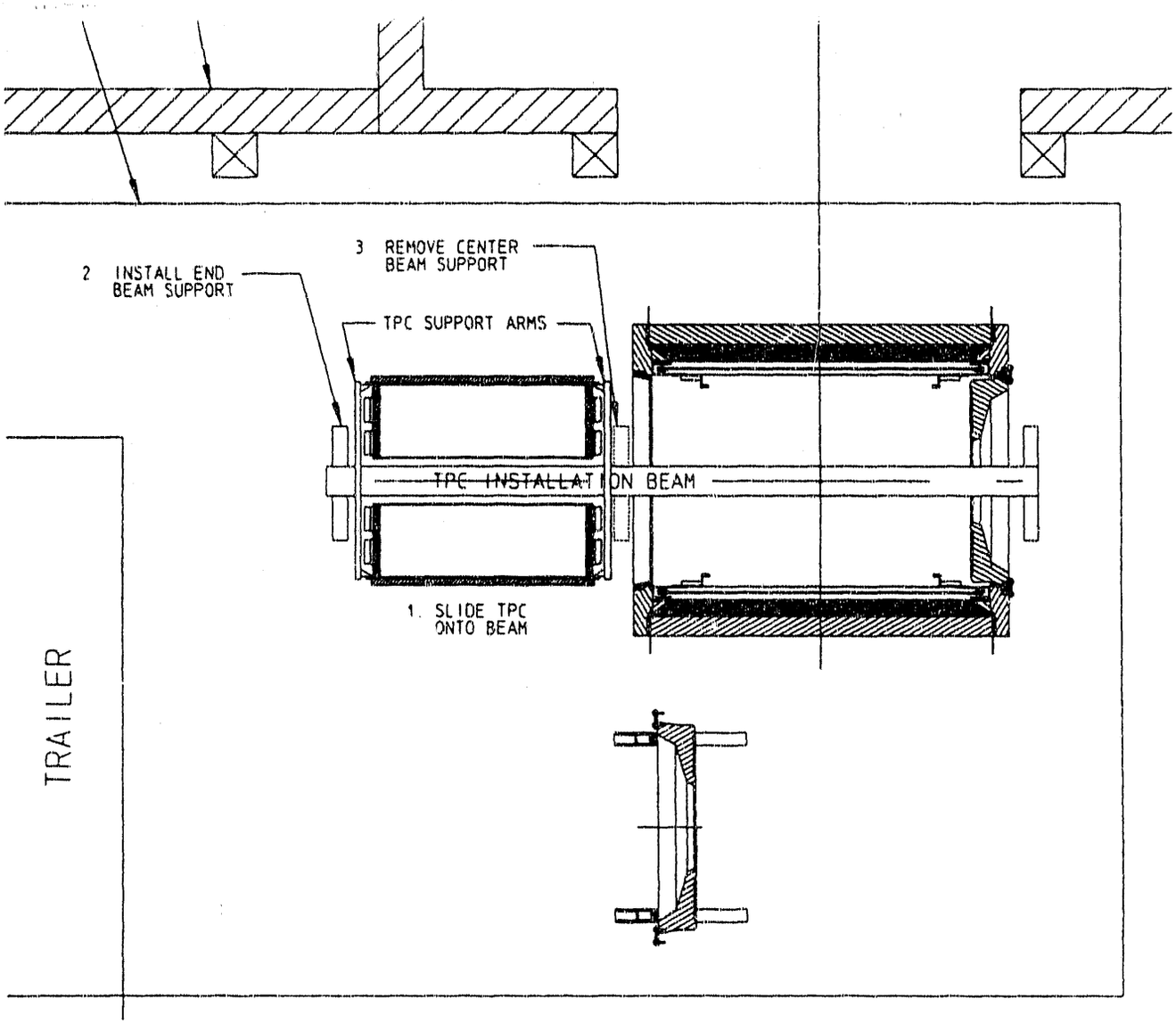

Figure 5-8 Installation of TPC onto installation beam.

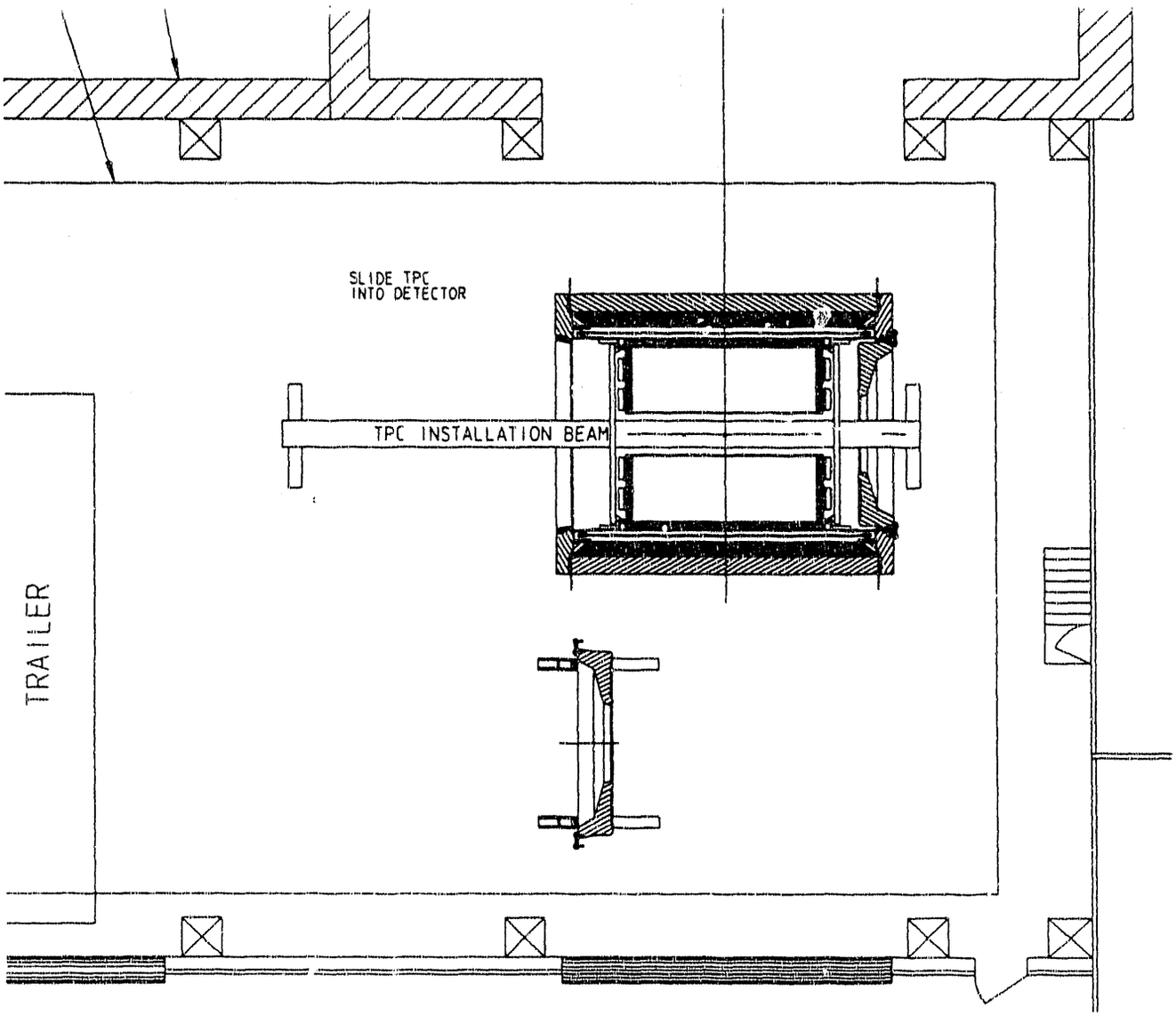

Figure 5-9 Installation of TPC into the detector.

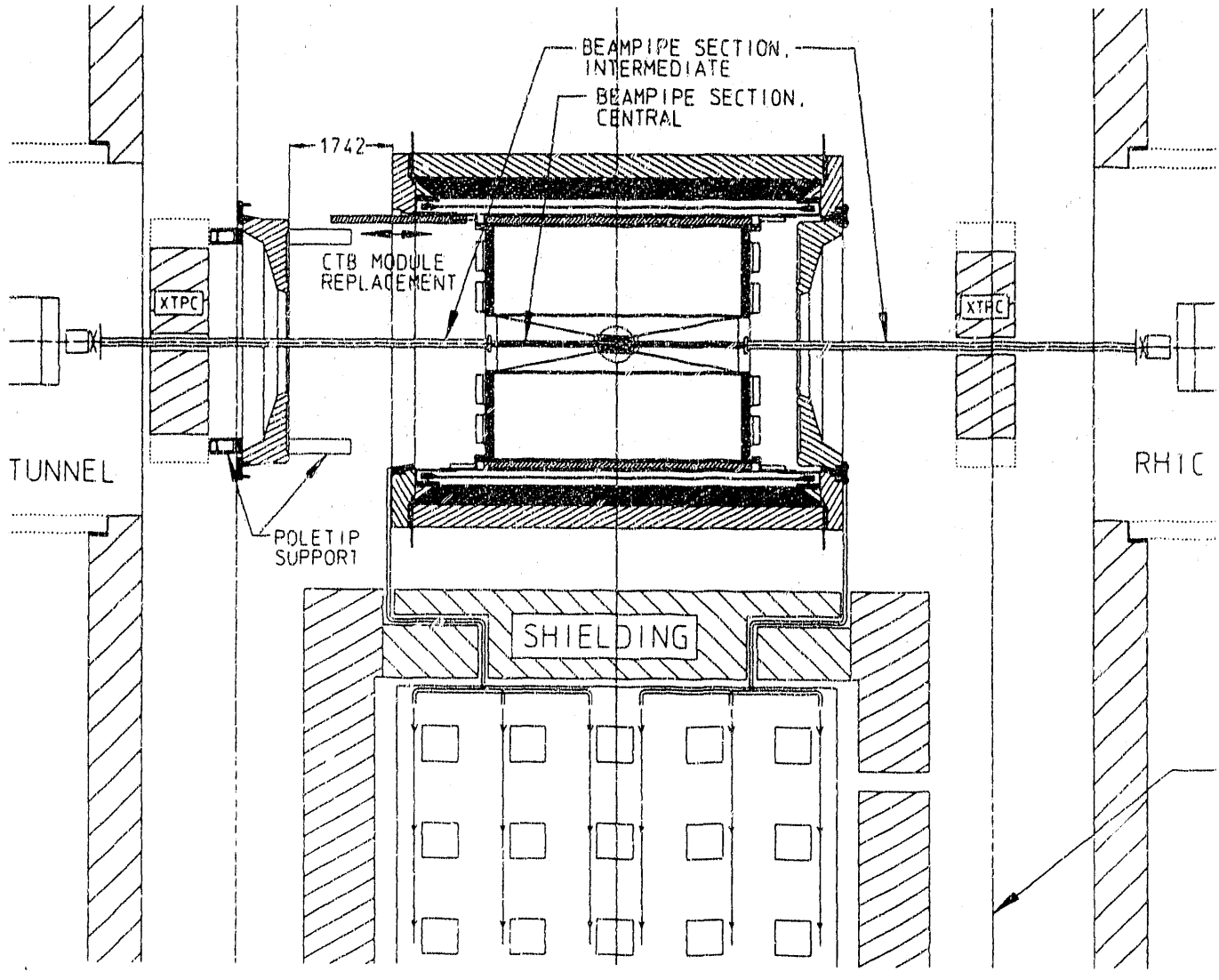

Figure 5-10 Minor service or TB/TOF upgrade scenario.

blocks and detector supports. The detector is then moved with the jacks, the jacks are retracted and the anchor blocks moved to the next set of holes, similar to the method used by the SLD, and D0 detectors.

5.B. Plumbing & Cabling Plans and Issues

Cable and pipe routing, provision for electronics power and cooling and ventilation needs are being developed. Three-D CAD solid modeling will be used to both visualize and check for interferences. A general concept has been developed for the routing of cables and pipes from the various subsystems to their respective electronics and service connections. Cables and pipes which service the SVT, TPC, and CTB will be routed between the end return iron segments, as shown in Figures 5-11 and 5-12. EMC PMT cables are already external to the detector and will be collected and routed directly to the electronics. EMC Shower Max cabling will start at each end of each EMC segment and be routed radially outward through the gaps between each barrel return iron segment. Solenoid services will require one or more slots, on one end only, in the top EMC/barrel return iron segment.

The slots between the end return iron (ERI) segments for the SVT, TPC, and CTB cables and pipes result in a loss of 25% of the iron circumferential flux return path at this radius. The remaining 75% iron area carries both higher overall field and a small amount of localized magnetic saturation which is not thought to adversely affect the operating field in the TPC . Should more cable area be necessary, the ERI segments can be made non-magnetic and coil current increased by about 1-2% to account for the resulting air gap. Again, it is felt that the field quality is not adversely affected. The ERI segments are designed to be removable, which allows CTB modules to be removed. These modules are removed by sliding them axially outward after removing first the poletip, and then the obstructing ERI segment. Figure 5-10 shows this concept. Some CTB modules will be blocked by cables and pipes as well. These pipes and cables will have to be made flexible enough to move laterally to the side after one or two ERI segments are removed.

After exiting the return iron, these cables will be routed along the ERI ring, as shown in Figure 5-12. The cables will collect at, and feed through the shielding wall, perhaps in a dogleg fashion (into the paper) to reach the electronics. The majority of the DAQ and power supply electronics for all the subsystems are located on the electronics trailer which travels with the detector when it is rolled off the beamline and into the assembly hall. The shielding wall and roof between the trailer and the detector allows safe access to the electronics during operation. The magnet power supply and control dewar are located at the top level of this trailer for cryogenic flow stability and to minimize the length of the coil leads.

5.C. Access and Maintenance Requirements.

There are three service scenarios which may occur. The first scenario requires the removal of the detector from the wide angle hall. This would be required in the case where a subsystem needs major service, such as a coil failure, or for a time consuming upgrade. The beampipe is removed, the shielding disassembled, and the detector rolled

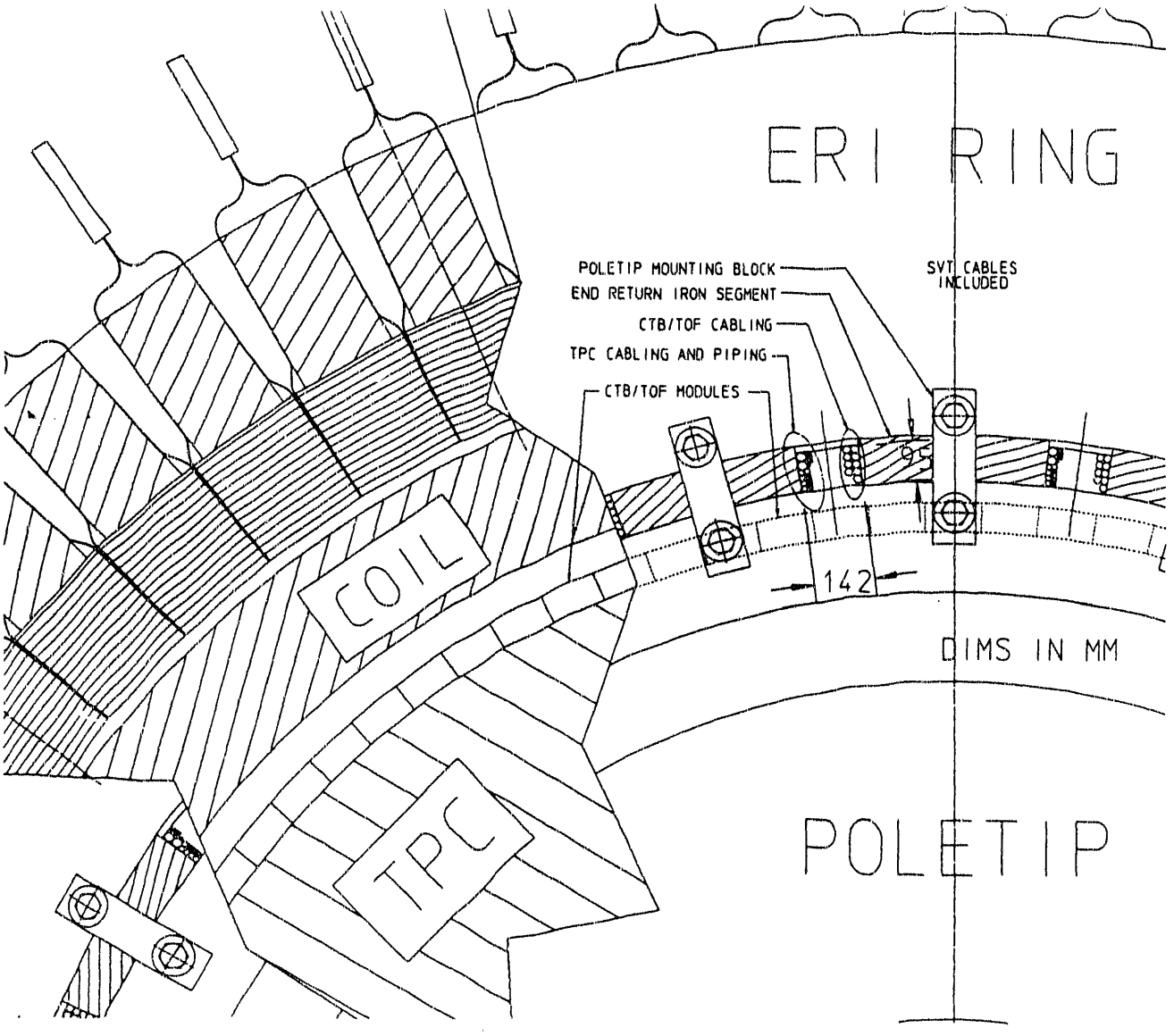

Figure 5-11 Cabling and piping through return iron.

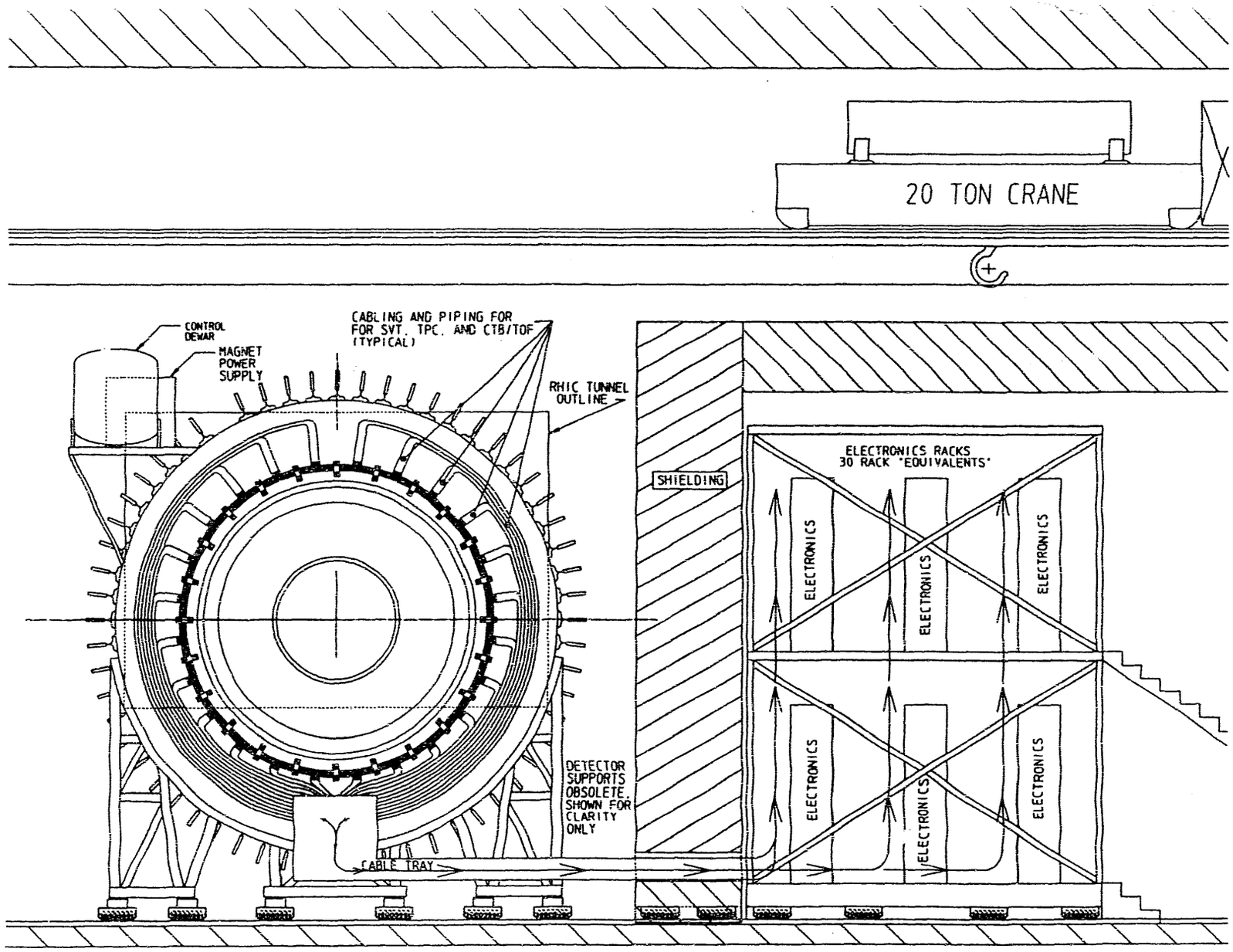

Figure 5-12 Detector cabling concept.

into the assembly building. As soon as the detector is off the beamline, the beampipe is replaced and the shielding rebuilt. It is estimated that the accelerator would be operational in 2-3 weeks.

The second type of service scenario is where quick access is needed to service SVT, TPC, and CTB electronics, or for replacement of a TPC sector and/or CTB module(s). Table 5-2 summarizes the STAR detector's expected service and repair time estimates.

Table 5-2

Service	Frequency	Repair Time
1. TPC electrical	biweekly	hours
2. EMC phototubes	bimonthly	hours-day
3. CTB /TOF phototubes	bimonthly	days
4. TPC pad planes	annually	days-week
5. SVT Electronics	bimonthly	hours-day

In this second scenario, the poletip(s) are retracted while the beampipe is left undisturbed. The XTPC's (if present) would first roll back on their own supports. Figure 5-10 shows the detector in this configuration with a CTB module being withdrawn for replacement. CTB segment removal will first require removal of the corresponding ERI segment(s) and temporary relocation of cables or pipes which might be in the way.

The third scenario is for removal and replacement of the (non-clamshelled) SVT. For this case, the intermediate beampipe sections would be removed and then the XTPC's and poletips would be moved off the beamline out of the way. The SVT can then be removed and replaced. The center beampipe section remains mounted within the SVT during these handling operations. Figure 5-13 shows this operation. The baseline SVT design is clamshell, however, and does not require removal of any beampipe sections.

5.D. Miscellaneous Subsystem Design

The integration group is currently taking on the task of initial design of two components. These two components are the return iron structure, which is being designed in conjunction with the EMC and SOL subgroups, and the detector support system which is being designed in conjunction with RHIC detector engineering. Design details for these subsystems are presented elsewhere in this report.

5.D.1. Return Iron Mechanical Design

The return iron for the solenoid serves several magnetic functions:

- Minimize solenoid electric current requirements
- Provide uniformity of the magnetic field (addition of poletips)
- Provide hole in poletip above $\eta = \pm 2.0$ for XTPC operation
- Minimize stray field

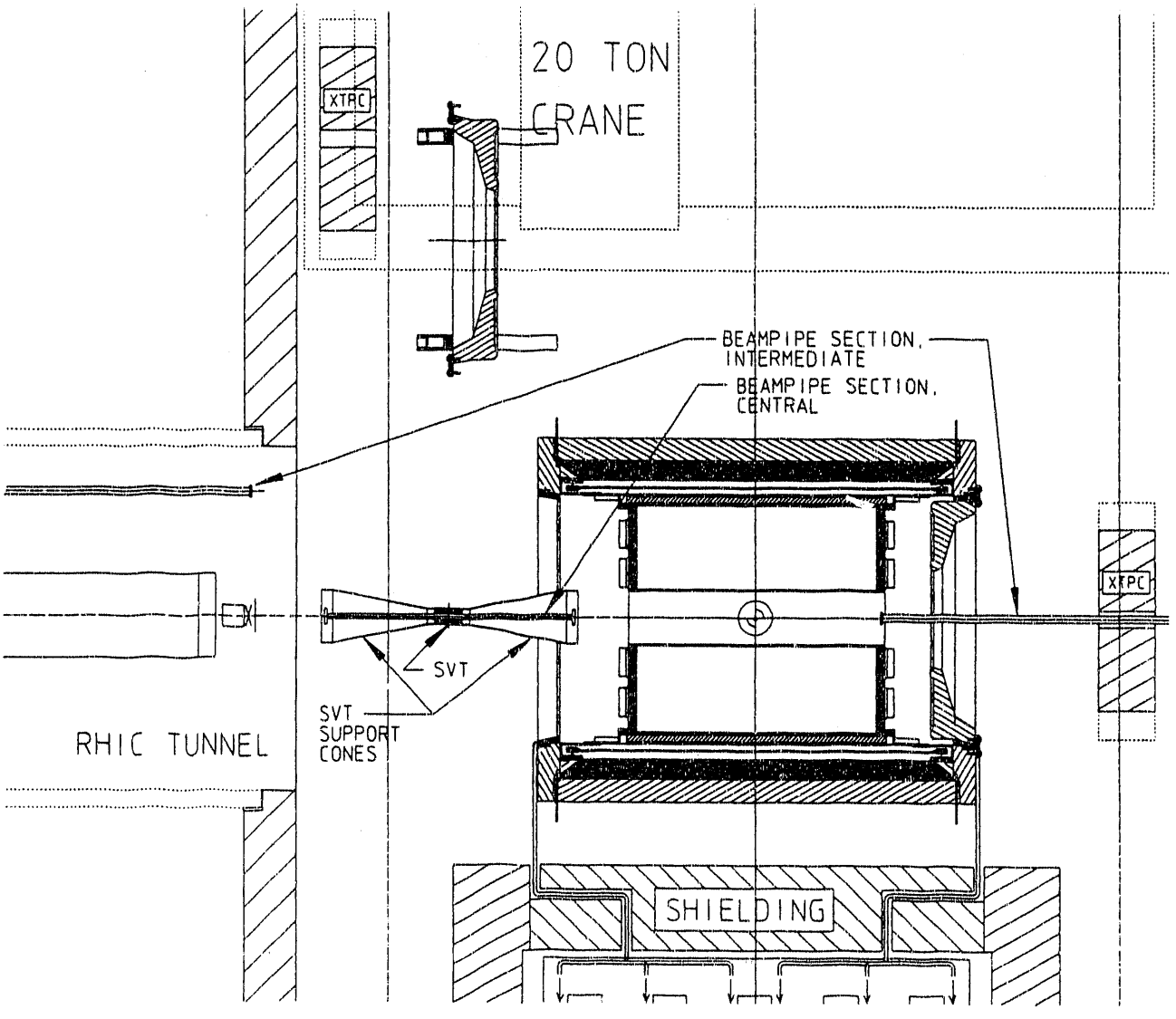

Figure 5-13 SVT replacement scenario.

The design of the return iron yoke must take into account several mechanical functions in addition to its magnetic ones:

- Provide support for all the major subsystems, except the XTPC's.
- Allow the poletips to be removed easily for servicing or removal of internal components.
- Accommodate cables and pipes for internal subsystems.
- Allow CTB segments to be easily removed
- Allow removal of individual EMC/BRI modules from the fully assembled detector

The return iron is composed of three major subparts: the poletip, the end return iron (ERI) ring, and the barrel return iron (BRI) segments. These are labeled in the detector cross-section illustration. The ERI rings are supported on the detector supports. Each ERI ring has 60 machined flats around the circumference to which the EMC/BRI segments are bolted. Additionally, bolted to each ERI ring are twelve adjustable mounts which support the solenoid coil cryostat on its outer end flanges. The BRI segments, as an ensemble, are expected to provide sufficient rigidity against forces in the axial and transverse directions, when bolted tightly to the end iron rings, as shown in Figure 5-14.

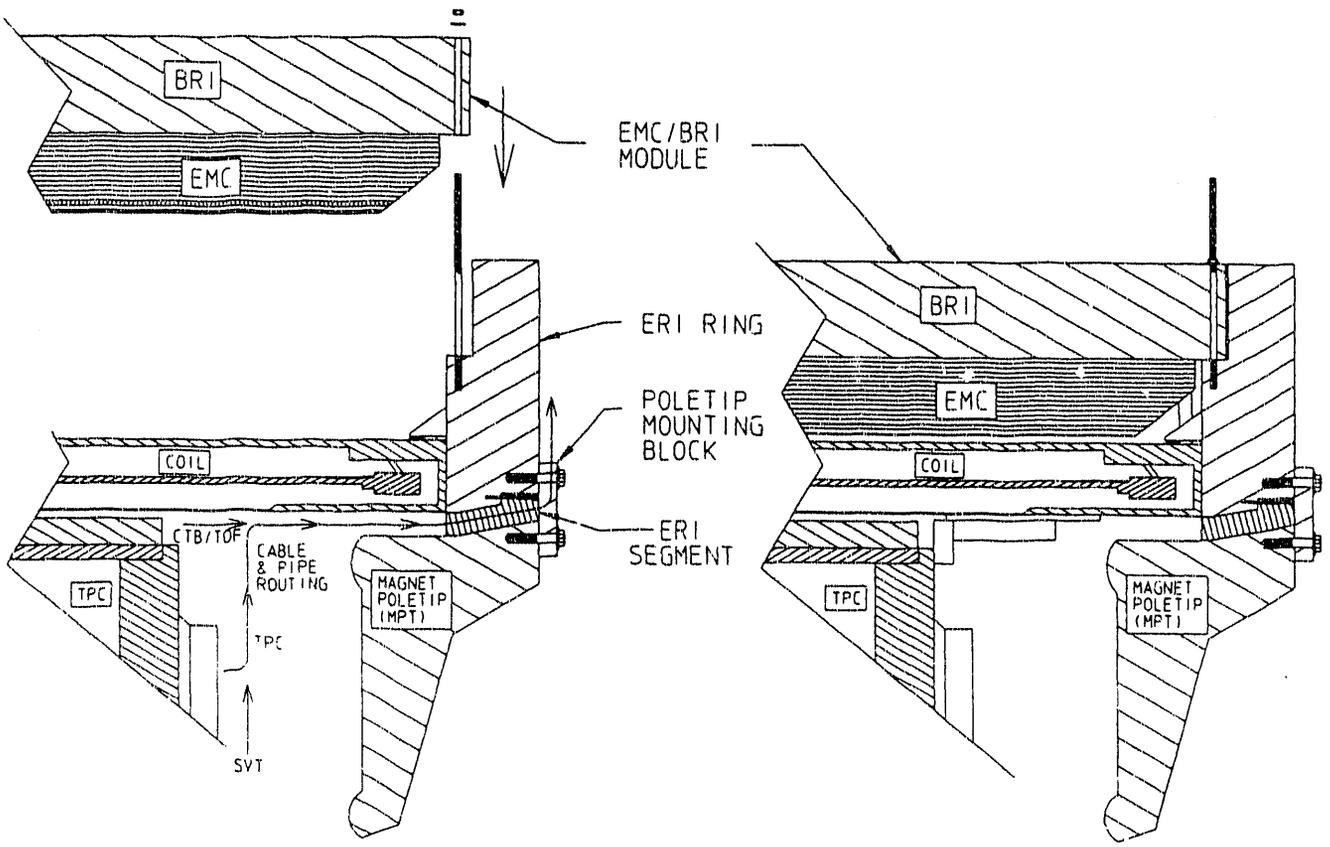

Figure 5-14 Barrel return iron (BRI) mounting concept.

These BRI segments can be connected together with tie plates (not shown) to provide additional lateral stability, if necessary.

The mating surfaces of the poletip and the ERI segments are tapered to allow insertion of the poletip without binding. To prevent the magnetic force (pulling the poletips inward) from locking the tapers together, the poletip will be mounted onto the ERI ring using mounting blocks which hold the poletip in axial alignment and prevent it from being pulled tightly into the taper. The tapered surface of the ERI segments hold the poletip in radial alignment, with a very small gap (of the order of a millimeter or less) between the tapered surfaces.

5.D.2. Detector Support Structure

The detector is supported by a structural steel assembly that will provide a stable support and will adequately distribute the weight of the detector on the floor.

The detector support will be designed to allow the detector to be assembled in the proposed Wide Angle Hall Assembly Building. The completed detector will then be rolled into the Wide Angle Hall and positioned on the beamline. The detector support structure will have the capability of not only rolling the detector (estimated weight of approximately 800 metric tons) but also positioning the overall detector to an accuracy of several millimeters, taking into account potential floor settlement. The supports will also allow removal of individual BRI/EMC modules without major detector disassembly.

The support structure is shown in Figures 5-15 and 5-16. This structure will be a welded array of four-inch mild carbon steel plate. The approximate weight of the support will be 38 metric tons. The structural steel will rest on twelve 75 ton Hilman type rollers. The rollers will allow horizontal motion of the detector during alignment. Located at each of the four corner posts of the detector will be a 300-ton Enerpac type hydraulic jack assembly. They will be used to provide vertical adjustment for the detector. Since it is expected that there will be an initial settlement of the detector, this arrangement will allow in situ vertical and horizontal adjustment of the fully assembled detector.

Between the structural steel and Hilman type rollers there will be rotating turntables that will allow the rollers to move both in the z and x direction (i.e., parallel and perpendicular to the accelerator beam line). With this arrangement the detector can be positioned very accurately. Lateral corrections can also be made while moving the detector into and out of the experimental hall.

The detector and detector support structure will require two reinforced concrete pads to be added as an upgrade to the WAH. They will provide a continuous path from the intersecting region of the Wide Angle Hall to the proposed Assembly Building. In order to roll the detector in and out of the intersecting region, there will be two horizontally mounted 100-ton hydraulic rams attached to the detector base plate.

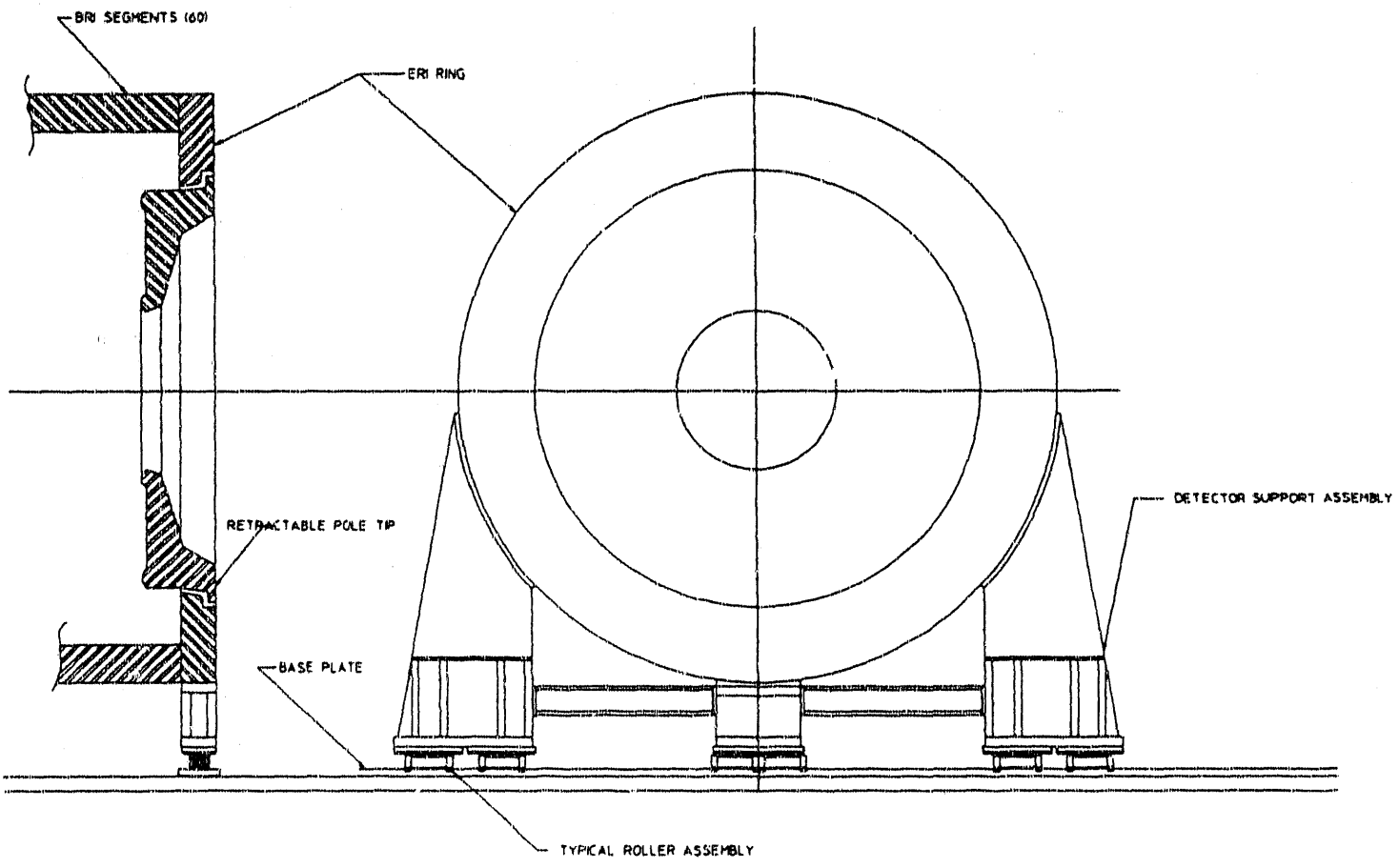

Figure 5-15 Detector support concept.

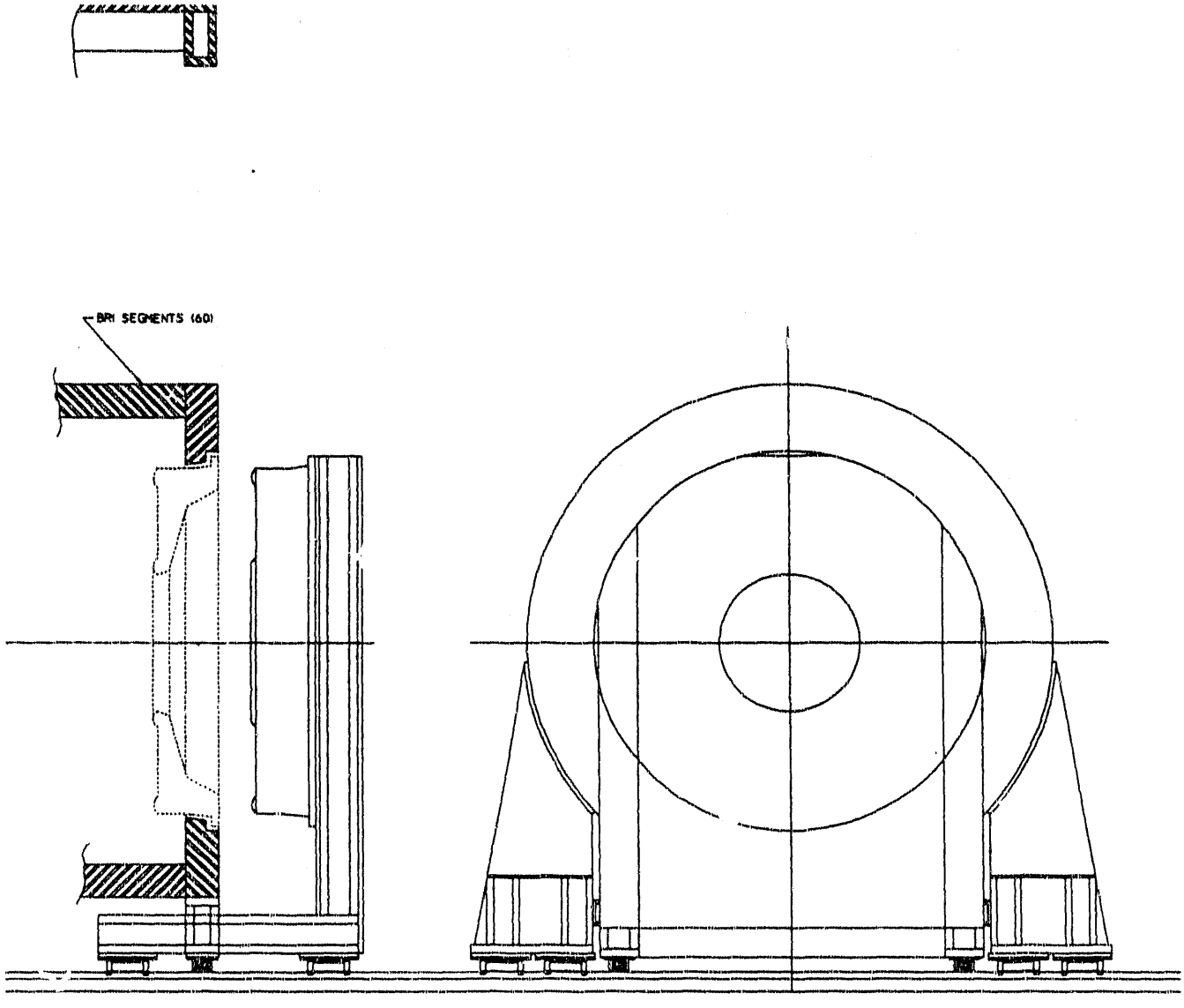

Figure 5-16 Detector and poletip support concept.

5.E. Detector Interface with Wide Angle Hall

5.E.1. Building Requirements

The Wide Angle hall has been selected by RHIC Management as the site for the STAR detector. Figures 5-17 and 5-18 show an "as is" layout of the hall and Table 5-3 lists the hall's major parameters. The beamline crosses the hall at approximately mid length, leaving little room on either end for assembly and service. The hall width is 53 ft, which limits the space needed to retract the pole tips for quick detector subsystem access. This constraint may impact the design of the XTPC and the fixture required to remove TPC sectors. Other hall constraints that may impact the detector operation are the limited crane capacity, the floor loading capacity, the size of the entry door and the clearance between the crane hook and the top of the detector. Because the south wing of the hall is too small for assembly/disassembly of the detector while the RHIC machine is operating, the detector will be assembled and cabled in a new assembly building which will be constructed adjoining the wide angle hall. After the detector is completely assembled, cabled, and tested, it will be rolled into position in the hall.

Table 5-3 Wide angle hall parameters.

Hall length and width	105 ft X 53 ft
Total area covered by crane	83 ft X 37 ft
Distance from floor to beamline	14 ft 2 in
Assumed distance from shield blocks to roll up door	47 ft
Roll up door dimension	27 ft W X 25 ft H
Floor thickness/Load capacity	1.0 ft / 5000 psf
Crane capacity	20 ton

At this time, the RHIC accelerator does not require any floor space in the hall to house machine-related equipment. The southern end of the hall which is inaccessible during operation, can be used for storing STAR assembly and handling fixtures and shielding blocks. The experiment requires power supplies and fast trigger electronic racks to be placed in the hall near the detector to minimize cable lengths. To facilitate assembly and testing of the detector in the assembly building, the electronics racks will be placed on a platform which will move along with the detector between the assembly building and the hall. Figure 5-2 shows a schematic layout of the detector and the rack platform. To allow access to the electronic crates during operation, a radiation shield will be built around the crates. The details of this shield are discussed in Section 6.A.

The load capacity of the hall's floor must be assessed by RHIC's facility structural engineers. If required, the floor will be upgraded to handle the ≈ 800 MT detector and shielding weight. Steel rails will have to be installed on the floor to facilitate detector movement between the assembly building and the hall. Other, more minor, modifications to the building will be discussed in a future document detailing the experimental facilities user requirement.

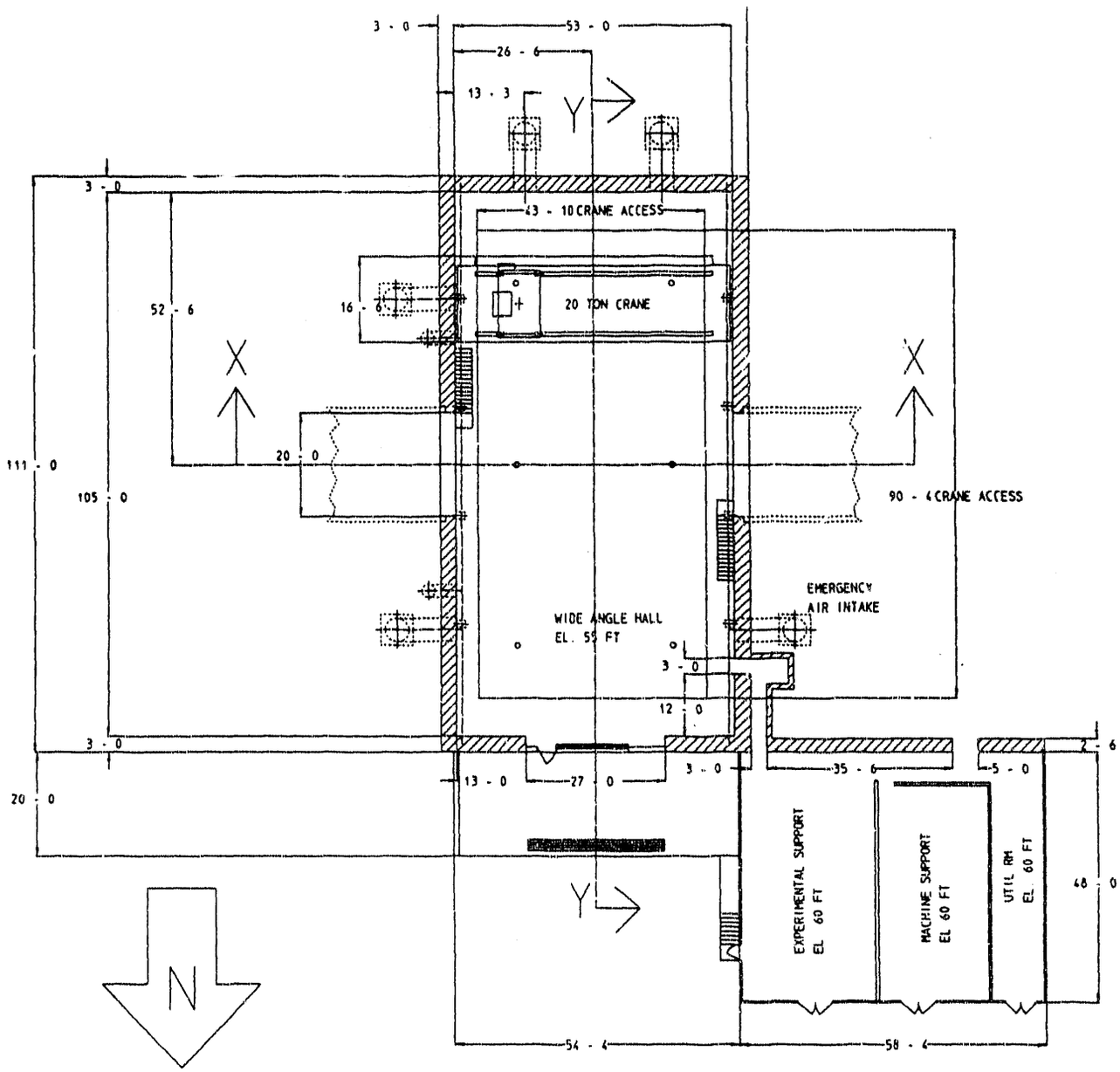

Figure 5-17 Wide Angle hall, as presently built, plan view.

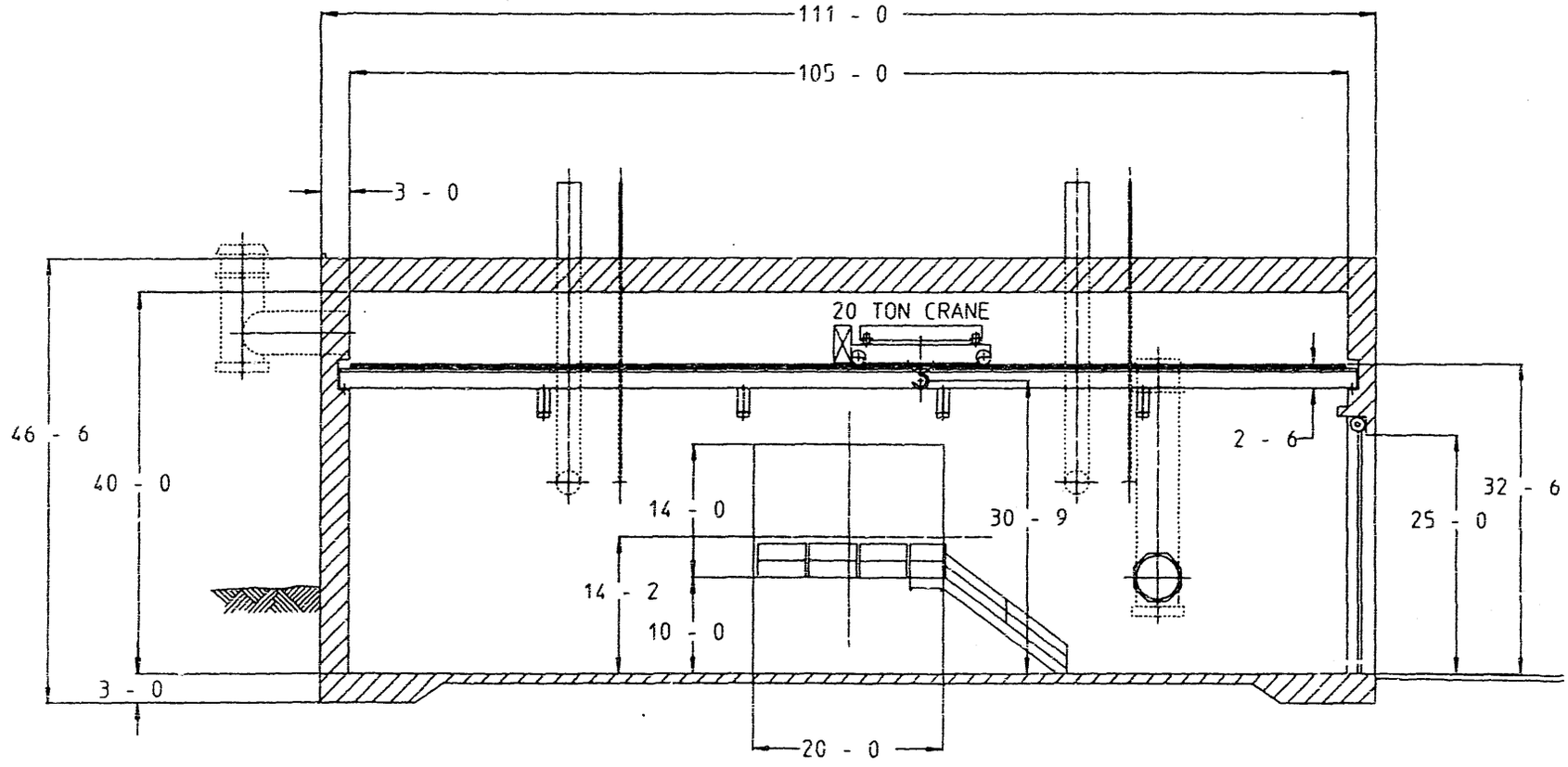

Figure 5-18 Wide Angle hall, as presently built, elevation view.

5.E.2. Hall Utilities Requirements:

The Wide Angle hall is equipped with basic utilities such as tap water, 120 psi compressed air supply line and electric power for conventional systems, such as lighting, crane and machine tools.

The STAR experiment is not expected to add much heat to the hall space since all electronics will be cooled locally using mixed chilled water loops. The maximum heat load added to the hall space air from electronics heat exchangers and PMT's is about 80 kW. Since the STAR detector cannot tolerate ambient temperature swings of more than a few degrees Fahrenheit, an HVAC system will be required to handle the 80 kW plus any heat load added to the hall from the outside world.

At the present time, only a humidity control system is available for the Wide Angle hall. This system must to be upgraded to include temperature control capability as well.

5.F. Interface with RHIC Accelerator

The interface between the RHIC accelerator and the STAR detector is basically limited to the beam pipe and possibly the cryogenic system, i.e. helium supply and return lines. All other accelerator equipment is located within the tunnel. Figures 5-19 and 5-20 show a layout of the beam pipe and the vacuum equipment near the beam pipe.

The details of the beampipe and its support structure within the detector have not yet been engineered. Preliminary layouts suggest a three piece beampipe, with the center narrow section being approximately 4 meters long and made of beryllium. None of the detector's subsystems require the removal of the beam pipe for routine service, with the exception of a non-clamshelled SVT. The impact on XTPC operation has not yet been determined.

Final engineering drawings of accelerator cryogenic bypass transfer lines and power cables are not available at this time. However, it is expected that this equipment will be located outside the hall to avoid any potential interference with the detector.

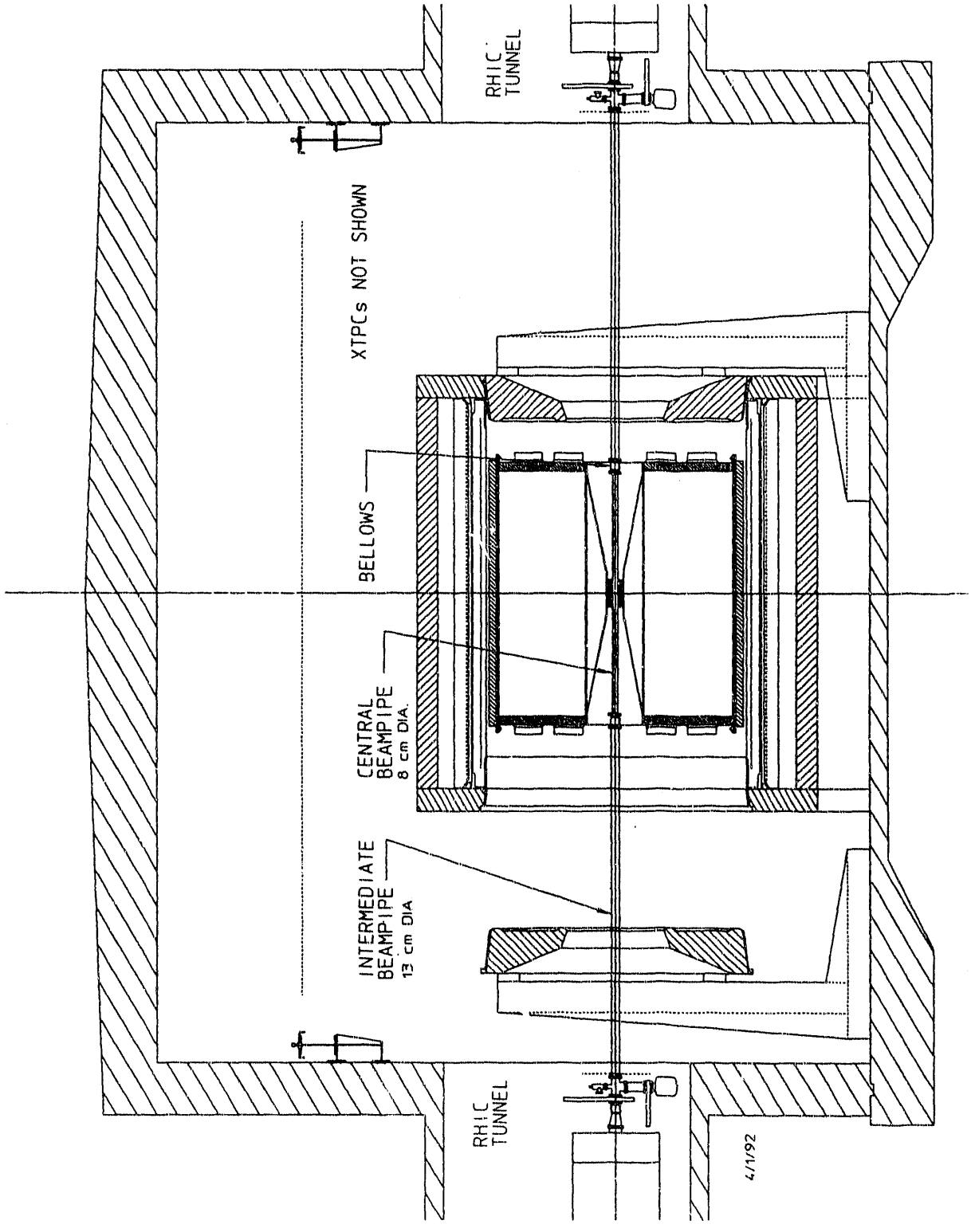

Figure 5-19 RHIC/STAR beampipe configuration.

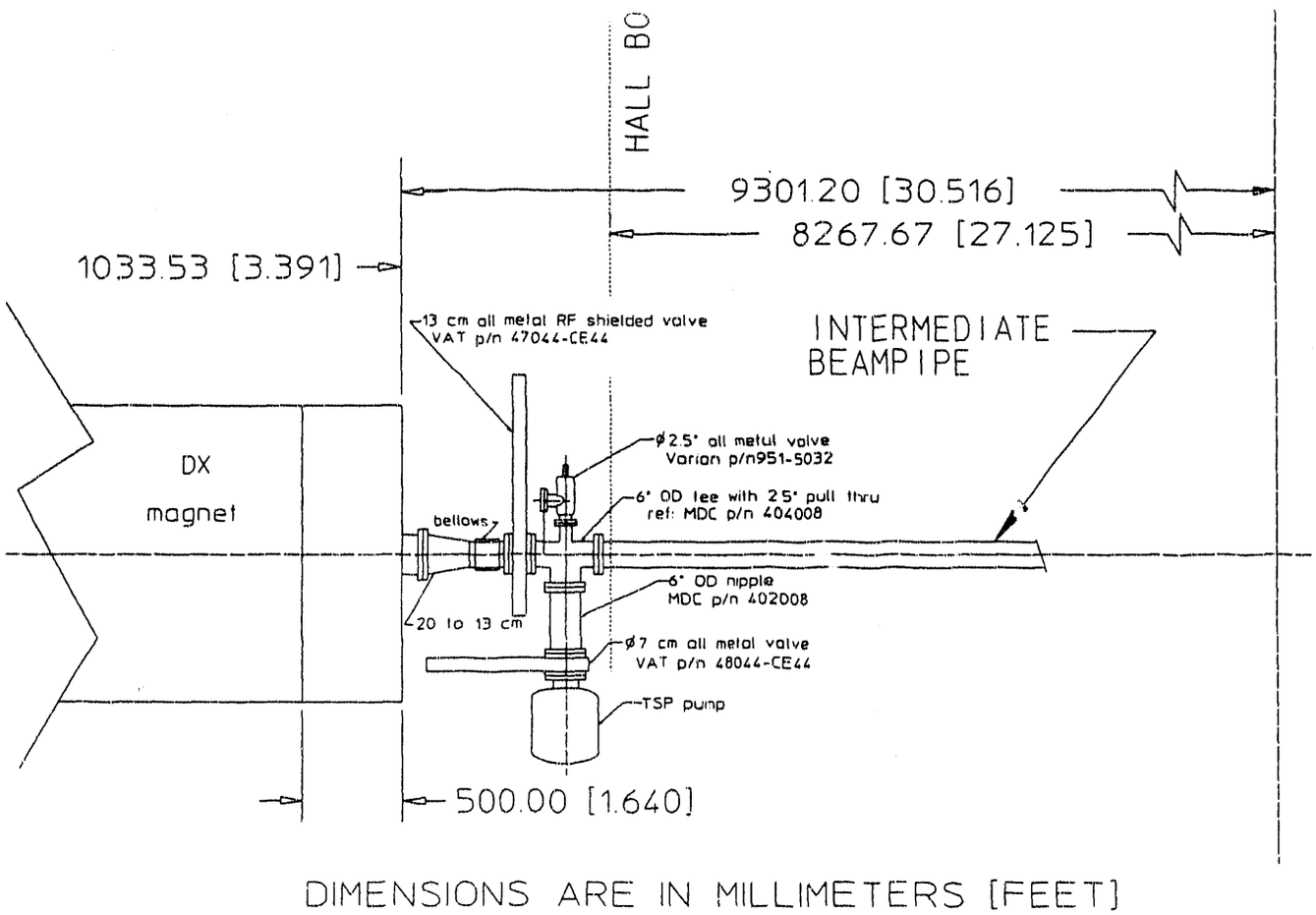

Figure 5-20 RHIC vacuum equipment, at each end of beampipe.

6. Facility Requirements

6. Facility Requirements

6.A. Assembly Areas

The proposed assembly building mentioned above needs a usable floor width, in the North/South direction, of at least 60 feet in order to accommodate the detector and its electronics trailer, as shown in Figure 5-2. This allows the detector to be fully cabled and tested inside the assembly hall before moving it into the wide angle hall. The proposed assembly building length of 120 ft is based on the space required to assemble the detector in the sequence described in Section 5.A, keeping in mind the assembly hall will also be used for storage of lifting fixtures, pipes, cables, electronics racks, etc. as they arrive. It will also be used for minor subassembly, modification and repair of various items as they are fitted to the detector. The assembly area also includes a clean room for TPC sector and SVT work. It is desirable to have crane coverage for the clean room.

Crane capacity requirements in the assembly building have not yet been finalized. However it will be necessary to have two separate bridge cranes, with the main rails for the bridges running along the length of the hall. This allows accurate positioning of long, large, components such as the coil, barrel return iron segments, and TPC installation beam(s), without building specialized lifting fixtures. It also allows lower capacity (20-30 MT) cranes to be used.

6.B. Shop Requirements

As the detector is built, many components/elements will need to be assembled, modified, repaired, re-fitted, etc. A mechanical shop located near or in the assembly building will be needed for this work. Similarly an electronics shop will be needed for ongoing work on the electronics. These are small shops, geared primarily for low-volume small fabrication/repair work. Each of these shops is estimated to require an area of approximately 400 sq. ft.

6.C. Computing Facility Requirements

Table 6-1 Design Parameters for STAR event analysis

Raw Data Size	
TPC (140k X 512 X 10 bits)	90 MB
SVT (72k X 256 X 10 bits)	23 MB
Zero Suppressed Data Size	
TPC (10% occupancy)	15 MB
SVT (1% occupancy)	3 MB
Recording (Tape limited) rate	1 Hz
Estimated Reconstruction CPU time per event	5 Gflop-seconds
# tracks/event	5000
# 4-byte words/track in DST	10
DST event size	0.2 MB
Data set	
running time	2000 hours
# events	7.20E+06
raw data size	108 TB
DST size	1.44 TB
Data access bandwidth	
processing raw data (at record rate)	15 MB/sec
search data set DST in 24 hours	17 MB/sec
search 10^5 DST events/hour	5.56 MB/sec
Storage requirements	
long term, archival for raw data	270 TB/year
rapid access for DST data	3.6 TB/year

The scale of computing required for timely analysis of a 1 Hz central Au-Au event rate is estimated to be 5 Gflops. Since this will involve processing thousands of equivalent events (both real data and Monte Carlo simulations) the computing is efficiently partitioned as a farm of inexpensive RISC processors. At the present time 20 Mflop workstations are common, so that 250 such processors would be needed. These nodes would be networked to three or four event-server machines which would have high speed tape I/O and large disks. The need for computation other than the analysis of raw event data, including especially event simulation, and the needs of other experiments sharing the offline facility could multiply the size by a factor of five or ten. By 1996, when acquisition of the facility should take place, individual nodes should be substantially more powerful so fewer would be required.

Equally as important as the magnitude of the processor power required is the need to move and manage a few times 10^{14} bytes of raw data per year and to provide

the databases and access to manage the processed data and extract the physics results. The raw data recording medium will be determined by the more critical rate requirements of the DAQ system. The data handling will mean massive amounts of conventional disk storage and 8 mm tape technology as well as newer storage media such as optical disks.

The aggregate data access bandwidth required for offline physics analysis is greater than the requirement for online recording. The offline system should be capable of supporting several physicists searching the central DST database at the rate of 10^5 events/hour. This sets the scale of the bandwidth at tens of MB/sec.

It is presently envisioned that a team of approximately 15 people will staff the STAR detector during running periods. These people will be responsible for monitoring the operation of the detector, the control and monitoring of data acquisition, and for quality assurance of the data. To accommodate these functions it is thought that approximately one workstation per person will be required in addition to a small number of electronics racks and communications equipment. Given these assumptions, the amount of space required is estimated to be approximately 3,000 sq. ft. at the detector site. The HVAC requirement to support these operations has not yet been calculated.

Given the experience of CDF and SLD, it will also be necessary to provide workspace for as many as 50 other physicists who travel to RHIC to participate during running periods. A conference room adequate for group meetings required to distribute information, results, and run plans will also be necessary. At present, the space necessary to accommodate these additional people has not been identified and requires additional discussion with RHIC/BNL management.

6.D. Utility Requirements (HVAC, water, power, gas, cryogenic, etc.)

6.D.1. Detector Cooling Requirement:

Cooling of electronics and computer systems will be done using mixed chilled water (CHW) @ 60°F. Table 6-2 shows the location and amount of the heat load in and around the detector. Approximately 350 kW (90% of the total heat load) will be removed from the electronics by the mixed chilled water. The mixed chilled water inlet temperature is 60°F or slightly higher than dew point temperature in the hall. Electronics racks will have main supply and return manifolds located on the detector and the electronics trailer. The manifolds will be connected to the main chilled water production plant via an independent circulation system to avoid damage from pressure surges.

The STAR air conditioning (HVAC) load is about 80 kW. This estimate is based on the sum of EMC PMT heat load plus 10% of the electronics heat load.

Industrial water (ICW) at about 100°F inlet temperature will be needed to cool the helium compressors. The capacity of this system is approximately 235 kW.

STAR Utilities

Table 6-2.

	Y	Z	AA	AB	AC	AD	AE	AF	AG	AH	AI	AJ	AK	AL	AM	AN	AO	AP	AQ	AR	AS	AT	AU
1	Cooling Needs			CHW					Dry A/C					ICW					LCW				
2	Primary Cooling			Frac	Load	T in	T out	Flow	Frac	Load	T in	T out	Flow	Frac	Load	T in	T out	Flow	Frac	Load	T in	T out	Flow
3	Location			%	KWatt	°F	°F	gpm	%	KWatt	°F	°F	CFM		KWatt	°F	°F	gpm		KWatt	°F	°F	gpm
4	INSIDE RETURN IRON																						
5																							
6	SVT																						
7			Preamps	90	8.1				10	0.9													
8			Shapers																				
9			Readout board																				
10																							
11	SVT Total				8.1					0.9													
12																							
13	TPC																						
14			End Caps	90	33.75				10	3.75													
15			Laser System																				
16																							
17	TPC Total				33.75					3.75													
18																							
19	TOF																						
20			PMT/Elec	90	9.113				10	1.013													
21																							
22	TOF Total				9.113					1.013													
23																							
24	Solenoid Magnet																						
25			Power leads																				
26																							
27	Solenoid Magnet Total																						
28																							
29	TOTAL INSIDE RETURN IRON				50.96					5.663													
30																							
31	OUTSIDE RETURN IRON																						
32																							
33	EM Calorimeter																						
34			PMT Bases						100	1.24													
35			Laser System																				
36			Source System																				
37																							
38	EM Cal Total									1.24													
39																							
40	XTPC																						
41			XTPC Electronics	90	13.5				10	1.5													
42																							
43																							
44	XTPC Total				13.5					1.5													
45																							
46	XTPC																						
47			Electronics	90	4.5				10	0.5													
48			XTPC PS	90	27				10	3													

* = Not included in power totals, for cooling estimate purpose. PF = Power Factor. Div = Diversity Factor. Eff = Power Supply Efficiency. Frac = Fraction of Cooling.

STAR Utilities

Table 6-2 cont.

	Y	Z	AA	AB	AC	AD	AE	AF	AG	AH	AI	AJ	AK	AL	AM	AN	AO	AP	AQ	AR	AS	AT	AU
1	Cooling Needs			CHW					Dry A/C					ICW					LCW				
2	Primary Cooling			Frac	Load	T in	T out	Flow	Frac	Load	T in	T out	Flow	Frac	Load	T in	T out	Flow	Frac	Load	T in	T out	Flow
3	Location			%	KWatt	°F	°F	gpm	%	KWatt	°F	°F	CFM		KWatt	°F	°F	gpm		KWatt	°F	°F	gpm
49			XTPC Electronics	90	27				10	3													
50			XTPC FE Electr	90	27				10	3													
51																							
52	XTPC Total				85.5					9.5													
53																							
54	Laser Systems, ETC.																						
55			TPC Laser						100	9.2													
56			XTPC Laser						100	9.2													
57																							
58			Vacuum Pumps						100	6													
59																							
60	Laser Systems Total									24.4													
61																							
62	Total Outside Return Iron				99					36.64													
63																							
64	Buildings																						
65																							
66	Electronic Cart																						
67																							
68	No. Racks and																						
69	Power/Rack, KW																						
70																							
71			SVT PS	90	22.5				10	2.5													
72			SVT Electronics	90	0				10	0													
73			SVT Misc	90	13.5				10	1.5													
74																							
75			TPC PS	90	67.5				10	7.5													
76			TPC Electronics	90	0				10	0													
77			TPC GGD	90	20.25				10	2.25													
78			TPC Misc	90	13.5				10	1.5													
79																							
80			TOF PS	90	18				10	2													
81			TOF Electronics	90	6.75				10	0.75													
82			TOF FE Electronics	90					10														
83																							
~~84~~			~~Solenoid Mag PS~~	~~90~~	~~36~~				10	4													
85			Solenoid Mag Elec	90	6.75				10	0.75													
86																							
87			EM PS	90	5.616				10	0.624													
88			EM Electronics	90	7.722				10	0.858													
89			EM FE Electronics	90	2.34				10	0.26													
90																							
91			Trigger Electronics	90	4.5				10	0.5													
92																							
93	Total Electronic Cart				224.9					24.99													

* = Not included in power totals, for cooling estimate purpose. PF = Power Factor. Div = Diversity Factor. Eff = Power Supply Efficiency. Frac = Fraction of Cooling.

Table 6-2 cont.

STAR Utilities

	Y	Z	AA	AB	AC	AD	AE	AF	AG	AH	AI	AJ	AK	AL	AM	AN	AO	AP	AQ	AR	AS	AT	AU
1	Cooling Needs			CHW					Dry A/C					ICW					LCW				
2	Primary Cooling			Frac	Load	T in	T out	Flow	Frac	Load	T in	T out	Flow	Frac	Load	T in	T out	Flow	Frac	Load	T in	T out	Flow
3	Location			%	KWatt	°F	°F	gpm	%	KWatt	°F	°F	CFM		KWatt	°F	°F	gpm		KWatt	°F	°F	gpm
94																							
95	DAQ Room																						
96																							
97																							
98			DAQ Level 2 and 3																				
99																							
100			SVT	90	4.5				10	0.5													
101			TPC	90	20.25				10	2.25													
102			TOF	90	4.5				10	0.5													
103			XTPC	90	6.75				10	0.75													
104			EM	90	4.5				10	0.5													
105			DAQ General	90	4.5				10	0.5													
106																							
107			Control Room																				
108			Monitoring																				
109			Computer System																				
110			Work Stations																				
111																							
112	Total DAQ Building				45					5													
113																							
114	Assembly Building																						
115																							
116			Cryogenic System																				
117			Control/Cold Box	1					100	4													
118			Auxiliary						100	4													
119			Crane																				
120			Lights																				
121			Safety																				
122																							
123	Total Assembly Building									8													
124																							
125	Utilities Building																						
126																							
127			Noninterruptable Pwr																				
128			Helium Compressors											100	200								
129			Water Pumps																				
130			Air Compressors																				
131			HVAC System																				
132			CHW Prod/Circ																				
133			Air Circ Fan																				
134			Util Water Pumps																				
135																							
136			Power Transformer																				
137			60 Hz Detector																				
138			60 Hz Other																				

* = Not included in power totals, for cooling estimate purpose. PF = Power Factor. Div = Diversity Factor. Eff = Power Supply Efficiency. Frac = Fraction of Cooling.

STAR Utilities

Table 6-2 cont.

	Y	Z	AA	AB	AC	AD	AE	AF	AG	AH	AI	AJ	AK	AL	AM	AN	AO	AP	AQ	AR	AS	AT	AU
1	Cooling Needs			CHW					Dry A/C					ICW					LCW				
2	Primary Cooling			Frac	Load	T in	T out	Flow	Frac	Load	T in	T out	Flow	Frac	Load	T in	T out	Flow	Frac	Load	T in	T out	Flow
3	Location			%	KWatt	°F	°F	gpm	%	KWatt	°F	°F	CFM		KWatt	°F	°F	gpm		KWatt	°F	°F	gpm
139	Vent. Fan																						
140																							
141	Total Utilities Building													100	200								
142																							
143	Buildings Total				270					38					200								
144																							
145					420					80					200								

* = Not included in power totals, for cooling estimate purpose. PF = Power Factor. Div = Diversity Factor. Eff = Power Supply Efficiency. Frac = Fraction of Cooling.

Table 6-3 summarizes the detector's total cooling requirement.

Table 6-3 Summary of detector cooling requirement.

Total CHW @ 60°F	350 kW
Total ICW @ 100°F	235 kW
Total HVAC	80 kW

6.D.2. Refrigeration requirements for the STAR solenoid Magnet

Several magnet cooling concepts were considered for the STAR detector[1,2]. The refrigeration requirements, assuming that STAR taps into the RHIC refrigeration capacity, are stated below.

During normal operation when the STAR solenoid is cold:

- The operating temperature is 4.7 K or below.
- The two phase helium should be delivered by the refrigerator J-T circuit to the STAR magnet control dewar at a rate of 15 grams per second.
- The refrigerator should deliver refrigeration as a refrigerator (with helium gas returning to it on the saturated vapor line at a temperature of 4.5 K or less) at a rate of 200 watts or more, and the refrigerator should provide liquefaction (where the helium gas is returned to the refrigerator compressor at a temperature of 273 K or higher) at the rate of 0.8 grams per second or more.
- In the event of a STAR solenoid quench, the quench gas should be exhausted to the atmosphere through a vent provided by RHIC which meets the Brookhaven safety standards. A schematic layout of the magnet cryogenic system is shown in Section 4.B.

During cool-down from room temperature to its normal operating temperature of 4.7 K or less:

- The RHIC refrigerator should be capable of delivering cold helium gas at a temperature of 4.7 K or less at a rate of 10 grams per second or more during the cool down of the STAR solenoid. During the early phases of the STAR magnet cool down, when the magnet cold mass temperature exceeds 100 K, the temperature of the gas leaving the RHIC refrigerator can be as high as 90 K.
- The pressure of the cold helium gas delivered by the RHIC refrigerator during the cool down should be as high as 1 MPa (about 10 bar).

---

1 M. A. Green, "STAR Refrigeration Requirements," STAR Note-0058, 21 April 1992.

2 M. A. Green, "Cryogenic System Options for the STAR Superconducting Thin Solenoid," STAR Note-0013, LBL Internal Report LBID-1841, 20 April 1992.

- The RHIC refrigeration system should be capable of delivering pure warm helium gas at a temperature of 273 K or above from the compressor at a pressure of 1 MPa (about 10 bar) or above. This warm helium can be mixed with the cold helium from the refrigerator so that helium gas at a controlled temperature can be delivered to the STAR solenoid during its cool down. The warm helium can also be used to warm up the STAR magnet.
- During the cool down and warm up, the STAR solenoid cryogenic system will deliver pure helium gas back to the compressor intake at a temperature of 273 K or higher.
- RHIC should provide an impure helium return line so that impure helium coming from STAR during the pump and purge phase before the cool down of the STAR solenoid can be returned to the RHIC helium system. If an impure helium return line is not provided by RHIC, it is assumed that the STAR experiment will dispose of the pump and purge helium by venting it to the atmosphere. RHIC should provide the vent line so that this venting can be done in accordance to Brookhaven safety requirements.

6.D.3. Electrical Power Requirement

For the purposes of this document, electrical power for the STAR Detector is divided into two parts; Facility Electrical Power (FEP) and Experiment Electrical Power (EEP).

FEP for the STAR detector will be provided by RHIC. FEP is defined as the supply and distribution network extending from the main feeder lines down to and including distribution panels and wall outlets. The network will supply both conventional power and isolated clean power for experiment electrical and electronic systems.

EEP for the STAR detector will be provided by the detector project. EEP is defined as the supply and distribution network extending from the FEP distribution panels and wall outlets down to and including electrical units and electronics systems power distribution centers. The EEP network will supply both conventional and isolated clean power to experiment systems.

The requirements described in this section are for the fully implemented detector including all future upgrades.

6.D.3.a. Conventional Power

Conventional power loads and their general location are presented in Table 6-4 and Figure 6-1. There are a number of items in the list which are not yet completely defined. Consequently, the total load estimate shown in the table is low. A reasonable assumption is that the final total load will be about 500 KVA, including a small amount of contingency.

6.D.3.b. Isolated Clean Power

The electronics systems used to collect experimental data are adversely affected by the electrical noise generated by conventional electrical equipment and by equipment which employ high power AC to DC converters. Therefore, an isolated, clean power distribution network will be required to supply power to these systems. Distribution panels will be located in the Experiment Hall and in the DAQ and Electronics Building. The loads for this network are described in Table 6-4.

Figure 6-1 shows a schematic layout of electrical power network.

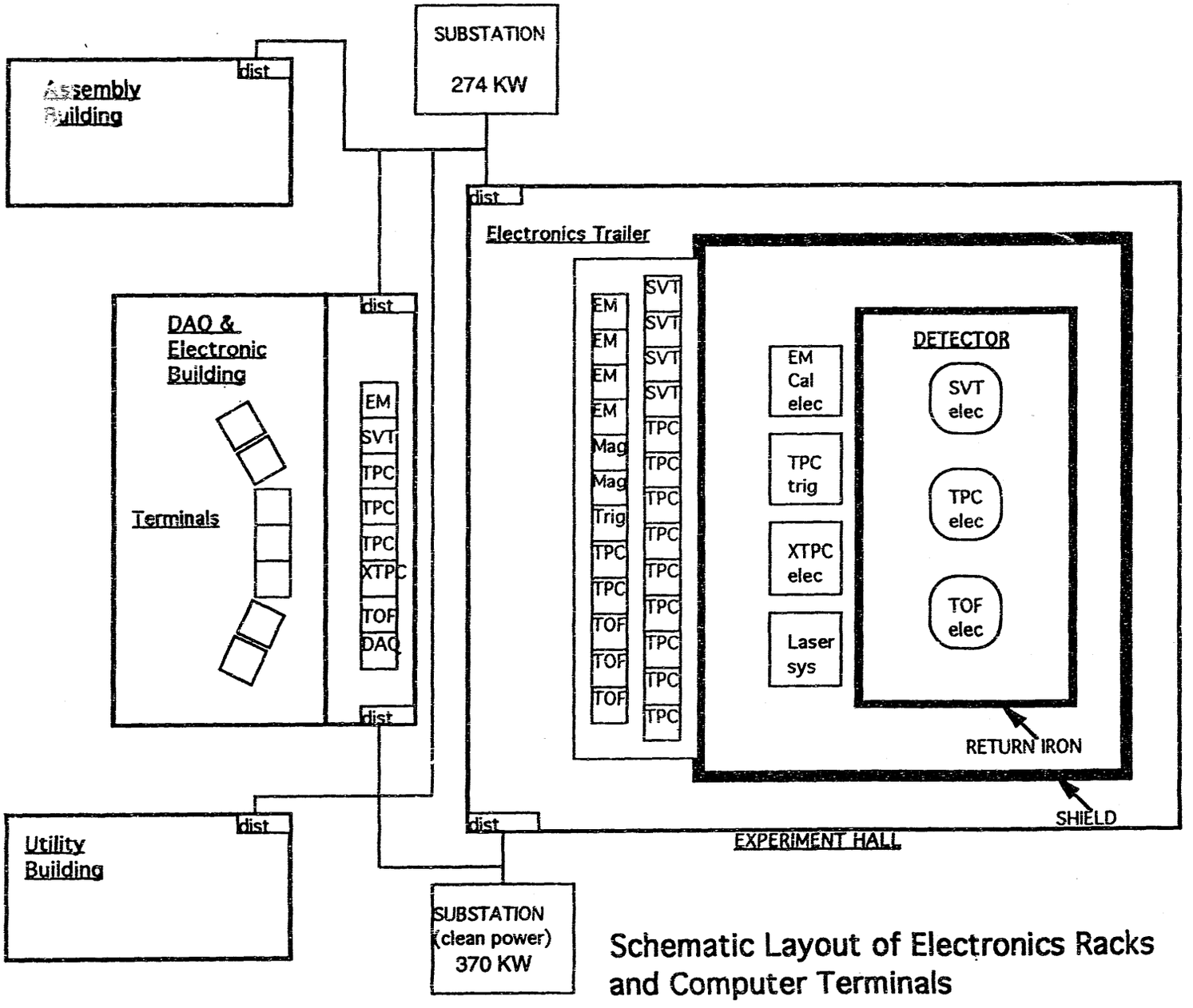

Schematic Layout of Electronics Racks and Computer Terminals

Fig. 6-1 Electric power distribution layout.

Table 6-4 STAR electrical power requirements.

	Clean			Conv.		
Load/Location	Load KWatt	Spare Frac	Total KWatt	Load KWatt	Spare KWatt	Total KWatt
INSIDE RETURN IRON						
SVT Preamps	7.2	0.25	9			
TPC End Caps	30	0.25	37.5			
TOF PMT/Elec	8.1	0.25	10.1			
TOTAL	45.3		56.6			
OUTSIDE RETURN IRON						
EM Calorimeter						
PMT Bases	0.24	0.25	0.3			
Laser System				1	0	1
Source System				1	0	1
EM Cal Total	0.24		0.3	2	0	2
TPC Trigger	12	0.25	15			
XTPC						
Electronics	4	0.25	5			
XTPC PS	24	0.25	30			
XTPC Electronics	24	0.25	30			
XTPC FE Electronics	24	0.25	30			
XTPC Total	76		95			
"Laser Systems, etc."						
TPC Laser				9.2	0	9.2
XTPC Laser				9.2	0	9.2
Mag Vacuum Pumps				4	2	6
Laser Systems Total				22.4	2	24.4
TOTAL	88.2		110	24.4	2	26.4

Table 6-4 (continued)

	Clean			Conv.		
Load/Location	Load KWatt	Spare Frac	Total KWatt	Load KWatt	Spare KWatt	Total KWatt
Buildings						
Electronic Cart						
SVT PS	20	0.25	25			
SVT Misc.	12	0.25	15			
TPC PS	60	0.25	75			
TPC GGD	18	0.25	22.5			
TPC Misc.	12	0.25	15			
TOF PS	16	0.25	20			
TOF Electronics	6	0.25	7.5			
Solenoid Mag PS	32	8	40			
Solenoid Mag Elec	6	0.25	7.5			
EM PS	4.8	0.3	6.24			
EM Electronics	6.6	0.3	8.58			
EM FE Electronics	2	0.3	2.6			
Trigger Electronics	4	0.25	5			
Total Electronic Cart	167		210	32	8	40
DAQ Room						
DAQ Levels 2 & 3						
SVT	4	0.25	5			
TPC	18	0.25	22.5			
TOF	4	0.25	5			
XTPC	6	0.25	7.5			
EM	4	0.25	5			
DAQ General	4	0.25	5			
Computer System			TBD			
Work Stations			TBD			
Total DAQ Building	40		50			

Table 6-4 (continued)

	Clean			Conv.		
Load/Location	Load KWatt	Spare Frac	Total KWatt	Load KWatt	Spare KWatt	Total KWatt
Assembly Building						
Cryogenic System						
Control/Cold Box				2	2	4
Auxillary				2	2	4
Crane						TBD
Safety						TBD
Total Assembly Building				4	4	8
Utilities Building						
Non-interrupt. Pwr						TBD
Helium Compressors				150	50	200
Water Pumps						TBD
Air Compressors						TBD
HVAC System						TBD
CHW Prod/Circ						TBD
Air Circ Fan						TBD
Utility Water Pumps						TBD
Safety						TBD
Total Utilities Building				150	50	200
Buildings Total	207		260	186	62	248
Total	296		370	210	64	274

7. Safety and Environmental Protection Issues

7. Safety and Environmental Protection Issues

The safety issues at STAR are the same as any other RHIC detector and have to be addressed in a RHIC-wide fashion. They include shielding requirements, access control, fire protection, laser's, cryogen's, electrical and mechanical hazards.

7.A. Shielding

There is a need for access during operation to an area as close to the detector as possible. Presently there is a proposal to build a shielded room for electronic racks that reaches from a few meters from the detector to the outside of the interaction hall. Exact distances from the detector and shield wall requirements will be determined by RHIC management. All other areas that are to be occupied during operation meet the standards for a low radiation environment.

7.B. Access Control

The major questions about access are how difficult it will be to gain access during short shut downs and what level of training and supervision will be required. STAR service scenarios call for retracting the pole tips 2.5 meters to allow for unrestricted access to the confined space within the detector. It is noted that there is a distinct danger of low levels of oxygen in parts of the hall and within the detector interior. Oxygen monitors will be placed in and around the detector to help ensure that safe operating conditions prevail during maintenance.

7.C. Hazardous Materials and Systems

7.C.1. Flammable Gas Systems

Fire Protection

There are many sources of ignition and a large supply of fuel in an experiment of this size and complexity including plastic construction materials, electronic circuits and large volumes of flammable gases [≈ 10,000 liters]. There are two experiment areas that require special fire protection: the detector and the gas handling facility. Since the detector will be enclosed to provide a controlled environment and will not be occupied during operation, it will be filled with dry nitrogen gas supplied from a liquid source. It is assumed that the system required to fill the central detector with nitrogen gas is a small modification to the environmental control system. The central detector systems are located in a magnetic field and therefore require special detection equipment that will need to be reviewed by the fire and safety engineers. This area will require oxygen deficiency hazard (ODH) monitors, alarms, and an access procedure which utilizes the information provided by these elements.

Major portions of the gas handling facility will be isolated from the rest of the buildings and will be protected with flammable gas detectors, emergency ventilation and sprinklers. Distribution will be done at the detector where flammable gas detection will be provided. All exhaust gases will be vented outside the building using an approved system. Presently, existing requirements of the BNL ES&H standards are

incorporated in the design and any additional requirements of the RHIC SEAPPM will be satisfied. This area will be supervised by a senior member of the BNL staff associated with STAR.

Lasers and Radioactive Sources

There will be at least one pulsed UV laser used for calibration and monitoring purposes. The laser will be supervised by a senior member of the collaboration and will have the optical path totally enclosed. Operation of the laser system will be in accordance with the BNL-ES&H Standards and the RHIC-SEAPPM.

There will be radioactive sources used for calibration, monitoring and setup purposes throughout the experiment. Many of these will be installed into individual detectors and will be supervised by a senior collaborator. General use sources will be secured in a storage area supervised by the STAR safety coordinator.

7.C.2. Cryogenics

Cryogenic Fluids

There will be at least three significant stores of cryogenic fluids associated with STAR. The first is the helium used to cool the magnet and will involve several hundred liters and will involve interaction with the machine system. The operation of this system will be done by experienced cryogenic technicians in accordance with the accepted Cryogenics Safety Codes. There will also be a several hundred liters of liquid argon and nitrogen used in the TPC gas supply system and for fire protection. These supplies will be located next to the gas mixing area and will be supervised by a senior member of the BNL staff associated with STAR in accordance with the applicable safety codes.

7.C.3. High Voltage/ High Current Power

Electrical and Mechanical Hazards

There are many low voltage high current supplies used to power the detector electronics. The output of these supplies is distributed to many individual circuit boards. Designs will include fuses or other devices that will limit the current in each lead to well within its rating. The main magnet uses a low voltage very high current supply and large bus bar conductors. All high current conductors will be covered to prevent accidental contact independent of the voltage. There are many high voltage power supply and distribution systems in use that will be built with devices that prevent accidental contact with live conductors. All electrical systems will be designed, built and operated in accordance with NEC, BNL-ES&H Standards and RHIC-SEAPPM.

The major mechanical hazards are associated with heavy objects and require that all people involved with handling them be properly trained and be provided with the required equipment. There are no large volumes of high pressure gases or liquids.

General Comment

It is assumed that general safety systems in the halls (such as the hall sprinkler system, ODH monitors and smoke alarms) will be provided by the RHIC project.

There will be an internal STAR Safety Committee that will review all systems from initial design to final operation to ensure that the system conforms to all applicable safety standards.

It will also be required that systems that have been disassembled for repair be inspected prior to operation in order to ensure that the safety related components are fully functional.

8. Management Structure of STAR

8. Management Structure of STAR

Displayed in Fig. 8-1 is the STAR management structure for the conceptual design phase. The STAR Council consists of representatives from each institution in STAR. A set of bylaws for governing the STAR Collaboration has been drawn up and ratified by the Council. A spokesman has been appointed to represent the Collaboration in all matters. It is expected that the structure on the technical side will evolve towards that shown in Fig. 8-2, which is expected to be in place for the construction project. Details of this plan will be presented in the STAR Project Plan.

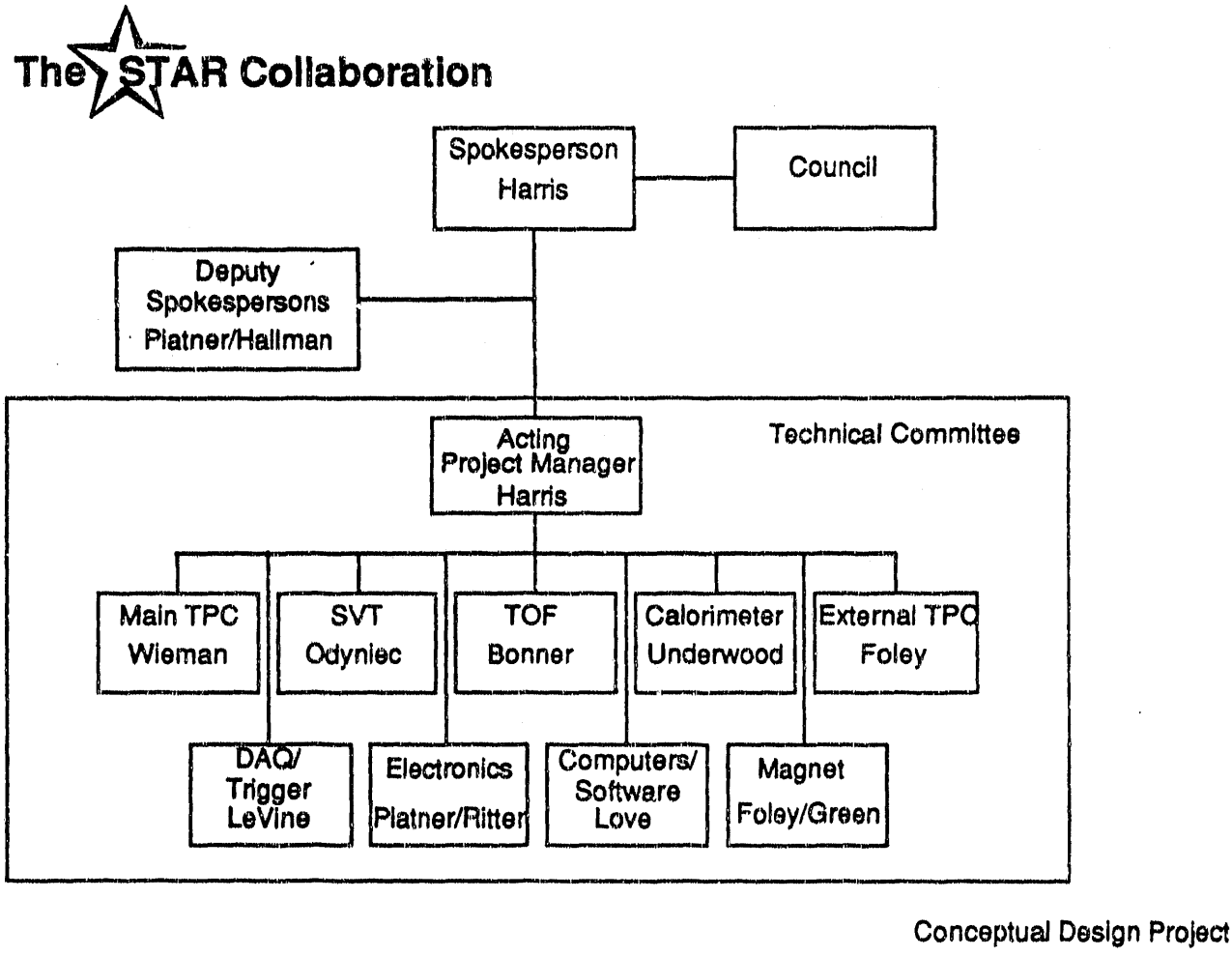

Fig. 8-1. Management structure of STAR for the conceptual design phase of the project.

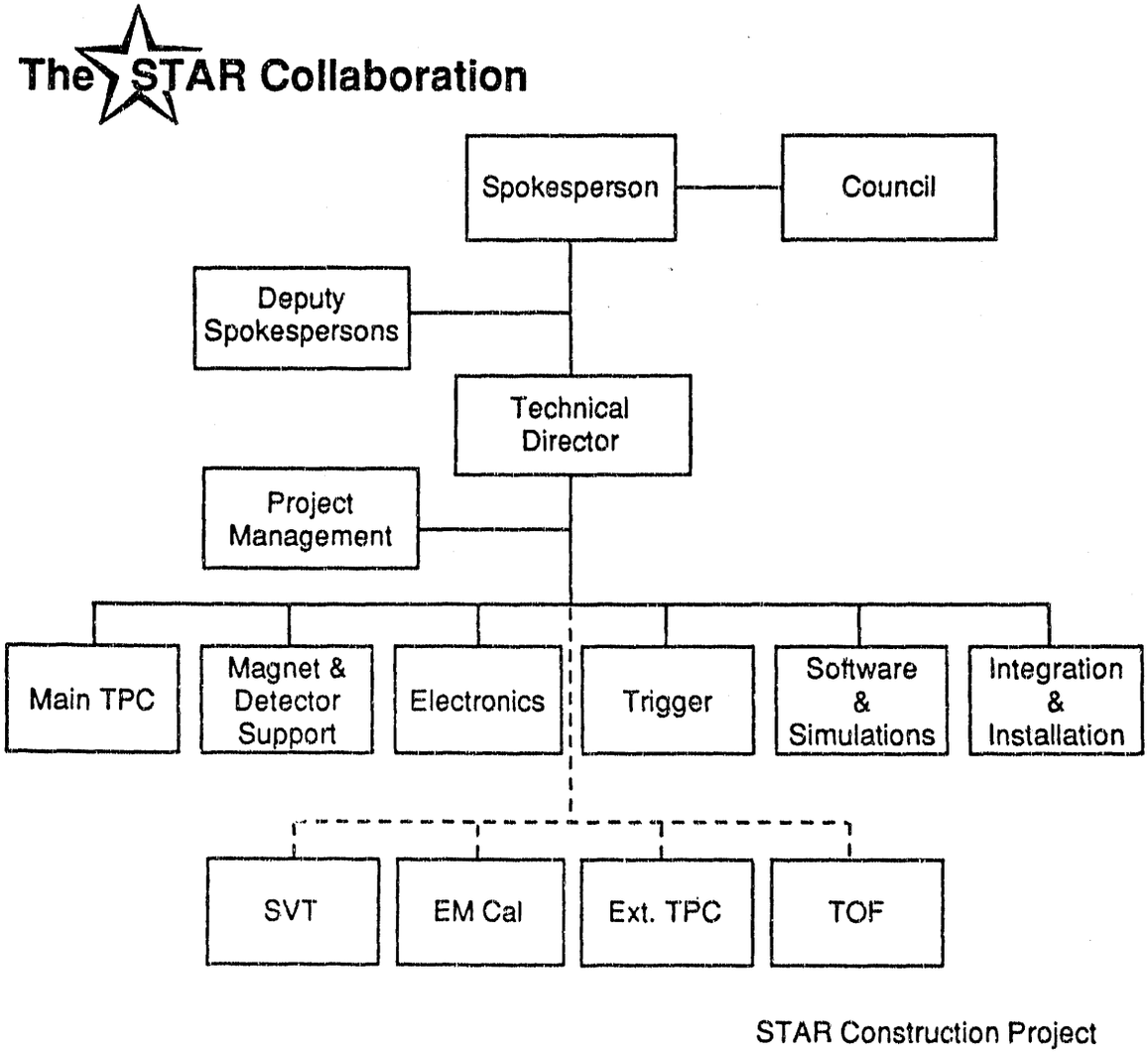

Fig. 8-2. Anticipated management structure of STAR for the construction project.

STAR

9. Cost, Schedule, Manpower and Funding

9. Cost, Schedule, Manpower and Funding

9.A. Detector Scope

The STAR Phase 1 detector includes the following detector subsystems and other necessary elements: Time Projection Chamber, Superconducting Solenoid and return iron, electronics, DAQ, trigger, slow controls, and computing for these detector subsystems, structure and utilities needed to support the detector in the Wide Angle Hall, installation and testing of the detector in the hall, systems integration and project management. Accounted for separately, but assumed to be constructed on a time scale coincident with STAR Phase 1, are the SVT and EM Calorimeter and their associated incremental electronics, DAQ, computing, and installation. The list of potential upgrades to Phase 1 include two stages of Time of Flight (TOF) detector (a patch and a full 7776 plus channel system), and an External TPC (XTP).

The cost estimate presented in the following section is based on the detector described above and throughout this CDR document. The cost is based on a point design, the scope of which is defined in the STAR Parameters Notebook. In a strict sense, modification of the detector scope would result in a different cost estimate based on a different point design. The funds set aside in contingency are not meant to take scope changes into account. In a more practical sense, some minor changes in scope on a subsystem level can be expected to be accounted for in the contingency. (This is because a factor has been added in the contingency analysis called design state which boosts the contingency percent early in the design process.) The addition or subtraction of an entire detector subsystem, or a major change in the dimensions or electronics channel count, cannot be expected to be taken into account in the contingency.

The cost estimate for the superconducting (SC) coil and cryostat is based on a budgetary quote received from a SC magnet vendor. Additional vendor budgetary quotes are expected in the near future and the estimate will continue to be updated based on this new information. A report will be issued when the first stage of this budgetary quote effort is completed, explaining the basis of our cost estimate assumptions.

9.B. Detector Summary Cost and Schedule Estimates

A cost estimating effort for the STAR detector was begun early in calendar year 1992. Formal cost and schedule (C/S) estimating guidelines[1] were published prior to beginning this effort. These guidelines have been reviewed by a subset of RHIC Project Management, and a favorable response has been received[2] , but the guidelines have not yet been formally approved. The Phase 1 detector cost estimate presented in this CDR represents the 4th formal iteration of the estimate and has thus received a fair amount of internal review. In section 9.B.1, the costs for constructing the Phase 1 detector are summarized by major subsystem (WBS level 2). Further details of the cost estimate can be found in the STAR Cost/Schedule Book, where each subsystem is presented to level

[1] STAR Cost & Schedule Procedure Manual, Draft Rev 1, March 20, 1992, W.R. Edwards and C. R. Barney.
[2] Tom Ludlam, private communication, May 1, 1992.

4 (5 in some cases). A detailed description of the individual WBS elements can be found in the STAR WBS Dictionary.

The cost estimate for the upgrade detector subsystems did not receive the same amount of review as the Phase 1 detector. Section 9.B.1 also includes discussion of the upgrade detector costs and presents these costs in terms of the detector, it's front end electronics, and incremental DAQ, computing, and installation. The Cost/Schedule Book presents further details on these upgrades. These cost estimates should be viewed as more preliminary than the Phase 1 detector cost estimate.

The schedule development effort was begun more recently. The schedule presented in section 9.B.2 is a high level summary only and is supported by detailed PERT[3] chart schedules for some subsystems, and summary level GANTT[4] charts for other subsystems. Schedule refinement and review will continue over the next several months until each subsystems' milestone/decision points, as well as their resource requirements by fiscal year, are well understood. Current subsystem summary level schedules are presented in the Cost/Schedule Book for each of the WBS level 2 subsystems (level 3 in the electronics areas).

9.B.1. Level 2 Cost Summary

A cost estimate summary for the STAR Phase 1 detector is presented in Table 9-1a. All estimates are in fiscal year 1992, US dollars, as defined in the C/S Procedure Manual. The estimates include materials, labor, EDIA and contingency, and are based on a variety of inputs including vendor quotes, estimates from comparable systems, and engineering estimates. The TPC, solenoid magnet, electronics, data acquisition, trigger system, controls, on-line computing, detector conventional systems, detector testing, detector installation, systems integration and project management will be funded primarily by the RHIC construction project. Funding for TOF, EMC, and external TPC systems will be sought from other sources. The SVT—which is especially important to the initial physics program—will be supported through the prototype phase by RHIC R&D funds and constructed thereafter using other resources.

The cost estimates for the portion of the detector to be funded from RHIC construction funds includes a detailed contingency analysis leading to an average contingency of 30%. Since the RHIC management will maintain $2M in reserves for the two large RHIC detectors, it has been agreed that the STAR contingency for the RHIC-funded part of the detector be reduced to 25%.

The estimated cost of the STAR Phase 1 detector, including an overall contingency of 25%, is $35.9M in FY92 dollars.

The STAR collaboration is investigating a warm-coil option for the solenoid magnet. Preliminary cost estimates of this option (without the iterations and reviews that characterize the superconducting-coil option) indicates that the warm-coil option could reduce the cost of the magnet by $2.1M in FY92 dollars provided that necessary

[3]PERT refers to a task logic chart format using task boxes and showing precessor/predecessor relationships of tasks.
[4] GANTT refers to a bar chart format showing dates and duration's only (not task logic).

facility/utility upgrades required by the warm-coil option are supplied by RHIC/BNL. Table 9-1b presents a comparison of conventional vs SC magnet costs. More refined estimates, and a decision between coil options will be completed in the near future.

The STAR collaboration has also evaluated the level of resources available within the collaboration to offset costs associated with the RHIC funded portion of the detector and found it to be approximately $2.5M. Therefore, assuming that the cost savings of the normal-coil option are confirmed with additional estimates and vendor quotes, the amount of capital funding required from the RHIC construction project for the STAR Phase 1 detector is $31.3M in FY92 dollars. In addition, an R&D budget of approximately $4.0M in the years FY93–95 is necessary and is expected to be provided by the RHIC project.

Presented in Table 9-1c are the cost estimates for the additions to the STAR Phase 1 detector. The total cost for the SVT in FY '92 capital equipment dollars is $4.84 M including $1.11 M in contingency. The total cost for the TOF patch upgrade is $1.0 M including $0.23 M in contingency, while the cost for the full TOF system upgrade is $10.4 M including $1.91 M held in contingency. For the EM Calorimeter, the total cost is $9.1 M including $2.02 M in contingency. The total cost of the XTP upgrade is $2.6 M including $0.72 M in contingency. Additionally, a portion of the $4.0 M in FY '93-95, discussed above, will go towards continuing the R&D activities on these upgrades. Construction efforts on these upgrades will begin as money becomes available.

The column headings in Table 9-1a (thru c) require some definition. The material column represents the sum of all costs associated with materials used in fabrication, procured items and expenses. The next column, Manufacturing Labor, represents all skilled (technician, machinist, and crafts) and unskilled labor used in the fabrication, assembly, test and installation efforts. The EDIA (Engineering, Design, Inspection and Administration) column represents the costs associated with engineering and design efforts, as well as the management and administrative efforts, for the life of the project. The next column, Subtotal, is the sum of the previous three columns. Contingency % is the weighted average value of contingency, and is presented as a percentage of the subtotal. When the dollar value of contingency is added to the Subtotal column, the result is the Total column.

WBS	DESCRIPTION	MATERIAL	MFG LABOR	EDIA	SUBTOTAL	CONT%	TOTAL
4.2	Time Projection Chamber	3,267	2,029	1,368	6,664	32.3	8,819
4.4	Solenoidal Magnet	5,597	258	828	6,682	32.4	8,848
4.7	Electronics	4,678	419	1,766	6,863	25.7	8,627
4.7.1	Front end electronics	2,170	123	751	3,044	23.0	3,745
4.7.2	DAQ System	1,271	92	735	2,098	24.5	2,611
4.7.3	Trigger Systems	1,137	204	280	1,621	32.1	2,141
4.7.4	Controls	100			100	30.0	130
4.8	Computing	1,058	398	515	1,971	35.6	2,673
4.9	Detector Conventional Systems	1,144	99	531	1,774	29.7	2,302
4.11	Detector Installation & Test	474	764	426	1,663	45.3	2,418
4.12	Project Management	258		1,281	1,539	13.0	1,738
4.13	Systems Integration	289		1,270	1,559	24.0	1,932
	TOTALS	**16,764**	**3,966**	**7,984**	**28,715**	**30.1**	**37,357**
	TOTAL WITH 25% CONTINGENCY				**28,715**	**25.0**	**35,893**

Table 9-1a STAR Phase 1 Detector cost summary (numbers in $K unless otherwise noted).

Warm Solenoid Option

WBS	DESCRIPTION	MATERIAL	MFG LABOR	EDIA	SUBTOTAL	CONT%	TOTAL
4.4	Solenoid Magnet						
4.4.1	Conventional Solenoid Coil	1,870		150	2,020	30.0	2,626
4.4.2	Return Iron	2,050		150	2,200	36.0	2,992
4.4.3	Cooling and Electrical Systems	350		45	395	36.0	537
4.4.4	Magnetic Field Measurement System	213	79	153	445	47.3	655
4.11.1.4	Solenoid Magnet Installation	15	64	23	102	40.0	143
4.11.2.4	Solenoid Magnet Test	100	20	28	148	34.0	198
	TOTALS	**4,598**	**163**	**549**	**5,310**	**34.7**	**7,152**

Superconducting Solenoid Option

WBS	DESCRIPTION	MATERIAL	MFG LABOR	EDIA	SUBTOTAL	CONT%	TOTAL
4.4	Solenoid Magnet						
4.4.1	Superconducting Coil & Cryostat	4,000		301	4,301	30.0	5,591
4.4.2	Return Iron	1,187		150	1,337	36.0	1,818
4.4.3	Cryogenic and Electrical Systems	257	179	224	660	32.2	873
4.4.4	Magnetic Field Measurement System	153	79	153	385	47.3	567
4.11.1.4	Solenoid Magnet Installation	15	64	23	102	39.7	142
4.11.2.4	Solenoid Magnet Test	100	30	38	168	34.0	225
	TOTALS	**5,712**	**352**	**889**	**6,953**	**32.6**	**9,217**

Table 9-1b Comparison of warm and superconducting solenoid costs for STAR Phase 1 Detector (numbers in $K unless otherwise noted).

WBS	DESCRIPTION	MATERIAL	MFG LABOR	EDIA	SUBTOTAL	CONT%	TOTAL
4.1	Silicon Vertex Tracker	797	241	383	1,421	33.1	1,891
4.7.1.1	SVT Front End Electronics	1,136	81	632	1,849	26.1	2,332
4.7.2.1	SVT DAQ	218	49	29	296	28.4	380
4.8.1	SVT Computing	20	34	45	100	42.3	142
4.11.1	SVT Installation & Test	25	18	20	63	47.6	94
	TOTALS	**2,196**	**423**	**1,109**	**3,729**	**29.8**	**4,839**
4.3	TOF Subsystem Upgrade- Option A	166	65	21	252	17.9	297
4.7.1.3	Time of Flight Electronics	100	25	125	250	31.1	328
4.7.2.3	TOF DAQ	58	7	18	82	25.6	104
4.8.3	TOF Computing	20	34	25	80	40.4	112
4.11.3	TOF Installation & Test	25	41	30	96	58.1	152
	TOTALS	**369**	**172**	**220**	**760**	**30.5**	**992**
4.3	TOF Subsystem Upgrade- Option B	4,174	850	24	5,048	16.5	5,883
4.7.1.3	Time of Flight Electronics	2,510	515	137	3,162	30.7	4,132
4.7.2.3	TOF DAQ	58	7	18	82	25.6	104
4.8.3	TOF Computing	20	34	25	80	40.4	112
4.11.3	TOF Installation & Test	25	41	30	96	58.1	152
	TOTALS	**6,787**	**1,447**	**235**	**8,469**	**22.6**	**10,382**

Table 9-1c Additions to the STAR Phase 1 Detector (numbers in $K unless otherwise noted).

WBS	DESCRIPTION	MATERIAL	MFG LABOR	EDIA	SUBTOTAL	CONT%	TOTAL
4.5.1	Barrel EM Calorimeter	3,583	811	972	5,365	27.0	6,812
4.7.1.5	EMC FEE	1,047	203	100	1,349	32.5	1,787
4.7.2.5	EMC DAQ	40	5	37	82	11.4	92
4.8.5	EMC Computing	20	39	54	114	43.3	163
4.11.5	EMC Installation & Test	30	103	20	152	48.8	226
	TOTALS	**4,720**	**1,160**	**1,183**	**7,063**	**28.6**	**9,080**
4.6	XTP Upgrade	522	389	156	1,066	38.3	1,475
4.7.1.6	XTP Front End Electronics FEE	268	55	90	413	41.0	582
4.7.2.6	XTP DAQ	117	13	18	148	27.8	189
4.8.6	XTP Computing	40	37	62	139	84.0	197
4.11.6	XTP Installation & Test	31	39	18	88	88.0	128
	TOTALS	**978**	**533**	**344**	**1,854**	**38.7**	**2,571**

Table 9-1c con't

9.B.2. STAR Schedule Summary

An overall project summary schedule is shown in Figure 9-1. Each of the lines in this project schedule show the full duration of each of the activities listed. In other words, the duration depicted in the design line, for example, is from the beginning of the earliest starting design task to the end of the latest finishing design task. A more detailed schedule for each subsystem is presented in the STAR Cost/Schedule Book.

The relatively aggressive schedule for STAR construction is based upon success and the receipt of funding necessary to support R&D, design and construction activities. Given the above assumptions, the schedule is possible but aggressive. It goes almost without saying then that delays in funding for any reason, will result in a corresponding delay in the completion date for STAR.

Recently, a slight slip in the commissioning complete date for the RHIC machine was announced. The new completion date is August 1997. This has been taken into account in the majority of the schedules presented in the Cost/Schedule Book and summarized here, but only by allowing an additional 4 months of testing and repairs to the completed detector. In other words, the delivery dates for individual elements of the detector have not changed since before the announcement. Bluntly, this serves as breathing room for final detector shakedown or schedule contingency for a late arriving critical element.

9.C Project Manpower Resources by Subsystem

Presently there are 24 institutions and 170 physicists and engineers in the STAR Collaboration. From this it is expected some amount of existing resources for constructing and operating the STAR detector will be available. A survey of collaboration resources has shown possible contributions in the areas of engineering, technical support, and computing. A precise accounting of the collaboration resources however, is complicated by the fact that for the resources to be effective they must be carefully matched with the projects outlined in the STAR Work Breakdown Structure (WBS).

The matching of resources and projects is a complex process. Account must be taken of institutional capabilities, time constraints, funding constraints, communications difficulties, and project scope. Additionally, it is necessary to account for the assumptions made in costing a given element of the STAR WBS in order to correctly credit resources which may be applied to that element.

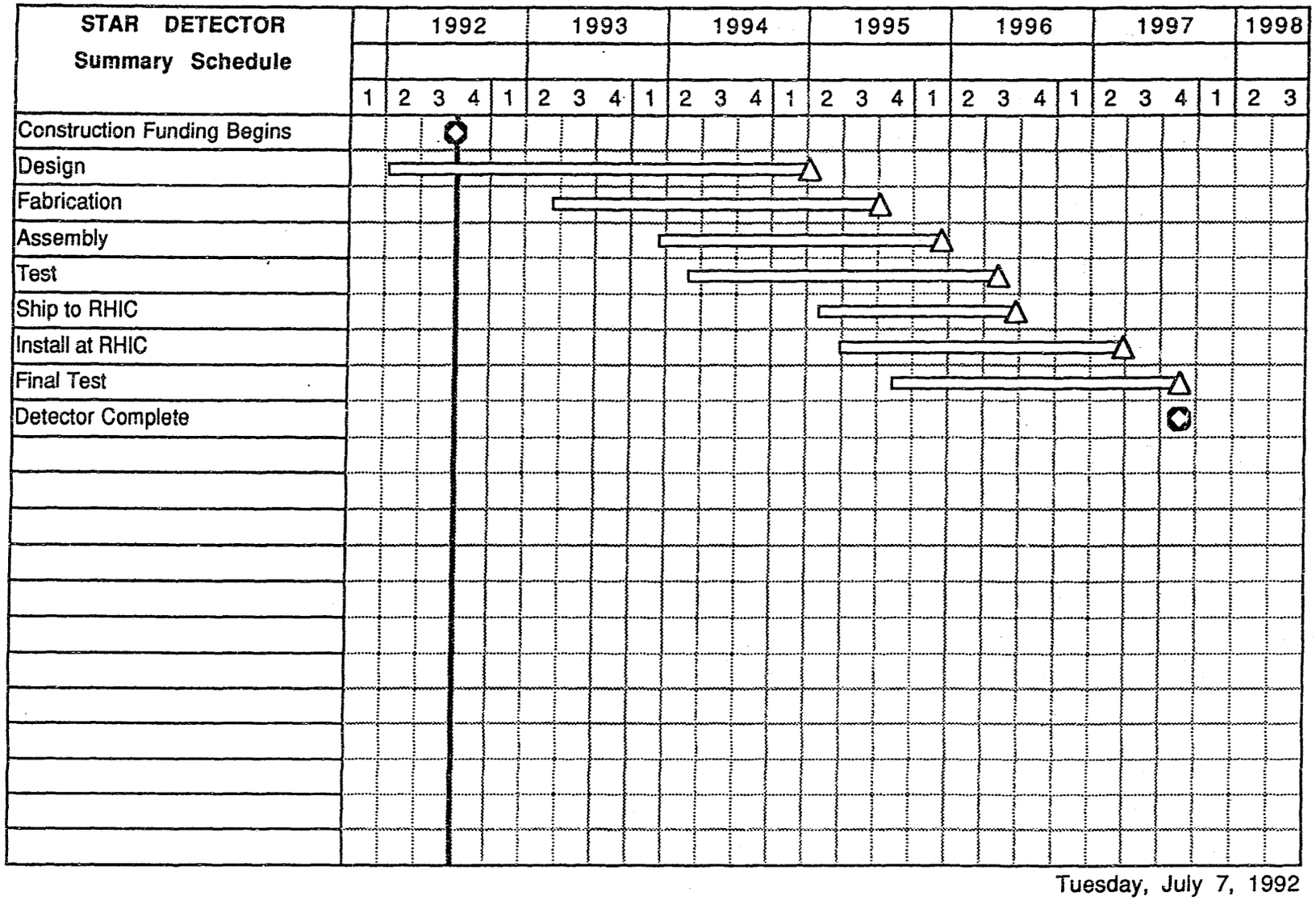

Figure 9-1 STAR Detector construction summary schedule.

The resources accounted for in the STAR Collaboration thus far sum to approximately $2.5 M. Areas in which the matching of resources has been possible include:

- Testing of TPC electronics
- Mapping of the STAR magnetic field
- Construction of a laser calibration system for the TPC
- Testing of the TPC pad plane sectors
- Professional software support
- Construction of the STAR trigger system

The process of identifying and applying resources will continue throughout the life of the project. It is expected that as details of the Project Plan for STAR are worked out, further areas will be identified where significant contributions from within the collaboration can be made, and the effort to apply resources to the STAR project will be accelerated. It is also expected that some resources will become available from the RHIC project through the operational support normally given to detector projects of this scope. The degree of support which may be expected from RHIC is presently under discussion.

9.D. Funding Profile

The current estimated funding profile for the STAR Detector is shown in Figure 9-2. This funding profile assumes that the detector is complete in August of 1997. Assembly of the detector will, for all intents and purposes, be completed in April of 1997, the following 4 months being spent performing tests at both the subsystem and system level and making last minute repairs.

As can be seen in Figure 9-2, the shape of the suggested RHIC Detector funding profile[5] is not completely inappropriate for STAR. However, if this proposed profile is flattened and drawn out because of DOE imposed RHIC project funding constraints, as stated previously, the STAR detector schedule will slip out beyond August of '97. In other words, there is very little leeway in this proposed funding plan. Table 9-2 presents a more detailed breakdown on a major subsystem level of the funding requirements.

In taking a more detailed look at Figure 9-2, the funding for the first 2 years is in excess of what we currently think we require; this is obviously not a problem. However, in years 3 & 4 (FY's '94 & '95), we see a discrepancy in proposed vs. required funding. The reserve from the previous 2 fiscal years does not make up for this discrepancy. Note also that implicit in these funding profile estimates is the assumption that large procurement contracts, which spread out over 2 or more fiscal years, can be paid for over the same period; in other words that progress payments can be negotiated between all involved parties. If this is an inappropriate assumption, the effect will be to move the profile forward to pay for these items in the fiscal year that the contract is initiated. This would most likely result in a need for a more forward loaded funding profile.

[5] As presented in the detector project CDR Guidelines from T. Ludlam.

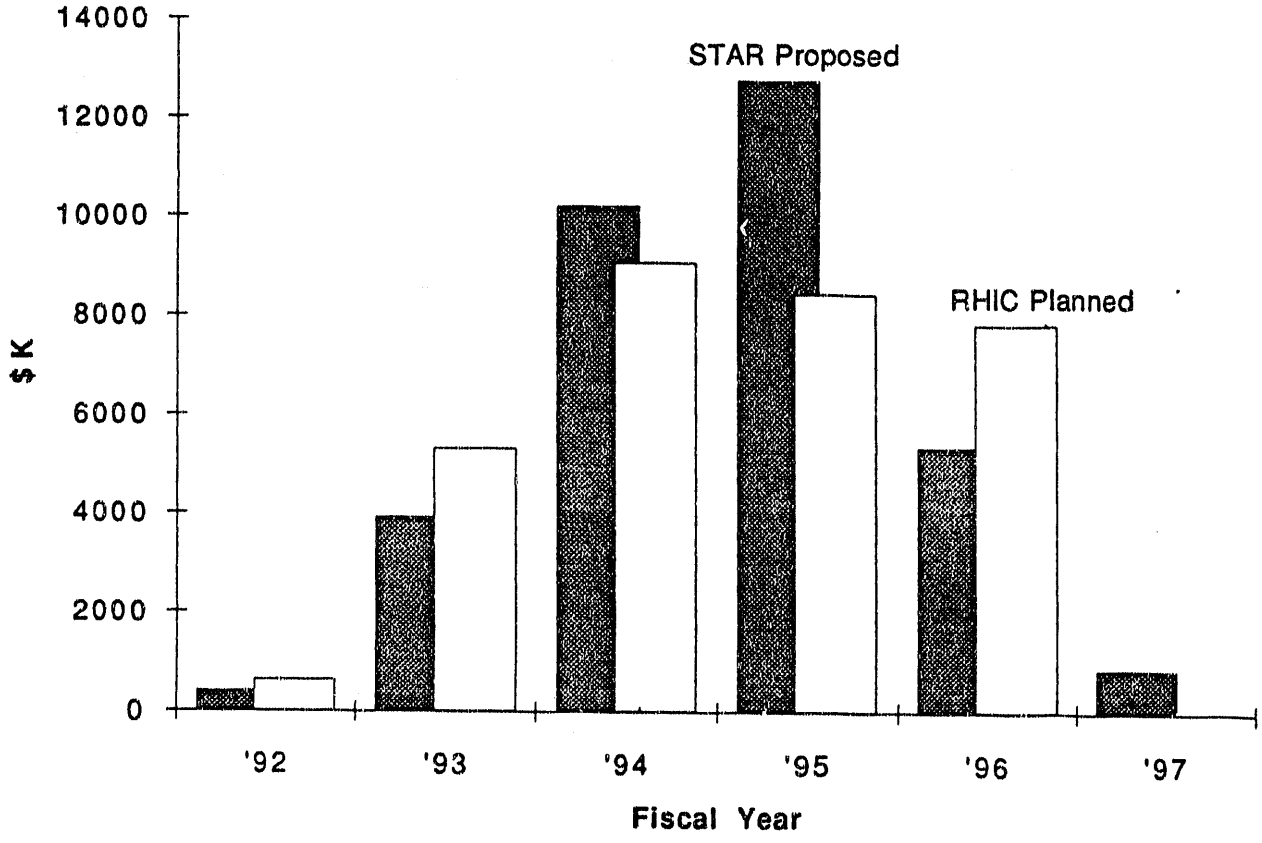

Figure 9-2 RHIC planned and STAR preferred funding profiles by fiscal year.

PRELIMINARY DRAFT Proposed Funding Profile for the STAR Detector						WRE 7/7/92	
		(Assuming August '97 Completion)					
Super Task or Subproject			Fiscal Year ($K)				
	'92	'93	'94	'95	'96	'97	Total:
Proj. Management	50	300	350	350	325	165	1540
Detector Integration	60	450	340	300	250	150	1550
SC Magnet Coil Procurement	20	900	2500	1500	400		5320
Return Yoke Design	15	75	50	10			150
Return Yoke Fabrication			700	485			1185
Supp't Str. & Alignment Sys Dsgn	10	100	100	80			290
Supp't Str. & Alignment Sys Fab			600	150			750
TPC Mech Design	100	525	450	225	100		1400
TPC Mech Fabrication		300	1500	3000	500		5300
TPC Electronics Design	50	200	200	200	100		750
TPC Electr. Fabrication		200	500	1200	400		2300
DAQ Dsgn & Fabrication		150	400	1000	550		2100
Trigger Detector Design		50	90	90	50		280
Trigger Det. Fabrication		60	300	700	280		1340
Controls System Fab.				100			100
Utilities/Safety Systems Design		50	50	60	20		180
Utilities/Safety Systems Fab			100	250	150	50	550
Computing Software Effort		150	200	175	125	50	700
Computing Hardware Procurement		100	150	550	470	0	1270
STAR Detector Installation				600	760	300	1660
Contingency (25%)	100	500	2200	2500	1500	400	7200
	'92	'93	'94	'95	'96	'97	
Total $ by Fiscal Year:	405	4110	10780	13525	5980	1115	35915
Free Resources by Fiscal Year:	0	200	600	800	650	250	2500
Net Funding Req'd by Fiscal Year:	405	3910	10180	12725	5330	865	33415
Total Planned $ by Fiscal Year:	*624*	*5304*	*9048*	*8424*	*7800*	*0*	*31200*
Percent of Project Total:	1.21	11.70	30.47	38.08	15.95	2.59	100
RHIC Planned Profile:	*2*	*17*	*29*	*27*	*25*	*0*	*100*

Table 9-2 The STAR preferred funding profile (all numbers in $K).

STAR

Appendices

Appendix 1: Hit-finding Algorithms in the Simulated TPC

The TPC response was simulated using the event generator FRITIOF for the case of central Au-Au collisions at $\sqrt{s_{nn}}$=200 GeV. Tracking of the particle trajectories was done using GEANT. A detailed study was carried out for one sector of the TPC, including all effects thought to be important; e.g., energy-loss fluctuations, diffusion, wire-crossing angle, dip angle, electronic shaping, amplitude binning. The pad geometry was 8x20 mm^2.

Figures A1-1 and A1-2 are linear plots of the pad response, in a restricted range of time bin (250-300) and pad number (40-80), for an Au-Au central collision, for padrows 20 and 22. Padrow 20 occurs at radius ~90 cm. Examination of these histograms produces the following observations:

1) Even at this small radius, most of the tracks produce hits which are cleanly separated from their neighbors.
2) Using the labels to aid in identifying hits, one notices that tracks which produce hits which are not cleanly separated in one padrow become detached within two padrows.

These observations provide a basis for optimism that, even in densely populated padrows, algorithms can be developed which can either ignore unresolved hits or use the information in neighboring padrows to unravel these compound clusters.

An attempt was made to find space points using the simulated pad response. The results shown in Fig. A1-2 represent pad row 50 (radius ~150 cm), also for the Au-Au central collision. Here the entire pad row is depicted. The rectangles represent peaks found by the candidate hit finder, in this case one adapted from the CERN NA35 TPC analysis program. These early results are encouraging; in particular, the success rate for finding space points at this outer radius is probably sufficiently good so that it can be used in a trigger decision application.

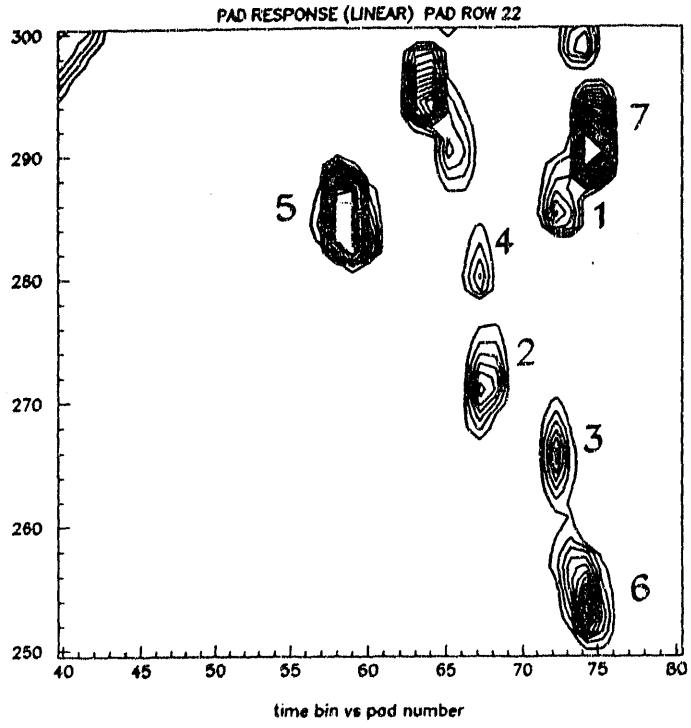

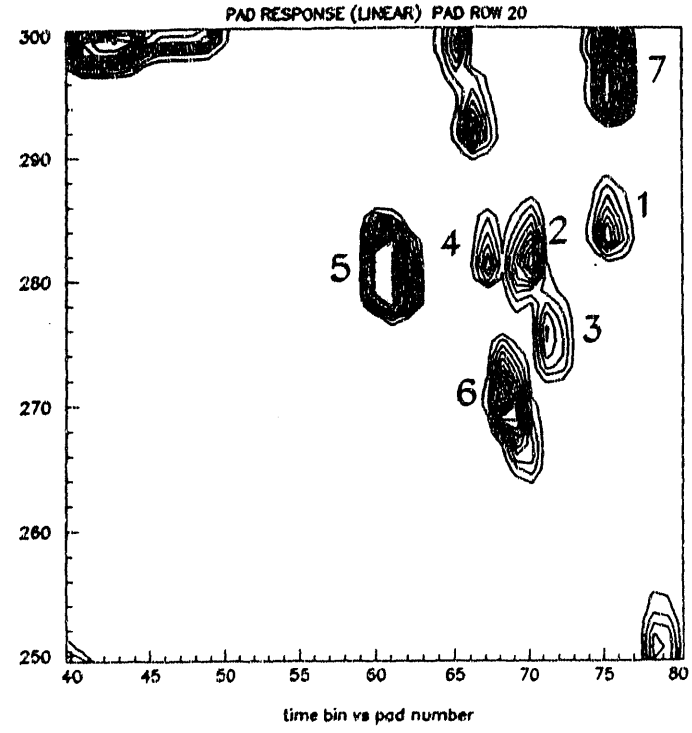

Figure A1-1 Linear plots of pad response for a portion of pad rows 20 and 22 for the case of a simulated Au-Au central collision.

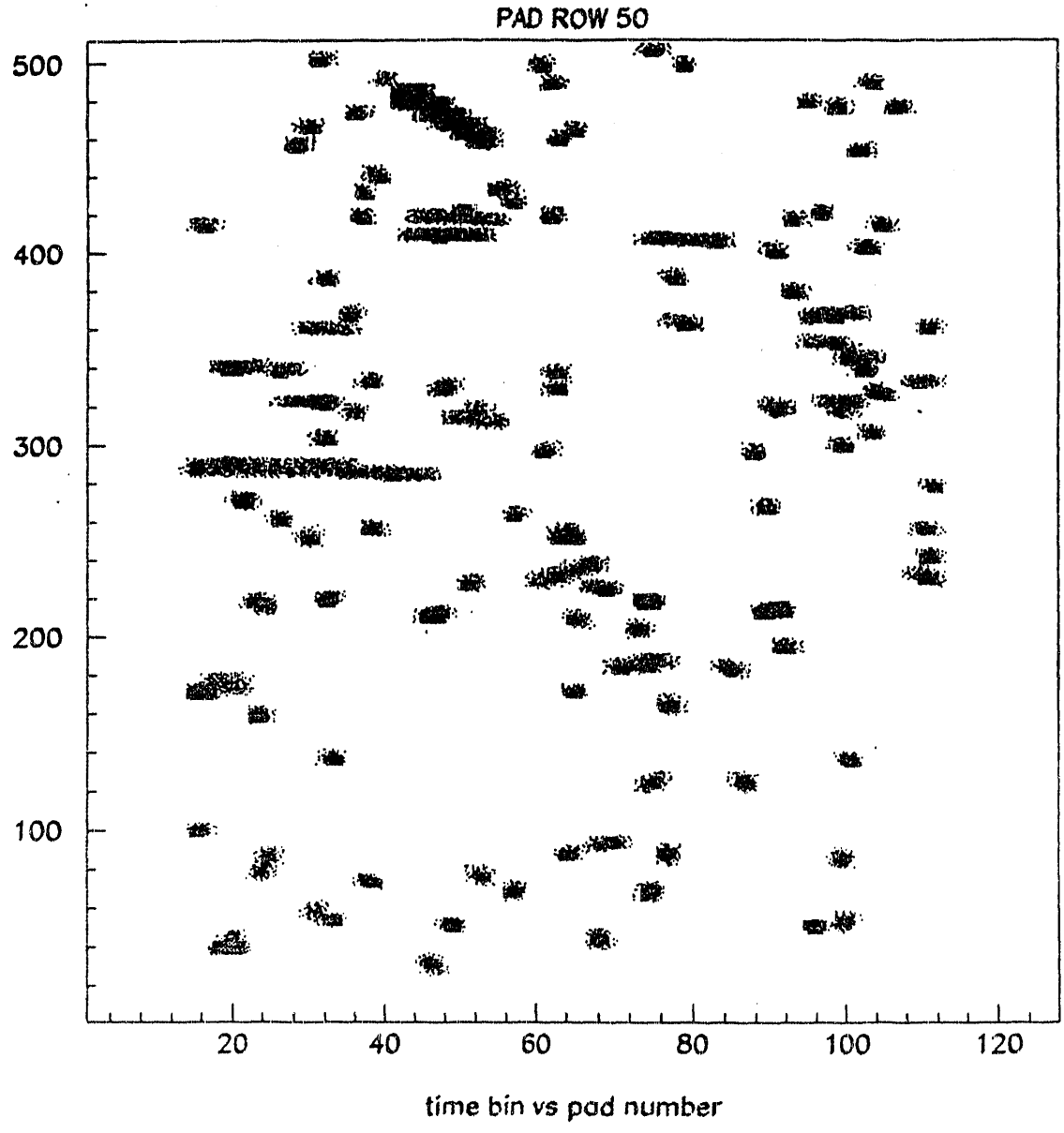

Figure A1-2 Responses on pad row 50 for a simulated Au-Au central event. Hits found by the algorithm described in the text are shown as superimposed rectangles.

Appendix 2: Alternate Technology Choices for the DAQ Architecture

Use of Fibre Channel Gigabit Networks in STAR DAQS

This investigation of appropriate technologies for STAR DAQS has been based on the following principle: the larger the application base for a particular technology, the more robust and cost-effective its implementations will be. Therefore, provided that technology choices meet STAR DAQS performance and cost goals, DAQS design should strive to maximize the use of commercially built and supported components.

Fibre Channel Gigabit Networks

Fibre Channel[1,2,3] is a new bi-directional serial data communications standard available at speeds of 132, 266, 531, and 1063 Mbits per second. In many respects, Fibre Channel can be viewed as logical outgrowth of the HIPPI (High Performance Parallel Interface) standard. Like the HIPPI standard, Fibre Channel provides a high-speed I/O channel between processors and/or peripherals. However, in addition to providing near-HIPPI performance, Fibre Channel also eliminates the reliability and length problems associated with parallel copper interconnects and bulky, expensive cable plants.

Early Fibre Channel connection topologies will be in the form of high performance cross point switches. These switches are based on multi-stage CLOS-switch designs (similar to telephone exchange designs) and can be configured to be completely non-blocking (e.g. all available inputs routable to all available outputs). A key feature of these switches is the ability to provide simultaneous full bandwidth communications channels between all connected input and output ports. Thus a 64 node switch has a bandwidth of 1 to 4 GByte/sec. These individual and aggregate channel rates make this standard a natural choice for exchanging large volumes of data between closely-coupled, high performance computers.

The switching time required to "make-up" or "tear-down" these connections is currently in the 100 μsec range and is expected to approach 10 μsec within several years. Note that the actual making and breaking of these connections is accomplished by the fabric itself as implied by the packet header information supplied by the sender. These fast switching times, combined with the high data transfer rates described above, make Fibre Channel an excellent commercial technology for distributing experimental data from a series of front-end processors to one or more event builder processors. The rapid connect times make it possible to "scale up" the available event builder processor bandwidth by the connection of additional processors to the Fibre Channel switch. The only architectural restriction on these additional processors is the amount of space

---

[1] "Effects of Various Event Building Techniques on Data Acquisition System Architectures", Ed Barsotti, Alexander Booth and Mark Bowden. In proceedings of CHEP 90, Santa Fe, April 90.
[2] "High-Performance Switching with Fibre Channel", Terry M. Anderson and Robert S. Cornelius. In proceedings of IEEE Spring CompCon 92, San Francisco, Feb. 92.
[3] "Distributed Computing with Fibre Channel Fabric", Kumar Malavalli and Bent Stovhase. In proceedings of IEEE Spring CompCon 92, San Francisco, Feb. 92.

required. Thus, event building capacity can be added as experiment requirements dictate by the addition of the latest, most cost-effective computing technology available.

Fibre Channel Performance

As with HIPPI, Fibre Channel design has been driven by the requirements of a very high speed I/O channel. The Fibre Channel protocol is based on variable length packets of up to 2148 bytes with a data payload of up to 2112 bytes. As this is a dedicated medium standard, packets can be sent almost back-to-back (6 intervening byte times required) to obtain data throughput rates very close to the medium's actual bit rate.

The protocol provides effective flow control based on the exchange of buffer availability information at the interface level and transmission sequences are only begun when sufficient receiver buffer memory is guaranteed to be available. Moreover, the requirements of such high data transfer rates has led to the inclusion of smart "scatter/gather" memory controllers in current Fibre Channel interface designs. The resulting designs are able to perform fully flow-controlled high speed data transfers from sender task memory directly to receiver task memory with no intervening data copy operations--exactly the kind of high performance data transfer design required for STAR DAQS.

DAQS Design

The Fig. A2-1 shows one possible implementation of a Fibre Channel-based DAQS. In this design, compressed data is sent from TPC readout boards over non-Fibre Channel optical links to a small set of sub-event builder systems. These sub-event builders would contain a readout board interface, a Fibre Channel interface, and sufficient buffer memory to contain the appropriate portion of a complete event. Within these sub-event builder systems, the readout board interfaces would receive event data from a number of readout boards and collect it into a single buffer memory (i.e. a sub-event). This sub-event would then be sent over the Fibre Channel interface to an event builder that had been selected to collect the entire event. The actual transfer from sub-event builder to event builder could be "pushed" (i.e. written) by the sub-event builder systems or "pulled" (i.e. read) by the particular event builder constructing a particular event. Several programming mechanisms could serve to insure the "pushing" or "pulling" of appropriate sub-event pieces during the event construction process. For event rejection purposes, readout boards containing TPC trigger information can be routed to a single sub-event builder, and that portion of the event can be sent to a dedicated trigger processor in addition to being sent to the event builder. Queues of accepted event id's can then be distributed to all event builders so that appropriate sub-events can be discarded or kept for complete event building and logging.

If Fibre Channel component costs fall quickly enough, it may be feasible to embed Fibre Channel interfaces in the chamber-mounted electronics. In this case, by collecting together data from a number of readout boards, data would flow off the chamber via Fibre Channel directly into a Fibre Channel switch ("fabric") and then to a number of commercial, high-performance compute servers that will function as event

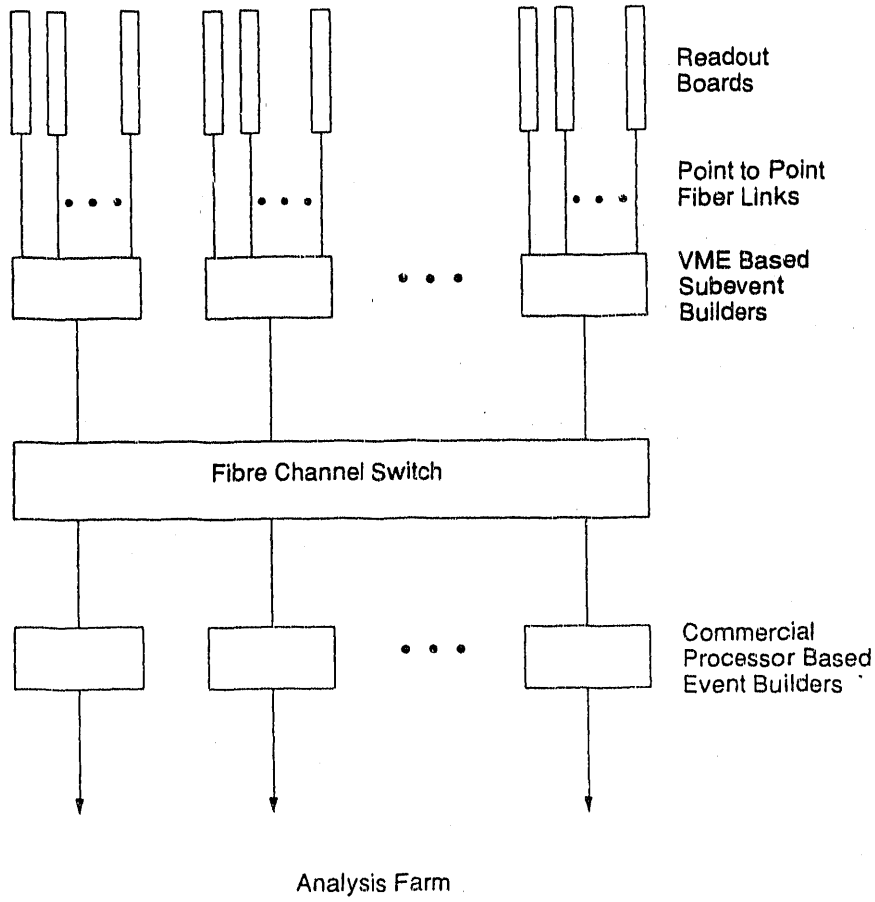

Figure A2-1 STAR Fiber Channel event builder.

builders. Once assembled, events will flow over the same fabric to workstations for further on-line analysis and to storage devices either attached directly to the fabric or attached to standard interfaces on other fabric nodes (see Fig. A2-2). Such a design would probably require a switch with a greater number of cross connects and design decisions would be based on implementation costs.

A Fibre Channel Testbed

Since the key architectural use of Fibre Channel in a high performance DAQ system is that of data transport to and from the event builder, our initial efforts will center on the design of a Fibre Channel event builder. We will begin by investigating the performance and reliability of a simple two front-end, one event builder system utilizing a 16 port Fibre Channel communications switch provided by Ancor Communications (see Fig. A2-3). Test front-ends will be VME-based systems with commercially built VME/Fibre Channel communications interfaces. This testbed will allow us to evaluate various techniques for buffering front-end data and performing event building during front-end readout. As we view the ability of scaling up event builder processor bandwidth as critical to the DAQS architecture design, we will follow these initial tests with an implementation of a multi-processor event builder system.

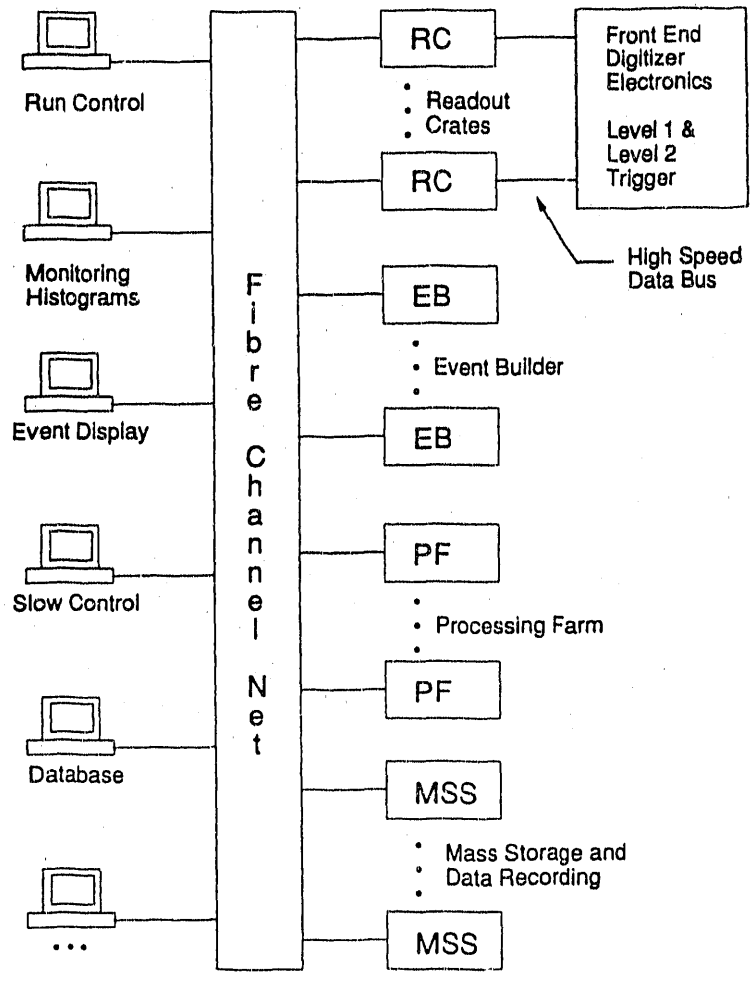

Figure A2-2 Fibre Channel based DAQ.

Since we believe that the STAR data acquisition system will benefit from the use of commercial computer standards and products, it is critical to have real "hands-on" experience prior to making technology choices.

DAQS Costs

Design of a Fibre Channel-based DAQS will be heavily driven by the degree of Fibre Channel's commercial acceptance. It appears that there will be strong initial interest in the 266 Mbit version of the standard. This will be based on the wide range of applications that will benefit from 25 Mbyte transfer rates (disk farms, imaging applications, etc.) and the relatively low cost of the 266 Mbit optical components. Further study will determine whether this version of Fibre Channel proves fast enough for most (or all) STAR data transport needs.

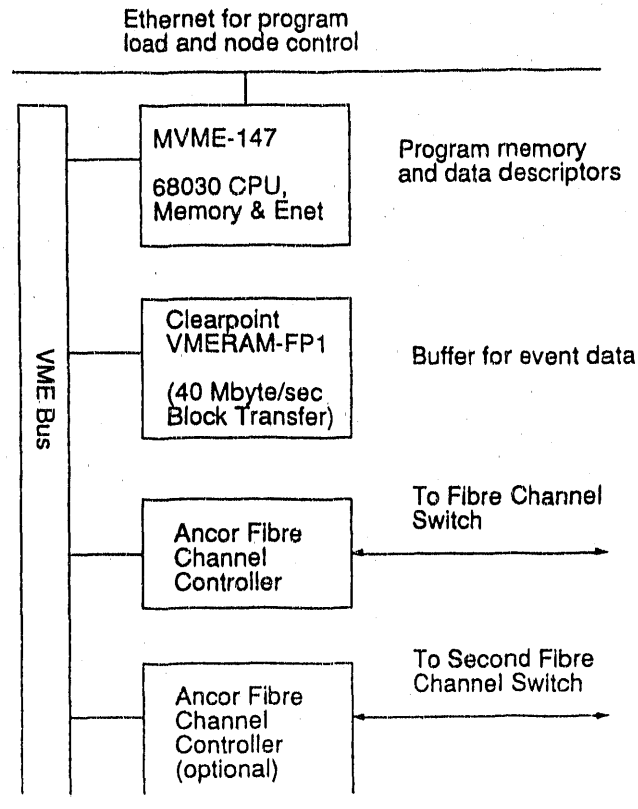

Figure A2-3 Test bed node.

Using current prices, Fibre Channel switch port connections are priced at about $1.5K per port. Approximately $1.1K of this cost is in the Fibre Channel controller interface with the remaining $400 for 266 Mbit optics parts. 1Gbit optics are currently priced at about $1K but reductions can be expected. Chamber-mounted embedded interfaces will be of the same order in cost.

Appendix 3 - SVT: Transport Code in Silicon

Simulations of Si Drift Detector Response

In order to optimize the design of the SVT and to interpret the results of laboratory tests it is necessary to have a software package which reproduces the expected response of the SDD. The development of this software will proceed in three steps. First, the current on the anodes of the SDD due to the passage of charged particles will be calculated using a simple simulation of electron transport in the detector. This simulation will include the detailed field due to the applied voltage, the field due to the charges themselves, the magnetic field of the solenoid, Landau fluctuations in the created charge, diffusion, and the anode geometry. Next, the anode current will be parameterized in terms of the position, angle, energy, and charge of the incident particle. Finally, this parameterization will be put through a software representation of the SDD electronics. The first step of the process is nearly complete, and will be outlined in this section.

The evolution of the electron cloud with time can be found by converting the continuity equation into a difference equation and using it to propagate the electron density on a 3 dimensional grid. We have rejected this approach due to the prohibitively large arrays needed to represent a SDD chip, and because the solution of the second order non-linear difference equation is unstable. Instead, we individually track the motions of the electrons, separating the drift due to the electric field and the diffusion into separate steps.

The electron cloud ρ produced by an ionizing particle in silicon evolves according to the following equations:

$$\frac{\partial \rho}{\partial t} = -\vec{\nabla} \cdot \vec{J}$$

$$\vec{J} = \vec{J}_{\text{drift}} + \vec{J}_{\text{diffusion}}$$

$$\vec{J}_{\text{drift}} = \vec{v}\rho = \mu \vec{E} \rho$$

$$\vec{J}_{\text{diffusion}} = D \vec{\nabla} \rho$$

Instead of following the evolution of ρ with time, we follow the trajectories of the individual electrons. The drift equation for an electron at r is simple:

$$\frac{d\,\vec{r}}{d\,t} = \mu \vec{E}$$

Therefore we only need to solve ***first order ordinary*** differential equations. The effects of diffusion over each time step can be added on at the end of each step using Monte Carlo techniques.

A sample simulation is shown in Fig. A3-1 for a 6 μm/ns drift velocity. The electron cloud is rapidly compressed into the central plane of the detector and transported towards the anodes on the right (not shown).

The expansion of the electron cloud due to its own Coulomb field can be added by applying Coulomb's law for the E field due to a point charge. For each electron, we can calculate the E field looping over all the other charges, and combine the result with the applied field before stepping to the next point. Unfortunately, this very CPU intensive operation goes as the square of the number of electrons. It is not feasible to carry out this calculation on the 25k electrons expected due to a minimum ionizing particle. However, instead of looping over all of the electrons, we can loop over a representative sample and increase the elementary charge to compensate for the smaller sample size. We have found that 100 sample electrons can be used to accurately represent the field.

Figure A3-2 shows the rms radius in the SDD plane for an initial track of 25,000 electrons as a function of time. The track was assumed to have normal incidence, and to produce a cylinder of electrons 1 μm in radius. The curve is the analytic result due to diffusion only, and closely matches the diffusion only simulation.

We have studied the influence of the angle of incidence on the width of the electron cloud. Tracks whose angle with respect to normal incidence exceeds 40° have significantly extended widths. Thus, it may be possible to actually recover the angle of incidence for some tracks using the deviation of its width from that expected due to normal incidence.

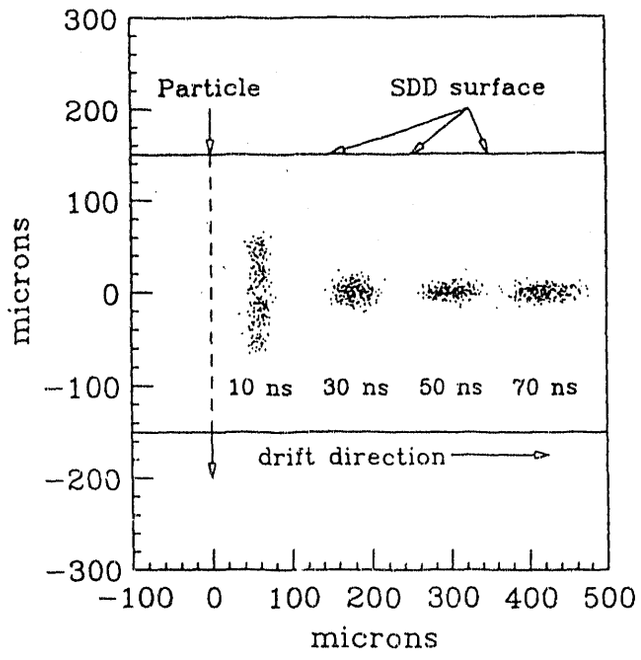

Figure A3-1 Sample SDD simulation for 6 μm/ns drift.

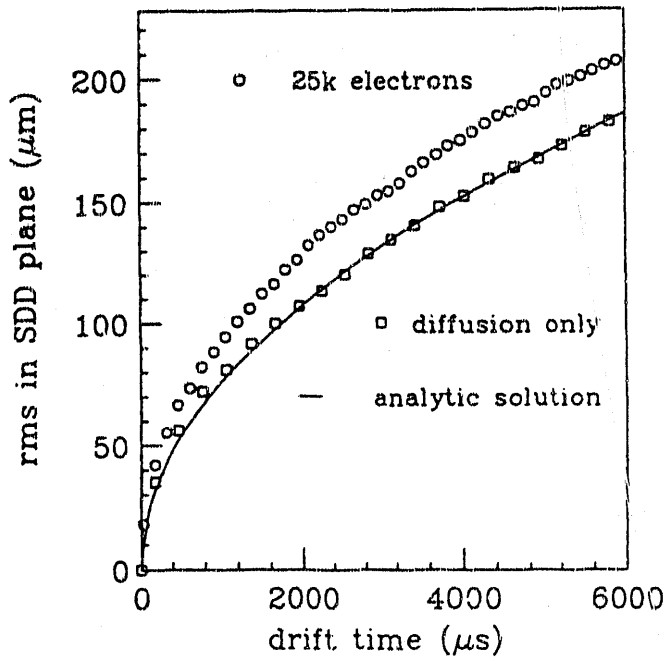

Figure A3-2 RMS radius for initial track of 25,000 electrons as a function of time.

The SDD will be placed in a 0.5 T field. The field will be parallel to the drift direction, causing the electrons to be deflected by the Lorentz angle only when they move perpendicular to the beam axis. Such movement occurs during the earliest stages of the drift, as can be seen in Figure A3-1. The effect on the final electron distribution collected at the anodes would be a slight broadening of the distribution. Our simulation shows the effect on the width of the distribution after 1 μs to be much less than the broadening due to diffusion. Non-perpendicular tracks are a much more significant source of broadening. The effects of Landau fluctuations along the ionization trail will be added before conclusions are drawn from the simulations.

The next step is to use the simulations to parameterize the current induced on the anode pads due to tracks at different distances from the pad rows and different angles of incidence. These calculations will provide a detailed understanding of the position resolution of the SDD chips. Thus we will be able to set the sampling frequency, drift voltage, and chip overlap (if any) to meet the resolution dictated by the STAR physics objectives.

Appendix 4

Table 4-1 Table of Materials at $\eta = 0$ in STAR.

Structure	Material	Length (cm)	Density (g/cm^3)	L_r (g/cm^2)	$L*\rho$ (g/cm2)	$L*\rho/L_r$ (%)
Beam pipe	Be	0.025	1.850	65.200	0.047	0.07
SVT	Silicon	0.090	2.330	21.820	0.210	0.96
SVT tube	Graphite	0.14	1.68	42.00	0.235	0.56
	epoxy					
Total SVT						1.52
Insulating gas	N2	30.000	0.001	37.99	0.038	0.10
TPC IFC	Aluminum	0.009	2.70	24.01	0.024	0.10
	Kapton	0.015	1.42	40.30	0.021	0.05
	Kevlar	0.061	1.44	41.30	0.088	0.21
	Nomex	0.635	0.05	40.00	0.030	0.08
	Adhesive	0.010	1.20	40.00	0.012	0.03
Total IFC						0.57
TPC Gas	P10	150.00	0.00178	19.55	0.267	1.37
TPC OFC	Copper	0.007	8.91	12.90	0.062	0.48
	Kapton	0.008	1.42	40.30	0.011	0.03
	Mylar	0.315	1.39	39.95	0.438	1.10
	Aluminum	0.4	2.59	24.01	1.036	4.31
	Honeycomb	4.8	0.037	24.01	0.178	0.74
	Adhesive	0.1143	1.20	40.00	0.137	0.34
Total TPC						8.37
Solenoid	Aluminum	6.3	2.59	24.01	16.317	67.96
Total						78.49

END

DATE FILMED

11/23/92